Gerhard A. Holzapfel · Ellen Kuhl *Editors*

Computer Models in Biomechanics

From Nano to Macro

Springer

Computer Models in Biomechanics

Gerhard A. Holzapfel • Ellen Kuhl
Editors

Computer Models in Biomechanics

From Nano to Macro

Springer

Editors
Gerhard A. Holzapfel
Institute of Biomechanics
Center of Biomedical Engineering
Graz University of Technology
Graz, Austria
url: http://www.biomech.tugraz.at
and
Chair of Biomechanics
Royal Institute of Technology (KTH)
Department of Solid Mechanics
School of Engineering Sciences
Stockholm, Sweden

Ellen Kuhl
Department of Mechanical Engineering
Department of Bioengineering (courtesy)
Department of Cardiothoracic Surgery
(courtesy)
Stanford University
Stanford, CA, USA
url:
http://biomechanics.stanford.edu/Main_Page

ISBN 978-94-007-5463-8 ISBN 978-94-007-5464-5 (eBook)
DOI 10.1007/978-94-007-5464-5
Springer Dordrecht Heidelberg New York London

Library of Congress Control Number: 2012950597

Printed on acid-free paper

Springer is part of Springer Science+Business Media (www.springer.com)

Preface

This book contains a collection of papers that were presented at the IUTAM Symposium on *Computer Models in Biomechanics: From Nano to Macro*, which was held at Stanford University, California, USA, from August 29 to September 2, 2011. The setting of Stanford University in Palo Alto and the San Francisco Bay Area of California is a rich melting-pot of culture, and an area with probably the highest density of stimulating experts and pioneers in the world, hence it is a magical place which has a lot to offer and which was very appropriate for the symposium. For example, in the 120 years since its founding, Stanford University has been home to 26 Nobel Laureates, 16 of whom are still alive. Palo Alto is also home to a number of high-tech Silicon Valley companies including Hewlett-Packard, founded by two Stanford graduates in a one-car garage in Palo Alto, and the biggest social-networking site, Facebook.

The IUTAM Symposium brought together 68 participants from universities, research centers and clinics in 14 countries. There were 35 invited oral presentations, including 5 keynote lectures to open the morning sessions throughout the week, and 33 young researchers to give poster presentations on the second afternoon of the meeting. The keynote lectures were given by P. Fratzl (Max Planck Institute, Potsdam, Germany), P. Hunter (University of Auckland, New Zealand), L. Taber (Washington University, St. Louis, USA), and A. Yoganathan (Georgia Institute of Technology, USA), while K. Parker (Harvard University, USA) could not come to give his keynote lecture due to the Hurricane Irene.

The computational modeling of biomechanics and mechanobiology is one of the most exciting multidisciplinary areas of this century. It is a rapidly expanding research area which involves researchers in engineering, physics, biology, medicine, applied mathematics and mechanics. Biomechanical modeling and computational simulations in biology hold promise to provide new insight into the complex multiscale and multiphysics phenomena of living tissue: the quantitative analysis of biomechanical processes on the molecular, cellular, tissue, and organ levels might enable reliable predictions of the progression of various types of disease. This may allow us to perform real-time, patient-specific simulations and to guide the design of optimal treatment strategies. The IUTAM Symposium aimed to bring together

young researchers and the world's leading experts working in the field, to provide a forum for discussion and to stimulate the study of challenging new topics in computational biomechanics.

One important aim was to provide computer algorithms, and the skill for implementations of biomechanical models in numerical codes; and this is essential because of the complexity of the materials and the geometries encountered in applications. Efficient computer models at the molecular, cellular, tissue and organ levels are key to better understand inter-relations between coupled processes such as growth, remodeling, and repair, and how mechanical information is processed and programmed by the cells (mechanobiology). Efficient computer models are one of the prerequisites for effective design and development of soft and hard tissue prostheses. Thematically, the IUTAM Symposium revealed a number of exciting new trends; several new aspects have been discussed in detail, which distinguish living biological materials from standard engineering materials such as adaptive responses (growth, remodeling) and active responses (force generation due to muscle contraction).

This volume includes topics on:

- *Protein and Cell Mechanics*

  One of the most promising trends to accurately characterize biomechanical phenomena is to explore their responses on the cellular level and to generate related computer models. Observations on the microscopic scale provide additional information, and, ideally, these observations feed back to macroscopic models that help to explain the biomechanical response of the overall tissue or organ. In the present volume this area is covered by the suggestion of a coarse-grained model for unfolded proteins, a collagen-proteoglycan model to capture the structural interaction in the human cornea, and a model to predict the values of forces generated by cells adhered on flat gels and on beds of micro-posts of variegated stiffness.
- *Muscle Mechanics*

  Computational models for smooth, cardiac and skeletal muscles are presented. In particular, a mathematical approach for studying Ca^{2+}-regulated smooth muscle contraction is reviewed and the chemomechanical model is implemented into a finite element (FE) program; 3D boundary-value problems are solved and the model is validated by experiments on porcine smooth muscle tissue strips. Finally, in regard to smooth muscle contraction, a homogeneous model is illustrated by using a continuum thermodynamical framework. An actomyosin model is studied to capture the mechanical contraction and energy consumption by the cardiomyocytes. Finally, two skeletal muscle models are presented; one is on the basis of electromechanics and the other combines principles of multi-body dynamics with continuum mechanics and the FE method to achieve a 3D forward-dynamics model of the musculoskeletal system.
- *Cardiovascular Mechanics*

  This topic is of major interest and is the most extensive area covered in this volume. It includes a review of continuum level models of arterial adaptations, their validations, and suggests an approach to incorporate molecular level information

within such models. The next chapter presents an experimental and computational framework to define and predict damage due to mechanical loading with an application to arterial clamping. Two chapters are devoted to aneurysms, in particular to the evaluation of dissection properties of human ascending thoracic aortas and to a computational methodology to remove an intracranial aneurysm and reconstruct the geometry of the healthy artery; a fluid-solid-growth framework for modeling aneurysm evolution is also outlined and its application to clinical cases illustrated. Two chapters focus on the mathematical modeling and computation of electromechanical mechanisms in the heart by considering the anisotropy of myocardial tissue. A computational fluid-solid-interaction model investigates possible effects on the hemodynamics within thoracic aorta and coronary, carotid and cerebral arteries due to a distal aortic coarctation. The last chapter within this topic shows the importance of combining medical imaging, computer graphics and computational fluid simulations to better guide surgical interventions such as the Fontan procedure.

- *Multiphasic Models*

  The next key topic deals with computational models required to analyze biological mixtures consisting of a porous (neutral and charged) deformable solid matrix and interstitial solvent and solutes. It starts by describing some features of the open source finite element program FEBio and continues with the presentation of an alternative approach to mixture theory-based poroelasticity in order to establish a basis for the development of constitutive equations for growth of tissues. A multiphasic modeling approach is used to analyze brain tissues considered as an elastic solid skeleton which is perfused by two liquids, the blood and the interstitial fluid. Special attention is focused on tumor therapies carried out by convection-enhanced delivery processes; 2D and 3D examples are discussed. A 3D computational model for remodeling of microperfusion is also presented. The biphasic model is based on the theory of porous media; application is shown by covering microcirculation in liver lobes. Next, the effectiveness of mechanotransport coupling in simulating biological growth, in particular tumor growth dynamics, is demonstrated. Thereby, the effectiveness of tools such as adaptive mesh refinement and automatic differentiation is also demonstrated. Finally, crack growth in a swelling porous medium such as the intervertebral disc is numerically analyzed and two options are discussed to account for the sharp pressure gradient around the crack.
- *Morphogenesis, Biological Tissues and Organs*

  Another challenging and trend-setting topic is the computational biomechanics of morphogenesis and development of various morphogenetic processes. Here, recent advances of the physical mechanisms of morphogenesis during brain development, in particular the formation of the primary brain vesicles and folding of the cerebral cortex, is discussed. Finally, mechanical characterization and predictive computer models of native and engineered anterior cruciate ligaments (ACLs), human liver, bone and lung are presented. In particular, a micromechanical constitutive model is reviewed to capture the inhomogeneous, nonlinear viscoelastic properties of native ACLs and of tissue engineered ligament grafts

upon explantation. Characterization of the *in vivo* mechanical behavior of human liver is conducted during open surgery using an aspiration device, and related histopathology is identified with biopsies taken at the measurement locations. Next, an *in vivo* validation framework for tissue level models such as bone remodeling and mechanobiology, based on true geometries, is analyzed. Finally, different types of overall lung models are reviewed concluding with an approach that couples 3D and lumped airway models.

The IUTAM Symposium provided scientific impetus, a good basis for generating new ideas for future research directions and some cultural impressions. It has also provided a unique forum to discuss mathematical equations that characterize (sub)cellular responses, specific biological tissues and computational tools that can be used to simulate their complex spatial and temporal responses. It created exciting new synergies and initiated new collaborations across disciplines and between young researchers and the world's leading experts in molecular, cellular, tissue, and organ biomechanics to shape pathways for the future multiscale and multiphysics modeling of biomechanical phenomena.

The organizers would like to thank the members of the Scientific Committee for their help in making the IUTAM Symposium such a success. They are J. Engelbrecht (Tallinn, Estonia), K. Garikipati (Ann Arbor, USA), P. Hunter (Auckland, New Zealand), A. Quarteroni (Lausanne, Switzerland), and Y. Ventikos (Oxford, UK). This volume has been made possible by the considerable efforts of all the authors; we are very grateful for their contributions. Special thanks also go to Jianhua Tong from the Institute of Biomechanics, Graz University of Technology, for his help in editing this volume using the document preparation system LaTeX. Financial support for the Symposium, in particular for the young researchers, was generously provided by IUTAM, Springer, and the National Science Foundation. Finally, we would like to thank Nathalie Jacobs, Senior Publishing Editor (Engineering) of Springer, for her encouragement to publish this volume.

Graz, Austria/Stockholm, Sweden — Gerhard A. Holzapfel
Stanford, USA — Ellen Kuhl
June, 2012

Contents

Part I
Protein and Cell Mechanics

Chapter 1
Towards a Coarse-Grained Model for Unfolded Proteins

Ali Ghavami, Erik Van der Giessen, and Patrick R. Onck

Abstract It is widely accepted that many biological systems benefit from the specific and unique properties of unfolded proteins. In order to study the conformational dynamics of these proteins, we propose an implicit solvent one-bead per amino-acid coarse-grained (CG) model. For the local backbone interactions, experimentally-obtained Ramachandran plots for the coil regions of proteins are converted into distributions of pseudo-bond and pseudo-dihedral angles between neighboring alpha-carbons in the CG chain. The obtained density plots are then used to derive bending and torsion potentials, which are residue- and sequence-specific. Our results show that the local interactions can be captured by specifically accounting for the presence of Proline and Glycine in the amino-acid sequence. An upper and lower bound is suggested for the radius of gyration of denatured proteins based on their specific sequence composition.

1.1 Introduction

In spite of the well-established relation between the biological function of proteins and their specific folded structure, the important role of unfolded proteins in many vital biological processes can not be ignored (Fink, 2005; Tompa, 2009). Rapid increase of our knowledge on the structure of proteins has revealed that many proteins and protein domains are intrinsically unstructured. The absence of a stable secondary structure in their polypeptide chain is the main reason behind the basic functions of unfolded proteins, which can be classified into four functional groups, namely molecular recognition, molecular assembly, protein modification and entropic chain activities (Dunker et al., 2002; Radivojac et al., 2007; Tompa, 2009).

Atomic-level molecular dynamics simulations provide detailed insight of the interactions and dynamics present in protein structures. However, because of the limitations in computational resources it is still not possible to reach biologically-interesting time and length scales. Unfolded proteins are even more dynamic and

A. Ghavami · E. Van der Giessen · P.R. Onck (✉)
Zernike Institute for Advanced Materials, University of Groningen, Groningen, The Netherlands
e-mail: p.r.onck@rug.nl

G.A. Holzapfel, E. Kuhl (eds.), *Computer Models in Biomechanics*,
DOI 10.1007/978-94-007-5464-5_1,

therefore even longer simulations are required in order to obtain statistically-meaningful results. The necessity to achieve biologically interesting time and length scales, have drawn the interest of researchers towards the development of coarse-grained (CG) models.

There is a limited set of available CG models that account for the disordered state of proteins. Simple models such as the elastic network and Go-models (Tirion, 1996) have been developed but their force fields are completely biased to a unique reference structure. In the more complex CG models like the MARTINI model (Monticelli et al., 2008), the Head-Gordon model (Yap et al., 2007) and the model developed by Korkut and Hendrickson (2009), a priori knowledge of the local secondary structure of the protein is required to perform the simulations. The CG models with more predictive power (Tozzini et al., 2006, 2007; Bereau and Deserno, 2009) are parametrized using databases of folded protein structures and therefore cannot be expected to reproduce the correct conformational dynamics of unfolded proteins.

In the present work, a one bead per amino-acid, implicit solvent model for unfolded proteins is proposed. Local interaction potentials are obtained by converting experimentally-obtained Ramachandran plots for the coil regions of proteins into distributions of pseudo-bond and pseudo-dihedral angles between neighboring α-carbons in the CG chain. These distributions are used to derive bending and torsion potentials, which are residue- and sequence-specific. As an example, the model is used to study the ensemble average gyration radius of denatured proteins as a function of the amino acid sequence.

1.2 Extraction Method to Obtain Coarse-Grained Potentials

In the following sections, the general methodology for extracting the CG potential functions from the Ramachandran data of coiled regions of proteins is summarized; more details can be found in (Ghavami et al., 2012).

1.2.1 Mapping Backbone Internal Degrees of Freedom (ϕ, ψ) to Pseudo Bending and Torsion Angles (θ, α)

A geometrical representation of the coarse-grained polypeptide chain together with the CG degrees of freedom are shown in Fig. 1.1. In the all-atom representation of the backbone (Fig. 1.1(a)), the bond lengths and bond angles display only a small variation from their average value so they are assumed to remain fixed in the present work (Finkelstein and Ptitsyn, 2002). The average bond lengths of C_α–N, C_α–C and C–N are 0.145 nm, 0.152 nm, 0.133 nm, respectively, with the average bond angles C_α–C–N $= 116°$, C–N–$C_\alpha = 122°$ and N–C_α–C $= \tau = 111°$. A Trans-conformation is presumed for the peptide bond ($\omega = 180°$) and the rare possibility of Cis-conformation is neglected. With the stated assumptions, it could be implied

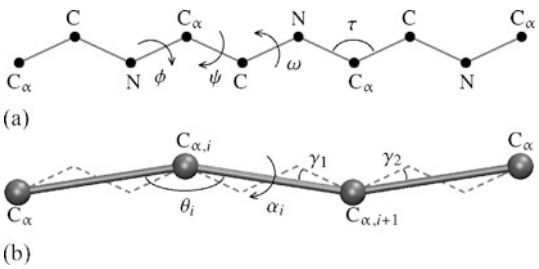

Fig. 1.1 All atom schematic of a polypeptide chain (**a**) and coarse-grained representation (**b**) of the backbone with pseudo-bending and torsion angles. Side chains are not shown in (**a**). In (**b**) the *dashed lines* represent the polypeptide chain and the bond angle θ and dihedral angle α represent the pseudo-bonds in the coarse-grained geometry

that ϕ and ψ dihedral angles are the only degrees of freedom of the all-atom backbone.

Figure 1.1(b) demonstrates the CG chain by connecting the α-carbons through pseudo-bonds. Since the all-atom bond lengths, bond angles and dihedral angle ω are not supposed to change, the pseudo-bond lengths between subsequent C_α's remain fixed at a distance of 0.38 nm. Also, the pseudo-bending angle θ and pseudo-dihedral angles α for the CG chain are defined between three and four consecutive C_α's, respectively. A geometrical expression can be established for the relationship between the CG (θ, α) and all-atom (ϕ, ψ) degrees of freedom as suggested by (Levitt, 1976; Tozzini et al., 2006). The pseudo-bending angle for the coarse-grained chain is given by

$$\begin{aligned}\cos\theta_i = &\cos\tau(\cos\gamma_1\cos\gamma_2 - \sin\gamma_1\sin\gamma_2\cos\phi_i\cos\psi_i)\\ &+ \sin\tau(\cos\psi_i\sin\gamma_1\cos\gamma_2 + \cos\phi_i\cos\gamma_1\sin\gamma_2)\\ &+ \sin\gamma_1\sin\gamma_2\sin\phi_i\sin\psi_i,\end{aligned} \tag{1.1}$$

where $\gamma_1 = 20.7°$, and $\gamma_2 = 14.7°$ are constant angles (see Fig. 1.1(b)). The exact formula for the pseudo-torsion angle is very complex, but the following approximate formula has been suggested by Tozzini et al. (2006):

$$\alpha_i = 180 + \phi_i + \psi_{i+1} + \gamma_1\sin\psi_{i+1} + \gamma_2\sin\phi_i. \tag{1.2}$$

It can be inferred from these equations that the pseudo-bending angle θ_i depends only on one set of backbone dihedral angles (ϕ_i, ψ_i), but the pseudo-torsion angle α_i is a function of two consecutive sets of backbone dihedral angles $(\phi_i, \psi_i, \phi_{i+1}, \psi_{i+1})$. It is worth noting that, in the force-fields developed specifically for well-defined secondary structures, the simplifying assumptions $(\phi_i = \phi_{i+1}, \psi_i = \psi_{i+1})$ are made for mapping α (Levitt, 1976; Tozzini et al., 2006). However, this assumption does not hold for proteins without any regular structure.

1.2.2 Coil Library

The ϕ and ψ dihedral angles of the backbone of protein structures are often presented in two-dimensional density plots, called Ramachandran plots. The Ramachandran space $[-180°, 180°) \rightarrow [-180°, 180°)$ is divided into several regions, each one referring to a specific secondary structure. The empty regions refer to the disfavored conformations which are mainly caused by the steric clash between neighboring side chains or steric hindrance to the formation of hydrogen bonds between peptide groups and water molecules (Avbelj et al., 2006). Here, these density plots are used to generate the mean force potentials for local interactions in the unfolded state. For this purpose, we adopt the Boltzmann inversion method

$$\mathrm{U}(q) = -k_{\mathrm{B}} T \ln\big[\mathrm{P}(q)\big], \tag{1.3}$$

where q is any desired degree of freedom, $\mathrm{P}(q)$ is the probability distribution for q, T is the temperature and k_{B} is the Boltzmann constant.

In order to obtain meaningful potentials for unfolded proteins, appropriate Ramachandran data must be extracted from the protein data bank. The required density plots should not be biased towards any secondary structure, while long-range effects (hydrophobic or electrostatic interactions) must be absent or have a negligible impact on the density plots. The data that satisfy these conditions best are for the coil regions of proteins. The coil regions are those parts of proteins that cannot be classified in any kind of known secondary structure. This implies that their backbone conformations are not biased to any regular structure. Also it has been shown that the intrinsic backbone preferences of di-peptides are strikingly similar to the backbone conformations of coil regions of proteins (Avbelj et al., 2006), confirming the assumption that long range hydrophobic or electrostatic interactions are negligible for this class of residues.

The DASSD library is used to extract Ramachandran plots of the coiled regions of proteins (Dayalan et al., 2006). This database contains dihedral angles of central residues of short amino-acid fragments (of length 1, 3 and 5), which gives the possibility to extract meaningful potentials by considering the effect of neighboring residues on the obtained potentials. The database is extracted from 5,227 non-redundant high resolution (less than 2 Å) protein structures and a secondary structure assignment is carried out using the STRIDE algorithm (Frishman and Argos, 1995).

1.2.3 Three-Letter Amino Acid Model

The current size of the coil library is not large enough to extract CG bending and torsion potentials for all 20 amino-acids accounting for all possible neighbors. Since the Ramachandran plots are the main input for the extraction of the CG potentials, they provide the best reference to compare different amino-acids and to categorize them into several sub-groups based on the similarities in their Ramachandran data.

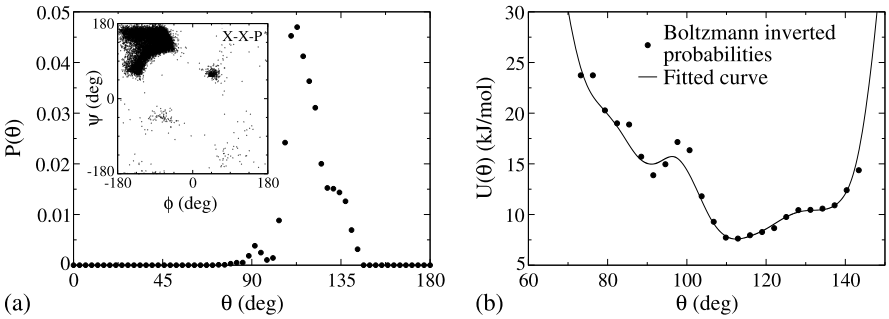

Fig. 1.2 Extraction procedure for the bending potential of X–X–P combinations. (**a**) Normalized distribution of the bending angle θ, which is obtained by mapping all the Ramachandran data (*inset*) to the pseudo-bending angle θ through Eq. (1.1). *Inset*: Ramachandran data for the central residue of X–X–P combinations extracted form the coil library. (**b**) Obtained bending potential, $U(\theta)$ after applying the Boltzmann-inversion method on the probability distribution $P(\theta)$ presented in (**a**)

Four basic types of Ramachandran plots have been reported in the literature depending on the stereo-chemistry of the amino-acids: Glycine, Proline, 'Generic' (which refers to the remaining 18 amino acids), and 'Pre-Proline' (which refers to residues preceding a Proline) (Ho and Brasseur, 2005). As a result, different potential functions are expected for Glycine (G), Proline (P), and the rest of the amino acids (X) depending on their neighboring residues.

1.2.4 Extraction of Potential Functions

Bending potentials for the pseudo-bond angles are obtained by Boltzmann-inversion of the θ probability distribution. Initially, ϕ and ψ dihedral angles for the central residue of different triple combinations of P, G and X are extracted from the 3-residue-fragments in the coil library. The extraction procedure is depicted schematically in Fig. 1.2 for X–X–P combinations. In Fig. 1.2(a-inset) the ϕ and ψ values are plotted for all X amino acids (i.e. those amino acids that are not P or G) that have an X preceding it and a P following it. In the next step, each datapoint in the Ramachandran space is mapped to θ using Eq. (1.1). Collecting all datapoints in data bins gives the θ probability distribution (Fig. 1.2(a)) which is then directly converted to the bending potential by Eq. (1.3) (see Fig. 1.2(b)).

In order to develop the bending potentials, one can consider different levels of accuracy. This could range from developing 27 bending potentials for all combinations of G, P and X to just three sets of potentials for our three letter amino-acid alphabet ignoring any neighbor dependence. Studying proteins with different amino-acid contents shows that including the neighbor-residue effect is important only if the considered residue is preceding a Proline residue. Therefore, 6 sets of bending potentials are suggested in which we distinguish those central residues that do and do not precede a Proline.

The same methodology is also applied to derive the pseudo-torsion potentials. The main difference with the bending procedure is that in Eq. (1.2) two separate sets of Ramachandran data (e.g., ϕ_i, ψ_i, ϕ_{i+1} and ψ_{i+1}) are required to convert the all-atom dihedral angles ϕ and ψ to the coarse-grained dihedral angle α. Studying different levels of accuracy resulted in torsion potentials for all possible double-combinations of X, P and G amino-acids, giving 9 different torsion potentials. The reader is referred to (Ghavami et al., 2012) for more background information.

1.3 Application to Denatured Proteins

High temperature, pressure or the presence of a chemical denaturing agent can break down the native structure of folded proteins. As a result, it will turn to a dynamic set of complex conformations which is called the denatured state of a protein (Rose, 2002). The addition of denaturants disrupts the native hydrogen bonds and weakens the hydrophobic forces in the protein (Das and Mukhopadhyay, 2008; Lim et al., 2009; Zangi et al., 2009). After denaturation, only local interactions that restrict the polypeptide backbone to limited regions of the conformational space are retained (Creamer, 2008). Experimental studies have revealed that the ensemble-average radius of gyration of denatured proteins follows a power-law scaling:

$$R_g = R_0 N^{\nu}, \tag{1.4}$$

where N is the number of residues, R_0 is a constant related to the persistence length of the polymer and ν is a scaling exponent.

The obtained potentials are used to study the effect of the composition of the protein sequence on the R_g of denatured proteins, with special emphasis on the role of Proline in enlarging and that of Glycine in reducing the conformational radius. A survey of protein sequences of folded and unfolded proteins shows that the amount of Proline and Glycine residues never exceeds 15 percent. In order to study the effect of sequence and composition on the R_g of unfolded proteins, a series of simulations has been performed on protein chains with different lengths, containing 15 percent of Glycine and Proline residues randomly distributed along the chain. As expected, the sequences rich in Proline residues lead to a higher R_g compared to the chains rich in Glycine, producing an upper and lower bound for the R_g of denatured proteins (see Fig. 1.3). Any chain with less than 15 percent Proline or 15 percent Glycine falls within this band. The experimental results of low-charge crosslink-free chemically unfolded proteins with sizes ranging from 16 to 549 residues, shows that R_g can be well fitted by the power-law relationship in Eq. (1.4) with $R_0 = 0.202 \pm 0.041$ nm and $\nu = 0.588 \pm 0.037$ (Kohn et al., 2004), which indeed falls in between the computed bounds in Fig. 1.3.

Recently, many studies have been conducted on poly-Proline proteins showing that these proteins form elongated left-handed helices with a very stiff backbone structure (Adzhubei and Sternberg, 1993). The current model is able to capture the helix conformation of poly-Proline proteins with a rise of 2.97 Å per Proline, which

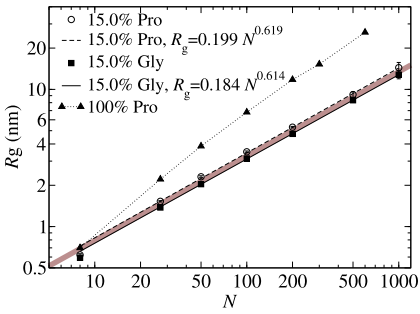

Fig. 1.3 Simulation results for chains rich in Proline and Glycine residues

is comparable to the 3.0 Å rise per Proline from atomistic simulations and 3.1 Å per Proline from experimental data (Dolghih et al., 2009). The dependence of the radius of gyration of poly-Proline proteins on the sequence length is also studied in Fig. 1.3. It clearly shows the higher dimensions of these synthetic proteins compared to natural proteins. It should be noticed that since Proline is considered a hydrophobic amino acid and the influence of solvent is not included in the present model, the predicted gyration radius is overestimating the R_g of poly-Proline proteins in aqueous solution.

1.4 Conclusion

In this paper, we have presented an implicit solvent, one-bead per amino-acid coarse-grained model to study the unfolded state of proteins. To ensure that the CG bending and torsion potential functions for bonded interactions are not biased to any specific secondary structure, the obtained potentials were extracted from Ramachandran data of the coil regions of proteins. The potential functions have been developed by accounting for the effect of neighboring residues, rendering the model to be residue- and sequence-specific. The model has been used to study the correlation between sequence composition and dimension of denatured proteins. Based on the Proline and Glycine content of the protein sequence, an upper and lower bound is constructed for the ensemble average R_g of denatured proteins, which is in agreement with the available experimental data. The developed model sets the stage for further developments towards the inclusion of electrostatic and hydrophobic interactions to study the characteristics of natively unfolded proteins under physiological conditions.

References

Adzhubei AA, Sternberg MJ (1993) Left-handed polyproline II helices commonly occur in globular proteins. J Mol Biol 229:472–493

Avbelj F, Grdadolnik SG, Grdadolnik J, Baldwi RL (2006) Intrinsic backbone preferences are fully present in blocked amino acids. Proc Natl Acad Sci USA 103:1272–1277

Bereau T, Deserno M (2009) Generic coarse-grained model for protein folding and aggregation. J Chem Phys 130:235106
Creamer T (2008). Unfolded proteins: from denatured to intrinsically disordered. Nova Publishers, Hanover
Das A, Mukhopadhyay C (2008) Atomistic mechanism of protein denaturation by urea. J Phys Chem B 112:7903–7908
Dayalan S, Gooneratne ND, Bevinakoppa S, Schroder H (2006) Dihedral angle and secondary structure database of short amino acid fragments. Bioinformation 1:78–80
Dolghih E, Ortiz W, Kim S, Krueger BP, Krause JL, Roitberg AE (2009) Theoretical studies of short polyproline systems: recalibration of a molecular ruler. J Phys Chem A 113:4639–4646
Dunker AK, Brown CJ, Lawson JD, Iakoucheva LM, Obradović Z (2002) Intrinsic disorder and protein function. Biochemistry 41:6573–6582
Fink AL (2005) Natively unfolded proteins. Curr Opin Struct Biol 15:35–41
Finkelstein AV, Ptitsyn O (2002) Protein physics: a course of lectures. Academic Press, San Diego
Frishman D, Argos P (1995) Knowledge-based protein secondary structure assignment. Proteins 23:566–579
Ghavami A, Van der Giessen E, Onck PR (2012) Coarse-grained potentials for local interactions in unfolded proteins (submitted for publication)
Ho BK, Brasseur R (2005) The Ramachandran plots of glycine and pre-proline. BMC Struct Biol 5:14
Kohn JE, Millett IS, Jacob J, Zagrovic B, Dillon TM, Cingel N, Dothager RS, Seifert S, Thiyagarajan P, Sosnick TR, Hasan MZ, Pande VS, Ruczinski I, Doniach S, Plaxco KW (2004) Random-coil behavior and the dimensions of chemically unfolded proteins. Proc Natl Acad Sci USA 101:12491–12496
Korkut A, Hendrickson WA (2009) A force field for virtual atom molecular mechanics of proteins. Proc Natl Acad Sci USA 106:15667–15672
Levitt M (1976) A simplified representation of protein conformations for rapid simulation of protein folding. J Mol Biol 104:59–107
Lim WK, Rösgen J, Englander SW (2009) Urea, but not guanidinium, destabilizes proteins by forming hydrogen bonds to the peptide group. Proc Natl Acad Sci USA 106:2595–2600
Monticelli L, Kandasamy SK, Periole X, Larson RG, Tieleman DP, Marrink S-J (2008) The MARTINI coarse-grained force field: extension to proteins. J Chem Theory Comput 4:819–834
Radivojac P, Iakoucheva LM, Oldfield CJ, Obradović Z, Uversky VN, Dunker AK (2007) Intrinsic disorder and functional proteomics. Biophys J 92:1439–1456
Rose GD (2002) Advances in protein chemistry, vol 62. Academic Press, San Diego
Tirion MM (1996) Large amplitude elastic motions in proteins from a single-parameter, atomic analysis. Phys Rev Lett 77:1905–1908
Tompa P (2009) Structure and function of intrinsically disordered proteins. Chapman & Hall/CRC, London
Tozzini V, Rocchia W, McCammon JA (2006) Mapping all-atom models onto one-bead coarse-grained models: general properties and applications to a minimal polypeptide model. J Chem Theory Comput 2:667–673
Tozzini V, Trylska J, Chang CE, McCammon JA (2007) Flap opening dynamics in HIV-1 protease explored with a coarse-grained model. J Struct Biol 157:606–615
Yap EH, Fawzi NL, Head-Gordon T (2007) A coarse-grained alpha-carbon protein model with anisotropic hydrogen-bonding. Proteins, Struct Funct Bioinform 70:626–638
Zangi R, Zhou R, Berne BJ (2009) Urea's action on hydrophobic interactions. J Am Chem Soc 131:1535–1541

Chapter 2
Modeling Collagen-Proteoglycan Structural Interactions in the Human Cornea

Xi Cheng, Hamed Hatami-Marbini, and Peter M. Pinsky

Abstract The cornea is a supremely organized connective tissue making it ideal for modeling and probing possible roles of collagen-PG interactions in the extracellular matrix. The cornea can be viewed as a reinforced electrolyte gel involving molecular-scale interactions between collagen fibrils, proteoglycans (PGs) and the mobile ions in the interfibrillar space. The swelling property of the tissue cannot be adequately predicted by Donnan theory for osmotic pressure. We propose an alternative unit cell approach based on a thermodynamic framework that employs a mean-field approximation for the electrostatic free energy and which accounts for a non-uniform electrostatic potential. The model is used to show that the equilibrium swelling pressure can be explained when the geometrical effect of electrolyte exclusion due to collagen fibril volume is considered. The model is further refined by dividing the PGs into collagen fibril coating and volumetric partitions. The model suggests that the PG coatings overlap at low hydration and set up repulsive forces that may act to maintain the collagen lattice order. Finally, we introduce a molecular-level unit cell in which volumetric domains within the unit cell are associated with the macromolecular GAGs and results from the continuum and molecular-level models are compared.

X. Cheng · H. Hatami-Marbini · P.M. Pinsky (✉)
Department of Mechanical Engineering, Stanford University, 496 Lomita Mall, Stanford, CA, USA
e-mail: pinsky@stanford.edu

X. Cheng
e-mail: cx1012@stanford.edu

Present address:
H. Hatami-Marbini
School of Mechanical and Aerospace Engineering, Oklahoma State University, 218 Engineering North, Stillwater, OK, USA
e-mail: hhatami@okstate.edu

G.A. Holzapfel, E. Kuhl (eds.), *Computer Models in Biomechanics*,
DOI 10.1007/978-94-007-5464-5_2,

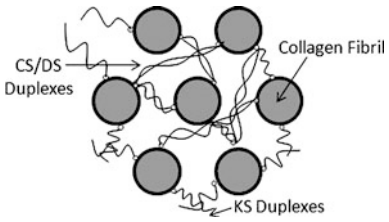

Fig. 2.1 Collagen-PG arrangement in the corneal stroma; some of the GAG chains may bridge fibrils by antiparallel duplexing (Scott, 1992)

2.1 Introduction

The extracellular matrix of the cornea is composed of two principal molecular components: type I collagen in the form of 25 nm diameter fibrils and small leucine-rich repeat proteoglycans (PGs). The corneal stroma is organized into approximately 500 lamellae (or fibers) through its thickness and within each lamella the collagen fibrils are maintained in almost perfect parallel arrays with a quasi-regular hexagonal packing arrangement. The collagen is responsible for carrying the tensile forces that are produced by the intraocular pressure. The corneal PGs consist of linear chains of disaccharide units covalently bound to a core protein. Predominant corneal glycosaminoglycan (GAG) components are dermatan sulfate (DS), chondroitin sulfate (CS) and keratan sulfate (KS). Scott (1992) proposed that some GAGs form interfibrillar bridges by duplexing and this has been supported by some evidence from imaging (Muller et al., 2004; Lewis et al., 2010). These arrangements are illustrated in Fig. 2.1. The DS, CS and KS disaccharide units are ionized at physiological pH and carry two negative charges per unit. The electrostatic interaction of these charges with ionic species gives rise to strong intermolecular forces that are responsible for the tissue osmotic pressure.

The transparency of the cornea requires that the collagen fibrils be maintained in their lattice-like arrangement. Modeling the forces of interaction between the collagen fibrils and GAGs may provide insights into the mechanisms underlying corneal transparency and is a primary goal of this work. The polyelectrolyte nature of the corneal stroma is well illustrated by its remarkable capacity for swelling when immersed in water or dilute salt solution. The tendency of the corneal stroma to swell can be characterized by the equilibrium swelling pressure. The equilibrium swelling pressure may be measured by compressing a piece of isolated corneal stroma in an ionic bath solution between permeable plates until equilibrium is reached (Hedbys and Dohlman, 1963). During the past several decades, the swelling pressure on various species have been measured experimentally (Hedbys and Dohlman, 1963; Fatt, 1968; Olsen and Sperling, 1987), and it has been observed that the swelling pressure is highly dependent on the tissue hydration.

Several previous investigations have aimed to create theoretical models for corneal swelling (Hart and Farrell, 1971; Hodson, 1971; Olsen and Sperling, 1987). It has been demonstrated that Donnan theory for osmotic pressure is incapable of fully explaining swelling pressure (Olsen and Sperling, 1987). In this work we propose a swelling pressure theory that is derived from a molecular-level description of

the polyelectrolyte system that recognizes the spatial heterogeneity of charge density that exists in the tissue. A similar thermodynamic approach was employed by Hart and Farrell (1971), but the present work uses an entirely different description of the electrostatic free energy. The electrostatic free energy of a polyelectrolyte found through a mean-field approximation can be expressed as a functional of the electrostatic potential, fixed charge density and local ionic concentrations (Che et al., 2008). The electrostatic potential is determined from solution of the Poisson-Boltzmann equation over a unit cell and the swelling pressure is found as the gradient of the free energy with respect to the swelling volume. By considering the volumetric domains of polyelectrolyte excluded by the collagen fibrils, the model finds excellent agreement with the experimental swelling pressure data.

In order to improve the model for low levels of hydration, we were lead by experimental observations to postulate that the stromal PGs are partitioned into two sets. One set is associated with PGs that bridge (perhaps by duplexing of the longer DS and CS GAGs) between neighboring collagen fibrils; these supply the charge density responsible for the osmotic pressure at physiological hydration. A second set produces a charge-rich coating around the collagen fibrils (perhaps formed primarily by the shorter KS GAGs). At physiological hydration, the coatings do not interact and add very little to the osmotic pressure. As hydration is reduced, the collagen fibrils come into closer proximity and the coatings will overlap producing a significant increase in local charge density and a concomitant increase in swelling pressure and electrostatic repulsion. We conclude that the PG-coatings may represent a mechanism to order the collagen fibril lattice as required in order for the cornea to be a good transmitter of light.

2.2 Comparison of Donnan and Poisson-Boltzmann Theories Applied to the Cornea

2.2.1 Donnan Theory

If a polyelectrolyte phase is in equilibrium with an external bath ionic solution, osmotic pressure will result from the polyelectrolyte fixed charges and the disparity of ionic concentrations in the two phases. Donnan theory may be employed to model the osmotic pressure under the assumption that the fixed charge density is spatially invariant. Consider a sample of isolated corneal stroma placed in a NaCl bath. Assuming ideal Donnan equilibrium, the distribution of mobile ions satisfies

$$\bar{C}_{\mathrm{Na+}}\bar{C}_{\mathrm{Cl-}} = C_0^2, \tag{2.1}$$

where $\bar{C}_{\mathrm{Na+}}$ and $\bar{C}_{\mathrm{Cl-}}$ are the mobile ion concentrations in the stroma and C_0 the ionic concentration in the bath. The GAG disaccharide units provide a fixed (nonmobile) negative charge density ρ_{f} and electroneutrality within the polyelectrolyte

phase requires,

$$\bar{C}_{\mathrm{Na+}} - \bar{C}_{\mathrm{Cl-}} + \frac{\rho_{\mathrm{f}}}{F} = 0, \tag{2.2}$$

where F is the Faraday constant. Equations (2.1) and (2.2) can be solved for the equilibrium mobile ion concentration (Buschmann and Grodzinsky, 1995) giving

$$\bar{C}_{\mathrm{Na+/Cl-}} = \mp\frac{\rho_{\mathrm{f}}}{2F} + \sqrt{\frac{\rho_{\mathrm{f}}^2}{4F^2} + C_0^2}. \tag{2.3}$$

The osmotic pressure in the two phases is given by

$$P_{\mathrm{poly}} = RT(\bar{C}_{\mathrm{Na+}} - \bar{C}_{\mathrm{Cl-}}), \qquad P_{\mathrm{bath}} = 2RTC_0, \tag{2.4}$$

where R is the gas constant and T is the absolute temperature. The osmotic pressure difference P_{os} between the two phases is then computed as

$$P_{\mathrm{os}} = P_{\mathrm{poly}} - P_{\mathrm{bath}} = 2RTC_0\left(\sqrt{\frac{\rho_{\mathrm{f}}^2}{4F^2C_0^2} + 1} - 1\right). \tag{2.5}$$

In Fig. 2.2 we depict experimental measurements and fitting curves for the equilibrium swelling pressure of human corneal stroma with a bath concentration of $C_0 = 0.15$ M as reported by Hedbys and Dohlman (1963) and Olsen and Sperling (1987). Letting ρ_0 represent the fixed charge density at physiological sample thickness $t_0 = 0.5$ mm, and letting ρ_{f} represent the charge density at tissue sample thickness t, we find by conservation of fixed charge that $\rho_{\mathrm{f}} = \rho_0(t_0/t)$. Using this result in Eq. (2.5), the osmotic pressure difference at thickness t may be estimated in terms of the physiological fixed charge density ρ_0. It has been shown that ρ_0 depends on the salt concentration in the bath through a process of ion binding. Hodson (1971) has estimated ρ_0/F for human stroma at physiological hydration and bath ionic concentration $C_0 = 0.15$ M to be approximately 48 mM. Values of ρ_0/F for bovine cornea have been measured at around 36 mM; see Elliott and Hodson (1998) for a review. The osmotic pressure difference P_{os} based on Donnan theory Eq. (2.5) with $\rho_0/F = 48$ mM is shown in Fig. 2.2. The prediction agrees well with the experimental data at physiological thickness $t = 0.5$ mm but deviates significantly for all other values, particularly for $t < 0.5$ mm. We conclude that Donnan theory is incapable of predicting swelling pressure accurately for lower thicknesses, which correspond to hydration levels lower than physiological.

2.2.2 Poisson-Boltzmann Theory

We now consider a thermodynamic framework for describing the swelling pressure experiment on corneal stroma. Consider a sample of isolated corneal stroma of area

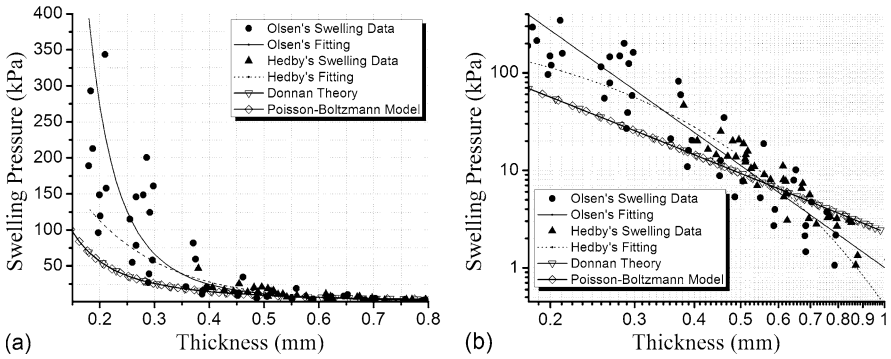

Fig. 2.2 Swelling pressure vs. thickness by Hedbys and Dohlman (1963) and Olsen and Sperling (1987), the Donnan model and the Poisson-Boltzmann (PB) model. Data plotted on the normal axis (**a**) and a log-log axis (**b**). Fitting curve by Olsen: $P_s = 7.56 \times t^{-3.48}$ mmHg and the fitting curve based on Hedbys' data (Fatt, 1968) $P_s = 1810 \times \exp(-H)$ mmHg. The hydration data from Hedbys and Dohlman (1963) is transformed to thickness by the linear relation $H = 7.00t - 0.64$ (Hedbys and Mishima, 1966). Charge density for Donnan model and the PB model is $\rho_0/F = 48$ mM

A_s immersed in an ionic solution and constrained by a porous piston to a thickness t. The total Gibbs free energy of the system is defined as

$$\mathscr{G} = \mathscr{F} + PV + P_s A_s t, \tag{2.6}$$

where $\mathscr{F}$ is the Helmholtz free energy, P and V are the atmosphere pressure and total system volume, respectively, and P_s is the pressure exerted by the piston on the sample (Katchalsky and Michaeli, 1955; Hart and Farrell, 1971). At equilibrium we require

$$P_s = -\frac{1}{A_s}\frac{\partial}{\partial t}(\mathscr{F} + PV). \tag{2.7}$$

At fixed temperature T and atmosphere pressure P, the PV term may be dropped and the swelling pressure is then expressed as

$$P_s = -\frac{1}{A_s}\frac{\partial \mathscr{F}}{\partial t}\bigg|_{T,P} = -\frac{\partial \mathscr{F}}{\partial V_t}\bigg|_{T,P}, \tag{2.8}$$

which is simply the derivative of the Helmholtz free energy with respect to the tissue volume V_t.

In general, the Helmholtz free energy $\mathscr{F}$ will have electrostatic $\mathscr{F}_{el}$ and chemo-mechanical components $\mathscr{F}_{cm}$ (Jin and Grodzinsky, 2001). The effective electrostatic free energy of a polyelectrolyte solution in a mean-field approximation can be expressed as a functional of the electrostatic potential φ and local ionic concentrations

$C_1, \ldots, C_M$ (Che et al., 2008)

$$\mathscr{F}_{\mathrm{el}}[\varphi, C_1, \ldots, C_M] = \int_\Omega \left\{ -\frac{\varepsilon}{2}|\nabla\varphi|^2 + \rho(r)\varphi + RT\sum_{i=1}^{M} C_i^\infty + RT\sum_{i=1}^{M} C_i\left[\ln\left(\Lambda^3 N_A C_i\right) - 1\right] - \sum_{i=1}^{M} \mu_i N_A C_i \right\} \mathrm{d}\Omega, \tag{2.9}$$

where ε is the dielectric permittivity of the solution, N_A is the Avogadro constant, C_i^∞ and μ_i are the bath concentration and chemical potential of the ith ionic species, respectively, and Λ is the thermal de Broglie wavelength. The local charge density $\rho(r)$ is given by

$$\rho(r) = \rho_{\mathrm{f}}(r) + \sum_{i=1}^{M} F z_i C_i(r), \tag{2.10}$$

where ρ_{f} is the fixed charge density from the GAG disaccharide units and z_i is the valence number for the ith ionic species. In Eq. (2.9), the first two terms are the internal electrostatic energy, the third term is the osmotic pressure from the mobile ions, the fourth term constitutes the ideal gas entropy and the last term accounts for the chemical potential. Setting the first variation of the free energy $\mathscr{G}$ with respect to the concentration C_i to zero leads to

$$C_i(r) = C_i^\infty \exp\left(-z_i \frac{F\varphi(r)}{RT}\right), \tag{2.11}$$

which is the Boltzmann distribution for the concentrations at equilibrium. The variation of $\mathscr{F}_{\mathrm{el}}$ with respect to the potential φ yields the Poisson equation

$$\nabla \cdot \varepsilon \nabla\varphi(r) = -\rho(r). \tag{2.12}$$

The Poisson-Boltzmann equation (PBE) is obtained by combining Eqs. (2.10)–(2.12),

$$-\varepsilon\nabla^2\varphi(r) = \rho_{\mathrm{f}}(r) + \sum_{i=1}^{M} F z_i C_i^\infty \exp\left(-z_i \frac{F\varphi(r)}{RT}\right). \tag{2.13}$$

Substituting Eqs. (2.10), (2.11) into (2.9), the free energy at equilibrium is obtained as

$$\mathscr{F}_{\mathrm{el}}[\varphi] = \int_\Omega \left\{ -\frac{\varepsilon}{2}|\nabla\varphi|^2 + \rho_{\mathrm{f}}\varphi - RT\sum_{j=1}^{M} C_j^\infty \left[\exp\left(-z_j \frac{F\varphi(r)}{RT}\right) - 1\right] \right\} \mathrm{d}\Omega. \tag{2.14}$$

It is remarked that this expression defines a concave functional; it has a unique equilibrium potential φ at which the functional is maximized (Fogolari and Briggs, 1997).

Specializing (2.13) and (2.14) to a binary electrolyte we find:

$$-\nabla^2\varphi = \frac{\rho_f}{\varepsilon} - \frac{2FC_0}{\varepsilon}\sinh\left(\frac{F\varphi(r)}{RT}\right), \tag{2.15}$$

and

$$\mathscr{F}_{el} = \int_\Omega \left\{-\frac{\varepsilon}{2}|\nabla\varphi|^2 + \rho_f\varphi - 2RTC_0\left[\cosh\left(\frac{F\varphi}{RT}\right) - 1\right]\right\} d\Omega. \tag{2.16}$$

Returning to the equilibrium swelling pressure problem and taking (as in the Donnan solution) a uniform fixed charge density of $\rho_f/F = 48$ mM and bath ionic concentration of $C_0 = 0.15$ M, the swelling pressure was computed using Eq. (2.8) and the results are shown for varying sample thickness t in Fig. 2.2. The derivative of the free energy $\mathscr{F}_{el}$ with respect to t was computed using central difference. As expected for this case of uniform charge density, the results are consistent with the Donnan prediction and confirm the thermodynamic framework provided by Eqs. (2.8) and (2.16).

2.2.3 An Unit Cell Model Based on Collagen Fibril Volume Exclusion

Both the Donnan and Poisson-Boltzmann (PB) theories confirm that the assumption of a spatially uniform charge distribution results in an unsatisfactory prediction of stromal swelling, especially for low levels of hydration. However, it is observed that the collagen fibrils occupy approximately 30 % of the stroma by volume (Meek and Leonard, 1993). As the tissue is compressed during the swelling pressure experiment, we argue that (i) the volume occupied of the collagen fibrils is unaffected by the change in stromal thickness, and (ii) the collagen fibrils maintain very few net ionized groups and contribute little or nothing to the electric balance within the tissue (Elliott and Hodson, 1998). Therefore, the GAG charges, which are conserved, must be restricted to the volumetric region between the collagen fibrils. Clearly, as the tissue is compressed, there will be a nonlinear increase in charge density due to the *geometric* effect of the collagen fibril volume exclusion.

Experimental estimation of the interfibrillar spacing l_c and radius of collagen fibril r_f in the human cornea suggest they lie in the ranges of $45 \sim 60$ nm and $11.5 \sim 15.0$ nm, respectively (Fratzl and Daxer, 1993; Elliott and Hodson, 1998; Muller et al., 2004). Consider a perfect hexagonal collagen lattice with $l_c = 53.0$ nm and $r_f = 12.5$ nm as shown in Fig. 2.3(a). Charge is now assumed to be uniformly distributed in the interfibrillar region $\Omega_s \in \mathbb{R}^3$ only and is zero in the fibril domains. The PB equation (2.13) was solved on a sequence of unit domains $\{\Omega_f^i\}$ in which

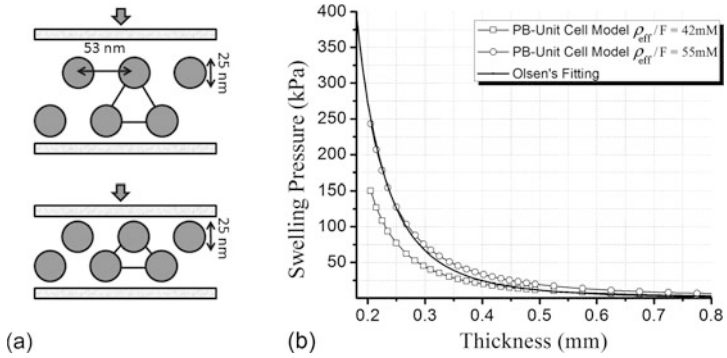

Fig. 2.3 (**a**) 2D illustration of the unit cell, charge distribution is uniform over the interstitial region Ω_s. The tissue is deformed by pressing the porous piston and the deformed unit cell is calculated from affine mapping; (**b**) Swelling pressure computed by PB-unit cell model based on collagen volume exclusion. The charge density is calibrated to be $\rho_{\text{eff}}/F = 42 \sim 55$ mM. The lower and upper bound of the ρ_{eff} are determined by fitting the result at physiological situation ($t = 0.5$ mm) and the low hydration situation ($t = 0.2$ mm) respectively. The interfibril spacing $l_c = 53$ nm and the collagen radius $r_f = 12.5$ nm

the total fixed charge Q_f is conserved and the charge density computed from $\rho_f^i = Q_f / V_f^i$, where V_f^i is the volume of Ω_f^i. The results are shown in Fig. 2.3(b) and labeled in terms of effective charge density ρ_{eff} defined by

$$\rho_{\text{eff}} = \frac{\rho_f V_f}{V_0}, \tag{2.17}$$

where V_0 is the total volume of the unit cell including the fibril volume at physiological thickness. Values of $\rho_{\text{eff}}/F = 42$ mM and 55 mM give best fits at physiological and low hydration, respectively, and produce predictions that are dramatically better than those of Donnan theory.

2.3 The Case for a PG-Coating of the Collagen Fibrils

Fratzl and Daxer (1993) describe X-ray scattering studies to measure the structural transformation of collagen fibrils under varying hydration produced by drying the tissue. The data strongly suggests that stromal PGs are heterogeneously distributed in the interfibrillar space. They appear in relatively high density in the vicinity of the fibrils where they may form a charge-rich effective PG coating surrounding each fibril. Hodson (1971) and Twersky (1975) have, much earlier, speculated on the existence of a such a fibril coating. Fratzl and Daxer (1993) estimated the radius of the coating as $r_c = 18$ nm. Interestingly, they showed that the coating radius r_c is insensitive to hydration over a wide range and this suggests that the charge density associated with the coating PGs will not change with variations in hydration. However, at low levels of hydration the coatings may overlap and interact, as described below.

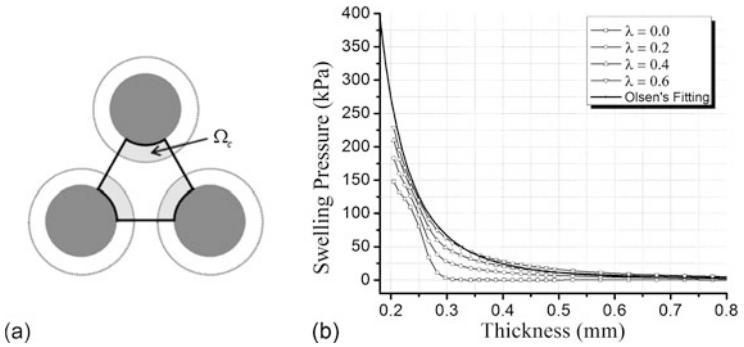

Fig. 2.4 (**a**) 2D illustration of the coating unit cell. Charges are distributed into the coating region Ω_c and the non-coating region $\Omega^i \backslash \Omega_c$. (**b**) Swelling pressure computed by the coating model under overall charge density $\rho_{\text{eff}}/F = 55$ mM. The coating radius is set to be 18 nm, and the charge fraction λ for the bridging GAGs varies from 0.0 to 0.6. The optimal fitting occurs at $\lambda = 0.6$

We propose a coating model in which the total unit cell charge Q is partitioned into two GAG-based classes: one based on charge derived from long interfibrillar bridging GAGs and one based on charge derived from short GAGs that form the coating. As in the previous model, we exclude the volume of the collagen fibrils in our analysis. A sequence of unit cell domains is defined by symmetry of the lattice and is denoted Ω^i with volume V^i. Here i is a configuration index corresponding to tissue thickness (and thus hydration). The coating subregion of the unit cell is denoted Ω_c and has volume V_c, which is *independent* of V^i in accordance with the findings of Fratzl and Daxer (1993). The setup is shown in Fig. 2.4(a). Letting $\lambda \in [0, 1]$ denote the charge fraction parameter, the unit cell has two charge densities computed as follows

$$\rho_s^i = \lambda \frac{Q}{V^i} \tag{2.18}$$

over Ω^i, and

$$\rho_c = (1 - \lambda) \frac{Q}{V_c} \tag{2.19}$$

over Ω_c. Clearly, the total charge in the unit cell Ω^i is conserved. Further, the coating charge density ρ_c is invariant with respect to hydration (i.e. index i). If the coating subdomains overlap at low thickness values, we assume that the charge density is additive in the overlap region in order to conserve total charge. The boundary value problem to be solved on each unit cell domain Ω^i is then

$$-\nabla^2 \varphi = \frac{\rho}{\varepsilon} - \frac{2FC_0}{\varepsilon} \sinh\left(\frac{F\varphi}{RT}\right), \quad \text{in } \Omega^i, \tag{2.20}$$

with the boundary conditions:

$$\big[|\varphi|\big] = 0, \qquad \big[|\nabla\varphi \cdot \mathbf{n}|\big] = 0, \quad \text{on } \Gamma_{\text{inner}}, \tag{2.21}$$

$$\nabla\varphi \cdot \mathbf{n} = 0, \qquad \text{on } \Gamma_{\text{outer}}, \tag{2.22}$$

and where Γ_{inner} and Γ_{outer} denote the inner and outer boundaries of the unit cell, respectively. The electrostatic free energy takes the form

$$\mathscr{F}_{\text{el}} = \int_{\Omega^i} \left[-\frac{\varepsilon}{2}|\nabla\varphi|^2 + \rho\varphi - 2RTC_0\left(\cosh\left(\frac{F\varphi}{RT}\right) - 1\right)\right] \mathrm{d}\Omega^i, \tag{2.23}$$

where the charge density distribution ρ in Eqs. (2.20) and (2.23) is given by

$$\rho^{(i)} = \begin{cases} \rho_{\text{s}}^i, & \text{in } \Omega^i \backslash \Omega_{\text{c}}, \\ \rho_{\text{s}}^i + \rho_{\text{c}}, & \text{on } \Omega_{\text{c}}, \\ 2(\rho_{\text{s}}^i + \rho_{\text{c}}), & \text{on } \Omega_{\text{c-c}}. \end{cases} \tag{2.24}$$

Here $\Omega_{\text{c-c}}$ refers to the subdomain of Ω_{c} resulting from the possible geometric intersection of coating domains as Ω^i is mapped to correspond to lower thickness values with increasing index i.

In this model, the coating radius is taken to be $r_{\text{c}} = 18.0$ nm. The effective charge density is again defined by $\rho_{\text{eff}} = Q/V_0$ and used for reporting results. The influence of the charge fraction λ on the swelling pressure is shown in Fig. 2.4 at the physiologically plausible $\rho_{\text{eff}}/F = 55$ nm. At $\lambda = 0$, all charge is concentrated in the coatings and the swelling pressure is zero until the coatings begin to interact at around $t = 0.3$ mm. As λ is increased the swelling pressure increases monotonically toward the experimental curve. At a value of $\lambda = 0.6$, the computed swelling pressure finds excellent agreement with the experimental curve and further improves on the result of the previous section.

2.4 Molecular-Level Unit Cell Model

Here we present a molecular-level unit cell model which explicitly considers the GAG chains that are bridging neighboring collagen fibrils. In this model, the bridging GAGs domains are approximated by an effective cylindrical volume (Hart and Farrell, 1971; Jin and Grodzinsky, 2001). The non-bridging GAGs that constitute the collagen fibril coating are modeled, as above, with a continuum description of the charge density. The charge density within the cylindrical GAG domain is denoted ρ_{g} and is determined by three parameters: the half length of the GAG disaccharide unit $b = 0.64$ nm (Jin and Grodzinsky, 2001), the cylinder radius r_{g} and a molecular ratio factor $\alpha = L_{\text{c}}/L_{\text{d}}$, where L_{c} is the contour length of the GAG chains and L_{d} is end-to-end distance. Then ρ_{g} may be computed from

$$\rho_{\text{g}} = \frac{\alpha e}{\pi b r_{\text{g}}^2}, \tag{2.25}$$

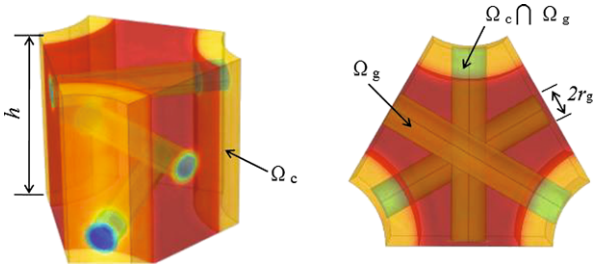

Fig. 2.5 Illustration of the molecular-level unit cell. The collagen fibrils are connected by the GAGs via next-nearest neighbor connectivity. The subdomains are: $\Omega_c \cap \Omega_g$—the overlapping domain of the coating and interconnecting GAGs; Ω_g—the region occupied only by interconnecting GAGs; Ω_c—the region occupied only by the coating GAGs

where e is the unit charge supplied by the disaccharide unit. The uniform charge density for the coating GAGs is

$$\rho_c = (1-\lambda)\frac{\rho_{\text{eff}} Ah}{V_c}, \tag{2.26}$$

where h is the length and Ah the volume of the unit cell, respectively. The bridging GAGs repeat along the axis of collagen fibrils with period h, which may be determined using the conservation of total charge

$$\rho_{\text{eff}} Ah\lambda = \frac{\sum_{i=1}^{N_{\text{gag}}} l_g^i \alpha e}{b}, \tag{2.27}$$

where λ is the charge fraction for the bridging GAGs and $\sum_{i=1}^{N_{\text{gag}}} l_g^i$ is the total length of the GAG rods over the unit cell. As an example, we employ a next-nearest neighbor topology for the interconnecting GAGs proposed by Muller et al. (2004). The 3-D unit cell model has uniform charge density ρ_c in the coating domain and ρ_g in the bridging GAG cylinders (Fig. 2.5).

The Poisson-Boltzmann equation is solved for the electrostatic potential φ over the cell subdomains with boundary conditions as described by Eqs. (2.21) and (2.22) and with fixed charge density ρ_f prescribed as,

$$\rho_f = \begin{cases} \rho_c & \text{on } \Omega_c, \\ \rho_g & \text{on } \Omega_g, \\ \rho_c + \rho_g & \text{on } \Omega_c \cap \Omega_g, \end{cases} \tag{2.28}$$

and $\rho_f = 0$ elsewhere. Charge conservation is applied to the bridging and coatings GAGs domains independently. As the unit cell is deformed, the charge density ρ_g changes due to the cylinder length change. The coating charge density ρ_c will not change, as discussed above. For simplicity, the GAG radius r_g is invariant during cell deformation.

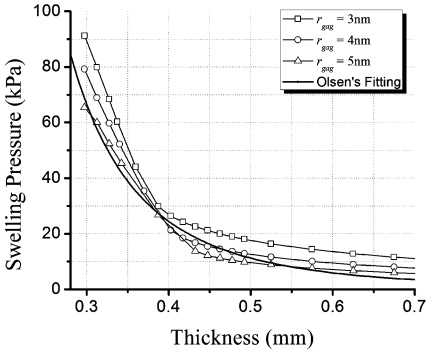

Fig. 2.6 Swelling pressure vs. corneal thickness around the physiological condition ($t = 0.5$ mm) by the molecular-level unit cell model. The average charge density $\rho_{\text{eff}}/F = 48$ mM and the radius of the GAGs rod varies from 3 to 5 nm, the ratio $\alpha = 4.0$ and charge fraction $\lambda = 0.5$

Figure 2.6 shows the computed swelling pressure versus the tissue thickness. The cell effective charge density is taken to be $\rho_{\text{eff}}/F = 48$ mM. The interfibrillar spacing $l_c = 53$ nm, radius of the collagen fibril $r_c = 12.5$ nm, and the coating radius $r_c = 18$ nm have the same values used in the previous models. The molecular length ratio is taken to be $\alpha = 4.0$, and the charge partition fraction $\lambda = 0.5$. We have studied the model under GAGs radii varying from 3 to 5 nm. The sensitivity of the results with respect to r_g is presented in Fig. 2.6. An increase in the effective GAG radius leads to a decrease in the computed swelling pressure, as expected, because the charge density ρ_g in the GAG cylinders drops. From Fig. 2.6, we observe that $r_g = 3 \sim 4$ nm gives a result that matches the experimental curve well.

2.5 Discussion

In this work we have compared predictions for equilibrium swelling pressure of the human stroma using three models. Each model provides a representation of the electrostatic forces arising from the charges associated with the linear GAG chains of the tissue PGs and with the mobile ions in the polyelectrolyte phase. The first to be considered was a continuum model based on Donnan equilibrium which requires the electrostatic potential to be spatially invariant. This allows no representation of molecular-level or microstructural-level information. This model was based on a uniform fixed charge density that has been reported from independent experimental measurement. The model equates the Donnan osmotic pressure difference between the polyelectrolyte phase and bath with the swelling pressure. The prediction for equilibrium swelling pressure at physiological hydration is reasonable but the approach severely underestimates swelling pressure at lower hydration levels.

The second model is also a continuum model. It is a unit cell approach and based on a thermodynamic derivation for the swelling pressure in which the swelling pressure emerges as the derivative of the electrostatic free energy with respect to the swelling volume. In this model, the electrostatic potential is found from the Poisson-Boltzmann equation. This model contains no molecular-level information but does describe the microstructure of the tissue. In particular, it accounts for the polyelectrolyte phase being excluded from the volume occupied by collagen fibrils. As the

hydration reduces, the volume containing the fixed charges decreases due to a geometrical effect. This model provides an accurate swelling pressure prediction over all ranges of hydration. The model is further improved by partitioning the charge into two GAG-based groups: one associated with a charge-dense coating of the collagen fibrils, in accordance with experimental evidence, and one dispersed over the interfibrillar volume and associated with GAGs which bridge fibrils, possibly by duplexing. This refinement gives a surprisingly accurate prediction for swelling pressure at $\lambda = 0.6$, when 40 % of the charge is in the coating region. This result implies that around physiological hydration ($t = 0.5$ mm), the swelling pressure primarily results from the bridging GAGs in the interfibrillar region. As the tissue is compressed toward $t \sim 0.25$ nm, the coatings start to play a role by mutually interacting and producing a local increase in charge density and a concomitant increase in swelling pressure.

The third model employs a molecular-level unit cell in which volumetric domains within the unit cell are associated with the macromolecular GAGs. The model is a hybrid approach in that it represents the fibril coating as a charge-dense region around the fibrils using a continuum description. The approach accounts for the spatially varying electrostatic potential between the explicit GAG domains and the mobile ions, again using the Poisson-Boltzmann equation. The results of this model applied to the case of next-nearest neighbor GAG connectivity, as proposed by Muller et al. (2004), are also quite accurate. This approach does introduce additional variables that are not readily estimated, including the GAG length ratio α, which describes the waviness of the GAG chains, and the radius of the effective GAG cylinder r_g. However, the length ratio α for the bridging GAGs is also a relevant parameter for estimating the entropic elasticity of the polymer chain using a theory such as the wormlike chain model.

In the present study, we have addressed the swelling problem in terms of the electrostatic component of the free energy alone. However, the chemomechanical free energy, which includes the entropic elasticity of the GAGs and the molecular mixing energy, will certainly have some influence on the swelling pressure (Hart and Farrell, 1971; Jin and Grodzinsky, 2001). Indeed, the GAG entropic elasticity will produce expansion-resisting forces that will contribute a 'negative' swelling pressure component (Hart and Farrell, 1971). These non-electrostatic components will be the subject of a future study.

Acknowledgements This research was supported by the Stanford University Bio-X Interdisciplinary Initiatives Program (PMP), which is gratefully acknowledged. XC also received support from a Stanford Graduate Fellowship.

References

Buschmann MD, Grodzinsky AJ (1995) A molecular model of proteoglycan-associated electrostatic forces in cartilage mechanics. J Biomech Eng 2:179–192

Che J, Dzubiella J, Li B, McCammom JA (2008) Electrostatic free energy and its variations in implicit solvent models. J Phys Chem B 112:3058–3069

Elliott GF, Hodson SA (1998) Cornea, and the swelling of polyelectrolyte gels of biological interest. Rep Math Phys 61:1325–1365

Fatt I (1968) Dynamics of water transport in the corneal stroma. Exp Eye Res 7:402–412

Fogolari F, Briggs JM (1997) On the variational approach to Poisson-Boltzmann free energies. Chem Phys Lett 281:135–139

Fratzl P, Daxer A (1993) Structural transformation of collage fibrils in corneal stroma during drying. Biophys J 64:1210–1214

Hart RW, Farrell RA (1971) Structural theory of the swelling pressure of corneal stroma in saline. Bull Math Biophys 33:165–186

Hedbys BO, Dohlman C (1963) A new method for the determination of the swelling pressure of the corneal stroma in *in vitro*. Exp Eye Res 2:122–129

Hedbys BO, Mishima S (1966) The thickness-hydration relationship of the cornea. Exp Eye Res 5:221–228

Hodson S (1971) Why the cornea swells. J Theor Biol 33:419–427

Jin M, Grodzinsky AJ (2001) Effect of electrostatic interactions between glycosaminoglycans on the shear stiffness of cartilage: a molecular model and experiments. Macromolecules 34:8330–8339

Katchalsky A, Michaeli I (1955) Polyelectrolyte gels in salt solutions. J Polym Sci 15:69–86

Lewis PN, Pinali C, Young RD, Meek KM, Quantock AJ, Knupp C (2010) Structural interactions between collagen and proteoglycans are elucidated by three-dimensional electron tomography of bovine cornea. Structure 18:239–245

Meek KM, Leonard DW (1993) Ultrastructure of the corneal stroma: a comparative study. Biophys J 64:273–280

Muller LJ, Pels E, Schurmans L, Vrensen G (2004) A new three-dimensional model of the organization of proteoglycans can collagen fibrils in the human corneal stroma. Exp Eye Res 78:493–501

Olsen T, Sperling S (1987) The swelling pressure of the human corneal stroma as determined by a new method. Exp Eye Res 44:481–490

Scott JE (1992) Morphometry of cupromeronic blue-stained proteoglycan molecules in animal corneas, versus that of purified proteoglycans stained *in vitro*, implies that tertiary structures contribute to corneal ultrastructure. J Anat 180:155–164

Twersky V (1975) Transparency of pair-correlated, random distributions of small scatterers, with applications to the cornea. J Opt Soc Am A 65:524–530

Chapter 3
Simulations of Cell Behavior on Substrates of Variegated Stiffness and Architecture

Amit Pathak, Vikram S. Deshpande, Anthony G. Evans, and Robert M. McMeeking

Abstract Several experimental studies have shown that cells adhered to stiffer substrates exert higher traction forces and simultaneously form more prominent focal adhesions and stress fibers. We employ a biochemomechanical model implemented in a finite element framework to simulate cell response on substrates of variegated stiffness and architecture. We perform simulations to generate stress fiber and focal adhesion distributions, and predict the values of forces generated by cells adhered on flat gels and on beds of micro-posts of variegated stiffness. We also demonstrate that our predictions agree well with the available experimental measurements obtained with the same cell-substrate setting. For a given, calibrated set of model parameters, our traction force predictions for cells adhered to post-beds of varying stiffness match with measurements from Saez et al. (Biophys. J. 89:L52–L54, 2005). Actin and focal adhesion distributions obtained from our simulations agree well with the patterns observed in the results of various visualization experiments available in the literature. Taken together, these findings suggest that our model captures well the

A.G. Evans deceased.

A. Pathak · A.G. Evans · R.M. McMeeking (✉)
Department of Mechanical Engineering, University of California, Santa Barbara, CA 93106, USA
e-mail: rmcm@engineering.ucsb.edu

A. Pathak
e-mail: amitp@berkeley.edu

V.S. Deshpande
Engineering Department, Cambridge University, Trumpington Street, Cambridge CB2 1PZ, UK
e-mail: vsd@eng.cam.ac.uk

A.G. Evans · R.M. McMeeking
Materials Department, University of California, Santa Barbara, CA 93106, USA

R.M. McMeeking
School of Engineering, King's College, Aberdeen University, Aberdeen AB24 3UE, UK

R.M. McMeeking
INM—Leibniz Institute for New Materials, Campus D2 2, 66123 Saarbrücken, Germany

G.A. Holzapfel, E. Kuhl (eds.), *Computer Models in Biomechanics*,
DOI 10.1007/978-94-007-5464-5_3,

intricate coupling mechanisms arising from cell-substrate interaction and intracellular machinery.

3.1 Introduction

Living cells interact with their environments over a wide range of stiffness, from soft skin through stiffer muscle to harder bone substrates. In such cellular interactions, adhesion of cells to substrates or to an extracellular matrix (ECM) is a critical feature in many cellular functions, ranging from migration and proliferation to apoptosis (Boudreau and Bissell, 1998; Schwartz and Ginsberg, 2002). Experimental studies have now shown that the mechanical compliance of the ECM or the substrate influences cell viability, differentiation and motility (Lo et al., 2000; Discher et al., 2005; Yeung et al., 2005). It is now widely accepted that cells exert a higher force, form larger focal adhesions and develop thicker stress fibers on stiffer substrates (Saez et al., 2005; Yeung et al., 2005). The relationship between stiffness and intracellular machinery regulates many important functions such as non-viral gene delivery (Kong et al., 2005) and growth of cancer cells (Paszek et al., 2005). Evidence suggests that increased rigidity may trigger malignant transformation (Paszek et al., 2005), attributable to increased cytoskeletal tension, integrin clustering and focal adhesion formation.

The experimental studies by Saez et al. (2005) and Yeung et al. (2005) clearly demonstrate a direct dependence of cell behavior on substrate stiffness. In these studies, cellular activity, measured in terms of the average force exerted by the cell on the substrate, the size of focal adhesions, and the concentration of stress fibers, rose to greater levels on stiffer substrates. In addition, the experimental studies of Tan et al. (2003) and Chen et al. (2003) provide further data regarding the shape and size of cell-substrate adhesions and the scaling of forces relative to the spread area of the cell.

A recently developed biochemomechanical model by Deshpande et al. (2006, 2007, 2008) characterizes the dynamically contractile stress fiber machinery made of actin-myosin filaments, giving rise to intracellular force generation, as well as focal adhesion assembly, the latter based on thermodynamic equilibrium between integrins in their low and high affinity states. This model has been successfully employed in simulations of experiments, including cell adhesion on V, T, Y and U-shaped patterned substrates (Pathak et al., 2008), and the formation of stress fibers upon cyclic stretching (Wei et al., 2008). We utilize a similar approach to simulate cell behavior on flat gel substrates, and on post-beds of variegated stiffness. While post-beds offer direct and readily quantifiable insights into the shapes and sizes of adhesions and the forces applied by a contractile cell, a flat substrate is relevant due to its presence in living organisms and its use for in vitro studies. Here, we present simulations for both flat substrates and post-beds, and predict trends in focal adhesion distribution, tractions and stress fiber distribution common to both types of substrate architecture.

3.2 A Biochemomechanical Model for the Cell

We envisage a well-spread, approximately two-dimensional cell, thickness b, lying on a substrate in the x_1–x_2 plane. The cell model comprises two major elements: (i) a constitutive model for the formation of stress fibers, their contractility and their spontaneous attachment to cell adhesion complexes; (ii) a cell adhesion model causing the cell to adhere to a substrate. In (i), following an activation signal, the model predicts the development of contractile, actin-myosin stress fibers by polymerization, subject to their spontaneous connection to transmembrane adhesions, and consistent with traction or displacement conditions imposed by these adhesions at the interface between the cell and its substrate. The outputs of this feature of the model are the spatial (position x_i) and temporal (time t) distributions of the stress fiber concentration, $\eta(x_i, \phi, t)$ and the Cauchy stresses $\Sigma_{ij}(x_i, t)$ generated by the resulting stress fiber contractility, where ϕ is the angle of orientation of a given family of stress fibers. In (ii), the stresses generated by the stress fiber model apply tractions to the focal adhesions to which the stress fibers are attached, and, thereby, control the spatial and temporal development of such adhesions, as parameterized through the high affinity integrin concentration on the cell membrane at the interface with the substrate. Such high affinity integrins are the transmembrane proteins, bound to stress fibers in the cell and substrate ligands outside it, that are the most important molecules forming the adhesion between the cell cytoskeleton and the substrate to which it is attached. Note that there are two main sources of mechano-sensitivity in the model as described below; tension in the stress fibers tends to inhibit their depolymerization, and tractions transmitted through adhesion complexes stabilizes them, encouraging formation of transmembrane integrins bound to ligands on the substrate.

The mechanical equilibrium equations for the cell are written as

$$b\left(\frac{\partial \Sigma_{11}}{\partial x_1} + \frac{\partial \Sigma_{12}}{\partial x_2}\right) = \xi_H F_1, \qquad b\left(\frac{\partial \Sigma_{12}}{\partial x_1} + \frac{\partial \Sigma_{22}}{\partial x_2}\right) = \xi_H F_2, \tag{3.1}$$

where $\xi_H(x_i, t)$, the concentration of high affinity, bound integrins, is their number per unit current area of the cell membrane, and F_i is the force per high affinity integrin applied by the cell to the substrate.

3.2.1 Stress Fiber Formation and Contractility

Stress fiber formation is initiated by a nervous impulse or a biochemical or mechanical perturbation that triggers a signaling cascade within the cell. We model this signal, C (which may be thought of as the concentration of Ca^{2+}) as a sudden rise to unity followed by an exponential decay, given by

$$C = \exp(-t_i/\theta), \tag{3.2}$$

where θ is the decay constant and t_i is the time after the onset of the most recent activation signal. We treat the signal as uniform throughout the cell, on the basis that diffusion of the signaling ions and proteins in the cytosol is fast enough to be non-rate limiting, as determined by Pathak et al. (2011).

The formation of stress fibers is parameterized by an activation level, designated η ($0 \leq \eta \leq 1$), defined as the ratio of the concentration of the polymerized actin and phosphorylated myosin within a stress fiber bundle to the maximum concentrations permitted by the bio-chemistry. The evolution of the stress fibers at an angle ϕ to the x_1 axis is characterized by a first-order kinetic equation

$$\dot{\eta}(\phi) = \big[1 - \eta(\phi)\big]\frac{C\overline{k}_f}{\theta} - \left(1 - \frac{\sigma(\phi)}{\sigma_0(\phi)}\right)\eta(\phi)\frac{\overline{k}_b}{\theta}, \tag{3.3}$$

where the overdot denotes time-differentiation at a fixed material point in the cell. In this formula, $\sigma(\phi)$ is the tension in the fiber bundle at orientation ϕ, while $\sigma_0(\phi) = \eta\sigma_{\max}$ is the corresponding isometric stress at activation level η, with $\sigma_{\max}$ being the isometric stress at full activation ($\eta = 1$). The dimensionless constants $\overline{k}_f$ and $\overline{k}_b$ govern the rates of stress fiber formation and dissociation, respectively. Note that mechano-sensitivity is present in the depolymerization term in (1), since a tensile stress σ will reduce the rate of dissociation of stress fibers; furthermore, a stress σ equal to σ_0 eliminates stress fiber depolymerization completely.

The stress σ in stress fibers is related to the fiber contraction/extension rate $\dot{\varepsilon}$ (positive during extension) by the cross-bridge cycling between the actin and myosin filaments. The simplified (but adequate) version of the Hill-like equation employed to model these dynamics is specified as

$$\frac{\sigma}{\sigma_0} = \begin{cases} 0 & \frac{\dot{\varepsilon}}{\dot{\varepsilon}_0} < -\frac{\eta}{\overline{k}_v}, \\ 1 + \frac{\overline{k}_v}{\eta}\left(\frac{\dot{\varepsilon}}{\dot{\varepsilon}_0}\right) & -\frac{\eta}{\overline{k}_v} \leq \frac{\dot{\varepsilon}}{\dot{\varepsilon}_0} \leq 0, \\ 1 & \frac{\dot{\varepsilon}}{\dot{\varepsilon}_0} > 0, \end{cases} \tag{3.4}$$

where the rate sensitivity coefficient $\overline{k}_v$ is the fractional reduction in fiber stress upon increasing the shortening rate by $\dot{\varepsilon}$. A 2D constitutive description for the stress fiber assembly uses the axial fiber strain rate $\dot{\varepsilon}$ at angle ϕ related to the strain rate $\dot{\varepsilon}_{ij}$ by

$$\dot{\varepsilon} = \dot{\varepsilon}_{11}\cos^2\phi + \dot{\varepsilon}_{22}\sin^2\phi + \dot{\varepsilon}_{12}\sin 2\phi. \tag{3.5}$$

The average stress generated by the fibers follows from a homogenization analysis as

$$\begin{pmatrix} S_{11} & S_{12} \\ S_{21} & S_{22} \end{pmatrix} = \frac{1}{\pi}\int_{-\pi/2}^{\pi/2} \begin{pmatrix} \sigma(\theta)\cos^2\phi & \frac{\sigma(\theta)}{2}\sin 2\phi \\ \frac{\sigma(\theta)}{2}\sin 2\phi & \sigma(\theta)\sin^2\phi \end{pmatrix} \mathrm{d}\phi. \tag{3.6}$$

The constitutive description for the cell is completed by including contributions from passive elasticity, attributed to intermediate filaments of the cytoskeleton attached to the nuclear and plasma membranes. These act in parallel with the active

elements, whereupon additive decomposition gives the total stress:

$$\Sigma_{ij} = S_{ij} + \left[\frac{E_c \nu_c}{(1-2\nu_c)(1+\nu_c)} \varepsilon_{kk} \delta_{ij} + \frac{E_c}{(1+\nu_c)} \varepsilon_{ij} \right], \tag{3.7}$$

where δ_{ij} is the Kronecker delta and (for a linear response) E_c is Young's modulus for the cell and ν_c the Poisson ratio. The above equations are valid in a small or infinitesimal deformation setting; readers are referred to Deshpande et al. (2006, 2007) for the finite strain and three-dimensional generalization.

3.2.2 Focal Adhesion Model

A viable model for the formation and growth of focal adhesions must account for the interaction between adhesions and cell contractility. The Deshpande et al. (2008) model relies on the existence of two conformational states for the integrins: low and high affinity. Only the high affinity integrins interact with ligand molecules on the substrate to form adhesions. The low affinity integrins remain unbound, and mobile on the membrane. The chemical potential of the low affinity integrins at concentration ξ_L is dependent on their internal energy and configurational entropy as (Gaskell, 1973)

$$\chi_L = \mu_L + kT \ln(\xi_L / \xi_R), \tag{3.8}$$

where μ_L is their reference chemical potential, ξ_R is a reference concentration, k is the Boltzmann constant and T the absolute temperature.

For geometrical reasons, the 'straight' architecture of the high affinity integrins permits the interaction of its receptor with ligand molecules on a substrate. Thus, the high affinity integrins have additional contributions to their chemical potential, involving the energy stored due to the stretching of the integrin-ligand complexes and a term related to the mechanical work done by the stress fibers. The ensuing potential is

$$\chi_H = \mu_H + kT \ln(\xi_H / \xi_R) + \Phi(\Delta_i) - F_i \Delta_i, \tag{3.9}$$

where μ_H is the reference chemical potential for high affinity integrins and $\Phi(\Delta_i)$ is the stretch energy stored in the integrin-ligand complex. The 'straight,' high affinity state of the integrins is less stable than the 'bent' or low affinity state (McCleverty and Liddington, 2003) so that the high affinity state has the higher reference chemical potential ($\mu_H > \mu_L$). The $-F_i \Delta_i$ term in Eq. (3.9) is the mechanical work representing the change in free energy due to the stretch Δ_i of the integrin-ligand complex acted upon by the force F_i. In molecular terms this implies that the stretch of the ligand-integrin complex can stabilize the adhesion by lowering the free energy ξ_H of bound integrins. The force F_i is related to the stretch Δ_i and the stored energy Φ via the relation

$$F_i = \partial \Phi / \partial \Delta_i. \tag{3.10}$$

The work term $-F_i \Delta_i$ term in Eq. (3.9) has been identified previously by Shemesh et al. (2005) as an important constituent of the thermodynamic state of focal adhesions.

The kinetics governing the diffusion of low affinity integrins in the cell membrane is typically fast compared to all other time-scales involved (Deshpande et al., 2008; Pathak et al., 2011). Consequently, we neglect the diffusion of the low affinity integrins and the kinetics between their low and high affinity states at any location on the plasma membrane. These simplifying assumptions imply that the concentrations are given by thermodynamic equilibrium between the low and high affinity binders, i.e. by

$$\chi_H = \chi_L, \tag{3.11}$$

which specifies that the integrin concentrations are related to the force F_i via

$$\xi_H = \frac{\xi_0}{\exp(\frac{\mu_H - \mu_L + \Phi - F_i \Delta_i}{kT}) + 1}, \tag{3.12}$$

$$\xi_L = \frac{\xi_0}{\exp(-\frac{\mu_H - \mu_L + \Phi - F_i \Delta_i}{kT}) + 1}, \tag{3.13}$$

respectively, where $\xi_0 = \xi_H + \xi_L$ is the fixed, total concentration of integrins. It is evident that with decreasing $\Phi - F_i \Delta_i$ (which typically occurs when the tensile force F_i increases), the concentration ξ_H of the high affinity integrins increases due to the conversion of the low affinity integrins to their high affinity state.

To complete the thermodynamic representation it remains to specify the form of the energy $\Phi(\Delta_i)$ and the associated force F_i in the integrin-ligand complex. Rather than employing a complex interaction, such as the Lennard-Jones (1931) potential, we utilize the simplest functional form. This is a piecewise quadratic potential expressed as (Deshpande et al., 2008)

$$\Phi = \begin{cases} (1/2)\kappa_s \Delta_e^2 & \Delta_e \le \Delta_n, \\ -\kappa_s \Delta_n^2 + 2\kappa_s \Delta_n \Delta_e - (1/2)\kappa_s \Delta_e^2 & \Delta_n < \Delta_e \le 2\Delta_n, \\ \kappa_s \Delta_n^2 & \Delta_e > 2\Delta_n, \end{cases} \tag{3.14}$$

where $\gamma \equiv \Phi(\Delta_i \to \infty) = \kappa_s \Delta_n^2$ is the surface energy due to high affinity integrins, the effective stretch $\Delta_e^2 = \Delta_1^2 + \Delta_2^2$, and κ_s is the stiffness of the integrin-ligand complex. The maximum force $\kappa_s \Delta_n$ occurs at a stretch $\Delta_e = \Delta_n$. We relate the evolution of the stretch Δ_i to the displacement u_i of the material point on the cell membrane in contact with the ligand patch on the substrate as (Deshpande et al., 2008)

$$\dot{\Delta}_i = \begin{cases} \dot{u}_i, & \Delta_e \le \Delta_n \text{ or } (\frac{\partial \Phi}{\partial \Delta_e} \dot{\Delta}_e < 0), \\ 0, & \text{otherwise}, \end{cases} \tag{3.15}$$

where we assume a rigid substrate (see Deshpande et al., 2008, for the generalization to a deformable substrate as used here).

Those integrins not in contact with the ligand patch are assumed to be isolated. Namely, they are unable to interact with any ligand molecules. Accordingly, we assume that these integrins are unbounded with $\Delta_i \to \infty$ such that the interaction force $F_i = 0$ and energy $\Phi = \gamma$. Their concentrations are then given by Eqs. (3.12) and (3.13) with such values inserted.

3.2.3 Finite Element Framework

The contractility model for the cell behavior is implemented in the ABAQUS finite element model using a user UMAT subroutine that calculates the material response of the cell in terms of actin polymerization and force generation. The interfacial behavior between the cell and a substrate is implemented via the UINTER subroutine, responsible for force equilibrium of the entire cell-substrate system and focal adhesion development at the cell-substrate interface. Parameters for the contractility and focal adhesion models are calibrated using the cell-on-posts simulation presented in Sect. 3.4. Based on this calibration study the following reference material parameters are chosen, with $T = 310$ K. The modulus $E_c = 0.9$ kPa and the Poisson ratio $\nu_c = 0.3$. The reaction rate constants are $\overline{k}_f = 10$, $\overline{k}_b = 1$, $\overline{k}_v = 6$ with $\dot{\varepsilon}_0 = 3.0 \times 10^{-3}$ s^{-1}, while the maximum tension exerted by the stress fibers is $\sigma_{\max} = 15$ kPa. For the focal adhesion model, the total concentration ξ_o is taken to be 5000 integrins/μm^2, and the difference in the reference chemical potentials is taken as $\mu_H - \mu_L = 5$ kT. We choose an integrin-ligand complex stiffness $\kappa_s = 0.015$ nNm^{-1}, and the stretch at maximum force $\Delta_n = 130$ nm, giving a bond strength ∼2 pN. Throughout the simulations presented in this article these parameters are kept constant and only the substrate properties are varied.

3.2.4 Correlation Between Model Parameters and Experimental Results

Focal adhesions are imaged in experiments by staining for the protein vinculin, which directly correlates to the concentration ξ_H of the high affinity integrins. The corresponding characterizing parameter for the stress fiber distributions is not chosen so straightforwardly. Most techniques only image the dominant stress fibers. The very fine mesh-work of actin filaments is not visible when standard epifluorescence or confocal microscopes are used. Thus, to correlate the observations with the predictions we define a circular variance $\Gamma = 1 - (\bar{\eta}/\eta_{\max})$, used by Pathak et al. (2008), that provides an estimate of how tightly the stress fibers are clustered around a particular orientation. Here $\eta_{\max}$ is the maximum polymerization level, which occurs at orientation ϕ_s, while $\bar{\eta}$ is an average value defined as $\bar{\eta} \equiv 1/\pi \int_{-\pi/2}^{\pi/2} \eta \mathrm{d}\phi$.

The value of Γ varies from 0 to 1, corresponding to perfectly uniform and totally aligned distributions, respectively.

3.3 Modeling Cell Behavior on Flat Substrates of Variegated Stiffness

We first investigate the cell-substrate interaction where a single cell is adhered to a flat surface. In our simulations, we utilize isotropic material properties for the flat substrate on which the cell attaches and forms focal adhesions. The stiffness of the substrate is prescribed by its Young's modulus.

3.3.1 Finite Element Implementation

The cell behavior is investigated in a finite strain setting (i.e. the effects of geometry changes on the momentum balance and constitutive behavior through material rotations are taken into account). We implement a 3D model of the gel using 8-noded linear brick elements, and a cell composed of membrane elements of unit thickness. We choose a circular cross-section for both the gel and the cell to obviate any geometrical irregularities in the simulations. The diameter of the cell is 34 μm. The gel diameter and thickness are taken to be approximately 350 μm to emulate the experiments where a cell is laid on a relatively thick gel substrate. Simulations based on the chosen geometry show that the reaction forces in the gel substrate are negligible away from the cell; thus, the chosen setup behaves like a cell lying on an infinitely thick gel substrate.

In each simulation, we start with a quiescent, stress free cell, having no stress fibers and a negligible quantity of adhesions (there exist a few that keep the cell located in place on the gel, consistent with Eqs. (3.12) and (3.13)). To commence the simulation, we turn on the signal in Eq. (3.2) at time $t = 0$, which has the effect of causing the formation of stress fibers and focal adhesions. Progressive polymerization and depolymerization of stress fibers, the growth of focal adhesions, and the generation of contractile stress take place within the cell. This process is continued in the simulation until a steady state is reached, with a stable configuration of stress fibers, mature focal adhesions, and a constant stress at any given location in the cell.

3.3.2 Simulation Results

We vary the stiffness of the gel, characterized by its Young's modulus E from 2 to 200 kPa and record the cell behavior. We calculate the focal adhesion distribution as the normalized concentration ξ_H/ξ_o of the high affinity integrins at each node, i.e. a

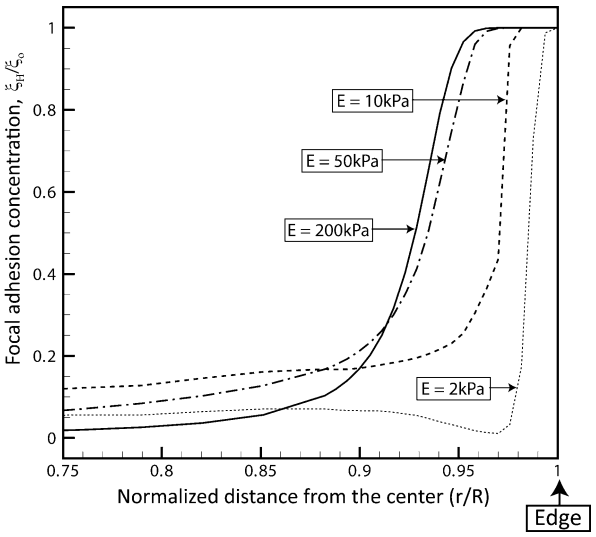

Fig. 3.1 Steady state focal adhesion distributions for a circular cell adhered to a flat gel substrate of Young's moduli varying from 2 to 200 kPa, where R is the radius of the cell

focal adhesion is taken as a region where ξ_H/ξ_o is high. The results are presented in Fig. 3.1, where axial symmetry permits the distributions to be plotted versus radial position. We find that on a relatively soft gel of $E = 2$ kPa, the cell does not develop prominent focal adhesions. However, on the stiffer gels focal adhesions develop to a much higher degree with their highest concentration at the periphery. The plot in Fig. 3.1 demonstrates that cells form larger focal adhesions on stiffer substrates, in qualitative agreement with many experimental studies, including that by Saez et al. (2005). To further elucidate this point we plot the cell total focal adhesion fraction ξ_T in steady state versus the stiffness of the substrate E in Fig. 3.2(a). Here, the cell total focal adhesion fraction ξ_T is calculated by integrating the concentration ξ_H over the entire cell area and dividing the result by the total number of integrins $\xi_o A$ on the cell membrane, where A is the area of the cell. As a result, ξ_T is the fraction of all integrins on the cell membrane that are in the high affinity state, and thus in focal adhesions. As expected, ξ_T increases for stiffer substrates, but reaches an asymptote at approximately $E = 50$ kPa. Any further rise in stiffness beyond this level does not change the overall focal adhesion distribution, a trend also apparent in Fig. 3.1.

We compute the magnitude of the cell traction applied to the substrate as $\xi_H(F_1^2 + F_2^2)^{1/2}$, and integrate this over the interface between the cell membrane and the gel to obtain a total force magnitude F_T applied by the cell to the substrate (we note here to avoid confusion that the total force vector applied by the cell to the gel is zero, but view the parameter F_T as a useful gauge of the intensity of force generation associated with the contractile machinery of the cell). We find that the total force F_T increases as the substrate stiffness E is increased, as shown in Fig. 3.2(b), but reaches an asymptote beyond $E = 50$ kPa. In addition, we also establish a linear correlation between focal adhesion assembly and force generation by plotting F_T versus ξ_T (not shown).

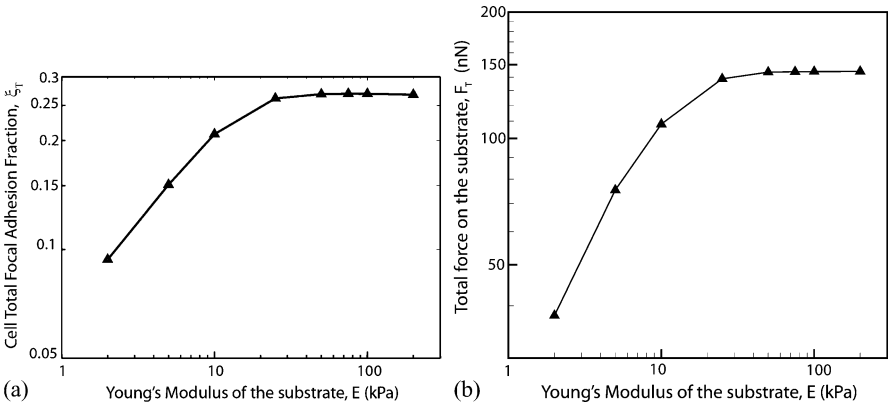

Fig. 3.2 (**a**) Cell total focal adhesion fraction F_T and (**b**) total force F_T exerted by a cell adhered to a flat gel substrate in steady state, where Young's modulus E of the gel is varied from 2 to 200 kPa

We note that the total force F_T applied by the cell to the gel is also an indicator of the degree of stress fiber development. Although we do not plot the results, we can confirm that in our simulations, cells on stiffer gels have higher average concentrations of stress fibers compared to cells on more compliant gels. Consistent with the trends in Figs. 3.1 and 3.2, the average concentration of stress fibers in a cell reaches an asymptote at a gel modulus of approximately 50 kPa.

3.4 Models of Cell Behavior on Micro-Posts

The distribution of traction forces exerted by a cell on its adhered substrate has been measured by seeding cells on a bed of micro-posts and determining the independent deflections of the posts (Tan et al., 2003; Saez et al., 2005). The isolated islands of cell-substrate interaction on post tops allow discrete measurement of tractions forces, and the size and shape of focal adhesions. In the experiments of Saez et al. (2005), the stiffness of the posts is varied and the average force per post F_{avg} exerted by the cell is recorded. This quantitative study demonstrates that the average force per post increases as the post stiffness is increased regardless of post-bed geometry or cell area. We use these measurements to test our model, and, as noted above, to calibrate it.

On top of the posts, the cell forms adhesions; the studies by Tan et al. (2003) and Chen et al. (2003) find that (a) focal adhesions, measured by vinculin staining, on top of posts near the edge of the cell are the largest, (b) posts interior to the cell have negligible focal adhesions, and (c) the focal adhesion distribution forms a horseshoe shape around the top perimeter of the posts. In addition, Tan et al. (2003) found that F_{avg} increases with the size of a cell, a behavior that can be rationalized by recognition that a larger cell pulls on more posts, so experiencing a stiffer environment.

3.4.1 Finite Element Setup for Cells on Posts

We use square cells having various areas, and model the posts as rigid circular discs of radius $a = 1$ μm constrained to move in the x_1–x_2 plane. The displacement d_i of the discs is constrained by a spring of stiffness k (SPRING1 option in ABAQUS) such that the force P_i applied by the cell is $P_i = kd_i$. We implement the adhesion between the cell and the disc surfaces by employing the user-defined interface (UINTER) option in ABAQUS, as before. Adhesions are allowed to form only where the cell is in contact with the discs. We keep the post area fraction, defined as the ratio of total surface area of the post-tops in contact with the cell to the total cell area, at approximately 25 % to match the characteristics of the post-bed used by Saez et al. (2005).

As in the simulations for cells on flat gel substrates, we commence with stress free, quiescent cells having neither stress fibers nor significant adhesions, and initiate the computation with a single signal. After transient behavior, a steady state sets in, with a constant stress state and stress fiber concentration and distribution at any point in the cell, a constant focal adhesion concentration at any point on the top of a post, and a constant deflection of the top of each post.

3.4.2 Simulation Results and Discussion

We first address simulations for a square cell of edge length $L = 30$ μm that covers an 8×8 post array.

3.4.2.1 Focal Adhesion and Stress Fiber Distribution

We consider first highly compliant posts having a spring constant $k = 2$ nN/μm. As shown in Fig. 3.3(a), a plot of the concentration of high affinity integrins in steady state, focal adhesions form a circular ring on each post with little polarization, and with relatively low densities of high affinity integrins. We interpret this to mean that the size of focal adhesions on these posts is small, even though they completely surround the tops of the posts. We implicate the very low stiffness of the posts used in this case for this behavior. Such compliant posts offer little resistance to stress fiber contractility, obviating the generation of tension in the stress fibers and allowing much depolymerization. The resulting lack of intracellular machinery in steady state is evident in the low stress fiber concentrations observed for this case, and in the lack of curvature along the edge of the cell, as depicted in Fig. 3.3(a). In Fig. 3.4(a) we show the distribution of stress fibers for this case, characterized by the parameter Γ. A modest degree of alignment of stress fibers is evident in this figure, but the significance of this is reduced by the fact that the stress fiber concentration at each point in the cell is relatively low. We note that each post top is interacting individually with the cell region that surrounds it, and there is little mechanical

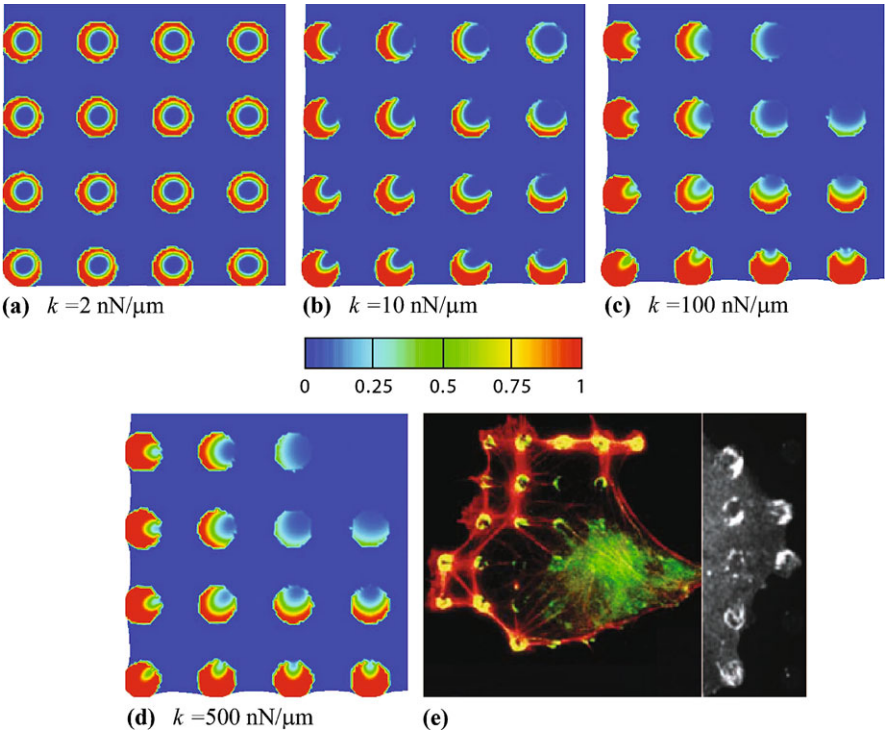

Fig. 3.3 Contour plots of focal adhesion concentration, defined by the quantity ξ_H/ξ_o, for a cell adhered in steady state to a post-bed with post stiffness (**a**) $k = 2$ nN/μm, (**b**) $k = 10$ nN/μm, (**c**) $k = 100$ nN/μm, and (**d**) $k = 500$ nN/μm. Only quarter segments of the square cells are shown. (**e**) Focal adhesion distributions on post tops from the experiments of Chen et al. (2003) and Tan et al. (2003)

communication among posts and between different locations in the cell. This feature explains the lack of polarization of the focal adhesions into a horseshoe shape on the post tops. The shape of the focal adhesion rings on the post tops and a lack of overall contractility in these simulations matches the experimental observations of Chen et al. (2003), where focal adhesions form uniformly in a ring shape on a circular substrate upon pharmacological inhibition of actomyosin contractility.

We next consider posts having a stiffness $k = 10$ nN/μm. Such posts are sufficiently stiff that the resistance they offer to cell contractility inhibits the rate of depolymerization of stress fibers, and allows the generation of higher contractile stress. As a result, the tractions applied to high affinity integrins are high enough to stabilize them, and significant focal adhesion form, as shown in Fig. 3.3(b). Note that the posts in the interior of the cell do not have significant focal adhesions, while posts near the cell perimeter have larger focal adhesions in a horseshoe shape with their open side directed towards the cell center, as in the experimental results of Chen et al. (2003), shown in Fig. 3.3(e). In these experiments, chemically boosted intracellular contractile activity causes significant stress in the cell, responsible for

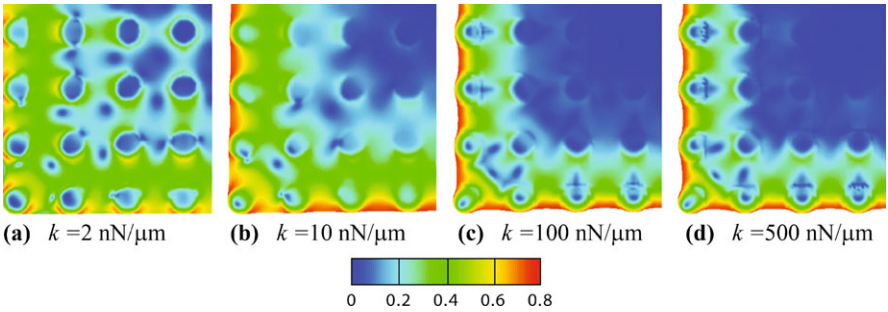

Fig. 3.4 Contour plots of the distribution of stress fiber orientations, characterized by the quantity Γ, for a cell in steady state adhered to a post-bed with post stiffness (**a**) $k = 2$ nN/μm, (**b**) $k = 10$ nN/μm, (**c**) $k = 100$ nN/μm, and (**d**) $k = 500$ nN/μm. Only quarter segments of the square cells are shown

higher focal adhesion densities near the cell periphery and the polarized horseshoe shape on individual posts. The fact that there is a significant density of contractile stress fibers is reflected in the curvature of the cell edge visible in Fig. 3.3(b). The heterogeneous nature of the cell response is more pronounced in this case than for the more compliant posts, evidenced by the degree of alignment of stress fibers shown in Fig. 3.4(b). The distribution of stress fiber orientations is almost uniform at the center of the cell, whereas they are highly aligned along the cell edge. This and other features visible in Figs. 3.3(b) and 3.4(b) indicate that posts near the cell perimeter are interacting with other perimeter posts to a significant degree via the stress fibers, and are interacting with the cell as a whole. Furthermore, the stress at the center of the cell is relatively high, only falling rapidly near the cell edges in a shear lag phenomenon. The stress gradient there is what gives rise to the horseshoe shape of the focal adhesions on posts near the cell perimeter, as the force applied by the cell to an individual post has a net resultant acting towards the open side of the horseshoe. A high, almost uniform stress at the cell center explains the relative lack of focal adhesions on posts near the cell center (Fig. 3.3(b)), as the absence of a stress gradient means that little force is being applied to the post tops in that area.

Next, we consider the simulations for posts with even higher stiffness, $k = 10$ nN/μm, with the focal adhesion distribution shown in Fig. 3.3(c). In this case, spatial gradients of stress near the cell perimeter are steeper than for more compliant posts. As a result, the concentration of focal adhesions on posts near the cell periphery is even higher than for the more compliant posts, and the horseshoe shape of the focal adhesion distribution on these posts is more distinct. Note also that the concentration of focal adhesions on posts near the center of the cell is lower than for the more compliant posts, indicating a more uniform stress there when the posts are stiff. The contractile stress and the concentration of stress fibers in the cell are greater than for the more compliant posts, as can be deduced from the higher curvature of the cell edge visible in Fig. 3.3(c). The heterogeneous nature of the response of the cell is apparent in the degree of alignment of the stress fibers, shown in Fig. 3.4(c), with an almost uniform distribution of orientations in a large patch at

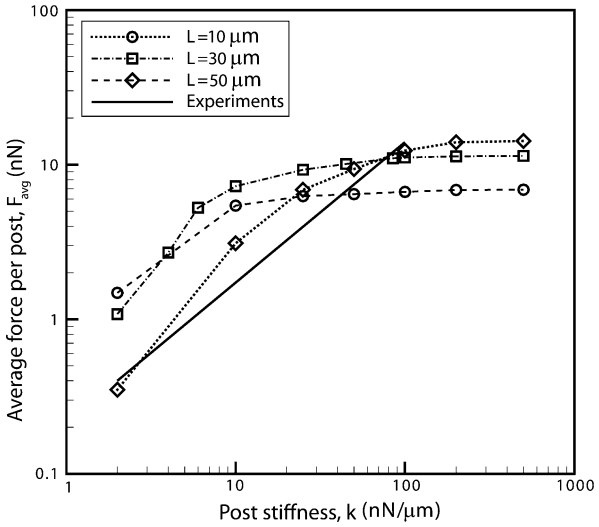

Fig. 3.5 Average force per post F_{avg} exerted by a square cell in steady state vs. post stiffness k for cells of edge lengths L

the center of the cell, and a high degree of alignment around the cell perimeter. This reflects the larger gradient of stress and stress fiber concentration near the cell edge in this case.

We find that increasing the post stiffness further to $k = 500$ nN/μm does not cause appreciable changes in the focal adhesion and stress fiber distributions, as shown in Figs. 3.3(d) and 3.4(d), respectively. Thus, the cellular response reaches an asymptote at a post stiffness of approximately $k = 100$ nN/μm. Further increases in the post stiffness above this level do not affect the cell response.

3.4.2.2 Average Force Versus Post Stiffness

We calculate the average force per post F_{avg} as the sum of the magnitude of the force exerted by the cell on each post in contact with the cell divided by the number of posts. In Fig. 3.5 we plot F_{avg} versus post stiffness k for square cells having various edge lengths. To vary cell size, we utilize square cells of edge length $L = 10$, 30 and 50 μm laid on 3×3, 8×8 and 14×14 post arrays, respectively. For each case, we vary the post stiffness from $k = 2$ nN/μm to $k = 500$ nN/μm and plot the resulting F_{avg} values in Fig. 3.5. In all cell sizes, we find a common trend between average force and post stiffness; namely, the average force per post F_{avg} increases with post stiffness, but reaches an asymptote. We also find that this trend prevails even if the post-bed parameters, such as post diameter and post density, are varied, but do not present these results here. The relationship between average force and post stiffness observed in our simulations agrees qualitatively as well as quantitatively with the experimental results of Saez et al. (2005), presented as a superimposed line in Fig. 3.5. It is this quantitative agreement that is used to justify the parameter calibration used throughout the simulations presented in this paper.

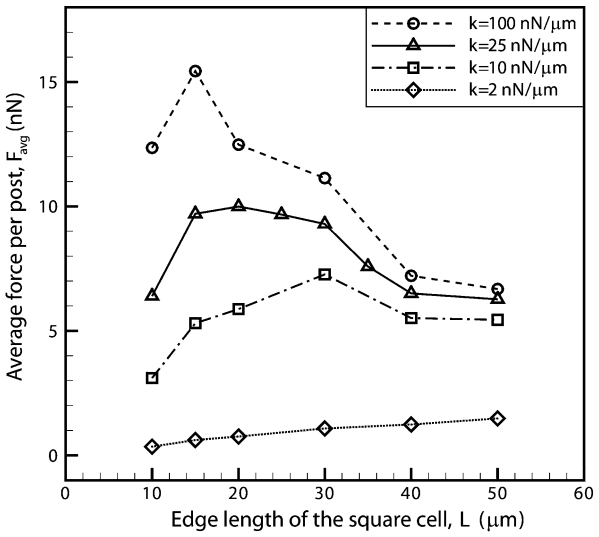

Fig. 3.6 Average force per post F_{avg} exerted by a square cell in steady state versus its edge length L plotted for post stiffness values $k = 2$, 10, 25 and 100 nN/μm

We note that the results of our simulations for cells on posts confirm that the average force generated by the cell is higher on stiffer substrates, and reaches a limit value beyond a critical value of substrate stiffness. This trend is consistent with our findings in the simulations for cells adhered on flat substrates, as presented in the previous section (Fig. 3.2(b)).

Tan et al. (2003) observed in experiments that the average force per post for a given post stiffness increases with cell size, and therefore with the number of posts to which the cell is adhered. Simulations by Deshpande et al. (2007) found the same trend, and they attributed this feature to the fact that a cell contracting on many posts senses a stiffer system than one contracting on a few posts. Deshpande et al. (2007) pointed out that this trend occurs despite the fact that many of the posts under well-spread cells engaging many posts are only lightly laden, due to the fact that these posts are in the central region of the cell where the cell stress is relatively uniform (see Fig. 3.4(c)). To further explore the effect of cell size on cellular contractility, we study how the average force per post varies with cell edge length for four post stiffnesses, with results shown in Fig. 3.6. We note that the cells engage 3×3, 4×4, 6×6, 8×8, 11×11 and 14×14 posts as they get larger. For each cell size the average force per post increases with post stiffness. Furthermore, as the smallest cell size is increased, the trend, the same for all post stiffnesses, is that the average force per post increases. In the case of the cell on the most compliant posts, this trend is monotonic. However, in all other cases, a peak in the average force per post is reached at an intermediate cell size, beyond which the average force per post falls.

The trend in which the average force per post increases with cell size, also observed by Deshpande et al. (2007), reflects the fact that a cell engaging more posts is interacting with a stiffer system. Since a stiffer environment induces in the cell a more robust cytoskeleton, and a higher level of contractile stress, the force per post goes up as the cell size increases. The trend in which the force per post declines as

the cell size increases reflects the fact that a cell engaging a larger number of posts has a larger number that are lightly laden because they are near the center of the cell in the region of uniform cell stress. Since an increasing number of posts has negligible force applied to them, the force per post goes down as the cell size increases. The results in Fig. 3.6 indicate that the former trend dominates for small cells engaging a small number of posts, but as the cell size increases, the latter trend takes over. The results in Fig. 3.6 also show that the transition point for these opposite trends depends on the stiffness of the posts. In a stiff environment, the changeover occurs at smaller cell size, whereas in a more compliant environment, a larger cell size is required for the transition.

3.5 Concluding Remarks

A biochemomechanical model is employed for modeling cell behavior in complex and diverse extracellular settings, and the effects of substrate stiffness, architecture of the substrate, and cell area are studied. Both on flat gel and micro-post substrates, cell contractility and focal adhesion assembly intensify as the stiffness of the environment is increased. The results of our simulations match key experimental data in the literature. We verify some well-established features regarding cell behavior in response to substrate stiffness-namely, (a) the intracellular force generation machinery exerts higher forces on stiffer substrates, (b) cells form larger and stronger focal adhesions on stiffer substrates, and (c) cells on stiffer substrates have more pronounced cytoskeletons in the form of higher concentrations of stress fibers. The response we have identified comes about because a stiff substrate presents resistance to the cell as it tries to contract, an effect that stabilizes a high degree of stress fiber polymerization and focal adhesion development. Such highly developed intracellular machinery then delivers a high level of traction to the substrate. We also find that monotonic increase of the stiffness of the substrate does not cause a monotonic enhancement of the cellular contractile machinery; an asymptote is reached at a critical value of substrate stiffness beyond which further enhancement of the cell contractile system ceases. Such a behavior is hinted at in the results from several experimental studies, such as that of Saez et al. (2005), but a conclusive dataset for a wide range of substrate stiffness values is currently unavailable. Our results not only agree qualitatively with many experimental findings, but have been calibrated quantitatively to the average force per post from Saez et al. (2005), where the stiffness of the posts is varied. This step enables us to assert that the cell model parameters used in our study are representative of the epithelial cells explored by Saez et al. (2005). The horseshoe focal adhesions on the post tops that we obtain in our simulations match the experimental images obtained by Tan et al. (2003) and Chen et al. (2003). Such results give us encouragement to believe that our model captures many elements of the contractile and adhesive behavior of cells, and may prove useful, eventually, in a wider setting of cell biology, medicine and disease.

Acknowledgements AP, AGE and RMM were supported by a Multi-University Research Initiative sponsored by the U.S. Army Research Office. RMM was also supported by Aberdeen University and by INM-Leibniz Institute for New Materials. VSD acknowledges the support of the Isaac Newton Trust, Trinity College, Cambridge.

References

Boudreau N, Bissell MJ (1998) Extracellular matrix signaling: integration of form and function in normal and malignant cells. Curr Opin Cell Biol 10:640–646

Chen CS, Alonso JL, Ostuni E, Whitesides GM, Ingber DE (2003) Cell shape provides global control of focal adhesion assembly. Biochem Biophys Res Commun 307:355–361

Deshpande VS, McMeeking RM, Evans AG (2006) A bio-chemo-mechanical model for cell contractility. Proc Natl Acad Sci USA 103:14015–14020

Deshpande VS, McMeeking RM, Evans AG (2007) A model for the contractility of the cytoskeleton including the effects of stress fiber formation and dissociation. Proc R Soc Lond A 463:787–815

Deshpande VS, Mrksich M, McMeeking RM, Evans AG (2008) A bio-mechanical model for coupling cell contractility with focal adhesion formation. J Mech Phys Solids 56:1484–1510

Discher DE, Janmey P, Wang Y-L (2005) Tissue cells feel and respond to the stiffness of their substrate. Science 310:1139–1143

Gaskell DR (1973) Introduction to metallurgical thermodynamics. McGraw-Hill, New York

Kong HJ, Liu J, Riddle K, Matsumoto T, Leach K, Mooney DJ (2005) Non-viral gene delivery regulated by stiffness of cell adhesion substrates. Nat Mater 4:460–464

Lennard-Jones JE (1931) Cohesion. Proc Phys Soc 43:461–482

Lo C-M, Wang H-B, Dembo M, Wang Y (2000) Cell movement is guided by the rigidity of the substrate. Biophys J 79:144–152

McCleverty CJ, Liddington RC (2003) Engineered allosteric mutants of the integrin $\alpha M\beta 2$ I domain: structural and functional studies. Biochem J 372:121–127

Paszek MJ, Zahir N, Johnson KR, Lakins JN, Rozenberg GI, Gefen A, Reinhart-King CA, Margulies SS, Dembo M, Boettiger D, Hammer DA, Weaver VM (2005) Tensional homeostasis and the malignant phenotype. Cancer Cell 8:241–254

Pathak A, Deshpande VS, McMeeking RM, Evans AG (2008) The simulation of stress fiber and focal adhesion development in cells on patterned substrates. J R Soc Interface 5:507–524

Pathak A, McMeeking RM, Evans AG, Deshpande VS (2011) An analysis of the cooperative mechano-sensitive feedback between intracellular signaling, focal adhesion development, and stress fiber contractility. J Appl Mech 78:041001

Saez A, Buguin A, Silberzan P, Ladoux B (2005) Is the mechanical activity of epithelial cells controlled by deformations or forces? Biophys J 89:L52–L54

Schwartz MA, Ginsberg MH (2002) Networks and crosstalk: integrin signaling spreads. Nat Cell Biol 4:E65–68

Shemesh T, Geiger B, Bershadsky AD, Kozlov MM (2005) Focal adhesions as mechanosensors: a physical mechanism. Proc Natl Acad Sci USA 102:12383–12388

Tan JL, Tien J, Pirone DM, Gray DS, Bhadriraju K, Chen CS (2003) Cells lying on a bed of microneedles: an approach to isolate mechanical force. Proc Natl Acad Sci USA 100:1484–1489

Wei Z, Deshpande VS, McMeeking RM, Evans AG (2008) Analysis and interpretation of stress fiber organization in cells subject to cyclic stretch. J Biomech Eng 130:031009

Yeung T, Georges PC, Flanagan LA, Marg B, Ortiz M, Funaki M, Zahir N, Ming W, Weaver V, Janmey PA (2005) Effects of substrate stiffness on cell morphology, cytoskeletal structure, and adhesion. Cell Motil Cytoskelet 60:24–34

Part II
Muscle Mechanics

Chapter 4
A Mathematical Approach for Studying Ca^{2+}-Regulated Smooth Muscle Contraction

Saeil C. Murtada and Gerhard A. Holzapfel

Abstract Smooth muscle is found in various organs. It has mutual purposes such as providing mechanical stability and regulating organ size. To better understand the physiology and the function of smooth muscle different experimental setups and techniques are available. However, to interpret and analyze the experimental results basic models of smooth muscle are necessary. Advanced mathematical models of smooth muscle contraction further allow, to not, only investigate the experimental behavior but also to simulate and predict behaviors in complex boundary conditions that are not easy or even impossible to perform through *in vitro* experiments. In this chapter the characteristic behaviors of vascular smooth muscle, specially those relevant from a biomechanical point of view, and the mathematical models able to simulate and mimic those behaviors are reviewed and studied.

4.1 Introduction

Smooth muscle has an important role in hollow organs where it determines the size and the wall tension of the organ. In blood vessels the smooth muscle has a critical role in regulating the diameter and the flow resistance which affect the blood pressure.

To increase the understanding of both basic and clinical/pathophysiological processes of smooth muscle, well defined chemomechanical models which couple

S.C. Murtada (✉)
Division Genetic Physiology, Department of Physiology and Pharmacology, Karolinska Institutet, von Eulers väg 8, 177 71 Stockholm, Sweden
e-mail: saeil.murtada@ki.se

G.A. Holzapfel
Institute of Biomechanics, Center of Biomedical Engineering, Graz University of Technology, Kronesgasse 5-I, 8010 Graz, Austria
e-mail: holzapfel@tugraz.at

G.A. Holzapfel
Department of Solid Mechanics, School of Engineering Sciences, Royal Institute of Technology (KTH), Osquars Backe 1, 100 44 Stockholm, Sweden

G.A. Holzapfel, E. Kuhl (eds.), *Computer Models in Biomechanics*,
DOI 10.1007/978-94-007-5464-5_4,

chemical activation with mechanical contraction and relaxation are needed. The properties of the passive arterial wall have been thoroughly explored both in structural and mechanical behavior, and there are models available to capture these behaviors (Holzapfel et al., 2000; Holzapfel and Ogden, 2010; Schriefl et al., 2012). The properties of the active tone, which mainly originate from the active smooth muscle, have been less explored in both structure and contractile behavior, and there is a pressing need for well-defined models of the smooth muscle to better understand its mechanical properties.

In the following sections the characteristic smooth muscle behavior is described and followed up with some approaches of modeling smooth muscle contraction and active tension development. The main part of this chapter reviews and analyzes a certain mechanochemical modeling approach for smooth muscle (Murtada et al., 2010a, 2010b, 2012) which is based on structural observations and experimental data. It is the single model found in the literature which is able to simulate a realistic behavior of both smooth muscle active tension development at different stretches and a realistic muscle length behavior during isotonic quick-releases.

4.2 Smooth Muscle Behavior

Smooth muscle behaves differently in both activation and contraction and has a different underlying structure compared to skeletal and cardiac muscles. Therefore, it is important, when modeling and studying smooth muscle behavior, to understand and consider the characteristic behaviors and parameters relevant for smooth muscle contraction.

4.2.1 Myosin Kinetics

Smooth muscle contraction is regulated through phosphorylation and dephosphorylation of the myosin regulatory light-chains (MRLC) which is governed by two main enzyme activities, the myosin light-chain kinase (MLCK) and the myosin light-chain phosphatase (MLCP). By changing the membrane potential through depolarization, certain voltage-operated Ca^{2+} channels are opened, allowing an influx of Ca^{2+} which increases the cytoplasmic calcium. When the cytoplasmic intracellular calcium increases through an influx of Ca^{2+} from the extracellular matrix, the Ca^{2+} bind to the messenger protein calmodulin (CaM), which activates the MLCK. An alternative way to increase the cytoplasmic intracellular Ca^{2+} is through agonist stimulation, e.g., histamine which attaches to G protein coupled receptors (GPCR) that activate phospholipase C (PLC) which in turn induces inositol 1,4,5-triphosphate ($InsP_3$) production and Ca^{2+} release from the sarcoplasmic reticulum (SR) (Somlyo and Somlyo, 2002), see also Fig. 4.1.

When the myosin is phosphorylated, it can attach to the smooth muscle actin filaments through load-bearing cross-bridges that are able to perform power-strokes

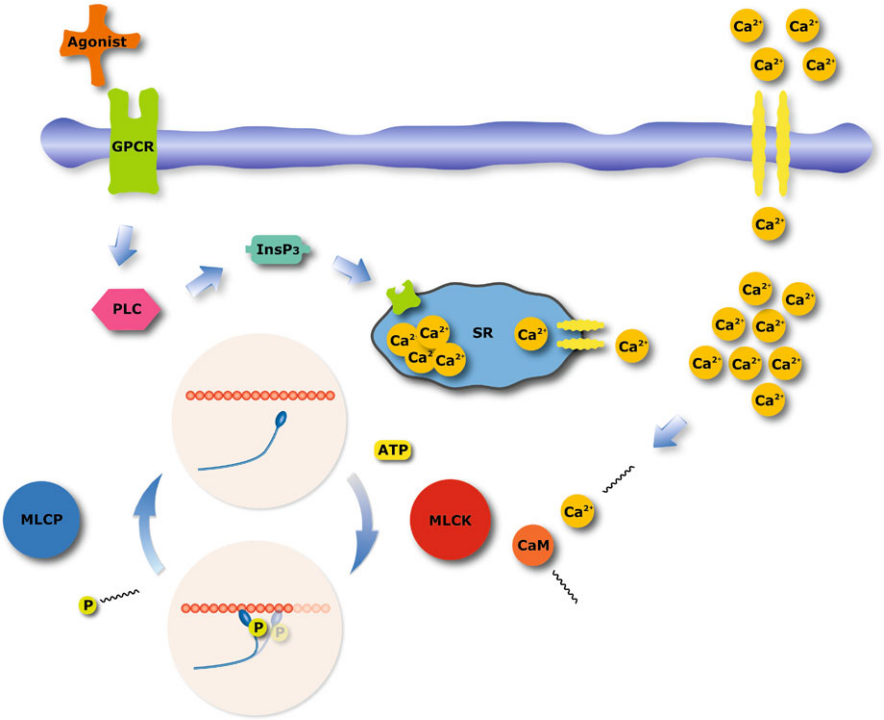

Fig. 4.1 Signaling pathways for Ca^{2+}-regulated myosin phosphorylation. Myosin phosphorylation/dephosphorylation is regulated by myosin light-chain kinase (MLCK) and myosin light-chain phosphatase (MLCP). MLCK is activated by a calmodulin (CaM)–Ca^{2+} complex which dependents on the level of intracellular [Ca^{2+}]. The intracellular Ca^{2+} may be influenced in different ways. Membrane depolarization and agonist stimulation through G protein coupled receptors (GPCR); during membrane depolarization certain channels on the cell membrane open resulting in an influx of Ca^{2+}. During agonist stimulation the GPCR activate phospholipase (PLC), which induces inositol 1,4,5-triphosphate ($InsP_3$) production and releases Ca^{2+} from the sarcoplasmic reticulum (SR)

through ATP hydrolysis, similar as in skeletal muscle, causing muscle contraction. The MLCP activity, which governs the dephosphorylation of the myosin regulatory light-chains, has an effect on the Ca^{2+} sensitivity for the MRLC phosphorylation. There are several pathways inhibiting the MLCP, such as Rho-Rho kinase and protein kinase C. However, here we are not considering variations in MLCP activity. Smooth muscle is able to maintain active tension while the myosin phosphorylation decreases. An explanation for this phenomenon was hypothesized by introducing an attached, non-cycling (or slow-cycling), dephosphorylated cross-bridge (also known as latch-bridge or latched cross-bridge), see Dillon et al. (1981). The introduction of such as latched cross-bridge also explains the different contractile behaviors observed for isotonic quick-releases performed at different time after isometric activation (Dillon et al., 1981).

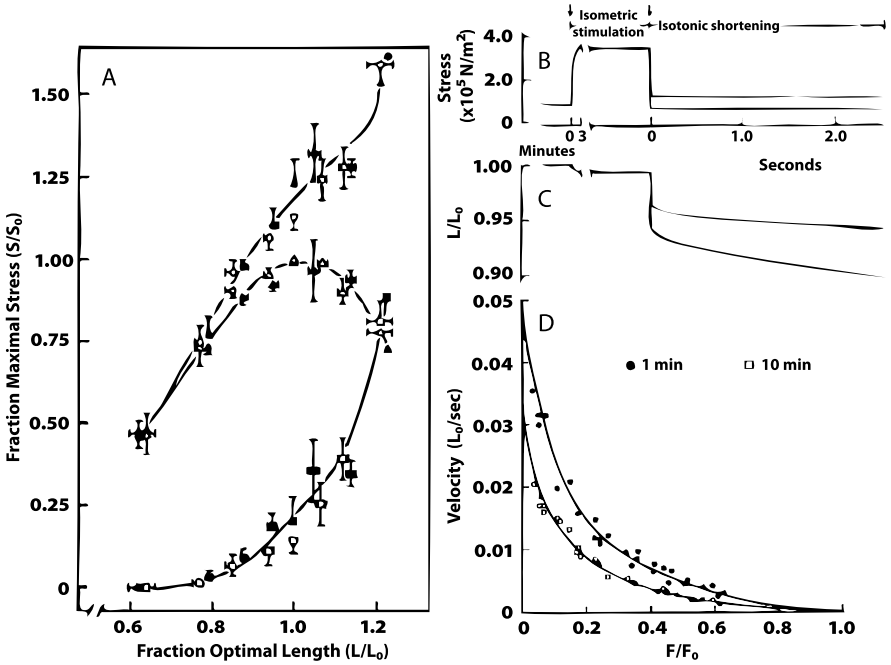

Fig. 4.2 **A**: length-tension behaviors of swine carotid media, where maximal steady-state active tension is obtained at a certain optimal length L_0. The *bottom curve* is the passive behavior, the *middle curve* is the active behavior and the *top curve* is the total behavior (passive and active) (Kamm et al., 1989). **B** and **C**: active stress development and stretch behavior during isometric stimulation and isotonic shortening for two different after-loads (Dillon et al., 1981). **D**: two force-velocity curves for isotonic quick-releases measured at 1 min and 10 min after isometric contraction at optimal length (Dillon et al., 1981)

4.2.2 Length-Tension Relationship

Smooth muscle is able to generate active tension over a broad range of muscle lengths. The active length-tension relationship has a parabolic behavior with maximal active tension at an optimal muscle length larger than the slack length, see Fig. 4.2A. In addition, Figs. 4.2B and C show the respective active stress development and stretch behavior during isometric stimulation and isotonic shortening for two different after-loads.

The origin of the active length-tension behavior, also found in skeletal muscle, is still not clearly distinguished but there are some hypothesis. One hypothesis is that the agonist sensitivity may be dependent on the stretch of the smooth muscle (Rembold and Murphy, 1990b). When the $[Ca^{2+}]$ was measured for the same concentration of agonist but at different muscle stretches, it was found that the magnitude of initial behavior of $[Ca^{2+}]$ function was different for different muscle stretches. Agonist stimulation (histamine, noradrenalin and so on) activates G protein-related pathways which leads to an increase in intracellular $[Ca^{2+}]$ to be different from

the direct membrane depolarizing stimulation (e.g., potassium) pathway, which also leads to an increase in intracellular [Ca^{2+}]. It should be noted that the length-tension relationship in smooth muscle is obtained for both membrane depolarization and agonist stimulation. A more plausible hypothesis is that the length-tension relationship may originate from the structural rearrangements within the smooth muscle contractile unit, when stretched. This would influence the filament overlap between the actin and myosin filaments in a smooth muscle contractile unit which has a direct relation to the number of attached cross-bridges, and hence the active tension produced by the smooth muscle. A connection between the length of the contractile unit (sarcomere) and the length-tension behavior in muscle has been hypothesized for a long time (Gordon et al., 1966).

4.2.3 Force-Velocity Relationship

The importance of the chemical and mechanical model combination is demonstrated when it comes to modeling the characteristic force-(shortening) velocity relationship of muscle. When the isotonic shortening velocity is measured for different forces (after-loads) a hyperbolic relationship of the force and the shortening velocity is obtained (Woledge et al., 1985). When extracting the force-velocity relationship, two certain times are of importance: (i) the time at which the quick-release is performed, i.e. the amount of time of isometric contraction before the quick-release, and (ii) the time at which the velocity is measured during the isotonic contraction.

When the force-velocity relationship is extracted at different time of isotonic quick-release, the relationship changes. The shortening velocity is higher when the quick-release is performed at an early stage of the isometric contraction rather than at a later stage, see Fig. 4.2D. This behavior supports the hypothesis of non-cycling latch cross-bridges which are dominant at a later stage of an isometric contraction.

4.2.4 Smooth Muscle Modeling

By assuming the well-established three-element Hill muscle characteristic, as described by Fung (1970) for smooth muscle, the smooth muscle contractile unit is represented by an elastic serial element and a contractile element. The active tension produced by the smooth muscle depends on two main principal parameters: (i) the number of attached load-carrying cross-bridges, and (ii) the (average) elastic elongation of the attached cross-bridges, both phosphorylated and dephosphorylated (cf. Rachev and Hayashi, 1999; Yang et al., 2003; Stålhand et al., 2008; Murtada et al., 2010a).

The kinetics of the smooth muscle myosin phosphorylation, which regulates the activation of smooth muscle contraction, can be used to define the number of attached load-carrying cross-bridges. The kinetics of myosin phosphorylation and

the number of load-bearing cross-bridges have been modeled through different approaches, see, e.g., Peterson (1982); Kato et al. (1984); Hai and Murphy (1988). In the myosin kinetics model by Hai and Murphy (1988) the latched cross-bridge was incorporated, and the myosin is described in four different functional states: (M) unattached and dephosphorylated, (Mp) unattached and phosphorylated, (AMp) attached and phosphorylated, (AM) attached and dephosphorylated. The two states where the myosin forms a cross-bride between the actin filament which can carry load are the attached states, AMp and AM. These functional states are coupled through different rate constants, where some can be related to the phosphorylating MLCK activity and some to dephosphorylating MLCP activity.

The average elastic elongation of the attached cross-bridges in the smooth muscle contractile unit is a key parameter to model the tension development in smooth muscle. It corresponds to the elastic serial element in the Hill muscle model. The average elastic elongation of the attached cross-bridges depends on the total deformation applied on the smooth muscle contractile unit and the sliding of actin and myosin filaments, which could be related to the contractile element in the Hill muscle model. It is necessary to model both the filament sliding and the average elastic elongation of the attached cross-bridges to simulate the length change and the tension development during muscle contraction. Among the smooth muscle models available in the literature there are some that also considers the filament sliding behavior to describe the active tension development and the total deformation of the smooth contractile unit (cf. Stålhand et al., 2008; Murtada et al., 2010a).

4.3 The Chemomechanical Response in Smooth Muscle—Results

In this section the modeling approach by Murtada et al. (2010a, 2010b, 2012) is briefly reviewed. This is an approach that is able to simulate both the length-tension and the force-velocity behavior of smooth muscle in addition to muscle contraction and relaxation regulated by $[Ca^{2+}]_i$.

In the work by Murtada et al. (2010a, 2010b, 2012), the model by Hai and Murphy (1988) was used to simulate the kinetics of the myosin functional states and the fraction of attached cross-bridges.

4.3.1 Cross-Bridge Kinetics Model

The active force produced by the smooth muscle is dependent on the number of attached cross-bridges in a smooth muscle contractile unit. The kinetics of attached cross-bridges is regulated by the MLCK and MLCP activity, which can be described by the cross-bridge kinetics model by Hai and Murphy (1988). Chemical kinetics

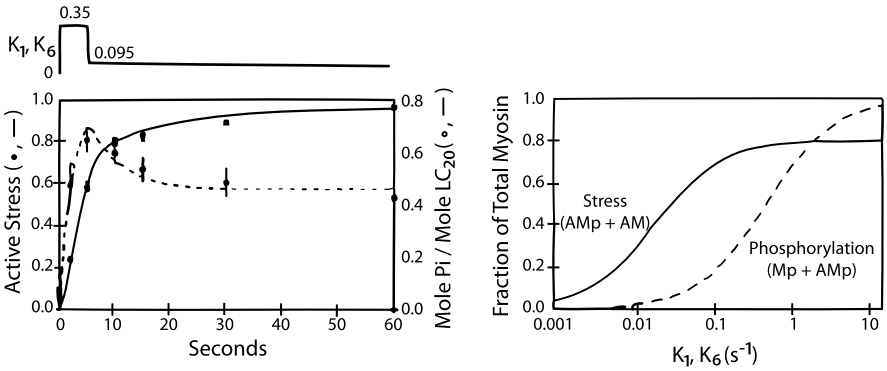

Fig. 4.3 *Left*: fitting results with the model by Hai and Murphy (1988) where the active stress is $n_{\mathrm{AMp}} + n_{\mathrm{AM}}$ and the myosin phosphorylation is $n_{\mathrm{Mp}} + n_{\mathrm{AMp}}$. The phosphorylating reaction rates k_1 and k_6 were set to 0.35 s^{-1} for 5 s followed by 0.085 s^{-1}. The other reaction rates were set to $k_2 = k_5 = 0.1$ s^{-1}, $k_4 = 0.11$ s^{-1}, $k_3 = 0.44$ s^{-1} and $k_7 = 0.005$ s^{-1}. *Right*: steady-state values of the sum of fractions $n_{\mathrm{AMp}} + n_{\mathrm{AM}}$ and $n_{\mathrm{Mp}} + n_{\mathrm{AMp}}$ for different values of the phosphorylating reaction rates k_1 and k_6 (Hai and Murphy, 1988)

can be summarized by the following system of differential equations, i.e.

$$\frac{\mathrm{d}}{\mathrm{d}t}\begin{bmatrix} n_{\mathrm{M}} \\ n_{\mathrm{Mp}} \\ n_{\mathrm{AMp}} \\ n_{\mathrm{AM}} \end{bmatrix} = \begin{bmatrix} -k_1 & k_2 & 0 & k_7 \\ k_1 & -(k_2+k_3) & k_4 & 0 \\ 0 & k_3 & -(k_4+k_5) & k_6 \\ 0 & 0 & k_5 & -(k_6+k_7) \end{bmatrix} \begin{bmatrix} n_{\mathrm{M}} \\ n_{\mathrm{Mp}} \\ n_{\mathrm{AMp}} \\ n_{\mathrm{AM}} \end{bmatrix}, \tag{4.1}$$

where n_{M}, n_{Mp}, n_{AMp} and n_{AM} are fractions of the myosin functional states M, Mp, AMp, AM, with the constraint $n_{\mathrm{M}} + n_{\mathrm{Mp}} + n_{\mathrm{AMp}} + n_{\mathrm{AM}} = 1$, $n_{\mathrm{i}} \geq 0$ and $k_1, \ldots, k_7$ are reaction rates describing the transition between the different functional states. Hence, the reaction rates k_1 and k_6 represents the phosphorylation of M to Mp and AM to AMp by the MLCK activity and the reaction rates k_2 and k_5 represents the dephosphorylation of Mp to M and AMp to AM by the MLCP activity. The reaction rates k_3 and k_4 represents the attachment and detachment of the cycling phosphorylated cross-bridges and the reaction rates k_7 represents the detachment of the latch-bridges. The phosphorylating reaction rates k_1 and k_6 can be coupled to the internal and also the external $[Ca^{2+}]$. Figure 4.3 shows the evolution of the different fraction of the functional states with time using the model by Hai and Murphy (1988).

When assuming maximal stimulated activation the phosphorylating MLCK activity can be related and coupled to the extracellular $[Ca^{2+}]$. In Murtada et al. (2010a) a Michaelis–Menten kinetics characteristic of the MLCK activity was implemented. The rate constants k_1 and k_6 are expressed as

$$k_1 = k_6 = \frac{[\mathrm{CaCaM}]^2}{[\mathrm{CaCaM}]^2 + K_{\mathrm{CaCaM}}^2}, \qquad [\mathrm{CaCaM}] = \alpha\left[\mathrm{Ca}^{2+}\right]_{\mathrm{e}}, \tag{4.2}$$

where [CaCaM] is the concentration of the calcium-calmodulin complex, K_{CaCaM} is the half-activation constant, α is a positive constant and $[\mathrm{Ca}^{2+}]_{\mathrm{e}}$ is the external calcium concentration. In (4.2), $[\mathrm{Ca}^{2+}]_{\mathrm{e}}$ is not a function of time and the MLCK reaction rates are constant values.

The MLCK-activity can also be related to the intracellular $[\mathrm{Ca}^{2+}]$ by using the first and fourth equations from (4.1) and setting $k_1 = k_6$ and $k_2 = k_5$. Thus (Murtada et al., 2010a),

$$k_1 = k_6 = \frac{k_2(n_{\mathrm{Mp}} + n_{\mathrm{AMp}}) - (\frac{\mathrm{d}}{\mathrm{d}t} n_{\mathrm{M}} + \frac{\mathrm{d}}{\mathrm{d}t} n_{\mathrm{AM}})}{n_{\mathrm{M}} + n_{\mathrm{AM}}}, \tag{4.3}$$

which in steady-state reduces to

$$k_1 = k_6 = \frac{k_2\,\mathrm{Phos}}{1 - \mathrm{Phos}}, \tag{4.4}$$

where $\mathrm{Phos} = (n_{\mathrm{Mp}} + n_{\mathrm{AMp}})$ is the fraction of phosphorylated cross-bridges (Rembold and Murphy, 1990a). The relationship between intracellular $[\mathrm{Ca}^{2+}]$ and Phos was estimated in swine carotid SM by measuring aequorin light signal into a sigmoidal function, i.e.

$$\mathrm{Phos} = -0.04 + \frac{0.686}{1 + 10^{-[3.645(0.004[\mathrm{Ca}^{2+}]_{\mathrm{i}} - 6.018) + 18.92]}}, \tag{4.5}$$

where $[\mathrm{Ca}^{2+}]_{\mathrm{i}}$ is the intracellular calcium concentration (Rembold and Murphy, 1990a). In a similar approach as for the external calcium concentration $[\mathrm{Ca}^{2+}]_{\mathrm{e}}$ in (4.2), the MLCK-activity can be related to the intracellular calcium concentration $[\mathrm{Ca}^{2+}]_{\mathrm{i}}$ according to

$$k_1 = k_6 = \varepsilon \frac{[\mathrm{Ca}^{2+}]_{\mathrm{i}}^{h}}{[\mathrm{Ca}^{2+}]_{\mathrm{i}}^{h} + (\mathrm{ED}_{50})^{h}}, \tag{4.6}$$

where ε is a fitting parameter describing the maximal MLCK activity, h is a parameter related to the steepness of the relationship and ED_{50} is the half-activation constant for $[\mathrm{Ca}^{2+}]_{\mathrm{i}}$ to MLCK.

Through these approaches the external and intracellular calcium concentrations can be coupled to the fraction of the attached cross-bridges $n_{\mathrm{AMp}} + n_{\mathrm{AM}}$ by fitting the chemical parameters against dose-response relationships (Murtada et al., 2010a) or by comparing to myosin phosphorylation data (Murtada et al., 2010b, 2012).

4.3.2 Mechanical Model of the Smooth Muscle Contractile Unit

To introduce a description of the average elastic elongation of the attached cross-bridges in a smooth muscle contractile unit, and a related framework of the filament sliding evolution law to simulate filament sliding during contraction and relaxation, a mechanical model is necessary.

4.3.2.1 Mechanical Framework

In the recent works by Murtada et al. (2010a, 2010b, 2012) a description of a smooth muscle contractile unit based on structural observations (Herrera et al., 2005) and filament sliding theory was presented. The model of the smooth muscle contractile unit consists of two thin actin filaments, each with a certain length, and one thick myosin filament, with a certain length, which are overlapped. The actin filaments are organized on each side of the myosin filament from which the filament overlap L_o can be distinguished. Based on the Hill's muscle model, the length-change in a smooth muscle contractile unit is described by the relative actin and myosin filament sliding u_{fs} caused by the phosphorylated cycling cross-bridges or by an external load/deformation, and the elastic elongation u_e of the attached cross-bridges. Hence, the stretch of a contractile unit with reference length L_{CU} can be expressed as

$$\lambda = \frac{l_{CU}}{L_{CU}} = \frac{L_{CU} + u_{fs} + u_e}{L_{CU}}, \tag{4.7}$$

where l_{CU} is the deformed length of a contractile unit. Note that u_{fs} is denoted positive in extension. When looking at a half contractile unit, the average elastic elongation of the attached cross-bridges can be described by the average force acting on the contractile unit and the total elastic stiffness from all the attached cross-bridges. Thus,

$$\frac{u_e}{2} = \frac{\frac{P_a}{N_{CU}}}{(n_{AMp} + n_{AM})\frac{L_o}{\delta} E_{cb}}, \tag{4.8}$$

where P_a is the measurable active (averaged) first Piola-Kirchhoff stress (engineering stress), N_{CU} is the number of contractile units per unit area in the reference configuration, δ is the average distance between the cross-bridges, $(n_{AMp} + n_{AM})L_o/\delta$ is the total number of the attached cross-bridges and E_{cb} is the elastic stiffness of a single phosphorylated/dephosphorylated cross-bridge with the unit force per length. Together with Eq. (4.7) the active stress P_a can be derived as a function of the filament sliding u_{fs} and the stretch λ, i.e.

$$P_a = \mu_a \bar{L}_o (n_{AMp} + n_{AM})(\lambda - \bar{u}_{fs} - 1), \tag{4.9}$$

where $\mu_a = L_{CU}^2 E_{cb} N_{CU}/(2\delta)$ is a stiffness constant, $\bar{u}_{fs} = u_{fs}/L_{CU}$ is the normalized filament sliding and $\bar{L}_o = L_o/L_{CU}$ is the normalized filament overlap.

4.3.2.2 Evolution Law of Filament Sliding

The normalized filament sliding $\bar{u}_{fs}$ depends on the mechanical state (contraction and relaxation) of the smooth muscle contractile unit. During muscle contraction, $\bar{u}_{fs}$ is driven by the difference of the internal force of the cycling phosphorylated cross-bridges (AMp) and any external force acting on the contractile unit. During

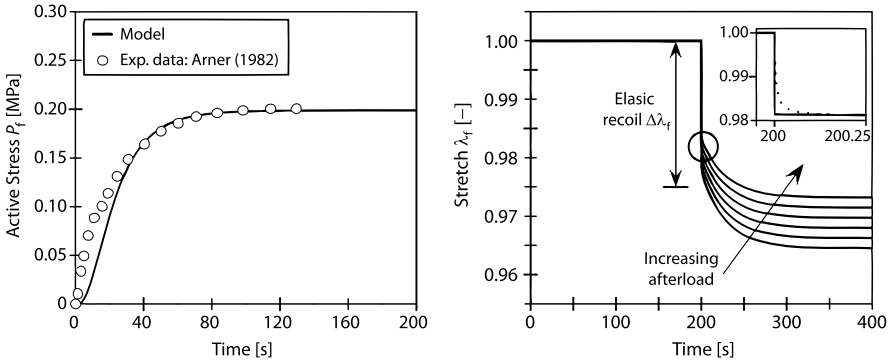

Fig. 4.4 *Left*: fitting results of the active stress development ($P_f = P_a$) using the model of Murtada et al. (2010a), with parameter values $\mu_a \bar{L}_o = 4.5$ MPa, $\eta = 60.0$ MPa s, $\kappa = 0.93$ MPa and $\mu_p = 0.90$ MPa. *Right*: isotonic stretch behavior ($\lambda_f = \lambda$) for different isotonic after-loads. The plot at the *top right corner* is an enlargement of the *encircled region* for a certain after-load (Murtada et al., 2010a). Compare with the experimental results presented in Figs. 4.2B and 4.2C

muscle relaxation (extension), $\bar{u}_{fs}$ is driven by the resulting force of the external force acting on the contractile unit, and the internal force from all the attached cross-bridges (AMp, AM). The evolution law of $\bar{u}_{fs}$ is summarized as an active dashpot where the normalized filament sliding velocity $\dot{\bar{u}}_{fs}$ is proportional to the difference of the internal force P_c and the external active force P_a such as

$$\eta \dot{\bar{u}}_{fs} = P_c - P_a, \tag{4.10}$$

with

$$P_c = \begin{cases} \kappa n_{AMp}, & \text{for } P_a < \kappa n_{AMp}, \\ P_a, & \text{for } \kappa n_{AMp} \le P_a \le \kappa (n_{AMp} + n_{AM}), \\ \kappa (n_{AMp} + n_{AM}), & \text{for } P_a > \kappa (n_{AMp} + n_{AM}), \end{cases} \tag{4.11}$$

where η is a positive material parameter and κ is a parameter related to the average driving/resisting force of the attached cycling and non-cycling cross-bridges (AMp, AM).

The material parameters were fitted to isometric and isotonic contraction data performed on intact smooth muscle taenia coli (Arner, 1982), resulting to $\mu_a \bar{L}_o = 4.5$ MPa, $\eta = 60.0$ MPa s, $\kappa = 0.93$ MPa and $\mu_p = 0.90$ MPa (the parameter μ_p is the shear modulus of the passive matrix material of the smooth muscle cells and the intermixed fibrous components).

The model was able to predict the active tension development during isometric contraction and a realistic behavior of the muscle length change during isotonic contraction for different after-loads, see Fig. 4.4. However, with the current description of the $\bar{u}_{fs}$ evolution law and the constant filament overlap, the model is not able to predict the nonlinear behavior of the length-tension and the force-(shortening) velocity behavior.

4.3.3 Length-Tension and Force-Velocity Relationships

The ability for smooth muscle to produce active tension over a broad range of muscle lengths, with a maximal active tension development at an optimal muscle length, is an important characteristic to capture when simulating active smooth muscle contraction under large deformation. We have worked out the modeling of the length-tension behavior through two different approaches, briefly reviewed here. The model of Murtada et al. (2010a) served as a basis.

In the first approach, the effect of the intracellular calcium concentration $[Ca^{2+}]_i$ and the dispersion of contractile fibers in smooth muscles was investigated (Murtada et al., 2010b). In the second approach, the effect of filament overlap and filament sliding behavior in the smooth muscle contractile unit was analyzed (Murtada et al., 2012).

4.3.3.1 Agonist Sensitivity and Dispersion of Contractile Fibers

In the first approach of Murtada et al. (2010b), two experimental studies of smooth muscle were used to analyze stretch-dependent agonist sensitivity and the dispersion effects of contractile fibers in smooth muscles, see Fig. 4.5. This was then used as a basis for studying the smooth muscle length-tension behavior.

The intracellular calcium measurements at different muscle lengths was coupled with the Hai and Murphy reaction rates k_1 through Eqs. (4.4) and (4.5). The smooth muscle contractile units were modeled as in Murtada et al. (2010a) with an equivalent evolution law for the filament sliding $\bar{u}_{\mathrm{fs}}$ and a constant filament overlap. The passive components in the surrounding matrix was modeled by elastin and one family of collagen fibers aligned along the main direction of the contractile units. The neo-Hookean material was used to model elastin and an anisotropic exponential function was used to model the anisotropic response (Holzapfel et al., 2000). The passive stress P_{p} of the surrounding matrix was derived as

$$P_{\mathrm{p}} = \mu_{\mathrm{p}}\left(\lambda - \frac{1}{\lambda^2}\right) + 2c_1\lambda\exp\left[c_2\left(\lambda^2-1\right)^2\right]\left(\lambda^2-1\right), \tag{4.12}$$

where λ denotes the stretch in the loading direction and μ_{p}, c_1 and c_1 are material parameters. The passive material parameters $(\mu_{\mathrm{p}}, c_1, c_2)$ were estimated by comparing the simulated stress-stretch behavior P_{p} through Eq. (4.12) with the passive length-tension experimental behavior of a carotid media (Kamm et al., 1989), with the results of $\mu_{\mathrm{p}} = 1680$ Pa, $c_1 = 5040$ Pa and $c_2 = 0.20$ Pa.

The contractile unit orientation dispersion was modeled by introducing an orientation density function $\rho(\theta, \gamma)$ with rotational symmetry as a function of the angle θ and the parameter γ which describes the shape of the density function. Hence, the active stress P_{a} was expressed as

$$P_{\mathrm{a}} = \mu_{\mathrm{a}}\bar{L}_{\mathrm{o}}(n_{\mathrm{AMp}} + n_{\mathrm{AM}})\frac{\lambda^{\star} + \bar{u}_{\mathrm{fs}} - 1}{\lambda^{\star}}\left[\chi\left(\lambda - \frac{1}{\lambda^2}\right) + (1-3\chi)\lambda\right], \tag{4.13}$$

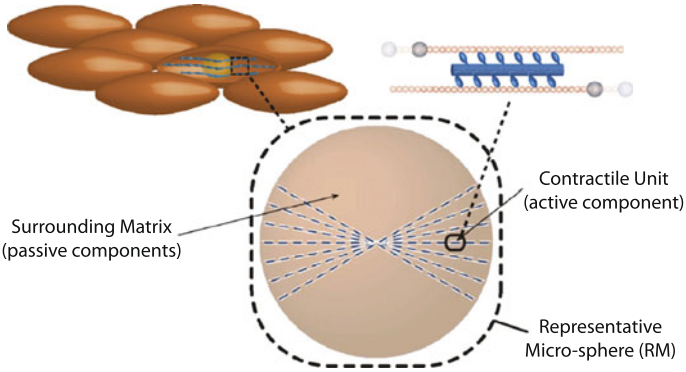

Fig. 4.5 According to Murtada et al. (2010b), smooth muscle cells are modeled through 'representative micro-spheres' which are divided into active and passive components. The active component is defined by the contractile units that are oriented in different directions and with a certain orientation density. The passive component is modeled by elastin and collagen fibers aligned in the main direction of the contractile units

where $\lambda^{\star} = [\lambda^2 + 2\chi(\lambda^{-1} - \lambda^2)]^{1/2}$, and $\chi \in [0, 1/3]$ is a dispersion parameter of the form

$$\chi = \pi \int_0^{\pi/2} \rho(\theta, \gamma) \sin^3 \theta \mathrm{d}\theta, \tag{4.14}$$

(cf. Gasser et al., 2006). For a detailed description of the choice and fitting of the orientation density function ρ see Murtada et al. (2010b).

The material parameters were estimated to fit the experimental data of active isometric tension development performed at two different muscle stretches, $\mu_a \bar{L}_o = 22.96$ MPa, $\eta = 2.215$ GPa s, $\kappa = 0.451$ MPa and $\chi = 0.016$. To study the effect of different orientation density functions ρ, the simulation was repeated for different values of γ, see Fig. 4.6.

When studying the length-tension behavior by modeling the stretch-dependent agonist sensitivity and the contractile unit orientation density function in smooth muscle, it was found that agonist sensitivity had a more significant effect on the length-tension behavior than the dispersion of the contractile units. The stretch-dependent agonist sensitivity could alone explain the length-tension behavior at the two studied muscle stretches. However, the $[Ca^{2+}]_i$ transient was only studied at two muscle stretches and it would be more convincing to study the agonist-sensitivity in smooth muscle with a more detailed set of experimental data of the $[Ca^{2+}]_i$ transient behavior for larger range muscle stretches. The length-tension behavior of smooth muscle exists for both agonist stimulations and membrane depolarization. However, studies show little significant change in the myosin phosphorylation behavior during potassium depolarization at different muscle lengths (Wingard et al., 1995), which contradicts a length-dependent sensitivity during membrane depolarization.

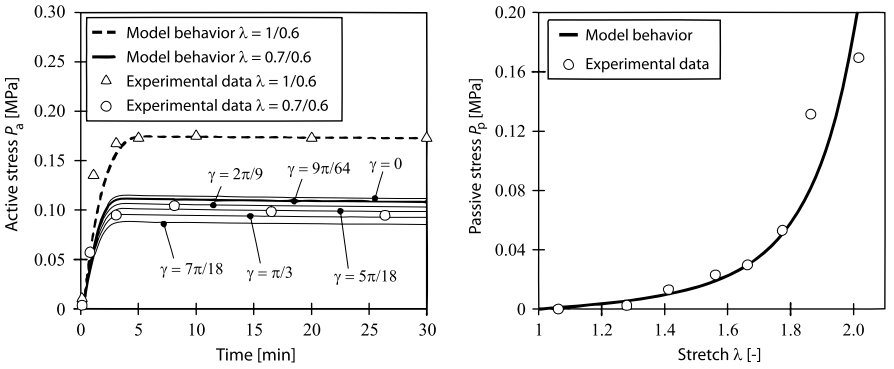

Fig. 4.6 *Left*: fitting results of the active stress developments at $\lambda = 1/0.6$ and $\lambda = 0.7/0.6$ by using the model of Murtada et al. (2010b). By repeating this for different orientation density functions $\rho(\gamma)$, where γ is a parameter describing the shape of the orientation density function, different behaviors of the predicted stress development at $\lambda = 0.7/0.6$ are obtained. *Right*: passive length-tension behavior (Murtada et al., 2010b). Compare with the passive length-tension behavior presented in Fig. 4.2A

4.3.3.2 Filament Overlap and Sliding Behavior

One common explanation for the length-tension behavior is the variation in the filament overlap in a contractile unit. This hypothesis was studied by introducing a filament overlap function $\bar{L}_o$ which defines the actin and myosin filament overlap and thereby the number of maximum possible attached cross-bridges in a contractile unit (Murtada et al., 2012). The filament overlap depends on the lengths of the actin and myosin filaments, and how these filaments slide with respect to each other, which was described by the normalized filament sliding $\bar{u}_{fs}$. An initial filament overlap $L_o(u_{fs} = 0) = x_0$ and an average optimal filament sliding u_{fs}^{opt}, for which optimal filament overlap is reached ($\partial L_o / \partial u_{fs}|_{u_{fs}=u_{fs}^{opt}} = 0$), were introduced. Thus the optimal filament overlap L_o^{opt} was defined as

$$L_o^{opt} = L_o\left(u_{fs} = u_{fs}^{opt}\right) = \frac{u_{fs}^{opt}}{2} + x_0. \tag{4.15}$$

Together with the boundary conditions, a continuous parabolic function of the filament overlap L_o was expressed as

$$L_o = u_{fs} - \frac{u_{fs}^2}{2u_{fs}^{opt}} + x_0 = \left(\bar{u}_{fs} - \frac{\bar{u}_{fs}^2}{2\bar{u}_{fs}^{opt}} + \bar{x}_0\right) L_{CU}, \tag{4.16}$$

where $\bar{x}_0 = x_0 / L_{CU}$ and $\bar{u}_{fs}^{opt} = u_{fs}^{opt} / L_{CU}$, see Fig. 4.7.

The initial filament overlap $\bar{x}_0$ and the optimal filament overlap $\bar{u}_{fs}^{opt}$ were defined through two equations: the definition of the stretch of a contractile unit (4.7) at

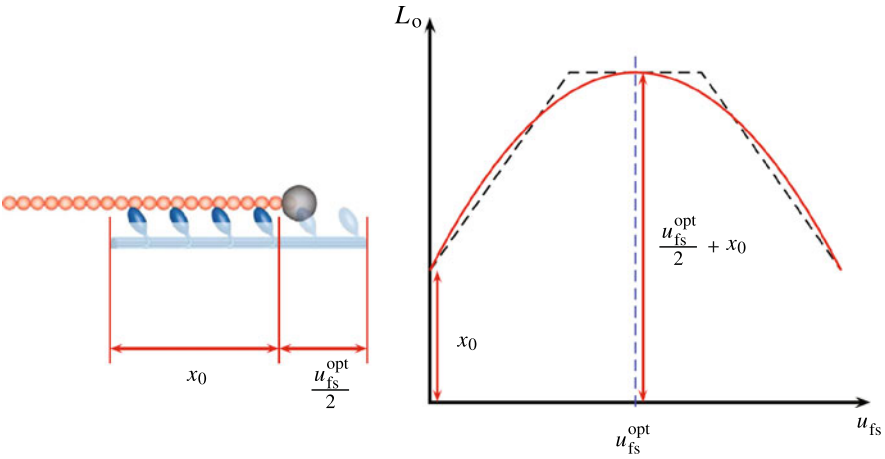

Fig. 4.7 Half contractile unit with the initial filament overlap x_0 between the myosin and actin filament. By introducing an optimal filament sliding distance u_{fs}^{opt} in a contractile unit, the filament overlap function L_o can be described by a parabolic function with an optimal filament overlap $u_{fs}^{opt}/2 + x_0$ (Murtada et al., 2012)

optimal muscle length, i.e.

$$\lambda_{opt} = 1 + \bar{u}_{fs}^{opt} + \bar{u}_{e}^{opt}, \tag{4.17}$$

where $\bar{u}_{e}^{opt} = u_{e}^{opt}/L_{CU}$, and by assuming that the fraction of the active stress at reference length P_0 and at the optimal length P_{opt} is equal to the fraction of the filament overlaps at the reference length and the optimal length, i.e.

$$\frac{P_0}{P_{opt}} = \frac{\bar{x}_0}{\bar{u}_{fs}^{opt}/2 + \bar{x}_0}. \tag{4.18}$$

Hence, the active stress of a contractile unit with varying filament overlap was expressed as

$$P_a = \mu_a \bar{L}_o(\bar{u}_{fs})(n_{AMp} + n_{AM})(\lambda - \bar{u}_{fs} - 1), \tag{4.19}$$

where $\bar{L}_o(\bar{u}_{fs}) = L_o(\bar{u}_{fs})/L_{CU}$.

One common way of studying the contractile mechanism in smooth muscle is to measure the shortening velocity during isotonic quick-release. The relationship between the shortening velocity and the after-load during isotonic quick-release can be described through a hyperbolic function, also known as Hill's equation (cf. Woledge et al., 1985), i.e.

$$(F + a)(v + b) = (F_0 + a)b, \tag{4.20}$$

where F is the isotonic after-load, F_0 is the isometric force at which the quick-release is performed, v is the muscle shortening velocity and a, b are fitting parameters. Based on the assumption that the velocity v reflects somewhat the behavior of

filament sliding $\bar{u}_{\mathrm{fs}}$, which was supported by Guilford and Warshaw (1998), a similar hyperbolic function was used to redefine the evolution law of the relative filament sliding $\bar{u}_{\mathrm{fs}}$, thus

$$(P_{\mathrm{a}} + \alpha)(-\dot{\bar{u}}_{\mathrm{fs}} + \beta) = (P_{\mathrm{c}} + \alpha)\beta, \tag{4.21}$$

which can be rewritten as

$$\dot{\bar{u}}_{\mathrm{fs}} = \beta \frac{P_{\mathrm{a}} - P_{\mathrm{c}}}{P_{\mathrm{a}} + \alpha}. \tag{4.22}$$

When comparing the evolution law of the filament sliding $\bar{u}_{\mathrm{fs}}$, as presented in Murtada et al. (2010a), with the updated evolution law (Murtada et al., 2012) it can be seen that the two evolution laws do not differ that much from each other.

The evolution law for $\bar{u}_{\mathrm{fs}}$ was further extended to also allow the simulation of isotonic muscle extension such as

$$\dot{\bar{u}}_{\mathrm{fs}} = \beta_1 \frac{P_{\mathrm{a}} - P_{\mathrm{c}}}{P_{\mathrm{a}} + \alpha} - \beta_2 \frac{P_{\mathrm{a}} - P_{\mathrm{c}}}{P_{\mathrm{a}} - P_{\mathrm{LBC}}}, \tag{4.23}$$

where P_{LBC} is the maximal load-bearing capacity of the contractile units (yield stress) (Dillon et al., 1981), and β_1 and β_2 are fitting parameters. The internal stress P_{c}, which is governed by the number of attached cycling and non-cycling cross-bridges (depending on the mechanical state of the smooth muscle) is dependent on the varying filament overlap $\bar{L}_{\mathrm{o}}$ as well. Hence, based on Eq. (4.11), the internal stress P_{c} during contraction was quantified as

$$P_{\mathrm{c}} = \kappa_{\mathrm{AMp}} \bar{L}_{\mathrm{o}}(\bar{u}_{\mathrm{fs}}) n_{\mathrm{AMp}}, \tag{4.24}$$

and during muscle relaxation (extension) as

$$P_{\mathrm{c}} = \kappa_{\mathrm{AMp}} \bar{L}_{\mathrm{o}}(\bar{u}_{\mathrm{fs}}) n_{\mathrm{AMp}} + \kappa_{\mathrm{AM}} \bar{L}_{\mathrm{o}}(\bar{u}_{\mathrm{fs}}) n_{\mathrm{AM}}, \tag{4.25}$$

where κ_{AMp} is a parameter related to the force due to a power-stroke of a single cross-bridge and κ_{AM} is related to the force-bearing capacity of a dephosphorylated attached (latch) cross-bridge during muscle extension.

The material parameters in the mechanical model were fitted to isometric tension development and to isotonic shortening velocities from swine carotid media (Dillon et al., 1981; Murtada et al., 2012), resulting in $\mu_{\mathrm{a}} = 5.3$ MPa, $\alpha = 26.7$ kPa, $\beta = \beta_1 = 0.0083\ \mathrm{s}^{-1}$ and $\kappa_{\mathrm{AMp}} = 204$ kPa. The material parameters β_2 and κ_{AM} were fitted to sudden extension experiments resulting to $\beta_2 = 0.0021\ \mathrm{s}^{-1}$ and $\kappa_{\mathrm{AM}} = 61.1$ kPa. The parameters in the filament overlap function $\bar{L}_{\mathrm{o}}$ were fitted to $\bar{u}_{\mathrm{fs}}^{\mathrm{opt}} = 0.48$ and $\bar{x}_0 = 0.8544$ by means of the conditions in Eqs. (4.17) and (4.18) together with length-tension experimental data from swine carotid media (Murtada et al., 2012). By using Eq. (4.19) together with a filament sliding evolution law and the kinetic model by Hai and Murphy (1988), the active stress P_{a} was simulated for different stretches λ, see Fig. 4.8. The simulated results show very good correlations with experimental data obtained from swine carotid media.

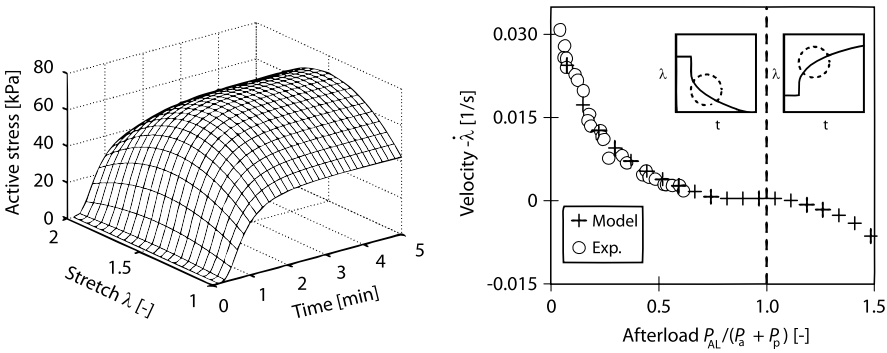

Fig. 4.8 *Left*: isometric active stress development for different muscle stretches λ activated by a certain intracellular calcium transient using the filament overlap model of Murtada et al. (2012); related material parameters are $\mu_a = 5.3$ MPa, $\alpha = 26.7$ kPa, $\beta = \beta_1 = 0.0083$ s^{-1} and $\kappa_{AMp} = 204$ kPa. *Right*: isotonic shortening and extension velocities for different after-loads (Murtada et al., 2012). Compare with the shortening velocity presented in Fig. 4.2D

Through the updated evolution law based on Hill's equation (4.22), the model was able to simulate a (very) realistic nonlinear behavior of the isotonic force-velocity relationship seen in smooth muscle. With the extended evolution law (4.23) a realistic behavior of the force development during sudden muscle extension and also the extension velocity were obtained. One of the advantages with the mathematical form of the extended filament sliding evolution law is the convenience of reducing it to its original form (4.22) when only simulating sudden muscle shortening.

4.4 Discussion and Concluding Remarks

In the present chapter, a review of a mathematical approach for studying smooth muscle contraction and relaxation was presented. There are several different smooth muscle models available in the literature and they have some characteristics in common, however the reviewed approach (Murtada et al. 2010a, 2010b, 2012) is one of the few which is able to simulate a realistic mechanochemical behavior of isometric contraction and relaxation at different muscle stretches and isotonic shortening/extension through one single model. The described approach models the active tension development by considering the number of attached cross-bridges, the average elastic elongation of attached cross-bridges and the filament sliding theory.

With the implemented filament overlap function, the model is able to simulate the well-known length-tension behavior which is very relevant for smooth muscle organs functioning at a large range of deformations. The model couples intracellular calcium [Ca^{2+}] with muscle contraction and relaxation through the Hai and Murphy myosin kinetics model (Hai and Murphy, 1988) and the smooth muscle model of Murtada et al. (2012). The myosin kinetics model describes the myosin

in four different functional states where two are load-bearings and coupled through seven reaction rates. The behavior of the active stress is proportional to the sum of the fractions of the load-bearing myosin functional states and is, therefore, very dependent on the behavior of the myosin kinetics model. However, it is not so trivial to define the reaction rates in the Hai and Murphy model and also to validate the simulated fraction values of attached cross-bridges. The Hai and Murphy kinetics model is rather old; it suggests the existence of a slower latch state myosin, where the myosin is dephosphorylated and attached, which has not been shown experimentally. In the last years several advances have been proposed in the understanding of myosin-actin kinetics so that an update of the myosin kinetics model would be a very valuable task.

The mechanical model presented in this chapter is based on structural observations and has a relatively low number of material parameters which can be related to the physical properties of the smooth muscle. For example, the physical parameter μ_a in the smooth muscle model (defined by the length of the contractile unit L_{CU}, the elastic stiffness of a single cross-bridge E_{cb}, the average distance between the cross-bridges δ and the contractile unit density N_{CU}) was investigated by comparing it with experimental data of L_{CU}, E_{cb}, δ and N_{CU}. It was found that it corresponds very well with the experimental data of the physical measurable units (Murtada et al., 2012) supporting the description and the fitted value of μ_a. However, there are still several items that can be improved such as an improved myosin kinetics model, which is not dependent on a latch state, and a further developed filament sliding evolution law.

With a realistic chemomechanical model of smooth muscle activity it is possible to study more complex boundary-value problems that are clinically and pathophysiologically relevant by implementing the coupled model into a three-dimensional finite element code. An implementation of the model into a finite element code also allows to study the effects of time-dependent changes in Ca^{2+} for different internal pressures of an intact artery that are relevant for both short-term and long-term changes in the vascular wall.

Acknowledgements Financial support for SCM was provided through a Project Grant (#20056167, #20094302) from the Swedish Research Council (VR) and the Swedish Heart-Lung Foundation. This support is gratefully acknowledged.

References

Arner A (1982) Mechanical characteristics of chemically skinned guinea-pig taenia coli. Eur J Physiol 395:277–284

Dillon PF, Aksoy MO, Driska SP, Murphy RA (1981) Myosin phosphorylation and the cross-bridge cycle in arterial smooth muscle. Science 211:495–497

Fung YC (1970) Mathematical representation of the mechanical properties of the heart muscle. J Biomech 269:441–515

Gasser TC, Ogden RW, Holzapfel GA (2006) Hyperelastic modelling of arterial layers with distributed collagen fibre orientations. J R Soc Interface 3:15–35

Gordon AM, Huxley AF, Julian FJ, (1966). The variation in isometric tension with sarcomere length in vertebrate muscle fibres. J Physiol 184:170–192

Guilford WH, Warshaw DM (1998) The molecular mechanics of smooth muscle myosin. Comp Biochem Physiol 119:451–458

Hai CM, Murphy RA (1988) Cross-bridge phosphorylation and regulation of latch state in smooth muscle. J Appl Physiol 254:C99–106

Herrera AM, McParland BE, Bienkowska A, Tait R, Paré PD, Seow CY (2005) Sarcomeres of smooth muscle: functional characteristics and ultrastructural evidence. J Cell Sci 118:2381–2392

Holzapfel GA, Gasser TC, Ogden RW (2000) A new constitutive framework for arterial wall mechanics and a comparative study of material models. J Elast 61:1–48

Holzapfel GA, Ogden RW (2010) Constitutive modelling of arteries. Proc R Soc A 466:1551–1597

Kamm KE, Gerthoffer WH, Murphy RA, Bohr DF (1989) Mechanical properties of carotid arteries from DOCA hypertensive swine. Hypertension 13:102–109

Kato S, Osa T, Ogasawara T (1984) Kinetic model for isometric contraction in smooth muscle on the basis of myosin phosphorylation hypothesis. Biophys J 46:35–44

Murtada S, Kroon M, Holzapfel GA (2010a) A calcium-driven mechanochemical model for prediction of force generation in smooth muscle. Biomech Model Mechanobiol 9:749–762

Murtada S, Kroon M, Holzapfel GA (2010b) Modeling the dispersion effects of contractile fibers in smooth muscles. J Mech Phys Solids 58:2065–2082

Murtada SC, Arner A, Holzapfel GA (2012) Experiments and mechanochemical modeling of smooth muscle contraction: significance of filament overlap. J Theor Biol 21:176–186

Peterson JW (1982) Simple model of smooth muscle myosin phosphorylation and dephosphorylation as rate-limiting mechanism. Biophys J 37:453–459

Rachev A, Hayashi K (1999) Theoretical study of the effects of vascular smooth muscle contraction on strain and stress distributions in arteries. Ann Biomed Eng 27:459–468

Rembold CM, Murphy RA (1990a) Latch-bridge model in smooth muscle: $[Ca^{2+}]_i$ can quantitatively predict stress. Am J Physiol 259:C251–C257

Rembold CM, Murphy RA (1990b) Muscle length, shortening, myoplasmic $[Ca^{2+}]$ and activation of arterial smooth muscle. Circ Res 66:1354–1361

Schriefl AJ, Zeindlinger G, Pierce DM, Regitnig P, Holzapfel GA (2012) Determination of the layer-specific distributed collagen fiber orientations in human thoracic and abdominal aortas and common iliac arteries. J R Soc Interface 9:1275–1286

Somlyo AP, Somlyo AV (2002) The sarcoplasmic reticulum: then and now. Novartis Found Symp 246:258–268

Stålhand J, Klarbring A, Holzapfel GA (2008) Smooth muscle contraction: mechanochemical formulation for homogeneous finite strains. Prog Biophys Mol Biol 96:465–481

Wingard CJ, Browne AK, Murphy RA (1995) Dependence of force on length at constant cross-bridge phosphorylation in the swine carotid media. J Physiol 488:729–739

Woledge RC, Curtin NA, Homsher E (1985) Energetic aspects of muscle contraction. Academic Press, San Diego

Yang J, Clark JW Jr, Bryan RM, Robertson C (2003) The myogenic response in isolated rat cerebrovascular arteries: smooth muscle cell model. Med Eng Phys 25:691–709

Chapter 5
A Coupled Chemomechanical Model for Smooth Muscle Contraction

Markus Böl and Andre Schmitz

Abstract This manuscript presents a chemomechanically coupled three-dimensional model, describing the contractile behavior of smooth muscles. It bases on a strain-energy function, additively decomposed into passive parts and an active calcium-driven part related to the chemical contraction of smooth muscle cells. For the description of the calcium phase the four state cross-bridge model of Hai and Murphy (Am. J. Physiol. 254:C99–106, 1988) has been used. Before the features and applicability of the proposed approach are illustrated in terms of three-dimensional boundary-value problems, the model is validated by experiments on porcine smooth muscle tissue strips.

5.1 Introduction

Many internal organs such as stomach, intestine, bronchia, urinary bladder, uterus, airways, or blood vessels are composed by multiple layers of spindle-shaped smooth muscle cells (SMCs). Focusing on vessel mechanics, vascular smooth muscle cells are the key component in the vascular system regulating the diameter of vessels, triggered by various neural, chemical and mechanical signals. Human arteries are comprised of three distinct layers, the intima, the media, and the adventitia, in which the proportion and structure of each varies with size and function of the particular artery.

From the mechanical perspective, the media is the most significant layer in human healthy arteries. It is the middle layer and is characterized by a complex three-dimensional network of smooth muscle cells embedded in a matrix of elastin and collagen fibers (Fritsch and Kuehnel, 2007). However, this architecture gives the media high passive strength and the ability to resists loads in multiple directions. Due to the existence of SMCs inside the media it is of particular interest related to smooth muscle (SM) activation, too. Focusing at cell level, SM contraction is

M. Böl (✉) · A. Schmitz
Institute of Solid Mechanics, Technische Universität Braunschweig, 38106 Braunschweig, Germany
e-mail: m.boel@tu-bs.de

G.A. Holzapfel, E. Kuhl (eds.), *Computer Models in Biomechanics*,
DOI 10.1007/978-94-007-5464-5_5,

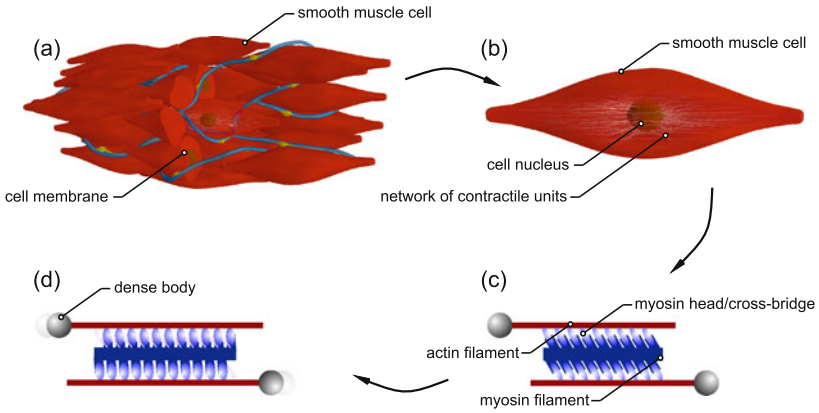

Fig. 5.1 Structural and geometrical characteristics of smooth muscles: (**a**) layers of smooth muscle cells; (**b**) isolated smooth muscle cell; (**c**) single, relaxed unit (myosin heads in skew position); (**d**) same contracted unit (myosin heads in vertical position)

rooted on one basic unit, the SMC, see Fig. 5.1(b). These spindle-shaped cells contains a single centrally positioned elongated nucleus and vary notably in size, from 30 µm length in walls of small vessels to 200 µm length and 5 µm width in the intestine, see Rhoades and Bell (2008). They are characterized by a fusiform shape. In the mid-region they are thickest and tapered at each end. SMs are built up of layers of cells (Fig. 5.1(a)) that are linked together by various junctional contacts that serve as points of cell to cell communication and mechanical linkages (dense plaque). The mechanical contraction is caused by contractile units which consist of two filaments: actin and myosin, see Fig. 5.1(c). These filaments are present in large numbers and roughly aligned with the long axis of the cell, see, e.g., Kuo and Seow (2004) and Seow and Paré (2007). They are loosely associated into thin myofibrils. These myofibrils consist of a centrally located myosin filament surrounded by multiple actin filaments. In electron micrographs (e.g., Bond and Somlyo, 1982; Hodgkinson et al., 1995; Herrera et al., 2005) numerous dense staining regions, known as dense bodies (Fig. 5.1(d)), can be identified scattered throughout the cytoplasm of the cell. In common with the Z-discs of skeletal muscles, these dense bodies contain the actin-binding protein α-actinin and appear to serve as anchorage points for actin filaments of myofibrils. Their association with the system of internal intermediate filaments essential serve to integrate contractions over the entire cell and allow the very high degree of shortening achieved by these cells. When actin filaments run into the cell membrane, they connect the dense bodies and dense plaques. Based on the coupling by pairs of opposed adjacent dense bodies located on neighboring cells force transmission is accomplished across cell boundary. Thus, it appears that SMs are composed on a huge number of contractile units in series as well as in parallel.

In comparison to experimental investigations there exist only a few approaches describing parts of the biochemical-mechanical process in SM activation by means of mathematical models. Looking at this type of models it stands out that a huge number of these models is realized in a one-dimensional framework, see, e.g., Fay

and Delise (1973), Gestrelius and Borgström (1986), Lee and Schmid-Schönbein (1996a,b), Miftakhov and Abdusheva (1996), Rachev and Hayashi (1999), Yang et al. (2003a,b), Zulliger et al. (2004), Herrera et al. (2005), Bates and Lauzon (2007), Bursztyn et al. (2007), Stålhand et al. (2008) and Murtada et al. (2010). All these models have the main restriction that they are implemented in form of so-called stand-alone programmes. Hence, only limited estimations are possible as the chemomechanical behaviors of smooth muscles significantly depend on their geometry undergoing large deformations it is essential to take a three-dimensional modeling approach into account. However, to the authors knowledge, there only exists one three-dimensional coupled chemomechanical modeling approach presenting three-dimensional boundary-value problems, see Schmitz and Böl (2011). Herein, *steady state* characteristics of the calcium concentration are presented, only.

The present contribution concentrated on the development of a three-dimensional chemomechanical SM model including *dynamic* behavior of the calcium concentration. Section 5.2 introduces the governing equations of a coupled boundary-value problem for SM chemomechanics. Before the manuscript is concluded with Sect. 5.4, Sect. 5.3 shows illustrative numerical examples.

5.2 Field Equations of Smooth Muscle Chemomechanics

5.2.1 Kinematics

As this work focuses on the modeling of vascular smooth muscle tissue, an anisotropic material with outstanding directions for collagen bundles and SMC layers has to be considered. Collagen bundles as well as SMC layers are aligned tangentially with the wall of the vessel (Herlihy and Murphy, 1973; Walmsley and Murphy, 1987; Dahl et al., 2007) accomplished by the angle Φ, see Fig. 1 in Schmitz and Böl (2011). The in-wall dispersions $\Theta_{\mathrm{c/s}}$ (c = collagen and s = SM layer) leading to arbitrary direction vectors which are able to describe the collagen and SMC orientations in the reference configuration using so-called unit direction vectors

$$\mathbf{M}_{\mathrm{c/s}} = \begin{pmatrix} \cos\Theta_{\mathrm{c/s}} \cos\Phi \\ \cos\Theta_{\mathrm{c/s}} \sin\Phi \\ \sin\Theta_{\mathrm{c/s}} \end{pmatrix}. \tag{5.1}$$

Consequently, the structural tensors

$$\mathbf{Z}_{\mathrm{c/s}} = \mathbf{M}_{\mathrm{c/s}} \otimes \mathbf{M}_{\mathrm{c/s}} \tag{5.2}$$

can be constructed by means of the dyadic product including the directional information of a certain SMC layer $\mathbf{M}_{\mathrm{s}}$ or collagen fiber bundle $\mathbf{M}_{\mathrm{c}}$. This allows the computation of corresponding stretches

$$\lambda^2_{\mathrm{c/s}} = I_{4,\mathrm{c/s}} = \mathbf{C} : \mathbf{Z}_{\mathrm{c/s}}, \tag{5.3}$$

where the fourth invariant $I_{4,\mathrm{c/s}}$ can be expressed as scalar product of the right Cauchy-Green tensor $\mathbf{C}$ and $\mathbf{Z}_{\mathrm{c/s}}$.

5.2.2 Balance Equations

Using classical non-linear continuum mechanics, a coupled problem of chemo-mechanical SM contraction is formulated in terms of two primary field variables, namely the placement $\boldsymbol{\varphi}(\mathbf{X}, t)$ and the calcium concentration $c(\mathbf{X}, t)$. Consequently, a chemomechanical state $\mathscr{S}$ of a material point $\mathbf{X}$ at the time t is defined as

$$\mathscr{S}(\mathbf{X}, t) = \big\{\boldsymbol{\varphi}(\mathbf{X}, t), c(\mathbf{X}, t)\big\}. \tag{5.4}$$

Spatial as well as temporal evolution of the primary field variables are governed by two basic field equations: the balance of linear momentum and the diffusion-type equation of excitation through calcium.

The balance of linear momentum in spatial form

$$\operatorname{div}\boldsymbol{\sigma} + \bar{\mathbf{b}} = \mathbf{0} \quad \text{in } \mathscr{B} \tag{5.5}$$

describes the quasi-static stress equilibrium. Herein $\bar{\mathbf{b}}$ is the given spatial body force per unit reference volume. The operator $\operatorname{div}[\bullet]$ indicates the divergence with respect to the spatial coordinates $\mathbf{x}$, and $\boldsymbol{\sigma}$ denotes the Cauchy stress tensor given as

$$\boldsymbol{\sigma} = 2J^{-1}\mathbf{F}\frac{\partial \Psi(\boldsymbol{\varphi})}{\partial \mathbf{C}}\mathbf{F}^{\mathrm{T}}, \tag{5.6}$$

depending on the deformation measures $\mathbf{C}$ and $\mathbf{F}$ as well as on a strain-energy function $\Psi(\boldsymbol{\varphi})$, see Sect. 5.2.3. The mechanical problem is completed by essential and natural boundary conditions,

$$\boldsymbol{\varphi} = \bar{\boldsymbol{\varphi}} \quad \text{on } \partial\mathscr{B}_{\varphi} \quad \text{and} \quad \mathbf{t} = \bar{\mathbf{t}} \quad \text{on } \partial\mathcal{B}_{\sigma}. \tag{5.7}$$

The surface stress traction vector $\bar{\mathbf{t}}$, defined on $\partial\mathscr{B}_{\sigma}$, is related to the Cauchy stress tensor $\boldsymbol{\sigma}$ via the Cauchy stress theorem $\bar{\mathbf{t}} := \boldsymbol{\sigma}\mathbf{n}$, where the outward surface normal is specified as $\mathbf{n}$.

The second field equation describes the calcium concentration inside the SM tissue. The well-known Fick's second law

$$\dot{c} = -\operatorname{div}\mathbf{q} \quad \text{in } \mathscr{B} \tag{5.8}$$

predicts how diffusion causes the concentration field c to change with time. Herein, the diffusion flux vector

$$\mathbf{q} = -\mathbf{d}(\boldsymbol{\varphi})\nabla_x c \tag{5.9}$$

relates to the calcium concentration gradient $\nabla_x c$ via the deformation dependent, anisotropic diffusion tensor $\mathbf{d}(\boldsymbol{\varphi})$. Based on the microstructure of SM tissue the diffusion tensor

$$\mathbf{d}(\boldsymbol{\varphi}) = d_{\text{iso}}\mathbf{I} + \frac{d_{\text{aniso}}}{n}\sum_{i=1}^{n}\mathbf{Z}_i^{\text{R}} \tag{5.10}$$

is additively decomposed into an isotropic (related to the elastin and matrix material) and an anisotropic part (related to the collagen fibers in SMCs) including the appropriate diffusion coefficients d_{iso} and d_{aniso}, respectively. The number of considered directions inside the SM tissue is controlled by n and $\mathbf{I}$ denotes the identity tensor. Further,

$$\mathbf{Z}_i^{\text{R}} = \mathbf{R}\mathbf{Z}_i\mathbf{R}^{\text{T}} = \frac{\mathbf{F}\mathbf{M}_i}{|\mathbf{F}\mathbf{M}_i|} \otimes \frac{\mathbf{F}\mathbf{M}_i}{|\mathbf{F}\mathbf{M}_i|} \tag{5.11}$$

are the rotated structural tensors without the stretch component $\mathbf{U}$ of the deformation gradient $\mathbf{F} = \mathbf{R}\mathbf{U}$, whereby $\mathbf{R}$ is the rotation tensor.

Analogously to the momentum balance, the calcium field equation also uses corresponding essential and natural boundary conditions

$$c = \bar{c} \quad \text{on } \partial\mathscr{B}_c \quad \text{and} \quad q = \bar{q} \quad \text{on } \partial\mathscr{B}_q. \tag{5.12}$$

The diffusion surface flux term $\bar{q}$ is related to the spatial flux vector through the Cauchy-type formula $\bar{q} := \mathbf{q} \cdot \mathbf{n}$.

5.2.3 An Active Artery Model

In this section we give a short review over the governing constitutive equations for the active artery model. Thus, the used strain-energy function for the media layer

$$\Psi(\boldsymbol{\varphi}) = \Psi_{\text{e}} + \Psi_{\text{c}} + \Psi_{\text{s}} \tag{5.13}$$

is additively decomposed in the three components: the load-bearing proteins elastin (Ψ_{e}) and collagen (Ψ_{c}) and the active, contractile SMCs (Ψ_{s}).

5.2.3.1 Elastin

The first component of the strain-energy function Ψ_{e} stays for elastin, a protein used to build up load-bearing structures in creature tissue. As flexible elastin molecules are randomly arranged in a three-dimensional network, the isotropic neo-Hookean material model

$$\Psi_{\text{e}} = \frac{\mu_{\text{e}}}{2}(I_1 - 3) \tag{5.14}$$

has been chosen to mirror such characteristics. Herein, the shear modulus μ_e as single material parameter seems sufficient. Further, the first invariant $I_1 = \mathrm{tr}\,\mathbf{C}$ is defined as the trace of $\mathbf{C}$.

5.2.3.2 Collagen

The second main connective tissue component in arteries, collagen (Ψ_c), dominates their mechanical behavior by a stress-stretch relation of exponential type along the fiber direction. Experimental observations by, e.g., Dahl et al. (2007) indicate that collagen fibers are preferably aligned with the vessels longitudinal axis, helically and circumferentially. Thus, the dispersion of the collagen fibers by incorporation angles $\Theta_{c,i}$ has been measured. In doing so, the relative frequency f_c has been regarded to fulfill the relation $\sum_{i=1}^{n_c} f_{c,i} = 1$ with n_c being the number of different directions i. For the modeling of such material characteristics, the used strain energy is weighted in every incorporated direction with the corresponding, measured collagen fraction $f_{c,i}$ and can be written as

$$\Psi_c = \sum_{i=1}^{n_c} f_{c,i}\,\Psi_{c,i}. \tag{5.15}$$

Herein, the strain-energy functions

$$\Psi_{c,i} = \begin{cases} \frac{c_1}{2c_2}\exp[c_2(\lambda_{c,i}^2 - 1)^2] & \text{if } \lambda_{c,i} \geq 1, \\ 0 & \text{else,} \end{cases} \tag{5.16}$$

depend on two material constants, c_1 and c_2, see Holzapfel et al. (2000).

5.2.3.3 Smooth Muscle Cells

The third component in arteries are mainly circumferentially oriented SMCs. However, it stands out that there is a certain stretch at which the generated force reaches a maximum value, see Schmitz and Böl (2011). Having those experimentally obtained force-stretch characteristics in mind, the strain-energy function of a single SMC or a layer of SMCs reads

$$\Psi_s = \sum_{j=1}^{n_s} f_{s,j}\,\Psi_{s,j}. \tag{5.17}$$

According to the findings of Walmsley and Murphy (1987) the active strain-energy function has been weighted with the SMC volume fractions $f_{s,j}$ in every incorporated direction j. Further, n_s denotes the number of considered directions and the

direction dependent strain-energy functions

$$\Psi_{\mathrm{s},j} = \frac{s_1}{2}(n_\mathrm{C}+n_\mathrm{D})\Bigg[\left(2+\lambda_{\max}^{s_2}\right)\left(\lambda_{\max}\lambda_{\mathrm{s},j}^2-\frac{1}{3}\lambda_{\mathrm{s},j}^3-\lambda_{\max}^2\lambda_{\mathrm{s},j}\right) + \frac{\lambda_{\mathrm{s},j}^{3+s_2}}{3+s_2}-\frac{2\lambda_{\max}\lambda_{\mathrm{s},j}^{2+s_2}}{2+s_2}+\frac{\lambda_{\max}^2\lambda_{\mathrm{s},j}^{1+s_2}}{1+s_2}\Bigg]+P_{\max}\lambda_{\mathrm{s},j}. \tag{5.18}$$

Herein, s_1 is a stress-like material parameter and s_2 is a dimensionless constant. Further, λ_s specifies the SMC stretch and $\lambda_{\max}$ defines the stretch at which the generated stress

$$P_{\max} = \kappa(n_\mathrm{C}+n_\mathrm{D}), \tag{5.19}$$

depending on the parameter κ, reaches its maximum. The whole contraction process is triggered by the chemical degree of activation $(n_\mathrm{C}+n_\mathrm{D})$ provided by Hai and Murphy (1988), describing the time and calcium dependent contraction kinetics. This model is described by the differential equation system

$$\begin{bmatrix}\dot{n}_\mathrm{A}\\ \dot{n}_\mathrm{B}\\ \dot{n}_\mathrm{C}\\ \dot{n}_\mathrm{D}\end{bmatrix} = \begin{bmatrix}-k_1 & k_2 & 0 & k_7\\ k_1 & -(k_2+k_3) & k_4 & 0\\ 0 & k_3 & -(k_4+k_5) & k_6\\ 0 & 0 & k_5 & -(k_6+k_7)\end{bmatrix}\begin{bmatrix}n_\mathrm{A}\\ n_\mathrm{B}\\ n_\mathrm{C}\\ n_\mathrm{D}\end{bmatrix}, \tag{5.20}$$

composed of four first order differential equations in time for four chemical states n_A, n_B, n_C, and n_D. As these are fractions, $n_\mathrm{A}+n_\mathrm{B}+n_\mathrm{C}+n_\mathrm{D}=1$ has to be hold. The first two, n_A and n_B, represent non-force generating states whereas the last two, n_C and n_D, are related to generated force and thus, be mechanically significant. Further the rate constant have been used as published in Schmitz and Böl (2011), in doing so $k_1=k_6$ and $k_2=k_5$. SMC contraction is triggered by an increase in intracellular calcium which is controlled by the calcium-dependent rate constants k_1 and k_6. Thus, a simple relation is given by

$$k_1 = k_6 = \frac{(\alpha[\mathrm{Ca}^{2+}])^2}{(\alpha[\mathrm{Ca}^{2+}])^2+K_{\mathrm{CaCaM}}^2}, \tag{5.21}$$

where $\alpha>0$ is a positive constant, $[\mathrm{Ca}^{2+}]$ characterizes the calcium concentration, and K_{CaCaM} denotes the half-activation constant for the calcium-calmodium complex [CaCaM]. In this approach the rate parameters k_i have to be identified by experimental data (Hai and Murphy, 1988; Yang et al., 2003a,b).

5.3 Numerical Examples

This section aims to study how the chemical excitation affects the mechanical behavior at muscle level. In doing so, we first validate the presented modeling approach with experiments by Herlihy and Murphy (1973) before in a second step the

Table 5.1 Material parameters for porcine carotid artery tissue. As the media and the adventitia exhibit a certain amount of elastin and collagen, the mechanical behavior of these two constituent is described by Eqs. (5.14) and (5.16), respectively. In order to distinct between the appropriate material parameters, upper indexes have been used, med = media and adv = adventitia

Parameter	Value	Unit	Reference
Media			
s_1	1247.6	kPa	Herlihy and Murphy (1973)
s_2	2.0	–	Herlihy and Murphy (1973)
κ	291.0	kPa	Herlihy and Murphy (1973)
$\lambda_{\max}$	1.248	–	Herlihy and Murphy (1973)
$\Theta^{\text{med}}_{\text{s},1/2}$	± 4.5	°	Herlihy and Murphy (1973)
$f^{\text{med}}_{\text{s},1/2}$	0.5	–	Herlihy and Murphy (1973)
c_1^{med}	23.7	kPa	Herlihy and Murphy (1973)
c_2^{med}	1.7	–	Herlihy and Murphy (1973)
$\Theta^{\text{med}}_{\text{c},i}$	cp. Fig. 6 in	°	Dahl et al. (2007)
$f^{\text{med}}_{\text{c},i}$	cp. Fig. 6 in	–	Dahl et al. (2007)
$\mu_{\text{e}}^{\text{med}}$	7.0	kPa	Herlihy and Murphy (1973)
Adventitia			
c_1^{adv}	4.74	kPa	Wang et al. (2006)
c_2^{adv}	1.7	–	Wang et al. (2006)
$\Theta^{\text{adv}}_{\text{c},1/2/3/4}$	$0/-45/45/90$	°	chosen
$f^{\text{adv}}_{\text{c},1/2/3/4}$	0.25/0.25/0.25/0.25	–	chosen
$\mu_{\text{e}}^{\text{adv}}$	0.7	kPa	Wang et al. (2006)

Table 5.2 Material parameters needed for the calcium diffusion inside the SM tissue

Parameter	Value	Unit	Reference
K_{CaCaM}	178.0	nMol	Yang et al. (2003a,b)
α	$35 \cdot 10^{-6}$	–	Arner (1982)
d_{iso}	$4.0 \cdot 10^{-3}$	mm^2/s	chosen
d_{aniso}	0.0	mm^2/s	chosen

dependence of the chemical activation on the contraction characteristics has been studied. If not otherwise specified, the material parameters listed in Tables 5.1 (mechanical parameters) and 5.2 (parameters for the calcium diffusion) are used for the following simulations.

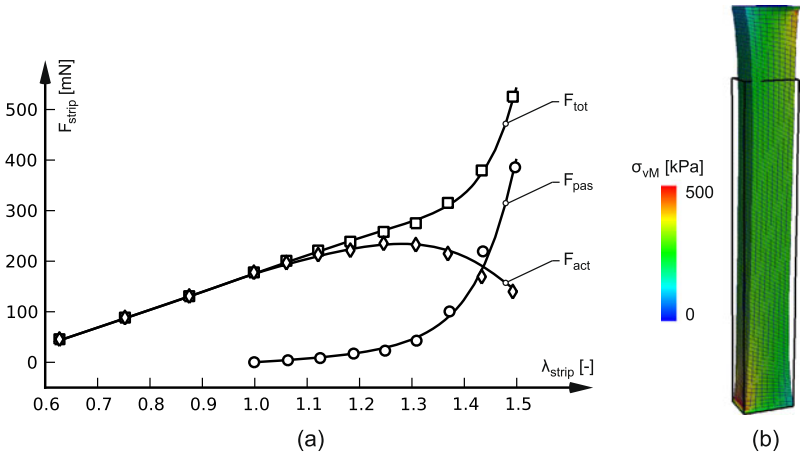

Fig. 5.2 Model validation using experimental data by Herlihy and Murphy (1973) obtained from medial strips ($\Theta_{\text{strip}} = 85.5°$): (**a**) force-stretch response from experiment and model and (**b**) results of the finite element simulation. Deformed shape and von Mises stress distribution at $\lambda_{\text{strip}} = 1.2$

5.3.1 Model Validation

For the model validation active and passive tension experiment performed on porcine medial strips (Herlihy and Murphy, 1973) have been used, see Fig. 5.2(a). Following the experimental protocol, the porcine strips have been completely activated so that a temporally converged contraction process is existent. Two main orientations ($\Theta_{\text{s},1/2} = \pm 4.5°$) of SMC layers with equal SMC fractions ($f_{\text{s},1/2} = 0.5$) have been measured. Strips with dimensions $h/w/t = 8.0/1.3/1.0$ mm have been dissected along the SMCs alignment, namely $\Theta_{\text{strip}} = 85.5°$. According to the experimental boundary conditions in Herlihy and Murphy (1973) we approximate them by fixing both ends of the strip in all directions. For the collagen dispersion of porcine, medial tissue experimental data by Dahl et al. (2007) have been used. The values for the rate constants of the chemical model have been taken from Hai and Murphy (1988) as these are rooted on data obtained by Singer and Murphy (1987) investigating swine tissue as well. Hence, a consistent parameter set is created, see Table 5.1.

Figure 5.2(a) indicates that the proposed model accurately captures the force-stretch behavior. As the tissue strip is aligned with the loading direction in the strips long axis high stress values can be identified, see Fig. 5.2(b).

5.3.2 Muscle Tissue Strip

In order to show the ability of the model a three-dimensional tissues example, dissected from vessels is used, see Fig. 5.3. The strip is characterized by two layers,

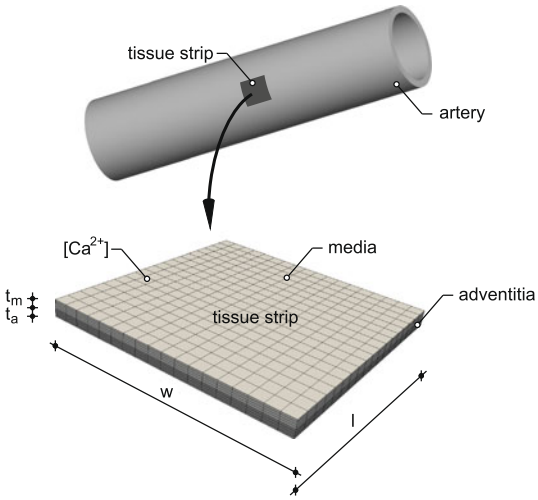

Fig. 5.3 Porcine tissue strip dissected from an artery. The strip has the dimensions $l/w/t_a/t_m = 3.0/3.0/0.1/0.1$ mm

the contractible media ($t_m = 0.1$ mm, light grey) and the adventitia ($t_a = 0.1$ mm, dark grey). In the proposed example we are interested in the tissue response when a completely deactivated strip with an extracellular calcium concentration being initially zero is exposed to an environment with an external calcium concentration of $[Ca^{2+}] = 500$ mMol. This example is closely related to the experimental work of Arner (1982).

In order to analyze the contraction process the main variables, i.e. the calcium concentration $[Ca^{2+}]$, the chemical concentrations $(n_C + n_D)$, and the equivalent von Mises stress σ_{vM} have been tracked during contraction. In doing so, Fig. 5.4 illustrated the results for four discrete time steps $t = 10/30/80/250$ s. Focusing on the calcium concentration (first line) a converged state is achieved in dependence on the choice of the diffusion coefficients, here this situation occurs at time $t = 80$ s. The chemical states $(n_C + n_D)$ in the second line display a small delay with respect to the calcium concentration, see, e.g., at time $t = 30$ s. Also here, the converged state arises after 80 seconds. In the third line the distribution of the equivalent von Mises stress is illustrated. Small stresses can be detected for the first time step (10 s). As the media differs from the adventitia by a higher stiffness also the stress values a higher. This is impressively documented at time $t = 30$ s where the maximum stress is achieved. The stress increases continuously until at 80 seconds a decrease can be observed. During further activation the stress again increases. Focusing on the overall deformation of the strip a clear bending deformation can be seen that continuously increases. This bending arises from the fact that the layers are aligned asymmetrical and that the media contracts, only.

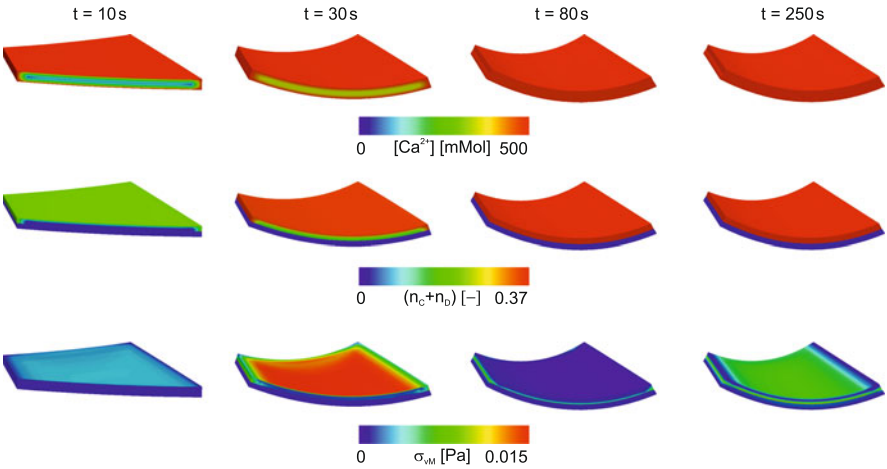

Fig. 5.4 Progress of the main variables $[Ca^{2+}]$, $(n_C + n_D)$, and σ_{vM} during SM contraction. For the sake of clarity the deformed strip has been cut virtually, so that the distribution of the appropriate variables can be identified

5.4 Conclusion

In this work, a monolithic coupled two field approach for the chemomechanical prediction of smooth muscle contraction has been developed and implemented into the framework of the finite element method. The strain-energy function of the mechanical model consists of three parts associated with the constituents inside a SM tissue. The chemical part has been represented using the four state model by Hai and Murphy (1988) triggered by the *dynamic* state of the calcium concentration inside the muscle.

It has been shown that the model shows an excellent agreement with experimental data. As the model is implemented into the finite element method it is possible to study the deformation behavior of SM contraction in a three-dimensional way. In doing so, deactivated tissue strips have been virtually loaded by an external calcium concentration, leading to a diffusion of the calcium trough the strip. As two layers, the media and the adventitia, have been considered the strip's deformation is dominated by a bending mode what seems to be a reasonable result.

We conclude by noting that such class of models in combination with the realistic three-dimensional SM geometries may provide significant contributions for the understanding, identification and treatment of SM activation.

References

Arner A (1982) Mechanical characteristics of chemically skinned guinea-pig taenia coli. Pflügers Arch 395:277–284

Bates JHT, Lauzon A-M (2007) Parenchymal tethering, airway wall stiffness, and the dynamics of bronchoconstriction. J Appl Physiol 102:1912–1920

Bursztyn L, Eytan O, Jaffa AJ, Elad D (2007) Mathematical model of excitation-contraction in a uterine smooth muscle cell. Am J Physiol, Cell Physiol 292:C1816–1829

Bond M, Somlyo AV (1982) Dense bodies and actin polarity in vertebrate smooth muscle. J Cell Biol 95:403–413

Dahl SLM, Vaughn ME, Niklason LE (2007) An ultrastructural analysis of collagen in tissue engineered arteries. Ann Biomed Eng 35:1749–1755

Fay FS, Delise CM (1973) Contraction of isolated smooth-muscle cells-structural changes. Proc Natl Acad Sci USA 70:641–645

Fritsch H, Kuehnel W (2007) Color atlas and textbook of human anatomy, vol 2. Internal organs. Thieme, Stuttgart

Gestrelius S, Borgström P (1986) A dynamic model of smooth muscle contraction. Biophys J 50:157–169

Hai CM, Murphy RA (1988) Cross-bridge phosphorylation and regulation of latch state in smooth muscle. Am J Physiol 254:C99–106

Herlihy JT, Murphy RA (1973) Length-tension relationship of smooth muscle of the hog carotid artery. Circ Res 33:275–283

Herrera AM, McParland BE, Bienkowska A, Tait R, Paré PD, Seow CY (2005) 'Sarcomeres' of smooth muscle: functional characteristics and ultrastructural evidence. J Cell Sci 118:2381–2392

Hodgkinson JL, Newman TM, Marston SB, Severs NJ (1995) The structure of the contractile apparatus in ultrarapidly frozen smooth muscle: freeze-fracture, deep-etch, and freeze-substitution studies. J Struct Biol 114:93–104

Holzapfel GA, Gasser TC, Ogden RW (2000) A new constitutive framework for arterial wall mechanics and a comparative study of material models. J Elast 61:1–48

Kuo K-H, Seow CY (2004) Contractile filament architecture and force transmission in swine airway smooth muscle. J Cell Sci 117:1503–1511

Lee S, Schmid-Schönbein GW (1996a) Biomechanical model for the myogenic response in the microcirculation: Part I—Formulation and initial testing. J Biomech Eng 118:145–151

Lee S, Schmid-Schönbein GW (1996b) Biomechanical model for the myogenic response in the microcirculation: Part II—Experimental evaluation in rat cremaster muscle. J Biomech Eng 118:152–157

Miftakhov RN, Abdusheva GR (1996) Numerical simulation of excitation-contraction coupling in a locus of the small bowel. Biol Cybern 74:455–467

Murtada S-I, Kroon M, Holzapfel GA (2010) A calcium-driven mechanochemical model for prediction of force generation in smooth muscle. Biomech Model Mechanobiol 9:749–762

Rachev A, Hayashi K (1999) Theoretical study of the effects of vascular smooth muscle contraction on strain and stress distributions in arteries. Ann Biomed Eng 27:459–468

Rhoades RA, Bell DR (2008) Medical physiology: principles for clinical medicine, 3rd edn. Lippincott Williams & Wilkins, Baltimore

Schmitz A, Böl M (2011) On a phenomenological model for active smooth muscle contraction. J Biomech 44:2090–2095

Seow CY, Paré PD (2007) Ultrastructural basis of airway smooth muscle contraction. Can J Physiol Pharm 85:659–665

Singer HA, Murphy RA (1987) Maximal rates of activation in electrically stimulated swine carotid media. Circ Res 60:438–445

Stålhand J, Klarbring A, Holzapfel GA (2008) Smooth muscle contraction: mechanochemical formulation for homogeneous finite strains. Prog Biophys Mol Biol 96:465–481

Walmsley JG, Murphy RA (1987) Force-length dependence of arterial lamellar smooth muscle and myofilament orientations. Am J Physiol 253:H1141–H1147

Wang C, Garcia M, Lu X, Lanir Y, Kassab GS (2006) Three-dimensional mechanical properties of porcine coronary arteries: a validated two-layer model. Am J Physiol, Heart Circ Physiol 291:H1200–1209

Yang J, Clark JW, Bryan RM, Robertson CS (2003a) The myogenic response in isolated rat cerebrovascular arteries: smooth muscle cell model. Med Eng Phys 25:691–709

Yang J, Clark JW, Bryan RM, Robertson CS (2003b) The myogenic response in isolated rat cerebrovascular arteries: vessel model. Med Eng Phys 25:711–717

Zulliger MA, Rachev A, Stergiopulos A (2004) A constitutive formulation of arterial mechanics including vascular smooth muscle tone. Am J Physiol, Heart Circ Physiol 287:H1335–H1343

Chapter 6
Modeling of Smooth Muscle Activation

Jonas Stålhand, Anders Klarbring, and Gerhard A. Holzapfel

Abstract Smooth muscle contraction is governed by a complex chain of events including both mechanical and electrochemical stimuli such as stretch and calcium ion concentration. A homogeneous model for smooth muscle contraction is derived in this paper by using a continuum thermodynamical framework. The model is based on an additive decomposition of the deformation, and balance laws for the mechanical and electrochemical scales are obtained using the principle of virtual power. Constitutive equations are derived by applying the dissipation inequality, and a first-order kinetic model for the chemical state of myosin and standard linear or nonlinear mechanical models for the tissue are introduced. The constitutive equations also provide couplings between the scales. The model includes experimentally observed features like stretch dependent active force generation and hyperbolic relation between shortening velocity and afterload. The model is applied to an experimentally relevant example to illustrate its potential.

6.1 Introduction

Smooth muscle cells are abundant throughout the human body and are found in hollow organs like the arteries, iris of the eye, gastrointestinal tract, and the urinary bladder. The main task for smooth muscles is to provide structural integrity and to

J. Stålhand (✉) · A. Klarbring
Division of Mechanics, Linköping Institute of Technology, 581 83 Linköping, Sweden
e-mail: jonas.stalhand@liu.se

A. Klarbring
e-mail: anders.klarbring@liu.se

G.A. Holzapfel
Institute of Biomechanics, Center of Biomedical Engineering, Graz University of Technology, Kronesgasse 5-I, 8010 Graz, Austria
e-mail: holzapfel@tugraz.at

G.A. Holzapfel
Department of Solid Mechanics, School of Engineering Sciences, Royal Institute of Technology (KTH), Osquars Backe 1, 100 44 Stockholm, Sweden

G.A. Holzapfel, E. Kuhl (eds.), *Computer Models in Biomechanics*,
DOI 10.1007/978-94-007-5464-5_6,

allow for active regulation of geometrical or mechanical properties. For example, arterial smooth muscle is known to contract in connection with acutely lowered blood pressure. This response is believed to work as a first line of defense restoring the transmural strain distribution and flow-induced shear stress back towards their homeostatic values (Rachev and Hayashi, 1999). Further, smooth muscle maintain a constant contraction in arteries. This basal tone together with the residual stress has been hypothesized to reduce the transmural stress gradient leading to a more uniform stress distribution (Humphrey and Wilson, 2003).

The muscle contraction is controlled by a complex chain of electrochemical events involving depolarization of the cell membrane, binding of calcium ions to calmodulin, phosphorylation of light myosin chains and ultimately formation of cross-bridges between actin and myosin filaments. Most of the myosin undergoes a continuous cross-bridge cycling where phosphorylated myosin heads attach actin, perform a force-related power stroke, and finally detach actin. It is the combined effect of all these cross-bridge cycles that generates active force and contraction. In addition to these electrochemical processes, mechanics also impact on the force generation, e.g., stretching the cell increases the phosphorylation rate and causes a sensitization with respect to the calcium ion concentration. This clearly shows that a reasonably complete smooth muscle model must be multi-scale and include properties from both the electrochemical and the mechanical scales.

Relatively few studies have modeled smooth muscle. Among the exceptions are studies by Gestrelius and Borgström (1986), Rachev and Hayashi (1999), Humphrey and Wilson (2003), and Yang et al. (2003). The models in these studies are based on experimental evidence and many constitutive equations are stated intuitively. For example, in Rachev and Hayashi (1999) and Humphrey and Wilson (2003), the effect of smooth muscle contraction is modeled by adding an active stress to the constitutive equation. This active stress has the form $t_0 f_\lambda f_{Ca^{2+}}$, where t_0 is the maximum isometric stress, $f_\lambda \in [0, 1]$ describes the bell-shaped stretch dependence associated with the filament overlap, and $f_{Ca^{2+}} \in [0, 1]$ is the calcium ion dependent activation level. Although this additive technique is both simple and flexible, it has some issues associated with it. First, the absence of a detailed kinematic description for smooth muscle contraction may lead us to believe that the stretch dependence observed in experiments is associated with the total stretch. A more detailed kinematic analysis, see, e.g., Stålhand et al. (2008) and Murtada et al. (2010), suggests that the total stretch should be decomposed into two pars: a filament translation and a stretching of myosin heads. With this decomposition it makes more sense to take the stretch dependence to be a function of the filament translation rather than the total stretch. Second, the coupling of the electrochemical and mechanical subproblems is made *ad hoc* and non-intuitive terms are easily overlooked, see Stålhand et al. (2008). By deriving the model in a continuum thermodynamic framework, this risk is minimized since couplings are implicitly given in the model. In addition, the continuum thermodynamic framework also give constraints on the constitutive equations which guarantee smooth muscle contraction to be dissipative. This is not guaranteed when adding extra terms to the constitutive equation but must be checked for each case. Third, to guarantee a physically reasonable behavior such as

frame-indifference and stress monotonicity, the model must satisfy objectivity and rank-one convexity. These condition may impose restrictions on the validity of the model, see Ambrosi and Pezzuto (2011).

In the proceeding sections, we will show how models for smooth muscle contraction can be derived by applying fundamental laws from mechanics and thermodynamics. The ideas presented herein are based on the works by Stålhand et al. (2008, 2011) and Murtada et al. (2010, 2012).

6.2 Continuum Model for Smooth Muscle Contraction

Contraction of smooth muscle is a coupled mechanical-chemical process. The contraction is intimately associated with two proteins: actin and myosin filaments. Unlike striated muscles, actin and myosin filaments are more smoothly organized and lacks the highly regular pattern evident in, e.g., skeletal muscles. Actin filaments span between anchoring points in the cell, usually referred to as dense bodies, with myosin filaments arranged along the actin (Alberts et al., 2008). Phosphorylated myosin can interact with actin through the head region of the myosin molecule which attaches to actin, forms strong bonds, or cross-bridges, and perform a power stroke which translates the filaments relative to each other (Alberts et al., 2008). After the power stroke, the myosin head can release actin and the cross-bridge cycle starts over again.

The continuum mechanical model starts by defining a mechanical element for the smooth muscle reflecting the physiological structure described above. The element has two sub-elements: a contractile unit and a parallel spring. The contractile unit comprises a friction clutch and a serial spring, see Fig. 6.1. The friction clutch represents the combined effect of all myosin heads exerting force on actin during the power stroke while the serial spring represents the elasticity of the myosin heads. There is evidence that filaments themselves may not be regarded as rigid structures and should, therefore, be included in the serial spring (Edman, 2009). Notwithstanding these evidence, we will assume the elastic deformation to be concentrated to the cross-bridges for simplicity. The second sub-element is a parallel spring which represents passive structures inside or outside the muscle cell, e.g., the cytoskeleton or connective tissue.

6.2.1 Myosin Kinetic Law

As indicated above, myosin must be both attached to actin and phosphorylated for the muscle to generate active contraction. It is, therefore, necessary to know the state of myosin. A simple but widely used model for this purpose was suggested by Hai and Murphy (1988). Therein, four discrete myosin states are introduced, namely, unphosphorylated and unattached myosin (A), phosphorylated

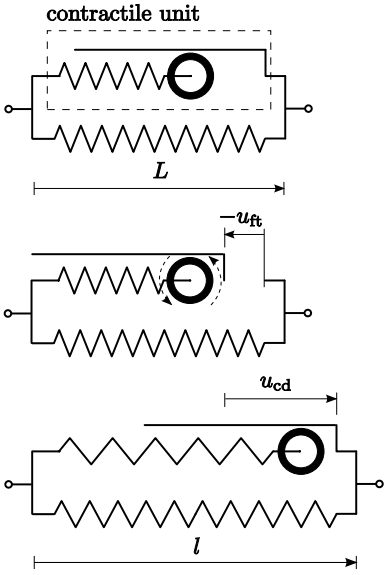

Fig. 6.1 The mechanical element for the smooth muscle comprising a contractile unit and a parallel spring. The reference length of the element is L (*top*). The filaments are first translated a distance $-u_{\mathrm{ft}}$ in the figure by the friction clutch (*middle*) followed by an extension of the cross-bridges a distance u_{cd} (*bottom*)

and unattached myosin (B), phosphorylated and attached myosin (C), and dephosphorylated and attached myosin (D). Because myosin must be attached to actin to generate force, only the states C and D are associated with force generation. The difference is that the myosin heads in state C undergo the cross-bridge cycle and generate force through the power stroke while myosin heads in state D are believed to be non-cycling and work as passive springs resisting extension. The latter state is, therefore, often referred to as the 'latch state'. The transformation between the four myosin states is given by a first-order kinetic model (Hai and Murphy, 1988),

$$\frac{\mathrm{d}}{\mathrm{d}t}\begin{bmatrix} n_{\mathrm{A}} \\ n_{\mathrm{B}} \\ n_{\mathrm{C}} \\ n_{\mathrm{D}} \end{bmatrix} = \begin{bmatrix} -k_1 & k_2 & 0 & k_7 \\ k_1 & -k_2-k_3 & k_4 & 0 \\ 0 & k_3 & -k_4-k_5 & k_6 \\ 0 & 0 & k_5 & -k_6-k_7 \end{bmatrix} \begin{bmatrix} n_{\mathrm{A}} \\ n_{\mathrm{B}} \\ n_{\mathrm{C}} \\ n_{\mathrm{D}} \end{bmatrix}, \tag{6.1}$$

where n_{A}, n_{B}, n_{C}, and n_{D} are the fractions of myosin in the states A, B, C, and D, respectively, and $k_1, \ldots, k_7$ are reaction rates. Since the myosin states are given as fractions, their sum must equal one, i.e.,

$$n_{\mathrm{A}} + n_{\mathrm{B}} + n_{\mathrm{C}} + n_{\mathrm{D}} = 1. \tag{6.2}$$

The reaction rates k_1 and k_6 in Eq. (6.1) control the phosphorylation of myosin. The phosphorylation is governed by a complex chain of events (Alberts et al., 2008) but is ultimately dependent on the intracellular calcium ion concentration in a sigmoid-shaped manner, see Arner (1982). This behavior can be modeled by taking the rate

constants to be (Murtada et al., 2012)

$$k_1 = k_6 = \eta \frac{q^4}{q^4 + q_{1/2}^4}, \tag{6.3}$$

where q is the intracellular calcium ion concentration, $\eta > 0$ is a constant and $q_{1/2}$ is the half-activation concentration.

6.2.2 Kinematics

The model presented herein is confined to homogeneous deformations and the smooth muscle contraction is, therefore, considered to be along a well-defined direction. For a fully three-dimensional smooth muscle contraction model, the interested reader is referred to Stålhand et al. (2011).

The active contraction is modeled as an additive two-step process. The first step is a filament translation u_{ft} where the friction clutch displaces actin along the myosin, and the second step is an elastic deformation u_{cd} of the cross-bridges. Note that the filament translation introduces an incompatibility in the strain field, indicated by the gap in the middle panel in Fig. 6.1. This incompatibility arises because it is assumed that the filament translation occurs without deforming the elastic springs. This has little significance here and compatibility is restored by stretching the cross-bridges. For three-dimensional contraction, however, the incompatibility becomes essential, see Stålhand et al. (2011).

If the reference length is taken to be L, the deformed length is given by $l = L + u_{\text{ft}} + u_{\text{cd}}$ and the total stretch can be obtained by dividing l by L giving

$$\lambda = 1 + \varepsilon_{\text{ft}} + \varepsilon_{\text{cd}}, \tag{6.4}$$

where $\varepsilon_{\text{ft}} = u_{\text{ft}}/L$ and $\varepsilon_{\text{cd}} = u_{\text{cd}}/L$. Note that ε_{ft} is defined to be negative in contraction. The time derivative of Eq. (6.4) gives the deformation rate

$$\dot{\lambda} = \dot{\varepsilon}_{\text{ft}} + \dot{\varepsilon}_{\text{cd}}, \tag{6.5}$$

where the superscribed dot denotes time derivative. Because of the side-polar arrangement of myosin heads (Xu et al., 1996), the power stroke can only generate contraction. Consequently, the friction clutch disc always rotates counter-clockwise in Fig. 6.1 and the velocity at the perimeter must be negative. The absolute value of the perimeter velocity v must be non-negative, however.

6.2.3 Balance Laws

The balance laws are derived using the principle of virtual power as stated by Germain (1973). The method is based on defining virtual velocity fields and assigning

power conjugated thermodynamic forces to these fields. By requiring the internal and external virtual powers to be equal and using the arbitrariness for the virtual velocity fields, balance laws can be obtained for very general situations where a classical free-body diagram will fail.

The virtual velocities in this model are taken to be $\delta\lambda$, $\delta\varepsilon_{\mathrm{ft}}$, $\delta\nu$, $\delta\mathbf{n}$, and δq, where $\mathbf{n} = (n_{\mathrm{A}}, n_{\mathrm{B}}, n_{\mathrm{C}}, n_{\mathrm{D}})$ and $\delta(\cdot)$ denotes the virtual velocity of $(\cdot)$. Using these velocities, we state the internal virtual power as

$$\hat{\mathscr{P}}_{\mathrm{int}} = T_{\mathrm{p}}\delta\lambda + T_{\mathrm{cd}}\delta\varepsilon_{\mathrm{cd}} + T_{\mathrm{ft}}(\delta\varepsilon_{\mathrm{ft}} + \delta\nu) + T_q\delta q, \tag{6.6}$$

where T_{p} is the stress in the parallel spring, T_{cd} is the elastic stress in the cross-bridges, T_{ft} is the stress associated with the friction clutch, and T_q is the internal force power conjugate with the calcium ion flux. The virtual velocity term $\delta\varepsilon_{\mathrm{cd}}$ in Eq. (6.6) is not an independent virtual velocity, as is clear from Eq. (6.5). It is merely introduced for convenience since it describes the strain rate associated with cross-bridge deformation. Furthermore, the term $\delta\varepsilon_{\mathrm{ft}} + \delta\nu$ is the relative velocity between the friction clutch disc and actin and is, therefore, the velocity power conjugate with T_{ft}. Next, we define the external virtual power to be

$$\hat{\mathscr{P}}_{\mathrm{ext}} = t\delta\lambda + t_{\mathrm{ft}}\delta\nu + t_q\delta q, \tag{6.7}$$

where t is the external force applied to the system, and t_{ft} and t_q are the thermodynamic forces power conjugate to $\delta\nu$ and δq, respectively. The second term on the right-hand side in (6.7) is the external power supplied to drive the friction clutch.

Setting Eqs. (6.6) and (6.7) equal and using the arbitrariness of the virtual velocity fields, we arrive at the force equilibrium equations

$$t = T_{\mathrm{p}} + T_{\mathrm{cd}}, \qquad T_{\mathrm{cd}} = T_{\mathrm{ft}}, \qquad t_{\mathrm{ft}} = T_{\mathrm{ft}}, \tag{6.8}$$

and an auxiliary equation for the electrochemical equilibrium

$$t_q = T_q. \tag{6.9}$$

The result above demonstrates the advantage of the virtual power method over the classical force equilibrium approach. Equations (6.8) can be obtained from a force equilibrium, but (6.9) cannot be obtained that way; it requires the electrochemical problem to be considered separately.

6.2.4 Constitutive Equations

With the kinematics and balance laws defined, it is time to focus on the constitutive equations. These equations are derived by applying the dissipation inequality which states that the free energy ψ must satisfy

$$\dot{\psi} \leq \mathscr{P}_{\mathrm{int}}, \tag{6.10}$$

for all admissible evolutions of the state variables. The term $\mathscr{P}_{\text{int}}$ in Eq. (6.10) is the internal power obtained by replacing the virtual velocities in Eq. (6.6) for their real counterparts. Following Stålhand et al. (2008) we take the free energy to be given by

$$\psi = \psi^{\text{p}}(\lambda) + f(\varepsilon_{\text{ft}})\psi^{\text{cb}}(\varepsilon_{\text{cd}}, \mathbf{n}) + \psi^{q}(q) + \sum_{i=\text{A}}^{\text{D}} \psi^{n}(n_i), \tag{6.11}$$

where ψ^{p} is the strain energy stored in the parallel spring, ψ^{cb} is the free energy for the cross-bridges, ψ^{q} and ψ^{n} are the free energies associated with the calcium ion concentration and myosin states, respectively, and $f \in [0, 1]$ describes the strain dependence of the force generation due to filament overlap. Replacing the virtual velocities in Eq. (6.6) for their true counterparts and substituting the result into (6.10) together with Eqs. (6.5) and (6.11), gives, after some rearrangement of the terms,

$$\begin{aligned}\left(T_{\text{p}} + T_{\text{cd}} - \frac{\partial \psi^{\text{p}}}{\partial \lambda} - f\frac{\partial \psi^{\text{cd}}}{\partial \varepsilon_{\text{cd}}}\right)\dot{\lambda} + \left(-T_{\text{cd}} - \frac{\partial f}{\partial \varepsilon_{\text{ft}}}\psi^{\text{cb}} + f\frac{\partial \psi^{\text{cd}}}{\partial \varepsilon_{\text{cd}}}\right)\dot{\varepsilon}_{\text{ft}} \\ + T_{\text{ft}}(\dot{\varepsilon}_{\text{ft}} + \nu) + \left(T_{q} - \frac{\partial \psi^{q}}{\partial q}\right)\dot{q} - \left(f\frac{\partial \psi^{\text{cb}}}{\partial \mathbf{n}} + \frac{\partial \psi^{n}}{\partial \mathbf{n}}\right)\cdot \dot{\mathbf{n}} \geq 0,\end{aligned} \tag{6.12}$$

where the dot denotes a scalar product. Assuming the first and fourth terms in Eq. (6.12) to be non-dissipative gives

$$t = \frac{\partial \psi^{\text{p}}}{\partial \lambda} - f\frac{\partial \psi^{\text{cd}}}{\partial \varepsilon_{\text{cd}}}, \tag{6.13}$$

and

$$t_q = \frac{\partial \psi^{q}}{\partial q}, \tag{6.14}$$

where Eqs. (6.8) have been substituted. Back-substitution of Eqs. (6.13) and (6.14) into (6.12) gives the reduced dissipation inequality

$$\left(-T_{\text{cd}} - \frac{\partial f}{\partial \varepsilon_{\text{ft}}}\psi^{\text{cb}} + f\frac{\partial \psi^{\text{cd}}}{\partial \varepsilon_{\text{cd}}}\right)\dot{\varepsilon}_{\text{ft}} + T_{\text{ft}}(\dot{\varepsilon}_{\text{ft}} + \nu) + \left(f\frac{\partial \psi^{\text{cb}}}{\partial \mathbf{n}} + \frac{\partial \psi^{n}}{\partial \mathbf{n}}\right)\cdot \dot{\mathbf{n}} \geq 0. \tag{6.15}$$

To guarantee that energy dissipates during contraction, first assume the stronger condition that each term in Eq. (6.15) satisfies the inequality, i.e., is greater than zero. Second, take the friction clutch stress to be

$$T_{\text{ft}} = \begin{cases} n_{\text{C}}\mu f(\dot{\varepsilon}_{\text{ft}} + \nu), & \text{if } \dot{\varepsilon}_{\text{ft}} \leq 0, \\ n_{\text{C}}\mu f(\dot{\varepsilon}_{\text{ft}} + \nu) + n_{\text{D}}\mu f\dot{\varepsilon}_{\text{ft}}, & \text{if } \dot{\varepsilon}_{\text{ft}} > 0, \end{cases} \tag{6.16}$$

where $\mu > 0$, and the factors $n_{\text{C}}\mu f$ and $n_{\text{D}}\mu f$ may be thought of as friction coefficients. Equation (6.16) is inspired by the contractile force in Murtada et al. (2010) and it is assumed that only cycling cross-bridges contribute to the force generation,

in contrast to extension, where both cycling and latched cross-bridges contribute to the force generation. Third, substituting Eqs. $(6.8)_2$ into (6.15) and taking the first term to be linear in $\dot{\varepsilon}_{\mathrm{ft}}$, gives

$$-T_{\mathrm{ft}} - \frac{\partial f}{\partial \varepsilon_{\mathrm{ft}}}\psi^{\mathrm{cb}} + f\frac{\partial \psi^{\mathrm{cd}}}{\partial \varepsilon_{\mathrm{ft}}} = g\dot{\varepsilon}_{\mathrm{ft}}, \tag{6.17}$$

where $g \geq 0$ is a function. Equation (6.17) constitutes an evolution law from which $\varepsilon_{\mathrm{ft}}$ can be computed. Finally, for the third term in Eq. (6.16), define

$$\frac{\partial \psi^{\mathrm{cb}}}{\partial \mathbf{n}} + \frac{\partial \psi^{n}}{\partial \mathbf{n}} - r\mathbf{1} = \mathsf{K}\dot{\mathbf{n}}, \tag{6.18}$$

where $\mathbf{1} = (1, 1, 1, 1)$, r is an arbitrary Lagrangian multiplier introduced to satisfy the constraint in Eq. (6.2), and K is a four-by-four positive definite matrix. Note that the term $-r\mathbf{1}$ disappears when Eq. (6.18) is substituted in (6.15) because $\mathbf{1}\cdot\dot{\mathbf{n}} = 0$ by Eq. (6.2). On closer inspection, the structure of Eq. (6.18) is reminicent of the kinetic evolution law by Hai and Murphy in Eq. (6.1), although the former is nonlinear. It is possible to recover Eq. (6.1) by linearizing the left-hand side of Eq. (6.18) around the experimental stretch in Hai and Murphy (1988) and choosing ψ^{cb} to be linear in $\mathbf{n}$, see Stålhand et al. (2008). After some straightforward but non-trivial steps, the result reads

$$\frac{\mathrm{d}}{\mathrm{d}t}\begin{bmatrix} n_{\mathrm{A}} \\ n_{\mathrm{B}} \\ n_{\mathrm{C}} \\ n_{\mathrm{D}} \end{bmatrix} = \begin{bmatrix} \mathbf{k}_1 & \mathbf{k}_2 & \mathbf{k}_3 & \mathbf{k}_4 \end{bmatrix}\begin{bmatrix} n_{\mathrm{A}} \\ n_{\mathrm{B}} \\ n_{\mathrm{C}} \\ n_{\mathrm{D}} \end{bmatrix}, \tag{6.19}$$

where $\mathbf{k}_m$ $(m = 1, 2, 3, 4)$ are the column vectors

$$\begin{aligned} \mathbf{k}_1 &= \eta_1\begin{bmatrix} -k_1, & k_1, & 0, & 0 \end{bmatrix}^{\mathrm{T}}, & \mathbf{k}_2 &= \eta_2\begin{bmatrix} k_2, & -k_2 - k_3, & k_3, & 0 \end{bmatrix}^{\mathrm{T}}, \\ \mathbf{k}_3 &= \eta_3\begin{bmatrix} 0, & k_4, & -k_4 - k_5, & k_5 \end{bmatrix}^{\mathrm{T}}, & \mathbf{k}_4 &= \eta_4\begin{bmatrix} k_7, & 0, & k_6, & -k_6 - k_7 \end{bmatrix}^{\mathrm{T}}, \end{aligned} \tag{6.20}$$

where a superscribed T denotes the transpose and $\eta_m = a_m(\lambda - \lambda_{\mathrm{HM}}) + 1$, where λ_{HM} is the stretch at which the experiments in Hai and Murphy (1988) are performed, see Stålhand et al. (2008). Note that the column vectors in Eq. (6.20) are equal to the column vectors in Eq. (6.1) when $\lambda = \lambda_{\mathrm{HM}}$.

In summary, the model presented is governed by Eq. (6.13) for the external stress, Eq. (6.14) for the calcium ion concentration, Eqs. (6.16) and (6.17) for the evolution of $\varepsilon_{\mathrm{ft}}$, and (6.19) for the myosin transformation. The unknowns variables in the model are λ, $\varepsilon_{\mathrm{ft}}$, $\mathbf{n}$, t, and t_q. In order to proceed, we must specify the model structure, i.e., what is considered as input and output. Further, we must also particularize the free-energy functions, μ, ν, and g. This will be exemplified in the next section.

6.3 A Numerical Example

In this section we describe a model tailored to simulate a type of smooth muscle experiment described in Arner (1982). Briefly, strips of skinned smooth muscles are stimulated in an open organ bath and contract isometrically at the optimal force generating length. The contraction is elicited by adding chemicals to the bath and the specimen is allowed to contract for three minutes after which it relaxes for seven minutes in a normalizing bath. This process is repeated several times. For this experiment, the model inputs are the isometric stretch and calcium ion concentration while the output is the total stress. The isometric stretch is taken to be $\lambda = 1.5$ and the calcium ion concentrations are taken to be 100 nM and 350 nM for the normalizing and contracting baths, respectively, see Murtada et al. (2012). Further, we assume $\lambda_{\mathrm{HM}} = 1.5$ and $a_m = 1$ in Eq. (6.20) to be consistent with the model in the same reference. All computations are summarized in Algorithm 6.1.

Algorithm 6.1 Given a stretch $\lambda(t)$ and the calcium ion concentration $q(t)$

Step 1. Compute consistent initial conditions at isometric conditions

- Step 1a. Set $\dot{\mathbf{n}} = \mathbf{0}$, $\dot{\varepsilon}_{\mathrm{ft}} = 0$ and $f = 1$
- Step 1b. Compute $\mathbf{n}(0)$ from the null space of the matrix in Eq. (6.19)
- Step 1c. Compute $\varepsilon_{\mathrm{ft}}(0)$ from Eq. (6.17)
- Step 1d. Set $\varepsilon_{\mathrm{ft},0} = \varepsilon_{\mathrm{ft}}(0)$

Step 2. For each time step k, compute

- Step 2a. $\dot{\mathbf{n}}(k)$ from Eq. (6.18), and
- Step 2b. $\dot{\varepsilon}_{\mathrm{ft}}(k)$ by using Eqs. (6.16) and (6.17)
- Step 2c. Compute $\mathbf{n}(k+1)$ and $\varepsilon_{\mathrm{ft}}(k+1)$ using a time-stepping scheme
- Step 2d. Compute the total stress $t(k)$ from Eq. (6.13)

The passive free-energy function is taken from Murtada et al. (2012), i.e.

$$\psi^{\mathrm{p}} = \frac{c_0}{2}\left(\lambda^2 + 2\lambda^{-1}\right) + \frac{c_1}{2c_2}\left\{\exp\left[c_2\left(\lambda^2 - 1\right)^2\right] - 1\right\}, \tag{6.21}$$

where $c_0, c_1, c_2 > 0$ are constants. Equation (6.21) is derived by specializing the three-dimensional strain energy proposed in Holzapfel et al. (2000) to a uniaxial extension case. For cross-bridges, assume the free energy to be

$$\psi^{\mathrm{cb}} = \frac{n_{\mathrm{C}} + n_{\mathrm{D}}}{2} E \varepsilon_{\mathrm{cd}}^2, \tag{6.22}$$

where E is the stiffness of the cross-bridges. The free energy in (6.22) gives a linear stress response in $\varepsilon_{\mathrm{cd}}$ which has been observed for cross-bridges in striated muscles using extremely small steps in quick-release experiments (McMahon, 1984).

Table 6.1 Constants used in the numerical example

Constant	Value	Unit	Reference
k_2	9.76	s^{-1}	Murtada et al. (2012)
k_3	4.00	s^{-1}	Murtada et al. (2012)
k_4	0.05	s^{-1}	Murtada et al. (2012)
k_5	9.76	s^{-1}	Murtada et al. (2012)
k_7	0.002	s^{-1}	Murtada et al. (2012)
η	21.55	s^{-1}	Murtada et al. (2012)
$q_{1/2}$	0.37	μM	Murtada et al. (2012)
c_0	0.84	kPa	Murtada et al. (2012)
c_1	3.15	kPa	Murtada et al. (2012)
c_2	0.035		Murtada et al. (2012)
E	5300	kPa	Murtada et al. (2012)
σ	0.25		see text
μ	6800	kPa	see text
ν	0.03	s^{-1}	Murtada et al. (2012)
b	5.0	s^{-1}	see text

The free energy for the calcium ion concentration is take to be the simplest form which allows for direct control of the intracellular calcium ion concentration, namely,

$$\psi^q = \frac{1}{2}q^2. \tag{6.23}$$

Note that the factor $1/2$ is not dimensionless but takes on the appropriate unit for ψ^q to be in Joule. The overlap function f must also be defined. It is generally reported to be bell-shaped (Rachev and Hayashi, 1999) or parabolic (Murtada et al., 2012) and, for simplicity, we take it to be the normal distribution

$$f = \exp\left[-(\varepsilon_{\mathrm{ft}} - \varepsilon_{\mathrm{ft},0})^2/\left(2\sigma^2\right)\right], \tag{6.24}$$

where $\varepsilon_{\mathrm{ft},0}$ is the strain at optimal force generation and $\sigma > 0$ is the width of the normal distribution taken to be 0.25. Finally, the constants ν and μ and the function g in Eq. (6.17) remains to be specified. To that end, assume ν to be the maximal shortening velocity for the smooth muscle and take it to be 0.03, see Fig. 9 in Murtada et al. (2012). This assumption is motivated by Eq. (6.16) since $\dot{\varepsilon}_{\mathrm{ft}} = -\nu$ is the maximal contraction velocity for which the friction clutch generates a contraction force. To determine μ, note that $\dot{\varepsilon}_{\mathrm{ft}} = 0$ in stationary isometric experiments and Eq. (6.16)[1] becomes $n_C \mu \nu f$. By comparing this result with Eq. (20) in Murtada et al. (2012) and substituting ν, the value for μ can be computed to be 6800 kPa. Finally, take the function g to be

$$g = \frac{f}{b}\frac{\partial \psi^{\mathrm{cb}}}{\partial \varepsilon_{\mathrm{cb}}}, \tag{6.25}$$

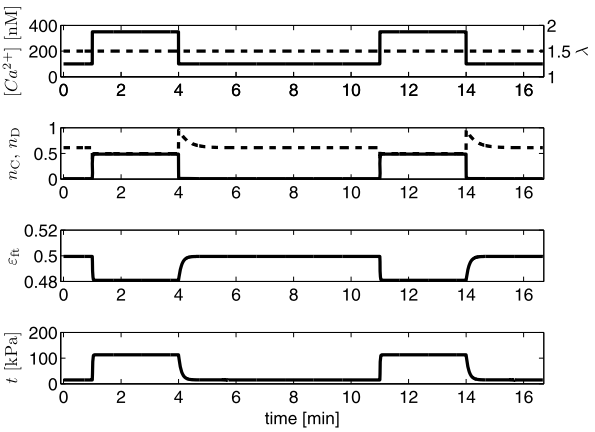

Fig. 6.2 Results from the numerical example. Only two pulses are shown in the interest of space. *Top panel*: calcium ion concentration (*solid line*) and isometric stretch (*dashed line*) inputs. *Second panel form top*: myosin fractions for states n_C (*solid line*) and n_D (*dashed curve*). *Third panel form top*: active filament translation strain ε_{ft}. *Bottom panel*: resulting stress t

where $b = 5$. This choice allows us to recover the same parabolic form for the evolution of ε_{ft} as for the shortening velocity in Hill's equation, see Remark 6.1.

All constants used in this example are listed in Table 6.1 and the results are shown in Fig. 6.2. The most notable result is the rapid transformation of myosin from state C to state D when the muscle relaxes (second panel, 4–11 minutes). From an energy point of view this is an efficient behavior. The majority of energy consumption is associated with cycling cross-bridges, i.e., states B and C, and the transformation allows the muscle to maintain a basal tone at low energy cost. Finally, ε_{ft} in the third panel undergoes a rapid shortening when the muscle is activated (at 1 and 11 minutes). The shortening takes about 10 s and has an exponential decay although it is difficult to see in the graph. This is in qualitative agreement with experimental studies, see, e.g., Arner (1982). If a better agreement is sought, a nonlinear parameter identification can be used to tune the model to experiments, but it is outside the scope of this paper. The interested reader is referred to Stålhand et al. (2008, 2011).

Remark 6.1 In quick-release experiments, smooth muscle show the same parabolic relation between shortening velocity and afterload as skeletal muscle, see Arner (1982). This parabolic relation is also known as Hill's equation and is given by

$$V = b\frac{T' - T_0}{T' + a}, \tag{6.26}$$

where V is the shortening velocity, T' and T_0 are the isometric stress and afterload, respectively, and a and b are constants. Note that the order of the terms in the nominator is shifted relative to the classical definition since contraction is defined as negative herein. Since the model presented herein uses stress and strain rather than force and velocity, V is replaced by $\dot{\lambda}$ in Eq. (6.26). Following Murtada et al. (2012), we choose to specialize the evolution law in Eq. (6.17) such that it has the same functional form as Eq. (6.26) under the assumption of negligible stress contribution from the parallel spring in Fig. 6.1. First, since Hill's equation applies to

contraction, substitute Eq. (6.16)[1] in (6.17) and rearrange the terms to have

$$(g + n_C \mu f)\dot{\varepsilon}_{ft} = f \frac{\partial \psi^{cb}}{\partial \varepsilon_{ft}} - n_C \mu f v. \tag{6.27}$$

The first term on the right-hand side can be interpreted as the stress measured in isotonic experiments and is, hence, associated with the constant afterload. The second term is the isometric force generated by the muscle which is obtained by setting $\dot{\varepsilon}_{ft} = 0$ in Eq. (6.16)[1]. Second, introduce $T_0 = n_C \mu f v$ and $T' = f\partial(\psi^{cb})/\partial\varepsilon_{cb}$ for the isometric stress and afterload, respectively, and take $a = n_C \mu f/b$ and $g = T'/b$. Finally, if the deformation rate in the cross-bridges $\dot{\varepsilon}_{cd}$ is assumed to be negligible after the elastic recoil, an initial step-like contraction following the quick release, Eq. (6.5) gives that $\dot{\varepsilon}_{ft}$ can be replaced by $\dot{\lambda}$ (McMahon, 1984). Equation (6.27), therefore, has the same functional form as Hill's equation.

6.4 Discussion

In this paper we have exemplified how a thermodynamically consistent model can be derived using a very general continuum thermodynamic framework. Despite the increased complexity, the model has several advantages compared to the models mentioned in Sect. 6.1. First, it has a clear kinematic description which is a cornerstone in any mechanical model, and particularly so for active materials. By considering an additive decomposition of the deformation, the model distinguishes between deformations associated with filament translation and force generation, i.e., cross-bridge deformation. This higher resolution allows for a model which is closer to the real physiological situation inside the muscle cell. Second, it has derived couplings between the electrochemical and the mechanical scales as can be seen in Eq. (6.16) or (6.20), for example. These coupling are still introduced intuitively to some extent in the free energies, but the kinematic analysis and the dissipation inequality restricts the number of appropriate choices for the free energies considerably.

The model presented in the previous sections is homogeneous and only accounts for muscle contraction along one direction. This is not as restrictive as may appear at first glance, however. Even though contractile units are less organized in a smooth muscle cell than in other muscle cells, they still have a preferred direction and a certain dispersion around this direction, see Walmsley and Murphy (1987). It is, therefore, possible to extend the smooth muscle model to three dimensions by considering λ to be the stretch along the preferred direction and include a fiber dispersion. The interested reader is referred to Murtada et al. (2010) for more information.

To show the parabolic behavior of the evolution law for ε_{ft}, it was assumed that the stress in the parallel spring was negligible. For skeletal muscle this is an acceptable assumption (McMahon, 1984) since passive structures are, generally, recruited further down on the descending portion of the bell-shaped function f. For smooth

muscle, this is not the case. Passive structures are recruited earlier and have a significant contribution to the isometric stress, see, e.g., Dobrin (1973). Nevertheless, smooth muscles still satisfy Hill's equation, see Arner (1982), and it makes sense to use Eq. (6.26) as an evolution law for $\varepsilon_{\mathrm{ft}}$. Note that the constants a and b in Hill's equation are not arbitrary, however. Only b can be chosen freely since a is defined by $a = n_{\mathrm{C}}\mu f/b$.

References

Alberts B, Johnson A, Lewis J, Raff M, Roberts K, Walter P (2008) Molecular biology of the cell, 5th edn. Garland Science, New York

Ambrosi D, Pezzuto S (2011) Active stress vs. active strain in mechanobiology: constitutive issues. J Elast 107:199–212

Arner A (1982) Mechanical characteristics of chemically skinned guinea-pig taenia coli. Eur J Physiol 395:277–284

Dobrin PB (1973) Influence of initial length on length-tension relationship of vascular smooth muscle. Am J Physiol 225:664–670

Edman KAP (2009) Non-linear myofilament elasticity in frog intact muscle fibres. J Exp Biol 212:1115–1119

Germain P (1973) The method of virtual power in continuum mechanics. Part 2: Microstructure. SIAM J Appl Math 25:556–574

Gestrelius S, Borgström P (1986) A dynamic model of smooth muscle contraction. Biophys J 50:157–169

Hai CM, Murphy RA (1988) Cross-bridge phosphorylation and regulation of latch state in smooth muscle. J Appl Physiol 254:C99–C106

Holzapfel GA, Gasser TC, Ogden RW (2000) A new constitutive framework for arterial wall mechanics and a comparative study of material models. J Elast 61:1–48

Humphrey JD, Wilson E (2003) A potential role of smooth muscle tone in early hypertension: a theoretical study. J Biomech 36:1595–1601

McMahon TA (1984) Muscles, reflexes, and locomotion. Princeton University Press, Chichester

Murtada S, Kroon M, Holzapfel GA (2010) Modeling the dispersion effects of contractile fibers in smooth muscles. J Mech Phys Solids 58:2065–2082

Murtada SC, Arner A, Holzapfel GA (2012) Experiments and mechanochemical modeling of smooth muscle contraction: significance of filament overlap. J Theor Biol 297:176–186

Rachev A, Hayashi K (1999) Theoretical study of the effects of vascular smooth muscle contraction on strain and stress distributions in arteries. Ann Biomed Eng 27:459–468

Stålhand J, Klarbring A, Holzapfel GA (2008) Smooth muscle contraction: mechanochemical formulation for homogeneous finite strains. Prog Biophys Mol Biol 96:465–481

Stålhand J, Klarbring A, Holzapfel GA (2011) A mechanochemical 3D continuum model for smooth muscle contraction under finite strains. J Theor Biol 268:120–130

Walmsley JG, Murphy RA (1987) Force-length dependence of arterial lamellar, smooth muscle, and myofilament orientations. Am J Physiol, Heart Circ Physiol 253:H1141–H1147

Xu JQ, Harder BA, Uman P, Craig R (1996) Myosin filament structure in vertebrate smooth muscle. J Cell Biol 134:53–66

Yang J, Clark JW Jr, Bryan RM, Robertson CS (2003) The myogenic response in isolated rat cerebrovascular arteries: smooth muscle cell model. Med Eng Phys 25:691–709

Chapter 7
A Cross-Bridge Model Describing the Mechanoenergetics of Actomyosin Interaction

Mari Kalda, Pearu Peterson, Jüri Engelbrecht, and Marko Vendelin

Abstract In order to study the mechanical contraction and energy consumption by the cardiomyocytes we further developed an actomyosin model of Vendelin et al. (Ann. Biomed. Eng. 28:629–640, 2000). The model is of a self-consistent Huxley-type and is based on Hill formalism linking the free energy profile of reactions and mechanical force. In several experimental studies it has been shown that the dependency between oxygen consumption and stress-strain area is linear and is the same for isometric and shortening contractions. We analyzed the free energy profiles of actomyosin interaction by changing free energies of intermediate states and activation of different reactions. The model is able to replicate the linear dependence between oxygen consumption and stress-strain area together with other important mechanical properties of a cardiac muscle.

7.1 Introduction

The intracellular environment of heart muscle cells is extensively compartmentalized with the several diffusion obstacles possibly separating mitochondria, the main source of ATP in mammalian heart, from ATPases (Kaasik et al., 2001; Vendelin and Birkedal, 2008; Sepp et al., 2010; Jepihhina et al., 2011). The compartmentation of

M. Kalda · P. Peterson · M. Vendelin
Laboratory of Systems Biology, Institute of Cybernetics, Tallinn University of Technology, Akadeemia 21, Tallinn, Estonia

M. Kalda
e-mail: mari@sysbio.ioc.ee

P. Peterson
e-mail: pearu@sysbio.ioc.ee

M. Vendelin
e-mail: markov@sysbio.ioc.ee

J. Engelbrecht (✉)
Centre for Nonlinear Studies, Institute of Cybernetics, Tallinn University of Technology, Akadeemia 21, Tallinn, Estonia
e-mail: je@ioc.ee

G.A. Holzapfel, E. Kuhl (eds.), *Computer Models in Biomechanics*,
DOI 10.1007/978-94-007-5464-5_7,

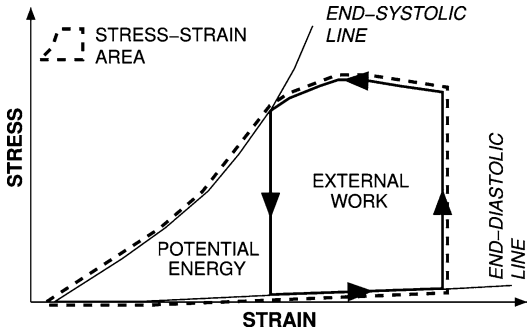

Fig. 7.1 A schematic representation of regional stress-strain trajectory loop. Stress-strain area (SSA) is the specific area in the stress-strain (SS) diagram surrounded by the end-systolic SS line, the end-diastolic SS line and the systolic segment of the SS trajectory for contraction (Delhaas et al., 1994)

the intracellular environment induced by the diffusion obstacles can be changed due to pathological conditions, such as ischemia or ischemia-reperfusion damage (Kay et al., 1997; Boudina et al., 2002). The kinetics of actomyosin ATPase, a main consumer of ATP in the cardiomyocytes (Suga, 1990), is also influenced by intracellular compartmentation as evidenced by strong coupling between creatine kinase and actomyosin (Ventura-Clapier et al., 1987). Studies of intracellular compartmentation has benefited from the development of several mathematical models that allowed us to analyze intracellular diffusion using a 2D (Vendelin et al., 2004) or 3D (Ramay and Vendelin, 2009) description of the intracellular environment and suggest the possible intracellular structures that can lead to compartmentalization of the cell (Ramay and Vendelin, 2009). However, this analysis so far has been limited to relaxed cardiomyocytes or fibers with the models taking into account only the endogenous ATPase activity at low calcium concentrations (Saks et al., 2003; Vendelin et al., 2004; Ramay and Vendelin, 2009; Sepp et al., 2010). To study intracellular energy fluxes and how they are changed depending on the contraction of the heart, the development of actomyosin models that are able to link ATPase activity of the muscle and mechanical performance are vital. Using such models, the changes in energy transfer pathways induced by variation in workload as demonstrated by ^{31}P-NMR inversion and saturation transfer experiments (Vendelin et al., 2010) can be analyzed using mechanistic models.

As an important link between mechanical contraction and ATPase activity of actomyosin, a linear relationship between pressure-volume area (PVA) and oxygen consumption of the heart during a single beat has been established experimentally (Suga, 1990). On a fiber level, the linear relationship between an analog of PVA—stress-strain area (SSA, see Fig. 7.1)—and oxygen consumption has been established (Hisano and Cooper, 1987).

There are several published models that link mechanical contraction and ATPase activity of actomyosin (Cooke and Pate, 1985; Taylor et al., 1993a,b; Landesberg and Sideman, 2000; Vendelin et al., 2000; Månsson, 2010; Tran et al., 2010). Several of these models are based on a Huxley description of the contraction and achieve thermodynamic consistency by applying Hill formalism (Hill, 1974; Eisenberg et al., 1980). That formalism involves describing the spatial dimension of cross-bridge placing and for that partial differential equations (PDE) were used. Solving PDEs is usually considered to be computationally expensive and for that many cross-bridge

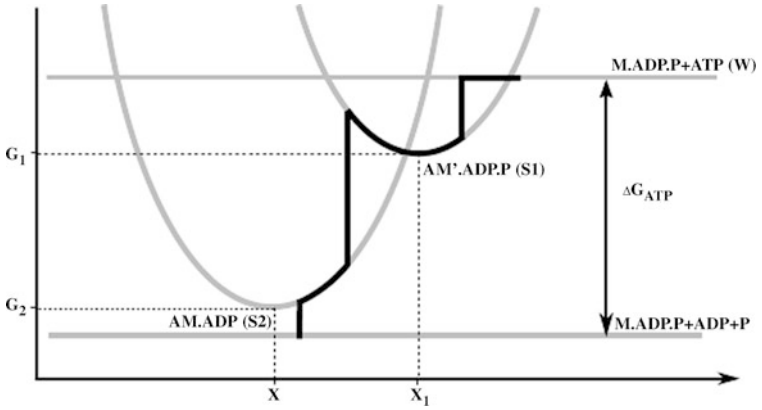

Fig. 7.2 Scheme of one possible set of free energy profiles and transition trajectory (*black solid line*) from state where considered cross-bridge is in the weakly bound state with ATP attached to myosin to weakly bound state without ATP attached to myosin. G_1, G_2, x and x_1 are parameters, that are describing the minimum points of free energy profiles for state S_1 and S_2. These parameters were found by optimization

models have made the simplification and neglected microscopic details of cross-bridge population distribution and instead describe it using average cross-bridge cycling governed by ordinary differential equation (ODE) systems. However, we have demonstrated that it is possible to use a Huxley-type model as a model describing the contraction in the 3D finite element model of the left ventricle (Vendelin et al., 2002). As a basis of actomyosin description in a 3D model, we used a model developed earlier on the basis Hill formalism (Vendelin et al., 2000). In that model, a linear relationship between SSA and ATP consumption during one beat was reproduced together with several other properties of cardiac muscle. Actually, we used a free energy profile of the actomyosin reaction that had two force producing states of the cross-bridge at the same displacement configuration. Namely, the free energy minimum was located at the same position relative to the binding site for the both force producing states. However, the configuration of the cross-bridge is changed during the stroke and to incorporate that into the model, the force producing states should have different free energy minima locations (Eisenberg et al., 1980; Pate and Cooke, 1989).

The aim of this work is to find the set of free energy profiles, with different minimum positions for force producing states of the cross-bridge (Fig. 7.2) that would allow one to replicate the linear dependence between oxygen consumption and stress-strain area in cardiac muscle. First, we give a short description of the theoretical formalism developed by Hill that allows us to link mechanical contraction and chemical energy consumption. Next, the model description and simulation results are presented.

7.2 Theoretical Background

According to the sliding filament theory, shortening in sarcomere length during contraction is caused by thick and thin filaments sliding along each other. Thick and thin filaments consist primarily of the protein myosin and actin, respectively. To slide along, the energy from ATP hydrolysis is used in the interaction between myosin heads and actin sites. One possibility to connect the energetic and mechanical behavior for the contraction process is to use a Huxley-type model and the Hill formalism to describe the actin-myosin interaction in a thermodynamically consistent way. Cross-bridges, as defined by Hill, represent the projection from thick filament, despite if it is attached or not to actin site (Hill, 1974).

The initial Huxley model involves two biochemical states for cross-bridges: one state where actin and myosin are not attached (W) and one where they are attached (S). The rate constants to describe the transition from one state to the other are functions of the relative distance between the nearest cross-bridge equilibrium position and actin binding site. In this formalism several assumptions have been made: the cross-bridge is considered to have only one head and this head has ability to bind to only one actin site with significant probability. Cross-bridge behavior is assumed not to depend on other cross-bridge behavior and each cross-bridge can be in different biochemical states. The force F_n produced by an attached cross-bridge in bound state S is assumed to be elastic and depends linearly on the axial distance x along the myosin and actin filaments between the equilibrium position of the myosin head and the nearest actin binding site.

According to Hill (1974), the force produced by the cross-bridge at position x is related to the free energy G in the corresponding state n: $F_n = \partial G_n / \partial x$. Hence the linear dependency of force on x, leads to a parabolic dependence of the free energy on x. Such a relationship between mechanical force and free energy links the chemical reactions with mechanics. Namely, the transition between states is described by forward and reverse rate constants k_{forward} and k_{reverse}, respectively. The ratio between rate constants is determined by the difference in free energies of biochemical states. If we consider a reaction between state W and S then the ratio between the rate constants of the reaction is defined as

$$\frac{k_{\text{forward}}}{k_{\text{reverse}}} = \exp\left[-\frac{G_S(x) - G_W(x)}{RT}\right], \tag{7.1}$$

where R and T are the universal gas constant and absolute temperature, respectively. It is clear from this relationship that only one of the rate constants can be given at each x with another one determined by the free energy difference. As there is no force associated with state W, the free energy for it is not dependent on x. For values of x, where $G_S < G_W$ the strongly bound state is thermodynamically more stable; otherwise the weakly bounded state is favorable.

To describe muscle contraction, we use a kinetic formalism developed by Hill (1974). In short, it is possible to divide cross-bridges into subensembles according to the distance x between cross-bridge and the closest actin binding site. The cross-bridges are in the same subensemble, if the distance is between x and $x + \mathrm{d}x$. For

the same $\mathrm{d}x$, the number of cross-bridges in subensembles is the same and constant for any x due to the lack of register between myosin and actin. Assuming that the cross-bridge can interact only with the closest actin binding site, the state of the cross-bridges can be described by fractions $n_j(x,t)$ giving the fraction of cross-bridges in state j (j is one of W, or S for two state model) at time t in subensemble at x to $x+\mathrm{d}x$. Taking that the distance between actin binding sites is d, fractions $n_j(x,t)$ are defined for x in the interval $(-d/2, d/2)$. At any time t, all cross-bridges are in one of the two states, $\sum_j n_j(x,t) = 1$. Changes in cross-bridge states are induced by chemical transition from one state to another or sliding of actin and myosin filaments relative to each other with the velocity v of sarcomere lengthening. For example, for state W, this would result in the following governing equation

$$\frac{\partial n_W}{\partial t} + \frac{\partial n_W}{\partial x} v(t) = k_{SW} n_S - k_{WS} n_W, \tag{7.2}$$

where k_{WS} and k_{SW} are the first order kinetic rate constants for transition from state W to state S.

The integral properties of the muscle, such as developed stress and ATPase rate could be found from integration over subensembles (Hill, 1974). The Cauchy stress σ_a developed by the cross-bridges in a half-sarcomere is, according to Zahalak and Ma (1990)

$$\sigma_\mathrm{a} = \frac{m l_s}{d}\left[\int_{-\frac{d}{2}}^{\frac{d}{2}} n_W(x,t) F_W \mathrm{d}x + \int_{-\frac{d}{2}}^{\frac{d}{2}} n_S(x,t) F_S(x) \mathrm{d}x\right], \tag{7.3}$$

where m is the number of cross-bridges in the unit volume and l_s is the length of the half-sarcomere. According to our assumptions F_W is zero because only the strong binding state generates force. Assuming that F_S is proportional to x with Hooke constant K, the stress equation will have the following form

$$\sigma_\mathrm{a} = \frac{m l_s K}{d} \int_{-\frac{d}{2}}^{\frac{d}{2}} n_S(x,t) x \mathrm{d}x. \tag{7.4}$$

The average cross-bridge ATP consumption rate is

$$V_\mathrm{ATP} = \frac{1}{d} \int_{-\frac{d}{2}}^{\frac{d}{2}} \left[k_{SW} n_S(x,t) - k_{WS} n_W(x,t)\right] \mathrm{d}x, \tag{7.5}$$

leading to the total ATP consumption per cross-bridge during a beat

$$V_\mathrm{ATP}^\mathrm{beat} = \frac{1}{d} \int_0^{T_c} \int_{-\frac{d}{2}}^{\frac{d}{2}} \left[k_{SW} n_S(x,t) - k_{WS} n_W(x,t)\right] \mathrm{d}x \mathrm{d}t, \tag{7.6}$$

where T_c is the period of a beat.

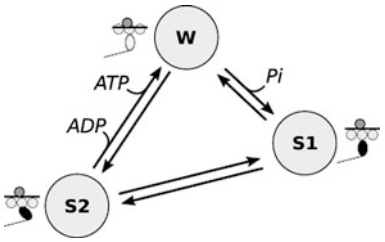

Fig. 7.3 Kinetic scheme of actin and myosin interaction used in three-state Huxley-type cross-bridge model: W is a weakly bound biochemical state, S_1 and S_2 are strongly bound states, where myosin head is able to generate force

7.3 Methods

7.3.1 Model Description

Our mathematical model of actomyosin interaction is a further development of the cross-bridge model of Vendelin et al. (2000). This model consists of a three state Huxley-type model with two strong binding states (S_1, S_2) and one weak binding state (W) for cross-bridge interaction and a model of Ca^{2+} induced activation (Fig. 7.3). According to Eq. (7.3), the Cauchy stress σ_a developed by the cross-bridges in a half-sarcomere for the considered three state model is

$$\sigma_a = \frac{ml_sK}{d}\left[\int_{-\frac{d}{2}}^{\frac{d}{2}} n_{S_1}(x,t)(x-x_1)\mathrm{d}x + \int_{-\frac{d}{2}}^{\frac{d}{2}} n_{S_2}(x,t)(x-x_2)\mathrm{d}x\right], \tag{7.7}$$

where x_1 and x_2 are the minimum positions of free energy profiles for biochemical states S_1 and S_2. The cross-bridge attachment and detachment in the muscle fiber are governed by the following system of equations

$$\frac{\partial n_{S_1}}{\partial t} = k_{WS_1}n_W + k_{S_2S_1}n_{S_2} - (k_{S_1W} + k_{S_1S_2})n_{S_1} - v\frac{\partial n_{S_1}}{\partial x}, \tag{7.8}$$

$$\frac{\partial n_{S_2}}{\partial t} = k_{s_1s_2}n_{S_1} + k_{WS_1}n_W - (k_{S_2S_1} + k_{S_2W})n_{S_2} - v\frac{\partial n_{S_2}}{\partial x}, \tag{7.9}$$

$$n_W = A - n_{S_1} - n_{S_2}, \tag{7.10}$$

where n_W, n_{S_1}, n_{S_2} are the fractions of the cross bridges in states W, S_1, S_2, respectively, A is the relative amount of activated cross bridges and v is the velocity of half sarcomere lengthening

$$v = \frac{\mathrm{d}l_s}{\mathrm{d}t}. \tag{7.11}$$

The rate constants are constrained as follows:

$$\frac{k_{WS_1}}{k_{S_1W}} = \exp\left[-\frac{G_{S_1}(x) - G_W(x)}{RT}\right], \tag{7.12}$$

$$\frac{k_{S_1S_2}}{k_{S_2S_1}} = \exp\left[-\frac{G_{S_2}(x) - G_{S_1}(x)}{RT}\right], \tag{7.13}$$

$$\frac{k_{S_2W}}{k_{WS_2}} = \exp\left[-\frac{G_W(x) - G_{S_2}(x)}{RT}\right]. \tag{7.14}$$

To describe the activation of the cross-bridges we use a phenomenological model, which is able to reproduce the main properties of heart muscle to generate the stress during the heart beat, which depends on time and the length of the sarcomere (Jewell, 1977). To activate the contraction, the concentration of Ca^{2+} changes. For that we use in the activation model the intermediate state B for reactions between tropomyosin C and Ca^{2+}

$$\frac{\mathrm{d}A}{\mathrm{d}t} = c_1 B(1 - A) - c_2(l_s)\frac{A}{Q + A}, \tag{7.15}$$

where c_2 is a function of sarcomere length l_s, i.e.

$$c_2 = c_{2MX} + c_{2F}\frac{l_{\max} - l_s}{l_s - l_{\min}}, \tag{7.16}$$

and normalized concentration B is a function of time, i.e.

$$B = \begin{cases} t \le T_{\mathrm{p}}, & \exp[-(\frac{t-T_{\mathrm{p}}}{T_{\mathrm{a}}})^2], \\ \text{otherwise}, & \exp[-(\frac{t-T_{\mathrm{p}}}{T_{\mathrm{D}}})^2]. \end{cases} \tag{7.17}$$

The symbols c_2, c_{2MX} and c_{2F} are rate constants for reactions between tropomyosin and Ca^{2+}, Q describes the cooperativity for Ca^{2+} to bind with tropomyosin C (Tobacman and Sawyer, 1990) and $l_{\max}$ and $l_{\min}$ are the maximum and minimum lengths of the half sarcomere, respectively. The constant T_{p} is the time that is needed to develop maximal contraction and T_{a} is a time constant. The characteristic time T_{D} is dependent on the half sarcomere length and is defined as

$$T_{\mathrm{D}} = T_{d0}\left(1 + T_{d1}\frac{l_s - l_{\min}}{l_{\max} - l_{\min}}\right), \tag{7.18}$$

where T_{d0} is a time constant and T_{d1} is a relative change of the time constant. The ATP consumption rate during one beat is according to Eq. (7.6)

$$V_{\mathrm{ATP}}^{\mathrm{beat}} = \frac{1}{d}\int_0^{T_c}\int_{-\frac{d}{2}}^{\frac{d}{2}}\left[k_{S_2W}n_{S_2}(x,t) - k_{WS_2}n_W(x,t)\right]\mathrm{d}x\,\mathrm{d}t. \tag{7.19}$$

7.3.2 Optimization Strategy

The goal of the optimization process is to find the set of model parameters for a cross-bridge model which allows us to replicate the experimentally measured linear dependence of oxygen consumption on SSA. For that we divided the model parameters into two sets: (a) parameters describing free energy profiles (Fig. 7.2) and

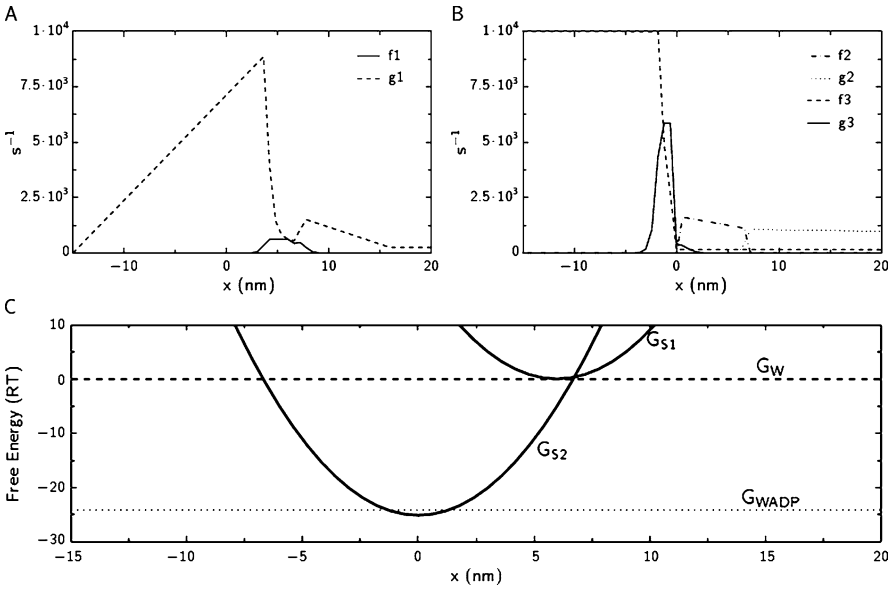

Fig. 7.4 (**A**), (**B**) cross-bridge cycling rates used in the model; (**C**) free energy profiles found by optimization of the mathematical model

(b) parameters describing Ca^{2+}—induced activation of the actomyosin complex and rate constants of the actomyosin complex state transformation reactions.

As a first step in the optimization, (b) parameters were optimized at different sets of parameters (a) by minimization of the different residual functions. After that, the best fit was picked out and all (a) and (b) parameters were optimized again. For finding the parameters for describing the rate constants between biochemical states we predescribed the shape of these functions. The relationship between rate constants pairs (Eq. (7.1)) declare that only one rate constants from the pair is independent. The shapes of the functions are shown at the Figs. 7.4(A) and (B).

To obtain the optimal model parameters we considered three fitting protocols. Simulation for isometric contraction were fitted against experimental data. The maximal total stress in isometric contraction was used for fitting the end-systolic points for isotonic contraction. And the linear relationship between SSA and ATP consumption was fitted against a pre-described linear line for all considered contraction types.

7.4 Results and Discussion

We considered three different type of contractions: isometric, isotonic and physiological. Under ‘physiologic’ contraction we mean the isotonic contraction until the minimal half sarcomere length is reached and isometric contraction after that moment.

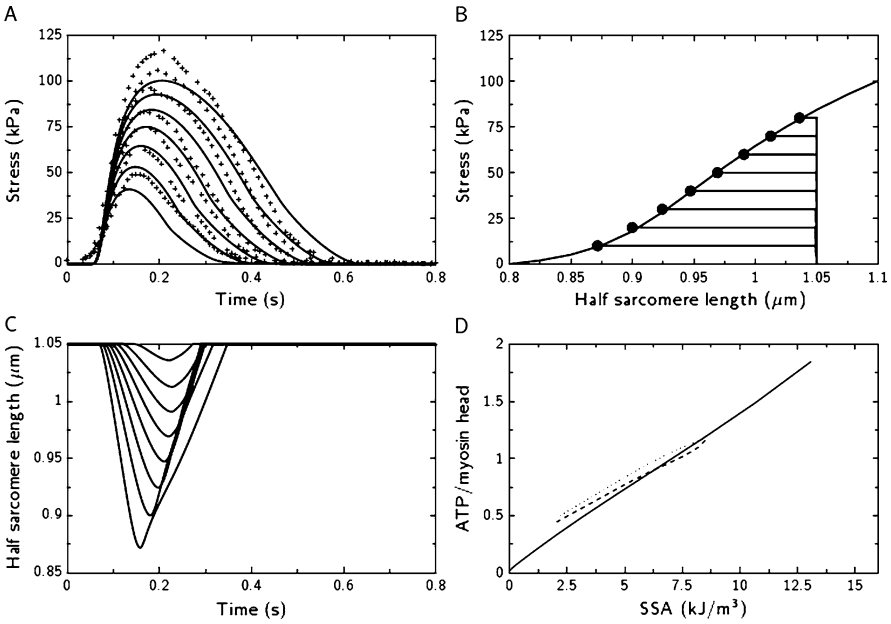

Fig. 7.5 Simulation results performed by mathematical model: (**A**) isometric contraction as a function of time at different half sarcomere lengths from 0.95 to 1.1 μm (*solid curves*) compared with experimental measurements (*crosses*) (Janssen and Hunter, 1995); (**B**) end-systolic curve for the isometric contractions and the isotonic contraction traces (end of the trace is marked with the symbol) at different afterloads from 10 to 80 kPa; (**C**) change in sarcomere length during the isotonic contraction at different afterloads; (**D**) total amount of consumed ATP molecules per myosin head during a cardiac cycle as a function of SSA for isometric (*solid curve*), isotonic (*dashed curve*) and physiologic (*dotted curve*) contraction

In Fig. 7.5(A) simulation of isometric contraction at different half sarcomere lengths from 0.95 to 1.1 μm (solid curve) is compared with experimental measurements (crosses) (Janssen and Hunter, 1995). Similar to experimental data, simulation results show that an increase in preload increases the maximal developed force and the twitch duration.

End-systolic curve for the isometric contractions and the isotonic contraction traces at different afterloads are compared in Fig. 7.5(B). End-systolic points for isotonic contraction lie close to the end-systolic curve for isometric contraction, which is in agreement with several experimental studies.

The isotonic contraction showed in Fig. 7.5(C) are simulated at afterloads from 10 to 80 kPa. To compare the contraction duration at isometric and isotonic contraction the duration is shorter in the isotonic case which is also in agreement with experimental results (Brutsaert et al., 1978).

A linear relationship between ATP consumption and SSA was replicated by our simulations for all considered contraction types (Fig. 7.5(D)). The linear fit for re-

lationship between ATP and SSA for isometric contraction is

$$V_{\mathrm{ATP}}^{\mathrm{beat}} = 0.103 + 0.140\left(\frac{SSA}{m\Delta G_{\mathrm{ATP}}}\right). \tag{7.20}$$

Taking into account the myosin ATPase concentration of 0.18 mol/m^3 (Velden et al., 1998) and free energy change during ATP hydrolysis of 60 kJ/mol (Gibbs and Barclay, 1995), the contraction efficiency calculated from the slope is 66 %. This value is in good agreement with experimental data (Suga, 1990), which demonstrates that the chemomechanical efficiency of cross-bridge cycling is in the range of 60–70 %.

The set of free energy profiles simulated are shown in Fig. 7.4(B). This set involves a configuration chance for cross-bridges during the stroke by having different free energy minimal location points for two strong binding biochemical states S_1 and S_2. It is important to note that the set of parameters found by the optimization may not be unique. In our work we tried to find cross-bridge rates with as simple shape as possible to fit the desired data. It is possible to use different functional forms to describe rate constants and still obtain good results.

7.5 Conclusion

Our mathematical model is able to replicate the classical measurements of SSA and oxygen consumption dependency. As a result of optimization, the model solution is in agreement with the behavior of cardiac muscle in isometric and shortening contractions.

Acknowledgements This research was supported by the European Union through the European Regional Development Fund and by the Estonian Science Foundation (Grant nr. 7344).

References

Boudina S, Laclau M, Tariosse L, Daret D, Gouverneur G, Bonoron-Adèle S, Saks V, Santos PD (2002) Alteration of mitochondrial function in a model of chronic ischemia in vivo in rat heart. Am J Physiol, Heart Circ Physiol 282:821–831

Brutsaert DL, Clerck NMD, Goethals MA, Housmans PR (1978) Relaxation of ventricular cardiac muscle. J Physiol (Lond) 283:469–480

Cooke R, Pate E (1985) The effects of ADP and phosphate on the contraction of muscle fibers. Biophys J 48:789–798

Delhaas T, Arts T, Prinzen FW, Reneman RS (1994) Regional fibre stress-fibre strain area as an estimate of regional blood flow and oxygen demand in the canine heart. J Physiol (Lond) 477:481–496

Eisenberg E, Hill TL, Chen Y (1980) Cross-bridge model of muscle contraction. Quantitative analysis. Biophys J 29:195–227

Gibbs CL, Barclay CJ (1995) Cardiac efficiency. Cardiovasc Res 30:627–634

Hill TL (1974) Theoretical formalism for the sliding filament model of contraction of striated muscle. Part I. Prog Biophys Mol Biol 28:267–340

Hisano R, Cooper G (1987) Correlation of force-length area with oxygen consumption in ferret papillary muscle. Circ Res 61:318–328

Janssen PM, Hunter WC (1995) Force, not sarcomere length, correlates with prolongation of isosarcometric contraction. Am J Physiol 269:676–685

Jepihhina N, Beraud N, Sepp M, Birkedal R, Vendelin M (2011) Permeabilized rat cardiomyocyte response demonstrates intracellular origin of diffusion obstacles. Biophys J 101:2112–2121

Jewell BR (1977) A reexamination of the influence of muscle length on myocardial performance. Circ Res 40:221–230

Kaasik A, Veksler V, Boehm E, Novotova M, Minajeva A, Ventura-Clapier R (2001) Energetic crosstalk between organelles: architectural integration of energy production and utilization. Circ Res 89:153–159

Kay L, Saks VA, Rossi A (1997) Early alteration of the control of mitochondrial function in myocardial ischemia. J Mol Cell Cardiol 29:3399–3411

Landesberg A, Sideman S (2000) Force-velocity relationship and biochemical-to-mechanical energy conversion by the sarcomere. Am J Physiol, Heart Circ Physiol 278:1274–1284

Månsson A (2010) Actomyosin-ADP states, interhead cooperativity, and the force-velocity relation of skeletal muscle. Biophys J 98:1237–1246

Pate E, Cooke R (1989) A model of crossbridge action: the effects of ATP, ADP and Pi. J Muscle Res Cell Motil 29:181–196

Ramay H, Vendelin M (2009) Diffusion restrictions surrounding mitochondria: a mathematical model of heart muscle fibers. Biophys J 97:443–452

Saks V, Kuznetsov A, Andrienko T, Usson Y, Appaix F, Guerrero K, Kaambre T, Sikk P, Lemba M, Vendelin M (2003) Heterogeneity of ADP diffusion and regulation of respiration in cardiac cells. Biophys J 84:3436–3456

Sepp M, Vendelin M, Vija H, Birkedal R (2010) ADP compartmentation analysis reveals coupling between pyruvate kinase and ATPases in heart muscle. Biophys J 98:2785–2793

Suga H (1990) Ventricular energetics. Physiol Rev 70:247–277

Taylor TW, Goto Y, Hata K, Takasago T, Saeki A, Nishioka T, Suga H (1993a) Comparison of the cardiac force-time integral with energetics using a cardiac muscle model. J Biomech 26:1217–1225

Taylor TW, Goto Y, Suga H (1993b) Variable cross-bridge cycling-ATP coupling accounts for cardiac mechanoenergetics. Am J Physiol 264:994–1004

Tobacman LS, Sawyer D (1990) Calcium binds cooperatively to the regulatory sites of the cardiac thin filament. J Biol Chem 265:931–939

Tran K, Smith N, Loiselle D, Crampin E (2010) A metabolite-sensitive, thermodynamically constrained model of cardiac cross-bridge cycling: implications for force development during ischemia. Biophys J 98:267–276

Velden JV, Moorman AF, Stienen GJ (1998) Age-dependent changes in myosin composition correlate with enhanced economy of contraction in guinea-pig hearts. J Physiol (Lond) 507:497–510

Vendelin M, Birkedal R (2008) Anisotropic diffusion of fluorescently labeled ATP in rat cardiomyocytes determined by raster image correlation spectroscopy. Am J Physiol, Cell Physiol 295:1302–1315

Vendelin M, Bovendeerd PHM, Arts T, Engelbrecht J, van Campen DH (2000) Cardiac mechanoenergetics replicated by cross-bridge model. Ann Biomed Eng 28:629–640

Vendelin M, Bovendeerd PHM, Engelbrecht J, Arts T (2002) Optimizing ventricular fibers: uniform strain or stress, but not ATP consumption, leads to high efficiency. Am J Physiol, Heart Circ Physiol 283:H1072–H1081

Vendelin M, Eimre M, Seppet E, Peet N, Andrienko T, Lemba M, Engelbrecht J, Seppet E, Saks V (2004). Intracellular diffusion of adenosine phosphates is locally restricted in cardiac muscle. Mol Cell Biochem 256–257:229–241

Vendelin M, Hoerter J, Mateo P, Soboll S, Gillet B, Mazet J (2010). Modulation of energy transfer pathways between mitochondria and myofibrils by changes in performance of perfused heart. J Biol Chem 285:37240–37250

Ventura-Clapier R, Mekhfi H, Vassort G (1987) Role of creatine kinase in force development in chemically skinned rat cardiac muscle. J Gen Physiol 89:815–837
Zahalak GI, Ma SP (1990) Muscle activation and contraction: constitutive relations based directly on cross-bridge kinetics. J Biomech Eng 112:52–62

Chapter 8
Multiscale Skeletal Muscle Modeling: From Cellular Level to a Multi-segment Skeletal Muscle Model of the Upper Limb

Oliver Röhrle, Michael Sprenger, Ellankavi Ramasamy, and Thomas Heidlauf

Abstract Modeling the biomechanical behavior of the musculoskeletal system requires a multiscale modeling approach spanning several length and time scales. Within this paper, two skeletal muscle models are presented. The first model is an electromechanical skeletal muscle model that couples neurophysiological recruitment principles and electrochemical processes of a sarcomere to the mechanical behavior of a single skeletal muscle through a multiscale continuum-mechanical constitutive law. The second model combines principles of multi-body dynamics and principles of continuum mechanics and the finite element method to achieve the first three-dimensional forward-dynamics model of a musculoskeletal system. Both muscle models can be coupled together in future research to obtain an overall skeletal muscle model spanning from cellular processes to a musculoskeletal system.

O. Röhrle · M. Sprenger · T. Heidlauf
Cluster of Excellence for Simulation Technology, University of Stuttgart, Pfaffenwaldring 5a, 70569 Stuttgart, Germany

O. Röhrle (✉) · M. Sprenger · T. Heidlauf
Institute of Applied Mechanics (CE), University of Stuttgart, Pfaffenwaldring 7, 70569 Stuttgart, Germany
e-mail: roehrle@mechbau.uni-stuttgart.de

M. Sprenger
e-mail: sprenger@mechbau.uni-stuttgart.de

T. Heidlauf
e-mail: heidlauf@mechbau.uni-stuttgart.de

O. Röhrle · E. Ramasamy
Fraunhofer Institute for Manufacturing Engineering and Automation IPA, Nobelstr. 12, 70569 Stuttgart, Germany

E. Ramasamy
e-mail: ellankavi.ramasamy@ipa.fraunhofer.de

G.A. Holzapfel, E. Kuhl (eds.), *Computer Models in Biomechanics*,
DOI 10.1007/978-94-007-5464-5_8,

8.1 Introduction

Dynamic human motion is achieved via the controlled activation of skeletal muscles. Activation of skeletal muscles is consciously initiated through neural impulses originating by the central nervous system causing skeletal muscles to shorten and/or to produce force in a controlled fashion. The muscle forces exerted through the contraction subsequently move the joints to accomplish predetermined tasks. These tasks are quite often required to take place against the action of external forces. The outcome of this entire process largely depends on the force-generation properties of the muscles, the anatomical and physiological features of the skeletal system and the underlying neuronal control system. To obtain a better understanding of the principles leading to dynamic motion, mathematical models play a crucial role.

In general, modeling the dynamics of the musculoskeletal system can be categorized into two methodologies: (i) inverse dynamics and (ii) forward dynamics. In inverse dynamics, the body motion and external forces are provided to compute joint forces and moments that produce the observed motion. Information about the level of activation of the involved muscles is typically not included in simulations appealing to inverse dynamics. Hence, the motion-based nature of such simulations provides limited information on the muscles' (material) behavior (actively contracting skeletal muscles are stiffer than non-activated ones). Without the knowledge of muscle activity many predictions concerning the mechanical behavior of the musculoskeletal system cannot be investigated. In forward dynamics, skeletal muscles are selectively activated and the resultant movement is computed. The activation pattern to achieve a specific target is either guided by a control algorithm, e.g., the λ-model (equilibrium point hypothesis) by Feldman (1974), or determined by an optimization procedure (e.g., Anderson and Pandy, 2001; Pandy, 2001; Erdemir et al., 2007). The cost function of the optimization needs to be specified to obtain meaningful solutions with respect to specific goals, e.g., energy minimization during walking or joint stability through co-contraction. The choice of the cost function can be quite subjective to the researcher's preference.

The parameters within the cost function depend on the modeling parameters of the musculoskeletal system, in particular the modeling parameters of the muscular actuators. In state-of-the-art mechanical skeletal muscle models, the anatomical and physiological complexity of the muscle is reduced to a few physiological parameters such as the point of origin, the direction of force, the average muscle length and the physiological cross-sectional area (PCSA). The point of origin, the direction of force, and the muscle insertion define the line of action (maybe redirected through via points) of such simplified skeletal muscle models. Hence, such models are often referred to as one-dimensional (1D) skeletal muscle models. The line of action and cross-sectional areas are typically obtained by means of magnetic resonance imaging (MRI) or examining cadavers. The magnitude of the exerted muscle forces is either linearly related to the PCSA (Barbenel, 1974) or obtained by 3-element Hill-type models (Zajac, 1989; Anderson and Pandy, 2001). The Hill-type models are by far the most commonly used skeletal muscle models for analyzing movement.

More recently, 3D continuum-mechanical models have been introduced to overcome the crude simplifications of 1D lumped-parameter models. The advantage

of continuum-mechanical models is their ability to represent structural aspects of a muscle's anatomy. Combined with macroscopic constitutive laws describing the stress-strain relationship of active and passive skeletal muscle tissue, the governing equations of finite elasticity, and the Finite Element (FE) method, the continuum-mechanical models provide new insights into stress and strain distributions (Blemker et al., 2005), predictions of a muscle's shape (Johansson et al., 2000; Oomens et al., 2003; Böl and Reese, 2007) or differences between 3D and 1D skeletal muscle models (Röhrle and Pullan, 2007).

Besides the Hill-type and continuum-mechanical models, there exist models that represent sub-cellular processes. For example, Hodgkin-Huxley-like models (e.g., Hodgkin and Huxley, 1952; Shorten et al., 2007) describe the ionic currents and kinetics on the (sub-)cellular scale using ordinary differential equations (ODE). Such models provide further insights into related processes or results of pathological conditions. Bridging the scales between cellular and continuum-mechanical skeletal muscle models opened recently a new field of modeling the skeletal muscle's electromechanical behavior by driving a contraction through muscle recruitment principles (Röhrle et al. 2008, 2012; Röhrle, 2010). The first and still only model that describes the electromechanical behavior of skeletal muscles and accounts for the unique manner in which skeletal muscles are activated, specifically the fact that neighboring fibers are electrically isolated and act independently, has been proposed by Röhrle et al. (2008, 2012) and Röhrle (2010).

However, all studies using state-of-the-art continuum-mechanical models instead of lumped-parameter models focus on inverse dynamics. No framework that appeals to forward dynamics and principles of continuum mechanics has been proposed so far. The research community investigating the dynamics of the musculoskeletal system is mainly focusing on analyzing motion (gait) and exhibits limited interest in computationally more expensive but structurally and functionally more accurate continuum-mechanical models. Considering the already significant computational costs of forward-dynamics simulations with lumped-parameter models, it is comprehensible that the lumped-parameter models cannot only be replaced by continuum-mechanical models. Novel and computationally efficient methodological approaches need to be developed.

For lumped-parameter models, alternative and cost effective strategies have been sought to estimate muscle forces. One of these alternative strategies is to use EMG recordings to predict muscle activity to be used as input in forward-dynamics simulations. Such EMG-driven forward-dynamics simulations (using rigid-body dynamics and lumped-parameter skeletal muscle models) have been proposed, among other musculoskeletal systems, to investigate elbow motion (Koo and Mak, 2005). While EMG data can reduce the computational cost and hence support the use of inverse dynamics within a clinical setting, concerns remain about EMG-driven approaches, in particular about inaccuracies of linking EMG data to muscle parameters of lumped-parameter models. The challenge of using EMG data in musculoskeletal simulations is often related to measuring, processing, and quantifying EMG signals.

The aim of this publication is to present in more detail two different methodological approaches of modeling skeletal muscle mechanics spanning from the cellular level, e.g., modeling the electrophysiological properties of a half-sarcomere,

to movement of a musculoskeletal system. The first methodology focuses in particular on modeling principles of skeletal muscle motor-unit recruitment to form a basis to further investigate the use of EMG signals in forward-dynamics simulations. The second one describes a new methodology to achieve forward-dynamics simulations, when the involved skeletal muscles are represented as three-dimensional continuum-mechanical models.

8.2 Constitutive Modeling of Skeletal Muscles

The continuum-mechanical models considered in this work are based on solving the governing equations of finite-elasticity theory using the FE method. Solving for the mechanical deformation due to skeletal muscle activity or due to a change in the muscle's attachment location, i.e. movement of a connected bone, requires the evaluation of a stress tensor, e.g., the second Piola-Kirchhoff stress tensor. In continuum mechanics, a relation between the applied strain and the corresponding stress has to be provided, which characterizes the behavior of the underlying material. Such a relation is commonly known as constitutive equation. In general, skeletal muscle tissue is modeled as a transversely isotropic and incompressible hyperelastic material. For hyperelastic materials, the constitutive equation can be derived from a Helmholtz free-energy function.

Given the ability of skeletal muscles to contract upon an externally induced stimulus, e.g., a nerve signal, the overall mechanical behavior of a skeletal muscle is typically split into two parts: a passive part describing the mechanical behavior of the so-called ground matrix of a skeletal muscle, $\mathbf{S}^{\text{matrix}}$, and an active part describing the contractile behavior of the muscle, $\mathbf{S}^{\text{active}}$.

The second Piola-Kirchhoff stress tensor used within the theory of finite elasticity is described herein by

$$\begin{aligned}\mathbf{S}^{\text{muscle}} &= 2\sum_{i=1}^{4}\frac{\partial \Psi^{\text{muscle}}(I_1,I_2,I_3,I_4,\alpha)}{\partial I_i}\frac{\partial I_i}{\partial \mathbf{C}}\\ &= \underbrace{c_1\mathbf{I}+c_2(I_1\mathbf{I}-\mathbf{C})-p\sqrt{I_3}\mathbf{C}^{-1}}_{=:\,\mathbf{S}^{\text{iso}}}+\underbrace{\left[\frac{\sigma^{ff}_{\text{pass}}}{I_4}f^{\text{passive}}(I_4)\right](\mathbf{a}_0\otimes\mathbf{a}_0)}_{=:\,\mathbf{S}^{\text{aniso}}}\\ &\quad+\underbrace{\alpha\left[\frac{\sigma^{ff}_{\text{ten}}}{I_4}f^{\text{active}}(I_4)\right](\mathbf{a}_0\otimes\mathbf{a}_0)}_{=:\,\mathbf{S}^{\text{active}}},\end{aligned}\tag{8.1}$$

where Ψ^{muscle} is the Helmholtz free-energy, I_1-I_4 are the standard invariants, $\mathbf{a}_0$ denotes the local direction of the skeletal muscle fibers, $\mathbf{C}$ is the right Cauchy-Green tensor, $\mathbf{I}$ is the identity tensor, $\sigma^{ff}_{\text{pass}}=\sigma^{ff}_{\text{ten}}=0.03$ MPa are the maximal passive

and active stiffnesses along the fiber direction, p is the hydrostatic pressure, and $\alpha \in [0, 1]$ is an internal variable that describes the level of activation. Further, $\lambda = \sqrt{\mathbf{a}_0 \cdot \mathbf{C}\mathbf{a}_0}$ is the fiber stretch, and f^{passive} and f^{active} are the normalized force-length relationships describing, for the active part, the overlap of actin and myosin, and hence the ability to generate tension through crossbridge dynamics. For the passive part, f^{passive} describes the nonlinear behavior of the skeletal muscle tissue due to stretch. The normalized force-length relationships are a common tool to incorporate the physiological behavior of the fiber stretch in the muscle's constitutive equation (e.g., Blemker et al., 2005; Röhrle and Pullan, 2007; Böl and Reese, 2007).

The second Piola-Kirchhoff stress tensor, as defined in Eq. (8.1), forms the basis for all continuum-mechanical investigations of skeletal muscle mechanics discussed in this work. In case of modeling the skeletal muscle as an electromechanical-active tissue, the activation parameter α is replaced by cellular variables (cf. Sect. 8.4).

8.3 The Electromechanical Skeletal Muscle Model

The cellular parameters within the continuum-mechanical model are based on functional and structural characteristics of skeletal muscles. Each skeletal muscle fiber is connected to an α-motoneuron at the neuromuscular junction at the middle of the fiber's length. Each α-motoneuron connects to a number of fibers that are distributed over some part of a muscle and transfers electrical signals from the central nervous system to these muscle fibers. Such an electrical signal induces a change in the membrane potential of the skeletal muscle fibers at the neuromuscular junction (stimulation). The potential change, referred to as action potential, spreads along the length of the fiber towards its ends, and induces a number of biophysical processes in the sarcomeres (basic units of a muscle fiber) eventually leading to a contraction. Hereby it is important to note that individual muscle fibers are electrically isolated from each other, i.e. a propagating action potential along one fiber does not induce an electrical signal in neighboring fibers, but mechanically coupled. To allow such a setting, in which electrical signals can independently propagate along the length of specific muscle fibers, one-dimensional structures representing the muscle fibers (the micro-structure) need to be embedded within the three-dimensional geometrical representation of the entire skeletal muscle.

For this purpose, a three-dimensional FE model of the tibialis anterior muscle (TA) has been generated based on the male Visible Human data set (Spitzer and Whitlock, 1998). Based on a manual digitization process, a tri-quadratic Lagrange FE representation of the superficial part and the deep part of the TA has been created using a least-squares fitting process similar to the one described by Bradley et al. (1997). Particular care was taken to align the ξ_1-local coordinate direction of the FE mesh with the anatomical muscle fiber direction of the TA's muscle fibers. This choice of aligning the muscle fibers with a local FE coordinate direction eased the embedding of the 1D fiber meshes and, later on, the numerical solution of action-potential propagation along the muscle fibers. The muscle-fiber distribution is based on published data obtained from diffusion-tensor MRI (Lansdown et al., 2007).

The smallest functional unit of a skeletal muscle is the motor unit (MU), which contains all muscle fibers within a muscle that are innervated by the same α-motoneuron. Therefore, to be able to model the physiological recruitment of MUs in a muscle, it is necessary to enhance the geometrical TA model with functional information of the MU distribution. As the fibers within one MU are distributed throughout the muscle, a muscle fiber assignment algorithm based on physiological properties has been developed by Röhrle et al. (2012). The key characteristics of the functional grouping include an exponential distribution of muscle fibers per MU, meaning that, in accordance with the work of Enoka and Fuglevand (2001), there exist many small MUs composed of slow-twitch muscle fibers with slow fatiguing properties and a few large MUs composed of fast-twitch fibers with fast fatiguing properties. The distribution of single MUs can be obtained experimentally. The experiments, however, are limited to determine the distribution of one/a few MUs per muscle. A thorough description is not available (cf., Monti et al., 2001). Hence, assigning the muscle fibers to MUs has been done based on published information on MU centers and MU territories. The reader is referred to Röhrle et al. (2012) for more details about the algorithm to assign muscle fibers to MUs.

The functional aspects of the skeletal muscle model can be described by three (sub-)models, which are coupled with each other. Firstly, the neuro-physiological model describes motor unit recruitment and rate coding. Secondly, the electrophysiological model of a single muscle fiber describes the major biochemical processes within a half-sarcomere, and, thirdly, the continuum-mechanical model links the neuro-physiological and electrophysiological model to muscle force generation. An overview on the key characteristics of each component and how the different components are linked to each other can be found in Fig. 8.1.

As depicted in Fig. 8.1, the skeletal muscle model is driven by the MU-recruitment model. As currently implemented, the recruitment model determines the times when single MUs fire, i.e. determining the efferent input. The MU recruitment model is currently only unidirectionally coupled to the electrophysiological and mechanical model. While providing the signals to recruit single fibers of a MU, it does not incorporate any feedback from the Golgi-tendon organ, muscle spindles, or other receptors, i.e. afferent input. Therefore, the link between the mechanical model and the motor recruitment model has been only indicated in Fig. 8.1 by a dashed arrow. This, however, is work in progress.

8.4 The Multiscale Constitutive Equation

As described above, the electrophysiological behavior on the cellular level is coupled to the continuum-mechanical model. Within this context, the coupling is achieved through a multiscale constitutive equation. As already indicated in Sect. 8.2, the 'macroscopic' α in Eq. (8.1) is replaced by an expression containing cellular parameters, specifically, the parameters A_1 and A_2, which describe the concentration of myosin heads in the attached pre- and post-powerstroke states. In

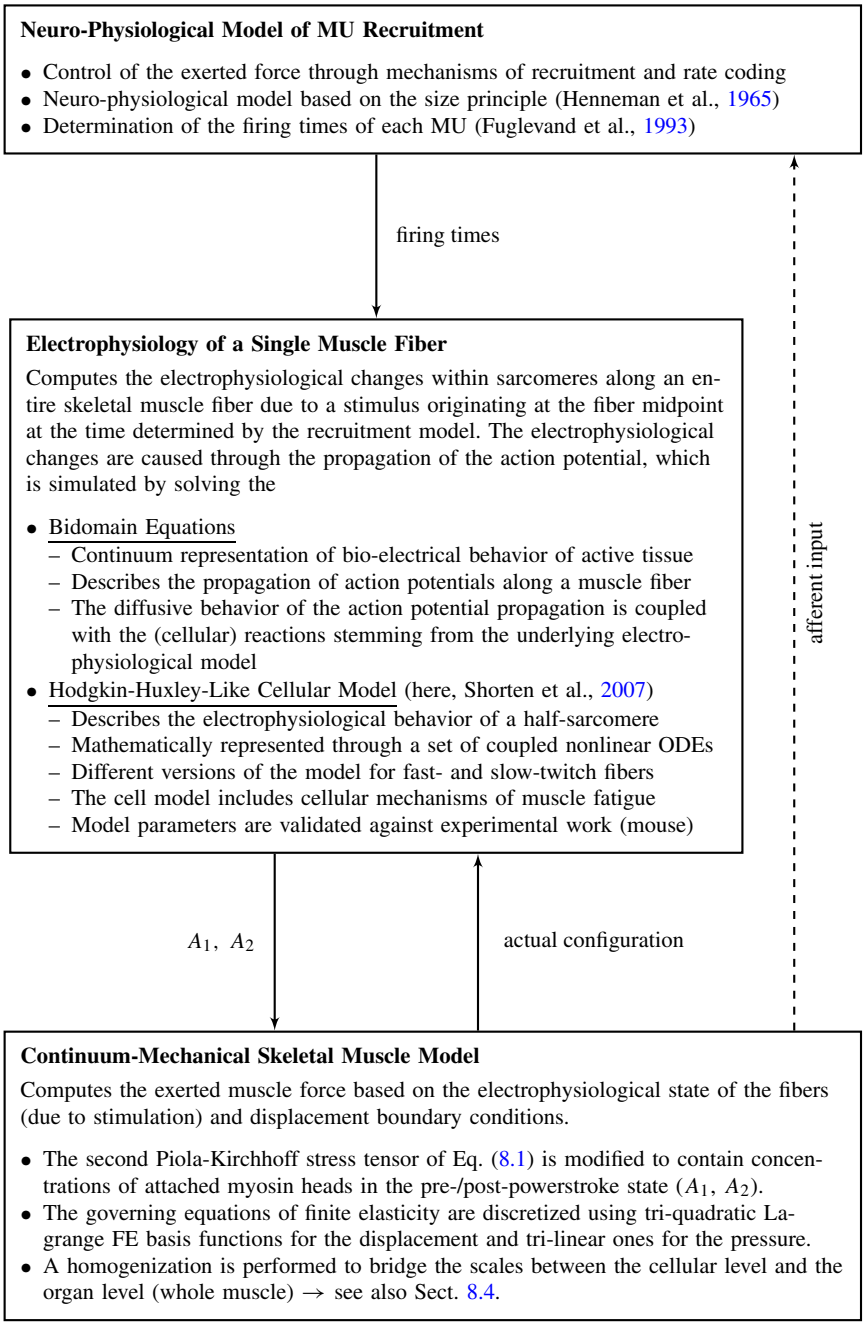

Fig. 8.1 Overview on the computational model to link motor unit recruitment with the continuum-mechanical model of a whole skeletal muscle

terms of cellular parameters, the second Piola-Kirchhoff stress tensor is given by:

$$\mathbf{S}^{\text{muscle}} = \mathbf{S}^{\text{iso}} + \left(\frac{A_1 + A_2}{c_{\text{trop}}} \frac{\sigma_{\text{pass}}^{ff}}{I_4} f^{\text{pass}}(I_4) + \frac{A_2}{A_2^{\max}} \frac{\sigma_{\text{ten}}^{ff}}{I_4} f^{\text{active}}(I_4) \right) \mathbf{a}_0 \otimes \mathbf{a}_0, \quad (8.2)$$

where c_{trop} is the amount of troponin present within a half-sarcomere and $A_2^{\max}$ is the maximal possible concentration of attached myosin heads in the post-powerstroke state. Further, the expression $A_2/A_2^{\max}$ in Eq. (8.2) is comparable to the α-term and presents a cellular-based activation variable that ranges between 0 and 1. The additional term containing $(A_1 + A_2)/c_{\text{trop}}$ can be interpreted as an additional passive stiffness that is induced by a specific contraction. The justification for this term is based on the assumption that each attached myosin head, either in the pre- or post-powerstroke state, adds additional passive stiffness to the system. Furthermore, the cellular parameters in the second Piola-Kirchhoff stress tensor (A_1 and A_2) are still multiplied by a rather macroscopic force-length relationship $f^{\text{active}}(I_4)$ and $f^{\text{pass}}(I_4)$, which are derived from experiments on whole muscles. The justification for doing so is that the model of Shorten et al. (2007) in its current form is only valid for isometric contractions. Therefore the pre- and post-powerstroke concentrations (A_1 and A_2) have been multiplied by the normalized force-length relationship for active contractions, i.e. $f^{\text{active}}(I_4)$, to account for the probability by how much the actin and myosin filaments overlap.

The cellular parameters A_1 and A_2 change from grid point to grid point along the 1D muscle fibers, and from 1D fiber to 1D fiber. A relative small grid spacing has to be used for the propagation of the action potential along the skeletal muscle fibers within the 1D grids, due to the sharp gradients occurring. Furthermore, a relative large number of fibers within a skeletal muscle have to be considered to represent physiological conditions. Due to the computational work involved, the second Piola-Kirchhoff stress tensor as given in Eq. (8.1), cannot be evaluated at each grid point of the 1D meshes. A FE discretization of the mechanical problem, in which each 1D grid point would coincide with a Gauss point of the 3D mesh, would lead to an overly large mechanical problem. Therefore, the cellular variables are homogenized. For all grid points of the 1D meshes, the closest Gauss point of the 3D mesh is sought, where the respective cellular values are homogenized by averaging. A grid convergence study justifying the proposed homogenization is presented in Röhrle et al. (2008).

An output of the above described electromechanical framework is given in Fig. 8.2. There, the stimulation times of every second motor unit are shown by vertical strikes on the horizontal lines (each line represents one MU). The simulation shows that, like in reality, the larger motor units (higher MU numbers) are activated later than the smaller motor units (lower MU numbers) and that the average recruitment frequency of all MUs increases, if a linear excitatory drive function as input to the Fuglevand et al. (1993) motor unit recruitment model is chosen. The resulting force output behaves sigmoidal with a slow average change in curvature at the beginning and end of the simulation and a relatively linear section in the middle.

The results in Fig. 8.2 essentially present the solution to a forward dynamics problem. The recruitment of particular motor units serves as input while the model's

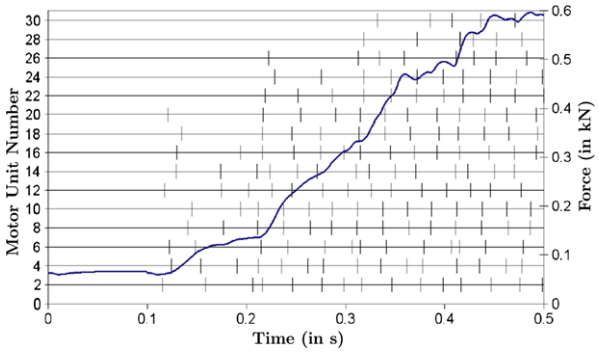

Fig. 8.2 The force output profiles of the TA with 30 motor units and a linear excitatory drive function as input to the Fuglevand et al. (1993) motor unit recruitment model. Figure is taken from Röhrle et al. (2012)

output is the resulting muscle force subject to zero-displacement boundary conditions (isometric contraction). The advantage of the modular framework, as presented in Fig. 8.1, is its versatility. For example, it is straight forward to exchange the MU recruitment model with a different neuro-physiological model of MU recruitment. Further, the knowledge of the action potential within the interior of the muscle can serve as source for the computation of a virtual EMG signal. Computing such a virtual EMG signal allows to test and investigate specific MU recruitment hypotheses—particularly in conjunction with experimental measurements. Further, by generating artificial EMG signals of multiple muscles within a musculoskeletal system, one can identify suitable EMG recording locations that minimize cross-talk. Further, such a model can provide the basis for investigating complex EMG signals taken from a musculoskeletal system, e.g., EMG signals taken from the biceps brachii and triceps brachii of the upper limb, which shall serve as input to forward-dynamics simulations of three-dimensional (continuum-mechanical) models.

8.5 A Multiscale Forward-Dynamics Musculoskeletal Simulation Framework

Without further investigating the ability to use EMG-signals in three-dimensional forward-dynamics simulations, it is more essential to develop a new and computationally efficient framework appealing to principles of forward dynamics and continuum-mechanics. In a first step, as outlined in the following, only activation-driven forward-dynamics simulations are considered. Full path-guided forward-dynamics simulations are subject to future work.

An efficient three-dimensional continuum-mechanical forward-dynamics simulation can be achieved by coupling the finite element method with rigid-body dynamics through nested iteration. The nested-iteration method is an efficient solution technique that aims to obtain a good initial guess for a nonlinear problem and mesh discretization by solving the problem on coarser meshes. Nested iteration builds on the idea that solutions on coarser meshes provide, through interpolation, a good initial guess to a nonlinear problem on a finer mesh. This provides two advantages:

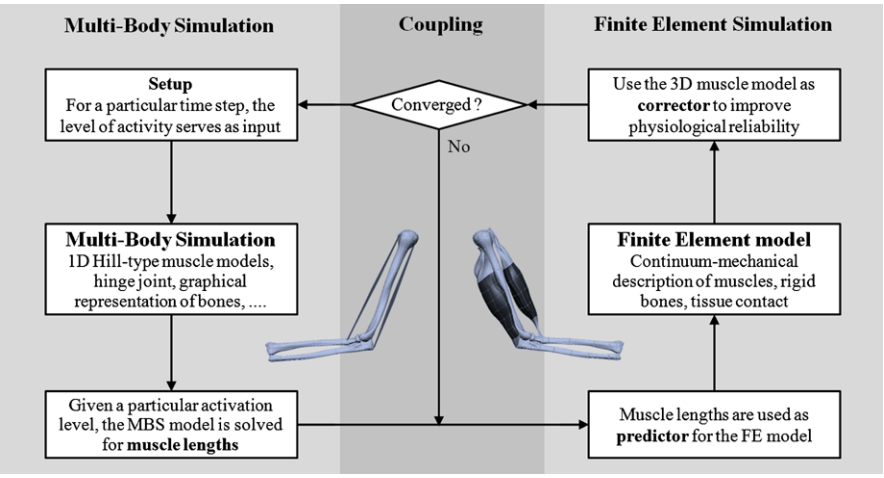

Fig. 8.3 Overview on the coupling of multi-body and FE simulations to achieve efficient forward-dynamics simulations within a continuum-mechanical framework. The coupling is achieved through a multi-physics nested-iteration approach

If the initial guess is close to the solution, Newton's method converges quadratically. Second, the initial guess for the nonlinear problem on the finest level is, if compared with one linearization step at the finest mesh resolution, obtained in a relative cheap manner as calculations on coarser meshes are much cheaper than on the finest mesh resolution. This is particularly true for three-dimensional problems. Such grid-continuation or nested-iteration methods have a great potential for reducing the number of necessary Newton iterations (Kim et al., 2006).

Within the context of modeling a musculoskeletal system, the nested-iteration algorithm as a sequence of predictions on successively finer meshes is extended from pure mesh refinement to a multi-physics approach. Now, the 'cheapest' solution of the coarsest mesh is substituted by a different solution methodology, here the rigid-body dynamics simulations. The key idea hereby is to predict the force and moment equilibrium within a given musculoskeletal system, i.e. the number of muscles and their respective levels of activation, using rigid-body dynamics. This procedure is efficient and, from a computational point of view, relative cheap. The solution of the multi-body problem serves within the nested-iteration algorithm as reasonable initial guess for the muscle displacement boundary conditions (still assuming the bony structures as rigid). Hence, the rigid-body model can be seen as a predictor for the continuum-mechanical model, and the continuum-mechanical model as a corrector. This way, model-inherent deficiencies of rigid-body dynamics simulations, e.g., the complex muscle-fiber distributions, contact with other surrounding tissues, or dynamically changing lines of action can be addressed in an appropriate way. On the other hand, by predicting an initial guess close to the correct solution, the FE method's CPU cost can be reduced.

As indicated in Fig. 8.3, initial tests on integrating such a multi-physics nested-iteration approach have been carried out on a two-muscle and one-degree of freedom

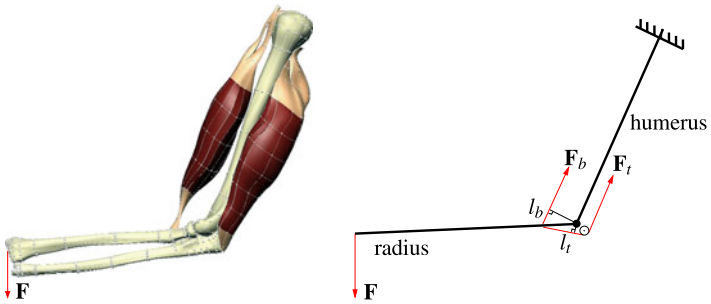

(a) 3D FE model (b) 1D model

Fig. 8.4 The detailed 3D FE model and the geometrically simplified upper limb model

(DOF) musculoskeletal system. The first musculoskeletal model consists of three-dimensional continuum-mechanical models of the biceps brachii and triceps brachii (including its tendons) as an antagonistic muscle pair, the humerus, radius and ulna as three-dimensional rigid representations of the involved bones, and the elbow joint as a one-DOF hinge joint. The prediction for the position of the radius and ulna stems from the 1-DOF-model depicted in Fig. 8.4.

8.6 Discussion

The strength of the electromechanical model is certainly its modular composition and flexibility. Any part of the model can be replaced by newly developed more sophisticated models, which for example describe the electrophysiology on the cellular level, the motor unit recruitment algorithm, or the continuum-mechanical constitutive equation. Furthermore, the framework can be extended to include further models, e.g., models of muscle spindles or Golgi tendon organs, or to incorporate afferent input in the MU recruitment model. Further, different neuro-physiological models, in particular models that are based on system-biological approaches like Cisi and Kohn (2008) can be investigated in much more detail. Understanding the recruitment principles of single muscles and within a musculoskeletal system enhances the applicability of the forward-dynamics simulations based on continuum-mechanical models.

In its current form, however, the electromechanical model also contains a number of weaknesses. Currently, some of the integrated models stem from models derived for different species. For example, the geometrical model is based on the human TA muscle while the electro-physiological model of Shorten et al. (2007) has been validated on mouse muscles. Moreover, when coupling different models, the number of parameters to be determined beforehand increases. The model of Shorten et al. (2007) by itself contains more than 50 ODEs and even more parameters. For many of these values and parameters of the other models, in particular on the motor unit distribution, only few data are available from the literature.

Considering the geometric model, the number of embedded 1D FE meshes within the 3D FE geometry cannot reach a physiological-realistic muscle fiber number. This is due to the computational load involved in solving the cellular model, which is an integral part of modeling the action potential propagation by means of the bidomain equations. Further, the assignment of muscle fibers to particular motor units has been based on physiological data published in the literature. Although much physiological information and knowledge has been included in constructing the geometrical model, there is still a considerable amount of uncertainty present. This stems mainly from the fact that muscle fibers associated with a motor unit can only be experimentally determined for one motor unit per muscle. This is due to the destructive nature of the experimental setup. Moreover, there exists a great inter-subject variability in muscle fiber distribution. Nevertheless, the model can be used to test different hypothesis and investigate the influence of different muscle fiber types in different regions of the muscle.

From a continuum-mechanical material modeling point of view, the constitutive equations presented in Eqs. (8.1), and (8.2) in case of modeling the electromechanical behavior of skeletal muscle, have been designed to describe the characteristic properties of skeletal muscle tissue in a phenomenological way. However, thorough validation of the active and passive behavior in conjunction with experiments is still missing. On the upside, the continuum-mechanical modeling framework of the musculoskeletal system provides the ability to include further mechanical features that cannot be included in multi-body dynamics simulations. For example, the mechanical behavior of skeletal muscles can now be easily subjected to other constraints and restrictions arising from the contact with neighboring structures such as adjacent muscles, bones, and skin. To realistically simulate the mechanical behavior of skeletal muscle in vivo, the influence of these structures has to be considered.

Both described models, e.g., the electromechanical single muscle model and the musculoskeletal system model of the upper arm, have not been validated against experimental data yet. Like for most biomechanical models, developing suitable experimental setups for validation is challenging. Here, however, there exist several different possibilities to validate the musculoskeletal system model of the upper arm through combined measurements of muscular activity (EMG) and motion (via motion capture). Further, other measuring modalities can be added to EMG and motion measurements. For example, pressure sensors or ultrasound devices, which have recently been used to investigate muscular contractions through the change in fiber angle, can significantly augment the EMG and motion measurements.

Although the electromechanical model is subject to restrictions, it provides a new basis to study motor unit recruitment principles and to simulate EMG-driven forward dynamics simulations of the musculoskeletal systems. By using multi-body simulations to cheaply describe overall characteristics and FE simulations to take into account local and structural information, the 3D forward-dynamics simulation framework will give rise to many new opportunities in investigating the musculoskeletal system and many biomechanical applications. For example, determining the dynamic loading conditions of joints during normal movement will play a crucial

role in the design process of new implants. The combination of multi-body simulations and FE methods will have a significant impact on investigating the musculoskeletal system as FE-only methodologies will remain a significant computational challenge for complex musculoskeletal systems for some time.

Acknowledgements The authors would like to thank the German Research Foundation (DFG) for financial support of the projects within the Cluster of Excellence in Simulation Technology (EXC 310/1) at the University of Stuttgart.

References

Anderson FC, Pandy MG (2001) Dynamic optimization of human walking. J Biomech Eng 123:381–390

Barbenel JC (1974) The mechanics of the temporomandibular joint. J Oral Rehabil 1:19–27

Blemker SS, Pinsky PM, Delp SL (2005) A 3D model of muscle reveals the causes of nonuniform strains in the biceps brachii. J Biomech 38:657–665

Böl M, Reese S (2007) A new approach for the simulation of skeletal muscles using the tool of statistical mechanics. Mat.-wiss. Werkstofftech. 38:955–964

Bradley CP, Pullan AJ, Hunter PJ (1997) Geometric modeling of the human torso using cubic hermite elements. Ann Biomed Eng 25:96–111

Cisi R, Kohn A (2008) Simulation system of spinal cord motor nuclei and associated nerves and muscles, in a web-based architecture. J Comput Neurosci 25:520–542

Enoka RM, Fuglevand AJ (2001) Motor unit physiology: some unresolved issues. Muscle Nerve 24:4–17

Erdemir A, McLean S, Herzog W, van den Bogert A (2007) Model-based estimation of muscle forces exerted during movements. Clin Biomech 22:131–154

Feldman A (1974) Control of the length of the muscle. Biophysics 19:766–771

Fuglevand AJ, Winter DA, Patla AE (1993) Models of recruitment and rate coding organization in motor unit pools. J Neurophysiol 70:2470–2488

Henneman E, Somjen G, Carpenter D (1965) Functional significance of cell size in spinal motoneurons. J Neurophysiol 28:560–580

Hodgkin A, Huxley A (1952) A quantitative description of membrane current and its application to conduction and excitation in nerve. J Physiol 117:500–544

Johansson T, Meier P, Blickhan R (2000) A finite-element model for the mechanical analysis of skeletal muscles. J Theor Biol 206:131–149

Kim S, Lee C, Manteuffel T, McCormick S, Röhrle O (2006) First-order system least squares for the Oseen equations. Numer Linear Algebra Appl 13:523–542

Koo TK, Mak AF (2005) Feasibility of using EMG driven neuromusculoskeletal model for prediction of dynamic movement of the elbow. J Electromyogr Kinesiol 15:12–26

Lansdown DA, Ding A, Wadington M, Hornberger JL, Damon BM (2007) Quantitative diffusion tensor MRI-based fiber tracking of human skeletal muscle. J Appl Physiol 103:673–681

Monti RJ, Roy RR, Edgerton VR (2001) Role of motor unit structure in defining function. Muscle Nerve 24:848–866

Oomens CWJ, Maenhout M, Van Oijen CH, Drost MR, Baaijens FP (2003) Finite element modelling of contracting skeletal muscle. Philos Trans R Soc B 358:1453–1460

Pandy MG (2001) Computer modeling and simulation of human movement. Annu Rev Biomed Eng 3:245–273

Röhrle O (2010) Simulating the electro-mechanical behavior of skeletal muscles. Comput Sci Eng 12:48–58

Röhrle O, Davidson JB, Pullan AJ (2008) Bridging scales: a three-dimensional electromechanical finite element model of skeletal muscle. SIAM J Sci Comput 30:2882–2904

Röhrle O, Davidson JB, Pullan AJ (2012) A physiologically based, multi-scale model of skeletal muscle structure and function. Preprint SimTech-2012, Cluster of Excellence for Simulation Technology (SimTech), University of Stuttgart, Germany

Röhrle O, Pullan AJ (2007) Three-dimensional finite element modelling of muscle forces during mastication. J Biomech 40:3363–3372

Shorten PR, O'Callaghan P, Davidson JB, Soboleva TK (2007) A mathematical model of fatigue in skeletal muscle force contraction. J Muscle Res Cell Motil 28:293–313

Spitzer VM, Whitlock DG (1998) National library of medicine: atlas of the visible human male-reverse engineering of the human body. Jones and Bartlett, Sudbury

Zajac F (1989) Muscle and tendon: properties, models, scaling, and application to biomechanics and motor control. Crit Rev Biomed Eng 17:359–411

Part III
Cardiovascular Mechanics

Chapter 9
Multiscale Modeling of Arterial Adaptations: Incorporating Molecular Mechanisms Within Continuum Biomechanical Models

Jay D. Humphrey

Abstract Continuum level biomechanical models of arterial adaptations are proving themselves vital both for understanding better the progression of disease and for improving the design of clinical interventions. Although these models are most appropriate to the clinical scale of observation, the underlying mechanisms responsible for such remodeling occur at the molecular scale. The goal of this chapter is to review a validated continuum level model of arterial adaptations and to suggest a straightforward approach to incorporate molecular level information within such models. In particular, it is shown that continuum mixture models reveal naturally a means to incorporate molecular information within fundamental constitutive relations within the continuum theory. There is, therefore, significant motivation to continue to formulate molecular level models that are necessary to inform models at scales that address the Physiome.

9.1 Introduction

The past four decades have brought forth tremendous advances in the continuum biomechanics of arteries (Humphrey, 2002). Nevertheless, three conspicuous shortcomings have persisted. First, most constitutive relations and stress analyses have focused on conditions at a single instant, not how the arterial properties and stress fields evolve due to normal development or in response to perturbed loads, disease, injury, or clinical treatment. Second, biomechanical analyses have been based on the assumption that arteries are materially uniform rather than consisting of many different constituents that turnover at different rates and to different extents while collectively defining the whole. Third, continuum biomechanical models have employed phenomenological constitutive relations that have not directly accounted for the many classes of molecules that control arterial adaptations, including vasoactive, mitogenic, proteolytic, and inflammatory molecules. The primary goal herein is to encourage a new direction in arterial research whereby one develops multiscale

J.D. Humphrey (✉)
Department of Biomedical Engineering, Yale University, New Haven, CT 06520, USA
e-mail: jay.humphrey@yale.edu

G.A. Holzapfel, E. Kuhl (eds.), *Computer Models in Biomechanics*,
DOI 10.1007/978-94-007-5464-5_9,

models that can predict time-dependent changes in composition, structure, geometry, and properties that occur in response to changes in the biochemomechanical environment. Although much more data will be needed to model precisely many of the underlying mechanisms that are responsible for such growth and remodeling (G&R), expanding data bases provide sufficient guidance on salient aspects of development, adaptation, and disease progression for us to begin to interpret these data within mathematical frameworks. Toward this end, here we consider a constrained mixture model of tissue-level arterial adaptations that can incorporate molecular information related to the underlying mechanisms. Areas requiring further research are then highlighted to encourage continued development of these models.

9.2 Continuum Framework

By growth, we mean a change in mass; by remodeling, we mean a change in structure. Notwithstanding the many associated complexities at different spatial and temporal scales, we begin by assuming that G&R occurs via quasi-static isothermal processes, which focuses our attention on equations of mass balance and linear momentum balance. Moreover, let us assume that the arterial wall can be modeled as a mixture consisting of N constituents, including $\alpha = 1, 2, \ldots, n$ insoluble but structurally significant constituents and $i = 1, 2, \ldots, N - n$ soluble but structurally insignificant constituents. Examples of the former are elastic fibers, fibrillar collagens, muscle fibers, and proteoglycans; examples of the latter include vasoactive, mitogenic, proteolytic, and inflammatory molecules. We have previously discussed the utility of employing full mixture equations to describe mass balance for both classes of constituents, but a rule-of-mixtures relation for the stress response that can be used to satisfy overall linear momentum balance (Humphrey and Rajagopal, 2002).

Mass balance, in spatial form, can be written as

$$\frac{\partial \rho^i}{\partial \tau} + \operatorname{div}\left(\rho^i v^i\right) = \bar{m}^i, \quad i = 1, 2, \ldots, N - n, \tag{9.1}$$

$$\frac{\partial \rho^\alpha}{\partial \tau} + \operatorname{div}\left(\rho^\alpha v^\alpha\right) = \bar{m}^\alpha, \quad \alpha = 1, 2, \ldots, n, \tag{9.2}$$

where ρ^i and ρ^α are so-called apparent mass densities (constituent mass per mixture volume) and $\bar{m}^i$ and $\bar{m}^\alpha$ are the so-called net rates of mass density production/removal (which can be positive, zero, or negative); $\tau \in [0, s]$ is the G&R time, which is typically much greater than the cardiac cycle timescale t.

Focusing first on the $N - n$ soluble constituents, i.e. Eq. (9.1), it is convenient to introduce the mass flux $\boldsymbol{j}^i = \rho^i(\mathbf{v}^i - \mathbf{v})$ where $\mathbf{v}^i - \mathbf{v}$ is sometimes called the 'diffusion velocity.' Regardless, Eq. (9.1) can be written at G&R time as

$$\frac{\partial \rho^i}{\partial \tau} + \operatorname{div}\left(\rho^i \mathbf{v}\right) = \bar{m}^i - \operatorname{div}\left(\boldsymbol{j}^i\right), \tag{9.3}$$

or if the mixture velocity $\mathbf{v}$ is negligible (consistent with a quasi-static assumption that is used for the structurally significant constituents)

$$\frac{\partial \rho^i}{\partial \tau} = \bar{m}^i - \operatorname{div}\left(\boldsymbol{j}^i\right). \tag{9.4}$$

Noting that we have $N-n$ equations to determine $N-n$ constituent mass densities ρ^i, we clearly must introduce additional (constitutive) relations for $\bar{m}^i$ and $\boldsymbol{j}^i$. For dilute solutions, the mass flux for diverse molecular species is often approximated by Fick's law, which is typically written in terms of molar, not mass, densities. Note, therefore, that the molar density $C^i \equiv \rho^i / MW^i$ where MW^i are molecular masses. Hence, the mass balance equation for the soluble constituents can be written

$$\frac{\partial C^i}{\partial \tau} = R^i - \operatorname{div}\left(\boldsymbol{J}^i\right), \tag{9.5}$$

where C^i are also called concentrations, R^i are reactions responsible for production/removal, and by Fick's law $\boldsymbol{J}^i = -D^i \operatorname{grad} C^i$, where D^i are the diffusivities. Hence, we obtain the classical reaction-diffusion equation

$$\boxed{\frac{\partial C^i}{\partial \tau} = R^i + D^i \nabla^2 C^i, \quad i = 1, 2, \ldots, N-n} \tag{9.6}$$

for all soluble constituents at G&R times $\tau \in [0, s]$.

The situation is very different for the insoluble, structurally significant, constituents, i.e. Eq. (9.2). We previously introduced an additional assumption that all structural constituents are constrained to move with the mixture (Humphrey and Rajagopal, 2002). This assumption coupled with the quasi-static assumption thus requires that the motions $\mathbf{x}^\alpha = \mathbf{x} = \mathbf{0}$, whereby velocities are similarly constrained: $\mathbf{v}^\alpha = \mathbf{v} = \mathbf{0}$. Equation (9.2) thus can be written

$$\frac{\partial \rho^\alpha}{\partial \tau} = \bar{m}^\alpha \quad \text{or} \quad \int \frac{\partial \rho^\alpha}{\partial \tau} \mathrm{d}\tau = \int \bar{m}^\alpha \mathrm{d}\tau. \tag{9.7}$$

We thus have n equations to determine n mass densities, which again necessitates the introduction of additional (constitutive) relations for the net production/removal function. Yet, because $\bar{m}^\alpha = 0$ during periods of tissue maintenance (i.e., balanced production and removal in unchanging configurations), we have shown previously that it is convenient to assume a separable representation $\bar{m}^\alpha(\tau) = m^\alpha(\tau) q^\alpha(s, \tau)$, where $m^\alpha(\tau) > 0$ is the true rate of mass density production and $q^\alpha(s, \tau) \in [0, 1]$ is a survival function that accounts for the fact that all cells and proteins have a finite half-life (Valentín et al., 2009). Hence, the survival function represents the percentage of constituents produced at time τ that survives to current time s.

It can be shown that use of the separable form for the net production term allows Eq. (9.7) to be written in a reduced form, namely

$$\boxed{\rho^\alpha(s) = \rho^\alpha(0) Q^\alpha(s) + \int_0^s m^\alpha(\tau) q^\alpha(s, \tau) \mathrm{d}\tau, \quad \forall \alpha = 1, 2, \ldots, n,} \tag{9.8}$$

which is to say that the current apparent mass density depends on its original value $\rho^\alpha(0)$ and the kinetic loss of the original material via $Q^\alpha(s) \in [0,1]$, as well as both the subsequent true production $m^\alpha(\tau)$ and associated loss $q^\alpha(s,\tau) \in [0,1]$ of material after $s = 0$ (the time at which a perturbation initiates G&R). Because the constituent mass densities are apparent, not true, densities, the total mass density is computed easily via

$$\rho(s) = \sum \rho^\alpha(s) \rightarrow 1 = \sum \phi^\alpha(s), \tag{9.9}$$

where $\phi^\alpha(s) = \rho^\alpha(s)/\rho(s)$ are usual mass fractions. Of course, we must recover $\rho^\alpha(0)$ at $s = 0$, which reveals that $Q^\alpha(0) = 1$ in Eq. (9.8).

Because we employ a rule-of-mixtures relation for the stress, linear momentum for quasi-static G&R is simply the same as that in classical continuum mechanics, namely $\operatorname{div}\mathbf{t} = \mathbf{0}$, where $\mathbf{t}$ is the Cauchy stress. As in most of biomechanics, therefore, the significant challenges lie first in formulating appropriate constitutive relations and second in solving initial-boundary value problems of interest.

Although it is natural to seek constitutive relations for stress directly (Humphrey and Rajagopal, 2002), it proves useful to follow advances in nonlinear elasticity and alternatively seek constitutive relations for the stored energy $W^\alpha(s)$, whereby a rule-of-mixtures approach can be written conceptually as

$$W(s) = \sum_{\alpha=1}^{n} \phi^\alpha(s)\hat{W}^\alpha(s), \tag{9.10}$$

noting of course that the stored energy depends on the (finite) deformation experienced by the material, which is to say each of its load-bearing constituents. Prior studies have suggested, however, that such an approach is limited in its ability to capture contributions of individual constituents that may turnover continuously at different rates and to different extents. Hence, following Baek et al. (2006), we let

$$W(s) = \sum_{\alpha=1}^{n} W^\alpha(s), \tag{9.11}$$

where we postulated, constituent-specific, forms motivated by Eq. (9.8) (which was derived directly), namely

$$\boxed{\begin{aligned} W^\alpha(s) = {} & \frac{\rho^\alpha(0)Q^\alpha(s)}{\rho(s)}\hat{W}^\alpha\left(\mathbf{C}^\alpha_{n(0)}(s)\right) \\ & + \int_0^s \frac{m^\alpha(\tau)q^\alpha(s-\tau)}{\rho(s)}\hat{W}^\alpha\left(\mathbf{C}^\alpha_{n(\tau)}(s)\right)\mathrm{d}\tau, \end{aligned}} \tag{9.12}$$

where the energy stored in individual constituents is assumed to depend on deformations experienced by those constituents, which by the principle of material frame indifference requires dependence on the deformation gradient through the

right Cauchy-Green tensor: $\mathbf{C}^{\alpha}_{n(\tau)}(s)$. In particular, $n(\tau)$ reminds us that this deformation is referred to the natural configuration $\kappa^{\alpha}_{n}(\tau)$ for that individual constituent at its time of deposition $\tau \in [0, s]$. To appreciate the assumed form in Eq. (9.12), note that if there is no G&R, then $s = 0$ and this equation reduces to

$$W^{\alpha}(0) = \frac{\rho^{\alpha}(0)\, Q^{\alpha}(0)}{\rho(0)}\, \hat{W}^{\alpha}\big(\mathbf{C}^{\alpha}_{n(0)}(0)\big) = \phi^{\alpha}(0)\, \hat{W}^{\alpha}\big(\mathbf{C}^{\alpha}_{n(0)}(0)\big) \tag{9.13}$$

(recalling that $Q^{\alpha}(0) \equiv 1$ by definition), which recovers a simple rule-of-mixtures relation as desired. It can be shown similarly that the simple rule-of-mixtures relation is recovered in the case of tissue maintenance, that is, balanced production and removal in unchanging configurations (Valentín et al., 2009).

Most importantly, Eqs. (9.8) and (9.12) reveal the need to determine three basic types of constitutive relations for each structurally significant constituent $\alpha = 1, 2, \ldots, n$, namely

$$m^{\alpha}(\tau), \qquad q^{\alpha}(s - \tau), \qquad \hat{W}^{\alpha}\big(\mathbf{C}^{\alpha}_{n(\tau)}(s)\big). \tag{9.14}$$

In our prior implementations (e.g., Baek et al., 2006; Valentín et al., 2009), we have used phenomenological constitutive relations motivated by tissue level observations of mechanobiological responses by arteries in response to diverse mechanical loads (Humphrey, 2008b). For example, we have modeled the energy stored in the elastin dominated amorphous matrix using a classical neo-Hookean relation and the energy stored in collagen fibers and passive smooth muscle using classical Fung-type exponential relations. For the present discussion, it is important to note that the neo-Hookean relation was first derived based on micromechanical arguments and exponential relations have been shown to capture well the net mechanical response of collections of fibers having linear behaviors but a distribution of undulations. It is suggested that increased attention should be given to the derivation of microstructurally based constitutive relations for the energy stored in individual constituents as well as interaction energies between constituents. Such relations would enable better modeling of many disease processes wherein either particular constituents are absence because of genetic mutations (e.g., fibrillin-1, which stabilizes elastic fibers, or collagen III, as in Marfan and Ehlers–Danlos IV syndromes, respectively) or chemomechanical injury (e.g., degradation or fatigue of elastic fibers in aging). Below, however, let us focus on constitutive relations for mass production and removal, which are unique to G&R theories.

9.3 Towards Multiscale Constitutive Relations

Two of the best studied arterial adaptations are responses to sustained alterations in blood pressure and flow, the former of which is particularly relevant to hypertension research. It is well accepted that large arteries tend to grow and remodel so as to keep the mean circumferential stress $\sigma_{\theta} = Pa/h$ and the wall shear stress

$\tau_w = 4\mu Q/\pi a^3$ each near target/homeostatic values (e.g., σ_θ^h and τ_w^h, respectively, where P, a, h, μ and Q are blood pressure, luminal radius, wall thickness, blood viscosity, and volumetric flow, respectively). As shown previously (Humphrey, 2008a), if we let parameterize the change in blood pressure from normal and parameterize the change in blood flow from normal (e.g., $\gamma = 1.5$ for a 50 % sustained increase in pressure), then it is easy to show that $a \to \varepsilon^{1/3} a_h$ and $h \to \gamma \varepsilon^{1/3} h_h$ (where the subscripts h denote homeostatic values) to maintain/restore the stresses to homeostatic targets in response to modest alterations in blood pressure or flow. Whereas these simple relations describe the extent of the morphological adaptations, they cannot describe the time-course of such changes or the associated changes in structure or properties. In contrast, the G&R framework described by Eqs. (9.8) and (9.12) can address both the extent and rate of each of these changes.

Fundamental to geometric and structural changes in arteries are changes in rates of turnover of structurally significant constituents such as the smooth muscle and fibrillar collagens. For example, we have shown that the following constitutive relations (cf. Eq. (9.14)) provide a good description of large artery adaptations to both altered blood pressure and flow:

$$m^\alpha(\tau) = m_B^\alpha \left(1 + K_\sigma^\alpha \Delta\sigma - K_{\tau_w}^\alpha \Delta\tau_w\right), \tag{9.15}$$

$$q^\alpha(s-\tau) = \exp\left[-\int_\tau^s K_q^\alpha \left(1 + \Delta\sigma(\tilde{\tau})^2\right) \mathrm{d}\tilde{\tau}\right], \tag{9.16}$$

where the stress differences are given by

$$\Delta\sigma = \frac{\sigma - \sigma^h}{\sigma^h}, \qquad \Delta\tau_w = \frac{\tau_w - \tau_w^h}{\tau_w^h}, \tag{9.17}$$

with σ an appropriate scalar metric of intramural stress. Note, too, that the gain-type parameters K in Eqs. (9.15) and (9.16) modulate the stress-mediated changes in mass production and removal. Although these particular functional forms are among the simplest possible, basal rates are recovered (m_B^α and K_q^α) when the stresses equal their homeostatic targets, as desired, and associated simulations have captured many salient aspects of observed adaptations (Valentín and Humphrey, 2009a,b). Note, too, that the survival function recovers first order kinetic decays as suggested by much of the data (cf. Humphrey, 2008b).

At this juncture, it is important to recognize that these constitutive relations are motivated by mechanobiological observations, yet they are phenomenological. For example, it is well known that collagen synthesis is increased by increases in cyclic stretch/stress of smooth muscle cells. It is also well known that increases in wall shear stress increase endothelial cell production of the vasodilator nitric oxide (NO) and decreases in wall shear stress increase endothelial cell production of the vasoconstrictor endothelin-1 (ET-1); see Fig. 9.1 and Humphrey (2008b). Moreover, NO decreases the production of collagen by smooth muscle cells whereas ET-1 increases the production rate (hence the minus sign in Eq. (9.15) for the shear stress mediated

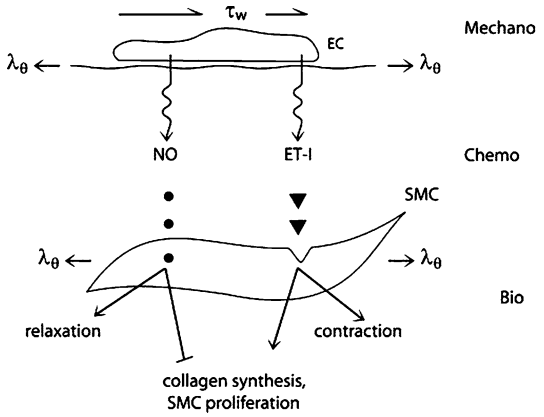

Fig. 9.1 Schema of possible mechano-induced production of vasoactive molecules, nitric oxide (NO) and endothelin-1 (ET-1), by endothelial cells (EC) in response to changes in cyclic wall shear stress and circumferential wall stretch. Diffusion and consumption of the vasoactive molecules results in stimulation of smooth muscle cell (SMC) vasoactivity and proliferation as well as synthesis of extracellular matrix proteins

term). It is also becoming increasingly clear that altered stress affects the production, activation, and effectiveness of proteolytic enzymes (e.g., matrix metalloproteinases; Humphrey, 2008b).

Whereas phenomenological equations can be very useful for simulations, as we learn more and more about the mechanobiology, there is an opportunity—indeed a responsibility—to move toward more mechanistic modeling. For example, it is now known that the increase in collagen synthesis by smooth muscle cells in response to increased mechanical stress/stretch (cf. Fig. 9.1) is mediated by complex signaling pathways that involve multiple vasoactive molecules and cytokines. For example, it appears that increased cyclic stress (as in hypertension due to increased pulse pressure) causes smooth muscle cells to increase their production of angiotensin-II and possibly to change associated receptor-ligand binding, which in turn stimulates the production of latent transforming growth factor beta (TGF-β) that can be activated by mechanical stress and ultimately lead to collagen production. Hence, there is an opportunity to use reaction-diffusion equations (9.6) to quantify local changes in 'effector molecules' that in turn influence directly the rates of mass production and removal (cf. Fig. 9.1). For example, one could consider mass density production for collagen ($\alpha = c$) such as

$$m^c(\tau) = m^c_B\big(1 + K^c_{\mathrm{TGF}}\Delta C^{\mathrm{TGF}} + K^c_{\mathrm{ET1}}\Delta C^{\mathrm{ET1}} - K^c_{\mathrm{NO}}\Delta C^{\mathrm{NO}} + \cdots\big). \quad (9.18)$$

Similarly for smooth muscle ($\alpha = m$), which depends in part on the concentration of platelet-derived growth factor (PDGF), one could consider

$$m^m(\tau) = m^m_B\big(1 + K^m_{\mathrm{PDGF}}\Delta C^{\mathrm{PDGF}} + K^m_{\mathrm{ET1}}\Delta C^{\mathrm{ET}} - K^m_{\mathrm{NO}}\Delta C^{\mathrm{NO}} + \cdots\big). \quad (9.19)$$

In other words, rather than purely phenomenological forms represented by Eq. (9.15), molecular level information could be used to inform the continuum level analysis. Similar relations could be determined for the survival function, which should include terms accounting for concentrations of active proteases. Moreover, relations for changes in molecular production can be derived from appropriate experiments, as, for example, studies of the effects of changing wall shear stress on the production of NO, as, for example (Humphrey, 2008b)

$$C^{\mathrm{NO}} = C_B^{\mathrm{NO}}\left\{\zeta + \beta\left[1 - \exp\left(-\delta\tau_w^2\right)\right]\right\}, \tag{9.20}$$

where (ζ, β, δ) are parameters required to fit the data (e.g., $\zeta, \beta, \delta = 0.37, 0.63$, and -8.89 as reported in Humphrey, 2008b). In this way, molecular level (mechanistic) relations can be combined simply with continuum level models that have already proven useful in modeling diverse aspects of arterial G&R.

9.4 Discussion

Bioengineers and clinicians must similarly address arterial adaptations at a macroscopic scale—including normal changes due to development or exercise as well as disease progression, responses to treatment, and so forth. Classical examples include quantification of wall thickening and stiffening in hypertension, changing caliber in exercise or arterio-venous fistulas, stenoses in vein grafts, evolving atherosclerotic plaques, aneurysms, and so forth (Taylor and Humphrey, 2009). Continuum level biomechanical modeling has proven fundamental to studying such tissue-level changes and will likely remain so for purposes of diagnosis, interventional planning, medical device design, and many other daily activities. Nevertheless, we must also exploit our growing understanding of the molecular level mechanisms that dictate macroscopic manifestations. We submit here that a consistent mixture theory framework for growth and remodeling allows one to account naturally for spatial and temporal changes in effector molecules via classical reaction-diffusion equations, which in turn can be used to inform improved constitutive relations for cell and matrix turnover that are fundamental to the tissue-level analyses that are vital for so many aspects of research and clinical care. Indeed, we emphasize that the present G&R framework, which focuses on changes to the arterial wall, is also easily coupled to sophisticated computational fluid dynamics simulations of the hemodynamics (Figueroa et al., 2009), thereby permitting both multiscale and multi-physics studies. Moreover, we emphasize that the multiscale approach presented here (focused mainly on informing continuum level constitutive relations with molecular level information) is but one possible multiscale approach. Hayenga et al. (2011), recently showed that agent based models can similarly be integrated with continuum level G&R models, hence providing yet another level of multiscale modeling.

In summary, there is a pressing need for continued research on the molecular mechanisms responsible for arterial adaptations and disease progression, particularly given the complex multifunctional capabilities of the large number of effector

molecules, including vasoactive, mitogenic, proteolytic, and inflammatory. Discovery of appropriate mechanobiological relations can and should be incorporated in continuum level models.

Acknowledgements This work was supported, in part, via NIH grants HL-086418 and HL-105297.

References

Baek S, Rajagopal KR, Humphrey JD (2006) A theoretical model of enlarging intracranial fusiform aneurysms. J Biomech Eng 128:142–149

Figueroa CA, Baek S, Taylor CA, Humphrey JD (2009) A computational framework for fluid-solid-growth modeling in cardiovascular simulations. Comput Methods Appl Mech Eng 198:3583–3602

Hayenga HN, Thorne BC, Peirce SM, Humphrey JD (2011) Ensuring congruency in multiscale modeling: towards linking agent based and continuum biomechanical models of arterial adaptation. Ann Biomed Eng 39:2669–2682

Humphrey JD (2002) Cardiovascular solid mechanics. Cells, tissues, and organs. Springer, New York

Humphrey JD (2008a) Mechanisms of arterial remodeling in hypertension: coupled roles of wall shear and intramural stress. Hypertension 52:195–200

Humphrey JD (2008b) Vascular adaptation and mechanical homeostasis at tissue, cellular, and sub-cellular levels. Cell Biochem Biophys 50:53–78

Humphrey JD, Rajagopal KR (2002) A constrained mixture model for growth and remodeling of soft tissues. Math Models Methods Appl Sci 12:407–430

Taylor CA, Humphrey JD (2009) Open problems in computational vascular biomechanics: hemodynamics and arterial wall mechanics. Comput Methods Appl Mech Eng 198:3514–3523

Valentín A, Cardamone L, Baek S, Humphrey JD (2009) Complementary vasoactivity and matrix remodelling in arterial adaptations to altered flow and pressure. J R Soc Interface 6:293–306

Valentín A, Humphrey JD (2009a) Evaluation of fundamental hypotheses underlying constrained mixture models of arterial growth and remodelling. Philos Trans R Soc A 367:3585–3606

Valentín A, Humphrey JD (2009b) Parameter sensitivity study of a constrained mixture model of arterial growth and remodeling. J Biomech Eng 131:101006

Chapter 10
Cardiovascular Tissue Damage: An Experimental and Computational Framework

Nele Famaey, Ellen Kuhl, Gerhard A. Holzapfel, and Jos Vander Sloten

Abstract Tissue overload during medical procedures can lead to severe complications. This chapter presents an experimental and computational framework to define and predict damage due to mechanical loading and applies this framework to arterial clamping. An extension of the Holzapfel-material model for arterial tissue is presented, incorporating smooth muscle cell activation and damage to the different constituents. It is implemented in a finite element framework and used to simulate arterial clamping and subsequent damage evaluation through an isometric contraction test. These simulations are compared to actual experiments and repeated for a different clamp design, thereby demonstrating the capability of the framework.

10.1 Introduction

In the USA in 2007, a 0.5 % chance existed to complications due to tissue overload during a medical procedure and 7 % of these complications had fatal consequences (Health Grades, 2012). In an effort to minimize this number, research has been directed towards decreasing unnecessary intraoperative trauma, by shifting towards

N. Famaey (✉) · J. Vander Sloten
Biomechanics Section, KU Leuven, Celestijnenlaan 300C, 3001 Heverlee, Belgium
e-mail: nele.famaey@mech.kuleuven.be

J. Vander Sloten
e-mail: Jos.VanderSloten@mech.kuleuven.be

E. Kuhl
Department of Mechanical Engineering, 496 Lomita Mall, Stanford, CA 94305, USA
e-mail: ekuhl@stanford.edu

G.A. Holzapfel
Institute of Biomechanics, Center of Biomedical Engineering, Graz University of Technology, Kronesgasse 5-I, 8010 Graz, Austria
e-mail: holzapfel@tugraz.at

G.A. Holzapfel
Department of Solid Mechanics, School of Engineering Sciences, Royal Institute of Technology (KTH), Osquars Backe 1, 100 44 Stockholm, Sweden

G.A. Holzapfel, E. Kuhl (eds.), *Computer Models in Biomechanics*,
DOI 10.1007/978-94-007-5464-5_10,

less invasive techniques and through the design of less traumatic instruments (Gupta et al., 1997). Obviously, the effectiveness of these new designs and techniques depends on how well damage mechanisms are understood and how accurately thresholds for safe tissue loading can be defined.

The implementation of safety thresholds during surgery obviously requires a consensus as to what these thresholds are. In current surgical practice, the amount of load that can safely be applied on a certain tissue is highly subjective, i.e. depending on the surgeon's experience and judgement. Several steps are needed to make this judgement more objective. This chapter describes an experimental and computational framework that allows a quantitative definition of damage to a certain tissue, as well as a simulation tool to estimate the amount of damage to a tissue due to a certain external load. Though generally applicable, we currently focus on the case study of arterial clamping.

Four main steps can be defined in the framework. First, a quantitative method to define damage for a certain tissue type is required. Next this quantitative damage must be related to the amount of mechanical loading previously applied to the tissue. This can be done experimentally for a specific loading situation, but to make the relation generally applicable, a simulation of the damage process due to the mechanical loading is needed. This requires a material model for cardiovascular tissue, which is capable of capturing the typical damage processes to the different constituents.

The first section of this chapter describes different damage quantification methods for arterial clamping. In the second section, one of these damage quantification methods is combined with an *in vivo* arterial clamping experiment, resulting in an experimental relation between damage and mechanical load. In the third section, an extension of the Holzapfel-material model for arterial tissue (Holzapfel et al., 2000) is described, incorporating smooth muscle cell activation according to Murtada et al. (2010) and damage according to Balzani et al. (2006). The model is suitable to simulate the damage process during the clamping of an artery. It captures the decrease of active force generation in smooth muscle cells due to the sustained damage. The fourth section shows how, embedded in a finite element environment, this new model provides a useful tool to simulate the amount of damage induced by a certain amount of mechanical load. Ultimately, the entire framework serves to define safe loading regimes for arterial tissue, which could be used to inform computer-enhanced surgical systems to minimize tissue damage in robotic surgery and to optimize surgical instrument design towards minimal trauma.

10.2 Damage Quantification

Damage is defined as 'injury or harm that reduces value or usefulness'. A quantification of damage can, therefore, be performed by assessing this reduction in value or usefulness. First of all, biological tissue is an integral part of a larger mechanical structure and, therefore, inherently has a (passive) mechanical function. Secondly,

each tissue type has one or multiple biological functions, i.e. any activity that contributes to the correct functioning of the organism. Damage to each of these functions requires an objective and quantitative method for evaluation. In both cases this can be done either directly, through functional assessment, or indirectly, through morphological assessment.

Damage to the mechanical function manifests itself through rupture or degradation of the mechanical constituents of the tissue. One way to quantitatively assess this form of damage is to perform mechanical tests of tissues before and after the induction of damage. For example, biaxial tensile testing on a patch of cardiovascular tissue can provide information on its stiffness in different directions. Excessive tension will cause the gradual rupture of more and more of the collagen fibers which will induce a measurable decrease in stiffness in the directions in which the collagen fibers contribute.

Another, indirect way to assess mechanical function is to assess the morphological integrity of the tissue. Imaging can provide insight into the composition of a tissue and expose fractures in the different constituents. A microscopic image of a patch of cardiovascular tissue can be stained to specifically show, for example, the collagen fiber component (Schriefl et al., 2012). If imaged when brought to excessive tension, image processing can reveal the percentage of collagen fibers that are still intact, providing a quantitative measure of the damage to this constituent.

Damage to the biological function manifests itself through malfunction, function switch or apoptosis of the involved cells. Quantification of the biological function before and after damaging the tissue provides a measure of the induced damage. Sometimes it is possible to directly measure this function. In other situations an indirect approach is taken, by measuring the concentration of certain products, or the expression of certain genes, as a biological function is often the result of a cell-biological cascade of events.

For the specific case of arterial tissue, functionality refers to the vasoregulating capability of the tissue, i.e., the potential of the smooth muscle cells to contract or relax in order to regulate the blood pressure. This vasoregulating capability can be quantified in an experimental setup, known as a ‘myograph’. Schematically shown in the top right image of Fig. 10.1, the myograph consists of a water-jacketed organ chamber in which an excised cylindrical section of an artery can be mounted such that isometric tension can be recorded. The sample is immersed in a Krebs buffer at 37 °C and continuously gassed with a mixture of 95 % oxygen and 5 % carbon dioxide. After stabilization at the optimal preload level, Phenylephrine (PE) at 10^{-6} M is added to the solution to induce contraction. PE is a contracting agent that acts directly on the smooth muscle cells. Sodium nitroprusside (SNP) (10^{-6} M) induces an endothelium-independent relaxation. Consequently, an adequate level of SNP-induced relaxation will indicate intactness of the smooth muscle cells (Callera et al., 2000). Absolute values of relaxation as well as the percentage of relaxation relative to the amount of contraction are recorded and provide a quantitative measure of the damage to the smooth muscle cells when comparing these values to those of an intact sample. More details on the experimental setup can be found in Famaey et al. (2010). A similar custom-designed device to test active force generation in response to electrical stimulation is reported in Böl et al. (2012).

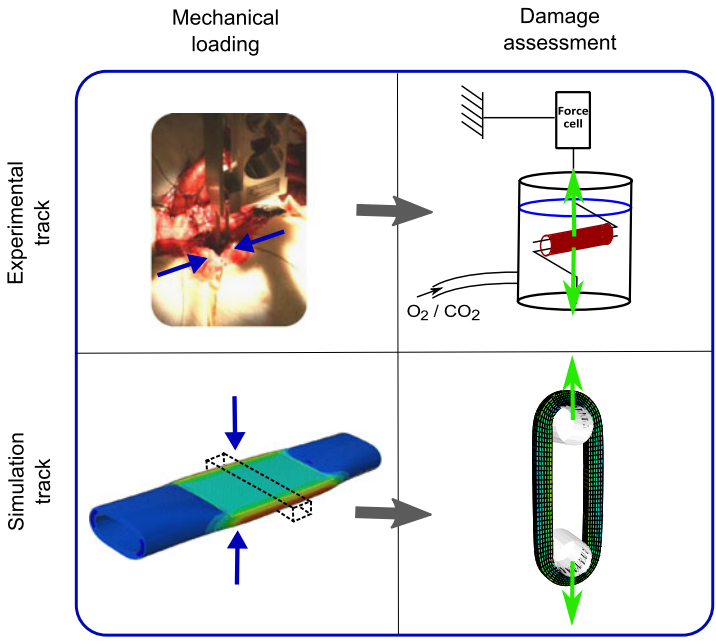

Fig. 10.1 Schematic overview of the framework. Mechanical loading of the artery is performed experimentally with a custom made clamp (*top left image*), and simulated with finite elements (*bottom left*). After mechanical loading, the damage to the tissue is assessed experimentally in a custom made functional testing device capable of recording isometric contraction (*top right image*). This isometric contraction experiment is also simulated with finite elements (*bottom right image*). Now, the simulation can be repeated for different loading situations, thereby predicting the amount of damage that will be induced

Another way to assess biological function is to study the condition of the tissue through morphological imaging. The spatial resolution of the imaging method determines how location-specific the damage can be assessed. Damage to certain constituents or processes can be imaged by applying specific stainings and visualizing through the corresponding microscopic techniques. For example, in immunofluorescence microscopy, specific antibodies can be labeled with a fluorophore, to visualize endothelial morphology (e.g., with CD31), the smooth muscle cells (e.g., with alpha-smooth muscle actin), elastin (e.g., with anti-elastin) and collagen (e.g., with anti-collagen IV). Cell-proliferation and cell-death can also be visualized through immunofluorescence microscopy, for example, with a TUNEL assay, or with a combined PI (propidium iodide) and syto 13 staining. Propidium iodide (PI) stains all cell nuclei red, whereas syto 13 stains only intact nuclei green. The combination of these two stainings therefore yields a 'live-dead'-staining, after which image processing can reveal the percentage of cell death in different regions (Megens et al., 2007, 2008).

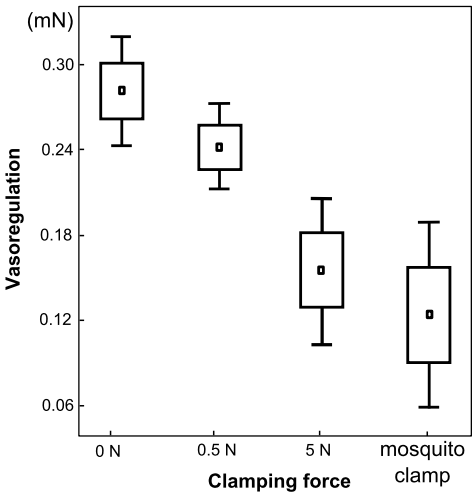

Fig. 10.2 Boxplots of the total relaxation due to the addition of SNP to the Krebs solution, i.e. a measure for the vasoregulating capability

10.3 Damage as a Function of the Mechanical Load

The previous section showed that damage can be evaluated quantitatively in multiple ways. This can facilitate a consensus as to how much damage is acceptable for a certain tissue. However, knowing this limit is only useful if the amount of mechanical load needed to induce this damage is known along with it. Therefore, in the experimental protocol for defining safety limits for tissue loading, there is a need for controllable force application and subsequent damage evaluation. This way, an unambiguous relation can be defined between mechanical loading and damage.

The mechanical load exerted during an experiment can be characterized with respect to location, magnitude, displacement boundary conditions, rate, and duration. These are all parameters that should be controlled or at least acquired during the experimental process. Ideally, the load should be applied *in vivo*, so that the induced damage can be solely attributed to the loading and not to non-physiological *ex vivo* conditions. If subsequent damage quantification requires excision of tissue, undamaged control segments should also be excised and tested, to rule out damage due to the excision process.

To clamp the artery in a controlled way, a hand-held mechanical device, shown in the top left image of Fig. 10.1, was designed that allows clamping of a rat abdominal artery in an *in vivo* setting to a known force (Famaey et al., 2010). By combining this experimental setup with the previous one, data can be collected regarding the degree of damage to the vasoregulating capability after different *in vivo* clamping forces. This type of data was collected for rat abdominal arteries, as described in Famaey et al. (2010). In total, 8 segments clamped at 0.5 N with the custom made clamping device, 6 segments at 5 N, 6 segments clamped with a typical mosquito clamp and 14 zero load control segments were tested in the functional setup. Figure 10.2 shows boxplots of the total relaxation due to the addition of SNP to the Krebs solution, i.e. a measure for the vasoregulating capability. Total relaxation due to SNP is significantly lower for the mosquito-group and for the 5 N-group compared to the zero

load control group ($p = 0.005$ and 0.003), but also significantly lower compared to the group clamped at 0.5 N ($p = 0.020$ and 0.020). There was no significant difference between the zero load control group and the 0.5 N-group. When repeated for more loading levels, these experiments will enable the definition of an unambiguous relation between mechanical loading and experimental clamping force.

This section showed how the relation between 'macroscopic' mechanical loading and 'macroscopic' damage can be found experimentally for a specific loading situation, but is not useful in general. When the boundary conditions of the mechanical loading change, or when the force is applied in a different location or with a different orientation, the connection between this new loading situation and the damage is still unknown.

10.4 A Material Model for Arteries

Practical and ethical issues impede the purely experimental characterization of this generalized relation between mechanical loading and damage and favor the use of numerical simulations. To this end, a realistic material model for arteries is required, capable of capturing features such as vasoregulation and damage. This section presents a material model suitable to simulate the damage process during the clamping of an artery.

Through an additive decomposition of the strain energy, the following constitutive model for active healthy and degraded arterial tissue characterizes the properties of (i) an isotropic matrix material constituent, (ii) an anisotropic constituent attributed to the dispersed collagen fibers and (iii) an anisotropic smooth muscle cell constituent. The first two constituents are motivated by the Holzapfel-material model as proposed in Holzapfel et al. (2000), whereas the third component is motivated by the mechanical smooth muscle activation model described by Murtada et al. (2010). The damage accumulating in the different constituents during mechanical loading is characterized through a strain-energy-driven damage function for each individual constituent, motivated by the formulation of Balzani et al. (2006). In the remainder of this chapter, the material model will be referred to as the three-constituent damage model.

10.4.1 Constitutive Equations

Since the tissue is assumed to be nearly incompressible, it is common to additively decompose the strain-energy function Ψ, i.e.

$$\Psi = \Psi^{\text{vol}} + \Psi^{\text{dev}} = \Psi^{\text{vol}} + \Psi^{\text{mat}} + \Psi^{\text{fib}_1} + \Psi^{\text{fib}_2} + \Psi^{\text{smc}}, \tag{10.1}$$

into a volumetric Ψ^{vol} and a deviatoric Ψ^{dev} part. The latter consists of an isotropic contribution of the matrix material Ψ^{mat}, an anisotropic contribution of two

families of collagen fibers Ψ^{fib_1} and Ψ^{fib_2}, and a contribution of the smooth muscle cells Ψ^{smc}. The individual contributions will be specified in detail in the following section.

10.4.1.1 Volumetric Bulk Material

The volumetric free energy Ψ^{vol} can, for example, be expressed as follows Arruda and Boyce (1993):

$$\Psi^{\text{vol}} = \Lambda\left[\frac{1}{2}\left(J^2 - 1\right) - \ln(J)\right], \tag{10.2}$$

where J is the determinant of the deformation gradient $\mathbf{F}$. The penalty parameter Λ corresponds to $\kappa/2$, with κ the bulk modulus (in MPa), and should be set high enough to ensure a nearly incompressible response.

Since this term is handled separately in an incompressible finite element formulation, we will now focus on the four contributions to the deviatoric energy Ψ^{dev}, which are the primary descriptors of the material behavior.

10.4.1.2 Damage to the Deviatoric Components

All deviatoric components are allowed to undergo degradation in the case of physiological overload. Simo and Ju (1987), in general, and Balzani et al. (2006) for arteries have described the approach of weighting the strain energy with a scalar-valued damage variable $(1 - d)$. This model builds upon the classical damage concept, and introduces an independent damage variable for each individual constituent. Thus,

$$\Psi^{\text{i}} = \left(1 - d^{\text{i}}\right)\widehat{\Psi}^{\text{i}}. \tag{10.3}$$

Here, $\widehat{\Psi}^{\text{i}}$ denotes the elastic energy of one of the deviatoric constituents (mat, fib_1, fib_2). The smooth muscle cells form an integral part of the matrix constituent, even in their passive state. Therefore, their degradation is assumed to depend on both the passive damage $d^{\text{smc}}_{\text{pas}}$ in the surrounding matrix and the active damage $d^{\text{smc}}_{\text{act}}$ in the smooth muscle cells themselves:

$$\Psi^{\text{smc}} = \left(1 - d^{\text{smc}}_{\text{pas}}\right)\left(1 - d^{\text{smc}}_{\text{act}}\right)\widehat{\Psi}^{\text{smc}}. \tag{10.4}$$

The evolution of the damage variable of each constituent d^{i} is driven by the undamaged elastic energy, as proposed by Balzani et al. (2006):

$$d^{\text{i}} = \gamma^{\text{i}}\left[1 - \exp\left(-\beta^{\text{i}}/m^{\text{i}}\right)\right] \quad \text{with } i = \text{mat}, \text{fib}_1, \text{fib}_2, {}^{\text{smc}}_{\text{pas}}, {}^{\text{smc}}_{\text{act}}. \tag{10.5}$$

The weighting factor γ^{i} (in kPa) can be used to tune the sensitivity to damage, $\gamma^{\text{i}} \in [0, 1]$, and m^{i} is a dimensionless parameter of the damage model. The variable β^{i} is

an internal variable keeping track of the maximum elastic strain energy experienced so far, within the time interval $0 \leq t \leq \tau$ (Balzani et al., 2006):

$$\beta^{\mathrm{i}} = \max_{0 \leq t \leq \tau} \left(\widehat{\Psi}^{\mathrm{i}}(t) - \Psi_0^{\mathrm{i}} \right) \quad \text{with } i = \mathrm{mat}, \mathrm{fib}_1, \mathrm{fib}_2, {}^{\mathrm{smc}}_{\mathrm{pas}}, {}^{\mathrm{smc}}_{\mathrm{act}}. \tag{10.6}$$

For the specific case of the smooth muscle cell contribution $\Psi^{\mathrm{smc}}_{\mathrm{pas}} = \Psi^{\mathrm{mat}}$ and $\Psi^{\mathrm{smc}}_{\mathrm{act}} = \Psi^{\mathrm{smc}}$.

Since it can be assumed that no damage occurs in the physiological range, the damage threshold Ψ_0^{i} is initialized with the strain energy in the respective constituent at systolic pressure. For heterogeneous problems, Ψ_0^{i} may, therefore, differ for each material point, and is thus not strictly a material property.

10.4.1.3 Elastic Energy of the Deviatoric Constituents

The elastic energy of the extracellular matrix is described by a neo-Hookean contribution:

$$\widehat{\Psi}^{\mathrm{mat}} = \frac{1}{2} c (\bar{I}_1 - 3), \tag{10.7}$$

where $c > 0$ characterizes the matrix stiffness (in kPa) and $\bar{I}_1$ is the first invariant of the modified right Cauchy-Green tensor.

10.4.1.4 Collagen Fibers

Collagen fibers will only contribute when under tension, where the free energy contributions of the two families of collagen fibers are formulated according to (Gasser et al., 2006)

$$\widehat{\Psi}^{\mathrm{fib}_{1,2}} = \frac{k_1}{2k_2} \left\{ \exp\left[k_2 \left(I_{4,6}^{\mathrm{fib}\star} - 1 \right)^2 \right] - 1 \right\}. \tag{10.8}$$

Here, $k_1 > 0$ characterizes the fiber stiffness (in kPa) and $k_2 > 0$ is a dimensionless parameter, while $I_{4,6}^{\mathrm{fib}\star}$ are pseudo-invariants for each of the two fiber families, accounting for fiber dispersion:

$$I_{4,6}^{\mathrm{fib}\star} = \kappa \, \bar{I}_1 + (1 - 3\kappa) \bar{I}_{4,6}^{\mathrm{fib}}, \tag{10.9}$$

with I_4 and I_6 the anisotropic invariants characterizing the stretches along the fiber directions:

$$\bar{I}_{4,6}^{\mathrm{fib}} = \lambda_\theta^2 \cos^2 \alpha^{\mathrm{fib}_{1,2}} + \lambda_z^2 \sin^2 \alpha^{\mathrm{fib}_{1,2}}. \tag{10.10}$$

Here, λ_θ and λ_z are the stretches in the circumferential and axial directions, respectively, and α^{fib_1} and α^{fib_2} denote the angles between the circumference and the mean directions of the fiber families. In the case of arteries, two fiber families are oriented symmetrically with respect to the cylinder axis, so that $\alpha^{\mathrm{fib}_1} = -\alpha^{\mathrm{fib}_2}$ and, consequently, $\bar{I}_4^{\mathrm{fib}} = \bar{I}_6^{\mathrm{fib}}$.

10.4.1.5 Smooth Muscle Cells

In the undamaged state, the energy of the smooth muscle cells $\widehat{\Psi}^{\text{smc}}$ can be expressed as follows (Murtada et al., 2010):

$$\widehat{\Psi}^{\text{smc}} = \frac{1}{2}\mu^{\text{smc}}(n_{\text{III}} + n_{\text{IV}})\left(\sqrt{I_4^{\text{smc}}} + u_{\text{rs}} - 1\right)^2, \tag{10.11}$$

where μ^{smc} characterizes the stiffness of the actin-myosin filament apparatus (in kPa). The kinetics of the actin-myosin powerstroke are modeled through a four-state model described by Hai and Murphy (1988) and adopted by Murtada et al. (2010) and Stålhand et al. (2011). This model describes the transitions between the four states n_{I}, n_{II}, n_{III} and n_{IV} of the myosin heads as a function of the calcium concentration as follows:

$$\begin{bmatrix} \dot{n}_{\text{I}} \\ \dot{n}_{\text{II}} \\ \dot{n}_{\text{III}} \\ \dot{n}_{\text{IV}} \end{bmatrix} = \begin{bmatrix} -\kappa_1 & \kappa_2 & 0 & \kappa_7 \\ \kappa_1 & -(\kappa_2+\kappa_3) & \kappa_4 & 0 \\ 0 & \kappa_3 & -(\kappa_4+\kappa_5) & \kappa_6 \\ 0 & 0 & \kappa_5 & -(\kappa_6+\kappa_7) \end{bmatrix} \begin{bmatrix} n_{\text{I}} \\ n_{\text{II}} \\ n_{\text{III}} \\ n_{\text{IV}} \end{bmatrix}. \tag{10.12}$$

Here, n are the fractions of the four states, which sum up to one, $\sum n_i = 1$. The κ_i (in s^{-1}) are the rate constants of the model, where κ_1 and κ_6 are a function of the calcium concentration. In particular, n_{I} and n_{II} are the fractions of dephosphorylated and phosphorylated myosin heads that are not attached to the actin filament, and thus not mechanically contributing, while n_{III} and n_{IV} are the fractions of phosphorylated and dephosphorylated myosin heads, or cross-bridges, attached to the actin filaments, and thus contributing to the stiffness. The power-stroke occurs through a conformational change in state III, after which the myosin heads transform back into state II. As long as the myosin heads remain phosphorylated, they cycle back and forth between states II and III, thus generating contraction. In state IV, the myosin heads are still attached to the actin filament but dephosphorylated and thus unable to perform a power stroke.

In Eq. (10.11), u_{rs} is the average normalized relative sliding between the myosin and the actin filaments. It follows a viscous evolution law:

$$\dot{u}_{\text{rs}} = \frac{1}{\eta}\left(P^{\text{smc}} - P^{\text{mat}}\right), \tag{10.13}$$

where η is a viscosity parameter (in MPa), P^{smc} denotes the active stress exerted by the attached myosin heads and P^{mat} denotes the stress from the surrounding matrix. The active stress P^{smc} can be approximated by the following step function

$$P^{\text{smc}} = \begin{cases} \kappa_c\, n_{\text{III}} & \text{for } P^{\text{mat}} < \kappa_c n_{\text{III}}, \\ P^{\text{mat}} & \text{else}, \\ \kappa_c(n_{\text{III}} + n_{\text{IV}}) & \text{for } \kappa_c/(n_{\text{III}} + n_{\text{IV}}) < P^{\text{mat}}, \end{cases} \tag{10.14}$$

where κ_c is a material parameter (in MPa) related to the driving force per myosin head, see Murtada et al. (2010) for details.

10.4.2 Implementation

The constitutive model is implemented in the Abaqus user subroutine `UANISOHYPER_INV` and `VUANISOHYPER_INV`, a family of subroutines designed for anisotropic, hyperelastic material models, in which the strain-energy function Ψ is formulated as a function of the strain invariants, written for Abaqus/Standard and Abaqus/Explicit, respectively. This subroutine can handle and update solution-dependent internal variables and requires that the derivatives of the strain-energy function are defined with respect to the scalar invariants $\bar{I}_1$, $\bar{I}_2$, $\bar{I}_3$, $\bar{I}_4^{\text{fib}}$, $\bar{I}_6^{\text{fib}}$, $\bar{I}_4^{\text{smc}}$, which are provided as input. It is called at each integration point during each load increment to calculate the total strain energy Ψ and its first and second derivatives with respect to the invariants $\partial\Psi/\partial\bar{I}_i$ and $\partial^2\Psi/\partial\bar{I}_i\partial\bar{I}_j$ for $i, j = 1, 2, 3, 4^{\text{fib}}, 6^{\text{fib}}, 4^{\text{smc}}$.

Through the input file, a local coordinate system must be set, containing the local directions α^{fib} for the collagen fibers and α^{smc} for the smooth muscle cells. When defining the material, memory must be allocated for nine solution-dependent state variables, namely the damage driving forces β^{mat}, β^{fib_1}, β^{fib_2}, and β^{smc}, and the damage thresholds Ψ_0^{mat}, $\Psi_0^{\text{fib}_1}$, $\Psi_0^{\text{fib}_2}$, and Ψ_0^{smc}. The ninth state dependent variable is the relative sliding u_{rs} in the actin-myosin complex, which needs to be stored because of its viscous nature.

The anisotropic, hyperelastic, user-defined material model must be specified with all the material parameters described above, choosing the options '`formulation = invariant`', '`local directions = 3`' and '`type = incompressible`'. A conceptual drawback of the `UANISOHYPER_INV` subroutine is that it does not provide access to the time step of the solution process, which should be known for correct programming of the viscous evolution law described in Eq. (10.13). This implies that the exact time step is only known if a fixed time increment is set, by adding the option '`direct`' to the keyword '`static`' in the input file. Otherwise, only the minimum and maximum allowable time step can be externally prescribed.

10.4.3 Parameter Selection

Table 10.1 gives an overview of all parameters of the material model. The first set of parameters are related to the extracellular matrix with two embedded fiber families. For the rat abdominal aorta, the main direction of the collagen fibers α^{fib} is set to $\pm 5°$, i.e., it is almost aligned with the circumferential direction, see O'Connell et al. (2008). The four remaining parameters are set to $\kappa = 0.16(-)$, $k_1 = 32.51$ kPa, $k_2 = 3.05(-)$ and $c = 23.63$ kPa, by using experimental data from extension-inflation tests, as described in Famaey et al. (2012a). Alternatively, a parameter set from human arteries can be found in Stålhand (2009).

The next set of parameters are the rate constants of the chemical model defining the fractions n_{III} and n_{IV} in Eq. (10.12). They are chosen according to Hai and Murphy (1988). These values led to the fractions of $n_{\text{III}} = 0.164$ and $n_{\text{IV}} = 0.547$, which

Table 10.1 Parameters used in the finite element model

Parameter	Value	Source
Matrix material		
c	23.63 kPa	Famaey et al. (2012a)
Collagen fibers		
α^{fib}	$\pm 5°$	O'Connell et al. (2008)
k_1	32.51 kPa	
k_2	$3.05(-)$	Famaey et al. (2012a)
κ	$0.16(-)$	
Smooth muscle cells—chemical rate constants		
κ_1, κ_6	$0.14\ \text{s}^{-1}$	Hai and Murphy (1988)
κ_2, κ_5	$0.5\ \text{s}^{-1}$	
$\kappa_3, 4\kappa_4$	$0.44\ \text{s}^{-1}$	
κ_7	$0.01\ \text{s}^{-1}$	
Smooth muscle cells—mechanical constants		
μ^{smc}	0.25 MPa	Famaey et al. (2012b)
κ_c	0.93 MPa	Famaey et al. (2012b)
η	60 MPa s	Murtada et al. (2010)
α^{smc}	$0°$	O'Connell et al. (2008)
$\gamma^{\text{smc}}_{\text{pas}}$	$0.9(-)$	Famaey et al. (2012b)
$m^{\text{smc}}_{\text{pas}}$	3.00 kPa	Famaey et al. (2012b)

were used as fixed input values into the mechanical model. Additional parameters are related to the mechanical model of the smooth muscle cell contribution. According to O'Connell et al. (2008), the smooth muscle cells of rat abdominal arteries are oriented circumferentially with $\alpha^{\text{smc}} = 0°$. The parameter μ^{smc} depending on the stiffness of the actin-myosin filament structure and the parameter κ_c related to the driving force per cross-bridge were both tuned to fit the experimental contraction measured in the myograph due to addition of PE for a previously undamaged segment, as described in Sect. 10.2. The viscous damping constant η was set to 60 MPa s, corresponding to the value used in Murtada et al. (2010).

To characterize damage progression appropriately, two parameters need to be calibrated for each constituent, plus two additional ones for the smooth muscle cells, resulting to ten parameters. Since the myograph experiment only allows for damage quantification in the smooth muscle cells, with the current setup, no reasonable damage parameters can be defined for the extracellular matrix and the collagen fibers. Additional complementary experiments will be needed for this task, as discussed in Sect. 10.7. Accordingly, here, γ^{mat} and γ^{fib} were set to zero, such that m^{mat} and m^{fib} can take any arbitrary value. Secondly, the assumption was made that, during clamping, the smooth muscle cells were completely passive, and thus not contributing to the stiffness. Consequently, no damage could accumulate here, so that $\gamma^{\text{smc}}_{\text{act}}$

could also be set to zero, and $m_{\text{act}}^{\text{smc}}$ to an arbitrary value. The two remaining parameters $\gamma_{\text{pas}}^{\text{smc}}$ and $m_{\text{pas}}^{\text{smc}}$ were then calibrated using the experimental data, as described in Famaey et al. (2012b). For a systematic approach to calibrate damage material parameters in a heterogeneous setting, the reader is referred to Mahnken and Kuhl (1999).

10.5 Finite Element Simulation

10.5.1 Arterial Clamping

With the material model described in Sect. 10.4, it becomes possible to simulate the experimental process described in Sect. 10.3. A three-dimensional finite element model was built in Abaqus/Standard $6.10-2$. Here, an idealized cylindrical geometry was used with an outer radius of 0.58 mm, a wall thickness of 0.14 mm and an initial length of 0.1 mm. These values were obtained from measurements on rat abdominal arteries described in Famaey et al. (2012a). Hexahedral `C3D8H` elements were used. Because of severe bending, six elements were taken across the thickness, and seeding in other dimensions was chosen to ensure regular elements. The numerical implementation of the arterial clamping is subdivided into two steps: (i) the setting of the initial damage level, (ii) the clamping process itself. Figure 10.3 shows all steps of the clamping simulation.

In the first part, an opened cylindrical segment with an opening angle of 60° is closed to account for the circumferential residual strains (Balzani et al., 2007). Next, the segment is longitudinally stretched by 50 %, to account for residual strains in the longitudinal direction. The values for the residual strains were obtained from experiments described in Famaey et al. (2012a). In the third step, the segment is inflated to an internal pressure of 16 kPa, which corresponds to physiological systolic blood pressure. The material model used in this step is the three-constituent damage model, as described above, however, without accumulation of damage. At the end of the third step, the undamaged elastic strain energy of each of the four constituents is written into a matrix of internal or 'solution dependent variables' for each integration point, using Python scripting. These are the initial damage threshold levels Ψ_0^i, described in Eq. (10.6), which will be used in step 4.

Step 4 starts with a new input file, in which the state of the artery after the first three steps is imported. By importing, the deformations are included as 'initial values' for the model. The solution dependent variables defined above contain the damage threshold levels Ψ_0^i specified as 'initial conditions' in the input file. The material model is now updated to enable damage accumulation, $\gamma^i > 0$, and four extra solution dependent variables, representing the β^i described in Eq. (10.6) are added. In addition, two extra parts are added to the assembly of the system, namely an upper and lower clamp, which are gradually moved towards each other during step 4, until a clamping force of 5 mN is reached. A friction coefficient of $\mu^{\text{clamp}} = 0.3$ is used between the clamp and the outer arterial surface. Finally, also the internal pressure

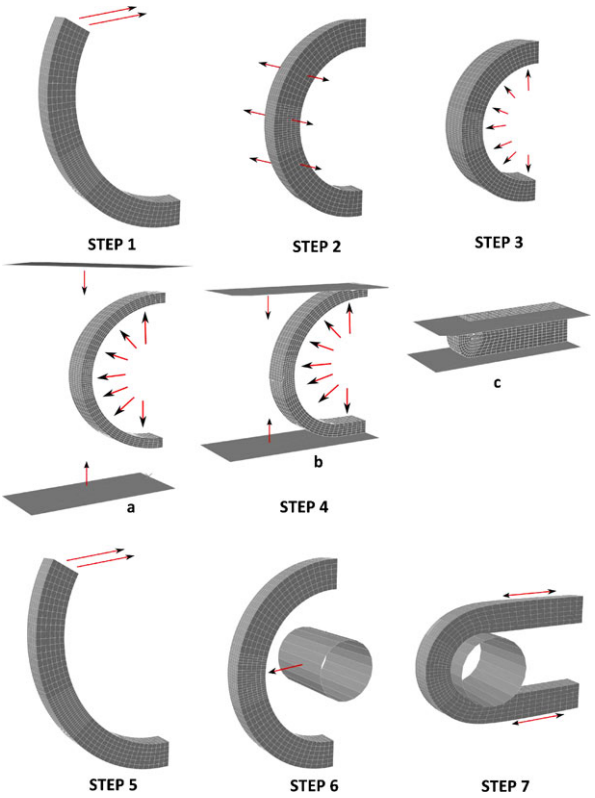

Fig. 10.3 Schematic overview of the seven steps in the FE simulation representing the loading history of arterial clamping (*steps 1–4*) and the functional damage assessment (*steps 5–7*)

boundary conditions are modified to a pulsating pressure between 10 and 16 kPa, that gradually decays to zero when the vessel is completely closed. To keep track of the maximum energy level reached for each constituent at every integration point of the system, the four extra solution dependent variables are updated and stored at each step as internal variables β^i. At the end of the simulation, these solution dependent variables are again written to a matrix using Python scripting to inform the next step.

10.5.2 Functional Damage Assessment

After clamping, damage has accumulated in the different constituents. For the smooth muscle cells, this amount of damage can be calibrated and validated in a myograph, as explained in Sect. 10.2. The simulation starts from the same mesh as in step 1 of Sect. 10.5.1. Initial conditions are specified for the solution dependent variables taking into account the earlier loading history through the internal variables β^i. The material model is adapted such that damage due to the energy

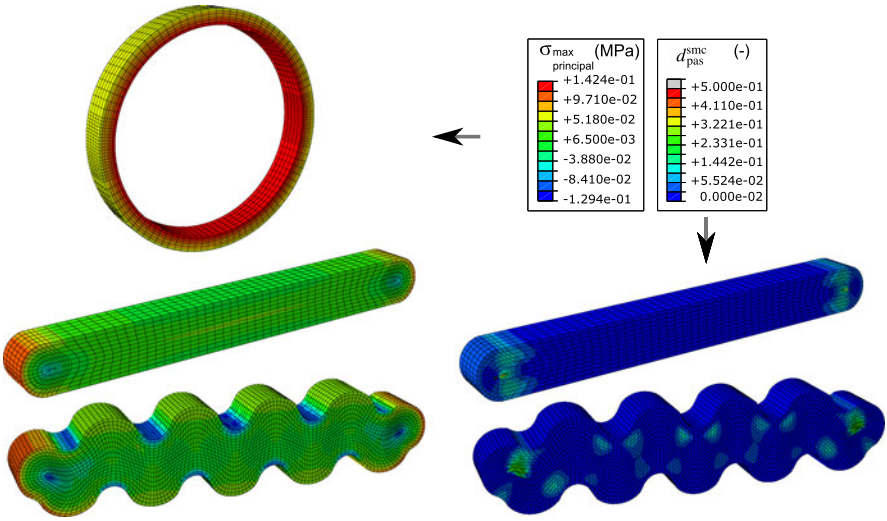

Fig. 10.4 Maximum principal stress in an arterial segment at systolic pressure (*top left*), when clamped up to a clamping force of 5 mN with a smooth clamp (*middle left*) and when clamped up to 5 mN with a mosquito clamp (*bottom left*). Damage variable $d_{\text{pas}}^{\text{smc}}$ in the same segment, for the smooth clamp design (*top right*) and for the wavy clamp design (*bottom right*)

accumulation of clamping is present, but no further damage is induced. Similar to step 1 of Sect. 10.5.1, the segment is closed to form a half cylinder in step 5, thus incorporating the circumferential residual stress. To reproduce the experimental situation, this time, no longitudinal stretch or internal pressure was added. Next, in step 6, a rod is translated radially from inside the section, pulling it until it exerts a certain load, corresponding to the experimentally measured value after complete relaxation due to the addition of SNP. A friction coefficient of $\mu^{\text{rod}} = 0.3$ is used between the rod and the outer arterial surface. Up to the end of step 6, no smooth muscle cell contribution is added in the material model. This is accomplished by multiplying the fractions n_{III} and n_{IV} with a switch function that is set to zero in steps 5 and 6.

After reaching the relaxed state, in the final step, the switch function is smoothly ramped to one, so that the smooth muscle cells reach the completely contracted state. Physiologically, this corresponds to the transition between the state after addition of SNP (completely relaxed) and the state after the addition of PE (completely contracted). In this step only, because of the time dependence of the evolution law for the relative sliding u_{rs}, the time step of the implicit solution scheme is fixed to $\Delta t = 10^{-5}$. Figure 10.3 gives a schematic overview of all seven steps of the simulation.

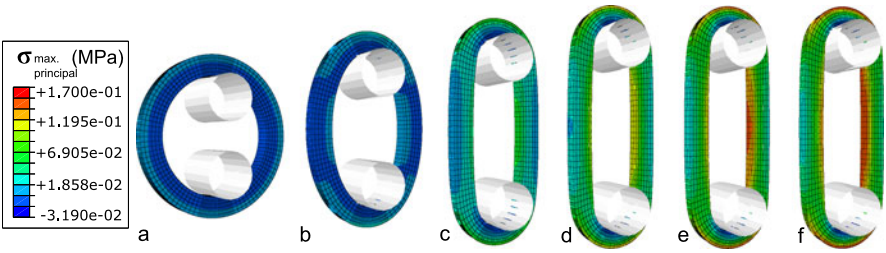

Fig. 10.5 Different stages of the myograph experiment, with the *color code* depicting the maximum principal stress. In stages *a*, *b* and *c* the rods are being pulled to the preload force (step 6 of the numerical simulation). In stages *d*, *e* and *f* the rods remain in position and the smooth muscle cells are activated (step 7 of the numerical simulation)

10.5.3 A Different Clamp Design

The power of the proposed framework is that damage assessment can be performed for different loading situations without having to perform new experiments. As a proof of concept, the simulations described above were repeated for the exact same geometry, but with a wavy clamp design, similar to a typical mosquito clamp used in surgery. Mesh density for this simulation was increased to nine elements through the thickness as more severe bending was expected. Clamping was simulated up to the same macroscopic clamping force as with the smooth clamp design. The clamping simulation was performed in Abaqus/Explicit, as it has a better capability of dealing with complex contact situations.

10.6 Results

The top left image in Fig. 10.4 shows the maximum principal stress in an arterial segment in the systolic physiological state. This state defines the free energy threshold above which damage is initiated. In the middle left image of the same figure, the maximum principal stress is shown for the same arterial segment when clamped up to a clamping force of 5 mN with a smooth clamp design. The bottom left image shows the segment when it is clamped to the same clamping force with a mosquito clamp. As shown in the right column of Fig. 10.4, the clamping induced an inhomogeneous damage pattern to the smooth muscle cells in both clamping cases.

Figure 10.5 shows snapshots of the myograph experiment, with the color code depicting the maximum principal stress. The right graph of Fig. 10.6 shows the force measured in the rods of the myograph as a function of time, for a previously undamaged segment, solid line, and for a segment that was previously clamped at 5 mN with a smooth clamp, dashed line, and for a segment that was previously clamped with a mosquito clamp, dotted line. The letters along the curve correspond to the stages shown in Fig. 10.5. The first section of the graph corresponds to step

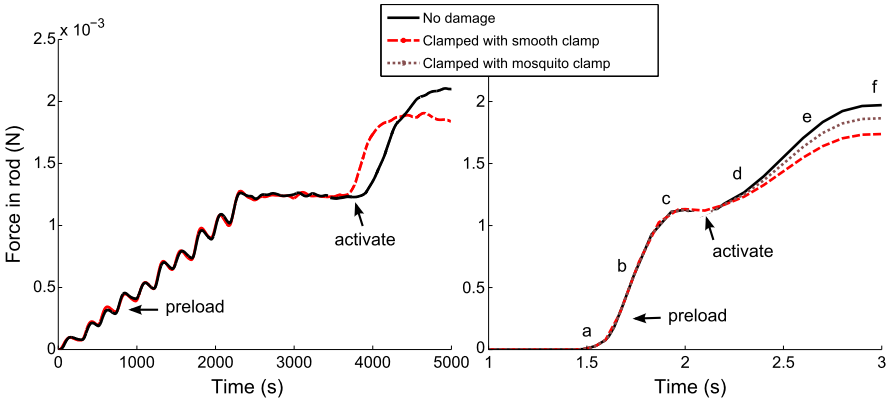

Fig. 10.6 The *left graph* shows the force measured in the rod during an experiment, for a segment that was previously clamped with the device described in Sect. 10.3 to a level of 5 mN and for a segment that was undamaged, both normalized to the width of the numerical model. The *right graph* shows the force in the rod of the myograph as a function of time calculated from the finite element simulation, for a previously undamaged segment (*solid line*), for a segment that was previously clamped at 5 mN with a smooth clamp (*dashed*) and for a segment that was previously clamped at 5 mN with a mosquito clamp (*dotted*). The *letters along the curve* correspond to the snapshots shown in Fig. 10.5

6 of the simulation, i.e., the pulling of the rod to the passive state. After 2 seconds, the smooth muscle cells are activated, corresponding to step 7.

The left graph of Fig. 10.6 shows the force measured in the rod for a segment that was previously clamped with the device described in Sect. 10.3 to a level of 5 mN, normalized to the width of the numerical model, and for a segment that was undamaged. The force in the rod was also normalized to the width of the numerical model. Again, in the first section of the graph, the rod is gradually pulled to reach the passive preload state. At the point indicated with the arrow, PE is added to the Krebs solution, triggering the activation of the smooth muscle cells. Note that the time scales in the two graphs do not agree. To calibrate the model appropriately, an additional time parameter would have to be included into the model. Here, however, we were only interested in the end result of the curve, rather than in calibrating the model to real physical times.

10.7 Discussion

This chapter outlined a framework to experimentally quantify and numerically simulate damage to cardiovascular tissue due to mechanical loading. Different experimental methods were described for the damage quantification of the different constituents of the tissue and explicit attention was given to the myograph setup, a device to test the vasoregulating capability of the artery. Next, it was shown how *in vivo* mechanical experiments can be performed to determine the experimental relation between a certain mechanical load and the induced damage.

To enable the simulation of the amount of induced damage due to any mechanical load without having to repeat a huge amount of experiments, a realistic material model incorporating damage to each of the constituents of the arterial tissue was introduced and incorporated into a finite element framework (Abaqus). It was used to simulate the clamping experiment as well as the myograph test, as described in the previous sections.

The material model described in Sect. 10.4 introduces a large set of parameters, which need to be experimentally defined for each tissue type. Extensive experimental data from a range of different experiments is required to correctly calibrate all parameters. Section 10.4.3 comments on the rationale behind the parameter selection for this study. The goal of this study was to demonstrate the feasibility of the proposed model and to illustrate a conceptual methodology for the damage characterization in smooth muscle cells. Accordingly, less emphasis was placed on the exact parameter identification for the other model parameters. As explained in Sect. 10.4.1, four damage processes can be captured by the model, one for each constituent. Each damage process is assumed to be driven by the individual free energy of that constituent. For smooth muscle cells, passive damage is also affected by the energy in the matrix constituent. Here, we focus in particular on this last passive part of damage, assuming that smooth muscle cells are inactive during the real clamping process. The damage parameters were chosen to correspond to the results of the *ex vivo* experiment. In the future, further experiments will be performed with different clamping force levels to calibrate the model for a wider loading range. To enable numerical comparison with higher clamping force levels, it will be necessary to remesh the clamped segment to avoid excessive element distortion. However, remeshing would require the mapping of the solution, both from the node points and from the integration points, onto the new mesh, a feature still lacking for anisotropic materials in Abaqus 6.10.

Aside from simulating with a smooth clamp similar to the experimental situation, a simulation was also performed with a wavy surface, as in a typical mosquito clamp. Results show how for the same amount of clamping force, less damage is induced in the tissue with the wavy clamp design and, consequently, a higher contractile force is achieved in the simulated isometric contraction test. Though perhaps counter-intuitive, the reason for this is that at the current clamping force, the tissue is still able to relax into the concave parts of the clamp and therefore gets less stretched towards the edges. One would expect the damage to become more severe as soon as these concave parts are entirely filled up by the material.

In order to accurately identify the damage parameters for the different constituents, different, ideally orthogonal, experiments are required that enable the extraction of this specific information. Damage in the collagen fibers under tension can possibly be studied using microscopic images of the tissue at different stages in the stretching process and assessing the images for collagen rupture. In fact, the extension-inflation tests that were used here to calibrate the undamaged baseline parameters of the Holzapfel-model most probably already induced damage to both collagen fibers and matrix in the higher pressure regimes. Damage in the collagen fibers and matrix should therefore ideally be calibrated simultaneously, possibly

through extension-inflation tests. Damage to the smooth muscle cells is assumed to depend on both damage of the passive extracellular matrix and damage of the active smooth muscle cells themselves. Damage in the passive regime has been observed and characterized experimentally in Famaey et al. (2010), and calibrated in this manuscript using these data. It results in a reduced activation capability, which will only become apparent upon activation. Damage in the active regime is caused by excessive tension in the direction of the contractile unit, which might cause ruptures in the myosin cross-bridges or rupture of the actin and myosin filaments. It is included here merely theoretically for the sake of completeness, but has not been calibrated yet. We are currently in the process of further investigating these phenomena to characterize the mechanisms underlying active damage.

Note also that in the finite element model, the artery was modeled as a single homogeneous layer, even though the wall consists of two solid mechanically relevant layers, i.e. the media and the adventitia. However, in the case of a rat abdominal artery, the complete wall thickness is only approximately 0.14 mm thick, and in contrast to human tissue, it is impossible to separate these two layers from each other. Therefore, the most accurate approach was to model the wall as a single layer. The assumption was also made that damage initiates once the energy level exceeds that of the energy level at systolic blood pressure. This was motivated by the fact that the morphology and properties of the arterial wall change due to chronic hypertension (Matsumoto and Hayashi, 1994), but whether this actually justifies this assumption for acute damage scenarios should still be experimentally validated.

Although the three-constituent damage model already captures a number of typical features of cardiovascular tissue, some characteristic aspects are still not included, and a few limitations remain. When qualitatively comparing a simulated homogeneous cyclic tension test performed on one element with the new material model to the experimental results of a uniaxial tensile test on a sheep carotid artery, shown in Fig. 10.7, it is clear that several features, e.g., tissue nonlinearity and discontinuous softening are accurately captured. However, in the tensile test on the sheep carotid artery, cycling up to a certain strain level was performed five times before the next strain level was reached, and clearly softening does continue in these cycles, even though the maximum energy level, the parameter β in our model, is not increased. This continuous damage behavior was not captured with the damage model used here. Moreover, the damage variables introduced in this model mainly capture acute effects, while chronic effects such as repair and/or remodeling have not been considered for the time being. These effects should be investigated, keeping in mind the trade-off between realism of the model and its usability. The correct identification of the material parameters obviously becomes more challenging as more effects are incorporated in the model.

Predictive computational modeling of tolerable damage thresholds is clinically relevant in two ways: on the one hand, in the short term, the proposed framework can be used as a simulation tool to optimize surgical tools, for example, to improve clamp design to minimize tissue damage. On the other hand, in the long term, the proposed framework could enable the prediction of surgically-induced damage evolution in real-time. This would allow loading thresholds to be imposed on surgical instruments during an operation in a robotic teleoperation setting. The actual

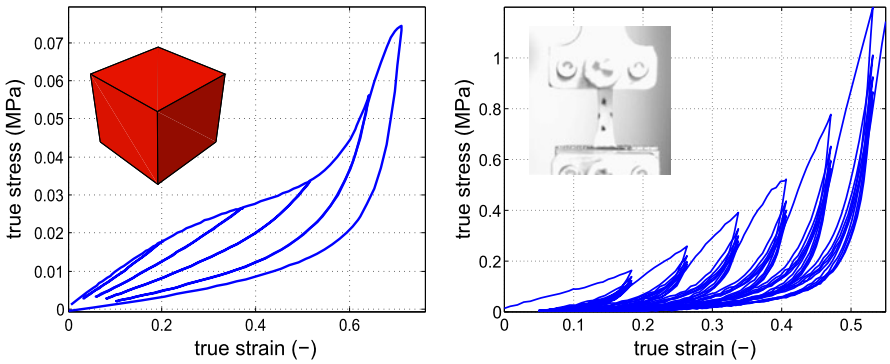

Fig. 10.7 Comparison of a simulated homogeneous cyclic tension test performed on one element with the new material model to a uniaxial tensile test on a circumferentially oriented strip of a sheep carotid artery. The experiment was performed on a tensile test bench (INSTRON 5567). Cyclic loading at gradually increasing levels of elongation was applied at a crosshead speed of 1 mm/s. The tests were performed with continuous recording of tensile force, with a 1 kN load cell and gauge length, based on crosshead displacement, at a sampling frequency of 10 Hz. Cycling up to a certain strain level was performed five times before the next strain level was reached, for six increasing levels of strain

value of these thresholds should be defined in close collaboration with surgeons and biomedical researchers, experimentally assessing the level of damage due to loading and defining which damage levels are still acceptable, taking into account long-term effects of damage accumulation but also self healing. These critical damage levels can then be correlated to the internal damage variables d. Once the damage variable of a constituent has reached a certain level robotic loading should be stopped automatically. Future research will therefore also be directed towards algorithm speed-up, e.g., through parallelized implementation in the GPU with NVIDIA Compute Unified Device Architecture.

References

Arruda EM, Boyce MC (1993) A three-dimensional constitutive model for the large stretch behavior of rubber elastic materials. J Mech Phys Solids 41:389–412

Balzani D, Schröder J, Gross D (2006) Simulation of discontinuous damage incorporating residual stresses in circumferentially overstretched atherosclerotic arteries. Acta Biomater 2:609–618

Balzani D, Schröder J, Gross D (2007) Numerical simulation of residual stresses in arterial walls. Comput Mater Sci 39:117–123

Böl M, Abilez OJ, Assar AN, Zarins CK, Kuhl E (2012) In vitro/in silico characterization of active and passive stresses in cardiac muscle. Int J Multiscale Comput Eng 10:171–188. doi:10.1615/IntJMultCompEng.2011002352

Callera GE, Varanda WA, Bendhack LM (2000) Impaired relaxation to acetylcholine in 2K-1C hypertensive rat aortas involves changes in membrane hyperpolarization instead of an abnormal contribution of endothelial factors. Gen Pharmacol 34:379–389

Famaey N, Sommer G, Vander Sloten J, Holzapfel GA (2012a) Arterial clamping: finite element simulation and in vivo validation. J Mech Behav Biomed Mat 12:107–118

Famaey N, Vander Sloten J, Kuhl E (2012b) A three-constituent damage model for arterial clamping. Biomech Model Mechanobiol (in press)
Famaey N, Verbeken E, Vinckier S, Willaert B, Herijgers P, Vander Sloten J (2010) In vivo soft tissue damage assessment for applications in surgery. Med Eng Phys 32:437–443
Gasser TC, Ogden RW, Holzapfel GA (2006) Hyperelastic modelling of arterial layers with distributed collagen fibre orientations. J R Soc Interface 3:15–35
Gupta V, Reddy NP, Batur P (1997) Forces in laparoscopic surgical tools. Presence 6:218–228
Hai CM, Murphy RA (1988) Cross-bridge phosphorylation and regulation of latch state in smooth muscle. Am J Physiol 254:C99–106
Health Grades (2012) Patient safety in American hospitals. Health grades quality study. Available at www.healthgrades.com Accessed April 2012
Holzapfel GA, Gasser TC, Ogden RW (2000) A new constitutive framework for arterial wall mechanics and a comparative study of material models. J Elast 61:1–48
Mahnken R, Kuhl E (1999) Parameter identification of gradient enhanced damage models with the finite element method. Eur J Mech A, Solids 18:819–835
Matsumoto T, Hayashi K (1994) Mechanical and dimensional adaptation of rat aorta to hypertension. J Biomech Eng 116:278–283
Megens RT, Reitsma S, Schiffers PH, Hilgers RH, De Mey JG, Slaaf DW, oude Egbrink MG, van Zandvoort MA (2007) Two-photon microscopy of vital murine elastic and muscular arteries. Combined structural and functional imaging with subcellular resolution. J Vasc Res 44:87–98
Megens RT, oude Egbrink MG, Merkx M, Slaaf DW, van Zandvoort MA (2008) Two-photon microscopy on vital carotid arteries: imaging the relationship between collagen and inflammatory cells in atherosclerotic plaques. J Biomed Opt 13:044022
Murtada S-I, Kroon M, Holzapfel GA (2010) A calcium-driven mechanochemical model for prediction of force generation in smooth muscle. Biomech Model Mechanobiol 9:749–762
O'Connell MK, Murthy S, Phan S, Xu C, Buchanan J, Spilker R, Dalman RL, Zarins CK, Denk W, Taylor CA (2008) The three-dimensional micro- and nanostructure of the aortic medial lamellar unit measured using 3D confocal and electron microscopy imaging. Matrix Biology 27:171–181
Schriefl AJ, Zeindlinger G, Pierce DM, Regitnig P, Holzapfel GA (2012) Determination of the layer-specific distributed collagen fiber orientations in human thoracic and abdominal aortas and common iliac arteries. J R Soc Interface 9:1275–1286
Simo J, Ju J (1987) Strain- and stress-based continuum damage models. Int J Solids Stuct 23:821–840
Stålhand J (2009) Determination of human arterial wall parameters from clinical data. Biomech Model Mechanobiol 8:141–148
Stålhand J, Klarbring A, Holzapfel GA (2011) A mechanochemical 3D continuum model for smooth muscle contraction under finite strains. J Theor Biol 268:120–130

Chapter 11
Mechanical Properties of Ascending Thoracic Aortic Aneurysm (ATAA): Association with Valve Morphology

Salvatore Pasta, Julie A. Phillipi, Thomas G. Gleason, and David A. Vorp

Abstract Type A aortic dissection (AoD) of an ascending thoracic aortic aneurysm (ATAA) is a life-threatening cardiovascular emergency with a high potential for death. AoD represents a devastating separation of elastic aortic layers occurring when the hemodynamic loads on the diseased wall exceed the adhesive strength between layers. The goal of this study was to evaluate and compare the dissection properties of non-aneurysmal and aneurysmal human ascending thoracic aortas from patients with bicuspid aortic valve (BAV) and normal tricuspid aortic valve (TAV) morphologies using biomechanical delamination testing. Following complete delamination of ATAA tissue samples, tensile tests were performed on each delaminated half for comparison of their tensile strengths. Results evinced that the aneurysmal aortas with BAV and TAV have lower delamination properties than non-aneurysmal aorta, and that ATAA with BAV has lower S_d than TAV, suggesting an apparent propensity of AoD.

11.1 Introduction

One of the most common lethal complications of an ascending thoracic aortic aneurysm (ATAA) is the aortic dissection (AoD), causing significant mortality

S. Pasta
Fondazione RiMED, Palermo, Italy
e-mail: sap62@pitt.edu

J.A. Phillipi · T.G. Gleason
Department of Cardiothoracic Surgery, University of Pittsburgh, Pittsburgh, USA

J.A. Phillipi
e-mail: phillippija@upmc.edu

T.G. Gleason
e-mail: gleasontg@upmc.edu

D.A. Vorp (✉)
Department of Bioengineering, University of Pittsburgh, Pittsburgh, USA
e-mail: vorpda@upmc.edu

G.A. Holzapfel, E. Kuhl (eds.), *Computer Models in Biomechanics*,
DOI 10.1007/978-94-007-5464-5_11,

despite advances in diagnostics and surgical management (Bonnichsen et al., 2011). The exact prevalence of AoD is difficult to determine, and most estimates are based on necropsy studies with evidence in 1–3 % of all cases. The incidence of AoD is believed to be 5–30 cases per 1 million people per year, typically presenting in elderly patients, and in males more frequently than females (ratio 3 : 1). AoD occurs more typically in elderly patients in the presence of a tricuspid aortic valve (TAV) and in relatively younger patients if a bicuspid aortic valve (BAV) is present. During the first 24 to 48 hours, the mortality in patients not treated surgically is as high as 74 % (Knipp et al., 2007). Even among patients treated with emergent aortic reconstruction, operative mortality averages 24 % worldwide as reported by the International Registry of Acute Aortic Dissection (Rampoldi et al., 2007).

Type A ascending aortic dissections originate with an intimal tear typically occurring near the sinotubular junction where the wall stresses are believed to be elevated (Coady et al., 1999). The intimal tear allows blood to enter the aortic wall, splitting the media and progressively separating the medial plane along the longitudinal direction of the aorta. This creates a new 'false lumen' which runs parallel to the true lumen. The false lumen can reenter the true lumen anywhere along the course of the AoD or exit through the adventitia resulting in frank rupture. As the dissection extends distally, its propagation and re-entry follows unpredictable courses that can result in life threatening ischemia of the heart, brain, abdominal viscera, spinal cord and extremities (Johansson, 1995). There are several risk factors predisposing patients to AoD. Among these are severe hypertension, connective tissue disorders such as the Marfan and Ehlers-Danlos syndromes, and bicuspid aortic valve (BAV). The congenital malformation, bicuspid aortic valve is distinctly associated with the development of ascending aortic dilatation imparting a marked risk of AoD (Cripe et al., 2004) and occurs in 1 to 2 % of the population, making it the most common congenital heart malformation (Bonderman et al., 1999; Ward, 2000). In the clinical practice of ATAA reported by Gleason (2005), over 40 % of patients undergoing elective surgical replacement of the ascending aorta indeed have BAV. Additionally, older necropsy studies shown a risk of fatal dissecting aneurysm in BAV patients nine times higher than patients with tricuspid aortic valve (TAV) (Edwards et al., 1978; Larson and Edwards, 1984). The histopathologic analyses of AoD and aneurysms appear strikingly different from those of abdominal aortic aneurysms (AAA). Thoracic aneurysms have distinct histopathologic characteristics classified as cystic medial degeneration, which is non-inflammatory and in stark contradistinction to AAAs showing inflammatory characteristics (Davies, 1998; El-Hamamsy and Yacoub, 2009).

From a biomechanical point-of-view, the AoD of ATAAs involves a separation (i.e. a delamination) of the elastic layers of the degenerated aortic wall that occurs when the hemodynamic loads exerted on the aneurysmal wall exceed adhesive forces that normally hold the mural layers together.

The purpose of this work was therefore to quantify the biomechanical properties of ATAA samples relative to non-aneurysmal human ascending aorta and to distinguish specific differences in the biomechanical properties of ATAAs from BAV and TAV patients. This was achieved performing biomechanical delamination tests, followed by tensile tests on the delaminated halves to show the distinct strengths of the

outer and inner aortic walls of the artificially created 'false lumen' for evaluating the propensity of either intimal flap propagation or frank disruption. SEM investigations was also performed to examine the failure modality of AoD.

11.2 Material and Methods

11.2.1 Human Aortic Tissue Specimens

All human ascending thoracic aorta tissue specimens were obtained after informed consent following guidelines of our Institutional Review Board and Center for Organ Recovery and Education. Segments of non-aneurysmal aorta (control) were collected from organ donor subjects whereas non-dissected ATAAs were collected from patients undergoing elective ascending aortic replacement at the University of Pittsburgh Medical Center. A total of 31 aortic segments (7 controls and 24 ATAAs) with age range of 41–79 yr, aortic diameter of 40–68 mm and gender comprised of 24 males and 7 females were analyzed. The aneurysmal groups were composed of 16 BAV and 8 TAV segments, respectively. All non-aneurysmal segments were collected from individuals with TAV. The aortic samples were tested within 48 hours of harvest after storing at 4 °C in a calcium-free and glucose-free 0.9 % physiological saline solution (Raghavan et al., 1996).

11.2.2 Biomechanical Testing

The harvested aortic segments were cut into long, thin, rectangular (approximately 30 × 6 mm) strips with their long axis in either longitudinal (LONG) or circumferential (CIRC) orientation with respect to that of the aorta. Generally, the same aortic segment was used to obtain strips of both orientations for direct comparison. To create an initial delamination plane, a delaminating incision was made with the aid of a surgical scalpel between elastic lamellae of each specimen, parallel with the plane of the aortic wall and 8–12 mm in length (Fig. 11.1).

Since the initial incision was made manually, there naturally was a moderate variation in terms of the exact location of the incision plane with respect to the center of the media or to the external or internal elastic lamina. However, the artificial delamination plane was reproducible. The dimension of each specimen (i.e., the width, thickness and length) were measured at three different locations using a dial caliper and then averaged and recorded before testing. The two free flaps of each delaminated half of the ATAA specimen were mounted between the grips of an Instron tensile system (model 5542) with a 5 N load cell. To avoid slipping of the specimen in the pneumatic grips, surfalloy jaw faces with gritty, sandpaper-like surfaces were used. During testing, the mounted specimens were submerged in 0.9 % physiological saline solution in a BioPuls bath under controlled temperature of 37 °C.

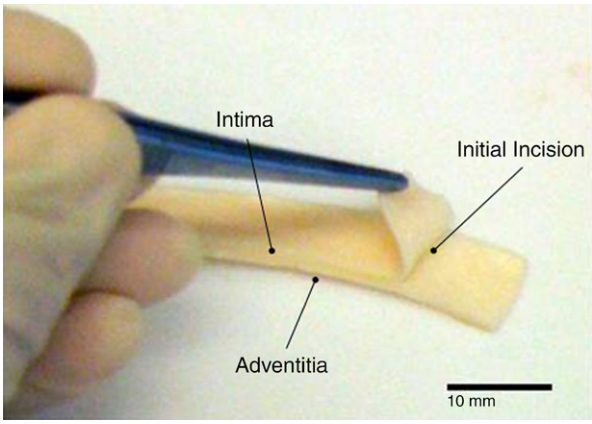

Fig. 11.1 Photography of a representative specimen for a delamination test showing the through-thickness incision for creating the initial dissection plane. Taken from Pasta et al. (2011)

A constant crosshead speed of 1 mm/min was used to pull apart the two free flaps of the tissue specimen whereas the applied load and resulting displacement were recorded continuously using the Instron-packaged software (Bluehill v.2). The two delaminated halves resulting from each delamination test (i.e., the one between the intimal surface and the delaminated plane (INT-DEL), and the one between the adventitial surface and the delaminated plane (ADV-DEL)) were stretched to failure in the uniaxial tensile testing system to evaluate the tensile strength of each. None of specimens failed for technical reason during biomechanical testing.

11.2.3 Data Analysis

'Delamination curves' were generated from each test, and consisted of a plot of the 'peel tension' (T_{peel}, defined as the applied force normalized by the width of the specimen) as function of the elongation (displacement). The mean value of T_{peel} after the initial peak was taken as the delamination strength S_{d} of the specimen. The S_{d} values calculated for multiple LONG and CIRC specimens tested for a given patient were taken as the overall $S_{\text{d,LONG}}$ and $S_{\text{d,CIRC}}$ for that specific patient. For the tensile tests, we utilized the approach published previously by our laboratory (Raghavan et al., 1996). In short, the Cauchy stress T was calculated as the applied force normalized by the deformed cross-sectional area, and stretch was calculated as the deformed length normalized by the original length of each specimen. The tensile strength S_{T} was taken as the peak value of stress attained prior to complete specimen failure.

One-way ANOVA, followed by Holm-Sidak post-hoc test for all pair-wise comparisons, was performed using SigmaPlot software (SYSTAT Software Inc., Chicago, Ill) to determine significance among groups. Level of statistical significance was set as $p = 0.05$. Data are shown as mean $\pm$ SEM.

11.2.4 SEM Imaging

Changes of tissue microstructure due to the propagation of the dissection were investigated observing the surfaces of delaminated halves of specimens from each group at SEM. The aortic tissues were fixed in 2.5 % glutaraldehyde for one hour, dehydrated in a graded series of ethanol/water solutions, dried, and then sputter coated with gold. The orientation of each specimen inside the microscope was aligned to that of the dissection propagation before imaging.

11.3 Results

Figure 11.2 shows representative delamination curves for three separate LONG and CIRC strips cut from an ATAA of a 56 yr old male patient with BAV and aortic diameter of 46 mm. The initial 'ramp' phase of the loading curve corresponds to stretching of the peel arms whereas the jagged plateau region shows the slow and controlled propagation of the AoD. In delamination testing, the oscillation is typical and is often referred in the rubber mechanics literature as unstable or 'stick-slip' tearing; i.e., the delamination does not propagate at a steady rate, but is arrested and re-initiated at irregular intervals.

A comparison of S_d between non-aneurysmal and ATAA with BAV and TAV in both LONG and CIRC directions was performed (Fig. 11.3). A significant difference was observed for the S_d (i.e. the resistance to AoD) in both LONG and CIRC directions of the non-aneurysmal aorta ($S_{d,LONG} = 149.0 \pm 7.6$ and $S_{d,CIRC} = 126.0 \pm 6.6$, $n = 7$) with respect to that of BAV ATAAs ($S_{d,LONG} = 100.0 \pm 4.1$ and $S_{d,CIRC} = 88.4 \pm 4.1$, $n = 16$) and with respect to that of TAV ATAAs ($S_{d,LONG} = 116.8 \pm 6.1$ and $S_{d,CIRC} = 109.1 \pm 5.2$, $n = 8$). Furthermore, the significant difference between LONG and CIRC strengths for the non-aneurysmal group indicates anisotropic (i.e., directionally-dependent) dissection properties of the human ascending thoracic aorta. However, the aneurysmal aorta displays isotropic dissection properties since both BAV and TAV groups are not statistically difference in LONG and CIRC orientations. The S_d of BAV ATAAs was significantly lower than TAV ATAAs in both orientations.

Patient age or aneurysm diameter could affect the delamination strength of the aneurysmal aorta. To determine if the difference in S_d between groups was age-dependent, the S_d data for the non-aneurysmal and BAV groups as a function of the patient age were fit by linear regression to calculate two new sets of extrapolated S_d for non-aneurysmal (non-aneurysmal$_{extr}$) and BAV ($BAV_{extr,\ age}$), respectively, at the ages of each of the TAV patients, see Fig. 11.4(A). To assess if the difference in S_d between aneurysmal groups was diameter-dependent, the S_d data for the BAV group as a function of the aneurysm diameter were fit by linear regression to obtain a new set of extrapolated S_d for BAV ($BAV_{extr,\ dia}$) at the aneurysm diameter of each of the TAV patients, see Fig. 11.4(B). For the latter analysis, the comparison was performed only between aneurysmal groups since the S_d can not be extrapolated for

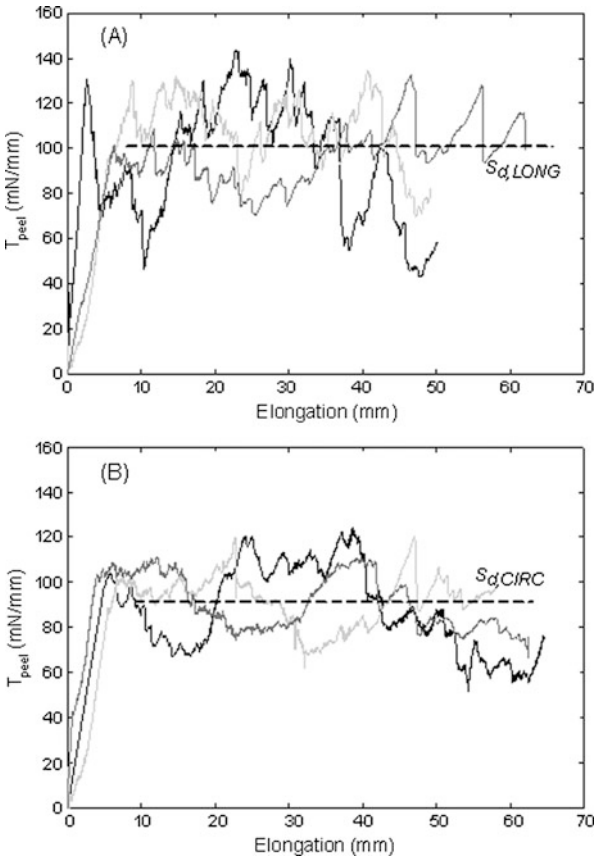

Fig. 11.2 Delamination profiles for (**A**) three LONG and (**B**) three CIRC strips cut from the same BAV aneurysm. The *dashed lines* represent the average of the mean values of T_{peel} for all LONG and CIRC strips and were taken as the S_d in LONG and CIRC directions for the patient, respectively. Taken from Pasta et al. (2011)

the non-aneurysmal aorta as a function of aortic diameter. Results suggest that even with corrections of age or aneurysm diameter the S_d of TAV ATAAs still remains higher than that of BAV_{ext}, see Figs. 11.4(A) and 11.4(B).

A comparison of S_T of non-aneurysmal and aneurysmal tissues for both INT-DEL and ADV-DEL halves following the delamination tests in LONG and CIRC orientations was performed, see Figs. 11.5(A) and 11.5(B). In all cases, the S_T of the CIRC strips was found to be higher than that of LONG specimens, and the INT-DEL half is significantly weaker than the ADV-DEL half. It should be also noted that the ultimate tensile strength of BAV ATAAs is higher than that of TAV ATAAs, though not significantly different. This trend is opposite of that observed for the delamination testing.

SEM imaging of the dissected surfaces for the healthy aorta reveals that the delamination in the LONG direction creates a remarkably 'rougher' surface compared to the surfaces from CIRC specimens (Fig. 11.6(A)). Similar failure surfaces were found for both BAV and TAV ATAAs; however, they appeared rougher than those of normal aorta (Fig. 11.6(A)). At high magnification, a 'fiber bridging' failure modality, which occurs when the dissection switches from one fiber/matrix interface to

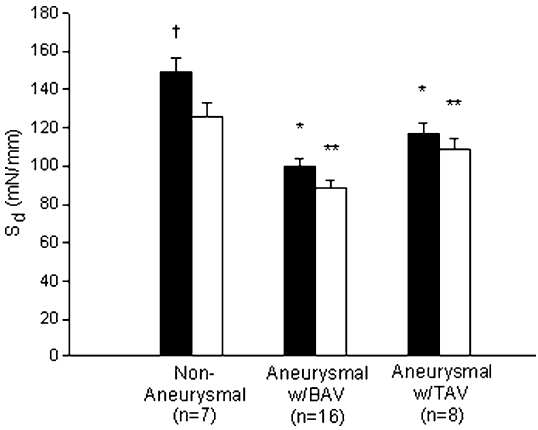

Fig. 11.3 Delamination strength in both LONG (■) and CIRC (□) orientations. * significantly different from LONG non-aneurysmal aorta ($p < 0.05$); ** significantly different from CIRC non-aneurysmal aorta ($p < 0.05$); † significantly different from CIRC non-aneurysmal aorta ($p < 0.05$). Taken from Pasta et al. (2011)

another and leaves behind the unbroken fibers to bridge the delamination, was observed for both non-diseased and aneurysmal aorta (Fig. 11.6(B)).

11.4 Discussion

The present investigation was performed to evaluate the delamination properties of the human ascending aorta to improve our understanding of the mechanics underlying aortic dissection in patients with ATAAs, and to compare these properties in patients with BAV and TAV. The mechanical integrity of the outer versus inner half of the dissected aorta was also explored to assess the relative probability of exit through the adventitia (frank disruption) versus propagation of the dissection flap, respectively, after the onset of AoD. Finally, the failure mechanisms during dissection were optically investigated. Our findings suggest that the propensity of AoD is greater in thoracic aneurysms compared to non-aneurysmal aorta, and is intrinsically greater for BAV ATAAs than those of TAV ATAAs. To our knowledge, these results have never been reported. Similar dissection properties for the human abdominal aorta were reported by Sommer et al. (2008).

The delamination curves (see Fig. 11.2) show an oscillation of T_{peel} about a mean 'plateau' value similar to the results found for tearing tests of the pig descending aorta (Purslow, 1983) and peeling tests of the human abdominal aorta (Sommer et al., 2008). Therefore, AoDs do not propagate at steady rates but arrest and re-initiate at somewhat regular intervals. The force necessary to drive the AoD appears to vary widely from a minimum at delamination arrest to a maximum at delamination initiation. This failure modality is mainly supported by the observation of a large amount of broken elastin fibers on the dissected tissue surfaces (see Fig. 11.6(B)) and is consistent with a fiber bridging failure modality (Gregory and Spearing, 2004). In this manner, the elastin fibers between halves may experience high stretch values during delamination testing with a consequent increase in the T_{peel} magnitude. Their subsequent failure induces a rapid decrease

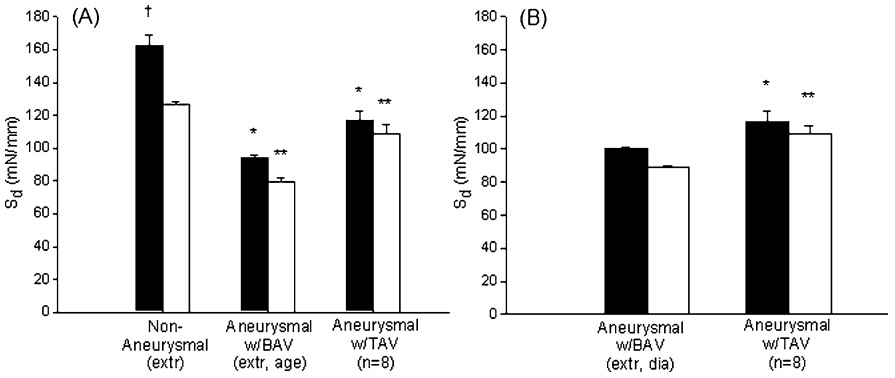

Fig. 11.4 (**A**) Delamination strength of aneurysmal aorta with BAV ($BAV_{extr,\ age}$) extrapolated (calculated) at the ages of each of the TAV patients in both LONG (■) and CIRC (□) directions for $n = 8$ specimens. ⋆ significantly different from LONG non-aneurysmal aorta ($p < 0.05$); ⋆⋆ significantly different from CIRC non-aneurysmal aorta ($p < 0.05$); † significantly different from CIRC non-aneurysmal aorta ($p < 0.05$); (**B**) delamination strength of aneurysmal aorta with BAV ($BAV_{ext,\ dia}$) extrapolated at the aneurysm diameter of each of the TAV patients in both LONG (■) and CIRC (□) directions for $n = 8$ specimens. ⋆ significantly different from LONG aneurysmal aorta with BAV_{ext} ($p < 0.05$); ⋆⋆ significantly different from CIRC aneurysmal aorta with BAV_{ext} ($p < 0.05$). Taken from Pasta et al. (2011)

in T_{peel} due to the reduced resistance to delamination, and this process repeats in intervals as the delamination propagates. Delamination was observed during the testing to propagate entirely within the medial layer of the aortic tissue specimens.

The significantly lower resistance to AoD of either type of aneurysm compared to that of healthy aorta (see Fig. 11.3) evinces that patients with ATAAs are more prone to AoD. Similar findings on the tensile strength of ATAAs were reported by our group and suggest that the propensity of rupture in thoracic aneurysm is 30 % higher than that of the non-aneurysmal ascending aorta (Vorp et al., 2003). Lower LONG tensile strength with aneurysm enlargement was also reported. This work suggests that a lower LONG tensile strength may be a cause of AoD in ATAAs (Iliopoulos et al., 2009). The fact that we found a $S_{d,CIRC}$ significantly lower than the $S_{d,LONG}$ is consistent with the notion that the pathogenesis of AoD is initiated by a transverse intimal tear on most of tear morphology seen clinically (Coady et al., 1999). Anisotropic dissection properties of the non-aneurysmal human ascending thoracic aorta are deduced by the significant difference of S_d in LONG and CIRC orientations (see Fig. 11.3). In contrast, aneurysmal disease leads to isotropic behavior of the aorta most likely due to a more disorganized microstructure, see Fig. 11.3. The most relevant finding is the difference in delamination propensity among BAV ATAAs compared to TAV ATAAs (Fig. 11.3), suggesting a greater propensity of AoD among BAV individuals. Furthermore, our deduction that age and aneurysm diameter are not key factors for AoD in patients with thoracic aneurysms (see Figs. 11.4(A) and (B), respectively) suggests that the higher propensity of aortic dissection in patients with BAV is related to lower delamination resistance that may

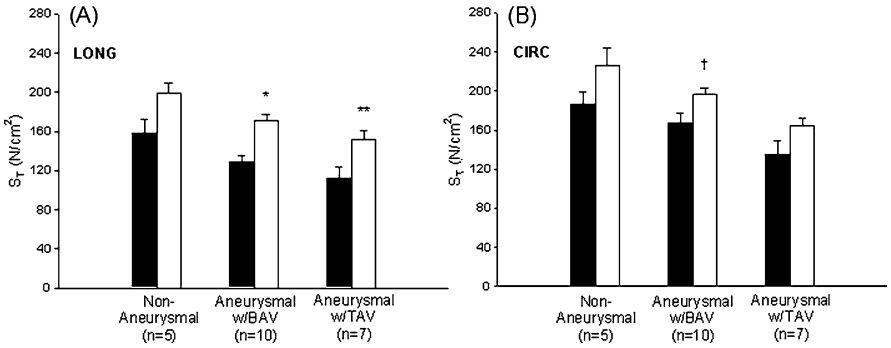

Fig. 11.5 (**A**) Tensile strength in LONG and (**B**) CIRC directions for INT-DEL halves (■) and ADV-DEL halves (□). * significantly different from INT-DEL LONG BAV ATAA ($p < 0.001$); ** significantly different from INT-DEL LONG BAV ATAA ($p = 0.016$); † significantly different from INT-DEL CIRC TAV ATAA ($p = 0.024$). Taken from Pasta et al. (2011)

be caused by predisposing structural disorders. A deficit in the smooth muscle cell response to the oxidative stress could be responsible for example of the inherent lower S_d in BAV tissues (Phillippi et al., 2009, 2010).

Our results demonstrate a weaker S_T of the intimal half of the aortic wall (i.e. the INT-DEL half; see Figs. 11.5(A) and (B)), imparting an apparent risk of the propagation of AoD. Exit through the outer residual layer (i.e. the ADV-DEL half) causing frank aortic disruption is less common than dissection propagation, and this may be explained by the relatively stronger S_T of the adventitial half of the aortic wall in this study. These results are consistent to the disparate strengths of healthy arterial layers found in the literature (Holzapfel et al., 2007).

Anisotropic dissection properties of the non-aneurysmal ascending aorta are consistent with SEM imaging results. Indeed, the elastin and collagen fibers are oriented mainly in the circumferential direction in the non-aneurysmal aortic wall and, as a result, may provide a greater strength to AoD in LONG direction. For the non-aneurysmal aorta, the creation of a rougher dissection surface may explain both higher mean and variance in S_d of LONG strips compared to those oriented in CIRC direction, see Fig. 11.2. The dissection in LONG direction frequently crosses the elastic layers while that in CIRC strips propagate mainly between adjacent elastic laminae (Fig. 11.6(A)) resulting in a 'flat' broken surface as found by Sommer et al. (2008) for the non-aneurysmal human abdominal aorta. Moreover, the fracture surfaces of both BAV and TAV ATAAs appear rougher than those for normal aorta (see Fig. 11.6(A)), likely due to the more disorganized microstructure caused by the disease. Disorganization of elastin and collagen fibers due to aneurysm appears to impact the mechanical properties of ATAAs. For the healthy aorta, the formation of a rougher surface may clarify the non-significant difference in S_d between the LONG and CIRC directions, suggesting isotropic dissection properties.

These results are limited by the fact that delamination testing does not accurately model the spontaneous initiation of AoD that occurs in vivo. Other models

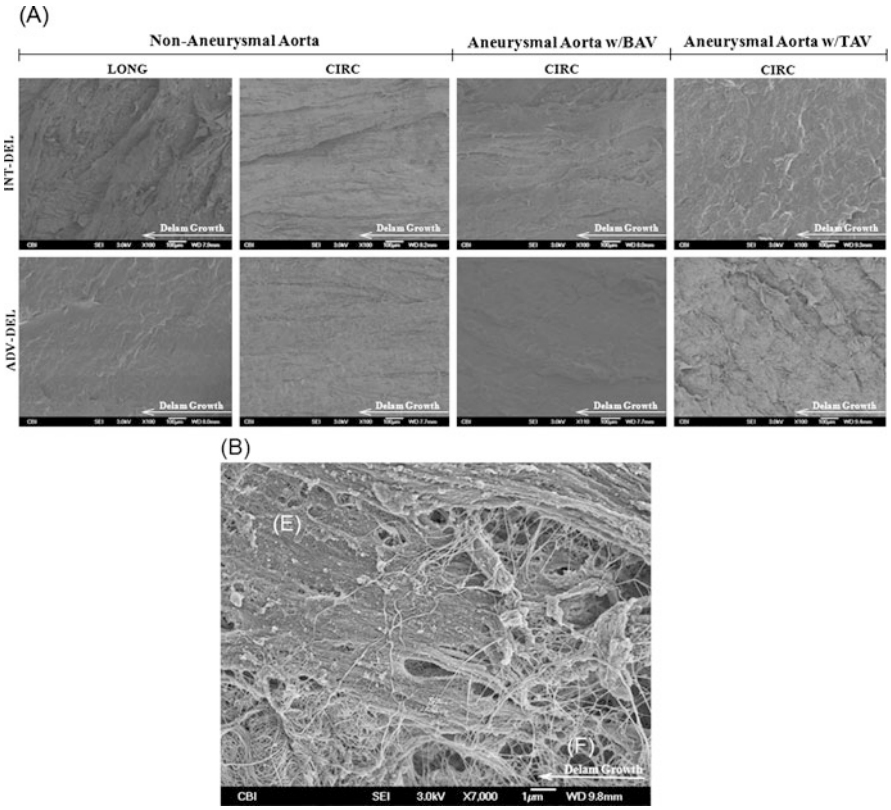

Fig. 11.6 (**A**) Representative SEM images of fracture surfaces of the non-aneurysmal and ATAA with BAV and TAV in LONG and CIRC direction; (**B**) high magnification image of a CIRC TAV ATAA for the INT-DEL half showing bundles of broken elastin fibers (**F**) existing between elastic sheets (**E**). The fibers act like a 'bridge' between halves in a fracture modality called 'fiber bridging' in delamination testing. Taken from Pasta et al. (2011)

of AoD have been described (Tiessen and Roach, 1993), but the onset of dissection was typically forced in these studies by injecting liquid with a syringe into the media to separate the aortic lamellae. Additionally, the stresses that lead to AoD are likely multi-factorial and could be composed of stresses due to blood pressure, shear stresses due to the blood flow field, torsion due to heart motion or propagation of the pressure pulse, etc. However, the purpose of this investigation was not to simulate these forces, but rather to measure the resistance of the tissue to stresses induced by delamination (i.e., bonding forces between the mural layers of the aortic wall, or the delamination strength). Future work could be to investigate correlation not observed in this investigation between tissue strength and aortic diseases as the aortic stenosis and regurgitation.

11.5 Conclusion

Thoracic aneurysms with BAV and TAV both have significantly altered biomechanical properties compared to normal ascending aorta, thus imparting their propensity of AoD. Moreover, BAV ATAAs have lower delamination strength than TAV ATAAs, rendering an apparently greater risk of AoD for BAV than TAV patients.

Acknowledgements The authors thank Mr. Jonathan Frank of the Center for Biologic Imaging of the University of Pittsburgh for his technical assistance with SEM investigation and Mr. Michael Eskay and Mr. Benjamin Green for assistance with aortic tissue acquisition and preparation. This research was funded in part by a grant from Fondazione RiMED provided to Drs. Pasta and Vorp.

References

Bonderman D, Gharehbaghi-Schnell E, Wollenek G, Maurer G, Baumgartner H, Lang IM (1999) Mechanisms underlying aortic dilatation in congenital aortic valve malformation. Circulation 99:2138–2143

Bonnichsen CR, Sundt TM 3rd, Anavekar NS, Foley TA, Morris MF, Martinez MW, Williamson EE, Glockner JF, Araoz PA (2011) Aneurysms of the ascending aorta and arch: the role of imaging in diagnosis and surgical management. Expert Rev Cardiovasc Ther 9:45–61

Coady MA, Rizzo JA, Goldstein LJ, Elefteriades JA (1999) Natural history, pathogenesis, and etiology of thoracic aortic aneurysms and dissections. Cardiol Clin 17:615–635

Cripe L, Andelfinger G, Martin LJ, Shooner K, Benson DW (2004) Bicuspid aortic valve is heritable. J Am Coll Cardiol 44:138–143

Davies MJ (1998) Aortic aneurysm formation: lessons from human studies and experimental models. Circulation 98:193–195

Edwards WD, Leaf DS, Edwards JE (1978) Dissecting aortic aneurysm associated with congenital bicuspid aortic valve. Circulation 57:1022–1025

El-Hamamsy I, Yacoub MH (2009) Cellular and molecular mechanisms of thoracic aortic aneurysms. Nat Rev Cardiol 6:771–786

Gleason TG (2005) Heritable disorders predisposing to aortic dissection. Semin Thorac Cardiovasc Surg 17:274–281

Gregory JR, Spearing SM (2004) A fiber bridging model for fatigue delamination in composite materials. Acta Mater 52:5493–5502

Holzapfel GA, Sommer G, Auer M, Regitnig P, Ogden RW (2007) Layer-specific 3D residual deformations of human aortas with non-atherosclerotic intimal thickening. Ann Biomed Eng 35:530–545

Iliopoulos DC, Deveja RP, Kritharis EP, Perrea D, Sionis GD, Toutouzas K, Stefanadis C, Sokolis DP (2009) Regional and directional variations in the mechanical properties of ascending thoracic aortic aneurysms. Med Eng Phys 31:1–9

Johansson G (1995) Ruptured thoracic aortic aneurysms: a study of incidence and mortality rates. J Vasc Surg 21:985–988

Knipp BS, Deeb GM, Prager RL, Williams CY, Upchurch GR, Patel HJ (2007) A contemporary analysis of outcomes for operative repair of type A aortic dissection in the united states. Surgery 142:524–528

Larson EW, Edwards WD (1984) Risk factors for aortic dissection: a necropsy study of 161 cases. Am J Cardiol 53:849–855

Pasta S, Phillippi JA, Gleason TG, Vorp DA (2011) Effect of aneurysm on the mechanical dissection properties of the human ascending thoracic aorta. J Thorac Cardiovasc Surg 143:460–467

Phillippi JA, Klyachko EA, Kenny JP, Eskay MA, Gorman RC, Gleason TG (2009) Basal and oxidative stress-induced expression of metallothionein is decreased in ascending aortic aneurysms of bicuspid aortic valve patients. Circulation 119:2498–2506

Phillippi JA, Eskay MA, Kubala AA, Pitt BR, Gleason TG (2010) Altered oxidative stress responses and increased type I collagen expression in bicuspid aortic valve patients. Ann Thorac Surg 90:1893–1898

Purslow PP (1983) Positional variations in fracture toughness, stiffness and strength of descending thoracic pig aorta. J Biomech 16:947–953

Raghavan ML, Webster MW, Vorp DA (1996) Ex vivo biomechanical behavior of abdominal aortic aneurysm: assessment using a new mathematical model. Ann Biomed Eng 24:573–582

Rampoldi V, Trimarchi S, Eagle KA, Nienaber CA, Oh JK, Bossone E, Myrmel T, Sangiorgi GM, De Vincentiis C, Cooper JV, Fang J, Smith D, Tsai T, Raghupathy A, Fattori R, Sechtem U, Deeb MG, Sundt TM 3rd, Isselbacher EM (International Registry of Acute Aortic Dissection (IRAD) Investigators) (2007) Simple risk models to predict surgical mortality in acute type A aortic dissection: the international registry of acute aortic dissection score. Ann Thorac Surg 83:55–61

Sommer G, Gasser TC, Regitnig P, Auer M, Holzapfel GA (2008) Dissection of the human aortic media: an experimental study. J Biomech Eng 130:021007

Tiessen IM, Roach MR (1993) Factors in the initiation and propagation of aortic dissections in human autopsy aortas. J Biomech Eng 115:123–125

Vorp DA, Schiro BJ, Ehrlich MP, Juvonen TS, Ergin MA, Griffith BP (2003) Effect of aneurysm on the tensile strength and biomechanical behavior of the ascending thoracic aorta. Ann Thorac Surg 75:1210–1214

Ward C (2000) Clinical significance of the bicuspid aortic valve. Heart 83:81–85

Chapter 12
Intracranial Aneurysms: Modeling Inception and Enlargement

Paul N. Watton, Haoyu Chen, Alisa Selimovic, Harry Thompson, and Yiannis Ventikos

Abstract Intracranial aneurysms (IAs) are abnormal dilatations of the cerebral vasculature. Computational modeling may shed light on the aetiology of the disease and lead to improved criteria to assist diagnostic decisions. We briefly review the literature and present novel models on two topical areas of research activity: modeling IA inception and modeling IA evolution. We present a novel computational methodology to remove an IA and reconstruct the geometry of the (unknown) healthy artery. This approach is applied to 22 clinical cases (the largest study of its kind to date) and we analyze whether spatial distributions of hemodynamic stimuli correlate with locations aneurysms are known, a priori, to form. In this study, locations of aneurysm formation are strongly correlated with regions of high wall shear stress (WSS) (19/22 positive correlations); however low correlations are observed with indices which characterize the oscillatory nature of the direction of the wall shear stress vector, e.g., oscillatory shear index (OSI) (7/22). We subsequently outline a fluid-solid-growth framework for modeling aneurysm evolution and illustrate its application to 4 clinical cases depicting IAs. We conclude with a discussion for the direction of future research in this field.

12.1 Introduction

Intracranial aneurysms (IAs) appear as sac-like outpouchings of the arterial wall inflated by the pressure of the blood. Prevalence rates in populations without comor-

P.N. Watton (✉) · H. Chen · A. Selimovic · H. Thompson · Y. Ventikos
Institute of Biomedical Engineering, Department of Engineering Science, University of Oxford, Oxford, UK
e-mail: Paul.Watton@eng.ox.ac.uk

H. Chen
e-mail: Haoyu.Chen@eng.ox.ac.uk

A. Selimovic
e-mail: Alisa.Selimovic@eng.ox.ac.uk

Y. Ventikos
e-mail: Yiannis.Ventikos@eng.ox.ac.uk

G.A. Holzapfel, E. Kuhl (eds.), *Computer Models in Biomechanics*,
DOI 10.1007/978-94-007-5464-5_12,

bidity are estimated to be 3.2 % (Vlak et al., 2011). Most remain asymptomatic; however, there is a small but inherent risk of rupture: 0.1 to 1 % of detected aneurysms rupture every year (Juvela, 2004). Subarachnoid haemorrhage (SAH) due to IA rupture is associated with a 50 % chance of fatality (Greving et al., 2009) and of those that survive, nearly half have long term physical and mental sequelae (Huang et al., 2011). Preemptive treatment may prevent aneurysm SAH and thus reduce the associated (large) financial burden, e.g., the total annual economic cost of aneurysm SAH is £510 M in the UK (Rivero-Arias et al., 2010). However, management of unruptured IAs by interventional procedures, i.e. minimally invasive endovascular approaches or surgical-clipping, is highly controversial and not without risk (Komotar et al., 2008). Given the very low risk of IA rupture, there is both a clinical and an economic need to identify those IAs which are actually in need of intervention.

Investigating the complex interplay of physical forces and their biological sequelae will aid further understanding of the formation and rupture of IAs and their management, and may lead to a cure (Krings et al., 2011). However, IAs may have heterogeneous hemodynamic, morphologic, and vascular characteristics associated with different mechanistic pathways (Sugiyama et al., 2011) and thus this is an extremely challenging complex problem. Computational models may yield insight into the aetiology of the disease and offer the potential to aid clinical decisions. Consequently, research in this area has grown extensively; for recent review articles see, e.g., Humphrey (2009); Sforza et al. (2011). In this article, we briefly review computational models which investigate IA inception and IA evolution and present our most recent models and findings on these topical areas of research.

12.2 IA Inception

IAs preferentially develop at specific locations in the Circle of Willis. Hence it appears that the hemodynamic environment plays a role in the pathophysiological processes that give rise to their formation. This has motivated the development of methodologies to reconstruct the original *healthy* geometry of the vasculature from a *diseased* geometry depicting an IA: computational fluid dynamic (CFD) analyzes proceed to investigate if particular patterns of hemodynamic stimuli (on the healthy vasculature) correlate with the location at which an IA is observed to develop, e.g., see the recent studies by Mantha et al. (2006); Baek et al. (2009); Ford et al. (2009); Shimogonya et al. (2009); Singh et al. (2010). Whilst all these studies have considered a limited number of clinical cases, i.e. between 1 and 5, interesting (although somewhat inconsistent) observations have been made (see Table 12.1). It has been concluded that locations susceptible to aneurysm formation are associated with: oscillatory wall shear stress (WSS) indicated by a novel index referred to as the aneurysm formation index (AFI) (Mantha et al., 2006); large temporal fluctuations of the direction of the spatial WSS gradient vector (WSSG) indicated by a novel index referred to as the gradient oscillatory number (GON) (Shimogonya

Table 12.1 Summary of IA inception studies. The spatial distributions of various hemodynamic indices have been compared with known locations of aneurysm formation. It can be seen that strong correlations are always observed in such studies. However, inconsistencies in conclusions are present and the study sizes are always small

Study	CFD index	Positive correlation
Mantha et al. (2006)	Low WSS, AFI	3/3
Shimogonya et al. (2009)	GON	1/1
Ford et al. (2009)	GON	4/5
Baek et al. (2009)	High WSS, High Pressure	2/2
Singh et al. (2010)	High WSS, High OSI	2/2

et al., 2009); elevated WSS and pressure (Baek et al., 2009); elevated WSS and oscillatory shear index (OSI) (Singh et al., 2010); the interested reader is referred to the relevant articles for specifics of how to calculate these hemodynamic indices.

Given the disparates in findings on CFD inception studies to date, there is clearly the need for a more comprehensive study: we consider a selection of 22 sidewall IAs, propose a novel method to reconstruct the hypothetical geometry of the artery without IA and analyze spatial distributions of hemodynamic stimuli on the healthy vasculature in the specific locations that the IAs are known, a priori, to develop.

12.2.1 Methodology

We have developed a novel approach to reconstruct the hypothetical geometry of the healthy artery prior to IA formation. Here we briefly outline the methodology (see Fig. 12.1 for graphical illustration). Clinical imaging data depicting an IA is segmented with the software suite @neufuse (developed for the European project @neurIST, www.aneurist.org 'Integrated Biomedical Informatics for the Management of Cerebral Aneurysms', see Villa-Uriol et al., 2011). A skeleton of the vasculature is created and the segment containing the IA is removed (see Fig. 12.1(b)). Given the position vectors of the center points of the upstream and downstream boundaries (neighboring the aneurysm section), $\mathbf{c}_0$ and $\mathbf{c}_1$, respectively, and unit normal vectors to the boundaries $\hat{\mathbf{n}}_0$ and $\hat{\mathbf{n}}_1$ (see Fig. 12.1(c)), a cubic curve $\mathbf{c}(t) = (a_{1j}t^j, a_{2j}t^j, a_{3j}t^j)$: $i = 1, 2, 3$; $j = 0, 1, 2, 3$; $t \in [0, 1]$ is constructed such that

$$\mathbf{c}(t=0) = \mathbf{c}_0, \qquad \mathbf{c}(t=1) = \mathbf{c}_1, \qquad \mathbf{c}'(t=0) = \kappa\hat{\mathbf{n}}_0, \qquad \mathbf{c}'(t=1) = \kappa\hat{\mathbf{n}}_1, \tag{12.1}$$

where $'$ denotes differentiation with respect to t and $\kappa = |\mathbf{c}_1 - \mathbf{c}_0|$. The 12 unknown coefficients $a_{ij} \in \mathbb{R}$ are uniquely determined by the 12 boundary conditions given by Eq. (12.1). A Frenet-Frame is then defined along the curve $\mathbf{c}$, i.e.

$$\mathbf{T}(t) = \frac{\mathbf{c}'(t)}{|\mathbf{c}'(t)|}, \qquad \mathbf{N}(t) = \frac{\mathbf{T}'(t)}{|\mathbf{T}'(t)|}, \qquad \mathbf{B}(t) = \mathbf{T}(t) \times \mathbf{N}(t). \tag{12.2}$$

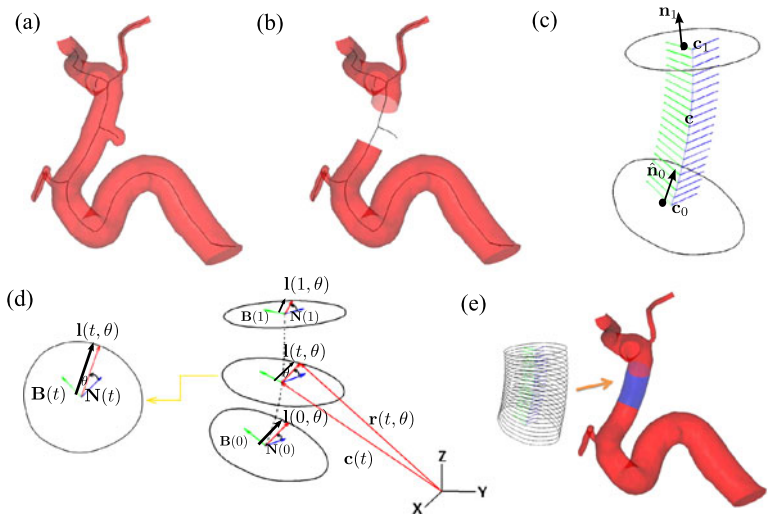

Fig. 12.1 Methodology to remove sidewall IA and reconstruct original healthy vessel: (**a**) segmented clinical image of vasculature depicting IA; (**b**) removal of section containing IA; (**c**) a Frenet-Frame is constructed along a curve $\mathbf{c}(s)$ between the upstream and downstream boundaries of the segment containing the IA that was removed; (**d**) methodology to smoothly morph the inlet boundary into the outlet boundary along $\mathbf{c}$; (**e**) reconstructed healthy vessel

The hypothetical healthy geometry is reconstructed by using the Frenet-Frame to propagate a closed curve in the **N**–**B** plane along $\mathbf{c}$ such that the upstream boundary smoothly morphs into the downstream boundary. This approach takes into account the natural tortuosity of the artery. The vector equation of the reconstructed healthy section of arterial surface $\mathbf{r}(t,\theta)$, $\theta \in [0, 2\pi)$ can be expressed as

$$\mathbf{r}(t,\theta) = \mathbf{c}(t) + \mathbf{l}(t,\theta), \tag{12.3}$$

where $\mathbf{l}(t,\theta)$ represents the position vectors of points on the boundary in the $\mathbf{N}(t)$–$\mathbf{B}(t)$ plane along $\mathbf{c}$. $\mathbf{l}(0,\theta)$ and $\mathbf{l}(1,\theta)$ are determined from the known position vectors of the upstream and downstream boundaries and we choose $\mathbf{l}(t,\theta)$ to be a linear combination of these:

$$\mathbf{l}(t,\theta) = \big|(1-t)\mathbf{l}(0,\theta) + t\mathbf{l}(1,\theta)\big|(\mathbf{N}\cos\theta + \mathbf{B}\sin\theta). \tag{12.4}$$

This novel reconstruction method is applied to 22 clinical cases depicting sidewall IAs. Figure 12.2 illustrates the application of the approach to 20 (segmented) clinical cases; the geometry of the IA is depicted in light blue whilst the geometry of the reconstructed segment of healthy artery is in depicted in dark blue.

12.2.1.1 Computational Fluid Dynamics

The methodological approach to solve the hemodynamics proceeds as follows. The geometry of the artery without IA is imported into ANSYS ICEM (ANSYS Inc.,

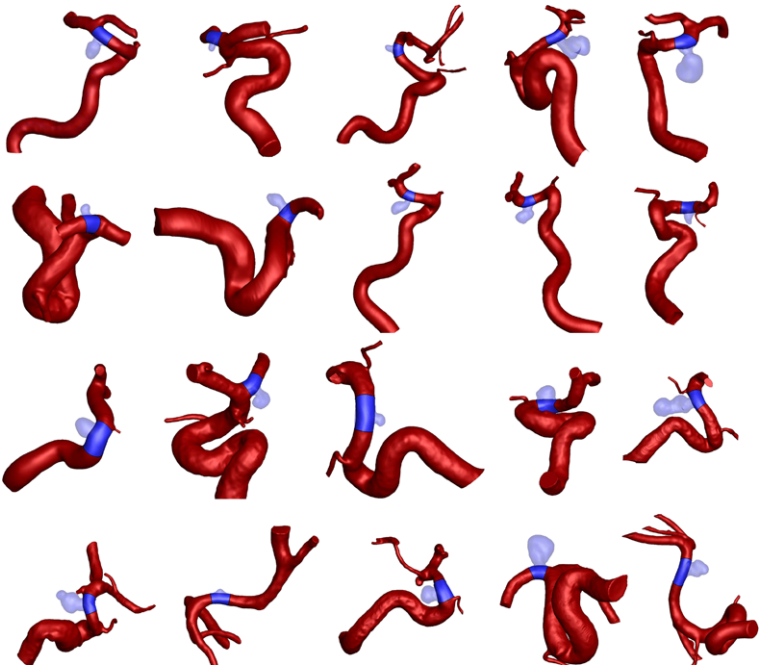

Fig. 12.2 An illustration of 20 cases with/without IAs. The reconstructed section is depicted in *dark blue* whilst the IA is depicted in *light blue*

Canonsburg, PA) and an unstructured tetrahedral mesh with prism layers lining the boundary is generated for the fluid domain. Blood is modeled as an incompressible Newtonian fluid with constant density $\rho = 1069\,\mathrm{kg\,m^{-3}}$ and viscosity $\eta = 0.0035\,\mathrm{Pa\,s}$. At the arterial wall, no slip, no-flux conditions are applied. Pulsatile flow and pressure boundary conditions for the inlets and outlets of the fluid domain are taken from a 1D model of the arterial tree (Reymond et al., 2009) which has been integrated into the software suite @neufuse. It solves the 1D form of the Navier-Stokes equation in a distributed model of the human systemic arteries, accounting for the ventricular-vascular interaction and wall viscoelasticity; it was recently validated through a comparison with in vivo flow measurements (Reymond et al., 2011). The incompressible Navier-Stokes equations which govern the flow are solved with ANSYS CFX (ANSYS Inc., Canonsburg, PA) using a finite volume formulation.

12.2.2 Results

CFD simulations are performed on 22 clinical cases with IAs removed. Spatial distributions of several hemodynamic indices are analyzed and compared with respect

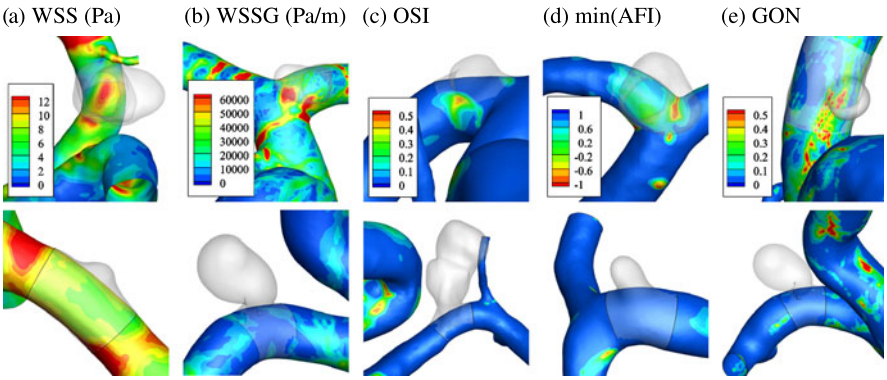

Fig. 12.3 Examples of spatial distributions of (**a**) WSS, (**b**) WSSG, (**c**) OSI, (**d**) min(AFI) and (**e**) GON (*left* to *right*, respectively) for reconstructed healthy vessels without IAs. The *upper row* illustrates cases where a positive correlation between an index and the location an IA evolves occurs whilst the *lower row* illustrates examples where no correlation is observed

to the known locations of aneurysm formation (LAF). Figure 12.3 illustrates examples of positive (upper row) and negative (lower row) correlations of the hemodynamic indices WSS, WSSG, OSI, minimum(AFI) and GON with the LAF. We observed that 19/22 IAs developed in regions that had locally elevated magnitudes of WSS and GON. However, fewer positive correlations were observed for other indices, i.e. 7/22 for elevated values of OSI, 7/22 for low values of min(AFI) and 8/22 for elevated values of WSSG.

Our study highlights that care should be taken when interpreting the conclusions and findings of smaller CFD studies in the literature. For example, we observed that low values of AFI were associated with 7/22 clinical cases whereas Mantha et al. (2006) observed correlations in all cases (3/3). Singh et al. (2010) observed a significant correlation with OSI (2/2) however we observed no such correlation. Consistent with Baek et al. (2009) we observed a positive correlation with regions subject to high WSS. Whilst we observed many positive correlations (19/22) with elevated GON, as observed and remarked by Ford et al. (2009), this index is elevated in many regions of the artery and thus the significance of this correlation is unclear and may merit further investigation.

12.3 IA Enlargement

To further our understanding of the aetiology of IA we must further our understanding of the physiological mechanisms that regulate the maintenance of arterial tissue in physiological and pathophysiological conditions. The structure of the artery is continually maintained by vascular cells. The morphology and functionality of vascular cells is intimately linked to their mechanical environment. Hemodynamic forces give rise to: cyclic stretching of the extra-cellular matrix (ECM); frictional

forces acting on the endothelial layer of the arterial wall; a normal hydrostatic pressure and interstitial fluid forces due to movement of fluid through the ECM. Mechanosensors convert the mechanical stimuli into chemical signals which lead to activation of genes that regulate cell functionality. The physiological mechanisms that give rise to the development of an aneurysm involve the complex interplay between the local mechanical forces acting on the arterial wall and the biological processes occurring at the cellular level. Consequently, models of aneurysm evolution must take into consideration: (i) the biomechanics of the arterial wall; (ii) the biology of the arterial wall and (iii) the complex interplay between (i) and (ii), i.e. the mechanobiology of the arterial wall. Humphrey and Taylor (2008) recently emphasized the need for a new class of fluid-solid-growth models to study aneurysm evolution and proposed the terminology FSG models. These combine fluid and solid mechanics analyzes of the vascular wall with descriptions of the kinetics of biological growth and remodeling (G&R).

12.3.1 Methodology

In this section, we describe our FSG computational framework for modeling IA evolution. It utilizes and extends the novel abdominal aortic aneurysm (AAA) evolution model developed by Watton et al. (2004) and Watton and Hill (2009) which was later adapted to model IA evolution (Watton et al., 2009b; Watton and Ventikos, 2009) and extended to consider transmural variations in G&R (Schmid et al., 2010, 2011). The aneurysm evolution model incorporates microstructural G&R variables into a realistic structural model of the arterial wall (Holzapfel et al., 2000). These describe the *normalized mass-density* and *natural reference configurations* of the load bearing constituents, and enable the G&R of the tissue to be simulated as an aneurysm evolves. More specifically, the natural reference configurations that collagen fibers are recruited to load bearing remodels to simulates the mechanical consequences of: (i) fiber deposition and degradation in altered configurations as the aneurysm enlarges; (ii) fibroblasts configuring the collagen to achieve a maximum strain during the cardiac cycle, denoted the attachment strain. The normalized mass-density evolves to simulate growth/atrophy of the constituents (elastin and collagen). The aneurysm evolution model has been integrated into a novel FSG framework (Watton et al., 2009a) so that G&R can be explicitly linked to hemodynamic stimuli. More recently, the G&R framework has been extended to link both *growth* and *remodeling* to cyclic deformation of vascular cells (see Watton et al., 2012).

Figure 12.4 depicts the FSG methodology. The computational modeling cycle begins with a structural analysis to solve the systolic and diastolic equilibrium deformation fields (of the artery/aneurysm) for given pressure and boundary conditions. The structural analysis quantifies the stress, stretch, and the cyclic deformation, of the constituents and vascular cells (each of which may have different natural reference configurations). The geometry of the aneurysm is subsequently exported to be prepared for hemodynamic analysis: first the geometry is integrated into a physiological geometrical domain; the domain is automatically meshed; physiological

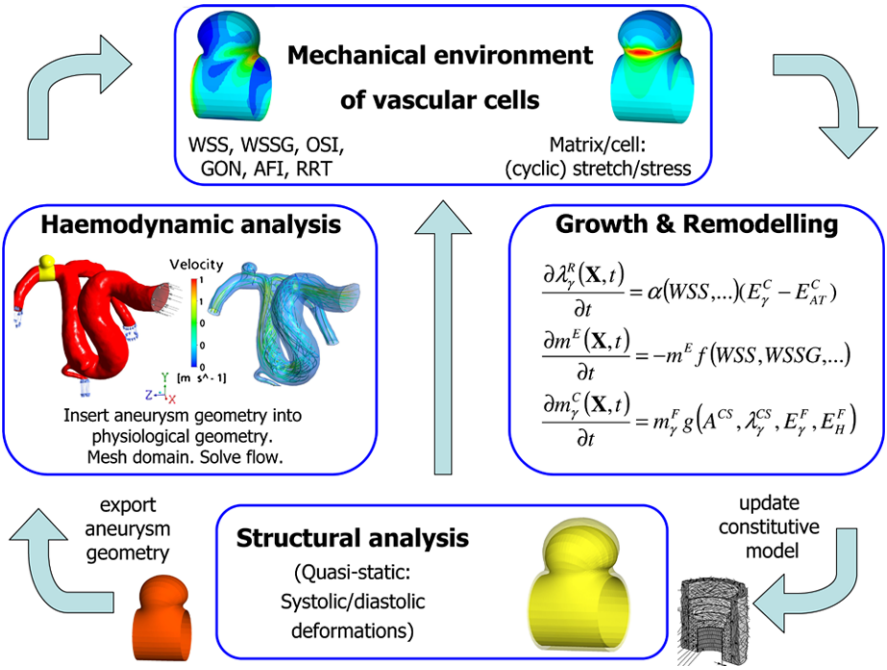

Fig. 12.4 Fluid-solid-growth computational framework for modeling aneurysm evolution

flow rate and pressure boundary conditions are applied; the flow is solved assuming rigid boundaries for the hemodynamic domain. The hemodynamic quantities of interest, e.g., WSS, WSSG are then exported and interpolated onto the nodes of the structural mesh: each node of the structural mesh contains information regarding the mechanical stimuli obtained from the hemodynamic and structural analyzes. G&R algorithms simulate cells responding to the mechanical stimuli and adapting the tissue: the constitutive model of the aneurysmal tissue is updated. The structural analysis is re-executed to calculate the new equilibrium deformation fields. The updated geometry is exported for hemodynamic analysis. The cycle continues and as the tissue adapts an aneurysm evolves.

Development of an IA is associated with apoptosis of vascular smooth muscle (VSM) cells (Kondo et al., 1998), disrupted internal elastic laminae, the breakage and elimination of elastin fibers (Frösen et al., 2004), a thinned medial layer and G&R of the collagen fabric (Juvela, 2004). The site of origin is strongly related to hemodynamic WSS (Kondo et al., 1997). It is postulated that high WSS is related to the initiation of IA formation (Ahn et al., 2007); note that this hypothesis is consistent with our observations in Sect. 12.2. However, whilst high WSS appears to be associated with the inception of an IA, low WSS is thought to give rise to its continued enlargement (Shojima et al., 2004).

To simulate IA inception, we prescribe a localized loss of elastin in a small circular patch of the arterial domain (the elastin is modeled with a neo-Hookean con-

stitutive model Watton et al., 2009c). The collagen fabric adapts to restore homeostasis and a small perturbation to the geometry alters the spatial distribution of hemodynamic stimuli that act on the lumenal layer of the artery. This enables subsequent degradation of elastin to be linked to deviations of hemodynamic stimuli from homeostatic levels via evolution equations. As the elastin degrades and the collagen fabric adapts (via G&R) an IA evolves. Watton et al. (2009a) adopted this approach to investigate the evolution of IAs assuming degradation of elastin was linked to high WSS or high WSSG. Given that a region of elevated WSS occurs downstream of the distal neck of the model IA and elevated spatial WSSGs occur in the proximal/distal neck regions, this approach led to IAs that enlarged axially along the arterial domain, i.e. it did not yield IA with characteristic 'berry' topologies. Consequently, Watton et al. (2011a) linked elastin degradation to low WSS and restricted the degradation of elastin to a localized region of the arterial domain: this yielded IAs of a characteristic saccular shape that enlarged and stabilized in size. Although interesting insights were obtained in both studies, an inherent limitation was that the IAs evolved on a cylindrical section of artery and consequently the spatial distribution of hemodynamic stimuli is non-physiological. This motivated the application of the FSG modeling framework to patient-specific vascular geometries. For a detailed description of the model methodology, we refer the interested reader to Watton et al. (2011b, 2012). Here we briefly illustrate the application of the FSG modeling framework to 4 clinical cases.

12.3.2 Examples of FSG Models of IA Evolution

Figure 12.5 (upper row) illustrates 4 clinical cases depicting IAs. The IA is removed (as in Fig. 12.1(b)) and replaced with a short cylindrical section on which IA evolution is simulated. The cylindrical section is smoothly reconnected to the upstream and downstream sections of the parent artery (middle row; see Selimovic et al., 2010, for methodology). In all four cases, IA inception is prescribed, i.e. an initial degradation of elastin is prescribed in a localized region of the domain, the collagen fabric adapts to restore homeostasis and a small localized outpouching of the artery develops. This perturbs the hemodynamic environment: subsequent degradation of elastin is linked to low levels of WSS. It can be seen that the modeling framework gives rise to IAs with different morphologies, i.e. IAs with: asymmetries in geometries (a_3, d_3); well-defined necks (b_3); no neck (c_3). For an in depth analysis of simulation results for case (a_3), e.g., evolution of elastin strains, collagen strains, concentrations of constituents and evolving diastolic/systolic geometries, the interested reader is referred to Watton et al. (2011b). Interestingly, for this particular case, which depicts an IA at (perhaps) a relatively early stage of formation (crudely inferred from its small size), the qualitative asymmetries of the simulated IA (see (a_3)) are in agreement with the patient aneurysm (a_1) and thus (tentatively) support the modeling hypotheses for elastin degradation (low WSS drives degradation) and collagen adaption.

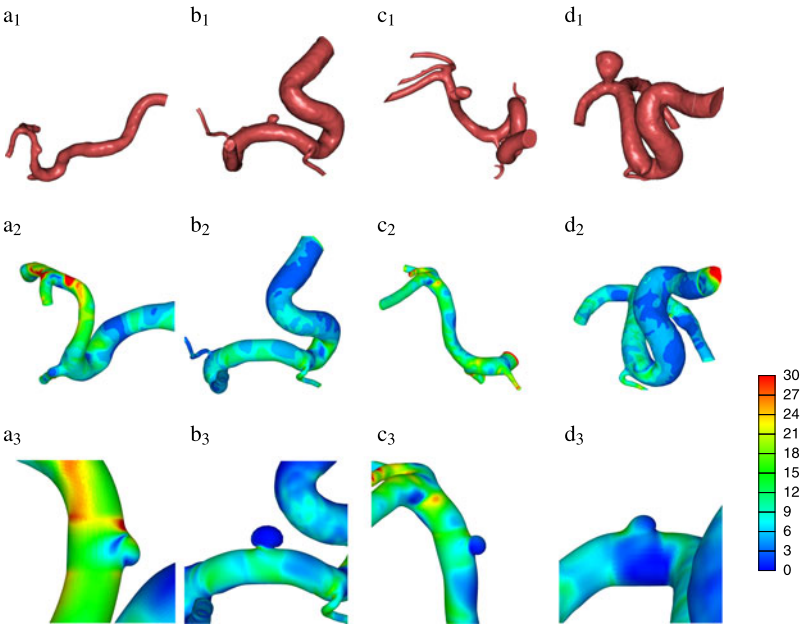

Fig. 12.5 Segmented clinical imaging data depicting IAs (a_1–d_1). IAs are removed the geometry of the healthy artery reconstructed (a_2–d_2). Computational models of IAs on patient specific geometries with degradation of elastin linked to low WSS (a_2–d_2). The color-map depicts WSS (Pa)

12.4 Discussion

In this chapter, we first (briefly) reviewed the application of CFD models to investigate IA inception and presented a novel methodology for reconstructing the geometry of the healthy artery prior to IA formation. We investigated the correlation between IA inception and the spatial distribution of several hemodynamic indices (WSS, WSSG, OSI, AFI and GON) for 22 clinical cases depicting sidewall IAs. To our knowledge this is the largest (and most complete) CFD inception study, of its kind, to date. Consistent with previous observations, we observed that locations of aneurysm formation (LAF) occur in regions of the artery subject to high WSS. However, correlation of LAF with indices that characterize the oscillatory nature of the flow, i.e. OSI and min(AFI), do not seem as strong as (sometimes) previously observed. Hence, we suggest care should be taken: (i) when interpreting conclusions of studies which have been deduced from a small number of clinical cases; (ii) articulating the significance of conclusions of CFD studies which involve relatively few cases. Moreover, we point out that whilst CFD has a role to play in guiding our understanding of vascular disease, it needs to be coupled with improved modeling (and understanding) of the mechanobiology of the arterial wall to gain real insight into the aetiology of vascular disease. This motivates the need for multi-scale models which integrate the biology and the (solid and fluid) biomechanics of the arterial

wall, i.e. FSG models, such as the one we presented. Such models provide the foundations to model not only aneurysm evolution but other vascular diseases.

It is envisaged that models of IA and AAA evolution may ultimately lead to predictive models that have diagnostic application on a patient specific basis. Given that this will yield very substantial healthcare and economic benefits, there is significant growth of research in this area. However, whilst models of aneurysm evolution have gained increasing sophistication over the past decade, many further improvements are still required. For instance, there is a need to incorporate explicit representations of vascular cells (endothelial cells, fibroblast cells and smooth muscle cells), their interactions and the signaling networks (Schmid et al., 2011) that link the stimuli acting on them to their functionality in physiological, supra-physiological and pathological conditions. There is also a need for implementation of more sophisticated constitutive models to represent, e.g., the collagen fiber recruitment distribution (Hill et al., 2012) and dispersion and the active and passive response of vascular smooth muscle cells (Murtada et al., 2010). Lastly, improved understanding and modeling of how this complex micro-structure adapts in pathological conditions is needed: the modeling framework needs to be validated and/or calibrated against physiological data; animal models undoubtedly have a role to play in this respect (Zeng et al., 2011). Such enhancements will offer the potential for patient-specific predictive models of vascular disease evolution and intervention. They will benefit patients immensely because the decision on whether to/how to intervene will be founded upon a robust concentration of knowledge with respect to patient-specific vascular physiology, biology and biomechanics. Of course, the challenging and multi-disciplinary nature of such research implies collaborations are essential.

Acknowledgements Paul N. Watton is funded by the Center of Excellence in Personalized Healthcare (funded by the Wellcome Trust and EPSRC, grant number WT 088877/Z/09/Z). This support is gratefully acknowledged.

References

Ahn S, Shin D, Tateshima S, Tanishita K, Vinuela F, Sinha S (2007) Fluid-induced WSS in anthropomorphic brain aneurysm models: MR phase-contrast study at 3T. J Musculoskel Neuron Interact 25:1120–1130

Baek H, Jayaraman MV, Karniadakis GE (2009) Wall shear stress and pressure distribution on aneurysms and infundiblae in the posterior communicating artery bifurcation. Ann Biomed Eng 37:2469–2487

Ford MD, Hoi Y, Piccinelli M, Antiga L, Steinman DA (2009) An objective approach to digital removal of saccular aneurysms: technique and applications. Br J Radiol 82:S55–S61

Frösen J, Piippo A, Paetau A, Kangasniemi M, Niemelä M, Hernesniemi J, Jääskeleläinen J (2004) Remodelling of saccular cerebral artery aneurysm wall is associated with rupture: histological analysis of 24 unruptured and 42 ruptured cases. Stroke 35:2287–2293

Greving JP, Rinkel GJE, Buskens E, Algra A (2009) Cost-effectiveness of preventive treatment of intracranial aneurysms: new data and uncertainties. Stroke 73:258–265

Hill MR, Duan X, Gibson GA, Watkins S, Robertson AM (2012) A theoretical and non-destructive experimental approach for direct inclusion of measured collagen orientation and recruitment into mechanical models of the artery wall. J Biomech 45:762–771

Holzapfel GA, Gasser TC, Ogden RW (2000) A new constitutive framework for arterial wall mechanics and a comparative study of material models. J Elast 61:1–48

Huang MC, Baaj AA, Downes K, Youssef AS, Sauvageau E, van Loveren HR, Agazzi S (2011) Paradoxical trends in the management of unruptured cerebral aneurysms in the united states. Stroke 42:1730–1735

Humphrey JD (2009) Coupling haemodynamics with vascular wall mechanics and mechanobiology to understand intracranial aneurysms. Int J Comput Fluid Dyn 23:569–581

Humphrey JD, Taylor CA (2008) Intracranial and abdominal aortic aneurysms: similarities, differences, and need for a new class of computational models. Annu Rev Biomed Eng 10:221–246

Juvela S (2004) Treatment options of unruptured intracranial aneurysms. Stroke 35:372–374

Komotar RJ, Mocco J, Solomon RA (2008) Guidelines for the surgical treatment of unruptured intracranial aneurysms: the first annual J. Lawrence pool memorial research symposium-controversies in the management of cerebral aneurysms. Neurosurgery 62:183–194

Kondo S, Hashimoto N, Kikuchi H, Hazama F, Nagata I, Kataoka H (1997) Cerebral aneurysms arising at nonbranching sites. An experimental study. Stroke 28:398–403

Kondo S, Hashimoto N, Kikuchi H, Hazama F, Nagata I, Kataoka H, Rosenblum WI (1998) Apoptosis of medial smooth muscle cells in the development of saccular cerebral aneurysms in rats. Stroke 29:181–189

Krings T, Mandell DM, Kiehl TR, Geibprasert S, Tymianski M, Alvarez H, terBrugge KG, Hans FJ (2011) Intracranial aneurysms: from vessel wall pathology to therapeutic approach. Neurosurgery 7:547–559

Mantha A, Karmonik C, Benndorf G, Strother C, Metcalfe R (2006) Hemodynamics in a cerebral artery before and after the formation of an aneurysm. Am J Neuroradiol 27:1113–1118

Murtada S, Kroon M, Holzapfel GA (2010) A calcium-driven mechanochemical model for prediction of force generation in smooth muscle. Biomech Model Mechanobiol 9:749–762

Reymond P, Merenda F, Perren F, Rüfenacht D, Stergiopulos N (2009) Validation of a one-dimensional model of the systemic arterial tree. Am J Physiol, Heart Circ Physiol 297:H208–H222

Reymond P, Bohraus Y, Perren F, Lazeyras F, Stergiopulos N (2011) Validation of a patient-specific one-dimensional model of the systemic arterial tree. Am J Physiol, Heart Circ Physiol 301:H1173–H1182

Rivero-Arias O, Gray A, Wolstenholme J (2010) Burden of disease and costs of aneurysmal subarachnoid haemorrhage (aSAH) in the united kingdom. Cost Eff Resour Allocation 8:6

Schmid H, Grytsan A, Postan E, Watton PN, Itskov M (2011) Influence of differing material properties in media and adventitia on arterial adaption: application to aneurysm formation and rupture. Comput Methods Biomech Biomed Eng. doi:10.1080/10255842.2011.603309

Schmid H, Watton PN, Maurer MM, Wimmer J, Winkler P, Wang YK, Roehrle O, Itskov M (2010) Impact of transmural heterogeneities on arterial adaptation: application to aneurysm formation. Biomech Model Mechanobiol 9:295–315

Selimovic A, Villa-Uriol M-C, Holzapfel GA, Ventikos Y, Watton PN (2010) A computational framework to explore the role of the pulsatile haemodynamic environment on the development of cerebral aneurysms for patient-specific arterial geometries. In: Lim CT, Goh JCH (eds) 6th world congress of biomechanics (WCB 2010), IFMBE proceedings, vol 31. Springer, Berlin, pp 759–762

Sforza DM, Putman CM, Cebral JR (2011) Computational fluid dynamics in brain aneurysms. Int J Numer Methods Biomed Eng 28:801–808

Shimogonya Y, Ishikawa T, Imai Y, Matsuki N, Yamaguchi T (2009) Can temporal fluctuation in spatial wall shear stress gradient initiate a cerebral aneurysm? A proposed novel hemodynamic index, the gradient oscillatory number (GON). J Biomech 42:550–554

Shojima M, Oshima M, Takagi K, Torii R, Hayakawa M, Katada K, Morita A, Kirino T (2004) Magnitude and role of WSS on cerebral aneurysm: computational fluid dynamic study of 20 middle cerebral artery aneurysms. Stroke 35:2500–2505

Singh PK, Marzo A, Howard B, Rufenacht DA, Bijlenga P, Frangi AF, Lawford PV, Coley SC, Hose DR, Patel UJ (2010) Effects of smoking and hypertension on wall shear stress and oscilla-

tory shear index at the site of intracranial aneurysm formation. Clin Neurol Neurosurg 112:306–313

Sugiyama SI, Meng H, Funamoto K, Inoue T, Fujimura M, Nakayama T, Omodaka S, Shimizu H, Takahashi A, Tominaga T (2011) Hemodynamic analysis of growing intracranial aneurysms arising from a posterior inferior cerebellar artery. World Neurosurg. doi:10.1016/j.wneu.2011.09.023

Villa-Uriol MC, Berti G, Hose DR, Marzo A, Chiarini A, Penrose J, Pozo J, Schmidt JG, Singh P, Lycett R, Larrabide I, Frangi AF (2011) @neurIST complex information processing toolchain for the integrated management of cerebral aneurysms. Inter Focus 1:308–319

Vlak MH, Algra A, Brandenburg R, Rinkel GJ (2011) Prevalence of unruptured intracranial aneurysms, with emphasis on sex, age, comorbidity, country, and time period: a systematic review and meta-analysis. Lancet Neurol 10:626–636

Watton PN, Hill NA (2009) Evolving mechanical properties of a model of abdominal aortic aneurysm. Biomech Model Mechanobiol 8:25–42

Watton PN, Ventikos Y (2009) Modelling evolution of saccular cerebral aneurysms. J Strain Anal 44:375–389

Watton PN, Hill NA, Heil M (2004) A mathematical model for the growth of the abdominal aortic aneurysm. Biomech Model Mechanobiol 3:98–113

Watton PN, Raberger NB, Holzapfel GA, Ventikos Y (2009a) Coupling the hemodynamic environment to the evolution of cerebral aneurysms: computational framework and numerical examples. J Biomech Eng 131:101003

Watton PN, Ventikos Y, Holzapfel GA (2009b) Modelling the growth and stabilisation of cerebral aneurysms. Math Med Biol 26:133–164

Watton PN, Ventikos Y, Holzapfel GA (2009c) Modelling the mechanical response of elastin for arterial tissue. J Biomech 42:1320–1325

Watton PN, Selimovic A, Raberger NB, Huang P, Holzapfel GA, Ventikos Y (2011a) Modelling evolution and the evolving mechanical environment of saccular cerebral aneurysms. Biomech Model Mechanobiol 10:109–132

Watton PN, Ventikos Y, Holzapfel GA (2011b) Modelling cerebral aneurysm evolution. In: McGloughlin T (ed) Biomechanics and mechanobiology of aneurysms. Springer, Heidelberg, pp 373–399

Watton PN, Huang H, Ventikos Y (2012) Multi-scale modelling of vascular disease: abdominal aortic aneurysm evolution. Springer, Heidelberg

Zeng Z, Kallmes DF, Durka MJ, Ding Y, Lewis DA, Kadirvel R, Robertson AM (2011) Hemodynamics and anatomy of elastase-induced rabbit aneurysm models-similarity to human cerebral aneurysms? Am J Neuroradiol 32:595–601

Chapter 13
Micro-structurally Based Kinematic Approaches to Electromechanics of the Heart

Serdar Göktepe, Andreas Menzel, and Ellen Kuhl

Abstract This contribution is concerned with a new kinematic approach to the computational cardiac electromechanics. To this end, the deformation gradient is multiplicatively decomposed into the active part and the passive part. The former is considered to be dependent on the transmembrane potential through a micro-mechanically motivated evolution equation. Moreover, the proposed kinematic framework incorporates the inherently anisotropic, active architecture of cardiac tissue. This kinematic setting is then embedded in the recently proposed, fully implicit, entirely finite-element-based coupled framework. The implicit numerical integration of the transient terms along with the internal variable formulation, and the monolithic solution of the resultant coupled set of algebraic equations result in an unconditionally stable, modular, and geometrically flexible structure. The capabilities of the proposed approach are demonstrated by the fully coupled electromechanical analysis of a generic heart model.

13.1 Introduction

Biological electro-active materials such as skeletal muscle and cardiac muscle commonly undergo remarkable deformations in response to electric stimulation.

S. Göktepe (✉)
Department of Civil Engineering, Middle East Technical University, 06800 Ankara, Turkey
e-mail: sgoktepe@metu.edu.tr

A. Menzel
Institute of Mechanics, TU Dortmund, Leonhard-Euler-Str. 5, 44227 Dortmund, Germany
e-mail: andreas.menzel@udo.edu

A. Menzel
Division of Solid Mechanics, Lund University, P.O. Box 118, 22100 Lund, Sweden

E. Kuhl
Departments of Mechanical Engineering, Bioengineering, and Cardiothoracic Surgery, Stanford University, Stanford, CA 94305, USA
e-mail: ekuhl@stanford.edu

G.A. Holzapfel, E. Kuhl (eds.), *Computer Models in Biomechanics*,
DOI 10.1007/978-94-007-5464-5_13,

Similarly, myocytes, for instance, are also capable of generating an electrical activity as subjected to mechanical loading. Apart from these strong coupling effects, the polarized nature of the externally applied electric field and the intrinsically anisotropic, actively deforming micro-structure of the myocardium, results in direction-dependent behavior (Nielsen et al., 1991; Rohmer et al., 2007). In the literature, the electromechanically coupled cardiac response is typically accounted for at a constitutive level through an additional transmembrane potential-dependent active stress term (Nash and Panfilov, 2004; Keldermann et al., 2007; Niederer and Smith, 2008; Göktepe and Kuhl, 2010).

In contrast to the active stress-based approaches, mentioned above, in this contribution, we propose a new, general kinematic approach to the computational modeling of electro-active materials. Inspired from the recent works of Cherubini et al. (2008), Ambrosi et al. (2011a), Stålhand et al. (2011), we decompose the total deformation gradient into the active and passive parts. The active part is considered to be dependent upon the electrical potential through a micro-mechanically motivated evolution equation. In addition, the proposed kinematic framework incorporates the inherently anisotropic, active architecture of the material. As opposed to the above mentioned works where merely the active-passive split of the deformation gradient has been utilized, we further additively decompose the free-energy function into passive and active parts. This decomposition allows us to recover the additive structure of the stress response. Therefore, the proposed formulation can be considered as the generalization of the approaches that employ either additive stress decomposition or multiplicative split of the deformation gradient to account for excitation-induced contraction. Furthermore, this kinematic setting is embedded in the recently proposed, fully implicit, entirely finite-element-based coupled framework, which has been originally developed in Göktepe and Kuhl (2010). The performance of the proposed formulation is demonstrated through the fully coupled finite element analyses of the nonlinear excitation-contraction of a generic heart model.

13.2 Coupled Cardiac Electromechanics

A coupled initial boundary-value problem of cardiac electromechanics within the mono-domain setting is formulated in terms of the two primary field variables, namely the placement $\varphi(\boldsymbol{X}, t)$ and the transmembrane potential $\Phi(\boldsymbol{X}, t)$. While the latter refers to a potential difference between the intracellular medium and the extracellular medium within the context of mono-domain formulations of cardiac electrophysiology, see Keener and Sneyd (1998), the former is the nonlinear deformation map, depicted in Fig. 13.1. Evolution of the primary field variables is governed by two basic field equations: the balance of linear momentum and the reaction-diffusion-type equation of excitation, which are introduced in Sect. 13.2.2.

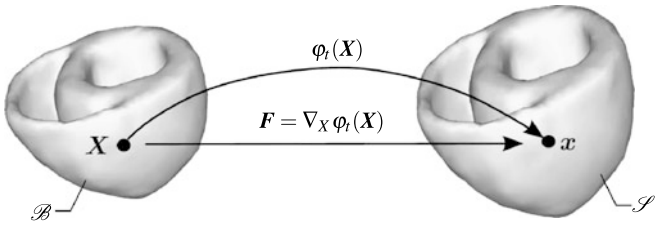

Fig. 13.1 Motion of an excitable and deformable solid body in the Euclidean space $\mathbb{R}^3$ through the nonlinear deformation map $\varphi_t(\boldsymbol{X})$ at time t. The deformation gradient $\boldsymbol{F} = \nabla_X \varphi_t(\boldsymbol{X})$ describes the tangent map between the respective tangent spaces

13.2.1 Kinematics: Active-Passive Decomposition

Let $\mathscr{B} \subset \mathbb{R}^3$ be the reference configuration of an excitable and deformable solid body that occupies the current configuration $\mathscr{S} \subset \mathbb{R}^3$ at time $t \in \mathbb{R}_+$ as shown Fig. 13.1. Accordingly, material points $\boldsymbol{X} \in \mathscr{B}$ are mapped onto their spatial positions $\boldsymbol{x} \in \mathscr{S}$ through the nonlinear deformation map $\boldsymbol{x} = \varphi_t(\boldsymbol{X}) : \mathscr{B} \to \mathscr{S}$ at time t. The deformation gradient $\boldsymbol{F} := \nabla_X \varphi_t(\boldsymbol{X}) : T_{\boldsymbol{X}}\mathscr{B} \to T_{\boldsymbol{x}}\mathscr{S}$ acts as the tangent map between the tangent spaces of the respective configurations. The gradient operator $\nabla_X[\bullet]$ denotes the spatial derivative with respect to the reference coordinates $\boldsymbol{X}$ and the Jacobian $J := \det \boldsymbol{F} > 0$ is the volume map.

Following the kinematics of finite plasticity (Kröner, 1960; Lee, 1969) and the recent work by Cherubini et al. (2008), the deformation gradient is multiplicatively decomposed into the passive part $\boldsymbol{F}^{\mathrm{e}}$ and the active part $\boldsymbol{F}^{\mathrm{a}}$, i.e.

$$\boldsymbol{F} = \boldsymbol{F}^{\mathrm{e}} \boldsymbol{F}^{\mathrm{a}}. \tag{13.1}$$

In this multiplicative decomposition, the active part evolves with the transmembrane potential Φ and reflects the underlying actively contracting anisotropic architecture of cardiac tissue through its dependence upon the second-order structural tensors $\boldsymbol{A}_{\mathrm{m}}$, $\boldsymbol{A}_{\mathrm{n}}$, and $\boldsymbol{A}_{\mathrm{k}}$

$$\boldsymbol{F}^{\mathrm{a}} = \hat{\boldsymbol{F}}^{\mathrm{a}}(\Phi, \boldsymbol{A}_{\mathrm{m}}, \boldsymbol{A}_{\mathrm{n}}, \boldsymbol{A}_{\mathrm{k}}). \tag{13.2}$$

For an orthotropic contractile material, the active part of the deformation gradient can be expressed as

$$\boldsymbol{F}^{\mathrm{a}} = \boldsymbol{1} + \big(\lambda^{\mathrm{a}}_{\mathrm{m}} - 1\big)\boldsymbol{A}_{\mathrm{m}} + \big(\lambda^{\mathrm{a}}_{\mathrm{n}} - 1\big)\boldsymbol{A}_{\mathrm{n}} + \big(\lambda^{\mathrm{a}}_{\mathrm{k}} - 1\big)\boldsymbol{A}_{\mathrm{k}}, \tag{13.3}$$

where $\lambda^{\mathrm{a}}_{\alpha} = \hat{\lambda}^{\mathrm{a}}_{\alpha}(\Phi)$ for $\alpha = \mathrm{m}, \mathrm{k}, \mathrm{n}$. Undoubtedly, the passive and active parts of the deformation gradient are not gradients of any nonlinear deformation map. Hence, the compatibility condition cannot be fulfilled by the active deformation. This leads to an incompatible fictitious intermediate configuration. The compatibility of the overall deformation, on the other hand, is satisfied by the passive part of the deformation gradient $\boldsymbol{F}^{\mathrm{e}}$. This is evident from the fact that while $\boldsymbol{F}^{\mathrm{a}}$ is rotation-free with respect to the material directions, $\boldsymbol{F}^{\mathrm{e}}$ embodies the rotational part.

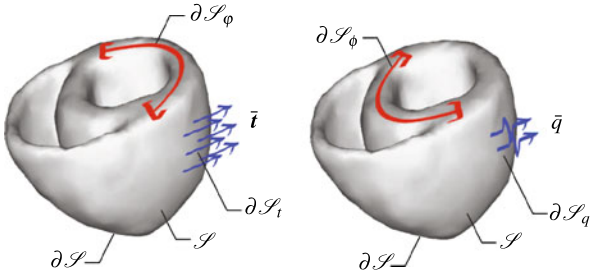

Fig. 13.2 Depiction of the mechanical (*left*) and electrophysiological (*right*) natural and essential boundary conditions

13.2.2 Governing Differential Equations

The balance of linear momentum with its following well-known local spatial form

$$J\,\mathrm{div}\big[J^{-1}\hat{\boldsymbol{\tau}}\big] + \boldsymbol{B} = \boldsymbol{0} \quad \text{in } \mathscr{B} \tag{13.4}$$

describes the quasi-static stress equilibrium in terms of the Eulerian Kirchhoff stress tensor $\hat{\boldsymbol{\tau}}$ and a given body force $\boldsymbol{B}$ per unit reference volume. The operator div[•] denotes the divergence with respect to the spatial coordinates $\boldsymbol{x}$. Note that the momentum balance depends on the primary field variables through the Kirchhoff stress tensor $\hat{\boldsymbol{\tau}}$, whose particular form is elaborated in Sect. 13.2.3. The essential (Dirichlet) and natural (Neumann) boundary conditions, see Fig. 13.2 (left),

$$\varphi = \bar{\varphi} \quad \text{on } \partial\mathscr{S}_\varphi \quad \text{and} \quad \boldsymbol{t} = \bar{\boldsymbol{t}} \quad \text{on } \partial\mathscr{S}_t, \tag{13.5}$$

complete the description of the mechanical problem. Clearly, the surface subdomains $\partial\mathscr{S}_\varphi$ and $\partial\mathscr{S}_t$ fulfill the conditions $\partial\mathscr{S} = \partial\mathscr{S}_\varphi \cup \partial\mathscr{S}_t$ and $\partial\mathscr{S}_\varphi \cap \partial\mathscr{S}_t = \emptyset$. The surface stress traction vector $\bar{\boldsymbol{t}}$, defined on $\partial\mathscr{S}_t$, is related to the Cauchy stress tensor through the Cauchy stress theorem $\bar{\boldsymbol{t}} := J^{-1}\boldsymbol{\tau}\cdot\boldsymbol{n}$ where $\boldsymbol{n}$ is the outward surface normal on $\partial\mathscr{S}$.

The second field equation of the coupled problem, the excitation equation of the following form

$$\dot{\Phi} - J\,\mathrm{div}\big[J^{-1}\hat{\boldsymbol{q}}\big] - \hat{I}^{\phi} = 0 \quad \text{in } \mathscr{B} \tag{13.6}$$

describes the spatio-temporal evolution of the action potential field $\Phi(\boldsymbol{X}, t)$ in terms of the diffusion term $\mathrm{div}[J^{-1}\hat{\boldsymbol{q}}]$ and the nonlinear current term $\hat{I}^{\phi}$. The notation $[\dot{\bullet}] := \mathrm{D}[\bullet]/\mathrm{D}t$ is utilized to express the material time derivative. Within the framework of Fitzhugh-Nagumo-type models of electrophysiology (Fitzhugh, 1961), the current source $\hat{I}^{\phi}$ controls characteristics of the action potential regarding its shape, duration, restitution, and hyperpolarization along with another variable, the so-called recovery variable r whose evolution is governed by an additional ordinary differential equation. Since the recovery variable r chiefly controls the local repolarization behavior of the action potential, we treat it as a local internal variable. This will be more transparent as we introduce the explicit functional form of $\hat{I}^{\phi}$ in

Sect. 13.3. Akin to the momentum balance, the equation of excitation is also furnished by the corresponding essential and natural boundary conditions, Fig. 13.2 (right),

$$\Phi = \bar{\Phi} \quad \text{on } \partial\mathscr{S}_\phi \quad \text{and} \quad q = \bar{q} \quad \text{on } \partial\mathscr{S}_q, \tag{13.7}$$

respectively. Evidently, the surface subdomains $\partial\mathscr{S}_\phi$ and $\partial\mathscr{S}_q$ are disjoint, $\partial\mathscr{S}_\phi \cap \partial\mathscr{S}_q = \emptyset$, and complementary, $\partial\mathscr{S} = \partial\mathscr{S}_\phi \cup \partial\mathscr{S}_t$. The electrical surface flux term $\bar{q}$ in $(13.7)_2$ is related to the spatial flux vector through the Cauchy-type formula $\bar{q} := \boldsymbol{J}^{-1}\hat{\boldsymbol{q}} \cdot \boldsymbol{n}$ in terms of the spatial surface normal $\boldsymbol{n}$. Owing to the transient term in the excitation Eq. (13.6), its solution necessitates an initial condition for the potential field at $t = t_0$

$$\Phi_0(\boldsymbol{X}) = \Phi(\boldsymbol{X}, t_0) \quad \text{in } \mathscr{B}. \tag{13.8}$$

Note that the 'hat' sign used along with the terms $\hat{\boldsymbol{\tau}}$, $\hat{\boldsymbol{q}}$, and $\hat{I}^\phi$ indicates that these variables are dependent on the primary fields.

13.2.3 Constitutive Equations

The solution of the field equations requires the knowledge of constitutive equations describing the Kirchhoff stress tensor $\hat{\boldsymbol{\tau}}$, the potential flux $\hat{\boldsymbol{q}}$, and the current source $\hat{I}^\phi$. In contrast to the constitutive approaches suggested in the literature (Cherubini et al., 2008; Ambrosi et al., 2011a), we additively decompose the free-energy function into the passive part ψ^{p} and the active part ψ^{a}, Ask et al. (2012a, 2012b),

$$\psi = \hat{\psi}^{\mathrm{p}}(\boldsymbol{g}; \boldsymbol{F}) + \hat{\psi}^{\mathrm{a}}\big(\boldsymbol{g}; \boldsymbol{F}^{\mathrm{e}}\big), \tag{13.9}$$

where the former depends solely on the total deformation gradient, while the latter depends on the elastic part of the deformation gradient, thus both on the deformation and on the potential. This additive form results in the decoupled stress response

$$\hat{\boldsymbol{\tau}} = \hat{\boldsymbol{\tau}}^{\mathrm{p}}(\boldsymbol{g}; \boldsymbol{F}) + \hat{\boldsymbol{\tau}}^{\mathrm{a}}\big(\boldsymbol{g}; \boldsymbol{F}^{\mathrm{e}}\big), \tag{13.10}$$

where the Kirchhoff stress tensor is obtained by the Doyle-Ericksen formula $\boldsymbol{\tau} := 2\partial_{\boldsymbol{g}}\psi$ and the elastic part of the deformation gradient is defined as $\boldsymbol{F}^{\mathrm{e}} = \boldsymbol{F}\boldsymbol{F}^{\mathrm{a}-1}$ from Eq. (13.1). Since the formulation is laid out in the Eulerian setting, the current metric $\boldsymbol{g}$ is explicitly included in the arguments of the constitutive functions.

The potential flux $\hat{\boldsymbol{q}}$ is assumed to depend linearly on the spatial potential gradient $\nabla_x \Phi$

$$\hat{\boldsymbol{q}} = \boldsymbol{D}(\boldsymbol{g}; \boldsymbol{F}) \cdot \nabla_x \Phi, \tag{13.11}$$

through the deformation-dependent anisotropic spatial conduction tensor $\boldsymbol{D}(\boldsymbol{g}; \boldsymbol{F})$ that governs the conduction speed of the non-planar depolarization front in three-dimensional anisotropic cardiac tissue.

The last constitutive relation describing the electrical source term of the Fitzhugh-Nagumo-type excitation Eq. (13.6) is additively decomposed into the excitation-induced purely electrical part $\hat{I}^{\phi}_{\mathrm{e}}(\Phi, r)$ and the stretch-induced mechano-electrical part $\hat{I}^{\phi}_{\mathrm{m}}(\boldsymbol{g}; \boldsymbol{F}, \Phi)$, i.e.

$$\hat{I}^{\phi} = \hat{I}^{\phi}_{\mathrm{e}}(\Phi, r) + \hat{I}^{\phi}_{\mathrm{m}}(\boldsymbol{g}; \boldsymbol{F}, \Phi). \tag{13.12}$$

The former describes the effective current generation due to the inward and outward flow of ions across the cell membrane. This ionic flow is triggered by a perturbation of the resting potential of an excitable cardiac muscle cell beyond some physical threshold upon the arrival of the depolarization front. The latter, on the other hand, incorporates the opening of ion channels under the action of deformation, see Kohl et al. (1999).

Apart from the primary field variables, the recovery variable r, which describes the repolarization response of the action potential, appears among the arguments of $\hat{I}^{\phi}_{\mathrm{e}}$ in Eq. (13.12). Evolution of the recovery variable r chiefly determines the shape and duration of the action potential locally inherent to each cardiac cell and may change throughout the heart. For this reason, evolution of the recovery variable r is commonly modeled by a local ordinary differential equation $\dot{r} = \hat{f}^{\mathrm{r}}(\Phi, r)$. From an algorithmic point of view, the local nature of this evolution equation allows us to treat the recovery variable as an internal variable. This is one of the key features of the proposed formulation that preserves the modular global structure of the field equations as set out in our recent works (Göktepe and Kuhl, 2009, 2010; Göktepe et al., 2010; Wong et al., 2011).

13.3 Model Problem of Cardiac Electromechanics

In this section, we present the specific constitutive equations that are utilized in the analysis of the representative numerical example in Sect. 13.4. In particular, we identify the specific expressions for the Kirchhoff stress $\hat{\boldsymbol{\tau}}$, the potential flux $\hat{\boldsymbol{q}}$, and the current source $\hat{I}^{\phi}$.

13.3.1 Active and Passive Stress Response

The ventricular myocardium can be conceived as a continuum with a hierarchical architecture where uni-directionally aligned muscle fibers are interconnected in the form of sheets. Loosely connected by perimysial collagen, these approximately four-cell-thick sheets can easily slide along each while being stiffest in the direction of the large coiled perimysial fibers aligned with the long axes of the cardiomyocytes, as depicted in Fig. 13.3. To model the passive response of myocardium, we employ the orthotropic model of hyperelasticity recently proposed by Holzapfel

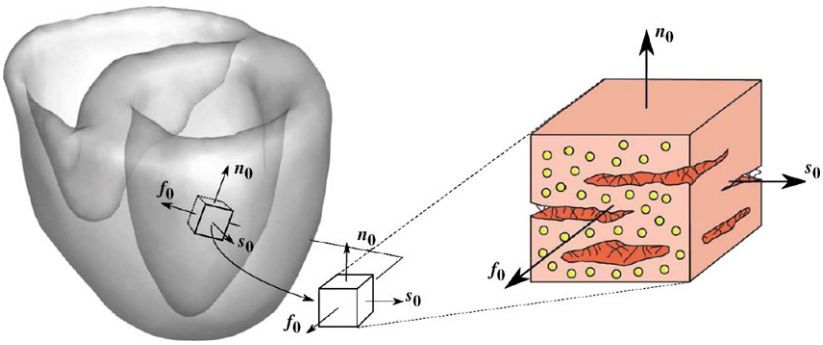

Fig. 13.3 Orthotropic architecture of the myocardium. The orthogonal unit vectors $\boldsymbol{f}_0$ and $\boldsymbol{s}_0$ designate the preferred fiber and sheet directions in the undeformed configuration, respectively. The third direction $\boldsymbol{n}_0$ is orthogonal to the latter by its definition $\boldsymbol{n}_0 := (\boldsymbol{f}_0 \times \boldsymbol{s}_0)/|\boldsymbol{f}_0 \times \boldsymbol{s}_0|$

and Ogden (2009). The specific form of this model can be expressed through the following free-energy function

$$\Psi^{\mathrm{p}}(\boldsymbol{g}; \boldsymbol{F}, \boldsymbol{M}, \boldsymbol{N}, \boldsymbol{K}) = U(J) + \tilde{\Psi}(I_1, I_{4\mathrm{m}}, I_{4\mathrm{n}}, I_{4\mathrm{k}}), \tag{13.13}$$

where $U(J)$ is the purely volumetric part and the orthotropic part is denoted by $\tilde{\Psi}(I_1, I_{4\mathrm{m}}, I_{4\mathrm{n}}, I_{4\mathrm{k}})$. The latter is defined as

$$\begin{aligned}\tilde{\Psi} = \frac{a}{2b}\exp\big[b(I_1 - 3)\big] + \sum_{i=\mathrm{m,n}} \frac{a_i}{2b_i}\big\{\exp\big[b_i(I_{4i} - 1)^2\big] - 1\big\} \\ + \frac{a_{\mathrm{k}}}{2b_{\mathrm{k}}}\big[\exp\big(b_{\mathrm{k}} I_{4\mathrm{k}}^2\big) - 1\big],\end{aligned} \tag{13.14}$$

in terms of the material parameters $a, b, a_{\mathrm{m}}, b_{\mathrm{m}}, a_{\mathrm{n}}, b_{\mathrm{n}}, a_{\mathrm{k}}, b_{\mathrm{k}}$ and the invariants $I_1, I_{4\mathrm{m}}, I_{4\mathrm{n}}$, and $I_{4\mathrm{k}}$, with

$$I_1 := \boldsymbol{g} : \boldsymbol{b}, \qquad I_{4\mathrm{m}} := \boldsymbol{g} : \boldsymbol{m}, \qquad I_{4\mathrm{n}} := \boldsymbol{g} : \boldsymbol{n}, \qquad I_{4\mathrm{k}} := \boldsymbol{g} : \boldsymbol{k}. \tag{13.15}$$

The Eulerian structural tensors $\boldsymbol{m}, \boldsymbol{n}$, and $\boldsymbol{k}$ are defined as the push-forward of the Lagrangian structural tensors

$$\boldsymbol{m} := \boldsymbol{F}\boldsymbol{M}\boldsymbol{F}^T, \qquad \boldsymbol{n} := \boldsymbol{F}\boldsymbol{N}\boldsymbol{F}^T, \qquad \boldsymbol{k} := \boldsymbol{F}\boldsymbol{K}\boldsymbol{F}^T, \tag{13.16}$$

and the Lagrangian structural tensors

$$\boldsymbol{M} := \boldsymbol{f}_0 \otimes \boldsymbol{f}_0, \qquad \boldsymbol{N} := \boldsymbol{s}_0 \otimes \boldsymbol{s}_0, \qquad \boldsymbol{K} := \mathrm{sym}(\boldsymbol{f}_0 \otimes \boldsymbol{s}_0) \tag{13.17}$$

reflect the underlying orthotropic micro-structure of the myocardium through the vectors $\boldsymbol{f}_0$ and $\boldsymbol{s}_0$ that denote the preferred fiber and sheet directions of the material micro-structure in the undeformed configuration as depicted in Fig. 13.3. For the explicit form of the passive Kirchhoff stress tensor $\hat{\boldsymbol{\tau}}^{\mathrm{p}}$ and the corresponding tangent

moduli, which can be obtained through the Doyle-Ericksen formula, the reader is referred to Göktepe et al. (2011).

For the active part of the free-energy function (13.9), we assume the following transversely isotropic function

$$\Psi^{\mathrm{a}}\big(\boldsymbol{g};\boldsymbol{F}^{\mathrm{e}},\boldsymbol{M}\big)=\frac{1}{2}\eta\big(I^{\mathrm{e}}_{4\mathrm{m}}-1\big)^2, \tag{13.18}$$

in terms of the material parameter η and the invariant $I^{\mathrm{e}}_{4\mathrm{m}}:=\boldsymbol{g}:\boldsymbol{m}^{\mathrm{e}}$ with $\boldsymbol{m}^{\mathrm{e}}:=\boldsymbol{F}^{\mathrm{e}}\boldsymbol{M}\boldsymbol{F}^{\mathrm{e}T}$. This leads to us to the active part of the Kirchhoff stress tensor (13.10)

$$\boldsymbol{\tau}^{\mathrm{a}}\big(\boldsymbol{g};\boldsymbol{F}^{\mathrm{e}},\boldsymbol{M}\big)=2\eta\big(I^{\mathrm{e}}_{4\mathrm{m}}-1\big)\boldsymbol{m}^{\mathrm{e}}. \tag{13.19}$$

Calculation of the active stress tensor necessitates the knowledge of the elastic part of the deformation gradient, which depends on the active part of the deformation gradient. As introduced in Eq. (13.2), the latter is assumed to be function of the transmembrane potential Φ through the following ansatz

$$\boldsymbol{F}^{\mathrm{a}}=\boldsymbol{1}+\big(\lambda^{\mathrm{a}}-1\big)\boldsymbol{M}. \tag{13.20}$$

The active fiber stretch λ^{a} is considered to be function of the normalized intracellular calcium concentration $\bar{c}$ through the following relationship

$$\lambda^{\mathrm{a}}=\frac{\xi}{1+f(\bar{c})(\xi-1)}\lambda^{\mathrm{a}}_{\mathrm{max}}, \tag{13.21}$$

where the functions f and ξ of the normalized calcium concentration $\bar{c}:=c/c_R$ are defined as

$$f(\bar{c}):=\frac{1}{2}+\frac{1}{\pi}\arctan(\beta\ln\bar{c})\quad\text{and}\quad\xi:=\frac{f(\bar{c}_0)-1}{f(\bar{c}_0)-\lambda^{\mathrm{a}}_{\mathrm{max}}}, \tag{13.22}$$

respectively. The evolution of the normalized calcium concentration $\bar{c}$ is modeled by the following ordinary differential equation, Pelce et al. (1995),

$$\dot{\bar{c}}=q\big(\Phi+\Phi^{\star}\big)-k\bar{c}\quad\text{with }\bar{c}(t_0)=\bar{c}_0. \tag{13.23}$$

In the algorithmic setting, this evolution equation is integrated locally by using the implicit Euler scheme. Having the active part of the deformation gradient at hand, the elastic part of the deformation gradient can be obtained as $\boldsymbol{F}^{\mathrm{e}}=\boldsymbol{F}\boldsymbol{F}^{\mathrm{a}-1}$ yielding the following closed-form expression

$$\boldsymbol{F}^{\mathrm{e}}=\boldsymbol{F}-\big(1-\lambda^{\mathrm{a}-1}\big)\boldsymbol{F}\boldsymbol{f}_0\otimes\boldsymbol{f}_0. \tag{13.24}$$

13.3.2 Spatial Potential Flux

We have already introduced the spatial potential flux $\hat{\boldsymbol{q}}$ in Eq. (13.11) as a function of the conduction tensor $\boldsymbol{D}$ and the potential gradient $\nabla_x\Phi$. For the model problem,

the second-order conduction tensor is split into the isotropic and anisotropic parts

$$\boldsymbol{D} = d_{\text{iso}}\boldsymbol{g}^{-1} + d_{\text{ani}}\boldsymbol{m}, \tag{13.25}$$

in terms of the scalar conduction coefficients d_{iso} and d_{ani}, where the latter accounts for the faster conduction along the myofiber directions.

13.3.3 Current Source

In order to complete the description of the model problem, we need to specify the constitutive equations for the electrical source term $\hat{I}^{\phi}$. In phenomenological electrophysiology, it is common practice to set up the model equations and parameters in the non-dimensional space. For this purpose, we introduce the non-dimensional transmembrane potential ϕ and the non-dimensional time τ through the following conversion formulas

$$\Phi = \beta_{\phi}\phi - \delta_{\phi} \quad \text{and} \quad t = \beta_t \tau. \tag{13.26}$$

The non-dimensional potential ϕ is related to the physical transmembrane potential Φ through the factor β_{ϕ} and the potential difference δ_{ϕ}, which are both in millivolt (mV). Likewise, the dimensionless time τ is converted to the physical time t by multiplying it with the factor β_t in millisecond (ms). Thus, the conversion formulae in Eq. (13.26) imply the equality $\hat{I}^{\phi} = (\beta_{\phi}/\beta_t)\hat{i}^{\phi}$ and the additive split of $\hat{I}^{\phi}$, introduced in Eq. (13.12) Sect. 13.2.3, becomes $\hat{i}^{\phi} = \hat{i}_{\text{e}}^{\phi} + \hat{i}_{\text{m}}^{\phi}$, which denote the purely electrical current source $\hat{i}_{\text{e}}^{\phi}$ and the stretch-induced mechano-electrical current source $\hat{i}_{\text{m}}^{\phi}$ in the non-dimensional setting.

In this model problem, we use the celebrated two-parameter model of Aliev and Panfilov (1996), which favorably captures the characteristic shape of the action potential in excitable ventricular cells,

$$\hat{i}_{\text{e}}^{\phi} = c\phi(\phi - \alpha)(1 - \phi) - r\phi, \tag{13.27}$$

where c, α are material parameters. The evolution of the recovery variable r is driven by the specific source term

$$\hat{i}^{\text{r}} = \left(\gamma + \frac{\mu_1 r}{\mu_2 + \phi}\right)\left[-r - c\phi(\phi - b - 1)\right]. \tag{13.28}$$

Analogous to the algorithmic update of $\bar{c}$, we use the backward Euler integration to calculate the current value of r. For the stretch-induced current generation $\hat{f}_{\text{m}}^{\phi}$, we adopt the formula proposed by Panfilov et al. (2005) and Keldermann et al. (2007)

$$\hat{i}_{\text{m}}^{\phi} = \vartheta G_{\text{s}}(\bar{\lambda} - 1)(\phi_{\text{s}} - \phi), \tag{13.29}$$

where G_s and ϕ_s denote the maximum conductance and the resting potential of the stretch-activated channels, separately. This contribution to the current source term is due to the opening of ion channels, and, therefore, exists only when myofibers are under tension.

13.4 Numerical Example: Excitation-Contraction of the Heart

This section is devoted to the coupled electromechanical analysis of a biventricular generic heart model that favorably illustrates the main physiological features of the overall response of the heart. For the material parameters that govern the passive stress response, we used the values given in Table 1 of Göktepe et al. (2011). The parameters governing the potential flux and the current source, outlined in Sects. 13.3.2 and 13.3.3, have been adopted from Table 4 of Göktepe and Kuhl (2010). The material parameters governing the active part in Eqs. (13.18)–(13.23) are taken as $\lambda^{a}_{max} = 0.70$, $\eta = 0.05$ MPa, $\beta = 6$, $q = 2$ $(\text{mVs})^{-1}$ and $k = 3.5$ s^{-1}.

The solid model of a biventricular generic heart is constructed by means of two truncated ellipsoids. The generic heart model whose dimensions and spatial discretization are depicted in Fig. 5 of Göktepe and Kuhl (2010) is meshed with 13 348 four-node coupled tetrahedral elements connected at 3 059 nodes. The unevenly distributed average orientation of contractile myocytes $\boldsymbol{f}_0$ is depicted with yellow lines in Fig. 13.4. This fiber organization is consistent with the myofiber orientation in the human heart where the fiber angle ranges from approximately $-70°$ in the epicardium to $+70°$ in the endocardium with respect to the longitudinal plane. Displacement degrees of freedom on the top base surface are restrained and the whole surface of the heart is assumed to be flux-free.

To initiate the excitation, the elevated initial value $\Phi_0 = -10$ mV of the transmembrane potential is assigned to the nodes located at the upper part of the septum as indicated by the partially depolarized region in the first panel in Fig. 13.4. The initial transmembrane potential at the remaining nodes is set to its resting value $\Phi_0 = -80$ mV. The excitation at the top of the septum generates the depolarization front traveling from the location of stimulation throughout the entire heart, thereby resulting in the contraction of the myocytes, see the snapshots in Fig. 13.4 corresponding to systole. At first glance, we observe that the contraction of myocytes gives rise to the upward motion of the apex. More importantly, we also note that the upward motion of the apex is accompanied by the physiologically observed wall thickening and the overall twisting of the heart. To appreciate these phenomena better, the two slices are presented in the complementary images shown in the lower rows of Figs. 13.4 and 13.5. Undoubtedly, it is the heterogeneous distribution of myocyte orientation that yields this physiological response through the non-uniform contraction of myofibers. The panels in Fig. 13.5 illustrate the relaxation of the heart during the course of repolarization.

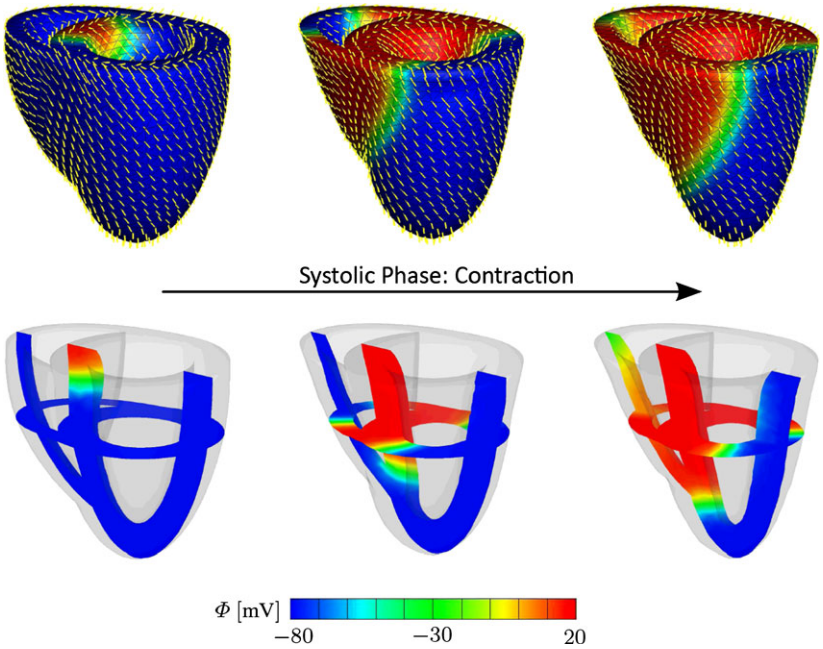

Fig. 13.4 Coupled excitation-induced contraction of generic heart model. Snapshots of the deformed model depict the action potential contours at different stages of depolarization. The *yellow lines* denote the spatial orientation $\boldsymbol{f}$ of contractile myofibers. The two slices in the translucent images in the *lower row* favorably depict the wall thickening and the twisting motion of the heart

13.5 Conclusion

In this contribution, we have proposed a new kinematic approach to the computational cardiac electromechanics. For this purpose, the deformation gradient has been multiplicatively decomposed into the active and passive parts. The evolution of the former has been considered to be function of the transmembrane potential. In addition, the inherently anisotropic, active architecture of cardiac tissue has been accounted for within the proposed kinematic framework. As opposed to the active-strain formulations proposed in the literature, the proposed formulation results in the additively decomposed stress response, which has been attributed to the active-stress formulations only. The proposed micro-structurally based kinematic approach to electro-active materials is believed to be advantageous over the entirely stress-based formulations, since the active deformation is more readily accessible through most experimental techniques at different scales. Therefore, the material parameters governing the generation of the active straining upon electrical stimulation can be favorably tuned to yield reliable, predictive simulations. The proposed kinematic setting has then been embedded in the fully implicit, entirely finite-element-based coupled framework. The implicit numerical integration of the transient terms and the monolithic solution of the resultant coupled algebraic equations has led us to an unconditionally stable and modular structure. The performance of the proposed model

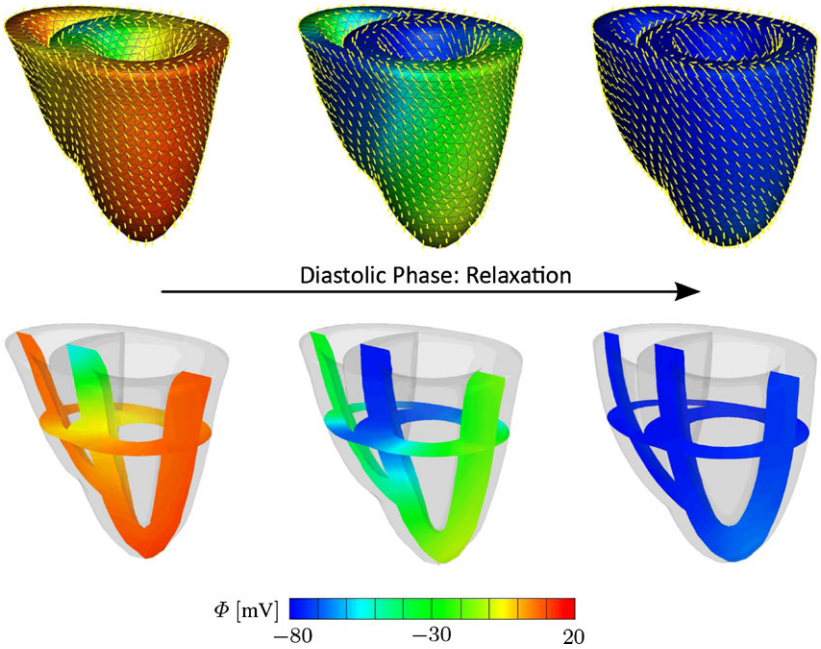

Fig. 13.5 Coupled excitation-induced contraction of generic heart model. Snapshots of the deformed model depict the action potential contours at different stages of repolarization. The *yellow lines* denote the spatial orientation $\boldsymbol{f}$ of contractile myofibers. The two slices in the translucent images in the *lower row* favorably depict the wall thickening and the twisting motion of the heart

has been demonstrated by the fully coupled finite element analysis of a generic heart model.

Acknowledgements The research by SG leading to these results has received funding from the European Union Seventh Framework Programme (FP7/2007-2013) under grant agreement no: PCIG09-GA-2011-294161. Work of EK has received financial support from the National Science Foundation CAREER award CMMI-0952021 and from the National Institutes of Health Grant U54 GM072970.

References

Aliev RR, Panfilov AV (1996) A simple two-variable model of cardiac excitation. Chaos Solitons Fractals 7:293–301

Ambrosi D, Arioli G, Nobile F, Quarteroni A (2011) Electromechanical coupling in cardiac dynamics: the active strain approach. SIAM J Appl Math 71:605–621

Ask A, Menzel A, Ristinmaa M (2012a) Electrostriction in electro-viscoelastic polymers. Mech Mater 50:9–21

Ask A, Menzel A, Ristinmaa M (2012b) Phenomenological modeling of viscous electrostrictive polymers. Int J Non-Linear Mech 47:156–165

Cherubini C, Filippi S, Nardinocchi P, Teresi L (2008) An electromechanical model of cardiac tissue: constitutive issues and electrophysiological effects. Prog Biophys Mol Biol 97:562–573

Fitzhugh R (1961) Impulses and physiological states in theoretical models of nerve induction. Biophys J 1:455–466
Göktepe S, Acharya SNS, Wong J, Kuhl E (2011) Computational modeling of passive myocardium. Int J Numer Methods Eng 27:1–12
Göktepe S, Kuhl E (2009) Computational modeling of cardiac electrophysiology: a novel finite element approach. Int J Numer Methods Eng 79:156–178
Göktepe S, Kuhl E (2010) Electromechanics of the heart: a unified approach to the strongly coupled excitation-contraction problem. Comput Mech 45:227–243
Göktepe S, Wong J, Kuhl E (2010) Atrial and ventricular fibrillation-computational simulation of spiral waves in cardiac tissue. Archive. Appl Mech 80:569–580
Holzapfel GA, Ogden RW (2009) Constitutive modelling of passive myocardium: a structurally based framework for material characterization. Philos T Roy Soc A 367:3445–3475
Keener JP, Sneyd J (1998) Mathematical physiology. Springer, New York
Keldermann RH, Nash MP, Panfilov AV (2007) Pacemakers in a reaction-diffusion mechanics system. J Stat Phys 128:375–392
Kohl P, Hunter P, Noble D (1999) Stretch-induced changes in heart rate and rhythm: clinical observations, experiments and mathematical models. Prog Biophys Mol Biol 71:91–138
Kröner E (1960) Allgemeine Kontinuumstheorie der Versetzungen und Eigenspannungen. Arch Ration Mech Anal 4:273–334
Lee EH (1969) Elastic-plastic deformation at finite strain. J Appl Mech 36:1–6
Nash MP, Panfilov AV (2004) Electromechanical model of excitable tissue to study reentrant cardiac arrhythmias. Prog Biophys Mol Biol 85:501–522
Niederer SA, Smith NP (2008) An improved numerical method for strong coupling of excitation and contraction models in the heart. Prog Biophys Mol Biol 96:90–111
Nielsen PMF, LeGrice IJ, Smaill BH, Hunter PJ (1991) Mathematical model of geometry and fibrous structure of the heart. Am J Physiol, Cell Physiol 260:H1365–H1378
Panfilov AV, Keldermann RH, Nash MP (2005) Self-organized pacemakers in a coupled reaction-diffusion-mechanics system. Phys Rev Lett 95:258104
Pelce P, Sun J, Langeveld C (1995) A simple model for excitation-contraction coupling in the heart. Chaos Solitons Fractals 5:383–391
Rohmer D, Sitek A, Gullberg GT (2007) Reconstruction and visualization of fiber and laminar structure in the normal human heart from ex vivo diffusion tensor magnetic resonance imaging (DTMRI) data. Invest Radiol 42:777–789
Stålhand J, Klarbring A, Holzapfel GA (2011) A mechanochemical 3D continuum model for smooth muscle contraction under finite strains. J Theor Biol 268:120–130
Wong J, Göktepe S, Kuhl E (2011) Computational modeling of electrochemical coupling: a novel finite element approach towards ionic models for cardiac electrophysiology. Comput Methods Appl Mech Eng 200:3139–3158

Chapter 14
Activation Models for the Numerical Simulation of Cardiac Electromechanical Interactions

Ricardo Ruiz-Baier, Davide Ambrosi, Simone Pezzuto, Simone Rossi, and Alfio Quarteroni

Abstract This contribution addresses the mathematical modeling and numerical approximation of the excitation-contraction coupling mechanisms in the heart. The main physiological issues are preliminarily sketched along with an extended overview to the relevant literature. Then we focus on the existing models for the electromechanical interaction, paying special attention to the active strain formulation that provides the link between mechanical response and electrophysiology. We further provide some critical insight on the expected mathematical properties of the model, the ability to provide physiological results, the accuracy and computational cost of the numerical simulations. This chapter ends with a numerical experiment studying the electromechanical coupling on the anisotropic myocardial tissue.

14.1 Introduction

The interaction mechanism between contraction of the cardiac muscle and electrical propagation is a complex multiscale phenomenon of vital importance in a wide range of medical applications (Smith et al., 2004). From a purely mechanical point of view, key features of muscle behavior include large deformations, fiber anisotropy, heterogeneity of the tissue, and the ability to shorten when a substantial

R. Ruiz-Baier (✉) · S. Rossi · A. Quarteroni
CMCS-MATHICSE-SB, Ecole Polytechnique Fédérale de Lausanne, 1015 Lausanne, Switzerland
e-mail: ricardo.ruiz@epfl.ch

A. Quarteroni
e-mail: alfio.quarteroni@epfl.ch

S. Rossi
e-mail: simone.rossi@epfl.ch

D. Ambrosi · S. Pezzuto · A. Quarteroni
MOX—Politecnico de Milano, piazza Leonardo da Vinci 32, 20133 Milano, Italy

D. Ambrosi
e-mail: davide.ambrosi@polimi.it

S. Pezzuto
e-mail: simone.pezzuto@mail.polimi.it

G.A. Holzapfel, E. Kuhl (eds.), *Computer Models in Biomechanics*,
DOI 10.1007/978-94-007-5464-5_14,

intracellular calcium concentration change occurs. The dynamics is driven by a traveling action potential, usually modeled by a reaction-diffusion equation, where the ions species diffusion activates the ionic currents reaction, which eventually dictate the depolarization and repolarization of the cells. Ionic currents depend on the jump in electric potential according to Ohm's law whereas the conductance is typically a highly nonlinear function of voltage described through gating variables or, more recently, by means of Markov models. Such a nonlinearity is responsible for the complex excitable behavior of the cardiac action potential cycle: rapid upstroke of depolarization, followed by a plateau phase and a repolarization of the cells when a voltage threshold is overcome. A variety of models exists in this respect, with increasing detail in the description of ionic channels and intracellular reactions taken into account (CellML, 2000; Rudy and Silva, 2006). Heuristic systems of equations, that only reproduce a qualitative pattern of the voltage wave, are very useful in providing a framework simple enough to allow for mathematical analysis. However, these kind of phenomenological models are not able to describe the correct behavior of the cell in a pathological condition, or correctly describe drug interactions; furthermore, the concentration of specific ions like intracellular calcium that induces contractions and relaxations of cardiomyocytes, is typically not present. Therefore a more detailed insight of several ionic currents is needed to provide the correct physiological contractility.

The numerical simulation of these complex multiphysics and multiscale systems poses a major challenge even if state-of-the-art computational techniques and computer architectures are employed. Finite element formulations of nonlinear elasticity for the myocardial tissue have been proposed since more than a decade (Nash and Hunter, 2000), followed by a series of works focusing on the integration of cardiac systems including elasticity, electricity, perfusion models, and on the close connection of the proposed models with experimental observations (see a review in Kerckhoffs et al., 2006). If a certain level of accuracy of the geometrical description of a patient specific model is desired and the solution is to be obtained within a reasonable amount of time, there is no way around using parallel computers (and suitable numerical techniques combined with scalable algorithms exploiting the underlying architectures). The public availability of scientific computing libraries such as, e.g., LifeV (2001), Continuity (2005) and Chaste (Pitt-Francis et al., 2009), represents a substantial step forward in this direction. Parallel algorithms capable of performing cardiac mechano-electrical simulations have recently been implemented reporting scalable behaviors in Chapelle et al. (2009); Reumann et al. (2009); Lafortune et al. (2012); Nobile et al. (2012).

In this paper we aim at investigating some features of the active strain formulation in cardiac electromechanics (Cherubini et al., 2008; Ambrosi et al., 2011; Nobile et al., 2012). Such approach is based on the assumption that the mechanical activation, laying in the core of the cell-level excitation-contraction mechanism, may be represented as a virtual multiplicative splitting of the deformation gradient into a passive elastic response, and an active deformation depending directly on the electrophysiology. Alternative options that avoid such decomposition at the deformation level are active-stress descriptions (see, e.g., Nash and Panfilov, 2004;

Pathmanathan and Whiteley, 2009; Land et al., 2012) where the stress is composed as a sum of a passive and an active part, the latter determined by the so-called active tension, also depending on the electrical activation of the cell. In this paper we address the feasibility of numerical simulations for the macroscopic coupling using the active strain approach, and we present in detail an example of the full electromechanical interaction. However, we will not discuss advantages and disadvantages of the different strategies, rather we refer to Ambrosi and Pezzuto (2012) and Rossi et al. (2012) for a thorough comparison.

This paper is organized as follows. In Sect. 14.2 we summarize the main mathematical characteristics of the electrical and mechanical problem and we detail the specific modeling strategy that we adopt. The electromechanical coupling, i.e. the cell contraction dictated by the electrical signal and the corresponding feedback (the stretch activated currents) are illustrated in Sect. 14.3. The computational method is outlined in Sect. 14.4 where we also present a numerical example, and we close with a discussion in Sect. 14.5.

14.2 Mathematical Models for Cardiac Electromechanics

Force balance equations for an elastic continuum medium are employed to describe large deformations of the myocardium under influence of the fluid pressure, the surrounding organs and its own contraction. Such framework has to be coupled with the macroscopic bidomain or monodomain equations accounting for the propagation of the electric potential and ionic currents.

14.2.1 Models for the Heart Electrophysiology

Starting from the pioneering work of Hodgkin and Huxley (1952) on the nerve axon model, several increasingly sophisticate models have been developed for the propagation of electrical signals in cardiac tissue. Here we separate between models for cardiac cell electrophysiology, and macroscopic tissue-level models based on continuum mechanics.

Popular cardiac cellular electrophysiology models include those based on experimental observations on animals (e.g., Luo and Rudy, 1991) and humans (see, e.g., Iyer et al., 2004; ten Tusscher et al., 2004). Such models address cell excitation in isolation from the rest of the cardiac function. They essentially include a description of the dynamics of ionic species (mainly potassium, calcium, and sodium) along with the gating processes of several proteins that are blocked or allowed to transport ions through the cellular membrane. A drastic decrease of computational cost can be obtained by using simplified low dimensional models based on phenomenological descriptions of such mechanisms (Rogers and McCulloch, 1994; Bueno-Orovio et al., 2008). The price to pay for this simplification, provided that a correct behavior of

the voltage field is reproduced, is that ionic species are not well resolved. Nevertheless, these types of electrical models are able to provide some specific information of interest, such as contractility.

Systems of ordinary differential equations (ODEs) of the form

$$\partial_t v - I_{\text{ion}}(v, \mathbf{w}) = 0, \qquad \partial_t \mathbf{w} - \mathbf{m}(v, \mathbf{w}) = \mathbf{0}, \tag{14.1}$$

are employed to describe these cellular models, without any spatial detail. Here v denotes the transmembrane potential field, $\mathbf{w}$ contains all gating variables and concentration of ionic species, and I_{ion} and $\mathbf{m}$ drive the kinetics of the system, its specific form depending on the chosen cellular model.

Models at the cell level can be incorporated into macroscopic descriptions for the propagation of electrical excitation throughout the cardiac muscle in the simplest way assuming homogeneous diffusion of ionic species on the microstructure of the substrate. The texture of the cardiac tissue can be incorporated observing that cellular and extracellular components are characterized by different diffusivities. A homogenization process yields the so-called bidomain equations (Tung, 1978):

$$\partial_t v - \nabla\cdot(\mathbf{D}_{\text{e}}\nabla u_{\text{e}}) + I_{\text{ion}} = I^{\text{i}}_{\text{app}}, \qquad \partial_t v + \nabla\cdot(\mathbf{D}_{\text{i}}\nabla u_{\text{i}}) + I_{\text{ion}} = I^{\text{e}}_{\text{app}}, \tag{14.2}$$

where u_{i} and u_{e} are the intra- and extracellular electric potentials (both defined in every point of the domain), and $(I^{\text{i}}_{\text{app}}, I^{\text{e}}_{\text{app}})$ are possible externally applied stimuli.

The cardiomyocytes are organized in fibers that originate the anisotropic conductivity in the electrophysiology of the heart. The myofiber angle varies continuously from about $-60°$ (inverse circumferential axis) at the epicardium, to about $70°$ at the endocardium. From the apical region, the myofibers that conform the tissue follow a right helical orientation towards the subendocardium and a left helical path parallel to the wall on the subepicardium. On the mid-wall region, cardiac fibers exhibit a circumferential orientation, and on the basal site fibers cross from subendocardial to the subepicardial region. Myocardial propagation velocities in the parallel and perpendicular myofiber directions can differ up to an order of magnitude. These geometrical features are encoded in the anisotropic conductivity tensors $\mathbf{D}_{\text{i}}$ and $\mathbf{D}_{\text{e}}$ (Colli Franzone and Pavarino, 2004).

14.2.2 Mechanical Response of the Myocardium

The characterization of the material properties of the cardiac tissue requires precise experimental settings that should reproduce physiological conditions as close as possible. Usual tests include uniaxial and biaxial tension experiments, as well as shear tests, from which it is possible to recover stress-strain relations on the different directions of the anisotropic medium (fiber, sheets, and sheet-normal axes).

The usual kinematics descriptors of a continuum medium placed in $\Omega_{\text{o}} \subset \mathbb{R}^3$ in its reference configuration are the deformation gradient of its motion $\mathbf{F}$ and the

right Cauchy-Green tensor $\mathbf{C} = \mathbf{F}^{\mathrm{T}}\mathbf{F}$. We denote by $I_1 = \operatorname{tr}\mathbf{C}$, $I_2 = \frac{1}{2}(I_1^2 - \operatorname{tr}\mathbf{C}^2)$, $I_3 = \det\mathbf{C}$, the principal invariants of $\mathbf{C}$.

Due to the alignment of cardiac fibers and their organization in sheets, the myocardium exhibits an orthotropic behavior that can be conveniently illustrated introducing the orthogonal unit vector fields $\mathbf{f}_0$ and $\mathbf{s}_0$ denoting the orientation of the fibers and collagen-sheets in the reference configuration. A hyperelastic material with constitutive response invariant with respect to rotations around $\mathbf{f}_0$ and $\mathbf{s}_0$ is described by a strain-energy function $\mathscr{W}(\mathbf{F})$ that depends on a set of invariant such as $I_{1,2,3}$, and also pseudo-invariants defined as follows:

$$I_{4,f} = \mathbf{C} : \mathbf{f}_0 \otimes \mathbf{f}_0, \qquad I_{5,f} = \mathbf{C}^2 : \mathbf{f}_0 \otimes \mathbf{f}_0, \qquad I_{8,fs} = \mathbf{C} : \operatorname{sym}(\mathbf{f}_0 \otimes \mathbf{s}_0), \quad (14.3)$$

and analogously $I_{4,s}$ and $I_{5,s}$.

Orthotropic strain-energy functions were suggested in Usyk et al. (2000); Costa et al. (2001); Holzapfel and Ogden (2009), that in addition are able to represent the behavior of the laminar sheets in which cardiac myofibers are structured. For instance, the energy function proposed by Holzapfel and Ogden (2009) is given by

$$\mathscr{W}(\mathbf{F}) = \frac{a}{2b}\left(\mathrm{e}^{b(I_1-3)} - 1\right) + \sum_{i=f,s} \frac{a_i}{2b_i}\left(\mathrm{e}^{b_i(I_{4,i}-1)^2} - 1\right) + \frac{a_{fs}}{2b_{fs}}\left(\mathrm{e}^{b_{fs}I_{8,fs}^2} - 1\right), \quad (14.4)$$

where the eight parameters a, b, a_f, b_f, a_s, b_s, a_{fs} and b_{fs} are experimentally fitted.

According to Ashikaga et al. (2008), the myocardium experiments a change in myocardial volume of up to 10 %. This is possibly due to blood-filled spaces within the myocardium which may communicate with the ventricular lumen or from the coronary arteries from which blood is expelled during systole. However incompressibility of the medium is often assumed as it is mainly constituted by water. In strictly incompressible models, the pressure field is the Lagrange multiplier enforcing the constraint, and in slightly compressible models a compressibility modulus penalizes the variation in density. For evident reasons, strict incompressibility is more popular when analytical methods are applied, as one degree of freedom drops out in homogeneous deformations, while penalization is often preferred in numerical codes, where no compatibility between spaces of representation of displacement and pressure fields must be abided.

14.3 Activation and Contraction

Myocardial systolic contraction is usually modeled at the macroscale by incorporating a possibly anisotropic, additive stress contribution in the force balance (Nash and Panfilov, 2004; Smith et al., 2004; Göktepe and Kuhl, 2010; Pathmanathan et al., 2010).

A different approach is to introduce a multiplicative decomposition of the strain. The active strain method, introduced in the context of biomechanics in Taber and

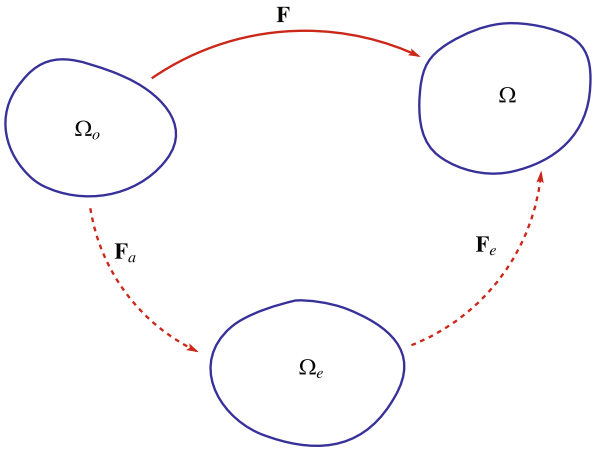

Fig. 14.1 Sketch of the active strain decomposition entailing an intermediate virtual configuration Ω_e between the reference state Ω_o and the current configuration Ω. Similar splittings have been proposed in finite elastoplasticity (Lee and Liu, 1967), growth and material remodeling (Taber and Perucchio, 2000; Menzel and Waffenschmidt, 2009), and mechano-chemical interactions (Murtada et al., 2010)

Perucchio (2000); Nardinocchi and Teresi (2007), assumes that the deformation gradient $\mathbf{F}$ can be rewritten in terms of a Lee-type multiplicative decomposition (Lee and Liu, 1967), i.e.

$$\mathbf{F} = \mathbf{F}_e \mathbf{F}_o, \tag{14.5}$$

where $\mathbf{F}_o$ is the active deformation, to be constitutively prescribed in terms of ionic species concentration, and $\mathbf{F}_e$ is the passive elastic deformation (see Fig. 14.1). Whichever approach that is chosen, the model should satisfy due mathematical properties (such as frame indifference and ellipticity of the total stress), and the constitutive laws need to recover physiological relevant behaviors (such as the Frank-Starling effect, where an increase of chamber volume at end-systolic pressure and stroke work reflects on the tissue as a monotonic increase in isometric tension), (Lee and Liu, 1967).

Comparisons between the usual active stress method and the active strain approach from a numerical viewpoints has been carried out in Rossi et al. (2012). Defining the variables γ_f, γ_s, γ_n as the relative displacements in the directions $\mathbf{f}_0$, $\mathbf{s}_0$, $\mathbf{n}_0$, (fibers, sheets and sheets-normal directions) of a single cell, respectively, the *local* deformation is

$$\mathbf{F}_o = \mathbf{I} + \gamma_f \mathbf{f}_0 \otimes \mathbf{f}_0 + \gamma_s \mathbf{s}_0 \otimes \mathbf{s}_0 + \gamma_n \mathbf{n}_0 \otimes \mathbf{n}_0. \tag{14.6}$$

Note that γ_f represents the active shortening of the cardiomyocytes, whereas γ_s, γ_n will take into account the associated thickening, in order to satisfy the incompressibility of the cell itself (Iribe et al., 2007; Smerup et al., 2009). In Nardinocchi and Teresi (2007), Evangelista et al. (2011) and Nobile et al. (2012), the contribution of the terms depending on γ_s and γ_n are not included. Analogously, for some activation models (see, e.g., Göktepe and Kuhl, 2010; Rausch et al., 2011), the active tension is assumed to act exclusively along the fibers direction. However, biaxial tests provide a measure of the active contributions in the transverse direction. This quantification can be obtained by either measuring the different rates of calcium

release in these directions (as done in Usyk et al., 2000) and then translating this information into active strains, or assuming transverse isotropy of the mechanical response at the cell level (as in Rossi et al., 2012). Moreover, if the components of the activated deformation $\mathbf{F}_\mathrm{o}$ satisfy the condition

$$(1+\gamma_f)(1+\gamma_s)(1+\gamma_n)=1, \tag{14.7}$$

then $\det\mathbf{F}_\mathrm{o}\equiv 1$, a very convenient choice from a numerical point of view for this nonlinear problem, since convergence has to be incrementally reached.

The thermodynamic assumption of the multiplicative decomposition (14.5) is that the active deformation $\det\mathbf{F}_\mathrm{o}$ stores no energy, so that the strain-energy function is $\widehat{\mathscr{W}}=\mathscr{W}(\mathbf{F}_\mathrm{e})$ and

$$\mathscr{W}_{\mathrm{strain}}=\det\mathbf{F}_\mathrm{o}\,\widehat{\mathscr{W}}=\det\mathbf{F}_\mathrm{o}\,\mathscr{W}\left(\mathbf{F}\mathbf{F}_\mathrm{o}^{-1}\right). \tag{14.8}$$

The activation γ_f depends on the concentration of ionic species as can be deduced from ordinary differential equation models (Rice et al., 2008; Murtada et al., 2010; Nobile et al., 2012), which can be summarized in the symbolic equation

$$\partial_t\gamma_f-G(\mathbf{w},\gamma_f)=0, \tag{14.9}$$

where G defines the activation dynamics depending on ionic concentrations denoted by the vector $\mathbf{w}$.

In the reference configuration Ω_o, the equations governing the electromechanical interaction under active strain read

$$\begin{cases} -\nabla\cdot\left(\det\mathbf{F}_\mathrm{o}\dfrac{\partial\mathscr{W}(\mathbf{F}\mathbf{F}_\mathrm{o}^{-1})}{\partial\mathbf{F}}-p\mathbf{F}^{-T}\right)=0, & \text{in } \Omega_\mathrm{o};\\ \det\mathbf{F}=1,\\ \chi c_\mathrm{m}\partial_t v-\nabla\cdot\left(\mathbf{F}^{-1}\mathbf{D}_\mathrm{e}\mathbf{F}^{-T}\nabla u_\mathrm{e}\right)+\chi(I_\mathrm{ion}+I_\mathrm{sac})=I_\mathrm{app}^\mathrm{i},\\ \chi c_\mathrm{m}\partial_t v+\nabla\cdot\left(\mathbf{F}^{-1}\mathbf{D}_\mathrm{i}\mathbf{F}^{-T}\nabla u_\mathrm{i}\right)+\chi(I_\mathrm{ion}+I_\mathrm{sac})=I_\mathrm{app}^\mathrm{e}, & \text{in } \Omega_\mathrm{o}\times(0,T).\\ \partial_t\mathbf{w}-\mathbf{m}(v,\mathbf{w})=0,\\ \partial_t\gamma_f-G(\mathbf{w},\gamma_f)=0, \end{cases} \tag{14.10}$$

System (14.10) is to be completed with suitable initial data for v, $\mathbf{w}$ as well as with boundary conditions for all fields. The usual prescription of voltage at the initial time is that a large enough perturbation is located at the apex, so that an electric wave starts traveling up to the base, producing the due ionic currents and mechanical contraction. This initial condition corresponds to immaterial assumption that the electric signal, actually produced at the sinoatrial node, has been traveling very fast along the Purkinje fibers down to the apex, where they finely branch producing a volumetric diffusion at $t=0$. Since the Purkinje fibers also branch up from the apex towards the base at the subepicardial level, different protocols are often used to

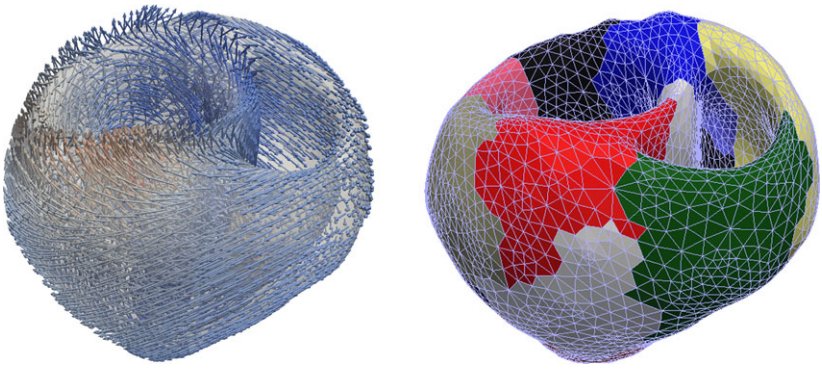

Fig. 14.2 Fiber distribution on the myocardium (*left panel*), and sketch of the geometrical domain decomposition of the corresponding mesh into 16 subdomains (*right panel*)

stimulate the entire endocardial surface. This is done either synchronously or with a slight delay going from apex to base. No-flux boundary conditions apply to the electric variables, while mixed boundary data are imposed to the displacement field. Robin conditions mimic the presence of the pericardial sac at the outer wall, while blood pressure inside the ventricles is computed on the basis of pressure-volume diagrams, relating the blood pressure depending to the ventricular volume.

14.4 Numerical Simulation

In what follows we present a simple numerical example illustrating the feasibility of electromechanical active strain models. The simulations reported in the present work are performed using the parallel finite element library LifeV (2001). We employed a biventricular geometry (originally from Sermesant, 2003) where the mesh consists of 29 504 tetrahedral elements. Myocardial fibers are distributed in the muscle following an analytical description so that the orientation varies linearly from an elevation angle (between the short axis plane and the fiber) of 65° in the epicardium, to −65° in the endocardium (see Fig. 14.2, left panel). The domain is then partitioned into 16 subdomains (Fig. 14.2, right panel).

Since we are interested in the myocardium activation more than the passive properties of the muscle, we consider a simple neo-Hookean material with strain-energy function $\mathscr{W} = \frac{\mu}{2}\mathbf{F} : \mathbf{F}$, where $\mu = 385$ kPa, in all regions of the cardiac muscle. Moreover, the active strain $\mathbf{F}_{\mathrm{o}}$ is chosen to be transversely isotropic, so $\gamma_s = \gamma_n = 0$ and therefore condition (14.7) is not needed. This means that the second Piola-Kirchhoff tensor reads:

$$\mathbf{S} = \mu(1-\gamma_f)\mathbf{I} + \mu\gamma_f \frac{2-\gamma_f}{1-\gamma_f}\mathbf{f}_0 \otimes \mathbf{f}_0. \tag{14.11}$$

The specifications for (14.1) are in accordance with the minimal model of Bueno-Orovio et al. (2008), a four-equations phenomenological model for human ventricles. The auxiliary variables are $\mathbf{w} = (w_1, w_2, w_3)$ which are phenomenological quantities (no direct physical interpretation), however w_3 behaves like a re-scaled intracellular calcium concentration. The reaction terms are defined as

$$I_{\text{ion}}(v, \mathbf{w}) = -w_1 H(v-\theta_1)(v-\theta_1)(v_v - v)/\tau_{fi} + (v - v_0)\big(1 - H(v-\theta_2)\big)/\tau_0 + H(v-\theta_2)/\tau_{3,0} - H(v-\theta_2)w_2 w_3/\tau_{si}, \tag{14.12}$$

and

$$\mathbf{m}(v, \mathbf{w}) = \begin{pmatrix} ((1 - H(v-\theta_1))(w_{1,\text{inf}} - w_1)/\tau_1^- - H(v-\theta_1)w_1/\tau_1^+ \\ (1 - H(v-\theta_2))(w_{2,\text{inf}} - w_2)/\tau_2^- - H(v-\theta_2)w_2/\tau_2^+ \\ ((1 + \tanh(k_3(v - v_3)))/2 - w_3)/\tau_3)^{\mathrm{T}} \end{pmatrix}, \tag{14.13}$$

where H stands for the usual Heaviside function. The switches and infinite values are defined as follows:

$$\tau_1^- = \big(1 - H\big(v - \theta_1^-\big)\big)\tau_{1,1}^- + H\big(v - \theta_1^-\big)\tau_{1,2}^- \tag{14.14}$$

$$\tau_2^- = \tau_{2,1}^- + \big(\tau_{2,2}^- - \tau_{2,1}^-\big)\big(1 + \tanh\big(k_2^-\big(v - v_2^-\big)\big)\big)/2 \tag{14.15}$$

$$\tau_{3,0} = \tau_{3,0,1} + (\tau_{3,0,2} - \tau_{3,0,1})\big(1 + \tanh\big(k_{3,0}(v - v_{3,0})\big)\big)/2 \tag{14.16}$$

$$\tau_3 = \big(1 - H(v-\theta_2)\big)\tau_{3,1} + H(v-\theta_2)\tau_{3,2} \tag{14.17}$$

$$\tau_0 = \big(1 - H(v-\theta_0)\big)\tau_{0,1} + H(v-\theta_0)\tau_{0,2} \tag{14.18}$$

$$w_{1,\text{inf}} = \begin{cases} 1, & v < \theta_1^- \\ 0, & u \geq \theta_1^- \end{cases} \tag{14.19}$$

$$w_{2,\text{inf}} = \big(1 - H(v-\theta_0)\big)(1 - v/\tau_{2,\infty}) + H(v-\theta_0)w_{2,\infty}^*. \tag{14.20}$$

The model reproduces the correct shape of the voltage wave. For the sake of simplicity, we use the epicardial parameters for the whole cardiac muscle: $\theta_0 = 0.005$, $\theta_1 = 0.3$, $\theta_2 = 0.13$, $\theta_1^- = 0.1$, $\tau_{3,0,1} = 91$, $\tau_{3,0,2} = 0.8$, $\tau_{3,1} = 2.7342$, $\tau_{3,2} = 4$, $\tau_{0,1} = 410$, $\tau_{0,2} = 7$, $w_{2,\infty}^* = 0.5$, $v_v = 1.61$, $\tau_{1,1}^- = 80$, $\tau_{1,2}^- = \tau_1^+ = 1.4506$, $\tau_{2,1}^- = 70$, $\tau_{2,2}^- = 8$, $\tau_2^+ = 280$, $k_2^- = 200$, $v_2^- = 0.016$, $\tau_{fi} = 0.078$, $k_{3,0} = 2.1$, $v_{3,0} = 0.6$, $k_3 = 2.0994$, $v_3 = 0.9087$, $\tau_{si} = 3.3849$, $\tau_{2,\infty} = 0.01$. The initial data corresponds to $w_1 = w_2 = 1$, $w_3 = 0$.

The governing ODE for the activation corresponds to (14.9), as introduced in Rossi et al. (2011) and Nobile et al. (2012), with the specification $G(\gamma_f, w_3) = -0.02w_3 - 0.04\gamma_f$.

The time sequence of transmembrane potential, activation γ_f and other ionic concentrations are illustrated in Fig. 14.3 for a point on the epicardial surface. The highest activation value is attained with a delay of about 120 ms with respect to that of the action potential.

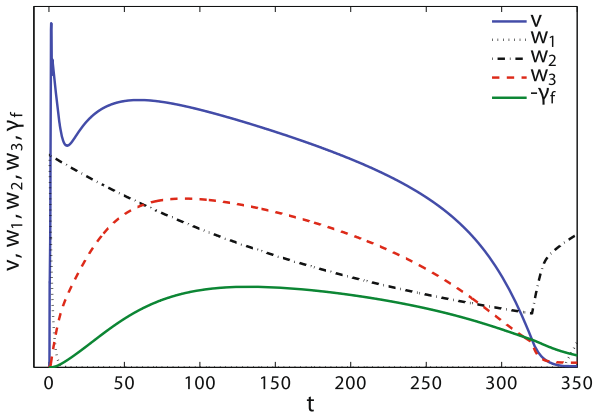

Fig. 14.3 Time evolution of the electric fields in a specific epicardial position of the tissue. Plotted quantities are the transmembrane potential v, gate variables $\mathbf{w} = (w_1, w_2, w_3)$ and the mechanical activation γ_f which are all presented in dimensionless form

Robin boundary condition $m\mathbf{u} + \mathbf{Pn} = \mathbf{0}$, with $m = \mu = 385$ kPa, has shown to yield a qualitatively correct end-systolic displacement magnitude (around 25 %) and rotation of the left ventricle, as reported in Rossi et al. (2012). Quadratic finite elements are used for displacement, whereas all other fields are discretized using continuous piecewise trilinear elements, in order to satisfy Brezzi-Babuška *inf-sup* condition. The timestep, fixed during the simulation, is $\Delta t = 0.01$ ms and, as usual in electromechanically coupled computational models (see, e.g., Nash and Panfilov, 2004; Cherubini et al., 2008; Pathmanathan and Whiteley, 2009; Land et al., 2012), we iterate between electrical and mechanical problems in a segregated mode. The nonlinear equations arising from the discretization of the mechanical problem are linearized using the Newton-Raphson method. We find that no more than 6 iterations are needed to converge with a tolerance of $\varepsilon_{\text{tol}} = 10^{-8}$, with the maximum number of iterations being always attained around the upstroke phase. The linear systems are solved using the GMRES iterative method (with a tolerance of $\hat{\varepsilon}_{\text{tol}} = 10^{-7}$). The average overall CPU time spent per time step is 3.5 seconds, using 32 cores distributed on 4 nodes on the Intel Harpertown cluster *Callisto* at EPFL.[1]

An external stimulus $I^{\text{e}}_{\text{app}} = -100$ μA is applied at the apex at $t = 0$, in order to generate a traveling wave for the transmembrane potential, initially everywhere at rest ($v = -84$ mV). Figure 14.4 presents three snapshots of the solution of the excitation-contraction problem at times $t = 1$, $t = 40$, $t = 230$ and $t = 540$ ms, where fiber directions are represented by the gray volume arrows and the color-map shows the values of the transmembrane potential v on the undeformed solid. Notice that the activation patterns adopt a profile dictated by the tissue anisotropy.

[1] http://hpc-dit.epfl.ch/clusters/callisto.php.

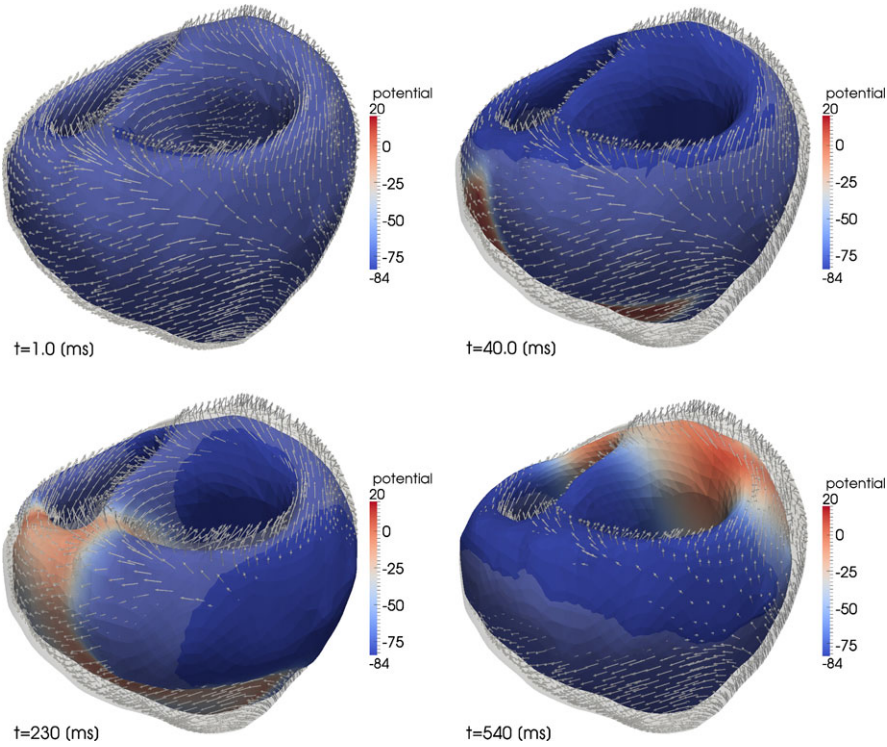

Fig. 14.4 Snapshots of the transmembrane potential field, plotted on the deformed configuration, and fiber distribution at times $t = 1, 40, 230, 540$ ms, plotted on the undeformed configuration

14.5 Conclusions and Future Directions

The material outlined in this paper reports some recent work in modeling and numerical simulation of cardiac electromechanics using the active strain approach. Even though several physical approximations apply, recently performed comparisons with experimental observations by Evangelista et al. (2011) (in terms of torsion of the left ventricle, endocardial volumes, and circumferential strains) and by Rossi et al. (2012) (in terms of end-systolic normal and shear strains) suggest the potential effectiveness of active-strain based models.

The effectiveness of an electromechanical model in capturing the key aspects of the physiology depends on several factors. In particular, we take electric models from a cell level and incorporate them in a force balance equation that holds at the macroscale. Yet, it is not obvious that such an uplift between spatial scales can be directly operated, without a suitable homogenization procedure. This is a concern shared by all current models of cardiac electromechanics, and needs to be addressed in further detail.

Acknowledgements The support by the European Research Council through the grant 'Mathcard, Mathematical Modelling and Simulation of the Cardiovascular System', ERC-2008-AdG 227058 is gratefully acknowledged.

References

Ambrosi D, Pezzuto S (2012) Active strain vs. active stress in mechanobiology: constitutive issues. J Elast 107:121–199

Ambrosi D, Arioli G, Nobile F, Quarteroni A (2011) Electromechanical coupling in cardiac dynamics: the active strain approach. SIAM J Appl Math 71:605–621

Ashikaga H, Coppola BA, Yamazaki KG, Villarreal FJ, Omens JH, Covell JW (2008) Changes in regional myocardial volume during the cardiac cycle: implications for transmural blood flow and cardiac structure. Am J Physiol, Heart Circ Physiol 295:H610–H618

Bueno-Orovio A, Cherry EM, Fenton FH (2008) Minimal model for human ventricular action potential in tissue. J Theor Biol 253:544–560

CellML (2000) (Language for storing and exchange of computer-based mathematical models). www.cellml.org

Chapelle D, Fernandez MA, Gerbeau JF, Moireau P, Sainte-Marie J, Zemzemi N (2009) Numerical simulation of the electromechanical activity of the heart. Lect Notes Comput Sci 5528:357–365

Cherubini C, Filippi S, Nardinocchi P, Teresi L (2008) An electromechanical model of cardiac tissue: constitutive issues and electrophysiological effects. Prog Biophys Mol Biol 97:562–573

Colli Franzone P, Pavarino LF (2004) A parallel solver for reaction-diffusion systems in computational electro-cardiology. Math Models Methods Appl Sci 14:883–911

Continuity (2005) (A problem-solving environment for multi-scale modeling in bioengineering and physiology). www.continuity.ucsd.edu/Continuity

Costa KD, Holmes JW, McCulloch AD (2001) Modelling cardiac mechanical properties in three dimensions. Philos Trans R Soc Lond A 359:1233–1250

Evangelista A, Nardinocchi P, Puddu PE, Teresi L, Torromeo C, Varano V (2011) Torsion of the human left ventricle: Experimental analysis and computational modelling. Prog Biophys Mol Biol 107:112–121

Göktepe S, Kuhl E (2010) Electromechanics of the heart: a unified approach to the strongly coupled excitation-contraction problem. Comput Mech 45:227–243

Hodgkin AL, Huxley AF (1952) A quantitative description of membrane current and its application to conductance and excitation in nerve. J Physiol 117:500–544

Holzapfel GA, Ogden RW (2009) Constitutive modelling of passive myocardium: a structurally based framework for material characterization. Philos Trans R Soc Lond A 367:3445–3475

Iribe G, Helmes M, Kohl P (2007) Force-length relations in isolated intact cardiomyocytes subjected to dynamic changes in mechanical load. Am J Physiol, Heart Circ Physiol 292:H1487–H1497

Iyer V, Mazhari R, Winslow RL (2004) A computational model of the human left ventricular epicardial myocyte. Biophys J 87:1507–1525

Kerckhoffs RCP, Healy SN, Usyk TP, McCulloch AD (2006) Computational methods for cardiac electromechanics. Proc IEEE 94:769–783

Lafortune P, Arís R, Vázquez M, Houzeaux G (2012) Coupled parallel electromechanical model of the heart. Int J Numer Methods Biomed Eng 28:72–86

Land S, Niederer SA, Smith NP (2012) Efficient computational methods for strongly coupled cardiac electromechanics. IEEE Trans Biomed Eng 59:1219–1228

Lee EH, Liu DT (1967) Finite strain elastic-plastic theory with application to plane-wave analysis. J Appl Phys 38:17–27

LifeV (2001) (A parallel finite element library). www.lifev.org

Luo C, Rudy Y (1991) A model of the ventricular cardiac action potential: depolarization, repolarization, and their interaction. Circ Res 68:1501–1526

Menzel A, Waffenschmidt T (2009) A micro-sphere-based remodelling formulation for anisotropic biological tissues. Philos Trans R Soc Lond A 367:3499–3523
Murtada S, Kroon M, Holzapfel GA (2010) A calcium-driven mechanochemical model for prediction of force generation in smooth muscle. Biomech Model Mechanobiol 9:749–762
Nardinocchi P, Teresi L (2007) On the active response of soft living tissues. J Elast 88:27–39
Nash MP, Hunter PJ (2000) Computational mechanics of the heart. J Elast 61:113–141
Nash MP, Panfilov AV (2004) Electromechanical model of excitable tissue to study reentrant cardiac arrhythmias. Prog Biophys Mol Biol 85:501–522
Nobile F, Quarteroni A, Ruiz-Baier R (2012) An active strain electromechanical model for cardiac tissue. Int J Numer Methods Biomed Eng 28:52–71
Pathmanathan P, Whiteley JP (2009) A numerical method for cardiac mechanoelectric simulations. Ann Biomed Eng 37:860–873
Pathmanathan P, Chapman SJ, Gavaghan D, Whiteley JP (2010) Cardiac electromechanics: the effect of contraction model on the mathematical problem and accuracy of the numerical scheme. Q J Mech Appl Math 63:375–399
Pitt-Francis J, Pathmanathan P, Bernabeu MO, Bordas R, Cooper J, Fletcher AG, Mirams GR, Murray P, Osbourne JM, Walter A, Chapman SJ, Garny A, van Leeuwen IMM, Maini PK, Rodriguez B, Waters SL, Whiteley JP, Byrne HM, Gavaghan D (2009) Chaste: a test-driven approach to software development for biological modelling. Comput Phys Commun 180:2452–2471. www.cs.ox.ac.uk/chaste
Rausch MK, Dam A, Göktepe S, Abilez OJ, Kuhl E (2011) Computational modeling of growth: systemic and pulmonary hypertension in the heart. Biomech Model Mechanobiol 10:799–811
Reumann M, Fitch BG, Rayshubskiy A, Keller D, Seemann G, Dossel O, Pitman MC, Rice JJ (2009) Strong scaling and speedup to 16,384 processors in cardiac electro-mechanical simulations. Proc IEEE 09:2795–2798
Rice JJ, Wang F, Bers DM, de Tombe PP (2008) Approximate model of cooperative activation and crossbridge cycling in cardiac muscle using ordinary differential equations. Biophys J 95:2368–2390
Rogers JM, McCulloch AD (1994) A collocation-Galerkin finite element model of cardiac action potential propagation. IEEE Trans Biomed Eng 41:743–757
Rossi S, Ruiz-Baier R, Pavarino LF, Quarteroni A (2011) Active strain and activation models in cardiac electromechanics. In Brenn G, Holzapfel GA, Schanz M, Steinbach O (eds) Proc Appl Math Mech, vol 11, pp 119–120
Rossi S, Ruiz-Baier R, Pavarino LF, Quarteroni A (2012) Orthotropic active strain models for the numerical simulation of cardiac biomechanics. Int J Numer Methods Biomed Eng 28:761–788
Rudy Y, Silva JR (2006) Computational biology in the study of cardiac ion channels and cell electrophysiology. Q Rev Biophys 39:57–116
Sermesant M (2003) Modèle électromécanique du coeur pour l'analyse d'image et la simulation. PhD Thesis, Université de Nice Sophia Antipolis, France
Smerup M, Nielsen E, Agger P, Frandsen J, Vestergaard-Poulsen P, Andersen J, Nyengaard J, Pedersen M, Ringgaard S, Hjortdal V, Lunkenheimer PP, Anderson RH (2009) The three-dimensional arrangement of the myocytes aggregated together within the mammalian ventricular myocardium. Anat Rec 292:1–11
Smith NP, Nickerson DP, Crampin EJ, Hunter PJ (2004) Multiscale computational modelling of the heart. Acta Numer 13:371–431
Taber LA, Perucchio R (2000) Modeling heart development. J Elast 61:165–197
ten Tusscher KH, Noble D, Noble PJ, Panfilov AV (2004) A model for human ventricular tissue. Am J Physiol, Heart Circ Physiol 286:H1573–H1589
Tung L (1978) A bi-domain model for describing ischemic myocardial D-C potentials. PhD Thesis, MIT, Cambridge, MA
Usyk TP, Mazhari R, McCulloch AD (2000) Effect of laminar orthotropic myofiber architecture on regional stress and strain in the canine left ventricle. J Elast 61:143–164

Chapter 15
Hemodynamic Alterations Associated with Coronary and Cerebral Arterial Remodeling Following a Surgically-Induced Aortic Coarctation

C. Alberto Figueroa, Jessica S. Coogan, and Jay D. Humphrey

Abstract Computational models promise to aid in the interpretation of the coupled interactions between evolving wall geometry, structure, material properties and hemodynamics seen in arterial adaptations. Motivated by recent aortic coarctation models in animals, we used a computational fluid-solid-interaction model to study possible local and systemic effects on the hemodynamics within the thoracic aorta and coronary, carotid, and cerebral arteries due to a distal aortic coarctation and subsequent spatial variations in wall adaptation. In particular, we studied an initial stage of acute cardiac compensation (maintenance of cardiac output) followed by early arterial wall remodeling (spatially varying wall thickening and stiffening).

15.1 Introduction

Although elevated mean arterial pressure (MAP) has traditionally been considered to be an important indicator or initiator of cardiovascular risk in hypertension, mounting evidence suggests that increased pulse pressure is as or more important (Safar, 2000; Dart and Kingwell, 2001; Safar and Boudier, 2005). Data from surgically created aortic coarctations in animals reveal striking evolutions of wall geometry, structure, and properties (Xu et al., 2000; Hu et al., 2008; Eberth et al., 2010) that appear to be driven primarily by increased pulse pressure, not MAP (Eberth et al., 2009). It also appears that the associated arterial adaptations progress at different rates and to different extents both temporally (first at basal rates, then rapidly, then

C.A. Figueroa (✉)
King's College London, London, SE16 7EH, UK
e-mail: alberto.figueroa@kcl.ac.uk

J.S. Coogan
Stanford University, Stanford, CA 94305, USA
e-mail: shihj@stanford.edu

J.D. Humphrey
Department of Biomedical Engineering, Yale University, New Haven, CT 06520, USA
e-mail: jay.humphrey@yale.edu

G.A. Holzapfel, E. Kuhl (eds.), *Computer Models in Biomechanics*,
DOI 10.1007/978-94-007-5464-5_15,

back to normal values) and spatially (from proximal to distal sites), see Hayenga (2010).

Although additional experimental data will be needed to understand better these spatio-temporal adaptations, computational fluid-solid-growth (FSG) models (Figueroa et al., 2009) offer considerable promise both in the design and interpretation of such experiments and in implicating possible biomechanical mechanisms.

Building on recent advances in computational modeling (Figueroa et al., 2006; Vignon-Clementel et al., 2006; Kim et al., 2009a,b; Moireau et al., 2012), the goal of this work was to simulate possible effects of a surgically created coarctation in the descending thoracic aorta on the hemodynamics within the proximal aorta and the coronary, carotid, and cerebral arteries following both an acute cardiac compensation (i.e., maintenance of cardiac output) and early arterial wall remodeling (i.e., spatially varying wall thickening and stiffening).

15.2 Methods

15.2.1 Model Geometry

15.2.1.1 Baseline Model

Computed tomographic (CT) images were collected from two adult male human subjects free of cardiovascular disease to collectively encompass all major arteries from the brain to the diaphragm. Separate 3D geometric models were constructed from the CT datasets using custom software based on a 2D vessel segmentation procedure, see Fig. 15.1. A finite element mesh was created by discretizing the 3D model coarsely, running a steady-state flow simulation, and then performing field-based adaptive mesh refinement (Sahni et al., 2006). The final finite element mesh consisted of 2,462,487 linear tetrahedral elements and 477,872 nodes.

15.2.1.2 Coarctation Model

A thoracic aortic coarctation was modeled by introducing a 75 % diameter narrowing in the aorta just above the diaphragm, consistent with both the location and the degree of a surgically induced coarctation in mini-pigs in studies that provide information on temporal and spatial changes in arterial wall composition (Hu et al., 2008; Hayenga, 2010).

15.2.2 Numerical Methods

Equations enforcing balance of mass and linear momentum (Navier-Stokes) were solved for the flow of an incompressible Newtonian fluid within a deformable domain using a stabilized finite element formulation implemented in the open-source

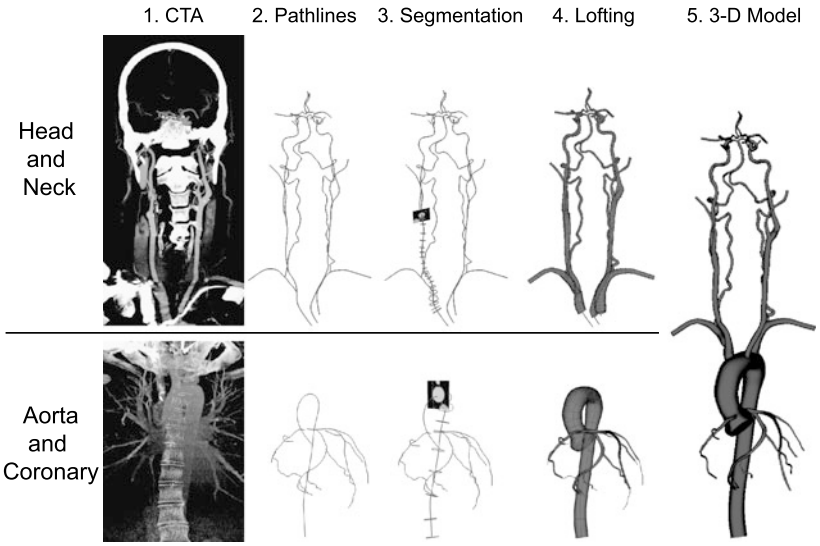

Fig. 15.1 3D computational model of the human thoracic aorta, coronary arteries, and head and neck vessels based on CT images from two normal male subjects. From Coogan et al. (2012)

code SimVascular (Figueroa et al., 2006). Computations were performed on a supercomputer (276 Dell PowerEdge 1950) typically using 96 cores. We utilized a time step size of 0.0001 seconds, and the simulations had an average residual of 0.005. Simulations were run for 7 cardiac cycles until achieving cycle-to-cycle periodicity in the pressure fields.

15.2.3 Fluid-Solid Models

Blood density was $\rho = 1.06$ kg/m^3 and blood viscosity was $\mu = 0.04$ P. We assumed typical baseline values for the linearized stiffness and thickness of the wall of each of the four primary vascular segments: thoracic aorta as well as coronary, neck, and cerebral arteries. A coupled momentum method was used (Figueroa et al., 2006) to model wall deformability and a coupled-multidomain formulation (Vignon-Clementel et al., 2006) was used to link Windkessel models for the heart and distal vessels to the 3D vascular model. The overall model thus required prescription of one inlet and 22 outlet boundary conditions. Numerical values for the lumped-parameter coefficients were determined iteratively to reach target values for flow and pressure.

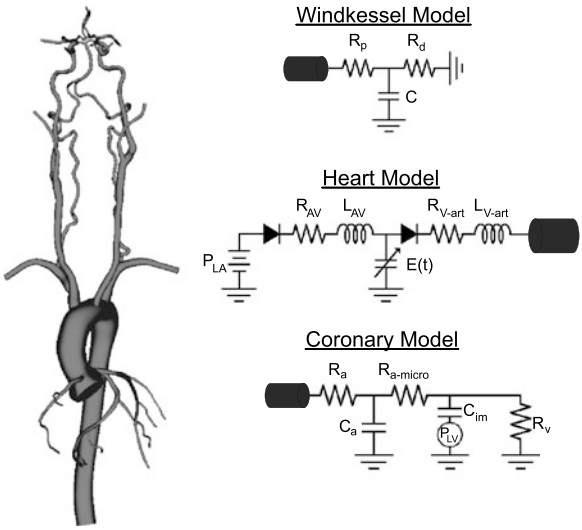

Fig. 15.2 Various lumped-parameter models utilized to specify boundary conditions for the 3D computational model. The Windkessel model was applied at all outlets except the coronary tree; the heart model was applied at the aortic root. From Coogan et al. (2012)

15.2.3.1 Heart Model

Overall function of the heart was simulated using a lumped parameter circuit model (Kim et al., 2009a) that includes resistors and inductors to represent the mitral and aortic valves (R_{AV}, $R_{\mathrm{V\text{-}Art}}$, L_{AV}, $L_{\mathrm{V\text{-}Art}}$), a pressure source that represents left atrial pressure P_{LA}, and a variable capacitance that represents left ventricular elastance/contractility $E(t)$, see Fig. 15.2. The initial left atrial pressure was assumed to be 10 mmHg. The final heart model parameters were $P_{\mathrm{LA}} = 11$ mmHg, maximum elastance of 1.25 mmHg/mL, and time-to-peak elastance of 0.4 s. A Lagrange profile constraint with a penalty number of 10,000 was used to stabilize the solution during the systolic phase of the cardiac cycle (Kim et al., 2009b).

15.2.3.2 Windkessel RCR Model

Hemodynamic conditions were prescribed at every outlet in the descending aorta, neck, and head vessels in terms of a proximal (larger arteries and arterioles) resistance R_{p}, a proximal vessel capacitance C, and a distal (small arterioles and capillaries) resistance R_{d} (cf. Fig. 15.2). A Lagrange profile constraint was used at the inlet and outlet of the aorta as well as at the outlets of the right and left subclavian and external carotid arteries. Such constraints stabilize the computed solution while affecting only the hemodynamics in a small region near the constraint (Kim et al., 2009b).

Table 15.1 Parameter values for the lumped parameter Windkessel and coronary models. The unit of resistance is 10^3 dynes s/cm^5 and the unit of capacitance is 10^{-6} cm^5/dynes

Windkessel parameters				Coronary parameters					
Outlet	R_p	R_d	C	Outlet	R_a	$R_{a\text{-micro}}$	R_v	C_a	C_{im}
Desc Aorta	0.25	2.48	500	LAD1	176	287	91	0.28	2.41
L Subclavian	1.88	19.0	44.7	LAD2	131	214	68	0.37	3.14
R Subclavian	1.88	19.0	48.3	LAD3	126	206	66	0.38	3.26
L Ext Carotid	4.39	44.4	15.0	LAD4	75	123	39	0.61	5.19
R Ext Carotid	4.39	44.4	13.9	LCX1	48	78	25	0.07	9.17
L Ant Cerebral	11.2	113	5.23	LCX2	159	260	83	0.41	3.50
R Ant Cerebral	11.2	113	5.05	LCX3	213	348	111	0.32	2.78
L Int Carotid	3.18	32.1	11.0	LCX4	167	272	87	0.39	3.38
R Int Carotid	3.18	32.1	10.3	RCA1	166	271	86	0.59	5.07
L Post Cerebral	8.29	83.8	5.41	RCA2	231	377	120	0.44	3.74
R Post Cerebral	8.29	83.8	6.13	RCA3	258	422	134	0.39	3.38

15.2.3.3 Coronary Model

A lumped parameter model of the coronary vascular bed (Kim et al., 2010) was prescribed at the outlets of the large coronary vessels (cf. Fig. 15.2). In addition to the resistors and capacitance of the Windkessel model, this model included the venous circulation and incorporated effects of left ventricular pressure. The latter is critical since contraction of the heart is one of the main determinants of coronary flow. The total resistance at each outlet R_{total} was again calculated assuming a MAP of 100 mmHg and that flow through each outlet scaled with cross-sectional area, with mean coronary flow comprising approximately 4.5 % of cardiac output (Guyton and Hall, 2006). The Windkessel portion of the lumped parameter coronary model was represented by R_a, C_a, and $R_{a\text{-micro}}$. The venous pressure defined the relationship between R_a, $R_{a\text{-micro}}$, and R_v and was assumed to be 15 mmHg. Two parameters, $C_{a\text{-total}}$ and $C_{im\text{-total}}$, were defined as the sum of all coronary arterial (C_a) and intramyocardial (C_{im}) compliances. An iterative tuning procedure was used to find values of $C_{a\text{-total}}$ and $C_{im\text{-total}}$ that yielded physiologic coronary flow waveforms. For the left coronary vessels, the left ventricular pressure found in the lumped parameter coronary model was equivalent to the pressure derived from the heart model. The boundary condition for the right coronary artery was based on a scaling of left ventricular pressure that was derived from the heart model, specifically $P_{RV} = 0.20 P_{LV}$. The final parameter values for the heart model and Windkessel models are listed in Table 15.1.

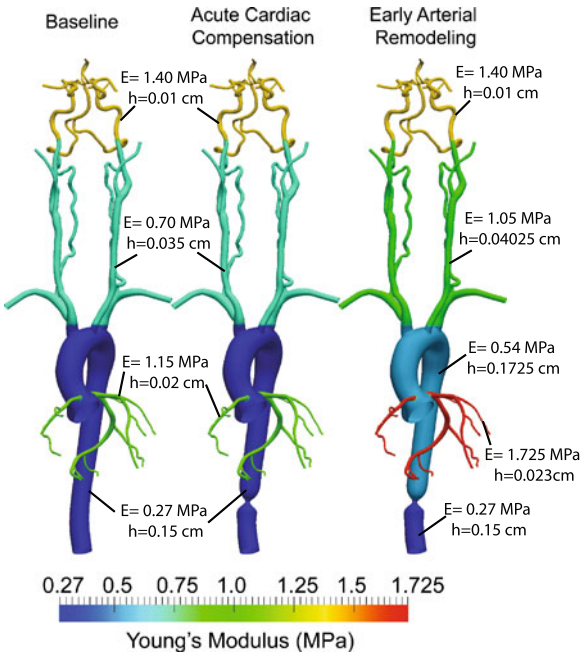

Fig. 15.3 Sections of the model with different wall properties. The acute cardiac compensation frame refers to the introduction of coarctation and subsequent cardiac compensation, the early arterial remodeling shows the differential stiffening observed in animal experiments in various vascular regions. From Coogan et al. (2012)

15.2.3.4 Vessel Wall Properties

Given current limitations in experimental data on regional variations in vascular mechanical properties and thickness, four sections of the vasculature were endowed with different but uniform wall properties, reflected by an effective constant stiffness and thickness of the wall (Fig. 15.3). The stiffness of the thoracic aorta was chosen to yield physiologic levels of strain over normal ranges of blood pressure (Redheuil et al., 2010) whereas moduli for coronary, neck, and cerebral vessels were based directly on data (Gow and Hadfield, 1979; Hayashi et al., 1980; Nichols and O'Rourke, 2005). The thickness of the vessel in each section was assumed to be 10 % of the mean radius within that section (Nichols and O'Rourke, 2005).

15.2.4 Acute Cardiac Compensation Following Coarctation

When first introducing the coarctation, parameters for the heart model were modified to simulate an acute cardiac compensation. This modification accounted for the increased work required of the heart to compensate for the increased afterload due to the coarctation. If the heart were not to adapt, then cardiac output would decrease due to the increased resistance in the aorta. Thus, the heart model was modified by iteratively increasing values of the maximum left ventricular elastance and left atrial pressure until cardiac output equaled that of the baseline model (Taylor and Donald,

1960). We assumed that cardiac output remained unchanged since the aortic stenosis was moderate and that it is unlikely that either the perfusion or the metabolic demands of the subject were altered significantly. It follows that, in order to maintain cardiac output, contractility of the heart (i.e., the elastance) must increase. In addition, changes in elastance affect filling of the heart, thus requiring an increase in left atrial pressure to maintain the same end diastolic volume. The final left atrial pressure was 14 mmHg and the maximum elastance was 1.52 mmHg/mL.

15.2.5 Early Arterial Remodeling

Early arterial vascular remodeling (i.e., within the first 10 days or so) was simulated by modifying wall properties to reflect stiffening and thickening of the thoracic aorta proximal to the coarctation, the coronary vessels, and the neck vessels. These changes were based on findings that the pulse wave velocity can increase by as much as two-fold with aging and that many adaptive processes associated with aging are similar to those associated with hypertension (Wolinsky, 1972; Nichols and O'Rourke, 2005). Updated values of stiffness and thickness are illustrated in Fig. 15.3. Briefly, the stiffness of the aortic arch, coronary tree, and neck vessels was increased by 100 %, 50 % and 50 %, respectively, while the thickness was increased 15 %. We assumed that the cerebral vasculature did not experience any changes in stiffness or thickness during this early period (Hayenga, 2010). We also did not prescribe any associated changes in vascular lumen largely because of the lack of associated experimental data and the possible competing effects of changes in distal resistances (e.g., cerebral autoregulation) and local shear-regulated vasodilatation. The prescribed changes in vascular stiffness and thickness affected cardiac afterload, hence additional cardiac compensation was required to maintain cardiac output after arterial remodeling. The final left atrial pressure was 16 mmHg and the maximum elastance was 1.82 mmHg/mL. All other outlet boundary conditions (arterial and coronary) remained the same for baseline, acute cardiac compensation, and early arterial remodeling.

15.2.6 Data Analysis

Simulation data were analyzed using the open-source software Paraview (Kitware, Inc. Clifton Park, NY). Pressure, flow, and cyclic wall strain were analyzed at five different locations within the vasculature (see Fig. 15.4): the proximal descending aorta (P-Ao), left anterior descending (LAD) coronary artery, left common carotid artery (LCCA), left middle cerebral artery (LMCA), and basilar artery (BA). Mean circumferential wall strain was calculated based on changes in the cross sectional area of the vessel over a cardiac cycle using the following Green-Lagrange type expression $E_{\theta\theta} = (A_t/A_{\mathrm{D}} - 1)/2$, where A_t is the cross sectional area at any given time t and A_{D} is a reference diastolic value (note: using area effectively represents radius squared as needed in the nonlinear measure of strain).

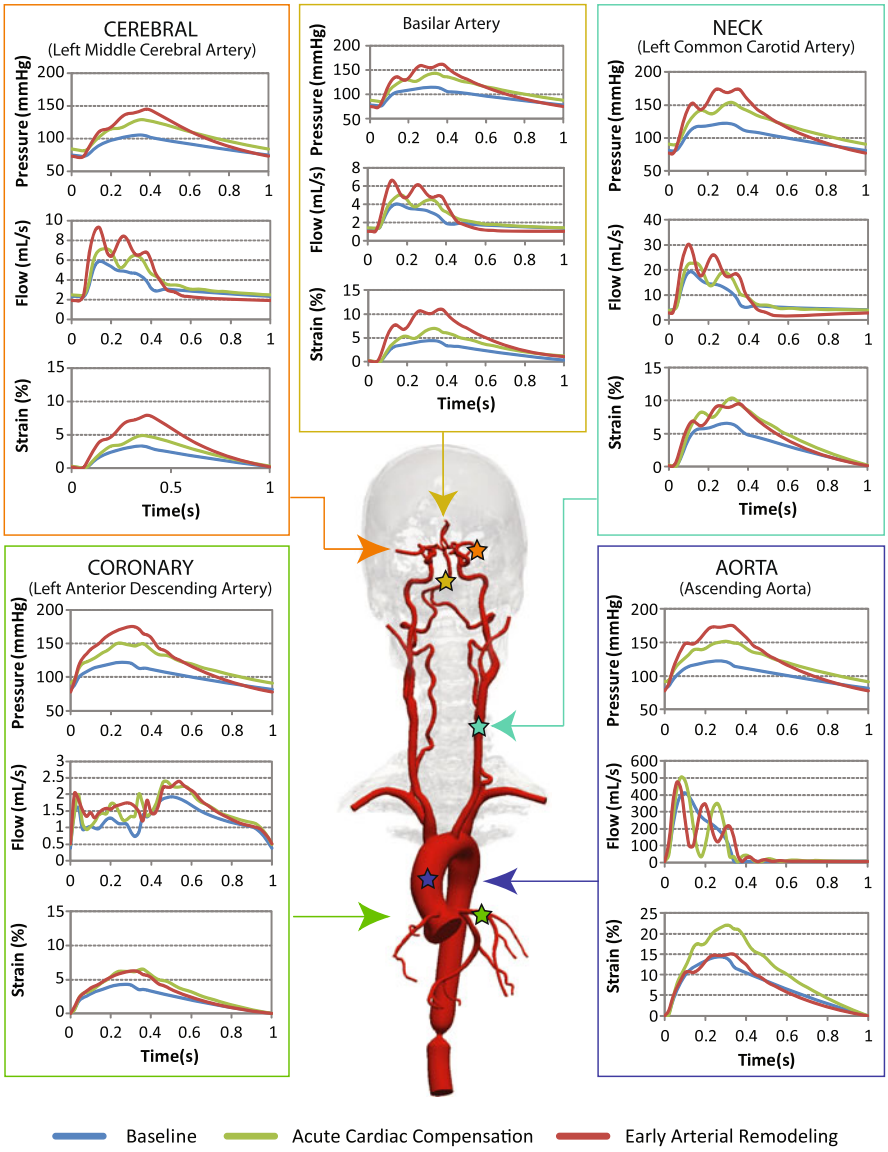

Fig. 15.4 Pressure, flow, and wall strain in baseline, acute cardiac compensation, and early arterial remodeling conditions. From Coogan et al. (2012)

15.3 Results

The baseline simulation provided a prototypical human aortic pressure of 120/80 mmHg, cardiac output of 5 L/min, and heart rate of 60 bpm. Associated pressure, flow, and strain waveforms also had realistic shapes (see blue plots in

Fig. 15.4). The P-Ao had the highest mean and peak strain, followed by the LCCA, BA, LAD, and LMCA. Conversely, the highest mean wall shear stress and mean circumferential stress were in the LMCA, followed by the BA, LAD, LCCA, and P-Ao. The coronary arteries exhibited realistic shapes and averages in the flow, pressure, and strain waveforms. In addition, equal regional blood flows were obtained in the left and right cerebral hemispheres, with mean and pulse pressure lower in the cerebral arteries than in other areas of the vasculature. These results are summarized in Fig. 15.4 and Table 15.2.

Cardiac output would have decreased from 5 to 4.46 L/min after introducing the 75 % aortic coarctation if no changes were made in the lumped parameter heart model. Increasing the maximum elastance of the heart from 1.25 to 1.52 mmHg/mL maintained cardiac output at 5 L/min, but increased blood pressure in the entire model (e.g., from 120/80 to ≈ 150/90 mmHg in the P-Ao). The pressure, flow, and strain waveforms exhibited more oscillations in each vascular territory, possibly due to the additional reflection site at the coarctation (Fig. 15.4). Similar to the baseline condition simulation, the P-Ao had the highest mean and peak strain, followed by the LCCA, BA, LAD, and LMCA, all with values higher than in baseline conditions. Interestingly, while the % increase in MAP was approximately the same throughout the model; the % increase in pulse pressure was greatest in the P-Ao, followed by the LCCA, BA, LAD, and LMCA (Table 15.3). Whereas flow increased through the LAD, LCCA, LMCA, and BA, it decreased in the P-Ao, thus indicating an early redistribution of flow due to the increased resistance at the coarctation. This redistribution also explained the smaller percentage increase in wall shear stress in the P-Ao compared to the other vascular territories. Cardiac workload, as measured by the area within the pressure-volume loop of the left ventricle, increased 17 % from 8476 to 9890 mmHg/mL.

In the early arterial remodeling case, had the heart model not been modified, the changes in arterial properties would have decreased cardiac output from 5 to 4.59 L/min. Additional cardiac compensation was thus introduced (e.g., increased maximum elastance to 1.82 mmHg/mL) to maintain cardiac output at 5 L/min. This change resulted in yet another increase in blood pressure throughout the model, with aortic blood pressure reaching ≈ 180/80 mmHg. Additional oscillations were seen in the pressure, flow, and strain waveforms compared with those found in the acute cardiac compensation stage (Fig. 15.4). The P-Ao again had the highest mean and peak strain, followed by the BA, LCCA, LMCA, and LAD. In this case, wall strain returned to near baseline levels in the P-Ao, whereas strains in the LCCA and LAD were approximately the same as for acute cardiac compensation despite the stiffening and thickening experienced by these arteries. Lastly, strains in the LMCA and BA were higher than those seen with acute cardiac compensation due to the higher mean and pulse pressures, but no changes in wall properties. The mean values of circumferential stress were between those for baseline and acute cardiac compensation for the P-Ao, LCCA, and LAD, but higher in the basilar artery and LMCA. When comparing acute cardiac compensation and early arterial remodeling, the % increase in mean pressure was nearly identical throughout the entire model but the % increase in pulse pressure differed regionally, see Table 15.3. This finding emphasizes that

Table 15.2 Results for the three simulated stages: P_{mean} = mean arterial pressure; PP = pulse pressure; Q_{mean} = flow; $E_{\theta\theta}$ = cyclic strain; $\boldsymbol{\tau}_{\text{mean}}$ = wall shear stress; σ_{mean} = circumferential wall stress

	Baseline					Acute cardiac compensation					Early arterial remodeling				
	Aorta	LAD	LCCA	LMCA	Basilar	Aorta	LAD	LCCA	LMCA	Basilar	Aorta	LAD	LCCA	LMCA	Basilar
P_{mean} (mmHg)	102	102	101	89	96	121	121	120	105	114	124	124	123	106	116
PP (mmHg)	42	40	42	33	38	70	60	65	47	58	101	97	97	74	88
Q_{mean} (mL/s)	54.5	1.2	7.5	3.4	2.1	47.7	1.5	8.9	4.0	2.5	45.6	1.5	9.0	4.0	2.6
$E_{\theta\theta}^{\text{mean}}$ (%)	5.9	2.2	3.2	1.7	2.3	8.9	3.2	4.8	2.4	3.6	5.8	2.9	4.4	3.7	5.3
$E_{\theta\theta}^{\text{peak}}$ (%)	12.0	4.3	6.6	3.4	4.5	20.6	6.6	10.3	4.9	7.1	12.6	6.2	9.5	8.0	10.9
$\boldsymbol{\tau}_{\text{mean}}$ (Pa)	0.98	1.12	1.11	9.57	3.59	1.01	1.40	1.41	11.82	4.56	0.78	1.43	1.58	12.58	4.91
σ_{mean} (kPa)	94	153	141	164	204	112	182	167	193	242	100	162	149	195	247

Table 15.3 Percent changes between baseline and acute cardiac compensation, baseline and early arterial remodeling, and acute cardiac compensation and early arterial remodeling

	Baseline vs. acute (%)					Baseline vs. early remodeling (%)					Acute vs. early remodeling (%)				
	Aorta	LAD	LCCA	LMCA	Basilar	Aorta	LAD	LCCA	LMCA	Basilar	Aorta	LAD	LCCA	LMCA	Basilar
ΔP_{mean}	19	19	19	18	19	22	22	22	19	21	2	2	3	1	2
ΔPP	67	26	55	42	53	140	143	131	124	132	44	62	49	57	52
ΔQ_{mean}	−12	26	19	16	19	−16	28	20	19	24	−4	2	1	2	4
$\Delta E_{\theta\theta}^{\text{mean}}$	51	45	50	41	52	−2	32	38	118	130	−35	−9	−8	54	51
$\Delta E_{\theta\theta}^{\text{peak}}$	72	53	56	44	58	5	44	44	135	142	−39	−6	−8	63	54
$\Delta \boldsymbol{\tau}_{\text{mean}}$	3	25	27	24	27	−20	28	42	31	37	−23	2	12	6	8
$\Delta \sigma_{\text{mean}}$	19	19	18	18	19	6	6	6	19	21	−11	−11	−11	1	2

possible differential changes in pulse, not mean, pressure throughout the vasculature might be responsible for different time courses of arterial remodeling. Flow through the LAD, LCCA, LMCA, and BA increased, whereas flow through the P-Ao decreased further. Cardiac workload increased 12 % from 9890 to 11059 mmHg/mL.

15.4 Discussion

Findings over the past few decades have revealed that vessels within the elastic, muscular arteries, arterioles, capillaries, venules or veins respond markedly differently to altered biomechanical stimuli. For example, whereas all arteries and arterioles tend to thicken in response to hypertension, the elastic arteries, muscular arteries, and arterioles tend to do so while increasing, maintaining, and decreasing their caliber, respectively (Humphrey, 2002). More recently, it has become apparent that differential remodeling responses can even occur within vessels of the same general classification and within close proximity to one another. For example, the ascending aorta (an elastic artery) appears to be the first central artery (i.e., of the rest of the aorta and carotids) to manifest aging related changes in structure that affect overall mechanical properties (Redheuil et al., 2010). Amongst the many effects of aging on arteries, including increased endothelial dysfunction and advanced glycation endproducts (Lakatta et al., 2009; Safar, 2010), it appears that fatigue-type damage to elastic fibers is particularly important (Arribas et al., 2006; O'Rourke and Hashimoto, 2007). Indeed, it may well be that the increased susceptibility of the ascending aorta to an aging related loss of elastic fiber integrity may explain in part the increased susceptibility of the same region to dilatation and dissection in Marfan syndrome (Pearson et al., 2008), which results from a genetic mutation in the fibrillin-1 gene (FBN1); fibrillin-1 appears to help stabilize elastic fibers, hence mutations in FBN1 also result in decreased elastic fiber integrity.

Understanding better the spatio-temporal progression of vascular changes in both adaptive and maladaptive G&R could impact clinical care significantly. For example, being able to identify early indicators of vascular disease or subsequent risk could allow earlier interventions, before the subsequent disease presents symptomatically as heart attack, stroke, or other life threatening condition. A long-term goal of this work is to build a new class of computational models that aid in understanding local and systemic effects of spatially and temporally progressive changes in large portions of the vascular tree and attendant changes in the hemodynamics, which in turn serve as strong mechanobiological stimuli for subsequent vascular growth and remodeling.

Toward that end, here we presented a zeroth order model wherein progressive changes in large segments of the vasculature were introduced based on limited observations in the literature to study possible consequences on the associated hemodynamics. Specifically, motivated by animal models of increased blood pressure/pulse pressure (Xu et al., 2000; Hu et al., 2008; Eberth et al., 2009; Hayenga, 2010), we studied the potential short-term effects of the abrupt creation of a 75 % coarctation in the human descending thoracic aorta.

Acknowledgements This work was supported by NIH grant HL-105297, the Benchmark Fellowship in Congenital Cardiovascular Engineering and the Vera Moulton Wall Center at Stanford University.

References

Arribas SM, Hinek A, Gonzalez MC (2006) Elastic fibres and vascular structure in hypertension. Pharmacol Ther 111:771–791

Coogan JS, Humphrey JD, Figueroa CA (2012) Computational simulations of hemodynamic changes within thoracic, coronary, and cerebral arteries following early wall remodeling in response to distal aortic coarctation. Biomech Model Mechanobiol (in press)

Dart AM, Kingwell BA (2001) Pulse pressure—a review of mechanisms and clinical relevance. J Am Coll Cardiol 37:975–984

Eberth JF, Gresham VC, Reddy AK, Popovic N, Wilson E, Humphrey JD (2009) Importance of pulsatility in hypertensive carotid artery growth and remodeling. J Hypertens 27:2010–2021

Eberth JF, Popovic N, Gresham VC, Wilson E, Humphrey JD (2010) Time course of carotid artery growth and remodeling in response to altered pulsatility. Am J Physiol, Heart Circ Physiol 299:1875–1883

Figueroa CA, Vignon-Clementel IE, Jansen KC, Hughes TJ, Taylor CA (2006) A coupled momentum method for modeling blood flow in three-dimensional deformable arteries. Comput Methods Appl Mech Eng 195:5685–5706

Figueroa CA, Baek S, Taylor CA, Humphrey JD (2009) A computational framework for fluid-solid-growth modeling in cardiovascular simulations. Comput Methods Appl Mech Eng 198:3583–3602

Gow BS, Hadfield CD (1979) The elasticity of canine and human coronary arteries with reference to postmortem changes. Circ Res 45:588–594

Guyton AC, Hall JE (eds) (2006) Textbook of medical physiology. Saunders, Philadelphia

Hayashi K, Hnada H, Nagasawa S, Okumura A, Moritake K (1980) Stiffness and elastic behaviour of human intracranial and extracranial arteries. J Biomech 13:175–184

Hayenga HN (2010) Mechanics of atherosclerosis, hypertension-induced growth, and arterial remodeling. Dissertation, Texas A&M University, TX

Hu J-J, Ambrus A, Fossum TW, Miller MW, Humphrey JD, Wilson E (2008) Time courses of growth and remodeling of porcine aortic media during hypertension: a quantitative immunohistochemical examination. J Histochem Cytochem 56:359–370

Humphrey JD (2002) Cardiovascular solid mechanics. Cells, tissues, and organs. Springer, New York

Kim HJ, Vignon-Clementel IE, Figueroa CA, LaDisa JF, Jansen KE, Feinstein JA, Taylor CA (2009a) On coupling a lumped parameter heart model and a three-dimensional finite element aorta model. Ann Biomed Eng 37:2153–2169

Kim T, Hwang W, Kamm RD (2009b) Computational analysis of a cross-linked actin-like network. Exp Mech 49:91–104

Kim HJ, Vignon-Clementel IE, Coogan JS, Figueroa CA, Jansen KE, Taylor CA (2010) Patient-specific modeling of blood flow and pressure in human coronary arteries. Ann Biomed Eng 38:3195–3209

Lakatta EG, Wang M, Najjar SS (2009) Arterial aging and subclinical arterial disease are fundamentally intertwined at macroscopic and molecular levels. Med Clin North Am 93:583–604

Moireau P, Xiao N, Astorino M, Figueroa CA, Chapelle D, Taylor CA, Gerbeau J-F (2012) External tissue support and fluid-structure simulation in blood flows. Biomech Model Mechanobiol 11:1–18

Nichols WW, O'Rourke MF (2005) McDonald's blood flow in arteries. Theoretical, experimental and clinical principles, 5th edn. Arnold, London, pp 73–97, Ch. 4

O'Rourke MF, Hashimoto J (2007) Mechanical factors in arterial aging: a clinical perspective. J Am Coll Cardiol 50:1–13

Pearson GD, Devereux R, Loeys B, Maslen C, Milewicz D, Pyeritz R, Ramirez F, Rifkin D, Sakai L, Svensson L, Wessels A, Van Eyk J, Dietz HC (National Heart, Lung, and Blood Institute), (National Marfan Foundation Working Group) (2008) Report of the National Heart, Lung, and Blood Institute and National Marfan Foundation Working Group on research in Marfan syndrome and related disorders. Circulation 118:785–791

Redheuil A, Yu W-C, Wu CO, Mousseaux E, de Cesare A, Yan R, Kachenoura N, Bluemke D, Lima JAC (2010) Reduced ascending aortic strain and distensibility: earliest manifestations of vascular aging in humans. Hypertension 55:319–326

Safar ME (2000) Pulse pressure, arterial stiffness, and cardiovascular risk. Curr Opin Cardiol 15:258–263

Safar ME (2010) Arterial aging-hemodynamic changes and therapeutic options. Nat Rev Cardiol 7:442–449

Safar ME, Boudier HS (2005) Vascular development, pulse pressure, and the mechanisms of hypertension. Hypertension 46:205–209

Sahni O, Muller J, Jansen KE, Shephard MS, Taylor CA (2006) Efficient anisotropic adaptive discretization of the cardiovascular system. Comput Methods Appl Mech Eng 195:5634–5655

Taylor SH, Donald KW (1960) Circulatory studies at rest and during exercise in coarctation of the aorta before and after operation. Br Heart J 22:117–139

Vignon-Clementel IE, Figueroa CA, Jansen KE, Taylor CA (2006) Outflow boundary conditions for three-dimensional finite element modeling of blood flow and pressure in arteries. Comput Methods Appl Mech Eng 195:3776–3796

Wolinsky H (1972) Long-term effects of hypertension on the rat aortic wall and their relation to concurrent aging changes. Morphological and chemical studies. Circ Res 30:301–309

Xu C, Zarins CK, Basiouny HS, Briggs WH, Reardon C, Glagov S (2000) Differential transmural distribution of gene expression for collagen types I and III proximal to aortic coarctation in the rabbit. J Vasc Res 37:170–182

Chapter 16
Patient-Specific Surgery Planning for the Fontan Procedure

Christopher M. Haggerty, Lucia Mirabella, Maria Restrepo, Diane A. de Zélicourt, Jarek Rossignac, Fotis Sotiropoulos, Thomas L. Spray, Kirk R. Kanter, Mark A. Fogel, and Ajit P. Yoganathan

Abstract For children born with single ventricle heart defects, the Fontan procedure (right heart bypass via connection of caval veins to pulmonary arteries) is the palliative procedure of choice. Previous research has demonstrated strong coupling

C.M. Haggerty · L. Mirabella · M. Restrepo · D.A. de Zélicourt · A.P. Yoganathan (✉)
Wallace H. Coulter School of Biomedical Engineering, Georgia Institute of Technology and Emory University, Atlanta, GA, USA
e-mail: ajit.yoganathan@bme.gatech.edu

C.M. Haggerty
e-mail: chaggerty3@gatech.edu

L. Mirabella
e-mail: lmirabella3@mail.gatech.edu

M. Restrepo
e-mail: mrestrepo3@gatech.edu

D.A. de Zélicourt
e-mail: diane.dezelicourt@gmail.com

J. Rossignac
College of Computing, Georgia Institute of Technology, Atlanta, GA, USA
e-mail: jarek@cc.gatech.edu

F. Sotiropoulos
Department of Civil Engineering, University of Minnesota, Minneapolis, MN, USA
e-mail: fotis@umn.edu

T.L. Spray · M.A. Fogel
Children's Hospital of Philadelphia, Philadelphia, PA, USA

T.L. Spray
e-mail: spray@email.chop.edu

M.A. Fogel
e-mail: fogel@email.chop.edu

K.R. Kanter
Children's Healthcare of Atlanta, Atlanta, GA, USA
e-mail: kkanter@emory.edu

G.A. Holzapfel, E. Kuhl (eds.), *Computer Models in Biomechanics*,
DOI 10.1007/978-94-007-5464-5_16,

between the geometric characteristics of the surgical construct and the resulting patient-specific hemodynamics, which may relate to the numerous chronic morbidities seen in these patients. The combination of medical imaging, computer graphics and computational fluid simulations has introduced a powerful new paradigm for these procedures: providing the means to model the various options and evaluate the resulting characteristics. This paper details these methodologies, their application to planning interventions, and their contributions to generalizable knowledge of Fontan hemodynamics.

16.1 Introduction

Single ventricle congenital heart defects are lethal if left untreated. The most common surgical intervention, known as the Fontan procedure, creates a right heart bypass by routing systemic venous return to the pulmonary arteries (Fontan and Baudet, 1971), creating the total cavopulmonary connection (TCPC) (de Leval et al., 1988). Despite acceptable operative outcomes, significant long-term complications are common, owing in part to the altered hemodynamics associated with Fontan physiology (Mair et al., 2001). Such complications include arrhythmias, ventricular dysfunction, exercise intolerance, protein-losing enteropathy, and pulmonary arteriovenous malformations (PAVM) (Gersony and Gersony, 2003).

Since its introduction, the TCPC has been the focus of large body of research in an effort to understand how the geometric characteristics of the surgical construct impact the hemodynamics within the connection (de Leval et al., 1996; Sharma et al., 1996; Migliavacca et al., 2003; de Zélicourt et al., 2005). With only one ventricle providing the driving pressure for both the systemic and pulmonary circulations, the general motivation and hypothesis behind such studies are that minimizing the hemodynamic power loss across the connection will provide long-term benefits for cardiovascular health. While many early studies relied on relatively simple models of idealized geometries, the current state-of-the-art employs patient-specific data for both the anatomic and physiologic boundary conditions for computational fluid solvers.

Through such advances, in conjunction with progress in computer science and free-form shape editing, it is now possible to both design and evaluate patient-specific TCPC models (Pekkan et al., 2008). In other words, these engineering tools can be used for prospective surgical planning by modeling any number of possible anatomic variations and characterizing their associated hemodynamics. The applications of such methods extend equally well to either a patient's initial Fontan procedure or, as shown by Sundareswaran et al. (2009a) and de Zélicourt et al. (2011), any subsequent surgical revisions, perhaps necessitated by deteriorating physiology (i.e., Fontan failure). As such, these techniques represent a powerful new paradigm for the approach to Fontan surgery and cardiothoracic surgery as a whole. The objective of this work is to detail the underlying methods and techniques upon which surgical planning builds. Different examples of each method are provided throughout to demonstrate their utility.

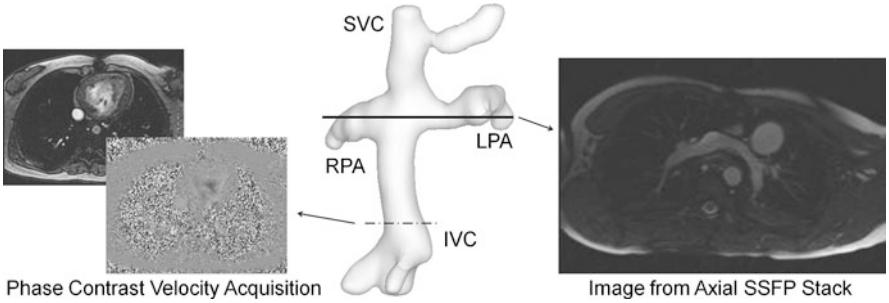

Fig. 16.1 Examples of typically acquired CMR images in relation to a patient-specific TCPC reconstruction (*central panel*). *Left*: magnitude and phase velocity images through the IVC. *Right*: axial steady-state free precession (SSFP) anatomic image through the right and left pulmonary arteries (RPA, LPA); SVC: superior vena cava

16.2 Methods and Results

The fundamental components of the current surgical planning procedure are the following: (i) cardiovascular magnetic resonance (CMR) image acquisition and reconstruction; (ii) virtual surgery, (iii) computational fluid dynamic (CFD) simulations.

16.2.1 CMR Imaging and Image Processing

Medical imaging provides the patient-specific anatomy and boundary conditions that inform the rest of the modeling. CMR is the preferred modality as it provides the means to both image the anatomic structures and make quantitative measurements of blood flow through variations in the sequence of magnetic field excitation. Figure 16.1 shows examples of these various image types in the context of the TCPC. The right image is taken from an axial stack of steady-state free precession images spanning the thorax. Here, the blood pool in the vessels produces a signal (without the use of a contrast agent), facilitating anatomical reconstruction (Frakes et al., 2005). The left set of images shows an instantaneous through-plane phase contrast measurement in a slice through the inferior vena cava (IVC). By acquiring such 2D images through each of the TCPC vessels, the local velocity fields (inlet/outlet boundary conditions) can be measured (Sundareswaran et al., 2009b).

These acquisitions provide the minimum information required to perform the subsequent anatomic and fluid mechanical modeling; however, advances in CMR sequence designs and image processing have provided additional means to directly assess *in vivo* flow patterns (Sundareswaran et al., 2012). Specifically, phase contrast sequences can be expanded to acquire three orthogonal components of the velocity vectors on a single slice; furthermore, the vector values between the slices can be interpolated using a novel divergence-free scheme. Therefore, a stack of such images spanning the TCPC can provide detailed 4D hemodynamic information throughout

the entire volume. As indicated by the recent work of Sundareswaran et al. (2012), these methods of 4D *in vivo* flow visualization and quantification have significant clinical potential. When acquired and analyzed over a larger series of patients, the results can be used to provide insights on a more generalizable level, such as the hemodynamic implications of different approaches to Fontan surgery (extra- vs. intra-cardiac) or the accuracy of computational fluid solvers for analyzing the same flow conditions. The increased availability of these 4D flow imaging sequences, and the development of volumetric phase contrast techniques (Markl et al., 2011), will make such analyses possible on a much broader scale in the near future.

Furthermore, for failing patients referred for surgical planning, these imaging techniques can be an invaluable means to directly identify adverse hemodynamic characteristics, as demonstrated in the following case study.

16.2.1.1 Patient-Specific Case Study

This was an eleven year old patient with bilateral superior vena cavae (SVC), interrupted IVC and azygos vein continuation, and a previous Fontan connection. In this rare and complex anatomy, the majority of inferior venous blood flow is carried by an enlarged azygos vein, which connects to one of the two SVCs. The Fontan baffle therefore carries only hepatic blood from the liver to the pulmonary arteries. Hemodynamic analysis was necessitated by the presence of PAVM in the right lung: arterial to venous shunts within the pulmonary vasculature that bypass the oxygenating alveolar beds, leading to progressive hypoxia. Studies suggest that this condition can develop because of a lack of hepatic blood flow, and a so-called 'hepatic factor', to either or both lungs (Duncan and Desai, 2003). This strong and well-characterized relationship between PAVM and the local TCPC hemodynamics has made it the primary indication in the preliminary series ($n = 15$) of patient-specific surgical planning; identifying connection designs that achieve a balanced hepatic flow distribution (HFD) has been shown to be effective in alleviating the disease state. Therefore, the objective of the analysis was to (i) confirm the unilateral distribution of hepatic flow from the liver, which is consistent with PAVM in the right lung; (ii) determine the factors mediating such undesirable hemodynamics.

Figure 16.2 (left panel) provides a single slice example of the coronal 4D MRI data acquired: the magnitude image is shown on top and the three orthogonal vector components (anatomically: anterior-posterior, foot-head, left-right) are shown at the bottom. The results from the volumetric interpolation are also shown (right panel) as instantaneous velocity streamlines, shaded based on the vessel of origin (LSVC flow omitted). The overlaid numbers report the time-averaged contribution of each vessel to the total flow, as determined from analysis of the through-plane phase contrast data.

From the reconstructed velocity field, it was appreciated that flow through the left-sided hepatic venous baffle (HepV; blue streamlines) was both very low in magnitude and heavily influenced by the momentum of the RSVC and Azygos (Azy)

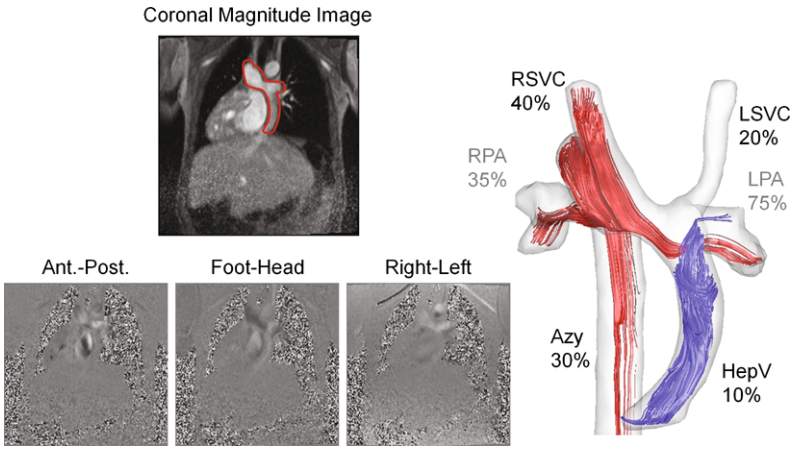

Fig. 16.2 *Left panel*: magnitude (*top*) and 3D phase contrast velocity (*bottom*) images for a single slice and cardiac phase from the coronal stack acquired. The TCPC is outlined in the magnitude image for reference. *Right panel*: TCPC reconstruction with instantaneous velocity streamlines from the 4D interpolation. Overlaid numbers represent time-averaged percentage contribution for each vessel to the total venous return. Azy-Azygos vein; HepV-Hepatic venous baffle

flows (red streamlines), which comprised 70 % of the total volume flow rate. Furthermore, only 35 % of flow through the connection exited the RPA, meaning that a significant portion of the RSVC + Azy flow had to traverse the connection to exit the LPA. This analysis is consistent with the right-to-left path of some of the red streamlines seen in Fig. 16.2, which influenced the hepatic streamlines and forced a unilateral (left) hepatic distribution, consistent with right-sided PAVM. Based on these observations, which were made possible by the ability to visualize the *in vivo* flow structures, it is evident that a successful surgical revision of this connection to address the PAVM must overcome: low momentum hepatic flow, high momentum superior venous flows, and potentially unfavorable results of their direct interaction.

16.2.2 Virtual Surgery

The use of CMR anatomical data to produce patient-specific models for detailed computational and/or experimental analyses has been a standard practice for the past decade (Frakes et al., 2003; de Zélicourt et al., 2005). However, such techniques can only measure and characterize the current physiology; to prospectively create connections in a realistic way to explore 'what if' scenarios required additional developments from the field of computer vision. To this end, a virtual interface was developed that allowed the user to import patient-specific anatomical reconstructions (e.g., the TCPC, single ventricle and atria, aorta, pulmonary veins) and mimic surgical gestures in the placement and deformation of the IVC baffle using free-form haptic devices (Pekkan et al., 2008). Thus, for a given patient anatomy: the size and

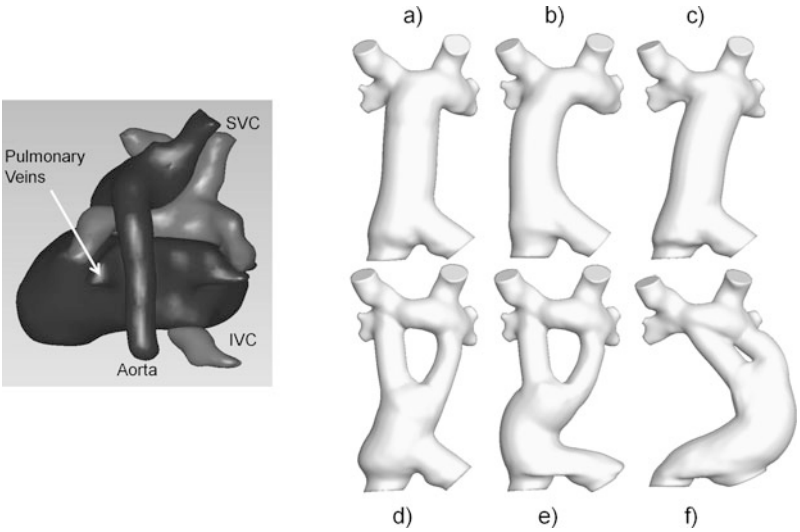

Fig. 16.3 *Left panel*: example of reconstructed TCPC and surrounding anatomy to be imported into virtual surgery interface for simulation of Fontan completion (IVC baffle to PA). *Right panel*: virtual options designed for a patient with bilateral SVCs and distinct atrial connections for the IVC and hepatic vein. Variations in IVC connection type (single baffle vs. Y-graft), baffle offset with respect to the PAs, and means of unifying IVC and hepatic flows are demonstrated

shape of the PAs, the orientation of the SVC-PA junction, and the size and location of surrounding anatomical structures, all potential options for the size and placement of the IVC baffle can be explored and generated in advance of the surgical procedure.

Figure 16.3 (left side) shows an example of the patient-specific reconstructions that are frequently incorporated into the virtual surgery interface. It is critical that surrounding structures, not simply the TCPC vessels, be included so as to visually provide the constraints and the relevant landmarks that surgeons rely on in the operating room. Otherwise, designing the connection 'in a vacuum' may yield unrealistic results. The right side of Fig. 16.3 provides a series of connections designed for a single patient with bilateral SVCs and separate IVC and hepatic connections to the atrium (prior to Fontan completion). These images serve to both demonstrate the capabilities of the software and emphasize its utility. In such complex anatomical configurations, it is possible to parametrically vary connection approach (top row vs. bottom row), baffle placement (a vs. b vs. c) or angle, and other patient-specific considerations: in this case, the means of joining the hepatic and IVC flows (a–d vs. e–f). Given that the examples shown are all reasonable approximations of the way in which any given surgeon might approach the connection of such a patient, the ability to both identify such options and, as detailed in the follow section, characterize the hemodynamic consequences a priori is a valuable asset.

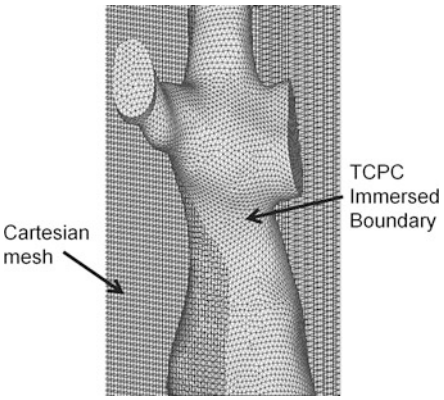

Fig. 16.4 Registration of TCPC surface mesh (*light gray*) within regular, background Cartesian grid

16.2.3 Computational Fluid Dynamics

The final critical component of the surgical planning tool set is the means to predict hemodynamic outcomes for all virtually designed connection options. For this, computational fluid dynamics (CFD) solvers play a central role. The subsequent sections provide descriptions of the important considerations inherent to such modeling, followed by selected results from preliminary experiences.

16.2.3.1 Solver Description

It is important to note that any validated computational fluid solver can be used to yield the needed results for these analyses; however, the program presently described has the advantage of simplifying the process of generating the discretized computational mesh. In cases where there are a large number of possible anatomic solutions to evaluate, this advantage is non-trivial.

The solver is based on the sharp-interface immersed boundary approach of Gilmanov and Sotiropoulos (2005). This method, rather than requiring a dense, high quality mesh of volume elements throughout the computational domain, only requires the boundary (i.e., the walls of the TCPC) to be discretized with two-dimensional triangular elements. This surface is then immersed and registered within a regular Cartesian grid (Fig. 16.4) to be segregated into fluid nodes (those falling within the boundaries), 'immersed boundary' (IB) nodes (nodes within the boundaries but immediately adjacent to the sharp-interface of the wall), and wall nodes (those external to the boundary). The 3D, unsteady incompressible Navier-Stokes equations must then only be solved on the internal fluid nodes (discretized in a hybrid staggered/non-staggered layout), with the wall boundary conditions (typically, the no-slip condition), imposed iteratively on the IB nodes. As described by de Zélicourt et al. (2009) this method is further simplified by recasting the problem into an unstructured Cartesian grid to reduced the required memory overhead of the discarded wall nodes.

16.2.3.2 Boundary Conditions

From the CMR analysis, specifically the through-plane phase contrast images, time-varying flow conditions across the cardiac cycle are known for all TCPC vessels of interest. The standard practice of TCPC simulations with this IB solver is to impose these flows (either as time-averaged or time-varying flat velocity profiles) at the inlets and the prescribed flow split at the outlets of the computational domain. Surgical modeling simulations present the additional challenge of physiologic changes (perhaps both acute and chronic) in the rest of the circulatory system in response to Fontan surgery. The work of Fogel et al. (1996) indicates that such changes have an impact on the cardiac output and thus systemic venous flows; the impact on the pulmonary vasculature and/or distribution has only be reported in a single patient case (Pennati et al., 2011) demonstrating unanticipated variations. In other words, simply imposing the measured flow conditions on the surgical model is unlikely to sufficiently represent the post-operative state.

There are thus several strategies that have been employed to combat this challenge. First is the parametric variation of the outflow distributions imposed: if a 60 %/40 % RPA/LPA distribution was measured pre-operatively, the proposed options might also be evaluated at 40/60, 50/50, and 70/30 to simulate possible outflow distributions. The finite and physiologically bounded nature of this parameter space facilitates these variations. The primary guide in making such determinations is the presence and hypothesized evolution of PAVMs in the given patient. For example, a presumed decrease in the number of malformations present would increase the effective vascular resistance of the pulmonary beds, leading to a decrease in local flow. Additionally, natural growth and development is likely to vary the relative distribution of pulmonary flows over the life of the patient, so identifying solutions that are robustly able to handle such variation is desirable.

Similarly, the inflow conditions can be selectively varied, both with respect to bulk flow rates and relative vessel distributions. However, it is important to note that the parameter space for the inlet values may not be as well constrained as the outlets, both with respect to magnitude and distribution variations, particularly as the number of inlet vessels increases (such as cases like in Fig. 16.2). Furthermore, the factors that mediate such changes, either at the level of the ventricular output or the relative compliances of the systemic vascular bed, are not as easy to define or predict, and no data yet exist in the literature to set a precedent.

Significant research and ongoing development efforts are focused on the use of multi-dimensional models to create a comprehensive view of the cardiovascular circuit (Laganà et al., 2005; Migliavacca et al., 2006; Kim et al., 2009). That is, the three-dimensional CFD domain is coupled with 0-dimensional lumped parameter models to capture the global hemodynamics. This multi-dimensional approach may address some of the limitations of prospective modeling efforts by providing a more rigorous means of determining the post-operative boundary conditions, particularly for the inlets. Of course, validation of such models will be critical and, as the work of Pennati et al. (2011) demonstrates, lumped parameter models alone may not be sufficient for capturing the range of possible patient-specific responses.

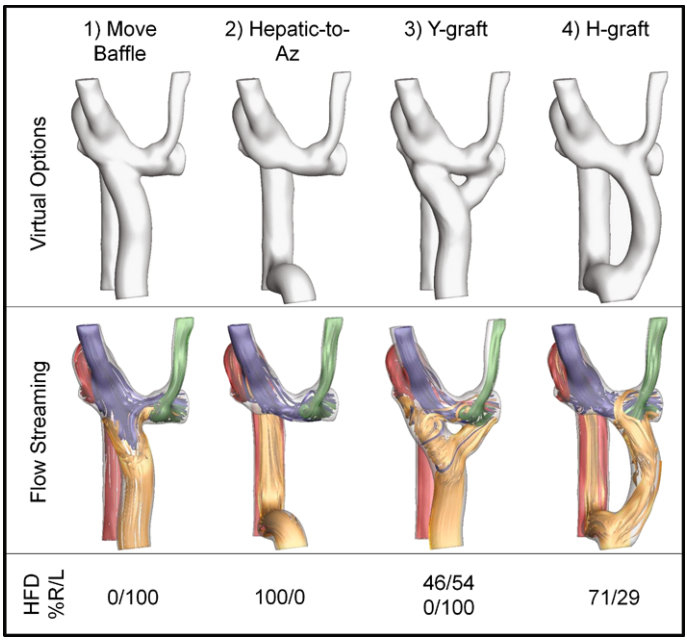

Fig. 16.5 *Top row*: a subset of the surgical models created for a failing patient with right lung PAVM. *Middle row*: flow streaming results (hepatic flow represented by gold streamlines) under equal pulmonary outflow conditions. *Bottom row*: quantitative flow distribution results as a percentage of hepatic flow exiting the right (R) or left (L) pulmonary artery. For option 3, the results of two possible variations on the same topology are shown

16.2.3.3 Patient-Specific Case Study

Returning to the patient case detailed in Sect. 16.2.1.1, Fig. 16.5 details a subset of the virtual surgical options created and their associated flow streaming results. The investigated options were intended to assess the impact of: (i) repositioning the hepatic baffle (option 1); (ii) merging the hepatic flow with another vessel to promote mixing (option 2); or (iii) bifurcating the hepatic flow laterally to either side of the connection (options 3 and 4). The gold streamlines in the middle row of Fig. 16.5 show the hepatic flow streaming results for each of these options with the quantitative results shown in the bottom row in terms of the percentage of hepatic flow perfusing the right or left pulmonary artery.

The results reveal substantial sensitivity of the flow streaming characteristics to the surgical baffle placement, underscoring both the significant challenge in surgically treating this particular patient, as well as the tremendous value of this modeling work in providing such information to the clinician. For option 1, simply repositioning the hepatic baffle closer to the RPA was shown to provide no benefit to hepatic-RPA flow because of the relative dominance of the RSVC and Azygos flows (blue streamlines seen impinging into the hepatic baffle). On the other hand, option 2 reached the opposite extreme in that all hepatic flow went to the RPA (by way of

the azygos vein). While this outcome would be acutely positive in addressing the right-sided PAVM, it is not a desirable long-term result as it presents a risk of future left lung PAVM development. Two different HFD values are provided for option 3 because multiple Y-graft designs were created and evaluated, with the right branch of the bifurcation being positioned slightly further to the right in one case (46 %) than the other (0 %). This drastic difference in potential outcome made such an approach undesirable given the uncertainty in how precisely the surgeon can mimic the virtual model in the operating room (i.e., the option was not robust with respect to the exact detail of surgical implementation). Finally, option 4 took an alternative approach to flow bifurcation by routing the right branch to the azygos vein (similar to option 2) while maintaining the original hepatic connection to provide flow to the left lung. Of the options tested, this design was predicted to yield the best outcome (71 % HFD to the RPA with a 50/50 outflow split of the total flow imposed as the boundary condition), presumably because it was successfully able to avoid direct competition between the low momentum hepatic flow and high momentum SVC/azygos flows. This 'H-graft' connection was ultimately selected for surgical implementation and, although no post-operative image data are available, arterial oxygen saturations were clinically seen to improve from 70 to 87 % four months post-operatively, which is indicative of regression of the PAVM, as predicted.

16.3 Conclusions

Through multi-disciplinary research collaborations and technological developments, image-based computational surgery planning for the Fontan procedure has become a reality. This ability greatly increases the resources available to clinicians in patient-specific decision making by supplementing intuition and experience with modeled predictions tailored to the specific case and intervention of interest. Obviously, these techniques have potential to extend far beyond Fontan surgery into the broader realm of cardiovascular procedures, but to do so requires a similar understanding of the specific hemodynamic end points that mediate the desired clinical outcome (as HFD relates to PAVM). Furthermore, surgical planning for the Fontan is still in its preliminary stages and much work remains to be done, perhaps most importantly, developing and validating the means of predicting what the post-operative boundary conditions will be. Nevertheless, the novelty and value of these techniques in translating engineering principles into actionable clinical tools are clear and the present an exciting new paradigm for cardiothoracic modeling and interventions.

Acknowledgements This work was supported by the National Heart, Lung, and Blood Institute through Grants HL67622 and HL098252, and through American Heart Association Pre-Doctoral Fellowships.

References

de Leval MR, Kilner P, Gewillig M, Bull C (1988) Total cavopulmonary connection: a logical alternative to atriopulmonary connection for complex Fontan operations. Experimental studies and early clinical experience. J Thorac Cardiovasc Surg 96:682–695

de Leval MR, Dubini G, Migliavacca F, Jalali H, Camporini G, Redington A, Pietrabissa R (1996) Use of computational fluid dynamics in the design of surgical procedures: application to the study of competitive flows in cavopulmonary connections. J Thorac Cardiovasc Surg 111:502–513

de Zélicourt DA, Pekkan K, Wills L, Kanter KR, Forbess J, Sharma S, Fogel MA, Yoganathan AP (2005) In vitro flow analysis of a patient-specific intraatrial total cavopulmonary connection. Ann Thorac Surg 79:2094–2102

de Zélicourt DA, Ge L, Wang C, Sotiropoulos F, Gilmanov A, Yoganathan AP (2009) Flow simulations in arbitrarily complex cardiovascular anatomies—an unstructured Cartesian grid approach. Comput & Fluids 38:1749–1762

de Zélicourt DA, Haggerty CM, Sundareswaran KS, Whited BS, Rossignac JR, Kanter KR, Gaynor JW, Spray TL, Sotiropoulos F, Fogel MA, Yoganathan AP (2011) Individualized computer-based surgical planning to address pulmonary arteriovenous malformations in patients with a single ventricle with an interrupted inferior vena cava and azygous continuation. J Thorac Cardiovasc Surg 141:1170–1177

Duncan BW, Desai S (2003) Pulmonary arteriovenous malformations after cavopulmonary anastomosis. Ann Thorac Surg 76:1759–1766

Fogel MA, Weinberg PM, Chin AJ, Fellows KE, Hoffman EA (1996) Late ventricular geometry and performance changes of functional single ventricle throughout staged Fontan reconstruction assessed by magnetic resonance imaging. J Am Coll Cardiol 28:212–221

Fontan F, Baudet E (1971) Surgical repair of tricuspid atresia. Thorax 26:240–248

Frakes DH, Conrad CP, Healy TM, Monaco JW, Fogel MA, Sharma S, Smith MJ, Yoganathan AP (2003) Application of an adaptive control grid interpolation technique to morphological vascular reconstruction. IEEE Trans Biomed Eng 50:197–206

Frakes DH, Smith MJ, Parks WJ, Sharma S, Fogel MA, Yoganathan AP (2005) New techniques for the reconstruction of complex vascular anatomies from MRI images. J Cardiovasc Magn Reson 7:425–432

Gersony DR, Gersony WM (2003) Management of the postoperative Fontan patient. Prog Ped Cardiol 17:73–79

Gilmanov A, Sotiropoulos F (2005) A hybrid Cartesian/immersed boundary method for simulating flows with 3D, geometrically complex, moving bodies. J Comput Phys 207:457–492

Kim HJ, Vignon-Clementel IE, Figueroa CA, LaDisa JF, Jansen KE, Feinstein JA, Taylor CA (2009) On coupling a lumped parameter heart model and a three-dimensional finite element aorta model. Ann Biomed Eng 37:2153–2169

Laganà K, Balossino R, Migliavacca F, Pennati G, Bove EL, de Leval MR, Dubini G (2005) Multiscale modeling of the cardiovascular system: application to the study of pulmonary and coronary perfusions in the univentricular circulation. J Biomech 38:1129–1141

Mair DD, Puga FJ, Danielson GK (2001) The Fontan procedure for tricuspid atresia: early and late results of a 25-year experience with 216 patients. J Am Coll Cardiol 37:933–939

Markl M, Geiger J, Kilner PJ, Foll D, Stiller B, Beyersdorf F, Arnold R, Frydrychowicz A (2011) Time-resolved three-dimensional magnetic resonance velocity mapping of cardiovascular flow paths in volunteers and patients with Fontan circulation. Eur J Cardiothorac Surg 39:206–212

Migliavacca F, Dubini G, Bove E, de Leval MR (2003) Computational fluid dynamics simulations in realistic 3-D geometries of the total cavopulmonary anastomosis: the influence of the inferior caval anastomosis. J Biomech Eng 125:803–813

Migliavacca F, Balossino R, Pennati G, Dubini G, Hsia TY, de Leval MR, Bove E (2006) Multiscale modelling in biofluidynamics: application to reconstructive paediatric cardiac surgery. J Biomech 39:1010–1020

Pekkan K, Whited B, Kanter KR, Sharma S, de Zélicourt DA, Sundareswaran KS, Frakes DH, Rossignac J, Yoganathan AP (2008) Patient-specific surgical planning and hemodynamic computational fluid dynamics optimization through free-form haptic anatomy editing tool (SURGEM). Med Biol Eng Comput 46:1139–1152

Pennati G, Corsini C, Cosentino D, Hsia TY, Luisi VS, Dubini G, Migliavacca F (2011) Boundary conditions of patient-specific fluid dynamics modelling of cavopulmonary connections: possible adaptation of pulmonary resistances is a critical issue for virtual surgical planning. Interface Focus 1:297–307

Sharma S, Goudy S, Walker P, Panchal S, Ensley A, Kanter KR, Tam V, Fyfe D, Yoganathan AP (1996) In vitro flow experiments for determination of optimal geometry of total cavopulmonary connection for surgical repair of children with functional single ventricle. J Am Coll Cardiol 27:1264–1269

Sundareswaran KS, de Zélicourt DA, Sharma S, Kanter KR, Spray TL, Rossignac J, Sotiropoulos F, Fogel MA, Yoganathan AP (2009a) Correction of pulmonary arteriovenous malformation using image-based surgical planning. JACC Cardiovasc Imaging 2:1024–1030

Sundareswaran KS, Frakes DH, Fogel MA, Soerensen D, Oshinski JN, Yoganathan AP (2009b) Optimum fuzzy filters for phase-contrast magnetic resonance imaging segmentation. J Magn Reson Imaging 29:155–165

Sundareswaran KS, Haggerty CM, de Zélicourt DA, Dasi LP, Pekkan K, Frakes DH, Powell AJ, Kanter KR, Fogel MA, Yoganathan AP (2012) Visualization of flow structures in Fontan patients using three-dimensional phase contrast magnetic resonance imaging. J Thorac Cardiovasc Surg 143:1108–1116

Part IV
Multiphasic Models

Chapter 17
Finite Element Modeling of Solutes in Hydrated Deformable Biological Tissues

Gerard A. Ateshian and Jeffrey A. Weiss

Abstract A broad range of biological processes result from a combination of passive (non-reactive) and active processes involving solvent and solutes, and the ability to model such processes in a general continuum framework represents an important tool for biomedical engineers and scientists. Yet, computational tools for modeling solute transport in neutral and charged deformable media are not widely available. In recent years, FEBio has been introduced as an open source finite element program in the public domain (www.febio.org), whose purpose is to provide such computational tools for the analysis of biological mixtures consisting of a porous deformable solid matrix and interstitial solvent and solutes. This article summarizes the background literature on this topic and describes the governing equations and some of the features of mixture analyses in FEBio.

17.1 Introduction

Most biological tissues are highly hydrated and their interstitial fluid contains a variety of inorganic and organic solutes. These solutes represent a broad range of constituents, such as nutrients, waste products, cytokines, and the building blocks of intracellular structures or extracellular matrix. At a fundamental level, most biological processes evolve from chemical reactions among various constituents of cells and tissues, and these chemical reactions generally involve any number of solutes. For example, cell and tissue metabolism, growth and degradation processes, active transport of solutes, active muscle contraction, mechanobiology, etc., represent broad categories of phenomena that involve the interaction of solutes with cell and tissue matrix constituents via reactive processes.

G.A. Ateshian (✉)
Columbia University, New York, NY 10027, USA
e-mail: ateshian@columbia.edu

J.A. Weiss
University of Utah, Salt Lake City, UT 84112, USA
e-mail: jeff.weiss@utah.edu

G.A. Holzapfel, E. Kuhl (eds.), *Computer Models in Biomechanics*,
DOI 10.1007/978-94-007-5464-5_17,

Passive processes involving solutes may also contribute significantly to the mechanics of biological tissues. Solutes are often charged and their transport through the tissue's porous solid matrix may be influenced by electrical charges fixed to this matrix. Depending on their concentration and charge, solutes may significantly influence the osmotic pressure of the interstitial fluid. In turn, this osmotic pressure can produce significant deformation of the tissue's solid matrix, demonstrating significant coupling of mechanochemical and mechanoelectrochemical phenomena. Large solute concentration gradients may induce significant flow of the solvent, a process known as osmosis. Charged solutes can also induce electrical potentials and carry electrical currents, or be driven by externally applied potentials or currents.

A broad range of biological processes thus result from a combination of passive (non-reactive) and active processes involving solvent and solutes, and the ability to model such processes in a general continuum framework represents an important tool for biomedical engineers and scientists. Yet, computational tools for modeling solute transport in neutral and charged deformable media are not widely available. In recent years, FEBio (Maas et al., 2012) has been introduced as an open source finite element program in the public domain (www.febio.org), whose purpose is to provide such computational tools for the analysis of biological mixtures consisting of a porous deformable solid matrix and interstitial solvent and solutes. This article summarizes the background literature on this topic and describes the governing equations and some of the features of mixture analyses in FEBio.

17.1.1 Solutes in Porous Media with Non-reactive Processes

In biomechanics, the study of interstitial fluid transport in deformable porous solids evolved from the mechanics of porous media, such as the consolidation theory derived from the work of Fillunger (1913), von Terzaghi (1933) and Biot (1941), and the biphasic theory of Mow et al. (1980), derived from the mixture theory of Truesdell (1960) and Bowen (1976). The biphasic theory has been applied to the study of creep and stress-relaxation responses of biological tissues under testing configurations such as confined (Mow et al., 1980) and unconfined (Armstrong et al., 1984; Cohen et al., 1998) compression, indentation (Mow et al., 1989; Athanasiou, 1991), and permeation (Lai and Mow, 1980) for the purpose of extracting material properties such as equilibrium modulus and hydraulic permeability. Biphasic contact analyses have been used to analyze articular contact mechanics in diarthrodial joints (Ateshian et al., 1994; Ateshian and Wang, 1995). Mixture and consolidation theories have also been used in the study of interstitial fluid transport in skin (Oomens et al., 1987), bone (Cowin, 1999), and cardiovascular tissues (Kenyon, 1976; Yang et al., 1994).

Electrokinetic phenomena were subsequently coupled with a porous media framework in the theory of Frank and Grodzinsky (1987a), by incorporating an equation relating the electric current density to gradients in electric potential and fluid pressure. Their framework was used to analyze phenomena such as streaming potentials and current-induced stresses in cartilage (Frank and Grodzinsky, 1987b).

In 1991, Lai and co-workers introduced their triphasic theory (Lai et al., 1991) to model mechanoelectrochemical phenomena in biological tissues. This framework, also based on mixture theory, explicitly modeled the charged solid matrix, neutral interstitial solvent, and two interstitial monovalent counter-ions, thus representing one of the earliest explicit models of solute transport in deformable porous media. The triphasic theory has been applied to the study of a variety of biological tissues, including articular cartilage, intervertebral disc, cornea, aorta, and brain. This framework has served as the basis for other related theories of swelling and charged solute transport in biological tissues (Huyghe and Janssen, 1997; Gu et al., 1998).

Mechanochemical phenomena associated with neutral solutes in porous deformable media may also be examined with mixture theory, as shown in the biphasic-solute framework of Mauck et al. (2003), which explicitly coupled the frictional interactions of the solute with the tissue's solid matrix and interstitial solvent. When adapted to semi-permeable membrane transport, this theory reproduced (Ateshian et al., 2006) the classical framework of Kedem and Katchalsky (1958). Biphasic-solute theory has been used to model the response of gels (Albro et al., 2007) and cells (Albro et al., 2009a) subjected to a change in their osmotic environment. This framework has also demonstrated that dynamic loading of a porous tissue may pump solute from a surrounding bath (Albro et al., 2008, 2010, 2011).

17.1.2 Finite Element Models for Solutes in Porous Media

Finite element implementations of charged porous media have been presented by several authors, which are applicable to infinitesimal deformations (Simon et al., 1996; Frijns et al., 1997; Sun et al., 1999; Kaasschieter et al., 2003; Yao and Gu, 2007; Magnier et al., 2009) and finite deformations (van Loon et al., 2003). Other investigators have used the analogy between thermal diffusion and solute transport to simulate a triphasic medium under infinitesimal deformation (Wu and Herzog, 2002), or have constrained their finite element analyses to modeling the equilibrium response to Donnan osmotic swelling under finite deformation (Azeloglu et al., 2008; Ateshian et al., 2009). The neutral transport of solutes in porous deformable media was addressed by Sengers et al. (2004), who formulated a finite element implementation of a biphasic (uncharged) medium, undergoing finite deformation, with solute transport and biosynthesis. Steck et al. (2003) and Zhang and Szeri (2005) used a commercial finite element code to combine mass (solute) transport with a poroelastic analysis using a two-stage solution procedure.

Recently, we developed a finite element implementation of neutral solute transport in deformable porous media that incorporated a number of important phenomena at the interface of mechanics and physical chemistry (Ateshian et al., 2011): (i) Solvent and neutral solute transport in deformable anisotropic media, including strain-induced alterations in permeability and diffusivity, and strain-induced anisotropy (Ateshian and Weiss, 2010). (ii) Momentum exchange between solutes and the solid matrix, which is responsible for increased hindrance to transport

(Deen, 1987; Mackie and Meares, 1955) as well as enhanced convection under dynamic loading (Mauck et al., 2003; Albro et al., 2008). (iii) Changes in tissue and cell volume due to alterations in their osmotic environment (Albro et al. 2007, 2009a). (iv) Partial solute exclusion from pore spaces due to steric volume and short-range electrostatic effects (Albro et al., 2009a), which may depend on solid matrix deformation and solute concentration (Lazzara and Deen, 2004; Albro et al., 2009b). (v) Deviation of the physicochemical responses of solutions from ideal behavior with varying solute concentration and solid matrix deformation. These features were incorporated into FEBio, under a framework described as a biphasic-solute material. This framework has now been extended to also include triphasic materials (Lai et al., 1991), as described below.

17.2 Mixture Models for Solutes in Porous Media

Mixture theory is able to describe the interaction of any number of solid of fluid constituents. Solutes may be modeled as fluid constituents in a mixture that also contains a porous solid and a solvent; when sufficiently dilute, the volume fraction of solutes may be neglected relative to that of the solid and solvent. In mixture theory, the axioms of mass balance and momentum balance must be satisfied for each constituent. Interactions among the constituents are represented by supply terms that represent exchanges of mass or momentum. In the mass balance equation, mass supplies occur only when chemical reactions take place among the mixture constituents which produce mass exchanges between reactants and products (Eringen and Ingram, 1965). In the linear momentum balance equation, momentum supplies may represent a combination of passive mechanisms, such as friction between constituents, and active mechanisms such as momentum supply from motors (Bowen, 1976; Ateshian et al., 2010).

In most applications of mixture theory for biological tissues, it has been assumed that each constituent of the mixture is intrinsically incompressible (Mow et al., 1980; Bowen, 1980; Lai et al., 1991). This assumption implies that the true density of each constituent is invariant in space and time, though heterogeneous mixtures may exhibit a spatial variation in mixture density. A saturated mixture of intrinsically incompressible constituents does not change in volume when subjected to a hydrostatic pressure. However, when a mixture includes a porous solid matrix, a material region defined on this solid may change in volume as fluid enters or leaves the pore space, depending on loading and boundary conditions.

One of the challenges of presenting mixture models is the choice of notation and the variety of ways that dependent variables describing the state of the mixture may be represented. Part of this challenge arises from the fact that mixture theory combines the classical fields of fluid mechanics, solid mechanics and chemistry. Each of these fields may have a preferred representation for the functions of state. Another challenge arises from the fact that intensive variables may be normalized in different, but equally valid ways when dealing with a mixture of multiple constituents.

For example, consider a mixture consisting of any number of constituents α. The *true density* of a specific constituent, ρ_T^α, represents the mass $\mathrm{d}m^\alpha$ of α, per volume $\mathrm{d}V^\alpha$ of α, in an elemental region $\mathrm{d}V$; thus, $\rho_T^\alpha = \mathrm{d}m^\alpha/\mathrm{d}V^\alpha$. The true density is an intrinsic property of constituent α. In a saturated mixture, the volume of the elemental region is the sum of the constituent volumes, $\mathrm{d}V = \sum_\alpha \mathrm{d}V^\alpha$. Therefore, it is also possible to define the *apparent density* of constituent α as $\rho^\alpha = \mathrm{d}m^\alpha/\mathrm{d}V$. The apparent density represents a measure of the relative content of α in the mixture. An alternative measure of relative content is the *volume fraction* $\varphi^\alpha = \mathrm{d}V^\alpha/\mathrm{d}V$. This measure is most useful when constituents are intrinsically incompressible, in which case $\rho^\alpha = \varphi^\alpha \rho_T^\alpha$; ρ^α and φ^α may be used interchangeably since ρ_T^α is invariant in that case. In a saturated mixture, the volume fractions satisfy $\sum_\alpha \varphi^\alpha = 1$; if the volume fraction of solutes is negligible, this relation reduces to $\varphi^s + \varphi^w \approx 1$, where $\alpha = s$ represents the porous solid matrix and $\alpha = w$ represents the solvent. Another common measure of relative content, normally used for solutes, is the *molar concentration* c^α, defined as the number of moles $\mathrm{d}n^\alpha$ in the elemental region, per volume of the solution; thus, $c^\alpha = \mathrm{d}n^\alpha/(\mathrm{d}V - \mathrm{d}V^s)$. Since the molar mass of α is defined as $M^\alpha = \mathrm{d}m^\alpha/\mathrm{d}n^\alpha$ (an invariant property), it follows that $\rho^\alpha = (1-\varphi^s)M^\alpha c^\alpha \approx \varphi^w M^\alpha c^\alpha$. Many classical relations from chemistry employ c^α as measure of solute content; some applications in bone mechanics employ ρ^s to describe trabecular bone density; and applications in cartilage mechanics use φ^s in the formulation of various constitutive relations. Other measures of relative content are also commonly used (e.g., molality, molar fraction, or mass fraction for solute content); thus, users of mixture theory must be comfortable switching among these various measures, depending on the needs of a particular analysis.

The motion of each constituent α of a mixture is given by $\boldsymbol{\chi}^\alpha(\mathbf{X}^\alpha, t)$, where $\boldsymbol{\chi}^\alpha$ represents the position at time t of a material point initially located at $\mathbf{X}^\alpha$. The velocity of α is given by $\mathbf{v}^\alpha = \partial \boldsymbol{\chi}^\alpha/\partial t$. In biological tissues, the mixture includes a solid matrix and the boundaries of the tissue are normally defined on that solid. Therefore, the solid may be viewed as a special constituent that may serve as a reference for the motion of the others. The mass flux of constituent α relative to the solid is given by $\mathbf{m}^\alpha = \rho^\alpha(\mathbf{v}^\alpha - \mathbf{v}^s)$; note here that the mass flux is defined as the rate of mass of α crossing a unit area of the mixture normal to the direction of $\mathbf{v}^\alpha - \mathbf{v}^s$. The volumetric flux of constituent α relative to the solid is given by $\mathbf{w}^\alpha = \varphi^\alpha(\mathbf{v}^\alpha - \mathbf{v}^s)$; and the molar flux is $\mathbf{j}^\alpha = (1-\varphi^s)c^\alpha(\mathbf{v}^\alpha - \mathbf{v}^s) \approx \varphi^w c^\alpha(\mathbf{v}^\alpha - \mathbf{v}^s)$. These fluxes are related by $\mathbf{m}^\alpha = \rho_T^\alpha \mathbf{w}^\alpha = M^\alpha \mathbf{j}^\alpha$.

17.2.1 Mass Balance

In the absence of chemical reactions, the differential statement of the axiom of mass balance for constituent α may be given by

$$\frac{\partial \rho^\alpha}{\partial t} + \operatorname{div}\left(\rho^\alpha \mathbf{v}^\alpha\right) = 0. \tag{17.1}$$

There are a number of alternative ways to write this equation, some of which may be more advantageous for interpreting and applying this axiom in mixture analyses. These alternative representations employ the deformation gradient for constituent α, given by $\mathbf{F}^\alpha = \partial \boldsymbol{\chi}^\alpha / \partial \mathbf{X}^\alpha$. For example, when using the material time derivative in the spatial frame following constituent α, the axiom of mass balance reduces to

$$\frac{D^\alpha}{Dt}\left(J^\alpha \rho^\alpha\right) = 0, \tag{17.2}$$

where $J^\alpha = \det \mathbf{F}^\alpha$ and $D^\alpha(\cdot)/Dt \equiv \partial(\cdot)/\partial t + \operatorname{grad}(\cdot) \cdot \mathbf{v}^\alpha$. This relation clearly shows that $J^\alpha \rho^\alpha$ remains invariant in the absence of mass supply to constituent α. For example, in the case of the solid matrix, this relation reproduces the classical statement $J^s \rho^s = \rho^s_r$, where ρ^s_r is the solid density in the reference configuration (when $\boldsymbol{\chi}^\alpha = \mathbf{X}^\alpha$ and $J^s = 1$). This means that the mass balance for the solid may also be expressed as $\varphi^s = \varphi^s_r / J^s$, where φ^s_r is the solid volume fraction in the reference state.

When using motion relative to the solid constituent, the mass balance equation for any constituent may also be written as

$$\frac{D^s}{Dt}\left(J^s \rho^\alpha\right) + J^s \operatorname{div} \mathbf{m}^\alpha = 0. \tag{17.3}$$

This relation is useful in finite element modeling of mixtures, when the mesh is defined on the solid matrix.

When the mixture constituents are intrinsically incompressible, the relation $\rho^\alpha = \varphi^\alpha \rho^\alpha_T$ may be substituted into Eq. (17.1) and the invariant ρ^α_T may be canceled out from the resulting expression. Taking the sum over all constituents and using the mixture saturation condition, $\sum_\alpha \varphi^\alpha = 1$, produces a mass balance relation for the mixture,

$$\operatorname{div}\left(\mathbf{v}^s + \sum_\alpha \mathbf{w}^\alpha\right) = 0. \tag{17.4}$$

When the solute volume fraction is negligible, the volume flux of solutes is negligible in comparison to that of the solvent, thus the net volume flux of interstitial fluid (solvent + solutes) relative to the solid, $\mathbf{w} \equiv \sum_\alpha \mathbf{w}^\alpha$, reduces to the flux of the solvent, $\mathbf{w} \approx \mathbf{w}^w$.

In a finite element modeling framework for intrinsically incompressible constituents, the mass balance equations that need to be enforced are Eq. (17.3) for each of the solutes, Eq. (17.4) for the mixture, and Eq. (17.2) applied to the solid. The intrinsic incompressibility constraint eliminates the need to explicitly enforce the balance of mass for the solvent.

17.2.2 Electroneutrality

When mixture constituents carry an electric charge, a charge number z^α may be associated with each constituent, which represents the number of charges per mole

of that constituent. If it is assumed that there can be no charge accumulation in the mixture, this electroneutrality condition must be enforced with the following constraint:

$$\sum_{\alpha} z^{\alpha} c^{\alpha} = 0. \tag{17.5}$$

Multiplying the mass balance in Eq. (17.3) with z^{α}/M^{α}, taking the sum over all constituents and making use of the above electroneutrality constraint produces $\operatorname{div} \sum_{\alpha} z^{\alpha} \mathbf{j}^{\alpha} = 0$, or equivalently,

$$\operatorname{div} \mathbf{I}_e = 0, \tag{17.6}$$

where $\mathbf{I}_e = F_c \sum_{\alpha} z^{\alpha} \mathbf{j}^{\alpha}$ is the electric current density (the net rate of flow of electric charge per unit area of the mixture) and F_c is Faraday's constant. Thus, the electroneutrality condition produces a constraint on the current density vector field in the mixture.

In most biological mixtures, the solvent is water and thus neutral ($z^w = 0$). The charge on the solid matrix is described as a net fixed charge density $c^F \equiv z^s c^s$. Thus, for solids, c^F may be used in lieu of a molar concentration and associated charge number.

17.2.3 Momentum Balance

Mixture models of biological tissues typically neglect the effects of the viscosity of fluid constituents in comparison to frictional interactions between constituents. The validity of this modeling assumption may be easily tested by performing comparisons of the orders of magnitude of these various terms, given representative values of the relevant material properties. For example, in a solid-fluid mixture of articular cartilage, the non-dimensional number representing the ratio of internal fluid friction (viscosity) to fluid-solid frictional drag is $\delta = \eta / h^2 K$ (Hou et al., 1989), where η is the fluid viscosity, h is a characteristic length, and K is the solid-fluid frictional drag coefficient. In articular cartilage, $\eta \approx 10^{-3}$ Pa · s, $h \approx 10^{-3}$ m, and $K \approx 10^{15}$ N · s/m^4, thus $\delta \approx 10^{-12}$, showing a very negligible relative contribution of fluid viscosity.

With negligible viscosity, the Cauchy stress tensor $\boldsymbol{\sigma}$ in a mixture of intrinsically incompressible constituents only includes two contributions: The hydrostatic pressure p in the fluid, and the Cauchy stress $\boldsymbol{\sigma}^s$ in the solid, thus $\boldsymbol{\sigma} = -p\mathbf{I} + \boldsymbol{\sigma}^s$, where $\mathbf{I}$ is the identity tensor. Under quasi-static conditions, and in the absence of external body forces, the momentum balance for the mixture is given by

$$\operatorname{div} \boldsymbol{\sigma} = -\operatorname{grad} p + \operatorname{div} \boldsymbol{\sigma}^s = \mathbf{0}. \tag{17.7}$$

A constitutive relation is needed to relate $\boldsymbol{\sigma}^s$ to the state variables adopted for a particular analysis, such as solid matrix strain.

For the fluid constituents of a mixture, the driving forces are the gradients in the constituents' mechanoelectrochemical potential, $\tilde{\mu}^\alpha$. This potential represents the sum of mechanical, electrical and chemical contributions, thus

$$\tilde{\mu}^\alpha = \frac{p}{\rho_T^\alpha} + \frac{z^\alpha}{M^\alpha} F_c \psi + \mu^\alpha. \tag{17.8}$$

In this expression, ψ is the electric potential in the mixture and μ^α is the chemical potential of constituent α. The mechanical contribution is evidently proportional to the fluid pressure p; the electrical contribution is proportional to ψ, but reduces to zero for a neutral constituent ($z^\alpha = 0$). The chemical potential represents the rate of change of the mixture free energy density with changes in the relative mass content (apparent density) of constituent α. A constitutive relation is needed for μ^α to relate it to the state variables in an analysis, such as solute concentrations. In the momentum equation for fluids, the gradient in the mechanoelectrochemical potential is balanced by the frictional interactions between constituents, inertia forces, external body forces, and the momentum supply from active transport (Bowen, 1976; Lai et al., 1991; Ateshian et al., 2010).

When the volume fraction of solutes is negligible, solute-solute frictional interactions may be neglected relative to solute-solvent, solute-solid, and solvent-solid interactions. Similarly, the mechanical potential of solutes in $\tilde{\mu}^\alpha$ becomes negligible. Under quasi-static conditions, in the absence of external body forces and active transport mechanisms, the resulting linear momentum balance equations may be inverted to produces the following expressions for the fluxes,

$$\mathbf{m}^w = -\tilde{\mathbf{k}} \cdot \left[\left(\rho_T^w\right)^2 \operatorname{grad} \tilde{\mu}^w + \frac{(\rho_T^w)^2}{\rho^w} \sum_{\alpha \neq s,w} \frac{\mathbf{d}^\alpha}{d_0^\alpha} \cdot \rho^\alpha \operatorname{grad} \tilde{\mu}^\alpha \right], \tag{17.9}$$

$$\mathbf{m}^\alpha = -\rho^\alpha \frac{M^\alpha}{R\theta} \mathbf{d}^\alpha \cdot \operatorname{grad} \tilde{\mu}^\alpha + \frac{\rho^\alpha}{\rho^w} \frac{\mathbf{d}^\alpha}{d_0^\alpha} \cdot \mathbf{m}^w, \quad \alpha \neq s, w, \tag{17.10}$$

where $\mathbf{d}^\alpha$ is the diffusivity tensor of solute α in the mixture (solid and fluid), d_0^α is the isotropic diffusivity of the solute in free solution (fluid), R is the universal gas constant, θ is the absolute temperature, and $\tilde{\mathbf{k}}$ is the hydraulic permeability tensor of the porous solid to the interstitial fluid (solvent and solutes), given by

$$\tilde{\mathbf{k}} = \left[\mathbf{k}^{-1} + \frac{R\theta}{\varphi^w} \sum_{\alpha \neq s,w} \frac{c^\alpha}{d_0^\alpha} \left(\mathbf{I} - \frac{\mathbf{d}^\alpha}{d_0^\alpha} \right) \right]^{-1}, \tag{17.11}$$

where $\mathbf{k}$ is the hydraulic permeability tensor of the porous solid to the interstitial solvent. Constitutive relations must be provided for $\mathbf{k}$, $\mathbf{d}^\alpha$, and d_0^α, which relate them to state variables such as solid matrix strain and suitable measures of solute concentrations.

In a finite element modeling framework, it is necessary to define nodal variables (degrees of freedom) that are continuous across the boundaries of elements. In a

mixture framework, variables that satisfy such continuity requirements are the solid displacement $\mathbf{u}$ and the mechanoelectrochemical potentials $\tilde{\mu}^\alpha$ of the solvent and solutes. In general, neither fluid pressure p nor solute concentrations c^α are continuous across boundaries (Lai et al., 1991). However, since $\tilde{\mu}^\alpha$'s are less practical to use as nodal variables, it is possible to define related nodal variables that represent effective measures of fluid pressure,

$$\tilde{p} = p - R\theta\, \Phi \sum_{\alpha \neq s,w} c^\alpha, \tag{17.12}$$

and solute concentration,

$$\tilde{c}^\alpha = \frac{c^\alpha}{\tilde{\kappa}^\alpha}, \quad \alpha \neq s, w. \tag{17.13}$$

These equivalent nodal variables are obtained by making use of standard constitutive relations from physical chemistry, for the chemical potential μ^α of the solvent and solute in dilute solutions (Sun et al., 1999; Yao and Gu, 2007; Ateshian et al., 2011). In these expressions, Φ is the *osmotic coefficient*, a non-dimensional property that describes the deviation of the osmotic pressure from the ideal behavior known as van't Hoff's law (McNaught and Wilkinson, 1997); $\tilde{\kappa}^\alpha$ is the *partition coefficient* of solute α relative to an ideal solution. This partition coefficient may be further described by

$$\tilde{\kappa}^\alpha = \frac{\kappa^\alpha}{\gamma^\alpha} \exp\left(-\frac{z^\alpha F_c \psi}{R\theta}\right), \tag{17.14}$$

where the non-dimensional property κ^α is the *solubility* of solute α in the mixture, representing the fraction of the interstitial pore volume which is accessible to the solute (Mauck et al., 2003); and γ^α is the *activity coefficient* of solute α, a non-dimensional property that describes the deviation of the solute chemical potential from the ideal behavior of a very dilute solution (Tinoco et al., 1995). The ratio $\hat{\kappa}^\alpha \equiv \kappa^\alpha/\gamma^\alpha$ may be interpreted as the *effective solubility* of solute α (Ateshian et al., 2011). Constitutive relations must be provided for Φ and $\hat{\kappa}^\alpha$. For a neutral solute ($z^\alpha = 0$), the partition coefficient reduces to the effective solubility. For *ideal mixtures* in the context of physical chemistry, $\Phi = 1$ and $\hat{\kappa}^\alpha = 1$.

Physically, since $R\theta\, \Phi \sum_{\alpha \neq s,w} c^\alpha$ is the osmotic (chemical) contribution to the fluid pressure, $\tilde{p}$ may be interpreted as that part of the total (mechanochemical) fluid pressure which does not result from osmotic effects; thus, it is the mechanical contribution to p. Similarly, the effective solute concentration $\tilde{c}^\alpha$ represents the true contribution of the molar solute content to its electrochemical potential. When using $\tilde{p}$ and $\tilde{c}^\alpha$ in lieu of mechanoelectrochemical potentials, the mass fluxes given in Eqs. (17.9), (17.10) may be represented by the equivalent fluid volume flux,

$$\mathbf{w} = -\tilde{\mathbf{k}} \cdot \left(\operatorname{grad} \tilde{p} + R\theta \sum_{\beta \neq s,w} \frac{\tilde{\kappa}^\beta}{d_0^\beta} \mathbf{d}^\beta \cdot \operatorname{grad} \tilde{c}^\beta\right), \tag{17.15}$$

and solute molar fluxes,

$$\mathbf{j}^{\alpha} = \tilde{\kappa}^{\alpha}\mathbf{d}^{\alpha} \cdot \left(-\varphi^{w}\,\mathrm{grad}\,\tilde{c}^{\alpha} + \frac{\tilde{c}^{\alpha}}{d_0^{\alpha}}\mathbf{w}\right), \quad \alpha \neq s, w. \tag{17.16}$$

These expressions are relatively compact, yet they describe a broad set of phenomena, including *permeation* (fluid flux driven by a pressure gradient), *osmosis* (fluid flux driven by solute concentration gradients), *electroosmosis* (fluid flux driven by an electric potential gradient), *diffusion* (solute flux driven by a concentration gradient), *electrophoresis* (solute flux driven by an electric potential gradient), and *barophoresis* (solute flux driven by a fluid pressure gradient).

17.3 Finite Element Formulation

The virtual work integral for a mixture of intrinsically incompressible constituents combines the balance of momentum for the mixture, the balance of mass for the mixture, and the balance of mass for each of the solutes. In addition, for charged mixtures, the current condition of Eq. (17.6) may be enforced as a penalty constraint on each solute mass balance equation:

$$\begin{aligned}\delta W = &-\int_b \delta\mathbf{v}\cdot\mathrm{div}\,\boldsymbol{\sigma}\,\mathrm{d}v\\ &-\int_b \delta\tilde{p}\;\mathrm{div}\big(\mathbf{v}^s+\mathbf{w}\big)\mathrm{d}v\\ &-\sum_{\alpha\neq s,w}\int_b \delta\tilde{c}^{\alpha}\left[\frac{1}{J^s}\frac{D^s}{Dt}\big(J^s\varphi^w\tilde{\kappa}^{\alpha}\tilde{c}^{\alpha}\big)+\mathrm{div}\,\mathbf{j}^{\alpha}+\sum_{\beta\neq s,w} z^{\beta}\,\mathrm{div}\,\mathbf{j}^{\beta}\right]\mathrm{d}v,\end{aligned} \tag{17.17}$$

where $\delta\mathbf{v}$ is the virtual velocity of the solid, $\delta\tilde{p}$ is the virtual effective fluid pressure, and $\delta\tilde{c}^{\alpha}$ is the virtual molar energy of solute α. Here, b represents the mixture domain in the spatial frame and $\mathrm{d}v$ is an elemental volume in b. Applying the divergence theorem, δW may be split into internal and external contributions to the virtual work, $\delta W = \delta W_{\mathrm{int}} - \delta W_{\mathrm{ext}}$, where

$$\begin{aligned}\delta W_{\mathrm{int}} = &\int_b \boldsymbol{\sigma} : \delta\mathbf{D}\mathrm{d}v + \int_b\left(\mathbf{w}\cdot\mathrm{grad}\,\delta\tilde{p} - \frac{\delta\tilde{p}}{J^s}\frac{D^sJ^s}{Dt}\right)\mathrm{d}v\\ &+\sum_{\alpha\neq s,w}\int_b\left[\mathbf{j}^{\alpha}\cdot\mathrm{grad}\,\delta\tilde{c}^{\alpha} - \frac{\delta\tilde{c}^{\alpha}}{J^s}\frac{D^s}{Dt}\big(J^s\varphi^w\tilde{\kappa}^{\alpha}\tilde{c}^{\alpha}\big)\right]\mathrm{d}v\\ &+\sum_{\alpha\neq s,w}\int_b \mathrm{grad}\,\delta\tilde{c}^{\alpha}\cdot\sum_{\beta\neq s,w} z^{\beta}\mathbf{j}^{\beta}\mathrm{d}v,\end{aligned} \tag{17.18}$$

$$\delta W_{\text{ext}} = \int_{\partial b} \left[\delta \mathbf{v} \cdot \mathbf{t} + \delta \tilde{p} w_n + \sum_{\alpha} \delta \tilde{c}^{\alpha} \left(j_n^{\alpha} + \sum_{\beta \neq s,w} z^{\beta} j_n^{\beta} \right) \right] \mathrm{d}a. \tag{17.19}$$

In these expressions, $\delta \mathbf{D} = (\operatorname{grad} \delta \mathbf{v} + \operatorname{grad}^{\mathrm{T}} \delta \mathbf{v})/2$, ∂b is the boundary of b, and $\mathrm{d}a$ is an elemental area on ∂b. In this finite element formulation, $\mathbf{u}$, $\tilde{p}$ and $\tilde{c}^{\alpha}$ are used as nodal variables, and essential boundary conditions may be prescribed on these variables. Natural boundary conditions are prescribed to the mixture traction, $\mathbf{t} = \boldsymbol{\sigma} \cdot \mathbf{n}$, normal fluid flux, $w_n = \mathbf{w} \cdot \mathbf{n}$, and normal solute flux, $j_n^{\alpha} = \mathbf{j}^{\alpha} \cdot \mathbf{n}$, where $\mathbf{n}$ is the outward unit normal to ∂b. To solve the system $\delta W = 0$ for nodal values of $\mathbf{u}$, $\tilde{p}$ and $\tilde{c}^{\alpha}$, it is necessary to linearize these equations (Bonet and Wood, 1997), as shown for example in Ateshian et al. (2011).

If the mixture is charged, it is also necessary to solve for the electric potential ψ using the electroneutrality condition in Eq. (17.5), which may be rewritten as

$$c^F + \sum_{\beta \neq s,w} z^{\beta} \tilde{\kappa}^{\beta} \tilde{c}^{\beta} = 0. \tag{17.20}$$

In the special case of a triphasic mixture, where solutes consist of two counter-ions ($\alpha = +, -$), this equation may be solved in closed form to produce

$$\psi = \frac{1}{z^{\alpha}} \frac{R\theta}{F_c} \ln \left(\frac{2 z^{\alpha} \hat{\kappa}^{\alpha} \tilde{c}^{\alpha}}{-c^F \pm \sqrt{(c^F)^2 + 4 (z^{\alpha})^2 (\hat{\kappa}^{+} \tilde{c}^{+})(\hat{\kappa}^{-} \tilde{c}^{-})}} \right), \quad \alpha = +, -. \tag{17.21}$$

Only the positive root is valid in the argument of the logarithm function.

This finite element formulation has been implemented in the public domain, open source finite element code FEBio (www.febio.org). To date, FEBio allows modeling of a biphasic-solute mixture consisting of a neutral porous solid, solvent, and a single neutral solute; and a triphasic mixture consisting of a charged porous solid, solvent, and two counter-ions (solutes with opposite charges).

17.4 Illustrations of Fundamental Phenomena

17.4.1 Permeation and Barophoresis

A permeation experiment may consist of prescribing a fluid pressure p_0 upstream of a tissue sample of thickness h, while maintaining the downstream side under atmospheric conditions. Thus, the tissue sample is exposed to an upstream bath with ambient pressure $p_u^* = p_0$, and a downstream bath with ambient pressure $p_d^* = 0$, where the asterisk denotes variables in the bath (Fig. 17.1). Consider that the fluid contains a single, neutral solute, whose concentration c_0 is the same in the upstream and downstream baths, thus, $c_u^* = c_d^* = c_0$. To set up this problem in a finite element analysis, it is necessary to identify the boundary conditions on the upstream and downstream faces of the tissue sample. Since pressure boundary conditions must be prescribed on the effective fluid pressure $\tilde{p}$ instead of p, Eq. (17.12) is used

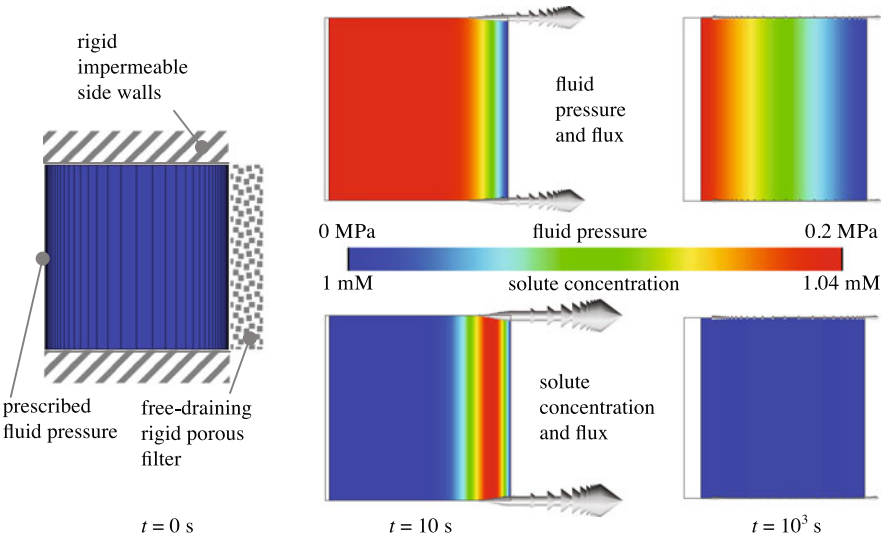

Fig. 17.1 Permeation analysis for a biphasic-solute tissue. The finite element mesh is shown at *left*. For this analysis, $h = 1$ mm, $p_0 = 0.2$ MPa, $c_0 = 1$ mM. The solid matrix is neo-Hookean with Young's modulus $= 1$ MPa and Poisson's ratio $= 0$; the initial solid volume fraction is $\varphi_r^s = 0.2$. The hydraulic permeability is 10^{-3} mm^4/N $\cdot$ s; the solute diffusivity in free solution is $d_0 = 10^{-3}$ mm^2/s, and the diffusivity in the tissue is $d = 0.5 \times 10^{-3}$ mm^2/s. At steady-state, the fluid flux and solute flux are uniform and equal to 0.22×10^{-3} mm/s and 0.11×10^{-3} nmol/mm^2 $\cdot$ s, respectively

to determine that the effective fluid pressure in the upstream bath is $\tilde{p}_u^* = p_0 - R\theta\Phi^* c_0$, and that in the downstream bath is $\tilde{p}_d^* = -R\theta\Phi^* c_0$. Since $\tilde{p}$ is a variable that remains continuous across boundaries, we may thus prescribe $\tilde{p}_u = \tilde{p}_u^*$ on the upstream face, and $\tilde{p}_d = \tilde{p}_d^*$ on the downstream face. Similarly, for the solute, the boundary conditions must be prescribed on the effective concentration $\tilde{c}$ instead of c. This is done using Eq. (17.13), thus $\tilde{c}_u = \tilde{c}_u^* = c_0$, and $\tilde{c}_d = \tilde{c}_d^* = c_0$, where we have made use of the fact that $\tilde{\kappa}^* = 1$ for a neutral solute in a fluid bath under ideal conditions ($\hat{\kappa}^* = 1$ and $\psi^* = 0$). Finally, it is also necessary to enforce traction and displacement boundary conditions: On the unconstrained upstream face, $\mathbf{t}_u = -p_0\mathbf{n}$, whereas on the constrained downstream face, the axial displacement is zero.

Initial conditions also need to be prescribed for this problem. It may be assumed initially that the upstream and downstream bath pressures are both atmospheric, thus $\tilde{p}_u = \tilde{p}_d = 0$. According to Eqs. (17.15), (17.16), equilibrium conditions (zero fluid and solute flux, and zero solid velocity) are achieved when there is no gradient in $\tilde{p}$ and $\tilde{c}$. Thus, based on the boundary conditions and the requirement for a uniform value of $\tilde{p}$ at equilibrium, it may be assumed initially that $\tilde{p} = 0$ throughout the tissue. By a similar argument, it may be assumed initially that $\tilde{c} = c_0$ throughout the tissue.

Upon the application of the fluid pressure upstream, a transient response ensues, whereby the tissue slowly compacts as interstitial fluid begins to exude from its

downstream side (Fig. 17.1, $t = 10$ s); as time progresses, fluid flux on the upstream side increases until, at steady-state, the fluid flux becomes uniform throughout the tissue thickness ($t = 10^3$ s). In FEBio, it is possible to request a full transient analysis, or to restrict the analysis only to the steady-state response. At steady-state, as expected, it is found that the fluid flux $\mathbf{w}$ along the thickness of the sample is directed from the high pressure fluid bath to the atmospheric fluid bath. This is the classical phenomenon known as permeation. Furthermore, despite the fact that the solute concentration returns to a uniform distribution at steady-state, the fluid pressure gradient continues to drives the solute from upstream to downstream, because of the frictional interactions between solvent and solute. This mechanism is generically known as the convective effect of the solvent on the solute; more specifically in this problem, this phenomenon may be described as barophoresis.

17.4.2 Diffusion and Osmosis

Diffusion represents the flux of solute in response to a gradient in its concentration. Consider a canonical problem of diffusion of a neutral solute across a tissue sample, from an upstream bath at a concentration c_0 to a downstream bath with negligible concentration. Both upstream and downstream baths are maintained at zero ambient pressure. Therefore, upstream boundary conditions are $\tilde{c}_u = c_0$, $\tilde{p}_u = -R\theta c_0$ (under ideal conditions, $\Phi^* = 1$), $\mathbf{t}_u = \mathbf{0}$, and downstream conditions are $\tilde{c}_d = 0$, $\tilde{p}_d = 0$, and zero axial displacement. Initial conditions may assume that the upstream bath also starts out with zero solute concentration, so that $\tilde{c} = 0$ and $\tilde{p} = 0$ throughout the tissue sample initially.

Upon raising the solute concentration to c_0 upstream, a transient response ensues whereby the solute begins to diffuse into the tissue on the upstream side. Over time, the solute concentration within the tissue evolves into a linear profile, producing a uniform solute flux across the entire thickness (Fig. 17.2). Simultaneously, it is observed that the solvent flows from the downstream side toward upstream (from the low concentration bath to the high concentration bath). This mechanism is known as osmosis.

17.4.3 Electrophoresis and Electroosmosis

To examine the phenomena of electrophoresis and electroosmosis, consider a tissue described by a triphasic material, where the ions represent Na^+ (with $z^{Na} = +1$) and Cl^- ($z^{Cl} = -1$) and the solid matrix is negatively charged. As in the above examples, the tissue is located between an upstream and a downstream bath. In these baths, due to electroneutrality and the absence of a charged solid matrix, the anion and cation concentrations must be the same. The salt concentrations in the upstream and downstream baths may also be taken to be the same, to prevent diffusion and

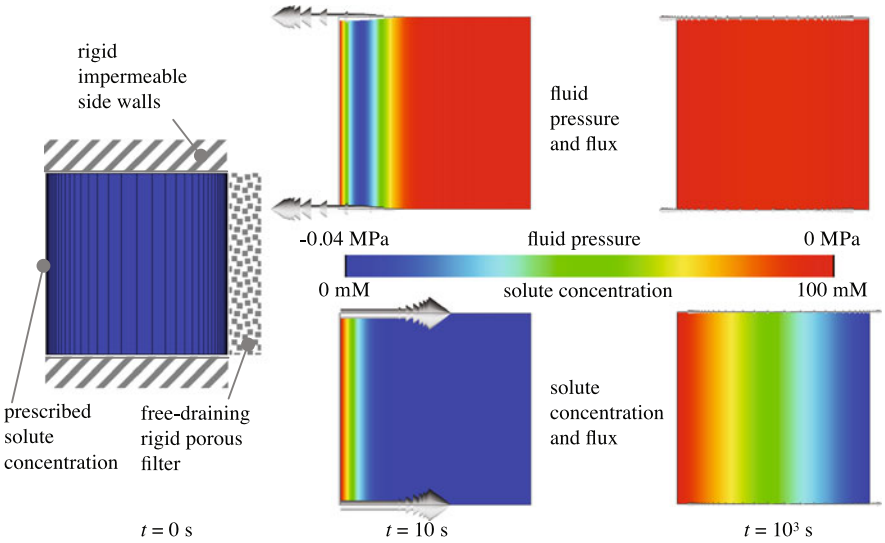

Fig. 17.2 Diffusion analysis for a biphasic-solute tissue. The finite element mesh is shown at *left*. For this analysis, $h = 1$ mm, the ambient pressure is zero, and $c_0 = 100$ mM on the *left* (upstream face), and zero on the *right* (downstream) face. The remaining properties are the same as in Fig. 17.1. These conditions produce solute flux (diffusion) from *left* to *right* and solvent flux (osmosis) from *right* to *left*. At steady-state, the fluid flux and solute flux are uniform and equal to -0.11×10^{-3} mm/s and 37×10^{-3} nmol/mm$^2 \cdot$ s, respectively

osmosis, thus $c_u^{\mathrm{Na}*} = c_u^{\mathrm{Cl}*} = c_0$ and $c_d^{\mathrm{Na}*} = c_d^{\mathrm{Cl}*} = c_0$. To produce electrophoresis and electroosmosis, let the electric potential in the upstream bath be $\psi_u^* = \psi_0$, whereas the downstream bath is maintained at a zero potential, $\psi_d^* = 0$, thereby creating an electric potential gradient across the tissue thickness. Also let the pressure equal ambient conditions in both baths, $p_u^* = 0$ and $p_d^* = 0$, to prevent permeation and barophoresis. All of these conditions may be combined to produce the following boundary conditions: On the upstream side, $\tilde{p}_u = -2R\theta c_0$, $\tilde{c}_u^{\mathrm{Na}} = c_0 e^{F_c\psi_0/R\theta}$, $\tilde{c}_u^{\mathrm{Cl}} = c_0 e^{-F_c\psi_0/R\theta}$, and on the downstream side, $\tilde{p}_d = -2R\theta c_0$, $\tilde{c}_d^{\mathrm{Na}} = c_0$, $\tilde{c}_d^{\mathrm{Cl}} = c_0$ (assuming $\Phi^* = 1$). For initial conditions, it may be assumed that the electric potential upstream is initially zero, thus $\tilde{p} = -2R\theta c_0$, $\tilde{c}^{\mathrm{Na}} = c_0$, and $\tilde{c}^{\mathrm{Cl}} = c_0$ throughout the tissue initially.

When performing finite element analyses with charged tissues, it is important to remember that a Donnan osmotic pressure arises between the tissue and its external bathing environment, due to the charged solute matrix. Since electroneutrality must be satisfied in the tissue and the bath, the tissue concentrations of anion and cation differ by the amount of the fixed charge, whereas the bath concentrations of anions and cations are the same; to satisfy both conditions simultaneously, while also satisfying continuity of solvent and solute mechanoelectrochemical potential, an imbalance in osmolarity and electric potential must exist between tissue and bath. This imbalance is responsible for the Donnan osmotic pressure and Donnan potential between the tissue and its surrounding environment. The Donnan pressure swells

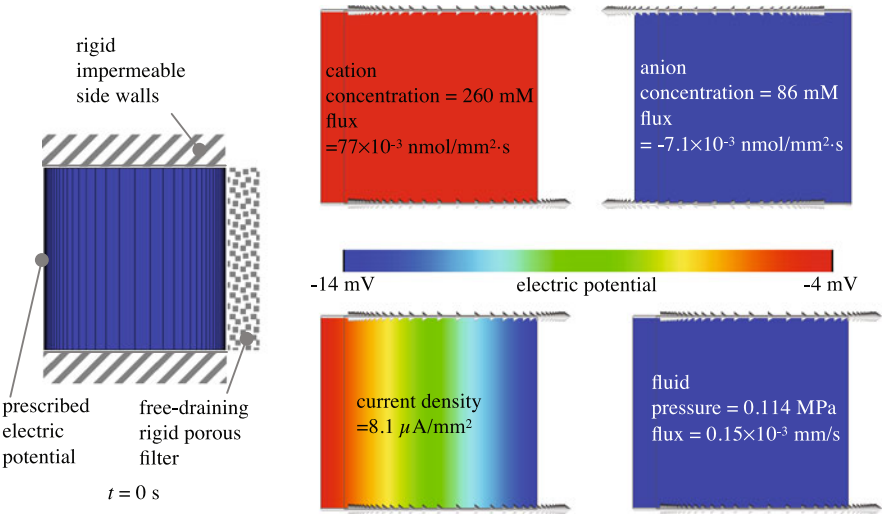

Fig. 17.3 Electrophoresis analysis for a triphasic tissue with monovalent counterions. The finite element mesh is shown at *left*, in its reference configuration. For this analysis, $h = 1$ mm, the ambient pressure is zero on *both sides*, the ambient concentration of cation and anion is 150 mM on *both sides*, and $\psi_0 = 10$ mV on the *left* (upstream face), and zero on the *right* (downstream) face. The fixed charge density in the reference configuration is $c_r^F = -200$ mEq/L. The solution at steady state (*4 panels at right*) demonstrates that the tissue is in a swollen state (swelling to the *left*) due to the Donnan osmotic pressure in the interstitial fluid (0.114 MPa). The cation flux (electrophoresis), current density (electric conduction), and fluid flux (electroosmosis) are directed from *left* to *right*, whereas the anion flux (electrophoresis) is in the opposite direction. The electric potential ψ inside the tissue differs from the externally applied potential ψ^* by the value of the Donnan potential

the tissue and is resisted by the solid matrix stress. Therefore, under traction-free swelling conditions, triphasic materials are not generally in a stress-free state, unless the fixed charge density is zero, or the external bath has an osmolarity far exceeding the tissue fixed charge density (theoretically, if the bath osmolarity is infinite).

In a finite element analysis, the initial state of the solid is stress-free (this is the reference state). Therefore, to achieve a traction-free swelling condition prior to subsequent loading, it is necessary to first perform an analysis whereby the fixed charged density is changed from zero to the desired value (or the bath osmolarity is decreased from a very high value down to the desired ambient conditions). Once this free-swelling equilibrium has been achieved, the desired electric potential difference may be applied between upstream and downstream baths. At steady-state, the following phenomena are observed (Fig. 17.3): (i) The positively charged cation flows from the higher to the lower electric potential, whereas the negatively charged anion flows in the opposite direction. This solute flux under the action of an externally applied electric potential is called electrophoresis. The cation and anion fluxes do not cancel out, as a net transport of charge is observed from the upstream to the downstream bath; this net flow is manifested by a non-zero current density $\mathbf{I}_e$, flow-

ing from upstream to downstream. (ii) At the boundaries with the baths, the electric potential ψ inside the tissue is not the same as the bath potential ψ^*, because of the fixed charge density in the tissue. The tissue *electric conductivity* may be evaluated from the ratio of $|\mathbf{I}_e|$ and the prescribed potential gradient, $(\psi_u^* - \psi_d^*)/h$, where h is the tissue thickness. (iii) The solvent also flows from the upstream to the downstream bath, due to the net frictional drag exerted on it by the solutes. This phenomenon is known as electroosmosis.

17.5 Conclusion

Finite element modeling of mechanoelectrochemical phenomena in deformable porous biological tissues and cells is a useful tool in the toolbox of biomedical engineers. The examples presented in this chapter provide only the most basic features of biphasic-solute and triphasic materials in FEBio. More elaborate analyses may be performed which combine any number of driving mechanisms for deformation and flow. The ability to describe transport of neutral or charged solutes within a porous deformable solid matrix, using a formulation that couples these mechanisms, makes it possible to address phenomena commonly observed in biology and physiology. FEBio provides this tool in the public domain, allowing users to exchange models and ideas in a common framework. Being open source, FEBio also allows users to extend its current capabilities, by adding new constitutive relations or extending existing frameworks to include additional mechanisms. Current efforts are under way to extend the existing biphasic-solute and triphasic frameworks to a more general multiphasic module, where any number of neutral or charged solutes may be modeled. Furthermore, the modeling of chemical reactions among any of the solid and solute constituents will be incorporated in future extensions of the code. These extensions will make it possible to model chemical kinetics and growth mechanics in deformable porous media, further extending the modeling capabilities into the realm of biology and physiology.

Acknowledgements The development of FEBio is supported by funds from the National Institute of General Medical Sciences (NIGMS) of the U.S. National Institutes of Health (GM083925).

References

Albro MB, Chahine NO, Caligaris M, Wei VI, Likhitpanichkul M, Ng KW, Hung CT, Ateshian GA (2007) Osmotic loading of spherical gels: a biomimetic study of hindered transport in the cell protoplasm. J Biomech Eng 129(4):503–510

Albro MB, Chahine NO, Li R, Yeager K, Hung CT, Ateshian GA (2008) Dynamic loading of deformable porous media can induce active solute transport. J Biomech 41(15):3152–3157

Albro MB, Petersen LE, Li R, Hung CT, Ateshian GA (2009a) Influence of the partitioning of osmolytes by the cytoplasm on the passive response of cells to osmotic loading. Biophys J 97(11):2886–2893

Albro MB, Rajan V, Li R, Hung CT, Ateshian GA (2009b) Characterization of the concentration-dependence of solute diffusivity and partitioning in a model dextran-agarose transport system. Cell Mol Bioeng 2(3):295–305

Albro MB, Li R, Banerjee RE, Hung CT, Ateshian GA (2010) Validation of theoretical framework explaining active solute uptake in dynamically loaded porous media. J Biomech 43(12):2267–2273

Albro MB, Banerjee RE, Li R, Oungoulian SR, Chen B, del Palomar AP, Hung CT, Ateshian GA (2011) Dynamic loading of immature epiphyseal cartilage pumps nutrients out of vascular canals. J Biomech 44(9):1654–1659

Armstrong CG, Lai WM, Mow VC (1984) An analysis of the unconfined compression of articular cartilage. J Biomech Eng 106(2):165–173

Ateshian GA, Wang H (1995) A theoretical solution for the frictionless rolling contact of cylindrical biphasic articular cartilage layers. J Biomech 28(11):1341–1355

Ateshian GA, Weiss JA (2010) Anisotropic hydraulic permeability under finite deformation. J Biomech Eng 132(11):111004

Ateshian GA, Lai WM, Zhu WB, Mow VC (1994) An asymptotic solution for the contact of two biphasic cartilage layers. J Biomech 27(11):1347–1360

Ateshian GA, Likhitpanichkul M, Hung CT (2006) A mixture theory analysis for passive transport in osmotic loading of cells. J Biomech 39(3):464–475

Ateshian GA, Rajan V, Chahine NO, Canal CE, Hung CT (2009) Modeling the matrix of articular cartilage using a continuous fiber angular distribution predicts many observed phenomena. J Biomech Eng 131(6):061003

Ateshian GA, Morrison B 3rd, Hung CT (2010) Modeling of active transmembrane transport in a mixture theory framework. Ann Biomed Eng 38(5):1801–1814

Ateshian GA, Albro MB, Maas S, Weiss JA (2011) Finite element implementation of mechanochemical phenomena in neutral deformable porous media under finite deformation. J Biomech Eng 133(8):081005

Athanasiou K (1991) Interspecies comparisons of in situ intrinsic mechanical properties of distal femoral cartilage. J Orthop Res 9:330–340

Azeloglu EU, Albro MB, Thimmappa VA, Ateshian GA, Costa KD (2008) Heterogeneous transmural proteoglycan distribution provides a mechanism for regulating residual stresses in the aorta. Am J Physiol, Heart Circ Physiol 294(3):H1197–H1205

Biot MA (1941) General theory of three-dimensional consolidation. J Appl Phys 12:155–164

Bonet J, Wood RD (1997) Nonlinear continuum mechanics for finite element analysis. Cambridge University Press, Cambridge

Bowen RM (1976) Theory of mixtures, vol 3. Academic Press, New York, pp 1–127

Bowen RM (1980) Incompressible porous media models by use of the theory of mixtures. Int J Eng Sci 18(9):1129–1148

Cohen B, Lai WM, Mow VC (1998) A transversely isotropic biphasic model for unconfined compression of growth plate and chondroepiphysis. J Biomech Eng 120(4):491–496

Cowin SC (1999) Bone poroelasticity. J Biomech 32(3):217–238

Deen WM (1987) Hindered transport of large molecules in liquid-filled pores. AIChE J 33(9):1409–1425

Eringen A, Ingram J (1965) Continuum theory of chemically reacting media—1. Int J Eng Sci 3:197–212

Fillunger P (1913) Der Auftrieb in Talsperren. Österr Wochenschrift öffentlichen Baudienst 19:532–556, 567–570

Frank EH, Grodzinsky AJ (1987a) Cartilage electromechanics—I. Electrokinetic transduction and the effects of electrolyte pH and ionic strength. J Biomech 20(6):615–627

Frank EH, Grodzinsky AJ (1987b) Cartilage electromechanics—II. A continuum model of cartilage electrokinetics and correlation with experiments. J Biomech 20(6):629–639

Frijns AJH, Huyghe JM, Janssen JD (1997) Validation of the quadriphasic mixture theory for intervertebral disc tissue. Int J Eng Sci 35(15):1419–1429

Gu WY, Lai WM, Mow VC (1998) A mixture theory for charged-hydrated soft tissues containing multi-electrolytes: passive transport and swelling behaviors. J Biomech Eng 120(2):169–180
Hou JS, Holmes MH, Lai WM, Mow VC (1989) Boundary conditions at the cartilage-synovial fluid interface for joint lubrication and theoretical verifications. J Biomech Eng 111(1):78–87
Huyghe JM, Janssen JD (1997) Quadriphasic mechanics of swelling incompressible porous media. Int J Eng Sci 35(8):793–802
Kaasschieter EF, Frijns AJH, Huyghe JM (2003) Mixed finite element modelling of cartilaginous tissues. Math Comput Simul 61(3–6):549–560
Kedem O, Katchalsky A (1958) Thermodynamic analysis of the permeability of biological membranes to non-electrolytes. Biochim Biophys Acta 27(2):229–246
Kenyon DE (1976) Transient filtration in a porous elastic cylinder. J Appl Mech 43Ser E (4):594–598
Lai WM, Hou JS, Mow VC (1991) A triphasic theory for the swelling and deformation behaviors of articular cartilage. J Biomech Eng 113(3):245–258
Lai WM, Mow VC (1980) Drag-induced compression of articular cartilage during a permeation experiment. Biorheology 17(1–2):111–123
Lazzara MJ, Deen WM (2004) Effects of concentration on the partitioning of macromolecule mixtures in agarose gels. J Colloid Interface Sci 272(2):288–297
Maas S, Ellis BJ, Ateshian GA, Weiss JA (2012) FEBio: finite elements for biomechanics. J Biomech Eng 134(1):011005
Mackie JS, Meares P (1955) The diffusion of electrolytes in a cation-exchange resin membrane. I. Theoretical. Proc R Soc Lond Ser A 232(1191):498–509
Magnier C, Boiron O, Wendling-Mansuy S, Chabrand P, Deplano V (2009) Nutrient distribution and metabolism in the intervertebral disc in the unloaded state: a parametric study. J Biomech 42(2):100–108
Mauck RL, Hung CT, Ateshian GA (2003) Modeling of neutral solute transport in a dynamically loaded porous permeable gel: implications for articular cartilage biosynthesis and tissue engineering. J Biomech Eng 125(5):602–614
McNaught AD, Wilkinson A (1997) Compendium of chemical terminology: IUPAC recommendations, 2nd edn. Blackwell Science, Oxford
Mow VC, Kuei SC, Lai WM, Armstrong CG (1980) Biphasic creep and stress relaxation of articular cartilage in compression: theory and experiments. J Biomech Eng 102(1):73–84
Mow VC, Gibbs MC, Lai WM, Zhu WB, Athanasiou KA (1989) Biphasic indentation of articular cartilage—II. A numerical algorithm and an experimental study. J Biomech 22(8–9):853–861
Oomens CW, van Campen DH, Grootenboer HJ (1987) A mixture approach to the mechanics of skin. J Biomech 20(9):877–885
Sengers BG, Oomens CW, Baaijens FP (2004) An integrated finite-element approach to mechanics, transport and biosynthesis in tissue engineering. J Biomech Eng 126(1):82–91
Simon BR, Liable JP, Pflaster D, Yuan Y, Krag MH (1996) A poroelastic finite element formulation including transport and swelling in soft tissue structures. J Biomech Eng 118(1):1–9
Steck R, Niederer P, Knothe Tate ML (2003) A finite element analysis for the prediction of load-induced fluid flow and mechanochemical transduction in bone. J Theor Biol 220(2):249–259
Sun DN, Gu WY, Guo XE, Lai WM, Mow VC (1999) A mixed finite element formulation of triphasic mechano-electrochemical theory for charged, hydrated biological soft tissues. Int J Numer Methods Eng 45(10):1375–1402
Tinoco I, Sauer K, Wang JC (1995) Physical chemistry: principles and applications in biological sciences, 3rd edn. Prentice Hall, Englewood Cliffs
Truesdell C, Toupin R (1960) The classical field theories. Springer, Berlin
van Loon R, Huyghe JM, Wijlaars MW, Baaijens FPT (2003) 3d FE implementation of an incompressible quadriphasic mixture model. Int J Numer Methods Eng 57(9):1243–1258
von Terzaghi K (1933) Auftrieb und Kapillardruck an betonierten Talsperren. Wasserwirtschaft 26:397–399
Wu JZ, Herzog W (2002) Simulating the swelling and deformation behaviour in soft tissues using a convective thermal analogy. Biomed Eng Online 1:8

Yang M, Taber LA, Clark EB (1994) A nonliner poroelastic model for the trabecular embryonic heart. J Biomech Eng 116(2):213–223

Yao H, Gu WY (2007) Three-dimensional inhomogeneous triphasic finite-element analysis of physical signals and solute transport in human intervertebral disc under axial compression. J Biomech 40(9):2071–2077

Zhang L, Szeri A (2005) Transport of neutral solute in articular cartilage: effects of loading and particle size. Proc R Soc Lond Ser A 461(2059):2021–2042

Chapter 18
Reformulation of Mixture Theory-Based Poroelasticity for Interstitial Tissue Growth

Stephen C. Cowin

Abstract This contribution presents an alternative approach to mixture theory-based poroelasticity by transferring some poroelastic concepts developed by Biot to mixture theory. These concepts are a larger RVE and the subRVE-RVE velocity average tensor, which Biot called the micro-macro velocity average tensor. This velocity average tensor is assumed here to depend upon the pore structure fabric. The formulation of mixture theory presented is directed toward the modeling of interstitial growth, that is to say changing mass and changing density of an organism. Growth is slow and accelerations are neglected in the applications. The velocity of a solid constituent is employed as the main reference velocity in preference to the mean velocity concept from the original formulation of mixture theory. The standard development of statements of the conservation principles and entropy inequality employed in mixture theory are easily modified to account for these kinematic changes and to allow for supplies of mass, momentum and energy to each constituent and to the mixture as a whole. The objective is to establish a basis for the development of constitutive equations for growth of tissues.

18.1 Introduction

The purpose of this contribution is to present an alternative approach to mixture theory-based poroelasticity by transferring some poroelastic concepts developed by Biot (1935, 1941, 1956a,b, 1962a,b) and Biot and Willis (1957) to mixture theory. The long-term objective of this study is facilitating the mixture modeling of biological growth phenomena. Since mixture theory was first presented by Truesdell (1957) its relationship to the previously established Biot's poroelasticity theory (Biot, 1941) has been a subject of discussion. In this contribution the overlap in the two theories is increased. In several important ways the mixture model of saturated porous media is more general than the Biot (1941) model of poroelasticity; Bowen (1980, 1982) recovered the model of Biot (1941) from the mixture theory approach.

S.C. Cowin (✉)
The Department of Biomedical Engineering, Grove School of Engineering of The City College and The Graduate School, The City University of New York, New York, NY 10031, USA
e-mail: sccowin@gmail.com

G.A. Holzapfel, E. Kuhl (eds.), *Computer Models in Biomechanics*,
DOI 10.1007/978-94-007-5464-5_18,

Fig. 18.1 A cartoon that illustrates the thesis of this contribution; the cartoon is a paradigm for the change in conceptual basis suggested for mixture theory based poroelasticity. The house being transported represents a significant structure of mixture theory being moved to a representative volume element viewpoint described in Biot (1941)

The most important way in which the mixture model is more general than the Biot poroelastic model is that the mixture model admits the possibility of following many solid and fluid constituents and it admits the possibility of having chemical reactions occurring. Thus some constituents might vanish and others might be created. The contrast with Biot theory is that Biot theory considers the single solid and fluid components to be chemically inert. In several important ways the poroelastic model of Biot (1941, 1956a,b, 1962a,b) and Biot and Willis (1957) offers better conceptual mechanisms for relating the elements of the physical situation to their mathematical representations, a principal example being a hierarchical structure that permits the distinction between the matrix, the drained and the undrained elastic constants. It is the objective of this contribution to transfer the selected Biot conceptual mechanisms to a mixture theory formulation of poroelasticity, thus combining the advantages of Biot's ideas with mixture theory.

The cartoon in Fig. 18.1 illustrates the thesis of this contribution; the cartoon is a paradigm for the change in conceptual basis suggested for mixture-theory based poroelasticity. The house being transported represents the significant structure of mixture theory. The foundation from which the house was removed represents the Eulerian point considered in the analysis of mixtures of fluids (Fig. 18.2). The foundation to which the house is moved represents the representative volume element (REV) employed in Biot's (1941) development of poroelasticity (Fig. 18.3). When a house is moved from one location to another the plumbing must be disengaged at the first location and reengaged at the new location. That is indeed the case for this change in conceptual basis suggested for mixture-theory based poroelasticity. However this change of plumbing for the theory is dealt with in a relatively simple and simplifying way as will be described.

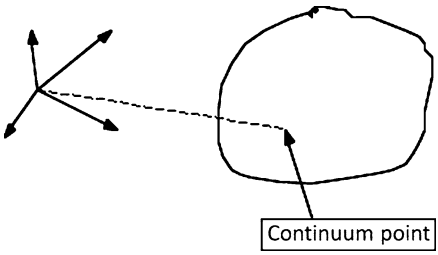

Fig. 18.2 The foundation from which the house was removed represents the Eulerian point considered in the analysis of mixtures of fluids

18.2 Mixture Theory

A mixture is a material with two or more ingredients, the particles of which are separable, independent, and uncompounded with each other. If the distinct phases of a mixture retain their identity, the mixture is said to be immiscible; if they lose their identity, the mixture is said to be miscible. The constituents include a porous solid of possibly a number of constituents, as well as solvents and solutes. The theory of mixtures is based on diffusion models and stems from a fluid mechanics and thermodynamics tradition and goes back to the century before last. Fick (1855) and Stefan (1871) suggested (Truesdell and Toupin, 1960, Sects. 158 and 295) that each place in a fixed spatial frame of reference might be occupied by several different particles, one for each constituent of the mixture (Fig. 18.2). Truesdell and Toupin (1960) assigned to each constituent of a mixture in motion a density, a body force density, a partial stress, a partial internal energy density, a partial heat flux and a partial heat supply density.

Truesdell and Toupin (1960) postulated equations of balance of mass, momentum and energy for each constituent and derived the necessary and sufficient conditions that the balance of mass, momentum and energy for the mixture be satisfied. Bowen (1967) summarized the formative years of this subject. A readable history of the subject and its applications in the period 1957–1975 is given by Atkin and Craine (1976a,b). De Boer (1996, 2000) has presented more up-to-date histories. Of key importance in the development of the mixture theories is the application by Bowen (1967, 1976, 1980, 1982) of a thermodynamically-based analytical approach developed by Coleman and Noll (1963) to restrict the form of constitutive equations.

There have been many notable contributions of the mixture theory approach to the modeling of tissue growth that are not cited here, as this is not a review of that broad subject. Others have employed some of the modifications of mixture theory employed here, but one would have to trace each modification through the literature to determine which authors first employed it. Such a review is not the objective of this contribution.

18.3 Poroelasticity

Poroelasticity is a theory that models the interaction of deformation and fluid flow in a fluid-saturated porous, elastic medium. The deformation of the medium influ-

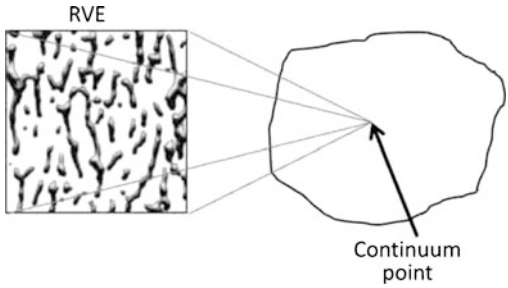

Fig. 18.3 The foundation to which the house is moved represents the representative volume element (RVE) employed in Biot's (1941) development of poroelasticity

ences the flow of the fluid and vice versa. The theory was proposed and developed by Biot (1941, 1956a,b, 1962a,b) and Biot and Willis (1957) as a theoretical extension of soil consolidation models for calculating the settlement of structures placed on fluid-saturated porous soils. The theory has been widely applied to geotechnical problems beyond soil consolidation, most notably problems in rock mechanics and wave propagation in porous media. There are thousands of papers, and a singular, but notable, book on the subject is that of Coussy (2004). The governing equations for anisotropic poroelasticity for quasi-static and dynamic poroelasticity were developed and extended to include the dependence of the constitutive relations upon a pore structure fabric tensor **F** as well as the porosity (Cowin 1985, 2004a; Cardoso and Cowin, 2011; Cowin and Cardoso, 2011).

18.4 The Alternative Formulation of Mixture Theory-Based Poroelasticity

In this alternative formulation of mixture theory-based poroelasticity, the Eulerian point used in mixture theory as a model of the continuum point (Fig. 18.2) is replaced by a larger RVE introduced by Biot as the model of the continuum point (Fig. 18.3). Further, Biot's concept of the RVE level representation of the fluid velocity as a function of the pore fluid velocities in the sub RVE pores is employed. Finally, the mixture theory concept of the mean velocity of the solid and fluid constituents is replaced by reference to the velocity of the solid and the diffusion velocities relative to a solid constituent.

This formulation of mixture theory is directed toward the modeling of biological growth, that is to say changing mass and changing density of an organism. Growth is slow, accelerationless from a mechanics viewpoint and therefore, although formulas for the acceleration are obtained (Cowin and Cardoso, 2012), accelerations will be neglected in the applications. The formulas for acceleration are obtained so that what is neglected is specially specified. The presentation of the theory of mixtures in Cowin and Cardoso (2012) is further restricted to the situation in which all the mixture constituents are compressible, immiscible, reacting (chemical reactions) and all are at the same temperature. It is assumed that terms proportional to the square of diffusion velocities will be negligible. Bowen (1976), see page 27 therein, considers

the case where they are not negligible. Interstitial flow is slow through a particular tissue because it is 8 liters per day or 5.55 cubic centimeters per minute for the entire human body (Levick, 1995; Cowin, 2011). The exact velocity ranges of this flow are unknown but measurements in limb tissue have suggested they are on the order of 0.1 to 2 microns per second (0.03 to 0.57 feet per day) (Levick, 1995; Cowin, 2011). Deformation-driven interstitial flows, such as those that occur in bone tissue, are greater, on the order of tens of microns per second. No tissue has a mass always composed of the same proteins and fluids; they are always changing, however slowly. Thus tissues form open systems.

For the growth of soft tissue it is reasonable to assume that the blood supply to the tissue will deliver the proteins and the supply of energy. If these proteins carried by the blood are not employed or deployed by the liver in their first pass through the tissue in need they will likely be transported across the blood vessel walls to pass into the interstitial fluid of another tissue. The interstitial fluid will then pass through the tissue to a collecting lymph node and then pass into the lymphatic system. The lymphatic system collects the lymph from all the tissues, concentrates the proteins and passes them back into the circulatory system at the left subclavian vein before it enters the heart. The tissue building proteins are then recirculated again and again before they find deployment in a tissue or are passed out of the body (Levick, 1995). The coupling of these related transport problems to growth problems is not difficult due to very slow transport velocities involved.

It is assumed that the stress tensor associated with each constituent is symmetric and that there are no action-at-a-distance couples, as there would be, for example, if the material contained electric dipoles and was subjected to an electrical field. The restrictions associated with each of these assumptions may be removed; they are imposed to restrict this presentation to an economical path for the development of a tissue-appropriate model for normal physiological growth phenomena.

18.4.1 Open and Closed System Models at the Constituent and Mixture Levels

Open systems permit the transport of mass, momentum and energy across their boundaries, closed systems do not. Bertalanffy (1950) pointed out that ‘From the physical point of view the characteristic state of the living organism is that of an open system’. Thus an open system model is desired to model growth. In traditional mixture theory (Truesdell and Toupin, 1960), each constituent is considered to be an open system, but the entire mixture is considered to be a closed system. In the Cowin and Cardoso (2012) development, the mixture is also considered to be an open system as a mechanism by which growth may be modeled. This means that the statements of the balance principles for the mixture may have supply terms as well as the statements of the balance principles for each constituent.

An alternative attractive approach to achieving an open system by allowing supply terms in the balance equations for the mixture is to, instead, allow the mixture to

be viewed as existing within a reservoir that is capable of supplying more mass of any constituent or being capable of resorbing some of the mass of any constituent. This was the approach taken in Cowin and Hegedus (1976) in the development of a growth model for bone tissue.

18.4.2 The Biot RVE for Poroelasticity and the Mixture Theory Approach

A key difference between the Biot effective parameter approach and the Eulerian point approach to mixture poroelastic models is the averaging process employed. The effective parameter approach illustrated in Fig. 18.3 is a schematic version of the viewpoint described in Biot (1941). He wrote, 'Consider a small cubic element of soil, its sides being parallel with the coordinate axes. This element is taken to be large enough compared to the size of the pores so that it may be treated as homogeneous, and at the same time small enough, compared to the scale of the macroscopic phenomena in which we are interested, so that it may be considered as infinitesimal in the mathematical treatment.' This prose written by Biot appears to be the first statement of what later came to be called the representative volume element (RVE) concept. In Biot's proposal a small but finite volume of the porous medium is used as a model for a continuum point in the development of constitutive equations for the fluid-infiltrated porous solid. These constitutive equations are then assumed to be valid at a point in the continuum. The length or size of the RVE is assumed to be many times larger than the length scale of the microstructure of the material, say the size of a pore. The length of the RVE is the length of the material structure over which the material microstructure is averaged or 'homogenized' in the process of forming a continuum model. The homogenization approach is illustrated in Fig. 18.3 by the dashed lines from the four corners of the RVE to the continuum point. The material parameters or constants associated with the solid phase are more numerous and difficult to evaluate compared to those associated with the fluid phase. The Biot-effective modulus approach provides a better understanding of the effective solid mechanical parameters like effective solid moduli than does the mixture theory approach.

The averaging process for the mixture approach is illustrated in Fig. 18.2. This is an Eulerian approach in that the flux of the various species toward and away from a spatial point is considered. The spatial point is shown in Fig. 18.2 and the vectors represent the velocities of various species passing through the referenced spatial point. In neither approach is a length scale specified, but an averaging length is implied in the Lagrangian material, Biot-effective modulus, approach because a finite material volume is employed as the domain to be averaged over. On the other hand the mixture theory is Eulerian and considers a fixed spatial point through which different materials pass and, as with the Biot approach, no length scale is suggested. It is difficult to imagine a length scale for the mixture theory approach other than one based on the mean free paths associated with the constituents. The

significantly different averaging lengths in the two approaches reflect the difference in the averaging methods.

18.4.3 The Larger RVE Hypothesis

The larger RVE for mixture theory-based poroelasticity is considered to have a length or size many times larger than the length scale of the pores (Fig. 18.3). It is assumed that the pores represent a lesser length scale that is sub RVE. The length of the RVE is the length of the material structure over which the porous microstructure is averaged or 'homogenized' in the process of forming a continuum model. The RVE is of sufficient size so that three sets of elastic constants (the drained and the undrained and those of the matrix material) may be represented as well as the porosity and the pore structure fabric tensor **F**. Pore structure fabric is a quantitative stereological measure of the degree of structural anisotropy in the pore architecture of a porous medium (Hilliard, 1967; Whitehouse, 1974; Whitehouse and Dyson, 1974; Oda, 1976; Cowin and Satake, 1978; Oda et al., 1980, 1985; Satake, 1982; Kanatani, 1983; Harrigan and Mann, 1984; Kanatani, 1984a,b, 1985; Odgaard 1997, 2001; Odgaard et al., 1997; Matsuura et al., 2008). The governing equations for anisotropic poroelasticity were developed and extended to include the dependence of the constitutive relations upon pore structure fabric (Cowin 1985, 2004a). Dynamic poroelasticity was extended by Cardoso and Cowin (2011) and Cowin and Cardoso (2011) to include the pore structure fabric tensor as a variable. The pore structure of the RVE is assumed to be characterized by porosity and a pore structure fabric tensor **F**.

18.5 The Hypothesis for Representing Microflows at the RVE Level

Let $\mathbf{v}^m_{(a/s)}$ denote the fluid sub RVE velocity of constituent 'a' relative to the selected (solid) constituent 's.' This is a velocity that exists only in the small pores of the solid matrix. The general hypothesis for representing microflows at the RVE level is that a homogenization process over the RVE may be constructed to determine the RVE level fluid velocity $\mathbf{v}_{(a/s)}$ from the fluid sub RVE velocity $\mathbf{v}^m_{(a/s)}$. This homogenization process will depend on the pore structure fabric tensor **F** of the RVE since the process is accomplished over the porous structure of the RVE.

The precise homogenization process employed is likely to depend upon the particular problem being studied so no general mathematical formulation is proposed here. For this presentation the Biot hypothesis (1956a) for representing sub RVE flows at the RVE scale is adopted:

$$\mathbf{v}_{(a/s)} = \mathbf{J} \cdot \mathbf{v}^m_{(a/s)}, \tag{18.1}$$

where **J** is the subRVE-RVE velocity average tensor; Biot (1962a) uses the term micro-macro velocity average tensor. **J** plays the role of a density distribution function that relates the relative micro-solid-fluid velocity to its RVE level bulk volume average $\mathbf{v}_{(a/s)}$. The subRVE-RVE velocity average tensor **J** is related to the pore structure fabric tensor **A** by (Cowin and Cardoso, 2011, Eq. (62))

$$\mathbf{J} = \mathbf{Q} \cdot \left(j_1 \mathbf{I} + j_2 \mathbf{A} + j_3 \mathbf{A}^2 \right), \tag{18.2}$$

where j_1, j_2 and j_3 are functions of I, II and III, where II and III are the second and third invariants of **A**; the first invariant is normalized to one. **Q** represents a rotation tensor associated with the transformation between the principal axes of **F** and the reference coordinate system used for **J**. In earlier work the governing equations for quasi-static (Cowin, 2004a) and dynamic (Cowin and Cardoso, 2011) linear theories of anisotropic poroelastic materials were developed and extended to include the dependence of the constitutive relations upon pore structure fabric (Cowin, 1985, 2004b). It is assumed there that any mixture theory growth model based on the present formulation will assume that all the constitutive equations will depend upon pore structure fabric. However, in the present contribution, the pore structure fabric tensor will only appear in Eq. (18.2) above for the purpose of explaining the nature of the subRVE-RVE velocity average tensor **J**. It was noted above that **J** functions like a density distribution function; that density distribution is determined by the pore structure fabric tensor **A**. It is possible that growth models will, in the future, include fabric tensors associated with particular constituents (e.g., collagen) as well as pore structure fabric.

18.6 The Mean Velocity of a Mixture

In the mixture theory it is customary to define the mean velocity of the mixture as the density-weighted average of the velocities of all the constituents,

$$\mathbf{v} = \frac{1}{\rho} \sum_{a=1}^{N} \rho_{(a)} \mathbf{v}_{(a)}. \tag{18.3}$$

There are two reasons why the concept of mean velocity is not employed in a significant way in this development. The first is its dubious physical significance when averaging over solid and fluid velocity components. The second is that its meaning as the mean velocity (18.3) is compromised when some of the RVE fluid velocities $\mathbf{v}_{(a/s)}$ are determined from the sub RVE fluid velocities $\mathbf{v}^m_{(a/s)}$ by a homogenization process. Given that the computation of the mean velocity employs RVE fluid velocities $\mathbf{v}_{(a/s)}$, which are determined from a homogenization process, renders the dubious physical significance of the mean velocity (18.3) more obscure. Here the velocity of the solid is used for reference velocity and the mean velocity of the mixture is generally avoided as has been assumed by a number of earlier mixture theory

authors, although we have not seen in previous publications all the consequences of that assumption that we record here. This option results in some complicated formulas for the acceleration of constituents, but the biological growth processes of interest are accelerationless.

18.7 Summary

This contribution presented an alternative approach to mixture theory-based poroelasticity by transferring some poroelastic concepts developed by Biot to mixture theory. These concepts were a larger RVE and the subRVE-RVE velocity average tensor, which was assumed to depend upon the pore structure fabric. The formulation of mixture theory presented, and detailed in Cowin and Cardoso (2012), was directed toward the modeling of interstitial growth, that is to say changing mass and changing density of an organism by the addition of mass to each constituent and to the total mixture. Traditional mixture theory considers constituents to be open systems, but the entire mixture is a closed system. In this development the mixture was also considered to be an open system as one possible mechanism for modeling growth. Growth is slow and accelerations are neglected in the applications. The standard kinematics of mixture theory was modified to account for the fact that pore fluid velocities generally occur at a scale below those of the solid velocities in poroelastic materials. Use of the velocity of the main solid constituent is employed as the main reference velocity in preference to the mean velocity concept from traditional mixture theory. The standard development of statements of the conservation principles and entropy inequality employed in mixture theory were modified in Cowin and Cardoso (2012) to account for these kinematic changes and to allow for supplies of mass, momentum and energy to each constituent and to the mixture as a whole. The basis for the development of constitutive equations for growth of tissues was thus partially established. There still remain the problems of specifying the supply terms for each constituent and for the mixture as a whole as well as the specification of how the building materials to be deposited are transported to their point of deposition.

Acknowledgements This work was supported by the National Science Foundation (PHY-0848491), the PSC-CUNY Research Award Program of the City University of New York.

References

Atkin RJ, Craine RE (1976a) Continuum theories of mixtures: applications. J Inst Math Appl 17:153–207

Atkin RJ, Craine RE (1976b) Continuum theories of mixtures: basic theory and historical development. Q J Mech Appl Math 29:209–244

Bertalanffy L (1950) The theory of open systems in physics and biology. Science 111:23–29

Biot MA (1935) Le problème de la consolidation des matières argileuses sous une charge. Ann Soc Sci Brux Sér I 55:110–113

Biot MA (1941) General theory of three-dimensional consolidation. J Appl Phys 12:155–164
Biot MA (1956a) Theory of propagation of elastic waves in a fluid-saturated porous solid. I. Low frequency range. J Acoust Soc Am 28:168–178
Biot MA (1956b) Theory of propagation of elastic waves in a fluid-saturated porous solid. II. Higher frequency range. J Acoust Soc Am 28:179–191
Biot MA (1962a) Generalized theory of acoustic propagation in porous dissipative media. J Acoust Soc Am 34:1254–1264
Biot MA (1962b) Mechanics of deformation and acoustic propagation in porous media. J Appl Mech 33:1482–1498
Biot MA, Willis DG (1957) The elastic coefficients of the theory of consolidation. J Appl Mech 24:594–601
Bowen RM (1967) Toward a thermodynamics and mechanics of mixtures. Arch Ration Mech Anal 24:370–403
Bowen RM (1976) Theory of mixtures. In: Eringen AC (ed) Continuum physics, vol III. Academic Press, New York, pp 1–127
Bowen RM (1980) Incompressible pourous media models by use of theory of mixture. Int J Eng Sci 18:1129–1148
Bowen RM (1982) Compressible porous media models by use of the theory of mixtures. Int J Eng Sci 20:697–735
Cardoso L, Cowin SC (2011) Fabric dependence of quasi-waves in anisotropic porous media. J Acoust Soc Am 129:3302–3316
Coleman BD, Noll W (1963) The thermodynamics of elastic materials with heat conduction and viscosity. Arch Ration Mech Anal 13:167–178
Coussy O (2004) Poromechanics. Wiley, New York
Cowin SC (1985) The relationship between the elasticity tensor and the fabric tensor. Mech Mater 4:137–147
Cowin SC (2004a) Anisotropic poroelasticity: fabric tensor formulation. Mech Mater 36:666–677
Cowin SC (2004b) Tissue growth and remodeling. Annu Rev Biomed Eng 6:77–107
Cowin SC (2011) The specific growth rates of tissues; a review and a reevaluation. J Biomech Eng 133:041001
Cowin SC, Cardoso L (2011) Fabric dependence of poroelastic wave propagation in anisotropic porous media. Biomech Model Mechanobiol 10:39–65
Cowin SC, Cardoso L (2012) Mixture theory-based poroelasticity as a model of interstitial tissue growth. Mech Mater 44:47–57
Cowin SC, Hegedus DH (1976) Bone remodelling I: Theory of adaptive elasticity. J Elast 6:313–326
Cowin SC, Satake M (eds) (1978) Continuum mechanical and statistical approaches in the mechanics of granular materials. Gakujutsu Bunken Fukyu-Kai, Tokyo
De Boer R (1996) Highlights in the historical development of the porous media theory: toward a consistent macroscopic theory. Appl Mech Rev 49:201–262
De Boer R (2000) Theory of porous media. Highlights in the historical development and current state. Springer, Heidelberg
Fick A (1855) Über Diffusion. Ann Phys 94:59–86
Harrigan TP, Mann RW (1984) Characterization of microstructural anisotropy in orthotropic materials using a second rank tensor. J Mater Sci 19:761–767
Hilliard JE (1967) Determination of structural anisotropy. In: Stereology—proceedings, 2nd international congress for stereology, Chicago, 1967. Springer, Berlin, p 219
Kanatani K (1983) Characterization of structural anisotropy by fabric tensors and their statistical test. J Jpn Solid Mech Found Eng 23:171–177
Kanatani K (1984a) Stereological determination of structural anisotropy. Int J Eng Sci 22:531–546
Kanatani K-I (1984b) Distribution of directional data and fabric tensors. Int J Eng Sci 22:149–164
Kanatani K (1985) Procedures for stereological estimation of structural anisotropy. Int J Eng Sci 23:587–598

Levick JR (1995) An introduction to cardiovascular physiology, 2nd edn. Butterworth-Heinemann, Boston

Matsuura M, Eckstein F, Lochmüller E-M, Zysset PK (2008) The role of fabric in the quasi-static compressive mechanical properties of human trabecular bone from various anatomical locations. Biomech Model Mechanobiol 7:27–42

Oda M (1976) Fabrics and their effects on the deformation behaviors of sand. Master Thesis, Department of Foundation Engr., Saitama University

Oda M, Konishi J, Nemat-Nasser S (1980) Some experimentally based fundamental results on the mechanical behavior of granular materials. Géotechnique 30:479–495

Oda M, Nemat-Nasser S, Konishi J (1985) Stress induced anisotropy in granular masses. Solid Mech Found 25:85–97

Odgaard A (1997) Three-dimensional methods for quantification of cancellous bone architecture. Bone 20:315–328

Odgaard A (2001) Quantification of cancellous bone architecture. In: Cowin SC (ed) Bone mechanics handbook. CRC Press, Boca Raton, pp 14-1–14-19

Odgaard A, Kabel J, van Rietbergen B, Dalstra M, Huiskes R (1997) Fabric and elastic principal directions of cancellous bone are closely related. J Biomech 30:487–495

Satake M (1982) Fabric tensor in granular materials. In: Vermeer PA, Lugar HJ (eds) Deformation and failure of granular materials. Balkema, Rotterdam, p 63

Stefan J (1871) Über das Gleichgewicht und Bewegung, insbesondere die Diffusion von Gemischen. Sitzgesber Akad Wiss Wien 63:63–124

Truesdell C, Toupin RA (1960) The classical field theories. In: Flügge S (ed) Encyclopedia of physics, vol III/1. Springer, Berlin, pp 226–793

Truesdell CA (1957) Sulle basi della termomeccania. Rend Lincei 22:33–38 1158–1166

Whitehouse WJ (1974) The quantitative morphology of anisotropic trabecular bone. J Microsc 101:153–168

Whitehouse WJ, Dyson ED (1974) Scanning electron microscope studies of trabecular bone in the proximal end of the human femur. J Anat 118:417–444

Chapter 19
Constitutive and Computational Aspects in Tumor Therapies of Multiphasic Brain Tissue

Wolfgang Ehlers and Arndt Wagner

Abstract The present contribution concerns the constitutive modeling and the numerical simulation of brain tissue with a specific focus on tumor therapies carried out by so-called convection-enhanced delivery processes (CED). The multiphasic modeling approach is based on the Theory of Porous Media (TPM) and proceeds from a volumetric homogenization of the underlying micro-structure. The brain tissue model exhibits an elastic solid skeleton (cells and vascular walls), which is perfused by two liquids, the blood and the interstitial fluid. The latter is treated as a mixture of two components, namely, a liquid solvent and a dissolved therapeutic solute. The inhomogeneous and anisotropic nature of the white-matter tracts is considered by a spatial diversification of the permeability tensors, obtained from Diffusion Tensor Imaging (DTI). Numerically, the strongly coupled solid-liquid-transport problem is simultaneously approximated in all primary unknowns (uppc-formulation) using mixed finite elements and solved in a monolithic manner with an implicit time-integration scheme. Within this procedure, numerical examples of the CED under two- and three-dimensional conditions are discussed.

19.1 Introduction and Treatment Options for Brain Tumors

After a medical detection of a brain tumor, the conventional treatment proceeds from a highly invasive removal of the tumor in combination with radiotherapy or chemotherapy. However, the healing success is still low, because malignant tumors are strongly resistant and regrow frequently. Therefore, the development of alternative and effective treatments is subject of current research.

Any suitable therapeutic agent reaching the malignant brain tumor can have the desired therapeutic outcome. Basically, there are several methods for the application

W. Ehlers (✉) · A. Wagner
Institute of Applied Mechanics (CE), University of Stuttgart, Pfaffenwaldring 7, 70569 Stuttgart, Germany
e-mail: Wolfgang.Ehlers@mechbau.uni-stuttgart.de

A. Wagner
e-mail: Arndt.Wagner@mechbau.uni-stuttgart.de

G.A. Holzapfel, E. Kuhl (eds.), *Computer Models in Biomechanics*,
DOI 10.1007/978-94-007-5464-5_19,

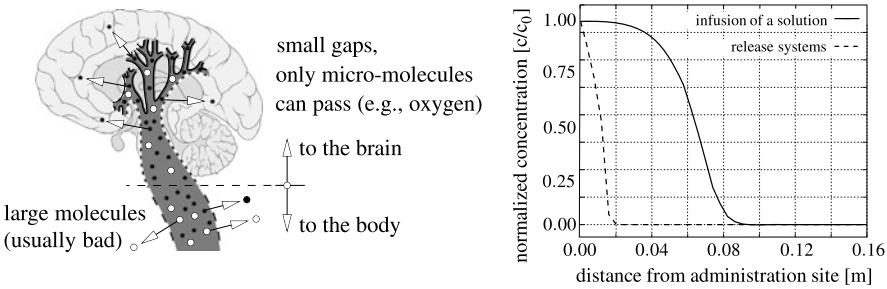

Fig. 19.1 *Left*: Sketch of limitations and characteristics of an intra-vascular medication. *Right*: Comparison of extra-vascular medications in the dispersion of therapeutics after the same time

of pharmaceuticals. Within chemotherapies, the most commonly used method is the intravenous application of drugs leading to a more or less regular distribution by the blood circulation. Within this method, only a part of the therapeutic agent reaches the target area. However, in case of brain tumors, the drugs have to pass the blood-brain barrier (BBB) to enter the tissue. Unfortunately, this is not possible for most of the commonly used therapeutic macro-molecules in brain-tumor therapies, cf. Fig. 19.1 (left).

A possible solution of the delivery problem is a direct insertion of therapeutic agents into the extra-vascular space in order to bypass the BBB. Herein, two different basic approaches can be distinguished:

- Implantation of release systems:
  - providing a constant concentration at the point of implantation
  - driving the distribution by diffusion as a result of concentration gradients
- Infusion of interstitial fluid with dissolved therapeutic agents:
  - distributing therapeutic agents by both concentration and pressure gradients
  - resulting in an extensive spreading of the therapeutic particles, see Fig. 19.1 (right)

The latter more promising approach represents the focus of this contribution and is generally known as convection-enhanced drug delivery (CED) of therapeutics. This pioneering method was introduced by Bobo et al. (1994) and clinically established by researchers from the National Institutes of Health (NIH). Through a small hole in the skull, a catheter is directly placed in the brain tissue, while the therapeutic solution is infused by an external medical pump. With this method, large target areas can be supplied. However, the prediction of the distribution profile is challenging since the distribution is affected by the complex nature of living brain tissue. Based on these remarks, the goal of this contribution is the continuum-mechanical and computational simulation of living brain tissue with application to the description of the CED process. We hope that a practising surgeon can be pre-operatively assisted in his decisions by our and comparable numerical studies.

19.2 Continuum-Mechanical Modeling of Human Brain Tissue

The continuum-mechanical description of human brain tissue was always an important task of biomechanical studies. In the context of the hydrocephalus problem, Hakim and Adams (1965) presented an early hypothesis that the occurring effects can only be described by the interplay of several brain-tissue components. The first satisfying mathematical approach, assuming the brain as a porous medium containing a viscous fluid in the extracellular space (ECS), was carried out two decades later by Nagashima et al. (1987) including a simple numerical simulation of a two-dimensional (2D) slice of the brain. Since then, various singlephasic and biphasic brain-tissue models (see, e.g., Taylor and Miller, 2004; Franceschini et al., 2006; Dutta-Roy et al., 2008) have been developed treating the hydrocephalus problem. For the specific application to CED, models have been proposed by, e.g., Smith and Humphrey (2007), Chen and Sarntinoranont (2007) or Linninger et al. (2008). However, there are still open questions concerning the coupling effects, the description of the deformable porous tissue and its entire pore content. To contribute to the solution of these questions, the present approach is based on the comprehensive Theory of Porous Media (TPM) in order to describe the multiphasic nature of brain tissue including the brain solid, the interstitial fluid and the vascular system.

19.2.1 Multiphasic Modeling Based on the TPM

The TPM is a macroscopic continuum theory, which is based on the Theory of Mixtures (TM), cf. Bowen (1976), combined with the concept of volume fractions. For more details on its foundation, cf., e.g., Ehlers (2002, 2009) and citations therein.

19.2.1.1 Basic Anatomy of the Human Brain Tissue

To obtain an overview of the modeling problem, the underlying structure of human brain tissue is briefly summarized. Situated in the rigid scull, the brain is surrounded by the cerebrospinal fluid (CSF), which is also found in the inner ventricles of the brain hemispheres. The intracellular space (ICS) of the nervous brain tissue consists of grey matter at the cerebral cortex (neural cell bodies) and of white-matter tracts (myelinated axons) in the inner regions. The ECS of the nervous brain tissue is filled with mobile interstitial fluid. Furthermore, the entire brain is crossed by a highly branched blood-vessel system.

19.2.1.2 Constituents, Volume Fractions and Densities

In order to enable the numerical simulation of the CED process, a biphasic four-constituent model is presented in accordance to Wagner and Ehlers (2010). The

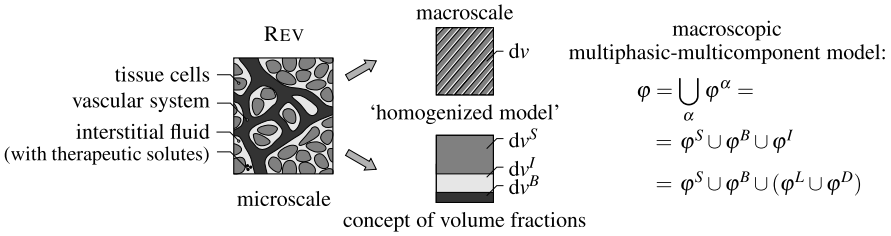

Fig. 19.2 Representative elementary volume (REV) with exemplarily displayed micro-structure of brain tissue and macroscopic multiphasic-multicomponent modeling approach

homogenization procedure of a representative brain-tissue sample is shown in Fig. 19.2, where a deformable solid skeleton φ^S consisting of tissue cells and vascular walls with hyperelastic properties is perfused by two mobile but separated liquid phases, the blood plasma φ^B and the overall interstitial fluid φ^I. The overall interstitial fluid φ^I is treated as a real chemical mixture of two components, the liquid solvent φ^L and the dissolved therapeutic solute φ^D. This leads to a ternary model $\varphi = \bigcup_\alpha \varphi^\alpha$ with $\alpha = \{S, B, I\}$ with four components initiated by φ^S, φ^B and $\varphi^I = \bigcup_\beta \varphi^\beta$ with $\beta = \{L, D\}$.

In order to account for the local compositions of the homogenized tissue, scalar volume fractions $n^\alpha = \mathrm{d}v^\alpha/\mathrm{d}v$ are introduced for the immiscible parts of the aggregate. Therein, $\mathrm{d}v^\alpha$ and $\mathrm{d}v$ are the local volume elements of φ^α and of the overall aggregate φ. Assuming fully saturated conditions, this leads to the well-known saturation condition

$$\sum_\alpha n^\alpha = n^S + n^B + n^I = 1. \tag{19.1}$$

With the aid of the volume fractions, two different densities can be distinguished relating the local masses $\mathrm{d}m^\alpha$ either to $\mathrm{d}v^\alpha$ or to $\mathrm{d}v$. These are the effective or realistic density $\rho^{\alpha R}$ and the partial density $\rho^\alpha = n^\alpha \rho^{\alpha R}$:

$$\rho^{\alpha R} = \mathrm{d}m^\alpha/\mathrm{d}v^\alpha, \qquad \rho^\alpha = \mathrm{d}m^\alpha/\mathrm{d}v. \tag{19.2}$$

Moreover, the sum of the partial densities yields the aggregate density $\rho = \sum_\alpha \rho^\alpha$.

To include the interstitial fluid mixture φ^I into the overall description, elements of the TM have to be embedded in the TPM (Ehlers, 2009). Following this, the amount of matter of φ^L and φ^D within φ^I has to be expressed by molar concentrations c_m^β and molar masses M_m^β. For this purpose, the partial densities ρ^β have to be related to the mixture volume of φ^I. In conclusion, this leads to

$$\rho^\beta = n^I \rho_I^\beta \quad \text{with } \rho_I^\beta = c_m^\beta M_m^\beta, \tag{19.3}$$

where ρ_I^β is the partial density of φ^β within φ^I. Finally, the effective density of the interstitial fluid mixture with respect to the overall aggregate yields $\rho^{IR} = \sum_\beta \rho_I^\beta$.

19.2.1.3 Kinematics of Superimposed Continua

Based on the fundamental assumption of superimposed continua, the TPM proceeds from the idea that any spatial point $\mathbf{x}$ of the current configuration is simultaneously occupied by material points of all constituents. However, each constituent follows its own motion such that $\mathbf{x} = \chi_\alpha(\mathbf{X}_\alpha, t)$ with $\mathbf{X}_\alpha$ as the reference position of the respective material point of φ^α and time t. This leads to the individual velocity fields $\overset{\prime}{\mathbf{x}}_\alpha = \mathrm{d}\chi_\alpha(\mathbf{X}_\alpha, t)/\mathrm{d}t$. The solid matrix is described by a Lagrangian formulation via the solid displacement $\mathbf{u}_S = \mathbf{x} - \mathbf{X}_S$ as the primary kinematic variable, while the pore-flow of blood and interstitial proceeds from a modified Eulerian setting via the seepage velocities $\mathbf{w}_\xi = \overset{\prime}{\mathbf{x}}_\xi - \overset{\prime}{\mathbf{x}}_S$ with $\xi = \{B, I\}$. Assuming the velocities of the liquid solvent and the interstitial fluid to be approximately identical, $\overset{\prime}{\mathbf{x}}_L \approx \overset{\prime}{\mathbf{x}}_I$ with $n^L \approx n^I$, the pore-diffusion velocity of the therapeutic solute φ^D reads $\mathbf{d}_{DI} = \overset{\prime}{\mathbf{x}}_D - \overset{\prime}{\mathbf{x}}_I$. This includes the possibility to define a seepage-like velocity $\mathbf{w}_D = \mathbf{d}_{DI} + \mathbf{w}_I$.

19.2.1.4 Balance Relations

The set of governing equations for the numerical treatment within the finite element method consists of the following balance equations, which are obtained from partial mass and momentum balances (e.g., Ehlers, 2009). Therein, materially incompressible constituents, no mass exchange between the constituents, quasi-static conditions and a uniform temperature are assumed.

- Concentration balance of the therapeutic agent φ^D:

$$0 = \left(n^I c_m^D\right)'_S + n^I c_m^D \operatorname{div}(\mathbf{u}_S)'_S + \operatorname{div}\left(n^I c_m^D \mathbf{w}_D\right) \tag{19.4}$$

- Volume balance of the overall interstitial fluid:

$$0 = \left(n^I\right)'_S + \operatorname{div}\left(n^I \mathbf{w}_I\right) + n^I \operatorname{div}(\mathbf{u}_S)'_S \tag{19.5}$$

- Volume balance of the blood plasma φ^B:

$$0 = \left(n^B\right)'_S + \operatorname{div}\left(n^B \mathbf{w}_B\right) + n^B \operatorname{div}(\mathbf{u}_S)'_S \tag{19.6}$$

- Momentum balance of the overall aggregate $\varphi = \bigcup_\alpha \varphi_\alpha$:

$$\mathbf{0} = \operatorname{div}\mathbf{T} + \rho\mathbf{g}. \tag{19.7}$$

  Therein, $\mathbf{T} = \sum_\alpha \mathbf{T}^\alpha$ is the overall Cauchy stress, while $\mathbf{b}^\alpha = \mathbf{g}$ characterizes uniform constant gravitational force.

19.2.1.5 Constitutive Settings

The presented balance equations need to be completed with admissible constitutive relations. An exploitation of the entropy inequality (Ehlers, 2002, 2009) yields restrictions and conditions for the formulation of constitutive equations such as the principle of effective stresses, viz.,

$$\mathbf{T}^S = \mathbf{T}^S_E - n^S p\,\mathbf{I} \quad \text{and} \quad \mathbf{T}^\xi = \mathbf{T}^\xi_E - n^\xi p^{\xi R}\mathbf{I}, \tag{19.8}$$

where $\mathbf{I}$ denotes the second-order identity. The extra-stresses $\mathbf{T}^\xi_E$ of the pore liquids are neglected due to dimensional reasons (e.g., Ehlers, 2002) as well as osmotic pressure contributions. The partial stress of the solid skeleton contains the pore pressure $p = (n^B p^{BR} + n^I p^{IR})/(1 - n^S)$. Following this,

$$\mathbf{T} = \mathbf{T}^S_E - p\mathbf{I}. \tag{19.9}$$

Therein, $\mathbf{T}^S_E$ is the effective stress governed by the solid deformation. Concerning the CED problem, use is made of the small-strain (linear) elasticity concept. In addition, although the brain tissue exhibits an inhomogeneous and anisotropic nature of the white-matter tracts, which strongly influences the pore-fluid and diffusion properties, it is assumed that a standard linear elasticity law in the Hookean sense is sufficient for the description of the brain deformation. Thus,

$$\mathbf{T}^S_E = 2\mu^S \boldsymbol{\varepsilon}_S + \lambda^S (\boldsymbol{\varepsilon}_S \cdot \mathbf{I})\mathbf{I}. \tag{19.10}$$

Therein, $\boldsymbol{\varepsilon}_S$ is the linear Green-Lagrangian strain, and μ^S and λ^S are the Lamé constants.

In this contribution, the main attention is drawn to the flow of the administered therapeutical including the drug. As a matter of fact, a slow infusion process with a slight application dose as is applied within the CED causes only small deformations in the solid skeleton (as is seen later in Fig. 19.7). However, if tumor growth or other diseases, i.e. hydrocephalus, have to be taken into consideration, the tissue model can be extended to finite elasticity or to finite viscoelasticity (see, e.g., Taylor and Miller, 2004; Ehlers et al., 2009). In both cases, the inclusion of solid anisotropy is possible.

Moreover, relations for the filter velocities $n^\xi \mathbf{w}_\xi$ of the pore fluids and for the drug diffusion $n^I c^D_m \mathbf{d}_{DI}$ need to be specified. Following the detailed constitutive modeling process described in Acartürk (2009) and Ehlers (2009), appropriate assumptions for the direct momentum production terms $\hat{\mathbf{p}}^\xi$ and $\hat{\mathbf{p}}^D$ have to be postulated and inserted into the respective partial momentum balances. In this regard, Darcy-like filter laws for the pore liquids are obtained in terms of

$$n^\xi \mathbf{w}_\xi = -\frac{\mathbf{K}^\xi}{\gamma^{\xi R}}\left(\operatorname{grad} p^{\xi R} - \rho^{\xi R}\mathbf{g}\right) \tag{19.11}$$

as well as a Fick-like diffusion law for the therapeutic agent:

$$n^I c^D_m \mathbf{d}_{DI} = -\mathbf{D}^D \operatorname{grad} c^D_m. \tag{19.12}$$

In the above equations, $\gamma^{\xi R}$ is the effective fluid weight and $\mathbf{K}^{\xi} = \gamma^{\xi R}\mathbf{K}^{S\xi}/\mu^{\xi R}$ is the Darcy permeability, involving the effective dynamic fluid viscosities $\mu^{\xi R}$ and the intrinsic permeabilities $\mathbf{K}^{S\xi}$. Since the permeabilities are related to the deformation of the solid skeleton, deformation-dependent intrinsic permeabilities (e.g., Markert, 2007) are included via

$$\mathbf{K}^{S\xi} = \mathbf{K}_{0S}^{S\xi}\left(\frac{n^{\xi}}{n_{0S}^{\xi}}\frac{n_{0S}^{S}}{n^{S}}\right)^{\kappa}. \tag{19.13}$$

Therein, $\mathbf{K}_{0S}^{S\xi}$ are the permeability tensors of the undeformed solid reference configuration, which need to be equipped with material parameters describing the initial (anisotropic) intrinsic permeability of the tissue perfusion by the interstitial fluid ($\mathbf{K}_{0S}^{SI}$) and by the blood plasma ($\mathbf{K}_{0S}^{SB}$). The exponent $\kappa \geq 0$ governs the non-linear deformation-dependent behavior. A possibility for a patient-specific determination of the coefficients of the permeability tensors and of the effective drug diffusion tensor $\mathbf{D}^{D}$ is described in Sect. 19.2.2.

Finally, there is a general need to express the volume fractions of all constituents either by primary variables and initial conditions or by constitutive equations. In case of an incompressible solid constituent with an initial volume fraction of n_{0S}^{S} in the solid reference configuration, $n^{S} = n_{0S}^{S}(\det\mathbf{F}_S)^{-1}$ holds and simplifies to $n^{S} = n_{0S}^{S}(1-\operatorname{div}\mathbf{u}_S)$ in case of small-strain theories. Thus, as a result of (19.1), n^{B} and n^{I} cannot be specified by primary variables individually but only as a sum: $n^{B}+n^{I} = 1-n^{S}$. Thus, additional constitutive information is needed. To solve this problem, it is assumed in the present study that the blood-vessel system is stable and inherent. Furthermore, since the blood plasma is assumed to incompressible, this leads to the assumption that $n^{B} = n_{0S}^{B}$ is constant. In particular, it is assumed that $n^{B} = n_{0S}^{B} = 0.05$, cf. Table 19.1.

19.2.2 Inhomogeneous and Anisotropic Perfusion Parameters

Regarding the micro-structural composition of the nervous brain tissue, one can assume that perfusion in grey matter (cell bodies) is isotropic. In contrast, white-matter perfusion is anisotropic due to a preferred flow direction in the ECS along the axonal fibers. The micro-structural information of the white-matter tracts can be provided by Diffusion Tensor Imaging (DTI), cf. Basser et al. (1994). The outstanding feature of DTI is the possibility to determine the diffusion tensor $\mathbf{D}_{\text{awd}}$ of water molecules in living biological tissue. The symmetric, positive definite apparent water-diffusion tensor $\mathbf{D}_{\text{awd}}^{\text{n}}$ of each voxel of the DTI can be written as

$$\mathbf{D}_{\text{awd}}^{\text{n}} = \begin{bmatrix} D_{11}^{\text{n}} & D_{12}^{\text{n}} & D_{13}^{\text{n}} \\ D_{21}^{\text{n}} & D_{22}^{\text{n}} & D_{23}^{\text{n}} \\ D_{31}^{\text{n}} & D_{32}^{\text{n}} & D_{33}^{\text{n}} \end{bmatrix} \mathbf{e}_i \otimes \mathbf{e}_k = \begin{bmatrix} \gamma_{1,\text{awd}}^{\text{n}} & 0 & 0 \\ 0 & \gamma_{2,\text{awd}}^{\text{n}} & 0 \\ 0 & 0 & \gamma_{3,\text{awd}}^{\text{n}} \end{bmatrix} \mathbf{v}_i^{\text{n}} \otimes \mathbf{v}_i^{\text{n}}. \tag{19.14}$$

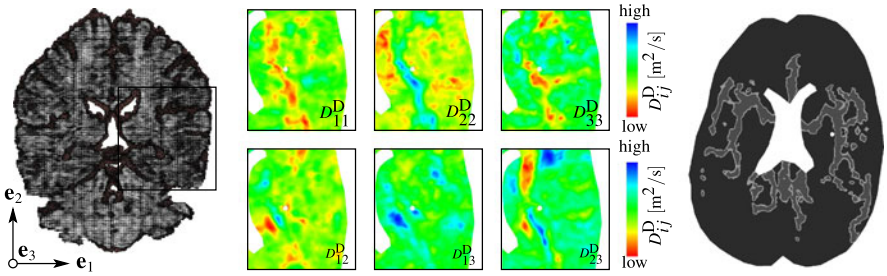

Fig. 19.3 *Left*: visualization of diffusion tensors as ellipsoids at a brain slice. *Middle*: selected values for all coefficients of the symmetric and anisotropic diffusion tensor $\mathbf{D}^{\mathrm{D}}$ obtained by DTI. *Right*: vascular (*grey*) and non-vascular (*black*) areas on a brain slice

Therein, n denotes the voxel number, $\mathbf{v}_i^{\mathrm{n}}$ are the eigenvectors and $\gamma_{i,\mathrm{awd}}^{\mathrm{n}}$ the eigenvalues of $\mathbf{D}_{\mathrm{awd}}^{\mathrm{n}}$ at each voxel. The basic assumption to obtain the required parameters is that $\mathbf{D}_{\mathrm{awd}}$ possesses the same eigenvectors as $\mathbf{D}^{\mathrm{D}}$ and $\mathbf{K}_{0S}^{SI}$, as it is proposed by Tuch et al. (2001). Therefore, a calibration as was shown by Sarntinoranont et al. (2006) or Linninger et al. (2008) is carried out via

$$\gamma_{i,\mathbf{D}^{\mathrm{D,n}}}^{\mathrm{n}} = \bar{D}^{\mathrm{D}} \frac{\gamma_{i,\mathrm{awd}}^{\mathrm{n}}}{\bar{\gamma}_{\mathrm{awd}}^{\mathrm{n}}} \quad \text{and} \quad \gamma_{i,\mathbf{K}^{\mathrm{I,n}}}^{\mathrm{n}} = \bar{K}^{I} \frac{\gamma_{i,\mathrm{awd}}^{\mathrm{n}}}{\bar{\gamma}_{\mathrm{awd}}^{\mathrm{n}}}, \tag{19.15}$$

where $\bar{\gamma}_{\mathrm{awd}}^{n}$ is the mean value of the eigenvalues and $\bar{D}^{\mathrm{D}}$ and $\bar{K}^{I}$ are adjusting reference values. Thus, the effective drug diffusion tensor $\mathbf{D}^{\mathrm{D,n}}$ and the anisotropic permeability tensor $\mathbf{K}_{0S}^{SI,\mathrm{n}}$ are computed for each evaluated voxel via

$$\mathbf{D}^{\mathrm{D,n}} = \sum_{i=1}^{3} \gamma_{i,\mathbf{D}^{\mathrm{D,n}}}^{\mathrm{n}} (\mathbf{v}_i \otimes \mathbf{v}_i) \quad \text{and} \quad \mathbf{K}_{0S}^{SI,\mathrm{n}} = \sum_{i=1}^{3} \gamma_{i,\mathbf{K}^{\mathrm{I,n}}}^{\mathrm{n}} (\mathbf{v}_i \otimes \mathbf{v}_i). \tag{19.16}$$

To show the general feasibility of this procedure, a patient-specific voxel data set is used here (available at http://www.sci.utah.edu/~gk/DTI-data/). In this regard, a custom MATLAB algorithm was programmed to process the raw binary data. Due to the irregular distribution of the anisotropic diffusion parameters, cf. Fig. 19.3 (left), it is not possible to define a closed analytical function for the anisotropic perfusion parameters. Therefore, the diffusion data is stored in a look-up table and loaded in a preceding calculation step to provide the full anisotropic perfusion parameters $\mathbf{D}^{\mathrm{D}}$ for the drug, cf. Fig. 19.3 (middle), and $\mathbf{K}_{0S}^{SI}$ for the interstitial fluid, respectively.

In order to include micro-structural information of the blood-vessel system, magnetic resonance angiography (MRA) is a promising in vivo approach to locate and image blood vessels within the brain tissue. In the present study, a blood-vessel segmentation of a MRA image was carried out using AMIRA, a software platform allowing for bio-medical data processing. With this tool, it is possible to assign vascular and non-vascular areas by varying blood perfusion parameters $\mathbf{K}_{0S}^{SB}$, cf. Fig. 19.3 (right). In this contribution, a microscopical isotropic perfusion is assumed, which varies in magnitude between vascular and non-vascular regions.

19.3 Numerical Application

In order to treat the strongly coupled multiphasic and multiphysical problem numerically, the FE solver PANDAS[1] is used. The primary variables of the present initial-boundary-value problem (IVBP) are the solid displacement $\mathbf{u}_S$ with corresponding test function $\delta\mathbf{u}_S$ associated with the momentum balance (19.7) of the overall aggregate, the effective pore pressures $p^{\xi R}$ with test functions $\delta p^{\xi R}$ corresponding to the volume balances (19.5) and (19.6) of the interstitial fluid and the blood plasma, and the concentration c_m^D with test function δc_m^D belonging to the concentration balance (19.4) of the therapeutic agent. After a transformation of the local balance equations into weak formulations, the momentum balance of the overall aggregate yields

$$\mathscr{G}_{\mathbf{u}_S} \equiv \int_\Omega \mathbf{T} \cdot \operatorname{grad} \delta\mathbf{u}_S \, \mathrm{d}v - \int_\Omega \rho\mathbf{g} \cdot \delta\mathbf{u}_S \, \mathrm{d}v - \int_{\Gamma_\mathbf{t}} \bar{\mathbf{t}} \cdot \delta\mathbf{u}_S \, \mathrm{d}a = 0, \tag{19.17}$$

where $\bar{\mathbf{t}} = \mathbf{T}\,\mathbf{n}$ is the external stress vector acting on the boundary of the overall aggregate and $\mathbf{n}$ is the outward-oriented unit surface normal. The weak form of the liquid constituents reads

$$\begin{aligned} \mathscr{G}_{p^\xi} \equiv & \int_\Omega \left[\left(n^\xi\right)'_S + n^\xi \operatorname{div}(\mathbf{u}_S)'_S \right] \delta p^{\xi R} \, \mathrm{d}v \\ & - \int_\Omega n^\xi \mathbf{w}_\xi \cdot \operatorname{grad} \delta p^{\xi R} \, \mathrm{d}v + \int_{\Gamma_{v^\xi}} \bar{v}^\xi \delta p^{\xi R} \, \mathrm{d}a = 0, \end{aligned} \tag{19.18}$$

where $\bar{v}^\xi = n^\xi \mathbf{w}_\xi \cdot \mathbf{n}$ is the efflux of liquid volume. Finally, the weak formulation of the concentration balance is

$$\begin{aligned} \mathscr{G}_{c_m^D} \equiv & \int_\Omega \left[\left(n^I c_m^D\right)'_S + n^I c_m^D \operatorname{div}(\mathbf{u}_S)'_S \right] \delta c_m^D \, \mathrm{d}v \\ & - \int_\Omega n^I c_m^D \mathbf{w}_D \cdot \operatorname{grad} \delta c_m^D \mathrm{d}v + \int_{\Gamma_{\bar{\imath}^D}} \bar{\imath}^D \delta c_m^D \, \mathrm{d}a = 0, \end{aligned} \tag{19.19}$$

where $\bar{\imath}^D = n^I c_m^D \, \mathbf{w}_D \cdot \mathbf{n}$ is the molar efflux of the therapeutic agent.

The spatial discretization of the coupled solid-fluid-transport problem within a $\mathbf{u}_S$–p^{BR}–p^{IR}–c_m^D-formulation requires mixed finite elements (see, e.g., Ellsiepen, 1999) with a simultaneous approximation of all primary variables. A standard Galerkin method is applied using extended Taylor-Hood elements with quadratic shape functions for $\mathbf{u}_S$ and linear shape functions for p^{IR}, p^{BR} and c_m^D in order to obtain a stable numerical solution. This leads to a differential-algebraic system of equations, which is solved in a monolithic manner with an implicit Euler time-integration scheme.

[1] **P**orous media **A**daptive **N**onlinear finite element solver based on **D**ifferential **A**lgebraic **S**ystems (http://www.get-pandas.com).

Table 19.1 Material parameters for numerical simulations of CED

Symbol	Value	Unit	Description/reference
ρ^{IR}	$0.993 \cdot 10^{+3}$	[kg/m^3]	effective density interstitial fluid (water at 37 °C) and
ρ^{BR}	$1.055 \cdot 10^{+3}$	[kg/m^3]	effective density of blood plasma according to *The Physics Factbook* by Glenn Elert (http://hypertextbook.com)
μ^{IR}	$0.7 \cdot 10^{-3}$	[Ns/m^2]	dynamic viscosity interstitial fluid (water at 37 °C) and
μ^{BR}	$3.5 \cdot 10^{-3}$	[Ns/m^2]	dynamic viscosity of blood at 37 °C according to *The Physics Hypertextbook* by Glenn Elert (http://physics.info/viscosity)
n^I_{0S}	0.20	[–]	initial interstitial fluid volume fraction, according to Baxter and Jain (1989) and citations therein
n^B_{0S}	0.05	[–]	initial blood volume fraction, according to Baxter and Jain (1989) and citations therein
n^S_{0S}	0.75	[–]	initial solidity (cells & vascular walls), remaining term in (19.1)
μ^S	$1.0 \cdot 10^{+3}$	[N/m^2]	elastic Lamé constants ($E = 2.8$ kPa; $\nu = 0.417$), chosen in
λ^S	$5.0 \cdot 10^{+3}$	[N/m^2]	magnitude according to Smith and Humphrey (2007), Chen and Sarntinoranont (2007) and citations therein
D^D_{ij}	10^{-11}–10^{-12}	[m^2/s]	order of magnitude of spatial varying drug diffusion coefficient, cf. Sect. 19.2.2, according to Baxter and Jain (1989) and citations therein
K^I_{ij}	10^{-7}–10^{-8}	[m/s]	order of magnitude of spatial varying Darcy permeability for the interstitial fluid, cf. Sect. 19.2.2, according to Kaczmarek et al. (1997)
K^B_{ii}	$3.0 \cdot 10^{-3}$	[m/s]	isotropic Darcy permeability coefficient, blood in vascular
	$3.0 \cdot 10^{-5}$	[m/s]	and non-vascular regions, based on Su and Payne (2009)
κ	1.4	[–]	deformation-dependent permeability (assumption)

19.3.1 Simulation of CED on a Human Brain Slice

As is well known in biomechanics, the in-vivo determination of patient-specific material data is an almost impossible task. Lacking of an alternative, the simulation parameters are predominantly extracted from the related literature on phantom experiments and numerical studies on animals or gels, see Table 19.1. However, since the focus of this contribution is mainly motivated by making available a modeling approach for numerical studies, we do not claim the accuracy for all included material parameters.

For the present numerical study, a realistic geometry of slice of a human brain is spatially discretized using 2,100 hexahedral Taylor-Hood elements (one element in thickness direction). As is shown in Fig. 19.4, the catheter is virtually placed in the brain tissue applying the corresponding boundary conditions for the CED. Furthermore, plane-strain conditions for the brain section are considered in combination with a horizontally fixed exterior of the brain (cortex). In addition, the blood flow is neglected in combination with a constant blood volume fraction. Figure 19.5 shows

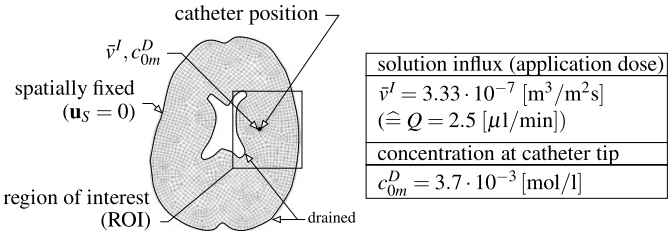

Fig. 19.4 Boundary conditions for CED on a horizontal brain section corresponding to a usual application dose. At the brain cortex and at the inner ventricle, an efflux of interstitial fluid and therapeutic agents over the surface is possible

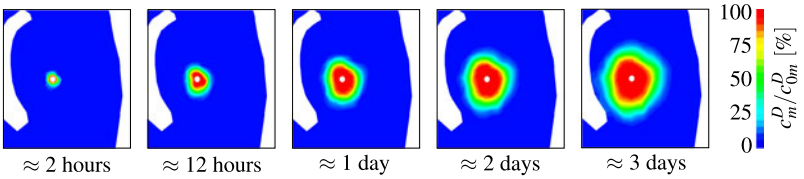

Fig. 19.5 Anisotropic distribution of the therapeutic agent during a CED process

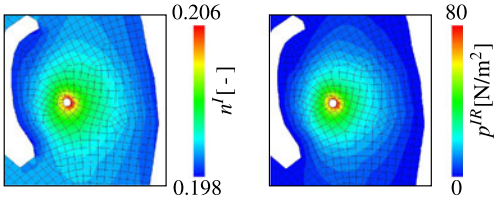

Fig. 19.6 *Left*: Volume fraction n^I of the interstitial fluid. *Right*: Interstitial fluid excess pressure p^{IR} during the infusion process

the anisotropic concentration profile in the region of interest (ROI) close to the infusion point at different time steps (in total three days). The therapeutic agent is distributed as expected in an irregular manner due to the anisotropic permeability parameters. Moreover, the propagation front is not smooth. The largest value of the interstitial fluid volume fraction, cf. Fig. 19.6, is found at the administration site of the catheter, as the solid constituent is dilated as a result of the infused solution. The excess pressure is a result of the infusion and naturally maximizes at the infusion site of the catheter, whereas the resulting pressure values are still moderate due to the small application rate. Note that the infusion pressure strongly depends on the infusion rate, the stiffness of the solid skeleton, and the tissue permeabilities. Note again that the present example is rather a numerical study than an approach on the basis of secure and patient-specific data. Nevertheless, numerical studies are important and provide the basis for a variety of computational results. For example, a decrease in the permeability parameters of the interstitial fluid would result in a faster increase of the infusion pressure, cf. Fig 19.7. This is an important aspect in the strategy of a clinical intervention, as a critical local pressure at the infusion site could lead to life-threatening effects due to large local dilatations of the tissue.

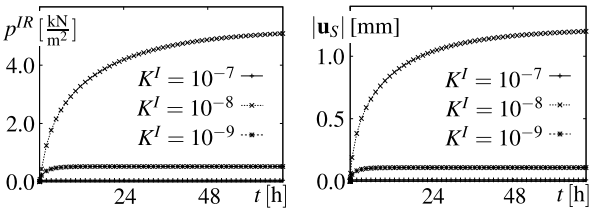

Fig. 19.7 Interstitial fluid excess pressure p^{IR} (*left*) and norm of the solid displacements $|\mathbf{u}_S|$ at varying permeabilities. Therein, K^I indicates the order of magnitude of the spatial varying Darcy permeability

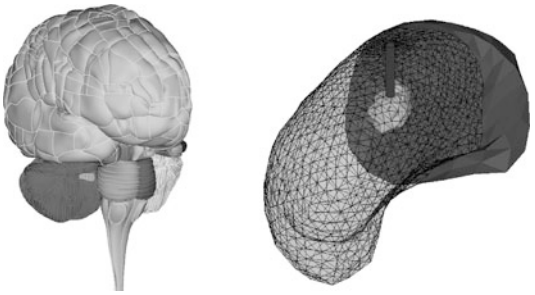

Fig. 19.8 *Left*: Geometrical preparation of the cerebral hemisphere for the finite-element meshing. *Right*: Numerical simulation results of a CED process, showing the spatial therapeutic agent distribution

19.3.2 Investigations on a Human Brain Hemisphere

For the sake of clarity, the simulation of a CED process was evaluated and discussed on a 2D brain slice. But since all formulations are derived in three dimensions, realistic geometries (e.g., of the human brain hemisphere) can be investigated. Therefore, a standard human brain (commercially available at www.anatomium.com) is used to survey the general physical behavior. The geometry was first adapted using the CAD software RHINOCEROS to prepare the cerebral hemisphere for the spatial discretization, cf. Fig. 19.8 (left). Afterwards, the geometry was exported into the mesh generation toolkit CUBIT and spatial discretized using tetrahedral Taylor-Hood elements. In the vicinity of the incorporated catheter, a finer grid was chosen. Boundary conditions and material parameters are applied according to Sect. 19.3.1. Realized numerical simulations show the 3D distribution front of therapeutic agents in the 3D brain model, cf. Fig. 19.8 (right).

19.4 Summary and Outlook

An appropriate constitutive model based on the TPM was presented, which is able to capture the infusion process of therapeutic agents into the brain tissue. All existing physical constituents are included in the modeling approach and a reasonable consideration of anisotropies and heterogeneities of the white-matter tracts was carried out, as this influences the observed irregular distribution of the infused therapeutic agents. The investigated model is able to describe the physical effects in a qualitative correct manner. If profound material parameters can be found in the future (by

appropriate clinical studies), the practising surgeons will benefit from preoperative studies, predicting the distribution of infused therapeutic agents.

Acknowledgements The diffusion tensor MRI brain dataset was obtained by courtesy of G. Kindlmann (Scientific Computing and Imaging Institute, University of Utah) and A. Alexander (W.M. Keck Laboratory for Functional Brain Imaging and Behavior, University of Wisconsin-Madison). Furthermore, proofreading by Dr. Nils Karajan is gratefully acknowledged.

References

Acartürk A (2009) Simulation of charged hydrated porous materials. Dissertation, Report No. II-18 of the Institute of Applied Mechanics (CE), Universität Stuttgart

Basser PJ, Mattielo J, Lebihan D (1994) Estimation of effective self-diffusion tensor from the NMR spin-echo. J Magn Reson 103:247–254

Baxter LT, Jain RK (1989) Transport of fluid and macromolecules in tumors: I. Role of interstitial pressure and convection. Microvasc Res 37:77–104

Bobo RH, Laske DW, Akbasak A, Morrison PF, Dedrick RL, Oldfield EH (1994) Convection-enhanced delivery of macromolecules in the brain. Proc Natl Acad Sci 91:2076–2080

Bowen RM (1976) Theory of mixtures. In: Eringen AC (ed) Continuum physics, vol. III. Academic Press, New York, pp 1–127

Chen X, Sarntinoranont M (2007) Biphasic finite element model of solute transport for direct infusion into nervous tissue. Ann Biomed Eng 35:2145–2158

Dutta-Roy T, Wittek A, Miller K (2008) Biomechanical modelling of normal pressure hydrocephalus. J Biomech 41:2263–2271

Ehlers W (2002) Foundations of multiphasic and porous materials. In: Ehlers W, Bluhm J (eds) Porous media: theory, experiments and numerical applications. Springer, Berlin, pp 3–86

Ehlers W (2009) Challenges of porous media models in geo- and biomechanical engineering including electro-chemically active polymers and gels. Int J Adv Eng Sci Appl Math 1:1–24

Ehlers W, Karajan N, Markert B (2009) An extended biphasic model for charged hydrated tissues with application to the intervertebral disc. Biomech Model Mechanobiol 8:233–251

Ellsiepen P (1999) *Zeit- und ortsadaptive Verfahren angewandt auf Mehrphasenprobleme poröser Medien*. Dissertation, Bericht Nr. II-3 aus dem Institut für Mechanik (Bauwesen), Universität Stuttgart

Franceschini G, Bigoni D, Regitnig P, Holzapfel GA (2006) Brain tissue deforms similarly to filled elastomers and follows consolidation theory. J Mech Phys Solids 54:2592–2620

Hakim S, Adams RD (1965) The special clinical problem of symptomatic hydrocephalus with normal cerebrospinal fluid pressure—observations on cerebrospinal fluid hydrodynamics. Neurol Sci 2:307–327

Kaczmarek M, Subramaniam RP, Neff SR (1997) The hydromechanics of hydrocephalus: steady-state solutions for cylindrical geometry. Bull Math Biol 59:295–323

Linninger AA, Somayaji MR, Mekarsk M, Zhang L (2008) Prediction of convection-enhanced drug delivery to the human brain. J Theor Biol 250:125–138

Markert B (2007) A constitutive approach to 3-D nonlinear fluid flow through finite deformable porous continua. Transp Porous Media 70:427–450

Nagashima T, Tamaki N, Matsumoto S, Horwitz B, Seguchi Y (1987) Biomechanics of hydrocephalus: a new theoretical model. Neurosurgery 21:898–903

Sarntinoranont M, Chen X, Zhao J, Mareci TM (2006) Computational model of interstitial transport in the spinal cord using diffusion tensor imaging. Ann Biomed Eng 34:1304–1321

Smith JH, Humphrey JA (2007) Interstitial transport and transvascular fluid exchange during infusion into brain and tumor tissue. Microvasc Res 73:58–73

Su S-W, Payne SJ (2009) A two phase model of oxygen transport in cerebral tissue. In: Annual international conference of the engineering in medicine and biology society, pp 4921–4924
Taylor Z, Miller K (2004) Reassessment of brain elasticity for analysis of biomechanics of hydocephalus. J Biomech 37:1263–1269
Tuch DS, Wedeen VJ, Dale AM, George JS, Belliveau JW (2001) Conductivity tensor mapping of the human brain using diffusion tensor MRI. Proc Natl Acad Sci USA 98:11697–11701
Wagner A, Ehlers W (2010) Continuum-mechanical analysis of human brain tissue. Proc Appl Math Mech 10:99–100

Chapter 20
A Biphasic 3D-FEM Model for the Remodeling of Microcirculation in Liver Lobes

Tim Ricken, Uta Dahmen, Olaf Dirsch, and Daniel Q. Werner

Abstract In this study we focus on a 3D computational model for the description of microperfusion and its application in liver lobes. The remodeling of microperfusion is initiated after a venous outflow obstruction. In particular, focal hepatovenous outflow obstruction can be caused by liver resection. Drainage of the obstructed territories is reestablished via dilatation of sinusoids connecting outflow obstructed territories to territories with normal hepatovenous outflow. Microperfusion is modeled by a homogenized biphasic approach based on the theory of porous media, see Ricken et al. (Biomech. Model. Mechanobiol. 9:435–450, 2010). Regarding the remodeling of microcirculation we make use of the phenomenological hypothesis that the blood pressure gradient is the main driving force for the formation of sinusoidal vascular canals. We recall the constitutive relations for the biphasic model including the solid stress, the transverse isotropic permeability law, and the remodeling algorithm. Finally, we present a numerical three-dimensional example covering microcirculation in seven liver lobes. After calculating the physiological status of the microcirculation in the liver lobes, we tested the hypothesis that the reorientation of blood flow mainly depends on the pressure gradient. Our findings support this hypothesis due to good agreement between experimental observation and computational results. Further investigations are needed to analyze functional processes such as cell metabolism.

T. Ricken (✉) · D.Q. Werner
Institute of Statics Mechanics Dynamics, TU Dortmund University, August-Schmidt-Str. 6, 44227 Dortmund, Germany
e-mail: tim.ricken@tu-dortmund.de

D.Q. Werner
e-mail: danielq.werner@tu-dortmund.de

U. Dahmen
Department of General, Visceral and Transplantation Surgery, University Hospital Jena, Drackendorfer Str. 1, 07747 Jena, Germany
e-mail: uta.dahmen@med.uni-jena.de

O. Dirsch
Institute of Pathology, University Hospital Jena, Ziegelmühlenweg 1, 07747 Jena, Germany
e-mail: olaf.dirsch@med.uni-jena.de

G.A. Holzapfel, E. Kuhl (eds.), *Computer Models in Biomechanics*,
DOI 10.1007/978-94-007-5464-5_20,

20.1 Introduction

The human liver receives its blood supply via the portal vein and the hepatic artery and is drained via the hepatic vein. The supplying and draining systems are connected via a delicate, highly organized vascular network. This vascular network consists of specific capillaries called sinusoids. Sinusoids are evenly distributed among liver cell plates, giving the liver 'sponge-like' properties.

Further, blood supply to the liver is delivered via two main branches of the portal vein and hepatic artery. These branches are the right and left portal vein, respectively, the right and left hepatic artery. Venous drainage of the liver is ensured by three hepatic veins, called the right, middle, and left hepatic veins. This two-to-three imparity is the anatomical basis of the focal outflow obstruction induced by resecting half of the liver. This surgical procedure is performed in extended liver resection and split liver transplantation. Resecting half of the liver requires the transection of the middle hepatic vein, leading to an outflow obstruction in the dependent hepatic territories.

Focal outflow obstruction induces hepatocellular damage in the respective drainage territories, leading to additional loss of functional liver tissue. This loss of functional liver mass adds to the loss caused by the resection itself. This combined loss of functional live mass can be detrimental for the patient undergoing extended liver resection, causing a small probability for size syndrome or even death. Liver resection itself causes portal hypertension, as half of the vascular bed is removed, forcing all blood from the intestine through a reduced vascular bed.

In Ricken et al. (2010) it was demonstrated that the proposed model applies to impaired perfusion of the liver after inducing focal outflow obstruction and the subsequent reestablishment of hepatic venous drainage. For the two-dimensional case, the results are closely compared to the results obtained in parallel, specifically designed experiments using our newly developed surgical model.

We created a surgical model of focal outflow obstruction in a rat, see Fig. 20.1. The rat liver consists of a median lobe which is—as is the human liver—supplied by two vessels, but drained by three vessels, and an additional three lobes supplied and drained separately. We incorporated focal outflow obstruction by ligating the right median hepatic vein and performed an additional 50 resection by removing the left lateral lobe to induce portal hypertension, cf. Dirsch et al. (2008). We were able to observe the extent of primary hepatic damage in the outflow obstructed area as well as the spontaneous recovery process consisting of reestablishment of venous drainage and parenchymal recovery from outflow obstruction. Further, volume recovery by growth of the liver (= regeneration) after liver resection was also observed.

Hepatic-venous drainage was reestablished within hours after ligation by redirecting sinusoidal blood flow via multiple-dilated sinusoids into the unobstructed neighboring territories. Within seven days the high number of dilated sinusoids was reduced to single vascularized sinusoidal canals. We postulated that the pressure gradient from the congested area to the neighboring normally drained territory in the hepatic 'sinusoid sponge' was the driving force for the formation of vascular

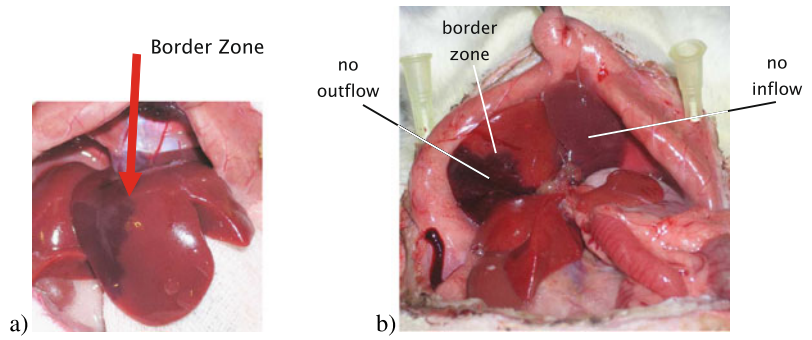

Fig. 20.1 (**a**) Congestion in the outflow disturbed territory (Dirsch et al., 2008); (**b**) animal model with defined perfusion defect after PH-30 %; provided from U. Dahmen

canals. Distension of sinusoids into sinusoidal canals was accompanied by a shift in gene and protein expression associated with a change in their wall structure, termed vascularization of sinusoidal canals. Vascularization of sinusoidal canals led to a thickening of the wall. Thickening of the sinusoidal wall is essential with respect to the change of function of this distended sinusoid aimed at draining the outflow-obstructed liver territory.

Changes in sinusoidal blood flow as well as the sinusoidal network were made visible by using orthogonal polarization spectroscopy (OPS), a technique for intravital microscopy. Changes in vascular structure and protein expression were observed using special histological and immunohistochemical staining methods.

The liver lobe is modeled as a sponge-like material with anisotropic perfusion behavior resulting from the inhomogeneous distribution of the sinusoidal network. This inner network structure of the liver admits such a high complexity that an accurate geometrical description in a continuum mechanical manner is impractical. Thus, a multiphase mixture theory based on the theory of porous media (TPM), see de Boer (1996, 2000) and Ehlers (2002), is used. Since the authors' past experience with the theory of porous media is highly satisfactory, especially regarding accuracy and thermodynamical consistency, we do not choose similar established multiphase theories describing biological tissues such as the mixture theory, cf. Mow et al. (1989) and Lai et al. (1991) or Biot's theory, cf. Biot (1935, 1941). The minor but significant differences between the three theories is the introduction of the constitutive framework; see de Boer (1996, 2000) or Lu and Hanyga (2005). Thus, under certain assumptions, the theories finally result in a set of field equations of similar type, cf. Bluhm and de Boer (1998) and Schanz and Diebels (2003). The choice of the theory of porous media should not be understood as a quantifying of these theories but as a practical choice founded on previous results.

It is well known that living tissue has the capacity to grow and to adapt to environmental changes by remodeling. In pathology, growth is understood as the increase of volume whereas remodeling defines the change in tissue structures like vessels or fibers, see, e.g., Majno and Joris (1996). In this paper we follow the definitions of growth and remodeling given by Humphrey and Rajagopal (2002). Therein, growth

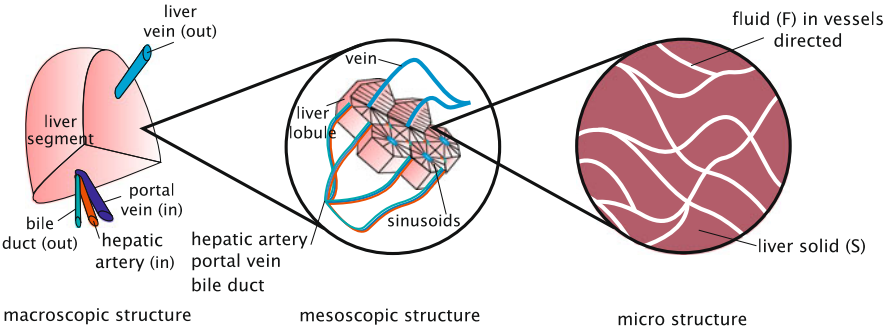

Fig. 20.2 Macro (liver, lobes and segments), meso (lobule) and micro (microcirculation in sinusoids) structure of the liver

in soft tissues is mathematically defined as the increase of mass via an increase of cells and/or via a synthesis of an extracellular matrix (ECM), whereas remodeling is characterized by a change in structure that is achieved by reorganizing existing constituents. As pointed out by Garikipati et al. (2006), remodeling and growth can be separated although they appear simultaneously in biological tissue. In this contribution we focus on remodeling the inner structure instead of the growth phenomenon as done by Epstein and Maugin (2000), Ambrosi and Mollica (2002), Kuhl and Steinmann (2003), Kuhl et al. (2003) regarding one phasic approaches, or Klisch et al. (2001), Humphrey and Rajagopal (2002), Guillou and Ogden (2006), Ehlers et al. (2003), Garikipati et al. (2004), or Ricken et al. (2007) for multiphase models.

The first descriptions of remodeling are given by Lee (1969) and Cowin and Hegedus (1976) in the context of plasticity. A general study of biological remodeling is given in Garikipati et al. (2006) where both evolution of the reference configuration and the concept of internal variables is investigated. In the present study, the latter concept has been used by integrating a preferred flow direction into the model.

Mechanical impact often influences the inner structures of biological tissues as, e.g., the remodeling of collagen fiber in arterial walls is considered stress driven where the fiber orientation follows the direction of principle stresses, see, e.g., Hariton et al. (2007). Gleason et al. (2004) suggested that carotid arteries be modeled as a flow-induced mixture in order to describe alterations in geometry, structure, and properties.

The simulation was based on the concept of mechanical-induced remodeling from Humphrey et al. (2009). The fluid is incorporated directly into the model as a solid-fluid mixture. We hypothesized that the reorientation of the sinusoidal flow and the remodeling of the sinusoidal structure depends mainly on the fluid pressure and the fluid pressure gradient caused by the outflow obstruction, see Dahmen et al. (2007) and Dirsch et al. (2008).

We tested this hypothesis with a numerical simulation and compared the results to the experimental findings. As we did not implement liver resection in the mathematical model presented here, but concentrated on focal outflow obstruction only, liver growth (= regeneration) was not addressed.

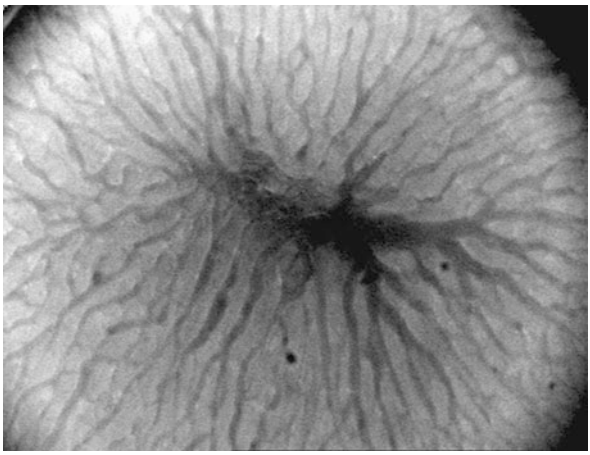

Fig. 20.3 Image of a liver lobule; the center shows the central vein surrounded by the sinusoids Hall (2006). The hepatic microcirculation was observed with an optical device using the technique of Orthogonal Polarization Spectral (OPS) Imaging (Cytoscan, Cytometrics, Inc., Philadelphia, PA, USA). This device allows real-time microscopic observation of the microcirculation of organ surfaces in vivo. The probe is gently placed on a serous organ surface and emits polarized light with a wavelength of 550 nanometers. Light penetrates into the tissue where most of it depolarizes and creates a virtual light source in the tissue

20.2 Methods

The general structure of the liver can be divided into a macroscopic, mesoscopic, and microscopic part as given in Fig. 20.2. At the macroscopic level, the human liver is divided in segments, whereas rodent livers consist of clearly separated liver lobes. Each lobule is connected with inflow vessels and one outflow vessel as shown in Fig. 20.2. Inside the liver lobule, the blood flows from the ingoing vessels (hepatic artery and portal vein) to the outgoing vessel (hepatic vein) through sinusoids; see the micro level in Fig. 20.2 and the OPS (orthogonal polarization spectroscopy, see, e.g., Nadeau and Groner, 2001) figure of the center of a lobule, see Fig. 20.3.

20.2.1 Biphasic Material Model for Liver

The two phases, namely the solid and the fluid phase, are presented as a biphasic continuum $\varphi = \varphi^{\mathrm{S}} + \varphi^{\mathrm{F}}$ which consists of the porous solid phase φ^{S} filled with the fluid phase (blood) φ^{F}. Both phases are assumed to be material incompressible see also Sect. 20.2.1.2. The solid phase represents the porous tissue structure with an anisotropic pore distribution since the blood flow is assumed so, but transversely isotropic in the direction of the vein. The fluid flow is influenced by both the outer pressure gradient and the anisotropic permeability. Here, we use the theory of porous media, a coupled, superimposed, continuum mechanical framework.

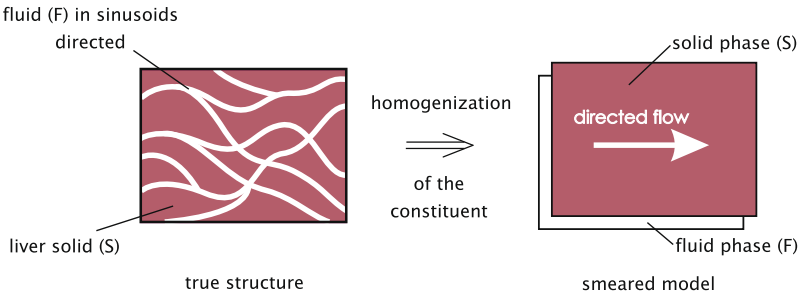

Fig. 20.4 Biphasic macromodel

20.2.1.1 Mixture Theory, Concept of Volume Fraction and Kinematics

The microscopic structure is represented within a statistical distribution of the constituents (solid and fluid) over a representative elementary volume (REV), see Fig. 20.4. The constituents φ^α will be represented by an averaging volume fraction n^α. Thereby, the volume fractions n^α refer to the volume elements dv^α of the individual constituents φ^α from the bulk volume element dv with

$$\mathrm{n}^\alpha(\mathbf{x},\mathrm{t}) = \frac{\mathrm{dv}^\alpha}{\mathrm{dv}}, \qquad \sum_{\alpha=1}^{\kappa} \mathrm{n}^\alpha(\mathbf{x},\mathrm{t}) = \sum_{\alpha=1}^{\kappa} \frac{\rho^\alpha}{\rho^{\alpha\mathrm{R}}} = 1, \quad \alpha \in \{\mathrm{S},\mathrm{F}\}, \tag{20.1}$$

where $\mathbf{x}$ is the position vector of the spatial point x in the actual placement and t is the time; we proceeded to a homogenized model with superimposed continua. The now separated partial volumes dv^α will again be interconnected constitutively by so-called interaction quantities. In general, these quantities are a mass exchange $\hat{\rho}^\alpha$, an interaction force $\hat{\mathbf{p}}^\alpha$, and an energy exchange $\hat{\mathrm{e}}^\alpha$. The volume fractions n^α in $(20.1)_1$ satisfy the volume fraction condition $(20.1)_2$ for κ constituents φ^α. Moreover, the partial density $\rho^\alpha = \mathrm{n}^\alpha \rho^{\alpha\mathrm{R}}$ of the constituent φ^α is related to the real density of the materials $\rho^{\alpha\mathrm{R}}$ involved via the volume fractions n^α; see $(20.1)_2$. Due to the volume fraction concept, all geometric and physical quantities, such as motion, deformation, and stress, are defined in the total control space. Thus, they can be interpreted as the statistical average values of the real quantities.

The saturated porous solid will be treated as an immiscible mixture of all constituents φ^α with particles X_α, where at any time t each spatial point X_S of the current solid placement is simultaneously occupied by fluid particles X_F. These particles proceed from different reference positions $\mathbf{X}_\alpha$ at time $\mathrm{t} = \mathrm{t}_0$.

Furthermore, the Jacobian is defined as $\mathrm{J}_\alpha = \det \mathbf{F}_\alpha$, where $\mathbf{F}_\alpha = (\partial \mathbf{x}_\alpha)/(\partial \mathbf{X}_\alpha) = \mathrm{Grad}_\alpha\, \boldsymbol{\chi}_\alpha$ is the deformation gradient of the constituent φ^α. During the deformation process $\mathbf{F}_\alpha$ is restricted to satisfy $\det \mathbf{F}_\alpha > 0$.

For scalar fields depending on $\mathbf{x}$ and t, the material time derivatives are defined as $(\ldots)'_\alpha = \partial(\ldots)/\partial \mathrm{t} + [\mathrm{grad}(\ldots)] \cdot \mathbf{x}'_\alpha$, with $\mathrm{grad}(\ldots) = \partial(\ldots)/\partial \mathbf{x}$. In order to use a

material objective measure of the fluid velocity with respect to the solid velocity, we introduce the seepage velocity $\mathbf{w}_{\mathrm{FS}}$, which describes the difference in velocity between the fluid phase $\mathbf{x}'_{\mathrm{F}}$ and the solid phase $\mathbf{x}'_{\mathrm{S}}$ S as $\mathbf{w}_{\mathrm{FS}} = \mathbf{x}'_{\mathrm{F}} - \mathbf{x}'_{\mathrm{S}}$. In connection with the fluid volume fraction this leads to the definition of the filtration velocity $\mathrm{n}^{\mathrm{F}}\,\mathbf{w}_{\mathrm{FS}}$. An extended explanation of the kinematics of porous media is given in de Boer (2000) or Ehlers (2002).

20.2.1.2 Assumptions

In general, we distinguish between four different types of biphasic materials: compressible (both components are compressible), hybrid type I (compressible solid and incompressible fluid), hybrid type II (incompressible solid and compressible fluid), and incompressible type (both components are incompressible). Since in most biological tissues the compressibility of the overall solid porous material is much higher in comparison with the material compressibility of the tissue material itself, see, e.g., Humphrey (2002), we assume a material incompressible solid tissue matrix ($(\rho^{\mathrm{SR}})'_{\mathrm{S}} = 0$) saturated by an incompressible pore fluid ($(\rho^{\mathrm{FR}})'_{\mathrm{F}} = 0$), i.e., the incompressible type. The volumetric deformation of the mixture body results from the change of pore space, namely a change of the volume fraction n^{α}, which leads to a macroscopic volumetric deformation. In liver tissue a volume deformation due to a physiologically hydrostatic pressure can also be observed.

With the assumption of material incompressibility on the solid skeleton, a compaction point must be introduced defining the state where all fluid is pressed out and all pores are closed so that no further compression occurs. The compaction point cannot be achieved physiologically since in biological tissues, neither the intracellular nor the interstitial fluid can be pressed out completely. Therefore, we used the Helmholtz free energy function formulated in Bluhm (2002), where an energy function based on Simo and Pister (1984) is extended to describe the compaction effect.

Since no mass or volumetric changes occurred during the remodeling of dilated sinusoids, we assume that mass exchanges between the solid and the fluid constituent is negligible. In general, remodeling requires cell proliferation as well as cell death. In the event of homeostatis, the balance of addition and depletion is equalized and no residual mass or volume change occurs over time. Thus, it is convenient to separate the phenomena of growth and remodeling for the modeling approach, see, e.g., Garikipati et al. (2006) or Kuhl and Holzapfel (2007).

Due to constant thermal conditions during the remodeling process, we further assume that interchanges of temperature and energy can be neglected among the constituents. Hence, energy supplies ($\hat{\mathrm{e}}^{\alpha}$) between the phases were not taken into account and we assumed an isothermal process with an equal temperature θ for solid (θ^{S}) and fluid phase (θ^{F}). Lastly, accelerations for all phases ($\mathbf{x}''_{\alpha} = \mathbf{o}$) were excluded.

20.2.2 Constitutive Modeling

With respect to thermodynamically consistent material laws we consider the entropy inequality, see Ricken et al. (2010). Thus, the thermodynamic restrictions

$$\mathbf{T}^{\mathrm{S}} = -\mathrm{n}^{\mathrm{S}}\lambda\mathbf{I} + 2\rho^{\mathrm{S}}\mathbf{F}_{\mathrm{S}}\frac{\partial\psi^{\mathrm{S}}}{\partial\mathbf{C}_{\mathrm{S}}}\mathbf{F}_{\mathrm{S}}^{\mathrm{T}}, \qquad \mathbf{T}^{\mathrm{F}} = -\mathrm{n}^{\mathrm{F}}\lambda\mathbf{I} \tag{20.2}$$

for the solid ($\mathbf{T}^{\mathrm{S}}$) and fluid ($\mathbf{T}^{\mathrm{F}}$) stress, respectively, as well as for the fluid interaction force $\hat{\mathbf{p}}^{\mathrm{F}} = -\hat{\mathbf{p}}^{\mathrm{S}}$ with

$$\hat{\mathbf{p}}^{\mathrm{F}} = \lambda\,\mathrm{grad}\,\mathrm{n}^{\mathrm{F}} - \mathbf{S}_{\mathrm{F}}\mathbf{w}_{\mathrm{FS}}, \tag{20.3}$$

must hold. In (20.2) and (20.3), $\mathbf{S}_{\mathrm{F}}$ denotes a positive definite material parameter tensor for permeability and λ represents the pressure.

On the one hand, the enlarged entropy inequality (20.2) forms the basic structure for the thermodynamically consistent constitutive modeling and provides the necessary restrictions for the material laws. On the other hand, biological tissues show highly coupled material behavior including anisotropy deformation response, viscoelasticity, anisotropic poroelasticity, osmosis, remodeling, and growth. For the description of the liver we confined ourself to a model including the anisotropy deformation response, anisotropic poroelasticity, and modeling of the poroelasticity. Although not all characteristics of the material are represented in the current model, we were able to describe the vascular behavior of the hepatic tissue in the case of outflow obstruction. The modeling of the anisotropic material behavior for stress which includes the compaction point is given in Ricken et al. (2010). Here, we will focus on the filter velocity, the transversely isotropic permeability, and the flow reorientation.

20.2.2.1 Filter Velocity and Transversely Isotropic Permeability

For the liver tissue we consider that the fluid flow is affected by two major mechanisms. Firstly, on the macroscale, blood is transported inside the liver from the main vessels (liver artery and portal vein; see Fig. 20.2) via smaller vessels into the lobar vessels. From here, the second mechanism starts: a micro-filter flow through the sinusoids; see Fig. 20.5. This filter flow forms the connection between the branches of the portal vein and liver artery with the branches of the liver vein. In the normal liver evenly and clearly directed, mostly straight perfusion of the sinusoids is seen by employing Orthogonal Polarization Spectroscopy (OPS) (Dirsch et al., 2008 and Dahmen et al., 2007). The 'sponge-like property' of the liver became more apparent, when observing the redirected blood flow of the liver with outflow obstruction using OPS (Dirsch et al., 2008). Redirection of flow leads not only to an actual change of direction—aiming for liver territories in which outflow is preserved—but also to a visible change in flow characteristics, like flow velocity, as well as a visible

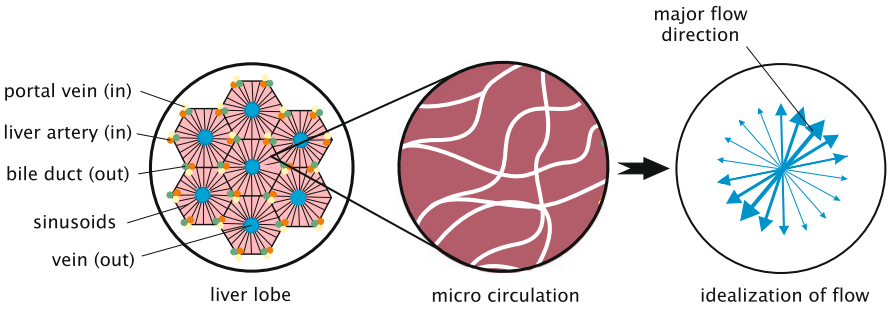

Fig. 20.5 Permeability in dependence on vessel and sinusoid distribution

change of the shape of the sinusoids. Although this connection is not straight linear, we mark an average major direction out, neglecting the waviness of the sinusoids. This major direction is neither fixed nor unique but underlies a varying dispersion as shown in Fig. 20.5. The major direction, dispersion, and diameter of the sinusoids are variable in time and space. Depending on boundary conditions, the liver tissue is able to change all three properties. In order to give a continuum representation of the sinusoidal orientation, we introduce a generalized structure tensor $\mathbf{M}_{\mathrm{F}} = \mathbf{a}_{\mathrm{F}} \otimes \mathbf{a}_{\mathrm{F}}$, where the arbitrary vector $\mathbf{a}_{\mathrm{F}} = \mathbf{F}_{\mathrm{S}}\, \mathbf{a}_{\mathrm{F0}}$, related to the arbitrary reference unit vector with $|\mathbf{a}_{\mathrm{F0}}| = 1$, represents the major distribution direction of the sinusoids. Due to the fact that the motions of both solid and fluid are connected by the interaction forces $\hat{\mathbf{p}}^{\mathrm{F}} = -\hat{\mathbf{p}}^{\mathrm{S}}$ and considering the thermodynamic restriction

$$\hat{\mathbf{p}}^{\mathrm{F}} = \lambda\, \mathrm{grad}\, \mathrm{n}^{\mathrm{F}} - \mathbf{S}_{\mathrm{F}} \mathbf{w}_{\mathrm{FS}} \tag{20.4}$$

(see (20.3) and Ricken and Bluhm 2009, 2010), we propose the representation of the anisotropic intrinsic permeability of the liver tissue as

$$\mathbf{S}_{\mathrm{F}} = \alpha_{\mathrm{F0}} \big[(1 - \alpha_{\mathrm{F}}) \mathbf{I} + \alpha_{\mathrm{F}} \mathbf{M}_{\mathrm{F}} \big]^{-1}. \tag{20.5}$$

The parameter $\alpha_{\mathrm{F}} \in [0, 1]$ defines the range between the fully isotropic state ($\alpha_{\mathrm{F}} = 0$) and the complete transverse isotropic state ($\alpha_{\mathrm{F}} = 1$). This parameter is suitable to adjust the direction distribution of sinusoids. In the case of a parallel distribution of all sinusoids, α_{F} becomes one, whereas for a random distribution, the condition $\alpha_{\mathrm{F}} = 0$ is assumed.

We derive the balance equation of momentum for the fluid phase with

$$\mathrm{div}\big(-\mathrm{n}^{\mathrm{F}} \lambda \mathbf{I}\big) + \rho^{\mathrm{F}} \mathbf{b} + \lambda\, \mathrm{grad}\, \mathrm{n}^{\mathrm{F}} - \big(\alpha_{\mathrm{F0}} \big[(1 - \alpha_{\mathrm{F}}) \mathbf{I} + \alpha_{\mathrm{F}} \mathbf{M}_{\mathrm{F}} \big]^{-1}\big) \mathbf{w}_{\mathrm{FS}} = \mathbf{0}, \tag{20.6}$$

see Ricken et al. (2010). In order to obtain a determination of the filter velocity $\mathrm{n}^{\mathrm{F}}\, \mathbf{w}_{\mathrm{FS}}$, we rearrange (20.6) into

$$\mathrm{n}^{\mathrm{F}} \mathbf{w}_{\mathrm{FS}} = \frac{(\mathrm{n}^{\mathrm{F}})^2}{\alpha_{\mathrm{F0}}} \big[(1 - \alpha_{\mathrm{F}}) \mathbf{I} + \alpha_{\mathrm{F}} \mathbf{M}_{\mathrm{F}} \big] \big(- \mathrm{grad}\, \lambda + \rho^{\mathrm{FR}} \mathbf{b} \big). \tag{20.7}$$

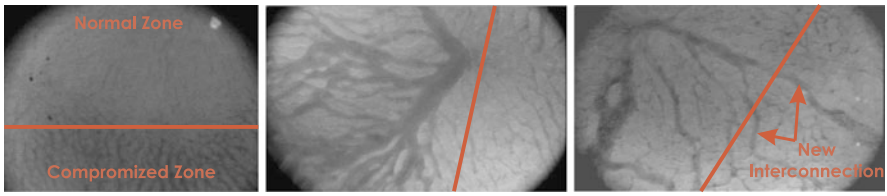

a) after ligation b) after 24h c) after 48h

Fig. 20.6 Remodeling of a sinusoid to a vessel (Dirsch et al., 2008)

The base permeability can either be described by using the initial Darcy permeability k^F_{0S} [m/s] and the specific weight γ^{FR} [N/m^3], or by use of the intrinsic solid permeability k^S_{0S} [m^2] and the effective shear viscosity μ^{FR} [Ns/m^2], where

$$\frac{(n^F)^2}{\alpha_{F0}} = \left(\frac{n^F}{1-n^S_{0S}}\right)^m \frac{k^F_{0S}}{\gamma^{FR}} = \left(\frac{n^F}{1-n^S_{0S}}\right)^m \frac{k^S_{0S}}{\mu^{FR}}, \tag{20.8}$$

where m denotes a dimensionless material parameter; see also, e.g., Eipper (1998). In (20.8), the term related to the volume fraction n^F is related to the change of permeability caused by the change of pore space, where n^S_{0S} denotes the reference solid volume fraction. Hence, an increasing fluid volume fraction is connected to a decrease of the permeability and vice versa.

20.2.2.2 Remodeling of Preferred Flow Direction

As shown in Dirsch et al. (2008), liver tissue undergoes a vascular remodeling process in response to focal outflow obstruction. After blocking the outflow, the dependent liver territory develops congestion with a clear demarcation line between properly drained areas and outflow obstructed areas (see Fig. 20.1a and Fig. 20.6a). Starting from universal sinusoidal dilatation in the border zone (Fig. 20.6b), single dilated sinusoids are transformed into vascularized sinusoidal canals which drain the congested area and therefore the obstructed zone recovers (Fig. 20.6c).

For the continuum mechanical description we consider a local pressure-modulated modeling approach. Since the time scale of the remodeling of the sinusoids is significantly higher than for the fluid flow, an artificial modeling time step is introduced in the definition of a remolding evolution relation for the preferred flow direction $\mathbf{a}_F$. Similar modeling approaches can be found, e.g., in Hariton et al. (2007) where a collagen fiber stress state depending on a reorientation approach in arterial walls is discussed, or in Himpel (2008) where a general kinematics-based reorientation approach can be found.

Here, we assume that the preferred flow direction develops in the liver lobule in order to minimize the flow dissipation, i.e., in order to find the optimal state with least resistance to blood flow. Therefore, the sinusoid tends to be oriented in the direction of the (normalized) pressure gradient $\mathbf{p}_0 = \|\mathrm{Grad}\lambda\|$ with $|\mathbf{p}_0| = 1$;

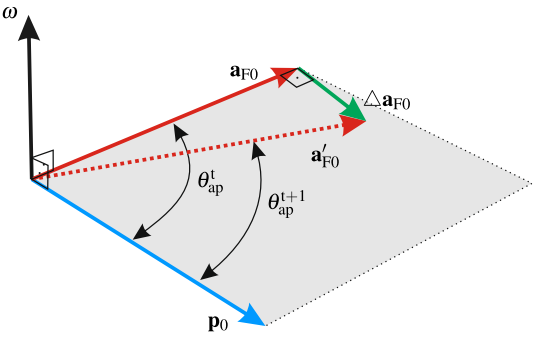

Fig. 20.7 Developing different angel θ^{t}_{ap} in the $\mathbf{a}_{F0} \times \mathbf{p}_0$ plain spanned by the pressure gradient $\mathbf{p}_0$ and preferred flow direction $\mathbf{a}_{F0}$ or $\mathbf{a}'_{F0}$

see Fig. 20.7. Thus, we postulate that the preferred flow direction $\mathbf{a}_F$ with $|\mathbf{a}_F| = 1$ develops in the direction of the pressure gradient $\mathbf{p}_0$ by $\mathbf{a}'_{F0}$. According to Himpel (2008) the merging process of both vectors is expressed by the relation

$$\mathbf{a}'_{F0} = \mathbf{a}_{F0} + \triangle\mathbf{a}_{F0}, \qquad \mathbf{a}_{F0} \cdot \triangle\mathbf{a}_{F0} = 0, \tag{20.9}$$

where $\triangle\mathbf{a}_{F0}$ denotes the incremental update of the preferred flow direction $\mathbf{a}_{F0}$. The incremental update can be expressed by a rigid body rotation of $\mathbf{a}_{F0}$ by

$$\triangle\mathbf{a}_{F0} = \boldsymbol{\omega} \times \mathbf{a}_{F0}, \tag{20.10}$$

where $\boldsymbol{\omega}$ denotes the angular velocity of reorientation. Since $\boldsymbol{\omega}$ is perpendicular to the plane spanned by $\mathbf{a}_{F0}$ and $\mathbf{p}_0$ the condition

$$\boldsymbol{\omega} = \delta_t(\mathbf{a}_{F0} \times \mathbf{p}_0) \tag{20.11}$$

must hold where δ_t denotes a virtual damping coefficient with respect to the time dependent model. Inserting (20.11) in (20.10) yields the direct evaluation of the incremental update with

$$\triangle\mathbf{a}_{F0} = \delta_t\big([\mathbf{a}_{F0} \times \mathbf{p}_0] \times \mathbf{a}_{F0}\big). \tag{20.12}$$

Thus, the new updated flow direction $\mathbf{a}'_{F0}$ can be expressed directly by $(20.9)_1$.

The governing weak formulations and their implementation into the FE-calculation program FEAP by Taylor (2012) are given in Ricken et al. (2010).

20.3 Numerical Example: Recovery of Liver Perfusion After Focal Outflow Obstruction

In the numerical example we consider the situation in a liver lobule (see Fig. 20.5) with the material parameters given in Table 20.1. The blood supply of the lobule is ensured via a small branch of the portal vein and the hepatic artery. The hepatic arterial and the portal venous blood come together in the sinusoids that supply the liver

Table 20.1 Parameters of liver lobule

Parameter	Value	Unit	Parameter	Value	Unit
μ^{S}	$1 \cdot 10^{6}$	Pa	k_{0S}^{F}	$1 \cdot 10^{7}$	m/s
λ^{S}	$1 \cdot 10^{4}$	Pa	γ^{FR}	$1 \cdot 10^{4}$	N/m^3
J_{cp}^{S}	0.0	–	α_1	0.0	Pa
ρ_{0S}^{SR}	$1 \cdot 10^{3}$	kg/m^3	α_2	0.0	–
ρ_{0S}^{FR}	$1 \cdot 10^{3}$	kg/m^3	n_{0S}^{S}	0.5	–
α_F	0.90	–	n_{0S}^{F}	0.5	–
δ_t	0.25	–			

cell plates. As mentioned in Sect. 20.2.2.2, sinusoids are oriented in the direction of the pressure gradient between portal tract and central vein.

In order to capture this physiological situation in the numerical model, we started with the unphysiological assumption that the direction of all sinusoids is horizontal. In Fig. 20.8a the different angle between pressure gradient and the direction of the sinusoids is plotted in the left column, the pressure is in the middle and on the right-hand side, the development of the norm of velocity is observed, each at three time steps: time $= 1, 5$ and 50, where in this approach the time has a virtual scale. At $t = 1$, the large difference angle causes a high resistance against the blood flow which causes a high pressure amplitude as well as local zones with high velocities. As time goes on, the sinusoids orient in the direction of the pressure gradient and the different angles, pressure, and the maximum of velocity all become smaller. Finally, the sinusoids are oriented parallel to the pressure gradient and no further reorientation occurs. This state can be defined as the optimal state and a reasonable physiological starting configuration.

In the next step, an outflow obstruction of the left lower vein is considered, see the black mark in Fig. 20.8b. Now the drainage of the liver lobule will only be realized with the remaining outflows. The obstruction first causes an increase of the pressure magnitude and then a new distribution of the pressure gradient. Again, the sinusoids follow the direction of the pressure gradient which can be seen at time $t = 55$. Finally, at $t = 100$, the sinusoids are oriented to the remaining outflow gates, so that a new optimized drainage has been established where the pressure and velocity magnitude are as low as possible.

We repeat this procedure by closing two more veins as given in Fig. 20.8c. Again, the same reorientation mechanism can be observed.

20.4 Discussion

Proceeding from the theory of porous media, the model equations for a fluid-saturated liver have been derived. In order to model the deformation of the solid, the diffusion flow of the fluid and the internal change of sinusoidal distribution comprise a two phase solid-fluid model that includes an evolutional transverse isotropic

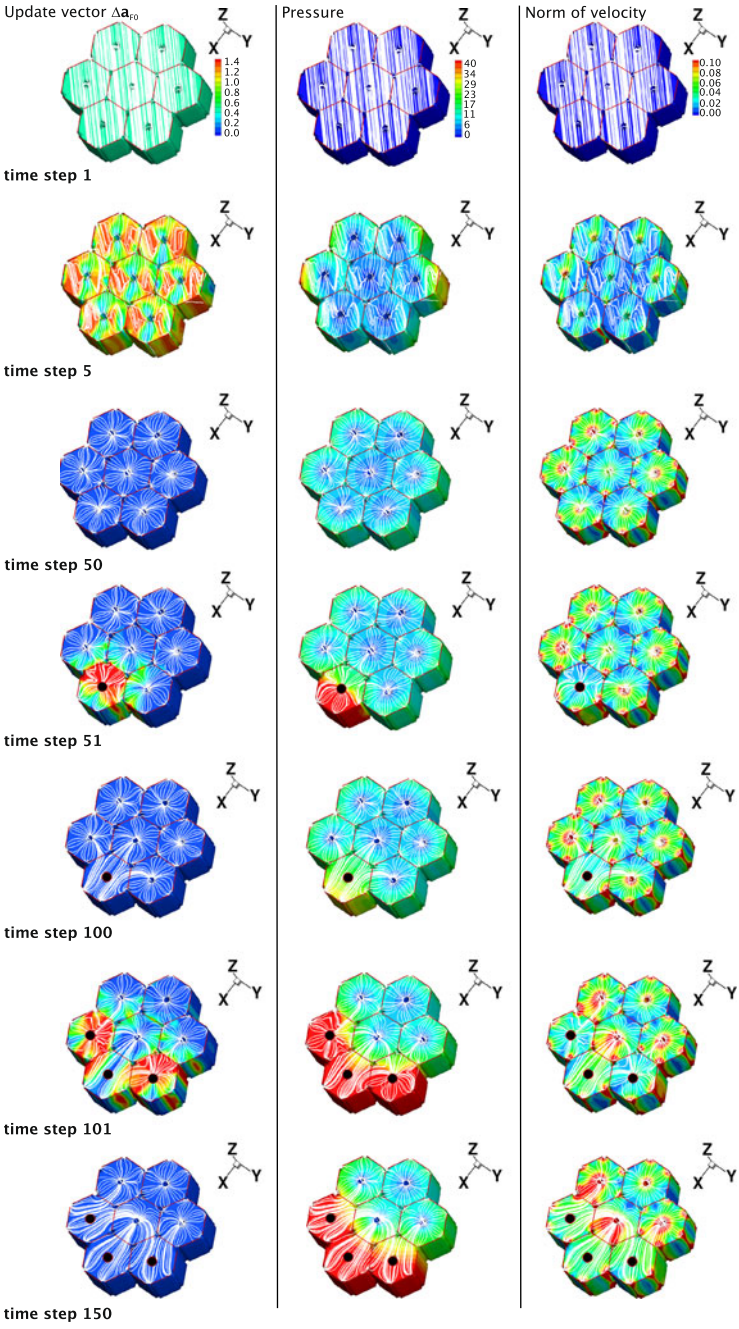

Fig. 20.8 Calculation of conditions in a liver lobule: (**a**) capturing physiological situation without outflow obstruction (time step 1–50), (**b**) after outflow obstruction of one portal vein (time step 51–100), (**c**) after outflow obstruction of three portal veins (time step 101–150)

permeability. The material modeling is derived from a thermo-mechanical investigation of the transversely isotropic biphasic mixture body. Thermodynamically consistent constitutive relations are formulated describing the anisotropic behavior of both the solid matrix and the fluid flow. In particular, a new description of the transverse isotropic permeability has been discussed and enhanced with an evolutionary approach for the preferred flow direction caused by the inner remodeling process.

In the framework of the finite element method, the governing model equations have been treated within a standard Galerkin procedure. This procedure leads to a system of algebraic differential equations in time which can be efficiently solved by an appropriate time integration scheme.

The numerical simulation model reflects the time-evolution of the hepatic vascular remodeling process in response to a focal outflow obstruction as observed by intravital microscopy. Philosophically speaking, the liver tries to 'escape' the increased sinusoidal pressure, caused by the obstruction, by forming new vascular structures called sinusoidal canals derived from multiple dilated sinusoids that follow the direction of the highest pressure gradient. Therefore, we hypothesized that the reorientation of the sinusoidal flow and the remodeling of the sinusoidal structure depends mainly on the fluid pressure and the fluid pressure gradient caused by the outflow obstruction. We tested this hypothesis with a numerical simulation and compared the results to experimental findings.

Due to the incorporated transverse isotropic permeability relation it was possible to define a remodeling approach that captured the process of re-establishing hepatic venous drainage via redirection of blood flow and formation of new vascular structures along fluid flow. It should be pointed out that the proposed model is based on a phenomenological description and macroscopic observations. Micromechanical influences are not taken into account at this stage.

In conclusion, we developed a modeling concept that reflects the experimental observation of the remodeling process. We propose to use this concept for future modeling steps on our way to simulate the individual response of a patient with focal outflow obstruction after liver resection. We aim to do so by integrating additional physiological data.

References

Ambrosi D, Mollica F (2002) On the mechanics of a growing tumor. Int J Eng Sci 40:1297–1316

Biot MA (1935) Le problème de la consolidation des matières argileuses sous une charge. Ann Soc Sci Brux Sér I 55:110–113

Biot MA (1941) General theory of three-dimensional consolidation. J Appl Phys 12:155–164

Bluhm J (2002) Modelling of saturated thermo-elastic porous solids with different phase temperatures. In: Ehlers W, Bluhm J (eds) Porous media: theory, experiments and numerical applications. Springer, Berlin

Bluhm J, de Boer R (1998) Biots poroelastizitätstheorie aus der Sicht der porösen Medien. Z Angew Math Mech 78:281–282

Cowin SC, Hegedus DH (1976) Bone remodelling I: theory of adaptive elasticity. J Elast 6:313–326

Dahmen U, Hall CA, Madrahimov N, Milekhin V, Dirsch O (2007) Regulation of hepatic microcirculation in stepwise liver resection. Acta Gastroenterol Belg 70:345–351

de Boer R (1996) Highlights in the historical development of the porous media theory: toward a consistent macroscopic theory. Appl Mech Rev 49:201–262

de Boer R (2000) Theory of porous media. Highlights in the historical development and current state. Springer, Heidelberg

Dirsch O, Madrahimov N, Chaudri N, Deng M, Madrahimova F, Schenk A, Dahmen U (2008) Recovery of liver perfusion after focal outflow obstruction and liver resection. Transplantation 85:748–756

Ehlers W (2002) Foundations of multiphasic and porous materials. In: Ehlers W, Bluhm J (eds) Porous media: theory, experiments and numerical applications. Springer, Berlin, pp 3–86

Ehlers W, Acartürk A, Markert B (2003) A continuum approach for swelling of charged hydrated media. In: Wendland W (ed) Multifield problems-state of the art. Springer, Berlin, pp 271–277

Eipper G (1998) Theorie und Numerik finiter elastischer Deformationen in fluidgesättigten porösen Festkörpern. Dissertation, Bericht Nr. II-1 aus dem Institut für Mechanik (Bauwesen), Universität Stuttgart

Epstein M, Maugin GA (2000) Thermomechanics of volumetric growth in uniform bodies. Int J Plast 16:951–978

Garikipati K, Arruda EM, Grosh K, Narayanan H, Calve SC (2004) A continuum treatment of growth in biological tissue: the coupling of mass transport and mechanics. J Mech Phys Solids 52:1595–1625

Garikipati K, Olberding JE, Narayanan H, Arruda EM, Grosh K, Calve S (2006) Biological remodelling: stationary energy, configurational change, internal variables and dissipation. J Mech Phys Solids 54:1493–1515

Gleason RL, Taber LA, Humphrey JD (2004) A 2-D model of flow-induced alterations in the geometry, structure, and properties of carotid arteries. J Biomech Eng 126:371–381

Guillou A, Ogden RW (2006) Growth in soft biological tissue and residual stress development. In: Holzapfel GA, Ogden RW (eds) Mechanics of biological tissue. Springer, Berlin, pp 47–62

Hall C (2006) Regulation der hepatischen Mikrozirkulation bei schrittweiser Resektion im Rattenlebermodell. Dissertation, Medizinische Fakultät der Universität Duisburg-Essen. Zentrum für Chirurgie Klinikum für Allgemeinchirurgie, Viszeral- und Transplantationschirurgie

Hariton I, deBotton G, Gasser TC, Holzapfel GA (2007) Stress-driven collagen fiber remodeling in arterial walls. Biomech Model Mechanobiol 6:163–175

Himpel G (2008) Computational modeling of biomechanical phenomena-remodeling, growth and reorientation. Dissertation, Fachbereich Maschinenbau und Verfahrenstechnik der Technischen Universität Kaiserslautern, Germany

Humphrey JD (2002) Cardiovascular solid mechanics. Cells, tissues, and organs. Springer, New York

Humphrey JD, Eberth JF, Dye WW, Gleason RL (2009) Fundamental role of axial stress in compensatory adaptations by arteries. J Biomech 42:1–8

Humphrey JD, Rajagopal KR (2002) A constrained mixture model for growth and remodeling of soft tissues. Math Models Methods Appl Sci 12:407–430

Klisch SM, Dyke TJV, Hoger A (2001) A theory of volumetric growth for compressible elastic biological materials. Math Mech Solids 6:551–575

Kuhl E, Holzapfel GA (2007) A continuum model for remodeling in living structures. J Mater Sci, Mater Med 42:8811–8823

Kuhl E, Menzel A, Steinmann P (2003) Computational modeling of growth—a critical review, a classification of concepts and two new consistent approaches. Comput Mech 32:71–88

Kuhl E, Steinmann P (2003) On spatial and material settings of thermohyperelastodynamics for open systems. Acta Mech 160:179–217

Lai WM, Hou JS, Mow VC (1991) A triphasic theory for the swelling and deformation behavior of articular cartilage. J Biomech Eng 113:245–258

Lee EH (1969) Elastic-plastic deformations at finite strains. J Appl Mech 36:1–6

Lu J-F, Hanyga A (2005) Linear dynamic model for porous media saturated by two immiscible fluids. Int J Solids Struct 42:2689–2709
Majno G, Joris I (1996) Cells, tissues, and disease. Blackwell Science, Oxford
Mow VC, Gibbs MC, Lai WM, Zhu WB, Athanasiou KA (1989) Biphasic indentation of articular cartilage-II. A numerical algorithm and an experimental study. J Biomech 22:853–861
Nadeau RG, Groner W (2001) The role of a new noninvasive imaging technology in the diagnosis of anemia. J Nutr 131:1610–1614
Ricken T, Bluhm J (2009) Evolutional growth and remodeling in multiphase living tissue. Comput Mater Sci 45:806–811
Ricken T, Bluhm J (2010) Remodeling and growth of living tissue: a multiphase theory. Arch Appl Mech 80:453–465
Ricken T, Schwarz A, Bluhm J (2007) A triphasic model of transversely isotropic biological tissue with applications to stress and biologically induced growth. Comput Mater Sci 39:124–136
Ricken T, Dahmen U, Dirsch O (2010) A biphasic model for sinusoidal liver perfusion remodeling after outflow obstruction. Biomech Model Mechanobiol 9:435–450
Schanz M, Diebels S (2003) A comparative study of biot's theory and the linear theory of porous media for wave propagation problems. Acta Mech 161:213–235
Simo JC, Pister KS (1984) Remarks on rate constitutive equations for finite deformation problems: computational implications. Comput Methods Appl Mech Eng 46:201–215
Taylor RL (2012) Feap—a finite element analysis program. http://www.ce.berkeley.edu/projects/feap/

Chapter 21
Multiphysics Modeling of Reactions, Mass Transport and Mechanics of Tumor Growth

Shiva Rudraraju, Kristen L. Mills, Ralf Kemkemer, and Krishna Garikipati

Abstract The biochemical dynamics involved in tumor growth can be broadly classified into three distinct spatial scales: the tumor scale, the cell-ECM interactions and the sub-cellular processes. This work presents the tumor scale investigations, which are expected to eventually lead to a system-level understanding of the progression of cancer. Many of the macroscopic phenomena of physiological relevance, such as tumor size and shape, formation of necrotic core and vascularization, proliferation and metastasis of cell populations, external mechanical interactions, etc., can be treated within a continuum framework by modeling the evolution of various species involved by transport equations coupled with mechanics. This framework is an extension of earlier work (Garikipati et al. in J. Mech. Phys. Solids 52:1595–1625, 2004; Narayanan et al. in Biomech. Model. Mechanobiol. 8:167–181, 2009, J. Phys. Condens. Matter. 22:194122, 2010) based on the continuum theory of mixtures for modeling biological growth. Specifically, the focus is on demonstrating the effectiveness of mechano-transport coupling in simulating tumor growth dynamics and explaining some *in vitro* observations like mechanics-induced ellipsoidal tumor shapes. Additionally, this work also seeks to demonstrate the effectiveness of tools like adaptive mesh refinement and automatic differentiation in handling highly nonlinear, coupled multiphysics systems.

21.1 Background

The primary biochemomechanical aspects of tumor growth involve (a) rapid cancer cell proliferation leading to formation of solid tumors, (b) metabolism by which cells consume nutrients like oxygen and glucose and create byproducts, (c) mechanical interactions between tumor mass, the extracellular matrix (ECM) and surrounding tissues, and (d) cell migration leading to formation of new tu-

S. Rudraraju · K. Garikipati (✉)
Department of Mechanical Engineering, University of Michigan, Ann Arbor, USA
e-mail: krishna@umich.edu

K.L. Mills · R. Kemkemer
Max Planck Institute for Intelligent Systems, New Materials and Biosystems, Stuttgart, Germany

G.A. Holzapfel, E. Kuhl (eds.), *Computer Models in Biomechanics*,
DOI 10.1007/978-94-007-5464-5_21,

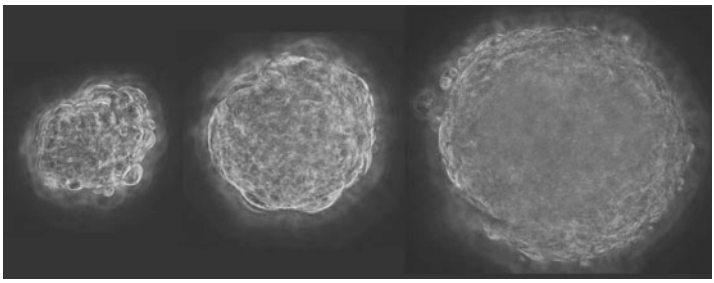

Fig. 21.1 Time progression of the growth of an LS174T tumor embedded in a 0.5 % agarose gel

mor colonies (metastasis). All these processes can be mathematically modeled as reaction-transport phenomena coupled with growth induced mechanics and mechanical interactions at the tumor scale, where the complex biophysical interactions between these processes are more broadly observable than in single-cell studies.

In vitro observations of prevascular tumor growth of human colon adenocarcinoma (LS174T, trypsinized variant of LS180) cells, involving multicellular tumor spheroids embedded in a tissue-mechanics-mimicking hydrogel (Mills et al., 2011, 2012), have shown strong influence of growth induced mechanics on the tumor scale growth dynamics, such as rate of tumor growth (Fig. 21.1) and evolution of different tumor shapes (Fig. 21.2). Our motivation in this work is to develop a quantitative understanding of these *in vitro* observations. The underlying physical processes that lead to these observations are also of interest because of their potential influence on the progression of the cancer. Towards this goal, we have been developing a coupled reaction-transport and finite deformation framework. The mathematical formulation and numerical implementation of this framework and a discussion of potential underlying mechanisms are presented here.

21.2 Mathematical Formulation

The formulation presented here is based on a broader treatment that was developed for the growth and remodeling of biological tissue. It is based on the continuum theory of mixtures and has been detailed in Garikipati et al. (2004) and Narayanan et al. (2009, 2010). The first step in this formulation is the identification of the various biological and chemical species involved and characterizing their sources, transport behavior and external interactions. The primary biological species are the cancer cells, represented as a concentration at the tumor scale. The two chemical species considered are the critical nutrients: oxygen and glucose. Over time, the cancer cells consume oxygen and glucose and produce many byproducts. In this study, the production of metabolic byproducts is not modeled; however, the production of ECM is modeled as it has an important role in the calculation of available free volume and the elastic compliance of the growth matrix. Cell death is tracked by considering

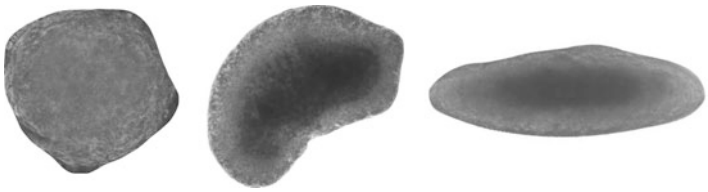

Fig. 21.2 Different *in vitro* shapes of LS174T tumors. In all cases, the initial tumor seed was spheroidal

dead cells as a separate concentration field. Also, keeping in view recent suggestions in the literature (Valastyan and Weinberg, 2011), a secondary cell population of more motile and proliferating cancer stem cells in considered in certain simulations. Now the reaction-transport equations and various source and sink terms are presented.

21.2.1 Species Transport

The evolution of these biological and chemical species is modeled using the following set of reaction-transport partial differential equations. The primary transport of these species is due to diffusion. However, to account for active transport of cells in response to mechanical/chemical signaling, advection terms have also been included. The concentrations of ECM and dead cells have no associated transport,

$$\dot{\rho}^c = \pi^c\left(\rho^c, \tau^c\right) - \pi^{c^n}\left(\rho^c, \sigma, \rho^o, \rho^g\right) - \nabla \cdot \left(-D^c \nabla \rho^c\right) - V^c(\sigma)\nabla\rho^c, \quad (21.1)$$

$$\dot{\rho}^s = \pi^s\left(\rho^s, \tau^s\right) - \pi^{s^n}\left(\rho^s, \sigma, \rho^o, \rho^g\right) - \nabla \cdot \left(-D^s \nabla \rho^s\right) - V^s(\sigma)\nabla\rho^s, \quad (21.2)$$

$$\dot{\rho}^e = \pi^e\left(\rho^c, \rho^s\right), \quad (21.3)$$

$$\dot{\rho}^n = \pi^{c^n}\left(\rho^c, \sigma, \rho^o, \rho^g\right) + \pi^{s^n}\left(\rho^s, \sigma, \rho^o, \rho^g\right), \quad (21.4)$$

$$\dot{\rho}^o = -\pi^o\left(\rho^c, \rho^s, \rho^o, \rho^g\right) - \nabla \cdot \left(-D^o \nabla \rho^o\right), \quad (21.5)$$

$$\dot{\rho}^g = -\pi^g\left(\rho^c, \rho^s, \rho^o, \rho^g\right) - \nabla \cdot \left(-D^g \nabla \rho^g\right). \quad (21.6)$$

Here, the species are identified by the superscripts: c-cancer cells (primary cell population), s-cancerous stem cells (secondary cell population), e-ECM, n-dead cells, o-oxygen and g-glucose. The subpopulations of dead cells are separately identified as c^n-dead cancer cells and s^n-dead stem cells. π^x are the species source terms, D^x and V^x the diffusivity and advective velocity, respectively. In addition, τ^x represents the cell doubling time which controls the proliferation rate and σ is the Cauchy stress induced due to growth and external interactions. As can be seen from the equations, the source terms control the growth dynamics via cell proliferation and nutrient consumption, hence a detailed discussion of these terms follows.

21.2.2 Species Sources and Chemomechanical Coupling

The source terms are expressed as mass rate per unit volume with units of $\mathrm{fg}/\mu\mathrm{m}^3\,\mathrm{s}$ (fg = femtogram). Many of the empirical relations listed here are from Casciari et al. (1992) or their modified relations from Narayanan et al. (2010). For brevity of the expressions, only the primary cancer cell population is considered in the source terms listed here. For the cell populations, the source terms model the initial stages of the tumor growth, characterized by exponential growth, i.e.

$$\pi^c\left(\rho^c, \tau^c\right) = \frac{\rho_0^c}{J}\frac{1}{\tau_{\text{inv}}^c}e^{t\tau_{\text{inv}}^c}, \qquad \tau_{\text{inv}}^c = 0.693/\tau^c, \qquad \tau^c = \frac{t_D^c}{\log 2}. \tag{21.7}$$

Here, ρ_0^c is the initial cell concentration and t_D^c is the doubling time of the cells, while J is the determinant of the deformation gradient, which is driven by volumetric growth of the tumor, in addition to its elastic deformation. The cell doubling time is dependent on the oxygen and glucose concentrations (Casciari et al., 1992), and the pH (ρ^{H^+}) of the medium (Casciari et al., 1992; Bourrat-Floeck et al., 1991). We have used the equation proposed by Casciari et al. (1992) for the doubling times:

$$t_D^c = \frac{t^{c^{\text{opt}}}}{0.014}\left(\frac{\rho^g + 1.8\cdot 10^{-2}}{\rho^g}\right)\left(\frac{\rho^o + 7.3\cdot 10^3}{\rho^o}\right)\left(\rho^{H^+}\right)^{0.46}. \tag{21.8}$$

This exponential growth is balanced by the sink π^{c^n}, representing the concentration of dead cells produced primarily due to aging, depletion of nutrients or environmental factors like surrounding pressure. These terms are modeled as follows:

$$\begin{aligned}\pi^{c^n}\left(\rho^c, \sigma, \rho^o, \rho^g\right) = {} & \rho^c\kappa\left\{1.0 - e^{2.0-[(\rho_0^o/\rho^o)^2+(\rho_0^g/\rho^g)^2]}\right\} \\ & + \rho^c\kappa\left[1.0 - e^{-(\sigma_{ii}/P_c)^2}\right].\end{aligned} \tag{21.9}$$

Here, the first term on the right hand side denotes cell death due to aging and the second term represents stress-driven cell death. Although it is known that cells have different tolerances to different stress states, here, stress-driven cell death is assumed to only depend on the hydrostatic component of the stress, represented by the trace σ_{ii} of the Cauchy stress, κ is the cell death rate constant and P_c is the threshold value of pressure at which stress-driven cell death is significant. Equation (21.9) represents a possible chemomechanical coupling which accounts for the effect of mechanics on cell proliferation.

The oxygen and glucose consumption rates were also adapted from Casciari et al. (1992) to be consistent with the different units used here, and scaled by the local cell concentration to be expressed as mass rates per unit volume. The resulting rate functions take on field values that vary over time and space, and have the forms

$$\pi^o\left(\rho^c\right) = -\rho^c\left(7.68\cdot 10^{-7} + \frac{3.84\cdot 10^{-15}}{\rho^g(\rho^{H^+})^{0.92}}\right)\left(\frac{\rho^o}{\rho^o + 1.47\cdot 10^{-4}}\right), \tag{21.10}$$

$$\pi^g(\rho^c) = -\rho^c\left(1.14\cdot 10^{-10} + \frac{3.65\cdot 10^{-17}}{\rho^o}\right)\left(\frac{\rho^g}{\rho^g + 7.21\cdot 10^{-3}}\right)\frac{1}{(\rho^{H^+})^{1.2}}. \tag{21.11}$$

The dependence of π^o on ρ^o, and π^g on ρ^g is 'Michaelis-Menten-like', giving rates that vary monotonically from zero to a maximum asymptotic value as the respective concentrations increase from $\rho^o, \rho^g = 0$.

Finally, the ECM production is assumed to be linearly proportional to the total living cell population and is given by

$$\pi^e(\rho^c) = 8.27\cdot 10^{-8}\rho^c. \tag{21.12}$$

21.2.3 Influence of Mechanics: Growth, Cell Death and Enhanced Motility

Tumors start as single cells or multi cell colonies and grow over time resulting in deformation of the tumor mass and the surrounding matrix due to growth. Biological growth is modeled by introducing a multiplicative split in the deformation gradient $\mathbf{F} = \mathbf{F}^{\mathrm{e}}\mathbf{F}^{\mathrm{g}}$, where $\mathbf{F}^{\mathrm{e}}$ and $\mathbf{F}^{\mathrm{g}}$ are the deformation gradients induced due to elastic strain and growth, respectively (Garikipati et al., 2004). Assuming only dilatational growth and resorption, $\mathbf{F}^{\mathrm{g}}$ is an isotropic tensor. It represents the kinematics of growth caused by cell proliferation, and is given by

$$\mathbf{F}^{\mathrm{g}} = G(\rho^c)\mathbf{I}, \tag{21.13}$$

where $\mathbf{I}$ is the second-order unit tensor, and G is any nonlinear function characterizing the swelling caused due to growth as a function of cell population. In this work, the following dependence is assumed:

$$G(\rho^c) = \begin{cases} 1, & \rho^c \le \rho_h. \\ \frac{1}{2}(1 + \frac{\rho^c}{\rho_h}), & \rho^c > \rho_h. \end{cases} \tag{21.14}$$

Here, ρ_h is the critical cell population density required to occupy all available free volume without causing any mechanical stress. This growth causes mechanical interactions with the surrounding growth matrix and results in significant compressive stresses, which, when beyond a certain threshold, can inhibit cell proliferation. This stress inhibited proliferation is modeled by Eq. (21.9), where the second term containing the trace of the Cauchy stress is only considered when it is compressive and above a threshold value. Further, as a possible explanation of symmetry-breaking in tumor shapes leading to ellipsoidal tumors, it is assumed that cancer cells, being highly motile, can migrate away from regions of high compressive stresses within the tumor mass. This is modeled by the advection terms in Eqs. (21.1) and (21.2), and given by

$$V^c(\sigma) = M\nabla\sigma_{ii}, \tag{21.15}$$

where M is a constant representing the motility of the cells. Further, tumor surface tension is modeled through localized enhancement of the Cauchy stress tensor, i.e. $\boldsymbol{\sigma}^{\mathrm{ST}}$, on the tumor surface and is given by

$$\boldsymbol{\sigma}^{\mathrm{ST}} = \gamma\left(\left|\nabla \rho^c\right|\right)(\mathbf{I} - \hat{\mathbf{n}} \otimes \hat{\mathbf{n}}), \tag{21.16}$$

where $\hat{\mathbf{n}}$ is the unit normal to the tumor surface and $\gamma(|\nabla \rho^c|)$ is the coefficient of surface tension, while $\gamma(|\nabla \rho^c|)$ is defined to be non-zero only in the neighborhood of the tumor boundary whose location is identified by the sharp gradient in cell concentration.

21.3 Numerical Framework

The coupled system of PDE's (Eqs. (21.1)–(21.6)) is solved using the Galerkin Finite Element Method and is integrated in time using the backward Euler scheme. The time steps were adaptively chosen to ensure near quadratic convergence. The code was based on the *deal.ii* (Bangerth et al., 2007) finite element library and heavily utilized its hanging nodes based adaptive mesh refinement capability (Fig. 21.3) and its suite of iterative solvers. A monolithic scheme was adopted to concurrently solve for the complete set of solution variables (ρ^c, ρ^s, ρ^n, ρ^e, ρ^o, ρ^g and $\bar{u}$). However, a matrix based monolithic scheme would require the computation of the Jacobian of the global residual equation. In this work, the exact Jacobian was computed using the Sacado (2011) automatic differentiation library which allows for efficient run time computation of the variational derivative of the residual equations.[1]

21.4 Simulations

The chemomechanical framework presented above is used to simulate tumor growth. Most of the growth related parameters, transport constants and elastic compliance values were obtained from the literature. The results presented in this work are primarily 2D simulations, however, a representative 3D simulation is also included at the end of this section. The problem geometry and the initial tumor seeding concentrations are depicted in Fig. 21.4. The initial tumor seed is a uniform spherical concentration of cells ($\rho^c = 250$ fg/μm^3) and the surrounding matrix is modeled as an elastic soft material ($E = 2.4 \cdot 10^{-8}$ N/μm^2, $\nu = 0.49$). To model the

[1] Automatic differentiation, also referred to as algorithmic differentiation, calculates derivatives of functions up to any order to within machine precision by reducing complex functions to elementary arithmetic operations and elementary functions by repeated application of the chain rule. It can result in significant speedup of multiphysics implementations by computing the Jacobian of finite element residuals. For variational problems, even greater ease of implementation is possible: only the energy functional needs to be coded, and the system of residual equations and the Jacobian can be computed by taking variational derivatives of the functional and residual equations, respectively.

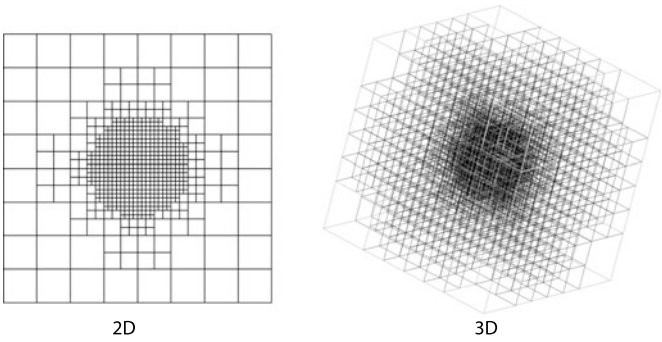

Fig. 21.3 Adaptively refined meshes with hanging nodes were used to discretize the problem domain. Such meshes involve minimal computational penalty while refining and coarsening, and the elements have a unit aspect ratio

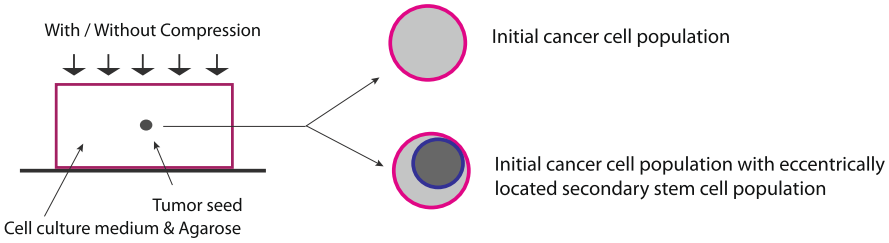

Fig. 21.4 The problem geometry and the initial tumor seeding. The problem domain dimensions are around 1000 μm

rise of a secondary stem cell population, some simulations consider an additional concentration of cancer stem cells ($\rho^s = 250$ fg/μm^3) located eccentrically with respect to the primary cancer cell population. Based on the experimental observations of change in tumor volume, the cell doubling times are assumed to be around one day ($t_D^c = 1.16$ days, $t_D^s = 1.04$ days). The results presented here can be broadly classified as follows:

- **Simulation of growth dynamics:** Initial simulations were geared towards reproducing experimentally observed growth dynamics (evolution of tumor size and shape, cell distribution within the tumor mass, etc.) (Mills et al., 2011, 2012) and were used to fine tune the various parameters controlling the species interactions and the effects of mechanics on cell proliferation. Figure 21.5 shows the distribution of various biological and chemical species after about 10 days of growth. As discussed in the introduction, a secondary population of tumor stem cells was also considered to study the effects of highly proliferating local cell populations on the overall tumor growth. Our computations (Fig. 21.6) show that the aggressive proliferation of these stem cells would tend to ultimately dominate the shape of the tumor, and depending on the relative proliferation rates of the two cell populations, the resulting shape may be different from a spheroid or ellipsoid.

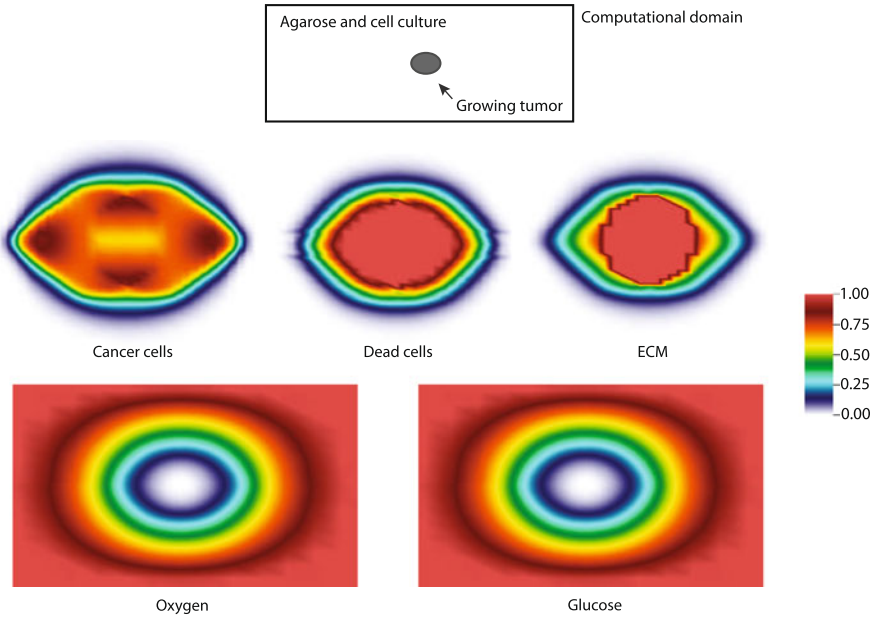

Fig. 21.5 Spatial distribution of species concentration after 10 days of growth. All the concentration values have been normalized. The formation of nutrient a depleted region at the center of the tumor leading to increased cell death can be observed

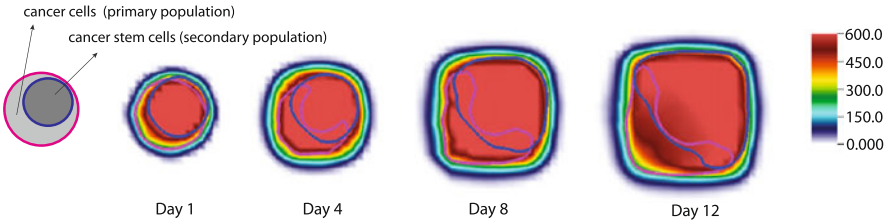

Fig. 21.6 Evolution of total cell concentration (cancer cells and stem cells) in the presence of an underlying secondary population of cancer stem cells. Also plotted are contour lines (*pink*-cancer cells, *blue*-stem cells) showing the dominant regions of the two cell populations. The stem cell population is assumed to be eccentrically-located in the initial tumor spheroid, and the stem cells are modeled to be more proliferative by reducing their doubling time by 10 % compared to the doubling time of the primary cancer cells

- **Study of proliferation and migration mechanisms:** One of our primary motivations for simulating tumor growth was to use the numerical framework to probe the possible mechanisms that cause symmetry-breaking in tumor shape leading to formation of ellipsoidally shaped tumors (Mills et al., 2012). The first mechanism we considered was the existence of microscopic compliant planes in the tumor growth matrix along which the stress produced by growth of tumors would be

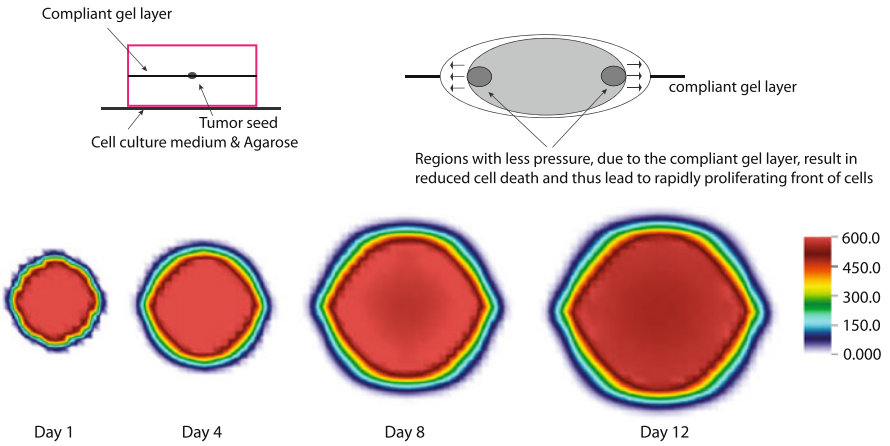

Fig. 21.7 Effect of microscopic complaint gel layers on tumor growth. Reduced cell death along these planes leads to enhanced proliferation and thus lead to ellipsoidal tumor shapes

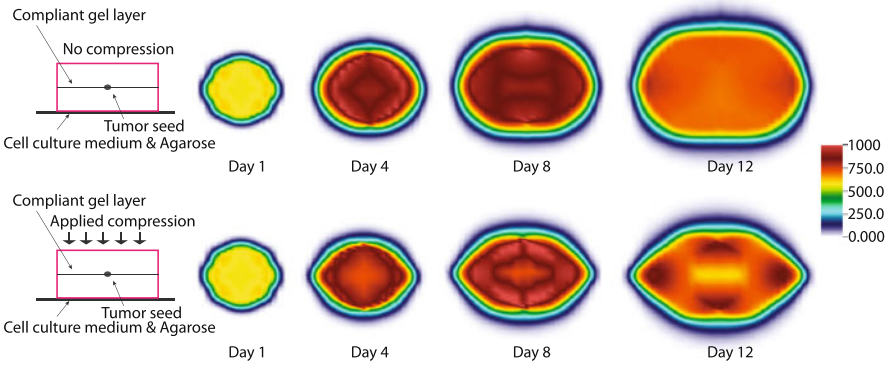

Fig. 21.8 Effect of high proliferation regions at symmetrically opposite ends of the tumor on the tumor shape evolution. The effect is becomes more predominant when the tumor growth matrix is subjected to compression

lower. If such regions of low stress exist, then they would act as enhanced cell proliferation fronts, as stress induced cell death in these regions would be relatively less compared to other regions of the tumor. This mechanism leads to symmetry-breaking in tumor shapes, as shown in Fig. 21.7. However, the observed ellipticity in the tumor shape was significantly less than the *in vitro* observations. To further understand the level of proliferation needed to produce significant ellipsoidal tumor growth, we conducted an inverse study, wherein we artificially created high proliferation regions at symmetrically opposite ends of the tumor, and it was seen that even a small reduction in the rate of cell death in these regions (10–20 %) leads to expected ellipsoidal shapes, as shown in Fig. 21.8. Lastly, cell migration from regions of high compressive stress to regions of lower compression/tension,

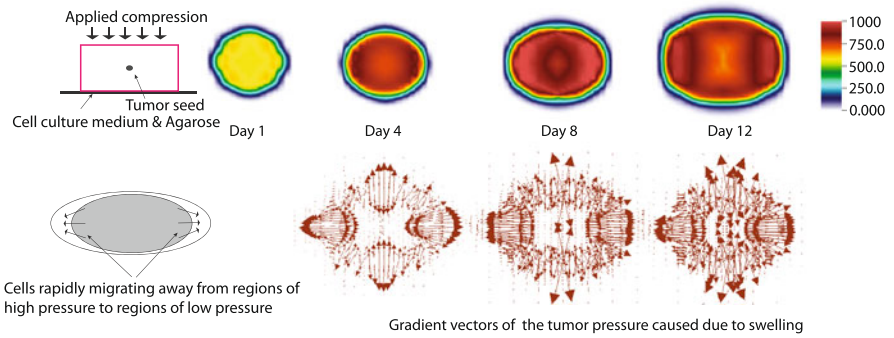

Fig. 21.9 Effect of cell migration from regions of high compressive stress to regions of lower compression/tension, modeled as pressure gradient driven advection

modeled as pressure gradient driven advection (Eq. (21.15)), was considered. The results in Fig. 21.9 show that such a stress-driven migratory behavior of cells can lead to preferred growth directions and thus may be a possible explanation for development of ellipsoidal tumor shapes.

Extension of the above formulation to 3D is only limited by available computational resources. A representative simulation of 3D tumor growth is shown in Fig. 21.10.

21.5 Discussion

The mathematical formulation based on multi-species reaction-transport equations and chemomechanical coupling presented here is to be seen as a generic framework for simulating tumor growth dynamics. The specific details of the source terms, transport properties and the influence of mechanics will depend on the type of the tumor, and one needs an extensive experimental program to fine tune various parameters and assumptions of inter-species interactions. The work presented here was part of a larger experimental program to investigate the growth of human colon adenocarcinoma tumors in agarose hydrogels, and thus the *in vitro* observations of tumor growth allowed us to set bounds on various chemical, transport and mechanical parameters. The simulations presented compared well with *in vitro* observations of tumor growth dynamics (tumor size and shape evolution, cell population distribution, etc.) (Mills et al., 2011, 2012). As a natural second step, this simulation framework is now being used to probe the possible mechanisms driving tumor growth, and our current interests include the evolution of various tumor shapes and effects of initial cell distributions (single cells, distributed colonies, secondary stem cell population, etc.). The results presented here seem to suggest that mechanics plays a critical role in evolution of these tumor shapes and various mechanics driven phenomena could possible explain some of the *in vitro* observations. One possible

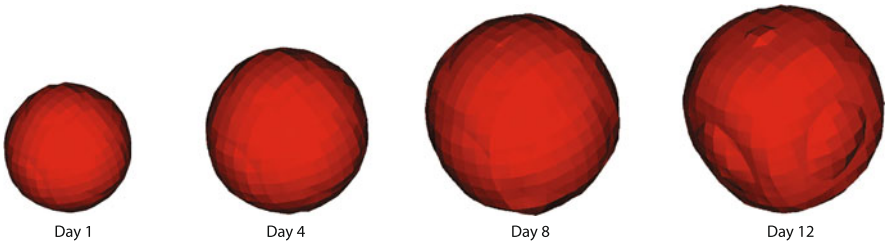

Fig. 21.10 Three-dimensional simulation of tumor growth. Shown is the evolution of the iso-surface of the total cell concentration

extension of the model being considered is the ability to simulate vascularization and surface migration of cancer cells.

References

Bangerth W, Hartmann R, Kanschat G (2007) deal.II–a general purpose object oriented finite element library. ACM Trans Math Softw 33:24

Bourrat-Floeck B, Groebbe K, Mueller-Klieser W (1991) Biological response of multicellular EMT6 spheroids to exogenous lactate. Int J Cancer 47:792–799

Casciari J, Sotirchos S, Sutherland R (1992) Variations in tumor cell growth rates and metabolism with oxygen concentration, glucose concentration, and extracellular pH. J Cell Physiol 151:386–394

Garikipati K, Arruda EM, Grosh K, Narayanan H, Calve SC (2004) A continuum treatment of growth in biological tissue: the coupling of mass transport and mechanics. J Mech Phys Solids 52:1595–1625

Mills KL, Garikipati K, Kemkemer R (2011) Experimental characterization of tumor spheroids for studies of the energetics of tumor growth. Int J Mater Res 7:889–895

Mills K, Kemkemer R, Rudraraju S, Garikipati K (2012) The growth of human colon adenocarcinoma tumors in agarose hydrogels (in preparation)

Narayanan H, Arruda EM, Grosh K, Garikipati K (2009) The micromechanics of fluid-solid interactions during growth in porous soft biological tissue. Biomech Model Mechanobiol 8:167–181

Narayanan H, Verner S, Mills K, Kemkemer R, Garikipati K (2010) In silico estimates of the free energy rates in growing tumor spheroids. J Phys Condens Matter 22:194122

Sacado (2011) Automatic differentiation tools for C++ applications. The Trilinos Project

Valastyan S, Weinberg RA (2011) Tumor metastasis: molecular insights and evolving paradigms. Cell 147:275–292

Chapter 22
Multicompartmental Poroelasticity as a Platform for the Integrative Modeling of Water Transport in the Brain

John C. Vardakis, Brett J. Tully, and Yiannis Ventikos

Abstract This work proposes the implementation of a multiple-network poroelastic theory (MPET) model for the purpose of investigating in detail the transport of water within the cerebral environment. The key advantage of using the MPET representation is that it accounts for fluid transport between CSF, brain parenchyma and cerebral blood. A further novelty in the model is the amalgamation of anatomically accurate Choroid Plexus regions, with their individual feeding arteries. This model is used to demonstrate and discuss the impact of aqueductal stenosis on the cerebral ventricles, along with possible future treatment techniques.

22.1 Introduction

Brain diseases affect over one quarter of the European population, at an estimated cost of over €450 billion (Gustavsson et al., 2011). Age-related changes are imposing huge challenges to the global healthcare system. Diseases of old-age, such as dementia and normal pressure hydrocephalus (NPH), are exerting substantial pressures on society through growing numbers and costs. At the same time, medical experts and policy makers are increasingly aware that the efficacy and economy of therapy is strongly connected with the personalization of treatment.

This research proposes a novel application of multiple-network poroelastic theory (MPET) to investigate cerebral fluid transport. A detailed investigation of multiscalar, spatio-temporal transport of fluid between the cerebral blood, cerebrospinal fluid (CSF) and brain parenchyma is conducted. Specifically, the MPET model of the cerebral tissue is coupled with a three-dimensional representation of the CSF

J.C. Vardakis · B.J. Tully · Y. Ventikos (✉)
Fluidics and Biocomplexity Group, Institute of Biomedical Engineering, Department of Engineering Science, University of Oxford, OX1 3PJ, Oxford, UK
e-mail: yiannis.ventikos@eng.ox.ac.uk

J.C. Vardakis
e-mail: john.vardakis@eng.ox.ac.uk

B.J. Tully
e-mail: brett.tully@magd.oxon.org

G.A. Holzapfel, E. Kuhl (eds.), *Computer Models in Biomechanics*,
DOI 10.1007/978-94-007-5464-5_22,

Fig. 22.1 CSF circulates through the four brain ventricles and in the subarachnoid space surrounding the brain and spinal cord. Most of the CSF is reabsorbed into the venous system through the arachnoid granulations and through the walls of the capillaries of the central nervous system and pia mater

flow patterns arising from the source of production within the patient-specific ventricular system.

A particular drawback of the majority of existing CSF transport models is the conflation of the cerebral blood network and the CSF. In comparison, MPET allows an elegant and novel extension of traditional poroelastic models to include detailed transfer mechanisms between the cerebral blood and extracellular fluid/CSF. The novelty of this approach leads to both a strength and a challenge, as many of the requisite material properties have never been recorded. Previous parametric studies (Tully and Ventikos, 2011) have identified both healthy and symptomatic ranges for these newly introduced parameters.

22.2 Background

22.2.1 Background to Cerebral Anatomy

Figure 22.1 illustrates a sagittal cut of the cranial area under consideration. As can be seen, the cerebral ventricles are the major CSF-containing spaces. It is known that when considering adults, the normal CSF circulation proceeds in a consistent and uniform manner. The classical hypothesis of CSF transport through the ventricles involves the production of CSF at the Choroid Plexuses of the lateral, third and fourth ventricles. CSF then flows out of the lateral ventricles via both the foramina of Monro and into the third ventricle. From there, CSF passes into the fourth ventricle via the aqueduct of Sylvius. The foramen of Magendie and the bilateral

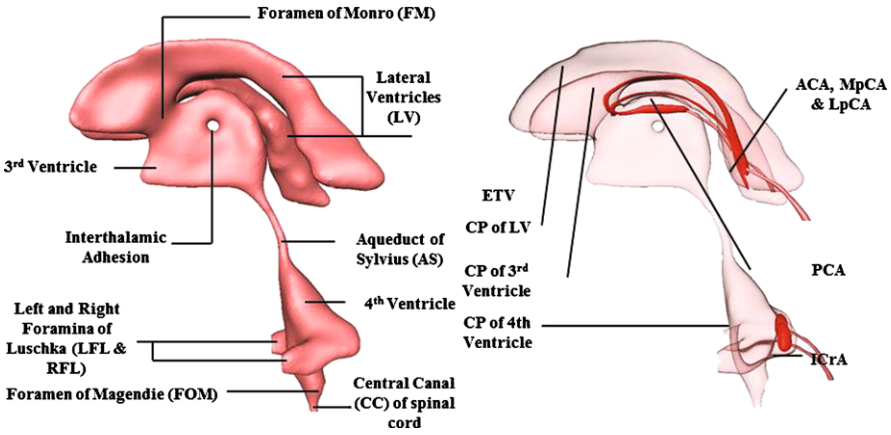

Fig. 22.2 (*Left*): Axial view of geometry of a human ventricular system showing key anatomical features. (*Right*): View of the ventricular system along with the choroid plexus of the lateral, third and fourth ventricle. The arteries supplying these plexuses are also shown

foramina of Luschka act as the final outlets of the CSF leading to the subarachnoid space. The central canal of the spinal cord also receives CSF from the fourth ventricle; however, in comparison to the foramen of Luschka and foramina of Magendie, this is a minute quantity. Once the CSF has exited from the cerebral ventricular system, it accumulates in the subarachnoid cisterns surrounding the brainstem (cisterna magna, medullary, pontine, interpeduncular, ambient and suprasellar cistern respectively). The choroid plexus is the main site of CSF production and is situated within the third, fourth and the underside of the lateral ventricles, see Figs. 22.1 and 22.2. CSF is also produced, to a lesser degree, within the bulk of the brain parenchyma (Irani, 2009). Once the CSF reaches the fourth ventricle, some of it exits through the central canal but the overwhelming proportion flows around the tentorium cerebelli in order for it to be absorbed by the arachnoid granulations and into the superior sagittal sinus (Rekate, 2008; Gupta et al., 2010).

Since this work will incorporate geometrically accurate choroid plexuses in all the aforementioned locations, the arterial supplies to these plexuses have to be included, see Fig. 22.2. For the lateral ventricle, the arterial supply is dominated by the anterior choroidal artery (ACA) and the medial and lateral posterior choroidal arteries (MpCA and LpCA). Likewise, the choroid plexus of the third and fourth ventricle is supplied by the posterior cerebral and inferior cerebellar arteries (PCA and ICrA) respectively (Irani, 2009).

22.2.2 Hydrocephalus (HCP)

HCP can be succinctly described as the abnormal accumulation (imbalance between production and circulation) of CSF within the brain (Rekate, 2008, 2009). This balance of CSF production and reabsorption allows for the CSF pressure to lie within

Table 22.1 Classification of hydrocephalus along with some examples within this classification

Obstructive HCP	Communicating HCP
Congenital	*Congenital*
Stenosis of aqueduct of Sylvius, TV[a] & FV[b]	Chiari malformations
Dandy Walker Syndrome, TV[a] & FV[b]	Venous hypertension
Acquired	*Acquired*
Midline supratentorial tumors	Subarachnoid haemorrhage
Posterior fossa tumors	Meningeal carcinomatosis

[a] Third ventricle, [b] Fourth ventricle

the 600–2000 Pa range (Irani, 2009). HCP cannot be considered a singular pathological entity, but instead, a consequence of a variety of congenital and acquired disorders present within the CNS (Thompson, 2009). What can be said with confidence is that HCP is classified with regards to whether the point of CSF obstruction lies within the ventricular system (obstructive) or not (communicating), see Table 22.1. HCP can be further sub classified as acute or chronic. The prior is caused by the obstruction of CSF flow pathways, whilst the latter is characterized by prolonged time scales for development. In addition, in most cases, this latter form of HCP possesses no radiographically identifiable flow obstruction.

Normal pressure HCP (NPH): this form was originally described by Hakim and Adams (1965). It aims to correlate a triad of disturbances, namely gait disturbance, dementia symptoms and urinary incontinence. The key point for NPH is that the aforementioned symptoms occur under the auspice of radiographic hydrocephalus with normal CSF pressure (Byrd, 2006). NPH can be either idiopathic (no clear aetiology and effects the elderly) or secondary (possesses an identifiable cause, e.g., subarachnoid haemorrhage). Some thoughts on the aetiology of NPH include the quashing of deep white matter ischemia as a cause, and instead focusing on the diminishing compliance of superficial veins or other progressive impairment of periventricular blood flow (Bradley, 2008). What is clear is that no matter what the encountered aetiology, the final result of NPH is ventriculomegaly (communicating HCP), which in turn may proceed in entertaining numerous manifestations of the disease.

Acute HCP: this form of HCP is unlike its chronic counterpart, since it presents clearly identifiable radiographical obstructions of the CSF flow pathways. The ventricular system itself is affected by the location of these obstructions, for instance, of the lateral ventricles and third ventricle, whilst an obstructed subarachnoid space (due to inflammatory or haemorrhagic fibrosing meningitis) may lead to widespread dilatation (Tully and Ventikos, 2011).

Surgical treatment is the preferred therapeutic option when treating hydrocephalus (Hamilton, 2009; Schödel et al., 2012), however this topic will not be elaborated here.

22.3 Mathematical Modeling and Anatomy Acquisition

22.3.1 Background

The primary theoretical development of the relationship between the pressure of a fluid permeating a solid matrix and its constituent displacement was established by Biot (1941). It is well known that a soil under an applied load does not conform to an instantaneous deflection. Instead, it settles gradually (due to the soil adapting to that load) at a variable rate. This settlement of soil to the load variation is termed consolidation. Consolidation is analogous to an elastic 'sponge' saturated with water deforming under load. The consequence of an applied load onto this system would yield a gradual settlement proportional to the rate of water being squeezed out of the voids of the elastic skeleton. Terzaghi (1943) initially applied the aforementioned principles on a restricted one-dimensional case of a column under an applied constant load. Biot extended Terzaghi's one-dimensional work to portray the number of physical constants necessary to determine the properties of the soil, along with the general equations necessary to predict the settlements and stresses in a three dimensional form. In doing so, he made the following assumptions regarding the soil: (i) isotropic; (ii) under the final equilibrium conditions, the stress-strain relationships (assumed linear) can be reversed, in addition, small strains are assumed; (iii) water in the pores is assumed incompressible; (iv) Darcy's law applies to water flowing through the porous skeleton. It must be noted that the assumption of isotropy is not a stringent one, and may be replaced by anisotropy. Assumptions (ii) and (iii) on the other hand warrant more attention. Surface tension forces allocate a soil grain configuration of minimum potential energy. This occurs since any changes would take place at an infinitely slow rate, and so the final state of the soil is independent of the path taken to reach this stage. This concept ties in well with assumption (ii), since if one considered the potential energy negligible in this case; energy could theoretically be drawn out of applied loading/unloading within a closed cycle. Reversibility is assigned on the basis of small strains, since a slight perturbation in the macroscopic sense is unlikely to disturb the existing grain configuration.

22.3.2 Multiple-Network Poroelastic Theory (MPET)

Regulation of CSF and tissue displacement within the cerebral environment was modeled by considering a spatio-temporal model. MPET theory is actively used in geotechnical engineering to model materials which have naturally fractured fluid passages of various sizes and which possess both storage and transport porosities. These reservoirs intrinsically contain various subdivisions of permeabilities and are, therefore, aptly suited to a multiple-poroelastic network (Bai et al., 1993). MPET amalgamates fundamental conservation of mass and momentum principles, stress-strain relationships, the Terzaghi effective stress principle and porous flow laws. In the system in question, a solid matrix (s) is permeated by $a = 1, \ldots, A$ number

of fluid networks. Each network has its own individual porosity n^a, density ρ^a, permeability k^a and finally fluid velocity relative to the aforementioned solid matrix w_i^a/n^a.

The complete system presents a highly non-linear set of equations which require vast computational effort. Fortunately, we are dealing with biological flows and so acceleration frequencies can be neglected and this can simplify the system to a concise set of $A+1$ equations, i.e.

$$\nabla \cdot \boldsymbol{\sigma}' - \sum_{a=1}^{A} \alpha^a \nabla p^a + \rho\left(\mathbf{b} - \frac{\partial^2 \mathbf{u}}{\partial t^2}\right) = \mathbf{0}, \tag{22.1}$$

$$\frac{1}{Q^a}\frac{\partial p^a}{\partial t} + \alpha^a \frac{\partial(\nabla \cdot \mathbf{u})}{\partial t} + \nabla \cdot \left[k^a \rho^a \left(\mathbf{b} - \frac{\partial^2 \mathbf{u}}{\partial t^2}\right) - k^a \nabla p^a\right] - \sum_{b=1, b\neq a}^{A} \dot{s}_{b\to a} = 0. \tag{22.2}$$

Here, $\boldsymbol{\sigma}'$ is the effective stress in the solid matrix, $\mathbf{b}$ is the local body force, $\mathbf{u}$ is the displacement vector of the solid matrix, $\rho = \sum_{a=1}^{A} n^a p^a + \rho_s(1-n)$ is the total density of the system, $n = \sum_{a=1}^{n} n^a$ is the total porosity of the combined fluid networks, ρ_s is the density of the solid, k is the isotropic permeability, Q is the combined compressibility of the system, $\partial(\nabla \cdot \mathbf{u})/\partial t = \dot{\boldsymbol{\epsilon}}$ is the strain rate in the solid matrix, α^a is the Biot parameter of the defined network a and finally $\dot{s}_{b\to a}$ is the rate of fluid exchange from network b to a (Tully and Ventikos, 2011).

The MPET framework strives to capture the independent nature of the fluid transfer within the brain. The quadruple MPET model takes into account the arterial blood network (a), the arteriole/capillary network (c), venous blood network (v) and extracellular/CSF network (e). To transform the system in Eqs. (22.1) and (22.2) into the quadruple MPET system required, one sets $A=4$ and $a=(a,c,v,e)$. In addition to this, further simplifications are made by assuming: a linear stress-strain relationship, isotropic permeability, no external forces on the system, negligible gravitational effects, stationary reference frame, quasi-steady system due to the large time scales in the development of HCP and physiology-derived constraints of specific directional transfer of water between networks in order to avoid breaches in continuity and finally a spherically symmetric geometry. This gives the following simplified relationships for the new quadruple MPET system, i.e.

$$\frac{\partial^2 u}{\partial r^2} + \frac{2}{r}\frac{\partial u}{\partial r} - \frac{2u}{r^2} - \frac{1-2\nu}{2G(1-\nu)}\left(\alpha^a \frac{\partial p^a}{\partial r} + \alpha^c \frac{\partial p^c}{\partial r} + \alpha^v \frac{\partial p^v}{\partial r} + \alpha^e \frac{\partial p^e}{\partial r}\right) = 0, \tag{22.3}$$

$$-k^a\left(\frac{\partial^2 p^a}{\partial r^2} + \frac{2}{r}\frac{\partial p^a}{\partial r}\right) + |\dot{s}_{a\to c}| = 0, \tag{22.4}$$

$$-k^c\left(\frac{\partial^2 p^c}{\partial r^2} + \frac{2}{r}\frac{\partial p^c}{\partial r}\right) - |\dot{s}_{a\to c}| + |\dot{s}_{c\to e}| + |\dot{s}_{c\to v}| = 0, \tag{22.5}$$

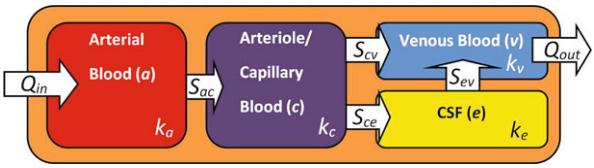

Fig. 22.3 Schematic represents the transfer restrictions placed on the MPET model. For example, it can be seen that there is no provision allowing for flow to occur between the CSF and arterial networks

$$-k^v\left(\frac{\partial^2 p^v}{\partial r^2}-\frac{2}{r}\frac{\partial p^v}{\partial r}\right)-|\dot{s}_{c\to e}|+|\dot{s}_{e\to v}|=0, \tag{22.6}$$

$$-k^e\left(\frac{\partial^2 p^e}{\partial r^2}-\frac{2}{r}\frac{\partial p^e}{\partial r}\right)-|\dot{s}_{c\to v}|-|\dot{s}_{e\to v}|=0. \tag{22.7}$$

In the above, G is the shear modulus and ν is the Poisson's ratio. In addition, if one observes the set of Eqs. (22.3)–(22.7), there is an evident alternation of signs for the $|\dot{s}|$ terms. A negative/positive sign indicates an addition/loss of fluid to that particular network, see Fig. 22.3. It is noted that in Eqs. (22.3)–(22.7), the transfer between networks is via a hydrostatic pressure gradient (for the current stata of development of the model), hence $\dot{s}_{s\to t}=\xi_{st}(p^t-p^s)$. Here, ξ_{st} is a constant scaling the flow between networks s and t.

22.3.3 Anatomy Acquisition

The three dimensional anatomy of the ventricular system, choroid plexuses and the arterial system was reconstructed from a series of 511(xy), 314(xz), 511(yz) DICOM files produced from a T2-weighted MRI scan of a healthy male volunteer aged in his sixties. The images of the entire cranial area were acquired in the sagittal, axial and coronal directions. The slice spacing was 0.5 mm. The acquired images were manually segmented for the ventricular system using Amira (Mercury Computer Systems, San Diego, CA, USA) and the raw segmented geometry from this process was saved as a stereo lithography (STL) file. In order to preserve key anatomical features such as the aqueduct of Sylvius, subsequent smoothing of the STL file was done using the open-source modeling software, Blender (The Blender Foundation, www.blender.org).

Owing to its powerful individual nodal manipulation capabilities, Blender was also used to apply the smooth and local stenosis (Tully and Ventikos, 2011) to the three-dimensional patient specific geometries for the cases involving the three degrees of HCP severity, namely open (3.00 mm diameter), mild (1.25 mm diameter) and severe (0.80 mm diameter). The aforementioned dimensions are those of the hydraulic diameter defined in Sect. 22.4. It must be noted that the current standard

voxel size produced from clinical imaging does not permit the accurate differentiation of different degrees of aqueductal stenosis. Finally, inlets and outlet boundaries were created using CFD-VisCART (ESI Group, Paris France), which was also used to generate non-conforming computational grids. The final smoothed STL file for an open aqueduct (i.e. no applied stenosis) is seen in Fig. 22.2, along with a clearer labeling technique.

22.3.4 Solution Method

The governing multicompartmental poroelastic equations are solved with an implicit second-order central finite differences scheme on the midpoints and forward/backward Euler used on the boundary nodes. The quasi-steady time discretization (for the temporally dependent terms in the boundary conditions) is performed via a first-order Euler approach.

Flow through the multidimensional aqueducts is solved using the multiphysics software CFD-ACE+ (ESI Group, Paris France) which is based on the finite volume approach, along with central spatial differentiating, algebraic multigrid scheme (Webster, 1994; Khandelwal and Visaria, 2006; Tu et al., 2008) and the SIMPLEC pressure-velocity coupling. The coupling between the poroelastic solver and the flow solver is achieved through the CFD-ACE+ user-defined subroutines (UDS's). This approach allows for the embedding of the patient-specific aqueduct of Sylvius into the model.

22.4 Results and Discussion for Aqueductal Stenosis

The results shown in Fig. 22.4 show the first application of the MPET model to acute HCP. The transfer of water between the four networks to mimic the cerebral environment reveals interesting features. The plots in Fig. 22.4 show the results of the ventricular displacement along with the corresponding CSF pressure for the three cases of stenosed aqueduct. The greatest displacement was witnessed for the severely stenosed case, which was $1.93 \cdot 10^{-4}$ m. The severe case also exhibited the highest ventricular CSF pressure, that being 1096 Pa.

The CSF pressure converges to 1089 Pa on the skull, for all cases, as expected since that value is connected with the venal absorption boundary condition. The ventricular displacement decreases to 0 m at the skull, since this is imposed as a rigid, adult skull boundary condition (skull radius of 10 cm).

The Reynolds number, defined as $R_e = \rho^e D_h v_p / \mu^e$, where v_p is the peak velocity flowing through the aqueduct, varied from 15 in the open case, 112 for the mild and 135 for the severely stenosed aqueduct. The peak velocities associated with these Reynolds numbers correspond to 4.4, 80 and 152 mm/s, respectively. The hydraulic diameter D_h is given by $D_h = 4A/P$, where A is the cross sectional

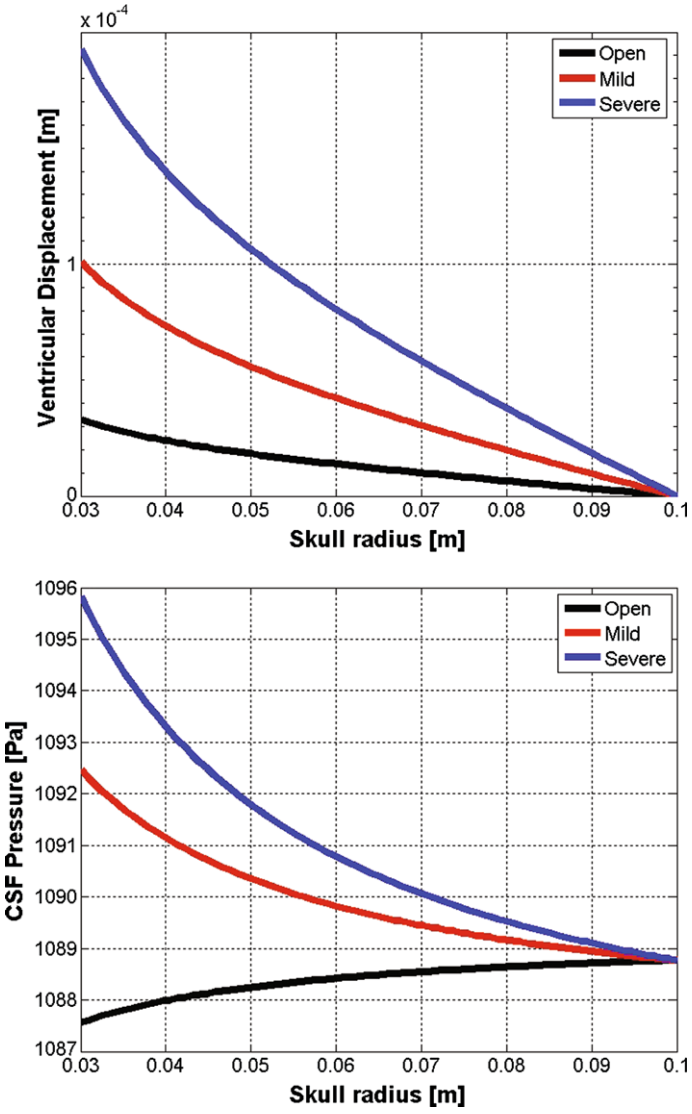

Fig. 22.4 Comparison of induced hydrocephalus behavior. The plots show results for ventricular displacement and CSF pressure when varying the degree of aqueductal stenosis

area and P is the perimeter, given by $P = 2\pi((a^2 + b^2)/2)^{1/2}$. Both a and b are the major and minor axis of an ellipse. Finally, μ^e is the dynamic viscosity of CSF, and is taken as $8.9 \cdot 10^{-4}$ Ns/m^2.

These results reasonably resemble those of Howden et al. (2007), although the artificially stenosed cases obviously differ due to differences in implementing the stenosis. It was also clear from the work currently undertaken that the central canal

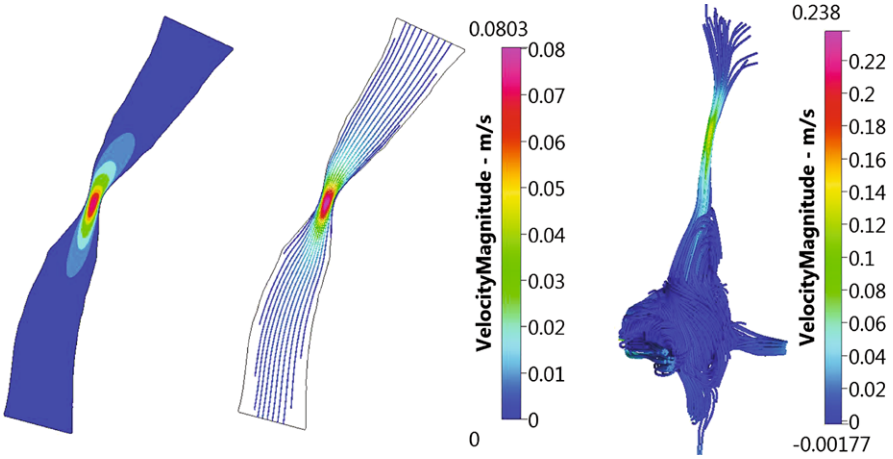

Fig. 22.5 (*Left*): Sagittal view of a z-slice of the mildly obstructed aqueduct of Sylvius. The contour lines denote velocity magnitude. (*Centre*): Lines tangent to the instantaneous velocity vector (at an instant coinciding with peak systole) in the aqueduct of Sylvius, indicating a smooth flow. (*Right*): Rotated view of lines tangent to the instantaneous velocity vector (at an instant coinciding with peak systole) in the aqueduct of Sylvius and fourth ventricle (open case)

displays the lowest peak velocities of all the outlets (did not exceed 0.02 m/s) throughout the different applied occlusions. From an anatomical perspective, this canal acts as a cushioning system for the spinal cord. This is in good agreement with similar inferences made in the literature (Loth et al., 2001; Gupta et al., 2009, 2010).

A final note is made on the complexity of the flow. The streamlines in Fig. 22.5 (right) show just how complicated and asymmetric the flow within the ventricular system is (namely in the fourth ventricle). Here, two vortices have developed, and they both rotate in an anti-clockwise direction. The other portion of CSF travels along the floor of the fourth ventricle and leaves via the three foramina. In the same figure, one can also appreciate how flow exits through the foramen of Magendie and in addition how a negligible amount leaves through the central canal. These visualizations of the cranio-caudal flow are in good agreement with the literature (Stadlbauer et al., 2010).

22.5 Future Work

The current MPET model can be extended to include a more varied range of hydrocephalic cases, namely those associated with atresia of the three foramina in the fourth ventricle and both the foramina of Monro, see Fig. 22.2. The effects of shunting, endoscopic third ventriculostomy (ETV) and a very recent development in fourth ventriculostomy (Giannetti et al., 2011) will be investigated. This investigation will be done in conjunction with the above cases of aqueductal stenosis, or

in addition, may form an integral part of a study addressing the direction of alleviating the symptoms of hydrocephalus when considering the aforementioned cases of atresia in the fourth ventricle. This model also allows for the natural incorporation of further, multiscalar detail by involving cellular level interactions such as aquaporin-centered transport, believed to facilitate rapid absorption from CSF and ISF.

The functional implications of the interthalamic adhesion (IA) and how it influences the CSF dynamics remains unclear. In the build-up to the current work, it was witnessed that varying the position of the IA varied the flow characteristics and pressure distribution quite considerably. Some very preliminary work has been carried out to link the IA with Chiari malformations (Cheng et al., 2010), and an appreciation of its imposing characteristics could prove pivotal when considering the pulsatile distribution of CSF within the ventricles during systole and diastole.

Acknowledgements This study is supported by the Digital Economy Programme; a Research Councils UK cross-Council initiative led by EPSRC and contributed to by AHRC, ESRC, and MRC. The EPSRC is further acknowledged for providing the resources necessary for the High Performance Computing simulations conducted in this study. The ESI Group and Dr. M. Megahed are kindly acknowledged for allowing the use of the CFD-ACE+ multiphysics suite.

References

Bai M, Elsworth D, Roegiers J (1993) Multiporosity/multipermiability approach to the simulation of naturally fractured reservoirs. Water Resour Res 29:1621–1633

Biot MA (1941) General theory of three-dimensional consolidation. J Appl Phys 12:155–164

Bradley WG Jr (2008) Idiopathic normal pressure hydrocephalus: new findings and thoughts on etiology. Am J Neuroradiol 29:1–3

Byrd C (2006) Normal pressure hydrocephalus: dementia's hidden cause. Nurse Pract 31:28–29, 31–35

Cheng S, Tan K, Bilston LE (2010) The effects of interthalamic adhesion position on cerebrospinal fluid dynamics in the cerebral ventricles. J Biomech 43:579–582

Giannetti AV, Malheiros JA, da Silva MC (2011) Fourth ventriculostomy: an alternative treatment for hydrocephalus due to atresia of the magendie and luschka foramina. J Neurosurg Pediatrics 7:152–156

Gupta S, Soellinger M, Boesiger P, Poulikakos D, Kurtcuoglu V (2009) Three-dimensional computational modeling of subject-specific cerebrospinal fluid flow in the subarachnoid space. J Biomech Eng 131:021010

Gupta S, Soellinger M, Grzybowski DM, Boesiger P, Biddiscombe J, Poulikakos D, Kurtcuoglu V (2010) Cerebrospinal fluid dynamics in the human cranial subarachnoid space: an overlooked mediator of cerebral disease. I. Computational model. J R Soc Interface 7:1195–1204

Gustavsson A, Svensson M, Jacobi F, Allgulander C, Alonso J, Beghi E, Dodel R, Ekman M, Faravelli C, Fratiglioni L, Gannon B, Jones DH, Jennum P, Jordanova A, Jönsson L, Karampampa K, Knapp M, Kobelt G, Kurth T, Lieb R, Linde M, Ljungcrantz C, Maercker A, Melin B, Moscarelli M, Musayev A, Norwood F, Preisig M, Pugliatti M, Rehm J, Salvador-Carulla L, Schlehofer B, Simon R, Steinhausen HC, Stovner LJ, Vallat JM, den Bergh PV, van Os J, Vos P, Xu W, Wittchen HU, Jönsson B, Olesen J (CDBE2010Study Group) (2011) Cost of disorders of the brain in Europe 2010. Eur Neuropsychopharmacology 21:718–779.

Hakim S, Adams R (1965) The special clinical problem of symptomatic hydrocephalus with normal cerebrospinal fluid pressure: observations on cerebrospinal fluid hydrodynamics. J Neurol Sci 2:307–327

Hamilton MG (2009) Treatment of hydrocephalus in adults. Semin Pediatr Neurol 16:34–41
Howden L, Giddings D, Power H, Aroussi A, Vloeberghs M, Garnett M, Walker D (2007) Three-dimensional cerebrospinal fluid flow within the human vetricular system. Comput Methods Biomech Biomed Eng 11:123–133
Irani DN (2009) Cerebrospinal fluid in clinical practice. Saunders Elsevier, Philadelphia
Khandelwal S, Visaria M (2006) Algebraic multigrid solver for structured meshes. Me608 final report, pp 1–7
Loth F, Yardimci MA, Alperin N (2001) Hydrodynamic modeling of cerebrospinal fluid motion within the spinal cavity. J Biomech Eng 123:71–79
Rekate HL (2008) The definition and classification of hydrocephalus: a personal recommendation to stimulate debate. Cerebrospinal Fluid Res 5:1–7
Rekate HL (2009) A contemporary definition and classification of hydrocephalus. Semin Pediatr Neurol 16:9–15
Schödel P, Proescholdt M, Ullrich OW, Brawanski A, Schebesch KM (2012) An outcome analysis of two different procedures of burr-hole trephine and external ventricular drainage in acute hydrocephalus. J Clin Neurosci 19:267–270
Stadlbauer A, Salomonowitz E, van der Riet W, Buchfelder M, Ganslandt O (2010) Insight into the patterns of cerebrospinal fluid flow in the human ventricular system using MR velocity mapping. Neuroimage 51:42–52
Terzaghi K (1943) Theoretical soil mechanics. Wiley, New York
Thompson D (2009) Hydrocephalus. Neurosurg 27:130–134
Tu J, Yeoh G, Liu C (2008) Computational fluid dynamics: a practical approach. Wiley, New York
Tully B, Ventikos Y (2011) Cerebral water transport using multiple-network poroelastic theory: application to normal pressure hydrocephalus. J Fluid Mech 667:188–215
Webster R (1994) An algebraic multigrid solver for Navier-Stokes problems. Int J Numer Methods Fluids 18:761–780

Chapter 23
Discontinuous Versus Continuous Chemical Potential Across a Crack in a Swelling Porous Medium

Jacques M. Huyghe, Famke Kraaijeveld, Joris J.C. Remmers, and René de Borst

Abstract Understanding and prediction of mechanisms of failure is needed to develop methods for prevention and treatment of failure. To increase the accuracy for the prediction of failure, advanced computational models are developed. Mesh-independent modeling of cracks in porous media is obtained by enriching the displacement field with a discontinuous shape function describing the crack. In a poroelastic finite element modeling, an enrichment of the pressure field is mandatory around the crack. Two options are available to account for the sharp pressure gradient around the crack. One is to resolve the pressure gradient using a continuous pressure enrichment, the other is not to resolve the steep gradients and use discontinuous jumps across the crack surface. In the latter case, analytical solutions of the pressure field at an interface is used to evaluate the real pressure gradient. This paper formulates criteria to decide whether to use one or the other approach. The techniques are applied to swelling media in which the pressure degree of freedom takes the form of a chemical potential.

23.1 Introduction

The mechanical causes of intervertebral disc (IVD) degeneration and herniation are poorly known (Urban and Roberts, 2003). The presence of fixed charges in the collagen network of tissues causes differences in ion concentrations with the surrounding fluid and, therefore, Donnan-osmotic pressure. This gives the IVD its prestress and its protective nature against crack growth. During degeneration a loss of fixed

J.M. Huyghe (✉) · F. Kraaijeveld · J.J.C. Remmers · R. de Borst
Eindhoven University of Technology, Eindhoven, The Netherlands
e-mail: j.m.r.huyghe@tue.nl

F. Kraaijeveld
e-mail: F.Kraaijeveld@tue.nl

J.J.C. Remmers
e-mail: J.J.C.Remmers@tue.nl

R. de Borst
e-mail: R.d.Borst@tue.nl

G.A. Holzapfel, E. Kuhl (eds.), *Computer Models in Biomechanics*,
DOI 10.1007/978-94-007-5464-5_23,

charges and hydration occurs. Understanding and prediction of failure of the IVD asks for the combination of experiments and computational models. Although finite element models of failure of the disc exist, the modeling has usually been restricted to stress analysis studies (Kim, 2000; Natarajan et al., 2007) or inserting contact elements as a model for lesions (Little et al., 2007). Accurate modeling of the crack improves the predictive behavior of those models. This is not only an issue in biomechanics, but there is a need for a good model for fracture in ionized porous media to study geotechnical issues as well.

A macro fracture in a continuum is often of interest and therefore a discrete fracture model is used. Herniation is not perfectly brittle. The macro-crack is preceded by a zone with small-scale yielding and micro-cracking. This process zone is simulated by a cohesive zone model, where the decrease of strength in the zone is lumped into a discrete line (in 2D modeling) and a stress-displacement relationship across this line. Larsson and Larsson (2000) introduced a discontinuity in the fluid by a regularized Dirac delta function. Armero and Callari (1999) assume only discontinuous displacement. Steinmann (1999) extended these embedded discontinuity models based on enhanced strains concepts without the restriction of locally drained or undrained behavior by a new interface law based on Darcy's law. To eliminate mesh dependency and artificial length scales, Babuska and Melenk (1997) introduced a discontinuity in a mesh free way by adding an enhanced field on top of the standard displacement (and pressure) field, in this case by a Heaviside function using the partition of unity property of the finite element shape functions. The number of degrees of freedom at the nodes whose support is crossed by a discontinuity is increased. Therefore, no new nodes are added during propagation. Belytschko and Black (1999) introduced this method for a solid together with an asymptotic enhancement of the displacement field at the crack tip. Wells and Sluys (2001) introduced cohesive segments within the finite elements followed by Remmers et al. (2003) who modeled the crack not as a single entity but as a collection of overlapping cohesive segments. A practical benefit of the method is that standard discretization is used and crack propagation is independent of the discretization. A downside of this method is that it is difficult to implement in commercial codes. Gasser and Holzapfel (2006, 2007) have applied the partition of unity finite element method to tissues, namely the fracture of an aortic wall and of bone. Réthoré et al. (2007) considered shear banding by using partition of unity with crack tip singularity for the solid phase and without crack tip singularity for the fluid phase, suggesting a discontinuity in the pressure field in case of shearing, combined with Darcy's law similar to the enhanced strain models. A diaphragm with low permeability at the discontinuity is assumed.

The above work has shown that the partition of unity approach is promising for crack propagation in porous media. Much discussion is still on the treatment of the fluid phase, because there is no comparison to a benchmark solution. In this research we analyze under which conditions a discontinuous enrichment of the pressure field should be preferred above a continuous. For the modeling of the osmoelastic behavior of the material, Lanir's plane strain model (Lanir, 1987) for small deformations is used. Lanir assumes incompressible constituents, namely the solid matrix and interstitial fluid, and neglects the influence of ion flow. Lanir's model coincides with

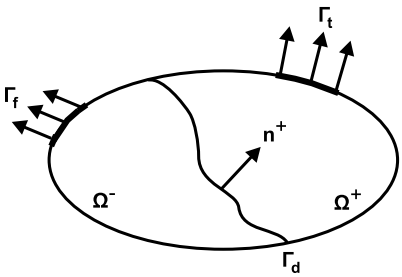

Fig. 23.1 Schematic representation of the body Ω: the two parts are Ω^+ and Ω^-, separated by crack Γ_d. A traction force holds on Γ_t and fluid supply at Γ_f

Biot's model if osmotic effects are neglected. This model is implemented with the cohesive segment model by Remmers et al. (2003) and de Borst et al. (2006) for the solid phase assuming quasi-brittle crack growth. Two cases are considered:

- A pressure discontinuity is introduced similarly to the displacement discontinuity. The flow across the crack surface is evaluated from Darcy's law where the pressure gradient follows from Terzaghi's one-dimensional consolidation.
- A continuous pressure enrichment is introduced which resolves the pressure gradient in the vicinity of the crack.

23.2 Governing Equations

The governing equations consist of equations for the bulk and for the discontinuity. Figure 23.1 shows a body Ω with external boundary Γ with a traction force on Γ_t and fluid supply on Γ_f, with $\mathbf{n}$ the normal unit vector on the boundary Γ directed outwards. The body is cut by a discontinuity Γ_d in two domains, Ω^+ and Ω^-. The normal of the discontinuity $\mathbf{n}^+$ is directed towards Ω^+.

23.2.1 Bulk Behavior

Osmoelastic media have large negatively charged groups fixed to the solid matrix. Counter charges are present in the fluid for electro-neutrality. Due to the fixed charges the total ion concentration inside the medium is higher than in the surrounding fluid. This leads to an osmotic pressure difference and therefore swelling of the medium. Lanir (1987) assumes in osmoelasticity that free ions are always in equilibrium with the external salt concentration. Ion contribution is therefore neglected and the medium is described by two constituents only: the solid (s) and the fluid (f). The constituents are assumed to be incompressible. The material is assumed linear elastic, isothermal, isotropic, homogeneous and fully saturated. The presence of the fixed charge causes a deformation dependent pressure difference between the sample and surrounding fluid. Van't Hoff relation defines the osmotic pressure in

terms of concentrations of free cations c^+, anions c^-, gas constant R and temperature T and depends indirectly on the fixed charge density c^{fc} and the external salt concentration c^{ex}, i.e.

$$\Delta\pi = \pi - \pi^{\mathrm{ex}} = RT\sqrt{\left(c^{\mathrm{fc}}\right)^2 + 4\left(c^{\mathrm{ex}}\right)^2} - 2RTc^{\mathrm{ex}}. \tag{23.1}$$

Not hydrostatic pressure, but the chemical potential of the fluid is the driving force for fluid flow. Chemical potential is a measure for the free energy of the fluid. The chemical potential of the fluid μ^{f} is defined per unit volume fluid

$$\overline{\mu}^{\mathrm{f}} = p - \pi, \tag{23.2}$$

where π is the osmotic pressure and p the hydrostatic pressure. The osmotic pressure is determined by the empirical Van't Hoff equation, which defines the osmotic pressure in terms of concentrations of free cations c^+, anions c^-, gas constant R and temperature T. Thus,

$$\pi = RT\left(c^+ + c^-\right), \quad c^+ + c^- = \sqrt{\left(c^{\mathrm{fc}}\right)^2 + 4\left(c^{\mathrm{ex}}\right)^2}. \tag{23.3}$$

This osmotic pressure holds outside as well as inside the medium, but outside the medium the fixed charge density c^{fc} is zero and the osmotic coefficient may be different. Electro-neutrality holds, therefore, the amount of negative charges are equal to the amount of positive charges: $c^- + c^{\mathrm{fc}} = c^+$. Furthermore we introduce $\Delta\pi = \pi - \pi^{\mathrm{ex}}$. The seepage flux $\mathbf{q}$ follows Darcy's law in the presence of concentration gradients. The total equations are given as:

$$\text{Momentum equation} \quad \nabla\cdot\boldsymbol{\sigma} = \nabla\cdot\boldsymbol{\sigma}_{\mathrm{e}} - \nabla\left(\mu^{\mathrm{f}} + \Delta\pi\right) = \mathbf{0}, \tag{23.4}$$

$$\text{Stress-strain relation} \quad \boldsymbol{\sigma}_{\mathrm{e}} = 2\mu\boldsymbol{\varepsilon} + \lambda\,\mathrm{tr}(\boldsymbol{\varepsilon})\mathbf{I}, \tag{23.5}$$

$$\text{Mass balance} \quad \nabla\cdot\frac{\partial\mathbf{u}}{\partial t} + \nabla\cdot\mathbf{q} = 0, \tag{23.6}$$

$$\text{Darcy's law} \quad \mathbf{q} = -\mathbf{K}\cdot\nabla\mu^{\mathrm{f}}, \tag{23.7}$$

$$\text{Swelling equation} \quad \Delta\pi = RT\sqrt{\left(c^{\mathrm{fc}}\right)^2 + 4\left(c^{\mathrm{ex}}\right)^2} - 2RTc^{\mathrm{ex}}, \tag{23.8}$$

$$\text{Fixed charge} \quad c^{\mathrm{fc}} = \frac{\phi_i^{\mathrm{f}} c_0^{\mathrm{fc}}}{\mathrm{tr}(\boldsymbol{\varepsilon}) + \phi_{\mathrm{i}}^{\mathrm{f}}}. \tag{23.9}$$

The parameters $\mu = E/2(1+\nu)$ and $\lambda = \mu 2\nu/(1-2\nu)$ are the Lamé constants, and E, ν and μ are the Young's modulus, Poisson's ratio and shear modulus, respectively. The tensor $\mathbf{K} = K\mathbf{I}$ denotes the permeability tensor and is assumed to be isotropic and constant in space and time.

The presence of ions fixed to the solid matrix results in prestress of the solid matrix at the initial condition. Therefore, $\boldsymbol{\varepsilon}$ is the strain tensor which is separated in an initial strain $\boldsymbol{\varepsilon}_{\mathrm{i}}$ and the deformation from an initial to the current state, i.e.

$\boldsymbol{\varepsilon}_\Delta = \boldsymbol{\varepsilon} - \boldsymbol{\varepsilon}_\mathrm{i} = \nabla^s \mathbf{u} = [\nabla \mathbf{u} + (\nabla \mathbf{u})^\mathrm{T}]/2$. Similarly, the fixed charge density is calculated from the fixed charge density c_0^fc at the stress-free configuration and the initial volume fraction $\phi_\mathrm{i}^\mathrm{f}$. Equations (23.4)–(23.8) may be reduced to

$$\frac{\partial \operatorname{tr}(\boldsymbol{\varepsilon})}{\partial t} - \nabla^s \cdot \left(\mathbf{K} \cdot \nabla^s \mu^\mathrm{f}\right) = 0, \tag{23.10}$$

$$2\mu \nabla^s \cdot \boldsymbol{\varepsilon} + \lambda \nabla^s \operatorname{tr}(\boldsymbol{\varepsilon}) - \nabla^s \left[\mu^\mathrm{f} + \Delta\pi(\boldsymbol{\varepsilon})\right] = \mathbf{0}. \tag{23.11}$$

The boundary and initial conditions are given by ($\Gamma_\mathrm{t} \cup \Gamma_u = \Gamma$, $\Gamma_\mathrm{t} \cap \Gamma_u = \emptyset$ and $\Gamma_\mathrm{f} \cup \Gamma_\mu = \Gamma$, $\Gamma_\mathrm{f} \cap \Gamma_\mu = \emptyset$),

$$\begin{array}{llll} \mathbf{u}(\mathbf{x},0) = \mathbf{u}_0(\mathbf{x}), & \mathbf{x} \in \Omega, & \mu^\mathrm{f}(\mathbf{x},0) = \mu_0^\mathrm{f}(\mathbf{x}), & \mathbf{x} \in \Omega, \\ \mathbf{u}(\mathbf{x},t) = \mathbf{u}_\gamma(\mathbf{x},t), & \mathbf{x} \in \Gamma_\mathrm{u}, & \mu^\mathrm{f}(\mathbf{x},t) = \mu_\gamma^\mathrm{f}(\mathbf{x},t), & \mathbf{x} \in \Gamma_\mu, \\ \left(\boldsymbol{\sigma}_\mathrm{e} - \left(\mu^\mathrm{f} + \Delta\pi\right)\mathbf{I}\right) \cdot \mathbf{n} = \mathbf{t}_\mathrm{t}(\mathbf{x},t), & \mathbf{x} \in \Gamma_\mathrm{t} & \mathbf{q} \cdot \mathbf{n} = f_\mathrm{f}(\mathbf{x},t), & \mathbf{x} \in \Gamma_\mathrm{f}. \end{array} \tag{23.12}$$

If the initial state is an unloaded state, where the material is in contact with a filter ($\mu_\mathrm{in}^\mathrm{f} = \mu_\mathrm{ex}^\mathrm{f}$), the next holds

$$\boldsymbol{\sigma}_\mathrm{e}(\boldsymbol{\varepsilon}_\mathrm{i}) - \Delta\pi(\boldsymbol{\varepsilon}_\mathrm{i})\mathbf{I} = \mathbf{0}, \tag{23.13}$$

provided that the medium is homogeneous. Then the initial strain tensor is given by

$$\boldsymbol{\varepsilon}_\mathrm{i} = \varepsilon_\mathrm{i}\mathbf{I}, \tag{23.14}$$

$$\varepsilon_\mathrm{i} = \frac{\Delta\pi_\mathrm{i}}{2\mu + 2\lambda}, \qquad \Delta\pi_\mathrm{i} = RT\sqrt{\left(c_\mathrm{i}^\mathrm{fc}\right)^2 + 4\left(c_\mathrm{i}^\mathrm{ex}\right)^2} - 2RTc_\mathrm{i}^\mathrm{ex}. \tag{23.15}$$

In the case that the swelling in one direction is obstructed, for instance by adjacent vertebrae, the initial strain is not isotropic.

23.2.2 Discontinuous Kinematics

A set basis or shape functions $\{N\}_{i=1}^n$, with n the number of integration points, form a partition of unity since $\sum_{i=1}^n N_i = 1$. A field v is interpolated as

$$v(\mathbf{x},t) = \sum_{i=1}^{n} N_i(\mathbf{x}) \left(a_i(t) + \sum_{k=1}^{m} \psi_k(\mathbf{x}) b_{ik}(t) \right), \tag{23.16}$$

with a_i the regular degrees of freedom (DOFs), $\{\psi\}_{k=1}^m$ additional basis functions and b_{ik} additional degrees of freedom (Babuska and Melenk, 1997). These additional basis functions may not originate from the span of the original set of basis functions.

Using these extra basis functions, the displacement field and the chemical potential distribution are separated into two different scales: the bulk behavior (standard field) and crack behavior (enhanced field). The opening or sliding of a crack can

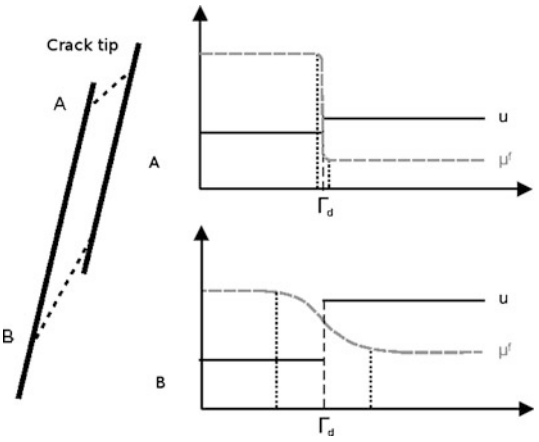

Fig. 23.2 When a shear band develops, the displacement jump becomes nonzero and a large gradient in chemical potential arises with a small transition zone (**A**). With time, the displacement jump grows, the gradient in chemical potential decreases and the transition zone widens (**B**)

be incorporated as a jump in the displacement. A jump in displacement is mathematically represented by the Heaviside function. We assume that the strain field is defined everywhere even at the surface across which the jump occurs. Then the displacement field $\mathbf{u}$ of the body can be additively decomposed into the continuous part $\hat{\mathbf{u}}$ and the enhanced part $\tilde{\mathbf{u}}$ (Remmers et al., 2003)

$$\mathbf{u}(\mathbf{x}) = \hat{\mathbf{u}}(\mathbf{x}, t) + \mathscr{H}_{\Gamma_\mathrm{d}}(\mathbf{x})\tilde{\mathbf{u}}(\mathbf{x}, t). \tag{23.17}$$

The Heaviside function $\mathscr{H}_{\Gamma_\mathrm{d}}$ is defined with the jump at the discontinuity as

$$\mathscr{H}_{\Gamma_\mathrm{d}} = \begin{cases} -h/2, & \mathbf{x} \in \Omega^+, \\ +h/2, & \mathbf{x} \in \Omega^-. \end{cases} \tag{23.18}$$

The Heaviside function is acting on the smooth function $\tilde{\mathbf{u}}(\mathbf{x}, t)$ keeping the crack surface continuous. The jump at the discontinuity Γ_d is given by $[\mathbf{u}]$ and represents the opening of the crack

$$\big[\mathbf{u}(\mathbf{x}, t)\big] = h\tilde{\mathbf{u}}(\mathbf{x}, t), \quad \mathbf{x} \in \Gamma_\mathrm{d}. \tag{23.19}$$

The strain becomes

$$\boldsymbol{\varepsilon} = \nabla^s \mathbf{u} = \nabla^s \hat{\mathbf{u}} + \mathscr{H}_{\Gamma_\mathrm{d}} \nabla^s \tilde{\mathbf{u}} + \delta_{\Gamma_\mathrm{d}} \big(\tilde{\mathbf{u}}\mathbf{n}^+\big)^s, \tag{23.20}$$

with $\mathbf{n}^+$ the normal at the crack surface directed inwards. The last term only has a contribution in the variational description at the discontinuity. The second degree of freedom that needs enrichment across the crack is the chemical potential, or in case of a non-swelling medium, the pressure. Figure 23.2 shows in two steps what happens at the crack. On initial growth a small opening arises, i.e. small displacement jump, and a steep gradient in the chemical potential occurs over a small transition zone (case A). While the opening grows, the gradient in the chemical potential decreases in magnitude and spreads over a wider transition zone. This is illustrated for

the case of mode II cracking in Fig. 23.2. The difficulty here lies in the fact that the most critical area of the crack, namely the crack tip has a jump in chemical potential that cannot be captured using continuous functions, and further away from the crack tip a discontinuous description fails as the chemical potential becomes increasingly continuous.

High gradients are either approximated by

- case 1: a jump $\tilde{\mu}^{\mathrm{f}}(\mathbf{x}, t)$ over the crack surfaces. In this case the decomposition becomes

$$\mu^{\mathrm{f}}(\mathbf{x}) = \hat{\mu}^{\mathrm{f}}(\mathbf{x}, t) + \mathscr{H}_{\Gamma_{\mathrm{d}}}(\mathbf{x})\tilde{\mu}^{\mathrm{f}}(\mathbf{x}, t), \tag{23.21}$$

  and the difference in chemical potential at the discontinuity is given by $[\mu^{\mathrm{f}}]$:

$$\left[\mu^{\mathrm{f}}(\mathbf{x}, t)\right] = h\tilde{\mu}^{\mathrm{f}}(\mathbf{x}, t), \quad \mathbf{x} \in \Gamma_{\mathrm{d}}. \tag{23.22}$$

  The gradient in the chemical potential becomes

$$\nabla^s \mu^{\mathrm{f}} = \nabla^s \hat{\mu}^{\mathrm{f}} + \mathscr{H}_{\Gamma_{\mathrm{d}}} \nabla^s \tilde{\mu}^{\mathrm{f}} + h\delta_{\Gamma_{\mathrm{d}}}\left(\tilde{\mu}^{\mathrm{f}}\mathbf{n}^+\right), \tag{23.23}$$

  or

- case 2: a continuous enrichment of the chemical potential. In this case the decomposition becomes

$$\mu^{\mathrm{f}}(\mathbf{x}) = \hat{\mu}^{\mathrm{f}}(\mathbf{x}, t) + \mathscr{D}_{\Gamma_{\mathrm{d}}}(\mathbf{x})\tilde{\mu}^{\mathrm{f}}(\mathbf{x}, t). \tag{23.24}$$

  The distance function is defined with respect to the coordinates of the crack $\mathbf{x}_\Gamma$, namely by

$$\mathscr{D}_{\Gamma_{\mathrm{d}}} = \frac{h}{2}\left|(\mathbf{x} - \mathbf{x}_\Gamma) \cdot \mathbf{n}^+\right|, \quad \mathbf{x} \in \Omega, \tag{23.25}$$

  with h the magnitude of the Heaviside jump. The gradient $\partial\mathscr{D}$ of the distance function is given by

$$\partial\mathscr{D} = \nabla^s \mathscr{D}_{\Gamma_{\mathrm{d}}} = \begin{cases} \frac{h}{2}\mathbf{n}^+ & \mathbf{x} \in \Omega^+ \\ \frac{h}{2}\mathbf{n}^- & \mathbf{x} \in \Omega^- \end{cases} = \mathscr{H}_{\Gamma_{\mathrm{d}}}\mathbf{n}^+, \tag{23.26}$$

  where $\nabla^s\mathbf{u} = [\nabla\mathbf{u} + (\nabla\mathbf{u})^{\mathrm{T}}]/2$ holds.

The Heaviside function results in a discontinuous distribution with a jump at the location of the crack and a linear distribution away from the crack (Fig. 23.3a). The distance function continuous distribution of the chemical potential with a nonlinear distribution of the chemical potential away from the crack (Fig. 23.3b).

23.2.3 Local Behavior at the Crack

A local coordinate system (n, s) is introduced where n is in the direction of the normal vector to Ω^+ and t is orthogonal in the direction of propagation. This means

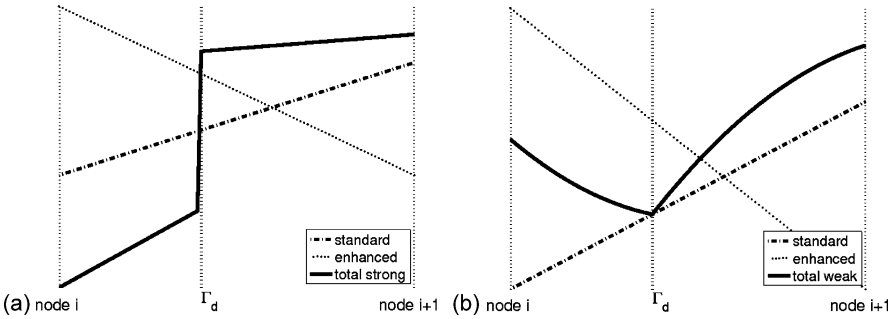

Fig. 23.3 A 1D representation of the effect of (**a**) the Heaviside function (case 1) and (**b**) the distance function (case 2). The total field is the additive result of the standard field and the enhanced field

a displacement jump is decoupled into

$$[\mathbf{u}] = [\mathbf{u}]_n \mathbf{n}^+ + [\mathbf{u}]_s \mathbf{t}^+, \tag{23.27}$$

with $\mathbf{n}^+ = -\mathbf{n}^-$ directed into the body and $\mathbf{t}^+$ is directed along the crack surface opposite to the direction of propagation. We define crack surfaces $\Gamma_{\mathrm{d}}^+ = \partial\Omega^+ \cap \Gamma_{\mathrm{d}}$ and $\Gamma_{\mathrm{d}}^- = \partial\Omega^- \cap \Gamma_{\mathrm{d}}$.

23.2.3.1 Local Mass Balance

Deformation around the discontinuity is strongly linked to fluid flow. Fluid flow takes place at the surface of the discontinuity from the medium into the crack and a flow along the crack when opening of the crack increases. When the crack is closed, the normal fluid flow $f_c^{\pm}$ over surface $\Gamma_{\mathrm{d}}^{\pm}$ determines the amount of fluid exchange. When the crack opens, additional terms are included. Figure 23.4 shows a schematic overview of the local mass balance. There is a balance between tangential flow and normal flow

$$\mathbf{q}_\Gamma \cdot \mathbf{n}^+ + \mathbf{q}_\Gamma \cdot \mathbf{n}^- = f_\Gamma^+ + f_\Gamma^- = -\frac{\partial \mathbf{q}_\Gamma \cdot \mathbf{t}^+}{\partial s} - [\dot{u}]_n, \tag{23.28}$$

$$\mathbf{q}_\Gamma \cdot \mathbf{t}^+ = -\left|[u]_n\right|^k K_{\mathrm{d}} \frac{\partial \mu_\Gamma^{\mathrm{f}}}{\partial s}, \tag{23.29}$$

where s represents the distance along the crack, with $s = 0$ the crack tip and s positive in direction of $\mathbf{t}^+$. Tangential flow is assumed of the Couette type. The fluid flows from the crack into the formation are calculated from Darcy's law. If the pressure gradient is resolved (case 2), then the resolved pressure gradient is used. If the pressure gradient is unresolved (case 1), then the pressure gradient is evaluated from Terzaghi's analytical solution of linear one-dimensional consolidation:

$$f_\Gamma^+(\mathbf{x}, t) = -K \frac{\mu^{\mathrm{f}+} - \mu^{\mathrm{f}\Gamma}}{\Delta x}, \qquad f_\Gamma^-(\mathbf{x}, t) = -K \frac{\mu^{\mathrm{f}-} - \mu^{\mathrm{f}\Gamma}}{\Delta x}, \tag{23.30}$$

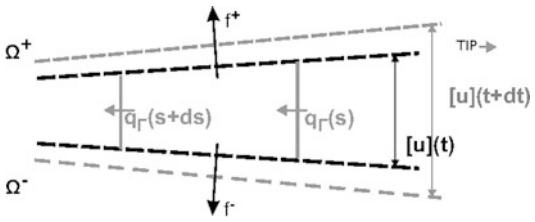

Fig. 23.4 Schematic representation of the fluid flow at the crack surface with parameter s the distance along the crack

where Δx is the width of the pressure gradient and depends on the time Δt since discontinuity developed at that place, the bulk permeability K and aggregate modulus of the material ($c = 2\mu + \lambda - \delta\pi/\delta\,\mathrm{tr}(\boldsymbol{\varepsilon})$), namely $\Delta x^2 \sim \Delta t\, K c$. In other words, at the crack tip, the pressure gradient is infinitely steep, while as one moves away from the crack tip, the pressure gradient is softening. Equation (23.30) can be rewritten in terms of an unresolved hydraulic permeability k_d:

$$f_\Gamma^+ = -k_\mathrm{d}\big(\mu^{\mathrm{f}+} - \mu^{\mathrm{f}-}\big) = -k_\mathrm{d}\big[\mu^\mathrm{f}\big] = -hk_\mathrm{d}\tilde{\mu}^\mathrm{f}. \tag{23.31}$$

23.2.3.2 Local Momentum Balance

A discrete crack is preceded by local damage. This micro-damage is lumped into one constitutive relation (cohesive zone) and projected onto the crack (Remmers et al., 2003). The model relates the decohesion, i.e. softening of the traction forces, as result of opening of the crack. For the traction forces at each surface holds $\boldsymbol{\sigma}\cdot\mathbf{n}^+ = \mathbf{t}_\Gamma^+ = -\mathbf{t}_\Gamma^- = -\boldsymbol{\sigma}\cdot\mathbf{n}^-$, i.e.

$$\big[\boldsymbol{\sigma}_\mathrm{e} - \big(\mu^\mathrm{f} + \Delta\pi\big)\mathbf{I}\big]^\pm \cdot \mathbf{n}^\pm = \mathbf{t}_\Gamma^\pm(\mathbf{x}, t), \quad \mathbf{x} \in \Gamma^\pm. \tag{23.32}$$

The cohesive law holds locally and is described in the local coordinate system of the discontinuity. The cohesive zone model is nonlinear and acts on the effective stress. For the cohesive damage model an exponential law similar to Xu and Needleman (1993) is used, see Fig. 23.5. This law denotes the softening behavior after reaching the critical stress state. Defined is critical length $\delta_s = \mathscr{G}_c/\tau_\mathrm{ult}$, with τ_ult the ultimate traction forces and $\mathscr{G}_c$ fracture toughness. The cohesive law is then

$$t_s = \tau_\mathrm{ult}\frac{[u]_s}{\delta_s}e^{-(\frac{[u]_s}{\delta_s})^2}. \tag{23.33}$$

Note that the surface underneath the curve is the fracture toughness $\mathscr{G}_c$:

$$\int_{-\infty}^{\infty} t_s \mathrm{d}[u]_s = \int_{-\infty}^{\infty} t_s \mathrm{d}[u]_s = \tau_\mathrm{ult}\delta_s 2\int_0^\infty \frac{r}{2}e^{-r^2}\mathrm{d}r = \tau_\mathrm{ult}\delta_s = \mathscr{G}_c. \tag{23.34}$$

A history parameter κ is introduced in case of unloading each time step the current opening κ_0 and traction τ_0 are remembered. When the new opening is smaller than

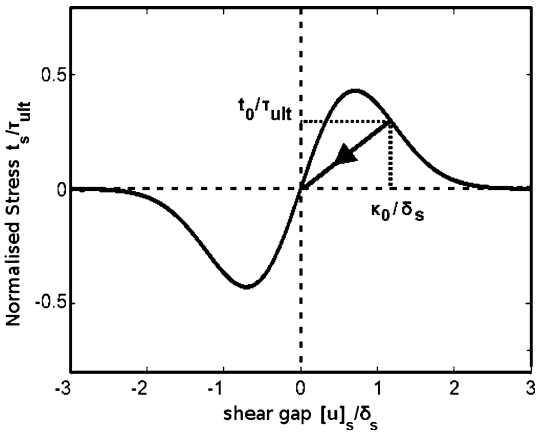

Fig. 23.5 Normalized distribution of the exponential cohesive law illustrated for shearing related traction forces and displacement

previous, then unloading takes place according to

$$t_s = \frac{\tau_0}{\kappa_0}[u]_s. \tag{23.35}$$

Damage is defined as

$$D = 1 - \frac{|t_s|}{\tau_{\text{ult}}}. \tag{23.36}$$

Macro crack is developed when the local damage approaches maximum ($D = 1$) and therefore when the exponential approaches zero. When locally the opening decreases compared to previous time step unloading takes place. The cohesive law parameters $\mathscr{G}_c$ and τ_{ult} can be obtained from experimental data.

23.2.3.3 Yield Criterion

Crack growth is determined by damage in the solid matrix. Therefore, the yield criterion, next to the cohesive zone, is related to the effective stress. The effective stress at the crack tip varies locally, therefore the critical effective stress state is calculated non-locally using Gaussian functions following Wells and Sluys (2001), i.e.

$$\boldsymbol{\sigma}_{\text{tip}} = \sum_{\text{i}=1}^{n_{\text{tot}}} \frac{w_{\text{i}}}{w_{\text{tot}}}\sigma_{\text{e1,2}}, \qquad w_{\text{tot}} = \sum_{j=1}^{n_{\text{tot}}} w_j, \qquad w_{\text{i}} = \frac{(2\pi)^{2/3}}{l_a^3} e^{-\frac{r_{\text{i}}^2}{2l_a^2}}, \tag{23.37}$$

with r_{i} the distance between integration point i and the crack tip and l_a is a length scale parameter which determines the influence of a sample point. $\sigma_{\text{e1,2}}$ and associated angle α_n is evaluated either from Camacho and Ortiz (1996) (mode I):

$$\sigma_{\text{e1,2}} = \frac{\sigma_{\text{e}x} - \sigma_{\text{e}y}}{2} \pm \sqrt{\left(\frac{\sigma_{\text{e}x} - \sigma_{\text{e}y}}{2}\right)^2 + \sigma_{\text{e}xy}^2}, \tag{23.38}$$

or by Tresca criterion (mode II). As soon as the criterion is met, the crack propagates to the next element boundary, additional enrichments are added to accommodate for the extra length of the crack and the criterion is tested for the next element.

23.3 Numerical Description

The weak form for the finite element method is derived by standard Galerkin approach. Then the weak equations are discretized leading to a time-dependent, nonlinear system. This is solved using a Crank-Nicolson scheme for time-integration and Newton-Raphson iteration within each time increment. A discretized form is derived by dividing body Ω into elements Ω_e, $e = 1, \ldots, n_e$ ($\Omega = \bigcup_1^{n_e} \Omega_e$). The result is that also the discontinuity is discretized in elements S_d and the boundary in elements S_e. The displacements, the chemical potential and their variations are discretized similarly (Bubnov-Galerkin approach) by

$$\hat{\mathbf{u}} = \underset{\sim}{N}^{\mathrm{T}} \underset{\sim}{a}_u, \qquad \tilde{\mathbf{u}} = \underset{\sim}{N}^{\mathrm{T}} \underset{\sim}{b}_u, \qquad \hat{\mu}^{\mathrm{f}} = \underset{\sim}{m}^{\mathrm{T}} \underset{\sim}{a}_\mu, \qquad \tilde{\mu}^{\mathrm{f}} = \underset{\sim}{m}^{\mathrm{T}} \underset{\sim}{b}_\mu, \tag{23.39}$$

where $\underset{\sim}{N} = [\underset{\sim}{N}_x \ \underset{\sim}{N}_y]$ contains the shape functions. The columns $\underset{\sim}{a}_u$ and $\underset{\sim}{b}_u$ contain the nodal values for bulk part and enhanced part, respectively. Similar are $\underset{\sim}{m}$, $\underset{\sim}{a}_\mu$ and $\underset{\sim}{b}_\mu$ columns of shape functions and nodal values. The introduction of fluid flow does demands a time stepping algorithm. Time stepping here is therefore driven by diffusion of the fluid and not dissipation of energy. The solution is sensitive to the magnitude of the time increment. A large time step leads to underestimation of fluid pressure in confined compression. Taking too small steps leads to initial oscillation. For stable time integration the following law has to be satisfied (Vermeer and Verruijt, 1981)

$$\Delta t > \frac{\Delta x^2}{cK}, \tag{23.40}$$

in which Δx is characteristic size of an element and Δt is the time step. A Crank-Nicolson scheme is used. Although the bulk material is assumed linear elastic, the presence of damage introduces nonlinearity. The system is therefore solved iteratively at each time step. The matrices involved are given elsewhere (Kraaijeveld et al., 2009). The model has been programmed using the Jem/Jive finite element toolkit which has been developed by Habanera (Rijswijk, Netherlands). For implementation aspects like the tracking of the crack tip, increasing the degrees of freedom or other propagation issues we refer to Remmers et al. (2003, 2008) and Remmers (2006).

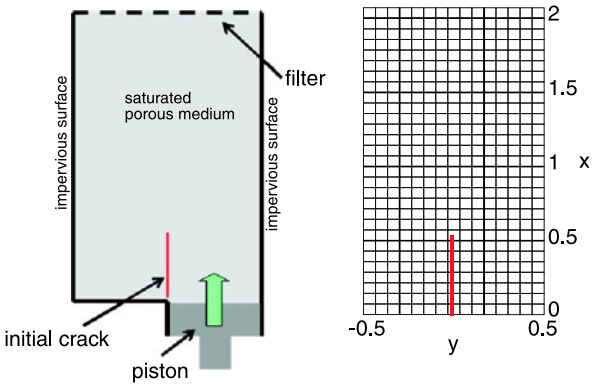

Fig. 23.6 *Left*: schematic representation of the compression test. *Right*: representation of the mesh for the compression test

23.4 Results

23.4.1 Shear Test Using Discontinuous Chemical Potential (Case 1)

For the shear test the sample is boxed except for the contact area with the piston. On the right the sample is in contact with a filter, which causes an equilibrium with an external salt solution ($\mu^{\mathrm{f}}_{\mathrm{in}} = \mu^{\mathrm{f}}_{\mathrm{ex}}$) and concomitant prestress is all directions. An initial crack is imposed away from element interfaces (Fig. 23.6).

The material properties are given in Table 23.1. External load is applied through the piston. The piston is moved with constant speed $v = 0.15 \cdot 10^{-3}$ mm/s. Crack growth is investigated in a free swollen sample. The initial size of the sample is the result of free swelling in both directions. The resulting pre-strain is $\varepsilon_{\mathrm{ix}} = \varepsilon_{\mathrm{ix}} = 1.2 \cdot 10^{-3}$. In Fig. 23.7 the distribution of the chemical potential is given. The movement of the piston results in initially straight crack growth which after a while deflects. At the crack tip a pressure gradient over the crack exists.

The fluid flow evolution in case of free swelling is considered across the crack $\mathbf{q} \cdot \mathbf{n}^{+}$ for two points, in the initial crack ($\mathrm{d}x = 0.28$ mm) and in the crack ($\mathrm{d}x = 0.48$ mm), see Fig. 23.8. The flow in the initial crack is nonzero. Every time the crack propagates a peak in flow takes place which is also felt in the already existing crack. The crack grows for several elements after which stress is built up again and in which the flow relaxes. The fluid flow is nonzero from start. When the local permeability is taken constant and similar to bulk permeability ($k_{\mathrm{d}} = K_{\mathrm{d}}$), the overall crack propagation is not changed much, but fluid exchange is lower and more slowly initiated. When the permeability is taken much lower, there is hardly any fluid flow.

There are two types of discretization sensitivity: in time and in space. Decreasing the time discretization by a factor 4 does not have any influence on bulk and crack behavior. Therefore, the time step is sufficiently small. Decreasing the mesh discretization size by a factor two, does not have a negligible effect. Decreasing the mesh size, but keeping the nonlocal length l_a (Eq. (23.37)) constant, increases the amount of integration points over which the stress at the crack tip is averaged.

Table 23.1 Material properties for shear test

$R = 8.3145$ Nmm/mmolK	$T = 298$ K
$E = 90.0$ MPa	$\nu = 0.20$
$\phi_{\mathrm{i}}^{\mathrm{f}} = 0.80$	$K = 0.28 \cdot 10^{-3}$ mm^4/Ns
$c^{\mathrm{ex}} = 0.15 \cdot 10^{-3}$ mmol/mm^3	$c_{\mathrm{i}}^{\mathrm{fc}} = -0.2 \cdot 10^{-3}$ mmol(eq)/mm^3
$K_{\mathrm{d}} = 0.28 \cdot 10^{-3}$ mm^3/Ns	
$\mathscr{G}_c = 0.002$ N/mm	$\tau_{\mathrm{ult}} = 0.4$ MPa
$l_a = 0.2$ mm	$v = 1.5 \cdot 10^{-3}$ mm/s

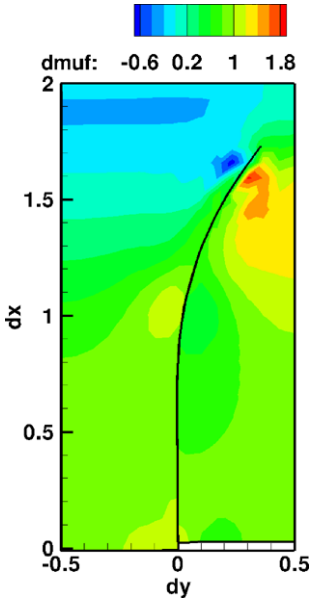

Fig. 23.7 Distribution of chemical potential (d$t = 16.6$ s). Crack-path is independent of mesh. Across the crack line a jump in chemical potential is observed

The result is that the stress at the crack tip is lower and, therefore, crack growth is slightly slower, but more constant. This has effect on the fluid flow. Decreasing the nonlocal length and the discretization size by a factor 2 causes faster crack growth.

23.4.2 Delamination Using Continuous Chemical Potential (Case 2)

A delamination test is performed with a predefined angle of 0°. An initial defect of length 13 mm is inserted on the left hand side, Fig. 23.9. The sample is fixed on the right hand side and is in contact with a filter ($\mu^{\mathrm{f}} = 0$). Crack propagation is initiated by pulling the sample on the top and bottom over approximate 8 mm with a fixed velocity of $1.0 \cdot 10^{-3}$ mm/s. The local fluid distribution is determined by Eqs. (23.28) and (23.29).

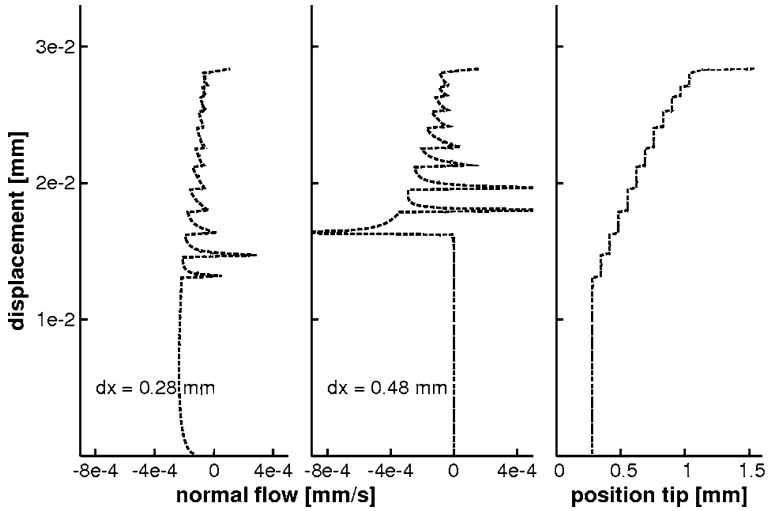

Fig. 23.8 Normal flow for free swelling along the crack at points $dx = 0.28$ mm and $dx = 0.48$ mm. Crack growth causes a peak in flow after which relaxation takes place. The jump in chemical potential imposed by the one-sided compressive load results in a nonzero initial flow and high peaks in case of crack growth followed by relaxation. The resulting crack-growth occurs in a staccato fashion. Crack growth over several elements followed by a pause during which the chemical potential jump diffuses away. This diffusion of the chemical potential leads to increasing load on the effective stress field of the solid, and hence failure of the solid

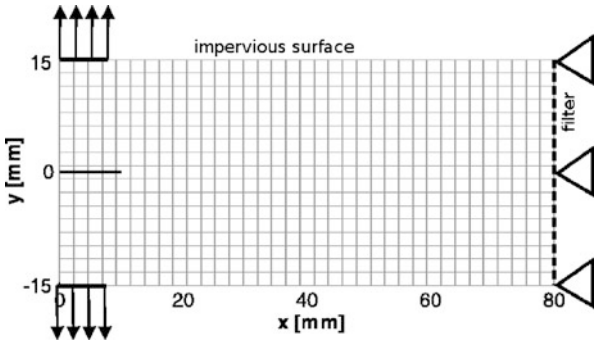

Fig. 23.9 The mesh and boundary conditions for delamination consisting of 575 elements. Material is pulled at the *top* and *bottom* on the *left* and is on the *right* in contact with a filter

The exact material properties are given in Table 23.2. This means that $2RT\Gamma c^{\text{ex}} = 4.96\ \text{N/mm}^2$ holds. A time step of 0.1 s is used.

The influence of mesh refinement, prestress and local boundary conditions on the crack is considered on crack propagation and flow around the crack. For the mesh refinement, the mesh of Fig. 23.9 is refined to 2701 elements. The corresponding time step is a quarter of the time step of the coarse mesh. For the influence of prestress four cases are compared, no prestress, prestress in both directions and prestress in either x- or y-direction. The modes of prestress are the result of different initial swellings, not the result of uneven distribution of fixed charges. Furthermore, the

Table 23.2 Material properties for delamination test

$R = 8.3145$ Nmm/mmolK	$T = 298$ K
$E = 1.4 \cdot 10^4$ MPa	$\nu = 0.33$
$\phi_{\mathrm{i}}^{\mathrm{f}} = 0.10$	$K = 0.2$ mm^4/Ns
$c^{\mathrm{ex}} = 1.0 \cdot 10^{-3}$ mmol/mm^3	$c_{\mathrm{i}}^{\mathrm{fc}} = -1.0 \cdot 10^{-3}$ mmol(eq)/mm^3
$K_{\mathrm{d}} = 0.2$ mm^3/Ns	$k = 2$
$\mathscr{G}_c = 0.020$ N/mm	$\tau_{\mathrm{ult}} = 1.1$ MPa
$l_a = 7.8$ mm	$v = 1.0 \cdot 10^{-3}$ mm/s

influence of local mass balance is considered by decreasing the local permeability with respect to the standard case or prescribing the chemical potential in the crack. Considering the chemical potential distribution, Fig. 23.10, the figures show localization at the crack tip with a negative chemical potential. This low chemical potential is relaxed by fluid redistribution towards the crack tip. The chemical potential is largest at the left due to largest opening of the crack.

Figure 23.11 shows the fracture length versus the pull displacement. Crack growth occurs slightly faster in the case of prestress. With further opening of the crack, the chemical potential decreases and the tangential flow increases. Numerical oscillations seem to be present, but the oscillations are actual changes in chemical potential due to crack growth and redistribution of load. These changes are less in the case of prestress than when there is no prestress present. In addition in the case without prestress the growth seems more smoothly. Furthermore, the chemical potential is nonzero from the start in case of prestress. When fluid is not taken into account, crack growth occurs faster, while the time to damage initiation is almost the same as in the case with fluid present.

23.5 Discussion

Computations of both mode I and mode II crack propagation in saturated porous media predict stepwise crack propagation, provided fluid exchange between crack and formation is accounted for. The time Δt during which the propagation pauses and the distance Δx over which the crack propagates in one step relates according to Terzaghi's relationship:

$$\Delta t = \frac{\Delta x^2}{cK}. \tag{23.41}$$

In mode I, the triaxial tensile stress state at the crack tip results in a strong underpressure in the fluid. This pressure (or chemical potential) dip at the crack tip attracts fluid, particularly from the crack itself, resulting on the one hand into a closing of the crack a short distance away from the tip, and on the other hand into a progressive transfer of the triaxial state of tensile stress from the fluid to the effective stress of the solid. This progressive transfer leads to failure of the solid and further propagation of the crack. The same scenario repeats itself all over again a little further into the material.

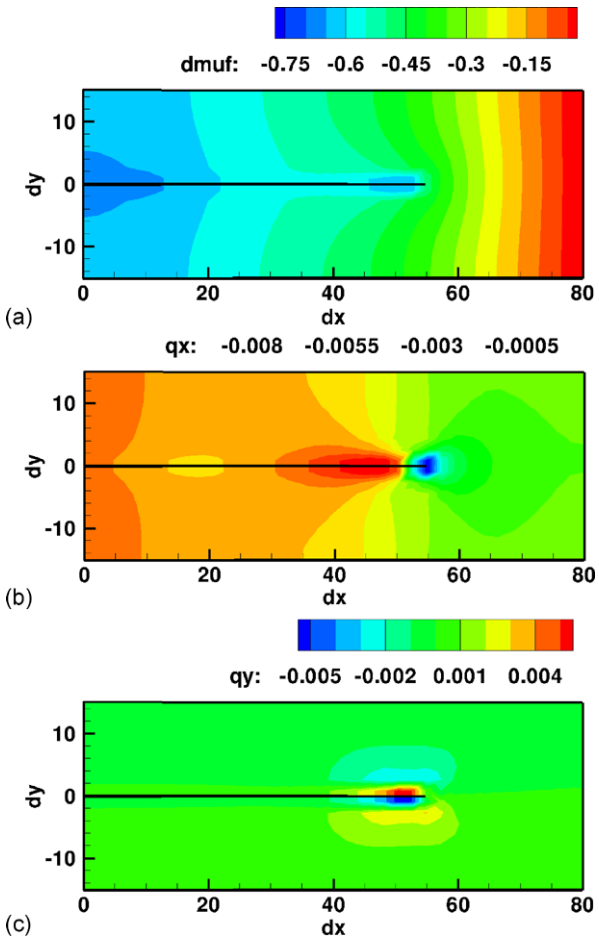

Fig. 23.10 Delamination in case of prestress in both directions after 950 time increments (i.e. $9.5 \cdot 10^{-2}$ mm displacement of top boundary). Distribution of (**a**) chemical potential (N/mm^2), (**b**) flow in the x-direction (mm/s), (**c**) flow in the y-direction (mm/s)

In mode II a very similar phenomenon occurs. A sharp pressure (or chemical potential) gradient develops as the shear band proceeds, causing a fluid flow across the band. This fluid flow transfers the stress concentration at the crack tip from the fluid to the effective stress, resulting in a (delayed) shear band propagation, recreating thereby the steep pressure gradient across the newly created shear band.

The crack chemical potential tracing in Fig. 23.11 are indicative of a model that cannot resolve the variations imposed by the stepwise progression of the crack. On the contrary, the flow tracings in Fig. 23.8 are obtained though discontinuous enrichment of the chemical potential field. This approach exempts from resolving the steep chemical potential gradients and reconstructs the steep gradients from the analytical solution of Terzaghi. From the poromechanical theory, we can infer that the continuous approach as taken in Fig. 23.11, can only capture the flow and pressure (or chemical potential) variations correctly if the time step is larger than $\Delta x^2/cK$, in which Δx is the characteristic mesh size. From this criterion we infer that for

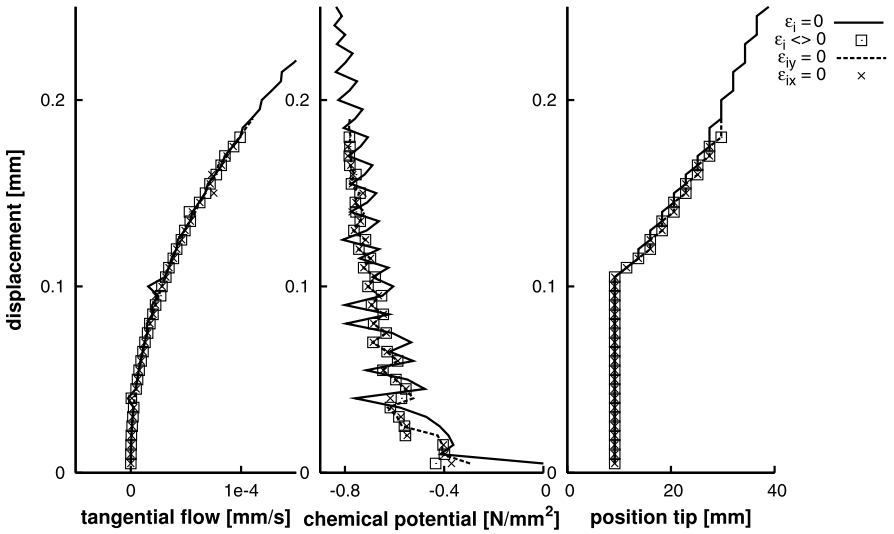

Fig. 23.11 Comparison of the effect of prestress for delamination d$x = 13.71$ mm (ahead of the initial crack) on tangential flow in the crack, chemical potential in the crack and crack growth against pull displacement at the top

adequate resolving of the chemical potential gradient, the time step should be larger than 180 s, which is not suitable for crack propagation. The only option left is to decrease Δx, in other words, increase the spatial resolution. Δx should decrease a factor $40 = \sqrt{180/0.1}$ in order to allow a time step of 0.1 s. If one does so through a mesh refinement, the advantage of partition of unity is largely lost. Choosing for high order polynomials for the enrichment function D is probably the only option to handle fracture in saturated porous media by means of continuous enrichment for the pressure. The lower the hydraulic permeability and the lower the Young's modulus of the porous medium, the higher the order of the polynomial has to be. The computationally more effective approach is the discontinuous enrichment function for the pressure.

Acknowledgements The authors acknowledge financial support from the Technology Foundation STW, the technological branch of the Netherlands Organization of Scientific Research NWO and the Ministry of Economic Affairs (DLR5790).

References

Armero F, Callari C (1999) An analysis of strong discontinuities in a saturated poro-plastic solid. Int J Numer Methods Eng 46:1673–1698

Babuska I, Melenk JM (1997) The partition of unity method. Int J Numer Methods Eng 40:727–758

Belytschko T, Black T (1999) Elastic crack growth in finite elements with minimal remeshing. Int J Numer Methods Eng 45:601–620

Camacho GT, Ortiz M (1996) Computational modelling of impact damage in brittle materials. Int J Solids Struct 33:2899–2938

de Borst R, Réthoré J, Abellan MA (2006) A numerical approach for arbitrary cracks in a fluid-saturated medium. Arch Appl Mech 75:595–606

Gasser TC, Holzapfel GA (2006) Modeling the propagation of arterial dissection. Eur J Mech A, Solids 25:617–633

Gasser TC, Holzapfel GA (2007) A numerical framework to model 3-D fracture in bone tissue with application to failure of the proximal femur. In: Combescure A, de Borst R, Belytschko T (eds) Discretization methods for evolving discontinuities. Springer, Dordrecht, pp 199–211

Kim Y (2000) Prediction of peripheral tears in the anulus of the intervertebral disc. Spine 25:1771–1774

Kraaijeveld F, Huyghe JM, Baaijens FPT (2009) Singularity solution of Lanir's osmoelasticity: verification of discontinuity simulations in soft tissues. J Biomech Eng 10:845–865

Lanir Y (1987) Biorheology and flux in swelling tissue. I. Biocomponent theory for small deformation including concentration effects. Biorheology 24:173–187

Larsson J, Larsson R (2000) Localization analysis of a fluid-saturated elastoplastic porous medium using regularized discontinuities. Mech Cohes-Frict Mater 5:565–582

Little JP, Adam CJ, Evans JH, Pettet GJ, Pearcy MJ (2007) Nonlinear finite element analysis of anular lesions in the 14/5 intervertebral disc. J Biomech 40:2744–2751

Natarajan RN, Williams JR, Lavender SA, Andersson GBJ (2007) Poro-elastic finite element model to predict the failure progression in a lumbar disc due to cyclic loading. Comput Struct 85:1142–1151

Remmers JJC (2006) Discontinuities in materials and structures. A unifying computational approach. PhD Thesis, Delft University of Technology, The Netherlands

Remmers JJC, de Borst R, Needleman A (2003) A cohesive segments method for the simulation of crack growth. Int J Numer Methods Eng 31:69–77

Remmers JJC, de Borst R, Needleman A (2008) The simulation of dynamic crack propagation using the cohesive segments method. J Mech Phys Solids 56:70–92

Réthoré J, de Borst R, Abellan, MA (2007) A discrete model for the dynamic propagation of shear bands in a fluid-saturated medium. Int J Numer Anal Methods Geomech 31:347–370

Steinmann P (1999) A finite element formulation for strong discontinuities in fluid-saturated porous media. Mech Cohes-Frict Mater 4:133–152

Urban JP, Roberts S (2003) Degeneration of the intervertebral disc. Arthritis Res Ther 5:120–130

Vermeer PA, Verruijt A (1981) An accuracy condition for consolidation by finite elements. Int J Numer Anal Methods Geomech 5:1–14

Wells GN, Sluys LJ (2001) Discontinuous analysis of softening solids under impact loading. Int J Numer Anal Methods 25:691–709

Xu XP, Needleman A (1993) Void nucleation by inclusion debonding in a crystal matrix. Model Simul Mater Sci Eng 1:111–132

Part V
Morphogenesis, Biological Tissues and Organs

Chapter 24
Mechanisms of Brain Morphogenesis

Benjamen A. Filas, Gang Xu, and Larry A. Taber

Abstract In structures with obvious mechanical function, like the heart and bone, the relationship of mechanical forces to growth and development has been well studied. In contrast, other than the problem of neurulation, the developmental mechanisms in the nervous system have received relatively little attention. In this review we discuss recent advances in our understanding of the physical mechanisms of morphogenesis during brain development. Specifically, we focus on two processes: formation of the primary brain vesicles and folding of the cerebral cortex.

24.1 Introduction

During development, the brain undergoes a dramatic transformation from a simple tubular structure to (in large mammals) a highly convoluted shape. Most investigators recognize that mechanics plays a major role in this process, but the physical mechanisms of brain morphogenesis remain poorly understood.

In this review, we discuss the state of the field and some of the current research challenges. Where appropriate, we emphasize interspecies differences in morphogenetic mechanisms, as understanding these differences can provide insight into the development of individual organisms (Lui et al., 2011). After discussing background and embryology we focus on the formation of the primary vesicles in the early brain and cortical folding, which occurs relatively late in development. These processes warrant further study, as abnormalities in brain shape and folding patterns have been linked to a wide array of neurological disorders including schizophrenia, epilepsy,

B.A. Filas · L.A. Taber (✉)
Department of Biomedical Engineering, Washington University, St. Louis, MO 63130, USA
e-mail: lat@wustl.edu

B.A. Filas
e-mail: baf1@cec.wustl.edu

G. Xu
Department of Mechanical Engineering and Materials Science, Washington University, St. Louis, MO 63130, USA
e-mail: gxu@seas.wustl.edu

G.A. Holzapfel, E. Kuhl (eds.), *Computer Models in Biomechanics*,
DOI 10.1007/978-94-007-5464-5_24,

autism, and mental retardation. Morphogenesis offers a number of challenges for computational modelers, and we hope this review stimulates more interest in these problems among biomechanical engineers.

24.2 Neurulation and Brain Tube Formation

Neurulation is the earliest stage of development specific to the nervous system. This process begins within the first three weeks of conception in humans, as a central region of ectoderm called the neural plate folds to create the neural tube (Fig. 24.1). The wall of the tube is a neuroepithelium composed of a single layer of undifferentiated neural progenitor cells (Lowery and Sive, 2009). The cells are columnar, and the cell nuclei migrate between the apical side (facing the lumen) and basal side (facing the exterior) during the cell cycle, giving the neuroepithelium a pseudostratified, or multi-layered appearance (Sauer, 1935; Miyata, 2008). Eventually, the anterior and posterior regions of the neural tube become the brain and spinal cord, respectively.

Morphogenesis of the neural tube occurs in a specific spatiotemporal pattern along the length of the embryo. In the chicken, mouse, and human embryo, the neural plate elevates, folds, and fuses to form a tube with a hollow lumen (Fig. 24.1A). Depending on the longitudinal position along the tube, this closure is facilitated by the formation of one or three hinge points (Fig. 24.1A, asterisks). Generally, multiple hinge points are present at the anterior end of the tube (prospective brain), while only one hinge point forms posteriorly (prospective spinal cord). The end result is a tube that decreases in cross-sectional area from the brain through the spinal cord. Collectively this folding is known as primary neurulation, which has been shown to require the coordination of forces intrinsic to the neuroepithelium as well as extrinsic forces generated by surrounding tissues (Schoenwolf and Smith, 1990).

In contrast, during later stages of development, an entirely different mechanism sculpts the furthest posterior spinal cord region. Here, undifferentiated mesenchymal (loosely connected, highly migratory) cells condense and cavitate to form an internal lumen in a process known as secondary neurulation (Fig. 24.1B). Hence, the anterior brain and spinal cord form via coordinated bending of the neuroepithelium, whereas the posterior end of the spinal cord forms via the agglomeration, cavitation, and epithelialization of loosely connected cells.

In species such as *Xenopus* (frog) and zebrafish, however, such a difference between neurulation mechanisms is not immediately apparent (Schmitz et al., 1993; Lowery and Sive, 2004; Harrington et al., 2009). Here, neural precursor cells migrate medially to form a neural keel (Fig. 24.1C, arrows), intercalate (exchange neighbors), and remodel to form a slit-like lumen. Interestingly, it remains controversial as to whether the brain forms via a primary or secondary neurulation mode in these species. Dynamic (time lapse) imaging studies suggest that these cells roll into a tube, as occurs during primary neurulation, but in doing so, the cells intercalate and migrate, displaying behaviors more typical of those involved in secondary

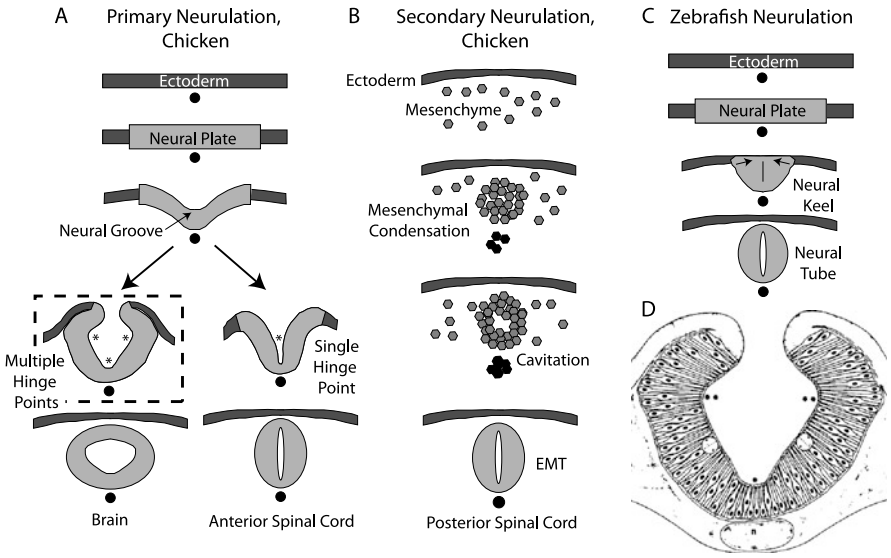

Fig. 24.1 Neurulation mechanisms. (**A**) Primary neurulation in the chicken. A central region of ectoderm (neural plate) bends to form the neural groove. Multiple (brain) or single hinge points (spinal cord) facilitate subsequent tube closure (*asterisks*). (**B**) Secondary neurulation in the chicken. Mesenchymal cells coalesce and cavitate to form the posterior spinal cord. (**C**) Neurulation in zebrafish. Cells migrate medially (*arrows*) to form the neural keel and reorganize to form a slit-like lumen. (**D**) Schematic from Schoenwolf and Smith (1990) showing representative cell morphologies during stages of hinge point formation in the prospective chicken brain, adapted with permission from Development. Interrelated processes of cell shape change, contraction at the apical (inner) wall, and nuclear positioning cooperatively shape the bending neuroepithelium

neurulation (Lowery and Sive, 2004; Harrington et al., 2009). Hence, neurulation in these species may involve a combination of the primary and secondary neurulation mechanisms. Computational models for neural tube closure in amphibians have provided insight into some of these processes (Clausi and Brodland, 1993; Chen and Brodland, 2008; Brodland et al., 2010).

What does seem to be clear, however, is that hinge points do not form during neural tube formation in *Xenopus* or zebrafish as occurs in chicken, mouse, and human embryos (Fig. 24.1A, C, Harrington et al., 2009). Hinge point formation is characterized by interrelated, intrinsic processes such as cell wedging, possibly caused by apical contraction or the radial positioning of nuclei in the neuroepithelial wall (interkinetic nuclear migration) (Fig. 24.1D, Schoenwolf and Smith, 1990). The nucleus constitutes the bulk of the cell volume (Fig. 24.1D) and its radial position in the neuroepithelial wall depends on the stage of the cell cycle. If, for example, a subset of cells takes longer to undergo DNA synthesis at the outer wall of the neuroepithelium, then the nucleus would force the basal side of these tall, thin cells to expand and potentially generate a hinge point (Smith and Schoenwolf, 1988). Apical narrowing via contraction may also be involved, however, as proteins that regulate cytoskeletal contraction (rho, phosphorylated myosin light chain, and F-actin)

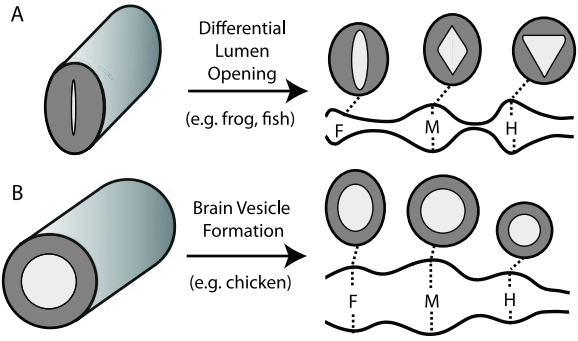

Fig. 24.2 Mechanisms of brain vesicle formation. (**A**) Differential opening of a slit-like brain tube is concomitant with primary vesicle formation in frog and fish. Shapes vary in transverse cross sections between the forebrain (*F*), midbrain (*M*), and hindbrain (*H*). (**B**) Primary brain vesicles similarly form in species with comparatively open brain tubes, but vesicle shapes are rounded and relatively homogeneous

colocalize and accumulate at the inner wall of the neuroepithelium at hinge points (Sadler et al., 1982; Lee and Nagele, 1985; Kinoshita et al., 2008). It is currently unclear whether hinge point formation acts as a driving or a stabilizing force during normal neural tube closure (Greene and Copp, 2009). Early finite element models have shown that apical constriction can produce invaginations (Odell et al., 1981) and hinge-like morphologies (Clausi and Brodland, 1993), but this mechanism warrants further study.

24.3 Brain Tube Morphogenesis

The brain tube of vertebrates subsequently subdivides into three primary vesicles (forebrain, midbrain, and hindbrain) (Fig. 24.2). Depending on the species, the brain vesicles develop from either a hollow tube or a comparatively closed, slit-like tube (Fig. 24.1). This suggests that, as in neurulation, morphogenetic mechanisms driving vesicle formation may vary between species.

24.3.1 Lumen Opening in Zebrafish Brains

To date, mechanistic studies of brain vesicle formation have been conducted primarily in zebrafish embryos. In this species, the internal lumen of the tube differentially opens to generate the primary vesicles. The lumen of the hindbrain opens first, followed closely by the midbrain and the forebrain (Lowery and Sive, 2005). Interestingly, the forebrain, midbrain, and hindbrain lumens open into different cross-sectional shapes (Fig. 24.2A). Specifically, the midbrain lumen is shaped like a diamond, the hindbrain a triangle, while the forebrain opens into a tear-drop shape

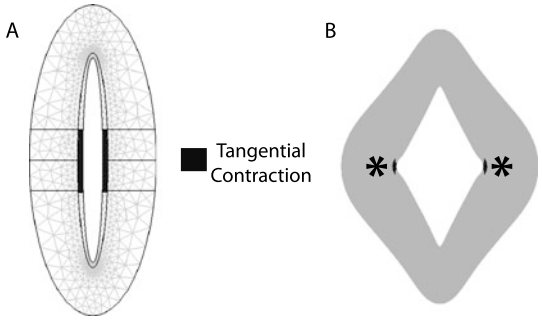

Fig. 24.3 Model for lumen opening. (**A**) Finite element model of a tube with a slit-like cross section. Tangential contraction is prescribed at the apical (inner wall) at two mediolateral (*darkened*) locations. (**B**) Local contraction generates lateral hinge points (*asterisks*) and opens the lumen into a *diamond shape*. Figure adapted from Filas et al. (2012), with permission from Biomechanics and Modeling in Mechanobiology

(Filas et al., 2012); see also Fig. 5G, J, M in Lowery and Sive (2005). It is currently unclear whether all regions initially open as diamonds (as occurs in the midbrain; Nyholm et al., 2009) and later remodel into different shapes, or if the shape inhomogeneities are preserved throughout the opening process. Moreover, the significance of regionally varying shapes along the length of the brain tube is not yet known. Notably, at comparable developmental stages, early chicken, mouse, and human brains are generally round in transverse cross section (Fig. 24.2B, Copp et al., 2003; Filas et al. 2011, 2012).

The morphogenetic mechanisms that drive luminal opening in the zebrafish midbrain are beginning to be uncovered. In particular, inhibiting myosin by blebbistatin exposure prevents this process (Nyholm et al., 2009). This result has led to speculation that cytoskeletal contraction at lateral hinge points may facilitate luminal opening in zebrafish (Nyholm et al., 2009). Consistent with this idea, finite element modeling has shown that simulating local contraction at the inner wall of a tube with an initially slit-like cross section generates lateral hinge points and a diamond-shaped lumen (Fig. 24.3).

Once the lumen opens, later expansion of the hindbrain requires relaxation of the cytoskeleton (Gutzman and Sive, 2010). Hence, it seems that the zebrafish brain tube actively contracts to establish a lumen, and later relaxes to facilitate expansion in response to increasing fluid pressure in the lumen (see Sect. 24.3.2).

24.3.2 Brain Vesicle Formation

Evidence suggests that brain tube morphology at the mid-hindbrain boundary in zebrafish is not purely a consequence of differential luminal expansion. The decreased radius in this region is associated with wedge-shaped cells produced by a combination of basal constriction and apical expansion (Gutzman et al., 2008). Actin

is concentrated on the basal side of these cells, consistent with actomyosin driven basal contraction. (Interestingly, in most other instances of invagination that involve cytoskeletal contraction, the contraction occurs at the cell apex, Davies, 2005.) In embryos that lack laminin, which is a major component of the basement membrane surrounding the outside (basal side) of the brain tube, the mid-hindbrain boundary still forms, but is not as sharp as in wild type embryos (Gutzman et al., 2008). Hence, differential lumen opening may set the initial pattern for the brain vesicles, while ongoing actomyosin activity remodels the tube into its characteristic three-dimensional structure.

Outside of zebrafish, however, the mechanisms of brain vesicle formation have received relatively little attention. To begin exploring this process, we measured morphogenetic strains at the inner wall of the neural tube during the stages of vesicle formation in the chicken embryo (Filas et al., 2008). As expected, negative circumferential strains occur at the mid-hindbrain boundary, with negative longitudinal strains in the surrounding ventricles. These results suggest that the brain may shorten in a specific, regionally dependent manner to facilitate vesicle formation. Corresponding changes in mechanical properties were measured by probing the stiffness of the neuroepithelium via microindentation (Xu et al., 2010a). Surprisingly, the characteristic brain geometry gives a nearly uniform indentation stiffness along the brain tube.

Recently, we have developed a finite element model for brain vesicle formation (BAF unpublished). The model consists of a circular tube with contraction simulated within a narrow region next to the lumen. When the mid-hindbrain boundary region undergoes circumferential contraction and the surrounding vesicles isotropic contraction (consistent with actin staining), the model yields geometric changes consistent with experimental measurements (Fig. 24.4B).

Extrinsic forces also may play a role in shaping the brain tube. The brain forms on the dorsal side of the embryo surrounded by a loosely packed network of cells and extracellular matrix known as the head mesenchyme. During vesicle formation in chicken and human embryos, the early brain seals at both ends to become a fluid-filled pressure vessel. The brain then begins a period of rapid expansion, and studies have shown that this growth depends on cerebrospinal fluid pressure (Gato and Desmond, 2009). Specifically, prematurely sealing the brain cavity causes the expansion to begin early (Desmond and Levitan, 2002), whereas relieving the pressure severely retards growth (Desmond and Jacobson, 1977).

In these embryos, however, the majority of vesicle morphogenesis occurs prior to the brain becoming a sealed, pressurized system. Hence, the primary source of external forces acting on the neuroepithelium during vesicle formation would likely be from surrounding tissues. To explore these effects, we removed the head mesenchyme and cultured isolated chicken brains through the stages of vesicle formation (Filas et al., 2011). In these brain tubes, the vesicles and overall morphology developed normally, suggesting that vesicle formation is intrinsic to the neuroepithelium.

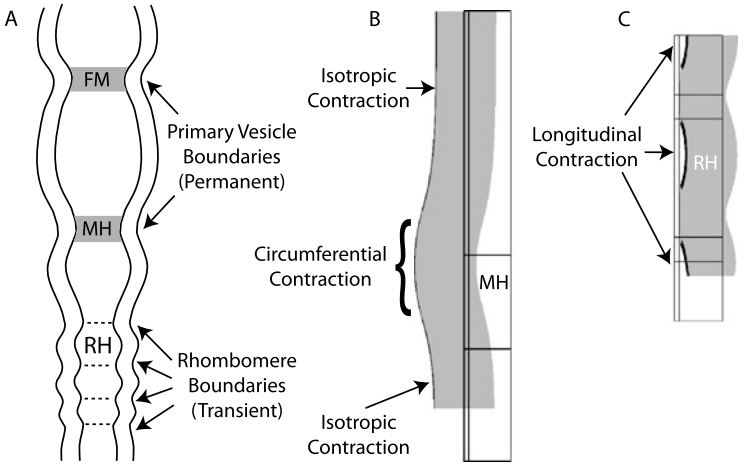

Fig. 24.4 Boundary formation in the brain tube of the chicken embryo. (**A**) The primary brain vesicles (forebrain, midbrain, and hindbrain) are separated by the permanent fore-midbrain (*FM*) and mid-hindbrain (*MH*) boundaries. Rhombomeres (*RH*) are transient, sequential bulges in the early hindbrain. (**B**, **C**) Axisymmetric finite element models of vesicle (**B**) and rhombomere (**C**) morphogenesis. Contraction occurs at the apical (inner) wall. (**B**) The mid-hindbrain boundary contracts in the circumferential direction, but the apical side of the wall contracts isotropically elsewhere to create vesicles. (**C**) Longitudinal contraction between the more passive rhombomere boundaries causes local bulges (rhombomeres) to form

24.3.3 Rhombomere Formation

As the primary brain vesicles form, a series of smaller, periodic bulges arise in the hindbrain. These rhombomeres (Fig. 24.4A), have received considerable attention since the early 1990s as regions of cell lineage restriction and differential gene expression (reviewed in Kiecker and Lumsden, 2005). With the spotlight on these structures as local signaling centers, interest in the morphogenetic mechanisms of rhombomere formation has receded. Still, some useful mechanistic details can be garnered from the earlier literature.

In rhombomeres of chicken embryos, cell proliferation rates and apical F-actin concentrations are higher in interboundary regions than in the boundaries (Guthrie et al., 1991). In addition, the amount of extracellular space between neighboring cells tends to increase in the boundaries during development (Heyman et al., 1993). These results led to early speculation that a bowing or buckling mechanism, due to constrained cell proliferation, drives rhombomere formation.

Alternatively, apical contraction between boundaries could play a role in rhombomere formation. For example, the model in Fig. 24.4C shows that longitudinal contraction along the inner wall between boundaries causes these regions to bend outward, producing a shape consistent with experimental observations.

Interestingly, rhombomeres are transient structures during brain development (as opposed to the primary vesicle boundaries which persist through maturity) (Kiecker

and Lumsden, 2005). Before they disappear, rhombomere boundaries facilitate spatially dependent patterns of axonal migration, cell differentiation, and gene expression. In a recent study in zebrafish, rhombomere boundaries abnormally persisted in hyper-contracted mutants (Gutzman and Sive, 2010), suggesting that rhombomere formation and subsequent dissolution may be a consequence of regulated patterns of cytoskeletal contraction.

24.4 Cortical Folding

24.4.1 Cerebral Cortex Development and Theories for Folding

Following vesicle formation, the brain rapidly expands due to an increasing lumen pressure. This expansion is primarily a growth response, rather than a simple inflation (Desmond and Jacobson, 1977; Pacheco et al., 1986). During these stages of rapid growth, the forebrain subdivides into the diencephalon and the more anterior telencephalon, which gives rise to the neocortex. Neurons generated in the developing neocortex differentiate and migrate along radially aligned glial fibers to form the characteristic layers of the mature brain in an inside-out manner (Bystron et al., 2008). In large mammals, folding of the cortex begins after these stages of neuronal migration and proliferation. The primary folding patterns are generally conserved across species, but secondary folds can differ considerably.

Several hypotheses have been proposed for cortical folding mechanisms, and many are based on the idea that folds are produced by differential or constrained growth. A straightforward idea is that the brain grows faster than the skull, which therefore exerts compressive forces on the brain that cause it to buckle. To study this hypothesis, Raghavan et al. (1997), modeled the cerebral cortex as a thin curved beam that grows within a semicircular boundary representing the skull. With some *ad hoc* assumptions, these authors obtained realistic folding patterns. Experimental evidence, however, indicates that the brain can fold without external constraints (Barron, 1950).

The cerebral cortex is more accurately modeled as a thin shell. Such a model was proposed by Richman et al. (1975), who assumed that the outer layers of the cortex grow faster than the inner layers, causing compressive stresses that buckle the cortex (Fig. 24.5A). Their analysis yielded wavelengths consistent with those measured in the normal brain, as well as in brains with a microgyric (short wavelength) or lissencephalic (long wavelength) cortex. However, these investigators neglected nonlinear effects, which become increasingly important as folds grow large.

Several other computational models for growth-driven cortical folding have been proposed. Toro and Burnod (2005) modeled the cortex as a ring of 2D truss elements with growth constrained by radially aligned elastoplastic fibers. Extending a similar model to 3D, Nie et al. (2009) examined the effects of constraint of skull constraint, growth rate, regional variations in growth, and initial geometry of folding patterns. In addition, Geng et al. (2009) examined folding of small 3D regions of the cortex

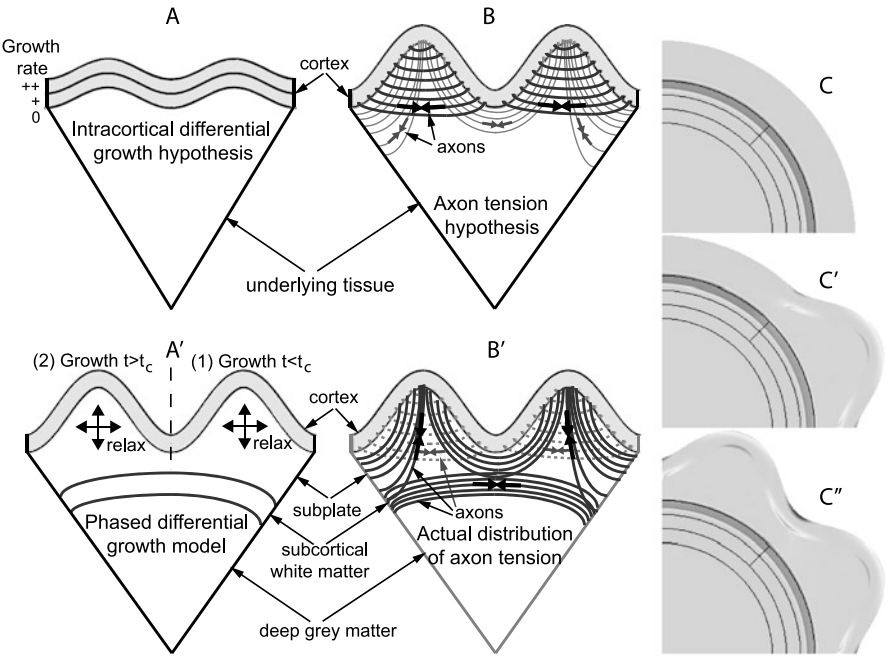

Fig. 24.5 Postulated models for cortical folding. (**A**) Intracortical differential growth hypothesis (Richman et al., 1975). Brain cortex is divided into two layers with the outer layer growing faster (indicated by ++) than the inner layer (+). Underlying tissue does not grow (*0*). Differential growth results in cortical buckling. (**B**) Axon tension hypothesis (Van Essen, 1997). Tension (*black arrows*) in axons pulls two cortical regions together to form an outward fold. The inward fold that forms between the outward folds separates weakly interconnected cortical regions (*grey arrows*). (**A′**) Phased differential growth model. Cortical growth in region 1 ($t < t_c$) followed by cortical growth in region 2 ($t > t_c$) produces two folds. The underlying subplate grows to relax the induced stresses. (**B′**) Experimental distributions of axon tension. Axons are under tension (*black arrows*) and aligned in the directions shown. Importantly, no circumferential tension (*grey arrows*) or axons (*grey dotted lines*) were detected in the cores (subplate) of the outward folds. (**C**–**C″**) Corresponding finite element model for cortical folding caused by phased differential growth. The *dark* and *light grey colors* indicate circumferential tension and compression, respectively (Xu et al., 2010b). Figure reproduced from Xu et al. (2010b), with permission from the Journal of Biomechanical Engineering, ASME

by combined osmotic expansion and artificially applied loads and constraints. It is important to note, however, that these models focus mainly on folding geometry and do not present stress distributions, which can be used to help distinguish between multiple solutions.

In an alternative hypothesis, Van Essen (1997) has postulated that the brain expands due to hydrostatic pressure and growth, but tension in axons restricts this expansion locally, forcing the cortex to fold (Fig. 24.5B). Consistent with observations, such a mechanism would tend to create outward folds in regions that are strongly interconnected, producing compact wiring, whereas inward folds form in

weakly connected regions. Until recently, this mechanism had not been tested experimentally (see Sect. 24.4.2).

24.4.2 Phased Differential Growth as a Mechanism for Cortical Folding

The ferret is a popular animal for studies of cortical folding, as the ferret brain does not begin to fold until after birth (Smart and McSherry, 1986a,b; Barnette et al., 2009). To test the axonal tension hypothesis, we used tissue dissection to determine stress patterns in the folding ferret brain. The results indicate that axonal tension is significant, but the principal directions of this tension (and the corresponding axon orientations) are different from those predicted by the axon tension hypothesis (Fig. 24.5B′; Xu et al., 2010b). Notably, there is no significant tension between the walls of the outward folds (gyri). This result suggests that, although axonal tension is present, it likely does not play the mechanistic role during folding proposed by Van Essen (1997).

Next, we proposed a new model for folding driven by differential growth. This model is similar to that of Richman et al. (1975) with the following exceptions: (i) Tangential growth in the cortex is out of phase between adjacent regions (phased differential growth); and (ii) the underlying subplate grows in response to the developed stresses. During the simulation, growth in one region produces an outward fold, which is then followed by a second growth-induced fold in the neighboring region, and so on (Fig. 24.5C). Consistent with this idea, imaging studies have shown that folds form in such a sequential manner during development (Neal et al., 2007; Kroenke et al., 2009). This model yields folding geometry and stress distributions that agree well with experimental results (Xu et al., 2010b). More recent data suggest, however, that the differential growth hypothesis may require further refinement to include a radial gradient in growth (Reillo et al., 2011).

24.5 Conclusions

In summary, results from a number of laboratories are providing new insights into the biomechanical mechanisms of brain morphogenesis. Careful consideration must be taken in interpreting the results from these studies, as brain morphology can be highly variable between different model organisms.

The treatment of the subject here is not exhaustive and much work remains to be done to fill in the gaps. Notably, we have omitted discussion of secondary vesicle generation in the brain tube, as well as secondary cortical folding. Deeper questions remain relatively unexplored, such as the possible role of mechanical feedback in driving and potentiating brain morphogenesis. Indeed, mounting evidence suggests that the neuroepithelium can actively respond to changes in mechanical stress (Filas

et al., 2011), and that changes in mechanical loading can directly affect cell proliferation rates (Desmond et al., 2005). Lastly, we note that the biomechanical events that cause folding anomalies associated with pathological conditions warrant further attention.

Acknowledgements We gratefully acknowledge funding support from NIH grants R01 GM075200 and R01 NS070918 (LAT), as well as a fellowship for BAF from NIH T90 DA022871 and the Mallinckrodt Institute of Radiology, Washington University.

References

Barnette AR, Neil JJ, Kroenke CD, Griffith JL, Epstein AA, Bayly PV, Knutsen AK, Inder TE (2009) Characterization of brain development in the ferret via MRI. Pediatr Res 66(1):80–84

Barron DH (1950) An experimental analysis of some factors involved in the development of the fissure pattern of the cerebral cortex. J Exp Zool 113:553–573

Brodland GW, Chen X, Lee P, Marsden M (2010) From genes to neural tube defects (NTDs): insights from multiscale computational modeling. HFSP J 4(3–4):142–152

Bystron I, Blakemore C, Rakic P (2008) Development of the human cerebral cortex: Boulder Committee revisited. Nat Rev, Neurosci 9(2):110–122

Chen X, Brodland GW (2008) Multi-scale finite element modeling allows the mechanics of amphibian neurulation to be elucidated. Phys Biol 5(19):15003

Clausi DA, Brodland GW (1993) Mechanical evaluation of theories of neurulation using computer simulations. Development 118:1013–1023

Copp AJ, Greene ND, Murdoch JN (2003) The genetic basis of mammalian neurulation. Nat Rev Genet 4:784–793

Davies JA (2005) Mechanisms of morphogenesis: the creation of biological form. Elsevier, San Diego

Desmond ME, Jacobson AG (1977) Embryonic brain enlargement requires cerebrospinal fluid pressure. Dev Biol 57(1):188–198

Desmond ME, Levitan ML (2002) Brain expansion in the chick embryo initiated by experimentally produced occlusion of the spinal neurocoel. Anat Rec 268(2):147–159

Desmond ME, Levitan ML, Haas AR (2005) Internal luminal pressure during early chick embryonic brain growth: descriptive and empirical observations. Anat Rec, Part a Discov Mol Cell Evol Biol 285(2):737–747

Filas BA, Knutsen AK, Bayly PV, Taber LA (2008) A new method for measuring deformation of folding surfaces during morphogenesis. J Biomech Eng 130:61010

Filas BA, Bayly PV, Taber LA (2011) Mechanical stress as a regulator of cytoskeletal contractility and nuclear shape in embryonic epithelia. Ann Biomed Eng 39:443–454

Filas BA, Oltean A, Beebe DC, Okamoto RJ, Bayly PV, Taber LA (2012) A potential role for differential contractility in early brain development and evolution. Biomech Model Mechanobiol (in press)

Gato A, Desmond ME (2009) Why the embryo still matters: CSF and the neuroepithelium as interdependent regulators of embryonic brain growth, morphogenesis and histiogenesis. Dev Biol 327(2):263–272

Geng G, Johnston LA, Yan E, Britto JM, Smith DW, Walker DW, Egan GF (2009) Biomechanisms for modelling cerebral cortical folding. Med Image Anal 13(6):920–930

Greene NDE, Copp AJ (2009) Development of the vertebrate central nervous system: formation of the neural tube. Prenat Diagn 29(4):303–311

Guthrie S, Butcher M, Lumsden A (1991) Patterns of cell division and interkinetic nuclear migration in the chick embryo hindbrain. J Neurobiol 22(7):742–754

Gutzman JH, Graeden EG, Lowery LA, Holley HS, Sive H (2008) Formation of the zebrafish midbrain-hindbrain boundary constriction requires laminin-dependent basal constriction. Mech Dev 125(11–12):974–983

Gutzman JH, Sive H (2010) Epithelial relaxation mediated by the myosin phosphatase regulator Mypt1 is required for brain ventricle lumen expansion and hindbrain morphogenesis. Development 137(5):795–804

Harrington MJ, Hong E, Brewster R (2009) Comparative analysis of neurulation: first impressions do not count. Mol Reprod Dev 76(10):954–965

Heyman I, Kent A, Lumsden A (1993) Cellular morphology and extracellular space at rhombomere boundaries in the chick embryo hindbrain. Dev Dyn 198(4):241–253

Kiecker C, Lumsden A (2005) Compartments and their boundaries in vertebrate brain development. Nat Rev, Neurosci 6(7):553–564

Kinoshita N, Sasai N, Misaki K, Yonemura S (2008) Apical accumulation of Rho in the neural plate is important for neural plate cell shape change and neural tube formation. Mol Biol Cell 19(5):2289–2299

Kroenke CD, Taber EN, Leigland LA, Knutsen AK, Bayly PV (2009) Regional patterns of cerebral cortical differentiation determined by diffusion tensor MRI. Cereb Cortex 19(12):2916–2929

Lee HY, Nagele RG (1985) Studies on the mechanisms of neurulation in the chick: interrelationship of contractile proteins, microfilaments, and the shape of neuroepithelial cells. J Exp Zool 235(2):205–215

Lowery LA, Sive H (2004) Strategies of vertebrate neurulation and a reevaluation of teleost neural tube formation. Mech Dev 121(10):1189–1197

Lowery LA, Sive H (2005) Initial formation of zebrafish brain ventricles occurs independently of circulation and requires the nagie oko and snakehead/atp1a1a.1 gene products. Development 132(9):2057–2067

Lowery LA, Sive H (2009) Totally tubular: the mystery behind function and origin of the brain ventricular system. BioEssays 31(4):446–458

Lui JH, Hansen DV, Kriegstein AR (2011) Development and evolution of the human neocortex. Cell 146(1):18–36

Miyata T (2008) Development of three-dimensional architecture of the neuroepithelium: role of pseudostratification and cellular 'community'. Dev Growth Differ 50(Suppl 1):S105–S112

Neal J, Takahashi M, Silva M, Tiao G, Walsh CA, Sheen VL (2007) Insights into the gyrification of developing ferret brain by magnetic resonance imaging. J Anat 210(1):66–77

Nie J, Li G, Guo L, Liu T (2009) A computational model of cerebral cortex folding. In: 12th international conference on medical image computing and computer-assisted intervention, 12(Pt 2). London, pp 458–465

Nyholm MK, Abdelilah-Seyfried S, Grinblat Y (2009) A novel genetic mechanism regulates dorsolateral hinge-point formation during zebrafish cranial neurulation. J Cell Sci 122(Pt 12):2137–2148

Odell GM, Oster G, Alberch P, Burnside B (1981) The mechanical basis of morphogenesis. I. Epithelial folding and invagination. Dev Biol 85:446–462

Pacheco MA, Marks RW, Schoenwolf GC, Desmond ME (1986) Quantification of the initial phases of rapid brain enlargement in the chick embryo. Am J Anat 175(4):403–411

Raghavan R, Lawton W, Ranjan SR, Viswanathan RR (1997) A continuum mechanics-based model for cortical growth. J Theor Biol 187(2):285–296

Reillo I, de Juan Romero C, García-Cabezas MÁ, Borrell V (2011) A role for intermediate radial glia in the tangential expansion of the mammalian cerebral cortex. Cereb Cortex 21(7):1674–1694

Richman DP, Stewart RM, Hutchinson JW, Caviness VS Jr (1975) Mechanical model of brain convolutional development. Science 189(4196):18–21

Sadler TW, Greenberg D, Coughlin P, Lessard JL (1982) Actin distribution patterns in the mouse neural tube during neurulation. Science 215(4529):172–174

Sauer FC (1935) Mitosis in the neural tube. J Comp Neurol 62(2):377–405

Schmitz B, Papan C, Campos-Ortega JA (1993) Neurulation in the anterior trunk region of the zebrafish brachydanio rerio. Roux's Arch Dev Biol 202(5):250–259
Schoenwolf GC, Smith JL (1990) Mechanisms of neurulation: traditional viewpoint and recent advances. Development 109:243–270
Smart IH, McSherry GM (1986a) Gyrus formation in the cerebral cortex in the ferret. I. Description of the external changes. J Anat 146:141–152
Smart IH, McSherry GM (1986b) Gyrus formation in the cerebral cortex of the ferret. II. Description of the internal histological changes. J Anat 147:27–43
Smith JL, Schoenwolf GC (1988) Role of cell-cycle in regulating neuroepithelial cell shape during bending of the chick neural plate. Connect Tissue Res 252(3):491–500
Toro R, Burnod Y (2005) A morphogenetic model for the development of cortical convolutions. Cereb Cortex 15(12):1900–1913
Van Essen DC (1997) A tension-based theory of morphogenesis and compact wiring in the central nervous system. Nature 385(6614):313–318
Xu G, Kemp PS, Hwu JA, Beagley AM, Bayly PV, Taber LA (2010a) Opening angles and material properties of the early embryonic chick brain. J Biomech Eng 132(1):011005
Xu G, Knutsen AK, Dikranian K, Kroenke CD, Bayly PV, Taber LA (2010b) Axons pull on the brain, but tension does not drive cortical folding. J Biomech Eng 132(7):071013

Chapter 25
A Micromechanical Viscoelastic Constitutive Model for Native and Engineered Anterior Cruciate Ligaments

Jinjin Ma and Ellen M. Arruda

Abstract Ligaments and tendons are soft tissues that are largely composed of aligned collagen and elastin. Due to this microstructure, they have nonlinear viscoelastic responses. We have developed a micromechanical constitutive model to capture the inhomogeneous, nonlinear viscoelastic properties of native ACL and of a tissue engineered ligament graft upon explantation. This constitutive model incorporates a viscoelastic collagen network and a nonlinear elastic elastin network. The model captures the nonlinear viscoelastic responses of these tissues using a limited number of parameters that can be interpreted in terms of physical properties of the collagen fibers and elastin. The parameters used to model the tissue engineered ligament response are similar to those found for the native ACL, indicating that the microstructure of the tissue engineered ligament graft has developed in vivo to match that of the native ACL.

25.1 Introduction

Ligaments and tendons are fibrous connective tissues that transmit forces from muscle to bone (tendon) or from bone to bone (ligament). In particular, the anterior cruciate ligament (ACL) is one of four major ligaments that stabilizes the knee. The ACL assists knee movement in anterior-posterior translation and constrains the tibia from excessive anterior motion relative to the femur. ACL tears (or ruptures) occur when the knee experiences a sudden landing with or without direction change. The incidents of ACL injury are on the rise and an ACL rupture is now one of the most common knee injuries in the US. Without a functional ACL, a patient's knee will experience abnormal joint movement and this may induce further knee complications such as osteoarthritis or multiple ligament tears. Eventually the knee may develop severe degenerative joint diseases that require a total knee replacement. The current

J. Ma · E.M. Arruda (✉)
University of Michigan, Ann Arbor, MI 48109, USA
e-mail: arruda@umich.edu

J. Ma
e-mail: jinjinma@umich.edu

G.A. Holzapfel, E. Kuhl (eds.), *Computer Models in Biomechanics*,
DOI 10.1007/978-94-007-5464-5_25,

treatment for ACL injuries uses a tendon graft to replace the torn ACL. Despite the generally good outcomes of the current method, several research and clinical reports have documented limitations of the treatment such as the high economic cost, donor-site morbidity, and the risk of osteoarthritis development (Wilder et al., 2002; NationalSurvey, 2004; Salgado et al., 2004; Roos, 2005; Moffat et al., 2008). A critical concern of the current tendon graft is that it is stiffer than the ACL it is replacing and, therefore, it is over-designed for its application. These limitations have led researchers to investigate the possibility of utilizing a tissue engineered ACL graft for ACL reconstruction. Recent work shows tissue engineered grafts have great potential to meet this unmet clinical need to restore native ACL anatomy and function (Goulet et al., 2004; Fan et al., 2008; Ma et al., 2012a).

An important goal of tissue engineering grafts for ACL replacement is that the biomechanical response of the graft match that of the native ACL. For the past few decades, efforts have contributed to elucidating the biomechanical behavior, remodeling process and failure mechanisms of native ACL and ACL grafts (Butler et al., 1992; Danto and Woo, 1993; Jackson et al., 1993). However, researchers have faced many challenges such as inaccurate strain and stress field measurements and the difficulty of mimicking a physiological loading condition (Weiss and Gardiner, 2001). Therefore, computational biomechanics has become an increasingly important tool to provide information to fill this gap. To further investigate the biomechanical response of the native ACL and to design and evaluate possible grafts in a 3D finite element framework, a constitutive model that can accurately describe the nonlinear viscoelastic behavior of the native and engineered ACLs is required to prescribe the material properties in the finite element analysis (FEA). Ligaments and tendons have nonlinear viscoelastic responses that can be characterized via stress-strain, load-unload, stress relaxation, and creep tests. Recent work has demonstrated that the viscoelastic responses of ligaments and tendons are both time and strain dependent and various viscoelastic constitutive laws have been proposed to capture these responses (Provenzano et al., 2001; Duenwald et al., 2009; Ma et al., 2012a).

The generalized Maxwell model that is shown schematically in Fig. 25.1 consists of multiple spring and dashpot combinations. It has been used to model inorganic polymer viscoelasticity and has been proposed for soft tissue (Corr et al., 2001; Tang et al., 2011; Sopakayang et al., 2012). In the latter modeling approach the multiple spring-dashpot elements are often thought of as representing the aligned fibrous structures of ligament or tendon. A generalized description of the model in 1D is expressed in Eq. (25.1), where k_i is the Young's modulus of the ith linear spring and η_i the viscosity of the ith linear dashpot. The advantage of this model is that it is simple and convenient to implement into computer programs and to auto-search the parameters to fit the experimental data. However, this model requires a fairly large number of parameters in order to capture both the load-unload and stress relaxation responses. Because the parameters are determined by fitting specific test data, these parameters often do not fully describe the responses of the specimen under different boundary conditions (Sopakayang et al., 2012). The generalized description of the

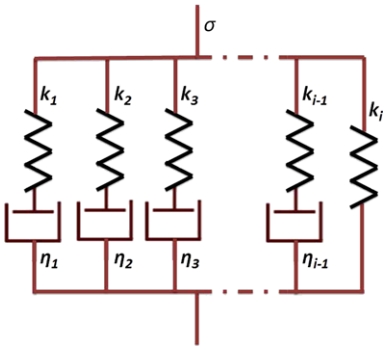

Fig. 25.1 Generalized Maxwell model

model is

$$\sigma(\varepsilon,t)=\left(k_1\exp\frac{-k_1t}{\eta_1}+k_2\exp\frac{-k_2t}{\eta_2}+\cdots+k_{i-1}\exp\frac{-k_{i-1}t}{\eta_{i-1}}+k_i\right)t. \quad (25.1)$$

To capture the nonlinear behavior with a reduced number of parameters, Fung's quasi-linear viscoelasticity (QLV) theory has been widely used (Fung, 1972). QLV theory assumes that the relaxation or creep response can be separated into strain-dependent and time-dependent components, as described in 1D as

$$\sigma(\varepsilon,t)=\int E_t(t-\tau)\frac{\mathrm{d}\sigma}{\mathrm{d}\varepsilon}\frac{\varepsilon(t)}{\mathrm{d}\tau}\,\mathrm{d}\tau, \quad (25.2)$$

where E_t is the reduced relaxation function that depends on time and $\mathrm{d}\sigma/\mathrm{d}\varepsilon$ is the instantaneous elastic response. Both functions are obtained by curve-fitting the experimental data. The QLV model is able to fit a single set of experimental data (Weiss and Gardiner, 2001) such as a stress relaxation experiment. However, this model cannot fully describe or predict stress or strain profiles at different constraint levels with the same set of parameters due to the fact that the reduced relaxation function E_t depends on time only (Provenzano et al., 2001) whereas the actual tissue response includes a strain-dependent relaxation function. The QLV model predicts the same relaxation or creep rate regardless of strain or stress levels.

Schapery's single integral nonlinear theory, or modified superposition theory (Provenzano et al., 2002; Duenwald et al., 2010), is similar to Schapery's single integral nonlinear theory and therefore in this paper, we use Schapery's single integral theory to demonstrate this class of constitutive models. In 1D uniaxial loading, Schapery's theory can be expressed as:

$$\sigma(\varepsilon,t)=h_e(\varepsilon)E_e\varepsilon+h_1(\varepsilon)\int\Delta E\big[\rho(t)-\rho'(\tau)\big]\frac{\mathrm{d}h_2(\varepsilon)\varepsilon}{\mathrm{d}\tau}\,\mathrm{d}\tau, \quad (25.3)$$

where the reduced time ρ and the reduced time variable of integration ρ' are functions of strain and time and are defined as:

$$\rho=\int_0^t\frac{\mathrm{d}t'}{a_e[\varepsilon(t')]},\qquad \rho'=\int_0^\tau\frac{\mathrm{d}t'}{a_e[\varepsilon(t')]}. \quad (25.4)$$

E_e is the final value of the elastic modulus and ΔE is the transient modulus during the relaxation between the initial and final values of the elastic modulus, while h_e, h_1, h_2 and a_e are strain-dependent material properties. A power law equation $\Delta E(\rho) = C\rho^n$ is used to fit a stress relaxation curve and the other material properties are fitted using the rest of the relaxation curves. To fit four different curves, a total of ten parameters are used and the relaxation function is obtained from curve-fitting the lowest relaxation profile. The model has been applied to ligament and can describe its strain and time dependent response (Provenzano et al., 2002; Duenwald et al., 2010). However, the relaxation function in the model is not unique. In fact, for four different relaxation curves, four different relaxation functions can be fit and, therefore, four separate sets of parameters would describe this behavior, indicating the method is essentially a curve-fitting based methodology.

The 1D models discussed above describe the uniaxial response of ligaments and tendons. They must be extended to 3D formulations to be used within a finite element framework or even to consider a different mode of deformation analytically, such as the anterior tibial translation deformation that results in ACL tears. Extending these models to 3D is likely to require the involvement of more parameters for describing the tissue responses in other orientations because, for instance, anisotropy is not addressed in these models in their present form. QLV viscoelastic models and modified QLV models have been implemented into 3D finite element modeling (Pioletti et al., 1998). These continuum models are able to describe the tissue behavior in 3D settings with curve-fitted parameters. However, because the QLV and modified QLV models are based on the separable relaxation function, they cannot fully predict the time and strain dependent responses of soft tissue.

To address this desire for a nonlinear viscoelastic model that can capture the 3D response of ligament and tendon with a reduced number of parameters, and moreover can potentially be predictive, we have taken a micromechanics approach that describes the deformation of aligned structural proteins such as collagen and elastin. Since these are macromolecules we describe their elastic response in terms of hyperelastic formulations that have been shown to be predictive of the nonlinear elasticity of biopolymers and inorganic elastomers alike (MacKintosh et al., 1995; von Lockette and Arruda, 1999a, 1999b, 2001, 2002; Bischoff et al., 2000, 2001, 2002a, 2002b, 2002c, 2004; Boyce and Arruda, 2000, 2001; Palmer and Boyce, 2008).

25.2 Constitutive Modeling of Mechanical Response

Ligaments and tendons are largely comprised of aligned viscoelastic collagen fibers and nonlinear elastic elastin networks. To capture their structure and nonlinear viscoelastic behavior, we have developed a micromechanical model incorporating collagen and elastin to describe the nonlinear viscoelastic response of ACLs and our tissue engineered grafts.

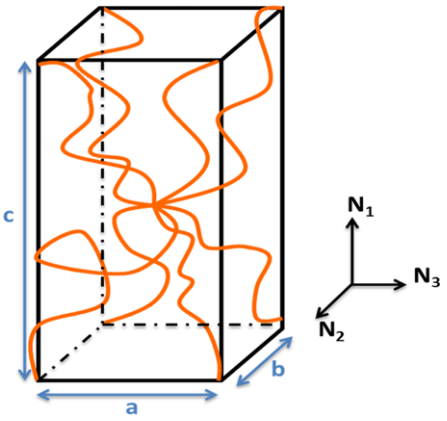

Fig. 25.2 An anisotropic representative volume element for a network of semi-flexible chains (Bischoff et al., 2002b, 2002c)

25.2.1 3D Hyperelastic Constitutive Models

Collagen fibers and elastin are long-chain molecules. Their mechanical responses can be categorized into three regimes: flexible, semi-flexible, and stiff (Palmer et al., 2010). Many biopolymer inspired constitutive models have been proposed, such as the freely jointed chain and semi-flexible chain models. MacKintosh et al. (1995) proposed a model that describes the nonlinear behavior of semi-flexible biopolymers at small strains well (MacKintosh et al., 1995). This model has been implemented in an eight-chain framework (Arruda and Boyce, 1993) to capture the response of an F-actin network (Palmer and Boyce, 2008). The Cauchy stress tensor $\mathbf{T}_A$ is expressed as

$$\mathbf{T}_A = \frac{nk\Theta_A}{3l_\mathrm{p}}\frac{r_0}{\lambda_\mathrm{c}}\frac{1}{4(1-\lambda_\mathrm{c}\lambda_0/L_\mathrm{c})^2}\frac{L_\mathrm{c}/l_\mathrm{p}-6(1-\lambda_\mathrm{c}r_0/L_\mathrm{c})}{L_\mathrm{c}/l_\mathrm{p}-2(1-\lambda_\mathrm{c}r_0/L_\mathrm{c})}\mathbf{B}-p\mathbf{I}, \quad (25.5)$$

$$\lambda_\mathrm{c} = \sqrt{\mathrm{tr}(\mathbf{B})/3}. \quad (25.6)$$

In this equation, n is the chain density of the network, k is Boltzmann's constant, Θ_A is the temperature, and p is the hydrostatic pressure. For the MacKintosh chain network l_p represents the persistence length, L_c represents the contour length, r_0 is the initial vector chain length and λ_c is the chain stretch. Since these are all physical parameters, potentially, they are measurable experimentally. The MacKintosh chain network of the micromechanical model is embedded within an initially isotropic or anisotropic 8-chain framework (Arruda and Boyce, 1993; Bischoff et al., 2002b, 2002c), as in Fig. 25.2 to mathematically model the mechanical behavior of a structural protein network or inorganic elastomer network.

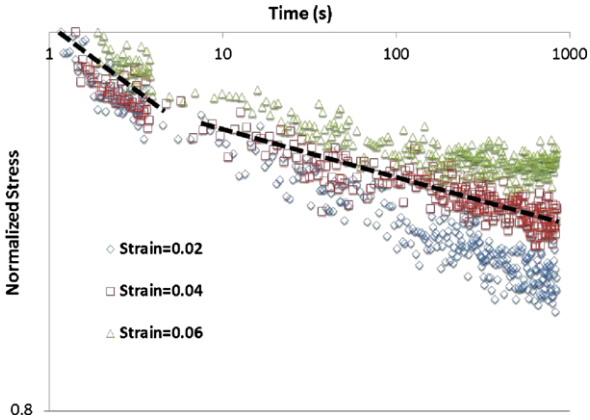

Fig. 25.3 Bi-linear stress relaxation response of native ACL

25.2.2 A 3D Viscoelastic Constitutive Model

The simplest viscoelastic model that can capture solid-like behavior is the standard linear solid model the 1D analog of which has two linear springs and a linear dashpot. The configuration of this model can be represented with springs of stiffness k_1 and k_2 and a dashpot with viscosity η_1, as in Fig. 25.1. The model describes the linear viscoelastic behavior of solids well. In the extension to 3D each spring becomes a 3D linear elastic stress-strain relationship (i.e. Hooke's law) and the dashpot becomes a 3D linear viscous element. Since the ACL and its grafts have a nonlinear viscoelastic behavior, we substitute a nonlinear MacKintosh semi-flexible network of Fig. 25.3 for one linear stress-strain relationship. We have examined various possibilities for the remaining elements in the three-element model and found the combination of a second nonlinear elastic network and a linear dashpot to capture ligament and tendon viscoelasticity reasonably well, but not fully accurately (Ma et al., 2010). Our previous stress relaxation experiments have demonstrated that ACLs and tissue engineered grafts have the distinct bi-linear relaxation behavior shown in Fig. 25.4 that may be captured by two linear elastic networks and two linear viscous elements. Therefore, the proposed model consists of five elements as illustrated in 1D in Fig. 25.4, a nonlinear elastic network, two linear elastic networks and two linear viscous elements.

In this model $\mathbf{F}^{\mathrm{e}}_B$ and $\mathbf{F}^{\mathrm{e}}_C$ are the elastic parts of the deformation gradient tensors and $\mathbf{F}^{\mathrm{v}}_B$ and $\mathbf{F}^{\mathrm{v}}_C$ are the viscous parts. From compatibility, the total deformation $\mathbf{F}$ is $\mathbf{F} = \mathbf{F}^{\mathrm{e}}_B\mathbf{F}^{\mathrm{v}}_B = \mathbf{F}^{\mathrm{e}}_C\mathbf{F}^{\mathrm{v}}_C$. The left Cauchy-Green tensor $\mathbf{B}$ is $\mathbf{B} = \mathbf{F}\mathbf{F}^{\mathrm{T}}$. From equilibrium of the system, the total Cauchy stress is given as $\mathbf{T} = \mathbf{T}_A + \mathbf{T}_B + \mathbf{T}_C$, where $\mathbf{T}_A$ is the Cauchy stress in the nonlinear spring network A, given by Fig. 25.4, and $\mathbf{T}_B$ and $\mathbf{T}_C$ are the Cauchy stresses in the linear spring networks B and C. The Cauchy stress tensors in the linear networks can be represented as follows:

$$\mathbf{T}_{B,C} = nk\Theta_{B,C}\mathbf{B}^{\mathrm{e}}_{B,C} - p\mathbf{I}. \tag{25.7}$$

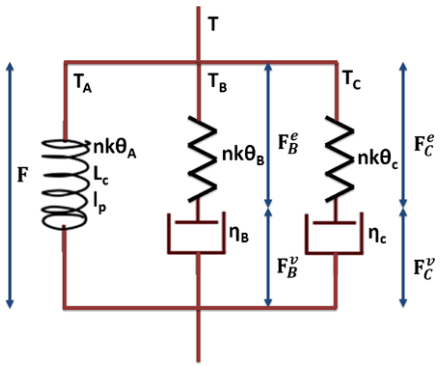

Fig. 25.4 A five-element nonlinear viscoelastic constitutive model

The linear dashpot constitutive equation for the viscous element B, C is $\mathbf{D}^{\mathrm{v}}_{B,C} = \mathbf{T}'_{B,C}/\eta_{B,C}$ where $\mathbf{D}^{\mathrm{v}}_{B,C}$ is the viscous shear strain rate, $\eta_{B,C}$ is the constant shear viscosity and $\mathbf{T}'_{B,C}$ is the equivalent shear stress. The network deformation is assumed to be incompressible. The model implementation and parameter determination will be presented in the next section.

25.3 Methods

25.3.1 Experimental Characterization of the ACL and Tissue Engineered Graft

We have previously developed a tissue engineered bone-ligament-bone (BLB) construct from bone marrow stromal cells and used it as a graft to replace the ACL in a sheep model. A detailed description can be found in Ma et al. (2012a, 2012b). After 9 months of implantation, the tissue engineered grafts and the contra-lateral ACLs were dissected with the femur and tibia attached for mechanical testing. The femur and tibia of each sample were fixed in a customized grip apparatus at a 30 degree knee flexion angle and the entire unit was installed onto an MTS 810 servo hydraulic test system with a 25 kN load cell. Uniaxial tension tests and stress relaxation tests were conducted to characterize the material properties of the samples. High-speed cameras were employed to measure the displacement at the tissue level. A speckle pattern made from waterproof India ink was applied on the surface of the samples. VIC-2D software (Correlated Solutions) was used for accurate tissue deformation determination via digital image correlation analysis and full-field strain contours of the tissue were obtained. The strain data of each test were then obtained by averaging all the data points on the tissue surface.

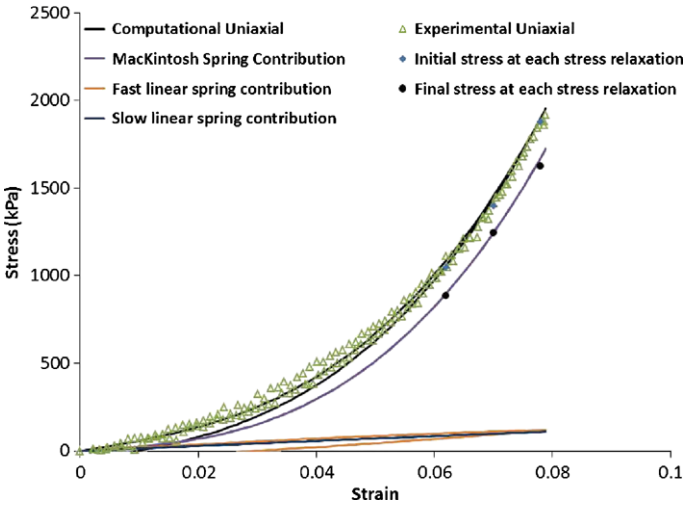

Fig. 25.5 Obtaining parameter constants from the instantaneous load-unload response (*triangles*) and the equilibrium response from the stress relaxation data (*circles*)

25.3.2 Determination of the Model Parameters

Stress and strain data from the uniaxial test and the final value of the stresses from each stress relaxation test conducted on the same specimen are used to determine the range of the model parameters. As shown in Fig. 25.5, first, the parameters of the MacKintosh 8-chain model, L_c, l_p, and $nk\Theta$, are determined by fitting the three final stress points shown in black dots to a nonlinear elastic MacKintosh model shown by the solid purple line in the figure. With these three parameters determined, the contributions of the two linear springs (yellow and blue curves) are added to the model to fit the uniaxial test data. The rate of the uniaxial test is 0.05 s^{-1}, therefore, one load-unload test ends within 4 seconds. The hysteresis of the uniaxial load-unload response can be fit using the viscosity of a fast linear dashpot. Finally, using the three sets of stress relaxation data, the parameters associated with the linear series spring-dashpot systems are adjusted so that the same set of seven parameters can fit all three stress relaxation response curves as well as the uniaxial tension response obtained from the same specimen.

A rate formulation is employed to compute the stress vs. strain responses of various tissues to a cyclic load/unload test. Time and the total stretch are prescribed so that $\mathbf{F}^v$ can be explicitly computed based on updating the rate of deformation of the viscous dashpots from the previous time step. $\mathbf{F}^e$ is, therefore, updated in the current time step using $\mathbf{F}^e = \mathbf{F}\mathbf{F}^{v^{-1}}$ and then used to compute the stresses. Once the total stress is calculated the deformation increments of the dashpots are updated based on the stress in each dashpot element and the next increment of viscous deformation, the $\mathbf{F}^v$ for each dashpot, is determined for the next time step.

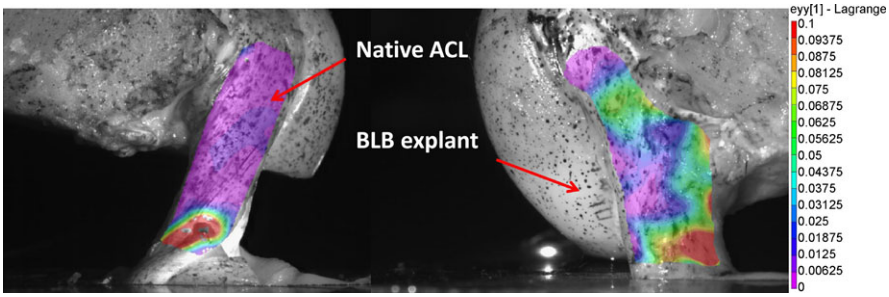

Fig. 25.6 Full-field deformation maps of the native ACL and tissue engineered BLB explant during the uniaxial loading (Ma et al., 2012b)

25.4 Results

Full-field deformation maps of the native ACL demonstrate that the native ACL is inhomogeneous and functionally graded with the most compliant region near the tibia insertion (Fig. 25.6). The contralateral tissue engineered BLB explant shows a similar full-filed deformation map. The micromechanical model proposed herein captures the uniaxial load-unload responses of the native ACL and the engineered BLB (Figs. 25.7A and C). With the same sets of the parameters, the model predicts the stress relaxation responses (Figs. 25.7B and D).

The parameters used to predict the engineered BLB response are very similar to those used to predict the native ACL response (Table 25.1). A total of 7 parameters are needed to capture these responses, but unlike the previous models discussed in the Introduction, the current formulation is 3D and additional model parameters are not needed to describe other deformation states.

25.5 Discussion

The conventional methods of strain measurement in soft tissues either record the displacement output from the testing machine itself or add fiduciary markers on the tissue surface as optical displacement trackers. Although gripping systems have become more advanced, tissue slip in the grips is still difficult to avoid. Experiments have shown that ligaments and tendons are highly nonlinear within their physiological range, which is a strain level of less than 0.05. Therefore, the displacements attributed to machine and grip compliances would largely affect the accuracy of mechanical characterization of these tissues. Therefore, we have employed optical strain measurements in our analysis. The ACL has a very complex geometry: the ligament portion consists of multiple fiber bundles twisting together and the insertions to the femur and tibia have irregular footprints. Using a speckle pattern and digital image correlation methods described elsewhere (Ma et al., 2012b), we are able to accurately capture the strain contours of the entire ACL surface. This information is critical for 3D finite element implementation. The full-field deformation

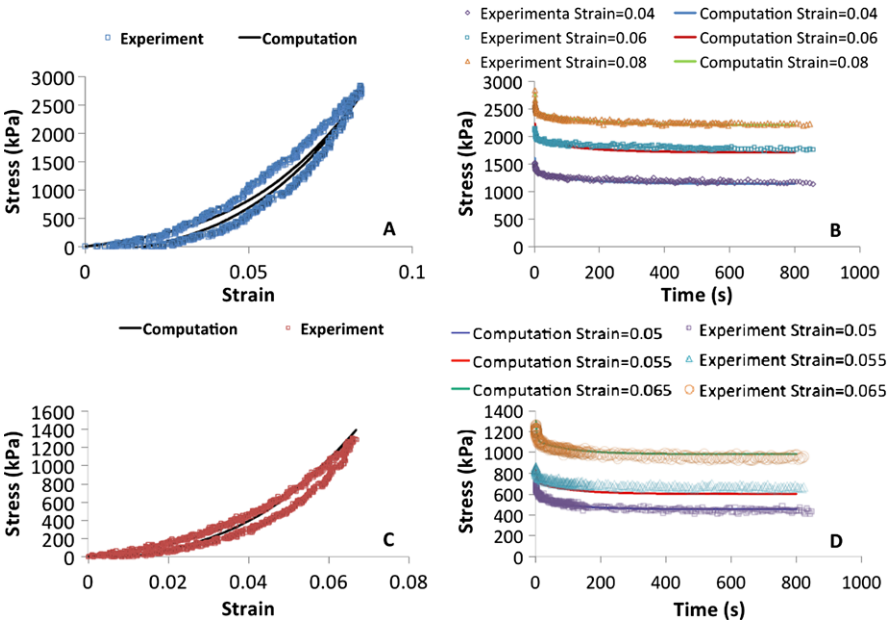

Fig. 25.7 Experimental response of native ACL (**A**) and (**B**) and BLB (**C**) and (**D**), and the computational predictions using the 3D micromechanical viscoelastic model

analysis also serves as an important tool to characterize the ACL graft locally to evaluate if it fully develops to match the biomechanical response of native ACL. The similar functionally graded strain pattern that our tissue engineered BLB has developed indicates its great potential to be used as the ACL graft (Fig. 25.6).

Previously we have developed a three-element viscoelastic model (Ma et al., 2010), for describing ligament and tendon response. This simple model qualitatively captured the nonlinear viscoelastic responses of ligaments and tendons. Experimental data from stress relaxation experiments demonstrate that these soft tissues possess a bi-linear relaxation pattern. This finding is in agreement with the results from collagen related research done by Shen et al. (2011) and Yang et al. (2012). Therefore, we added another linear series spring-dashpot system to the existing model as this two time constant feature fits the data well as seen in Fig. 25.3. The nonlinear strain-dependent viscoelastic responses of ligaments and tendons are captured by the nonlinear MacKintosh network representing the collagen components of the structure.

Our previous study shows the tissue engineered BLB, after 9 months of in vivo recovery, has developed a similar microstructure to that of the native ACL as indicated from longitudinally and sectionally stained tissue samples for both collagen and elastin (Ma et al., 2012b). Vascularization and innervation are also developed in these engineered BLBs and provide nutrition from the host body to further mature the engineered BLBs in vivo. The tangent modulus of the engineered BLB attains 52 % of that of the contralateral ACL. The parameters of our microstructural consti-

Table 25.1 Model parameter comparison between native ACL and engineered BLB

Tissue type	MacKintosh spring			Fast spring	Fast dashpot	Slow spring	Slow dashpot
	$nk\Theta_A$ (kPa)	L_c (–)	l_p (–)	$nk\Theta_B$ (kPa)	η_B (kPa/s)	$nk\Theta_C$ (kPa)	η_C (kPa/s)
Native ACL	5000	12.5	8	5000	1000	8000	280000
Engineered BLB	5000	12.4	8	3500	1000	2000	150000

tutive model are in agreement with the previous biological and mechanical studies. The model parameters used to capture the native ACL and engineered BLB response show the three parameters for the MacKintosh network are indeed very similar, indicating the engineered BLBs have remodeled in vivo and have developed mechanical properties that are very similar to that of the native ACL. The BLB parameters indicate a more compliant response than do those of the ACL, indicating a longer recovery time may be needed for our BLBs to fully develop to native ACLs.

The seven model parameters needed to capture the nonlinear response of these tissues are intended to capture the full 3D response of these tissues, however they assume initial isotropy. The modeling framework does allow for initial anisotropy, as seen in Fig. 25.2, without adding several more parameters. A transversely isotropic ligament or tendon would incur an additional parameter, which is the ratio of the representative volume element dimensions in the direction of the fibers versus perpendicular to them. In ongoing work we intend to implement this model into a commercially available finite element program to simulate the complicated inhomogeneous response of the knee during an anterior tibial translation, the motion that results in ACL failure. We will assess the initial anisotropy requirements needed to capture this response.

25.6 Conclusions

Experimental results show the mechanical response of ligaments and tendons is nonlinear, viscoelastic and functionally graded. Moreover, engineered ligaments used as an ACL replacement rapidly develop in vivo to obtain similar structure and function to native ACL. Our micromechanical computational model of connective tissue has been used to explore the rich mechanical response of native and engineered ligaments from a microstructural point of view and is in agreement with the findings in histological studies.

Acknowledgements We thank MICHR and Coulter Foundation for their generous financial support.

References

Arruda EM, Boyce MC (1993) A three-dimensional constitutive model for the large stretch behavior of rubber elastic materials. J Mech Phys Solids 41:389–412

Bischoff JE, Arruda EM, Grosh K (2000) Finite element modelling of human skin using a nonlinear elastic constitutive model. J Biomech 33:645–652

Bischoff JE, Arruda EM, Grosh K (2001) A new constitutive model for the compressibility of elastomers at finite deformations. Rubber Chem Technol 74:541–559

Bischoff JE, Arruda EM, Grosh K (2002a) Finite element simulations of orthotropic hyperelasticity. Finite Elem Anal Des 38:983–998

Bischoff JE, Arruda EM, Grosh K (2002b) A microstructurally based orthotropic hyperelastic constitutive law. J Appl Mech 69:570–579

Bischoff JE, Arruda EM, Grosh K (2002c) Orthotropic hyperelasticity in terms of an arbitrary molecular chain model. J Appl Mech 69:198–201

Bischoff JE, Arruda EM, Grosh K (2004) A rheological network model for the continuum anisotropic and viscoelastic behavior of soft tissue. Biomech Model Mechanobiol 3:56–65

Boyce MC, Arruda EM (2000) Constitutive models of rubber elasticity: a review. Rubber Chem Technol 73:504–523

Boyce MC, Arruda EM (2001) Swelling and mechanical stretching of elastomeric materials. Math Mech Solids 6:641–659

Butler DL, Guan Y, Kay MD, Cummings JF (1992) Location-dependent variations in the material properties of the anterior cruciate ligament. J Biomech 25:511–518

Corr DT, Strarr MJ, Vanderby RJ, Best TM (2001) A nonlinear generalized maxwell fluid model for viscoelastic materials. J Appl Mech 68:787–790

Danto MI, Woo SL-Y (1993) The mechanical properties of skeletally mature rabbit anterior cruciate ligament and patellar tendon over a range of strain rates. J Orthop Res 11:58–67

Duenwald SE, Vanderby RJ, Lakes RS (2009) Viscoelastic relaxation and recovery of tendon. Ann Biomed Eng 37:1131–1140

Duenwald SE, Vanderby RJ, Lakes RS (2010) Stress relaxation and recovery in tendon and ligament: experiment and modeling. Biorheology 47:1–14

Fan H, Liu H, Wong EJW, Toh SL, Goh JCH (2008) In vivo study of anterior cruciate ligament regeneration using mesenchymal stem cells and silk scaffold. Biomaterials 29:3324–3337

Fung YC (1972) Stress strain history relations of soft tissues in simple elongation. In: Fung YC, Perrone N, Anliker M (eds) Biomechanics: its foundations and objectives. Prentice-Hall, Englewood Cliffs

Goulet F, Rancourt D, Cloutier R, Tremblay P, Belzil AM, Lamontagne J, Bouchard M, Tremblay J, Stevens L, Labrosse J, Langelier E, McKee MD (2004) Torn ACL: a new bioengineered substitute brought from the laboratory to the knee joint. Appl Bionics Biomech 1:115–121

Jackson DW, Grood ES, Goldstein JD, Rosen MA, Kurzweil PR, Cummings JF, Simon TM (1993) A comparison of patellar tendon autograft and allograft used for anterior cruciate ligament reconstruction in the goat model. Am J Sports Med 21:176–185

Ma J, Narayanan H, Garikipati K, Grosh K, Arruda EM (2010) Experimental and computational investigation of viscoelasticity of native and engineered ligament and tendon. In: Garikipati K, Arruda EM (eds) Proceedings of the IUTAM symposium on cellular, molecular and tissue mechanics. Springer, New York, pp 3–17

Ma J, Smietana MJ, Kostrominova TY, Wojtys EM, Larkin LM, Arruda EM (2012a) In vivo study of anterior cruciate ligament regeneration using mesenchymal stem cells and silk scaffold. Tissue Eng Part A 18:103–116

Ma J, Smietana MJ, Swinehart IT, Kostrominova TY, Wellik DM, Wojtys EM, Larkin LM, Arruda EM (2012b) A comparison of tissue engineered scaffold-less bone-ligament-bone constructs and patellar tendon autografts used for anterior cruciate ligament replacement in sheep (submitted)

MacKintosh FC, Käs J, Janmey PA (1995) Elasticity of semiflexible biopolymer networks. Phys Rev Lett 75:4425–4428

Moffat KL, Sun WH, Pena PE, Chahine NO, Doty SB, Ateshian GA, Hung CT, Lu H (2008) Characterization of the structure-function relationship at the ligament-to-bone interface. Proc Natl Acad Sci USA 105:7947–7952

NationalSurvey (2004) National ambulatory medical care survey. Available on the American Association of Orthopaedic Surgeons web page at aaos.org. National Center for Health Statistics

Palmer JS, Boyce MC (2008) Constitutive modeling of the stress-strain behavior of F-actin filament networks. Acta Biomater 4:597–612

Palmer JS, Castro CE, Arslan M, Boyce MC (2010) Constitutive models for the force-extension behavior of biological filaments. In: Garikipati K, Arruda EM (eds) Proceedings of the IUTAM symposium on cellular, molecular and tissue mechanics. Springer, New York, pp 141–159

Pioletti DP, Rakotomanana LR, Benvenuti J-F, Leyvraz P-F (1998) Viscoelastic constitutive law in large deformations: application to human ligaments and tendons. J Biomech 31:753–757

Provenzano P, Lakes RS, Keenan T, Vanderby R (2001) Non-linear ligament viscoelasticity. Ann Biomed Eng 28:908–914

Provenzano PP, Lakes RS, Corr DT, Vanderby R Jr (2002) Application of nonlinear viscoelastic models to describe ligament behavior. Biomech Model Mechanobiol 1:45–57

Roos EM (2005) Joint injury causes knee osteoarthritis in young adults. Curr Opin Rheumatol 17:195–200

Salgado AJ, Coutinho OP, Reis RL (2004) Bone tissue engineering: state of the art and future trends. Macromol Biosci 9:743–765

Shen ZL, Kahn H, Ballarini R, Eppell SJ (2011) Viscoelastic properties of isolated collagen fibrils. Biophys J 100:3008–3015

Sopakayang R, Vita RD, Kwansa A, Freeman JW (2012) Elastic and viscoelastic properties of a type I collagen fiber. J Theor Biol 293:197–205

Tang CY, Ng GY, Wang ZW, Tsui CP, Zhang G (2011) Parameter optimization for the visco-hyperelastic constitutive model of tendon using FEM. Bio-Med Mat Eng 21:9–24

von Lockette PR, Arruda EM (1999a) A network description of the non-Gaussian stress-optic and Raman scattering responses of elastomer networks. Acta Mech 134:81–107

von Lockette PR, Arruda EM (1999b) Topological studies of bimodal networks. Macromolecules 32:1990–1999

von Lockette PR, Arruda EM (2001) Computational annealing of simulated unimodal and bimodal networks. Comput Theor Polymer Sci 11:415–428

von Lockette PR, Arruda EM (2002) Mesoscale modeling of bimodal elastomer networks: constitutive and optical theories and results. Macromolecules 35:7100–7109

Weiss JA, Gardiner JC (2001) Computational modeling of ligament mechanics. Crit Rev Biomed Eng 29:303–371

Wilder FV, Hall BJ, Barrett JP Jr, Lemrow NB (2002) History of acute knee injury and osteoarthritis of the knee: a prospective epidemiological assessment. Osteoarthr Cartil 10:611–616

Yang L, van der Werf KO, Dijkstra PJ, Bennink JFML (2012) Micromechanical analysis of native and cross-linked collagen type I fibrils supports the existence of microfibrils. J Mech Beh Biomed Mat 6:148–158

Chapter 26
Mechanical Characterization of the Human Liver

Marc Hollenstein and Edoardo Mazza

Abstract The aspiration technique was used to characterize the mechanical behavior of the liver. Intra-operative application on human organs aimed at (i) tissue classification towards development of novel diagnostic procedures, and (ii) constitutive modeling of liver tissue. The first goal was achieved using scalar parameters extracted from time histories of aspiration pressure and deformation. Determination of parameters for nonlinear time dependent constitutive model formulations required solving the inverse problem. Glisson's capsule was analyzed separately from parenchyma and was shown to behave as I_2-material. 207 aspiration measurements were performed on 33 patients. The influence of the contact force between the aspiration device and the liver was kept minimal in order to achieve a high reproducibility of the mechanical measurements. Histopathological characterization with biopsies taken at the measurement location allowed analyzing the influence of tissue microstructure. Tumors with high connective tissue content were shown to significantly affect the mechanical response.

26.1 Introduction

Simulation based planning and virtual reality training of minimally invasive hepatic surgery requires realistic constitutive models formulation and corresponding parameters (Schwartz et al., 2005). Recent advances in diagnostic procedures rely on the characterization of hepatic tissue's mechanical response, such as in dynamic magnetic resonance elastography for the detection of liver fibrosis (Huwart et al., 2006; Rouvière et al., 2006). Knowledge of the mechanical behavior of human liver might also contribute to improvements in radiation therapy. In fact, 4D CT or MRI is used for evaluation of organ displacement due to respiratory motion (von Siebenthal et al., 2007) and realistic mechanical models of liver tissue could improve the predictive capabilities of the algorithms used for tumor localization.

M. Hollenstein · E. Mazza (✉)
Institute of Mechanical Systems, ETH Zurich, Zurich, Switzerland
e-mail: emazza@ethz.ch

G.A. Holzapfel, E. Kuhl (eds.), *Computer Models in Biomechanics*,
DOI 10.1007/978-94-007-5464-5_26,

Experimental observations of the mechanical response of hepatic tissue are essential for determining model parameters of phenomenological model equations and are useful for verifying the predictive capabilities of model formulations proposed in the literature. Constitutive equations often aim at describing the *in vivo* mechanical behavior of tissues and organs when subjected to physiological conditions of loading and deformation. Mechanical measurements must be characterized by well defined kinematic and kinetic boundary conditions so to allow the inverse problem to be solved. Many experimental studies were performed to characterize the mechanical behavior of liver tissue, see, e.g., Chui et al. (2007) and Gao et al. (2010). Most of these involved *ex vivo* measurements on animal tissue. Data from *ex vivo* experiments, without physiological blood perfusion, might provide inappropriate results for mechanical modeling of the liver, as analyzed by Kerdok et al. (2006). This motivates the development of experimental techniques for *in vivo* mechanical testing. Account on the state of the art in measuring the deformation behavior of soft biological tissue, in particular liver, is given in Hollenstein (2011). Among the procedures proposed for *in vivo* liver characterization a few works shall be mentioned here: in Brown et al. (2003) an endoscopic grasper is used for experiments on porcine liver. Ottensmeyer (2002) and Samur et al. (2007) present indentation tests on animal organs. Carter et al. (2001) performed first intra-operative *in vivo* experiments on human liver. They used an indentation device and calculated a value of approximately 270 kPa for the linear elastic modulus of human liver. In contrast, dynamic elastography experiments on human liver, Huwart et al. (2006) and Rouvière et al. (2006), indicated that the linear elastic modulus of healthy human liver is in the range of 6 kPa.

In our laboratory, first *in vivo* mechanical experiments on human liver performed during open surgery using the so called 'aspiration device' were reported in Mazza et al. (2007) and Nava et al. (2008). Data from 23 measurements on 6 healthy organs were analyzed in Nava et al. (2008) and a constitutive model for 'average liver tissue' determined. Two main factors affect the corresponding results: (i) the liver was modeled as a homogeneous deformable solid without consideration of the mechanical resistance of the Glisson's capsule (the connective tissue layer that covers the organ); (ii) the initial deformation of the liver tissue, due to the compressive force applied to ensure a good initial contact between aspiration device and liver, was not considered for the inverse problem.

Results from our latest clinical study with aspiration experiments on the liver during open abdominal surgery are presented in this paper. An extensive experimental campaign with measurements on patients undergoing hepatic resection has been recently completed. In total the livers of 33 patients at the age of 38–82 years have been tested *in vivo* at the beginning of the surgical procedure. Measurements were taken on one normal reference site and one or two target sites with lesion leading to a total of 207 realizations of the aspiration experiment during open surgery on the human liver in this study.

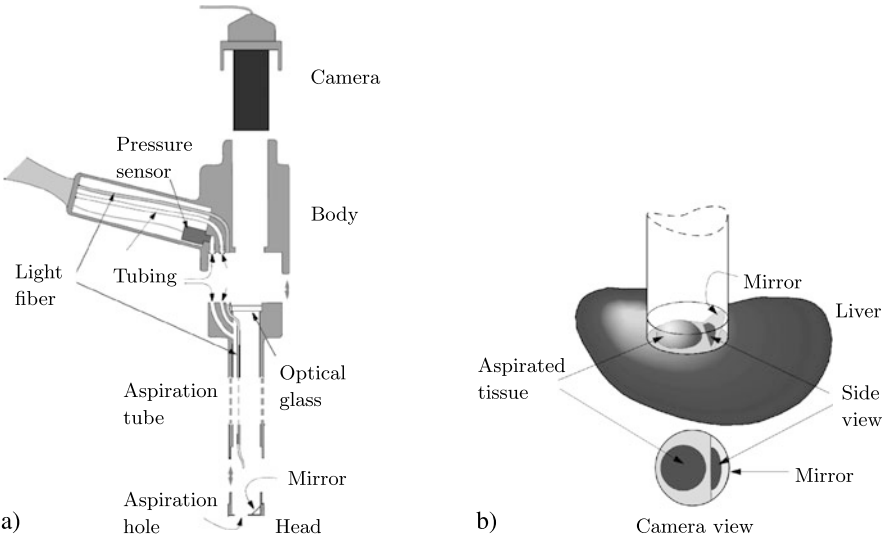

Fig. 26.1 Measuring principle, components, and assembly of the aspiration probe. (**a**) The CCD-camera is non-sterile mounted to the assembled probe through a long sterile bag taped to the rear probe end and sealed from the aspiration tube via an optical glass. (**b**) The tissue is aspirated through a 10 mm hole and the resulting deformation side view profile captured as it is reflected in an optical prism to the camera mounted at the top of the probe

26.2 Methods

This section introduces the experimental methods for intraoperative aspiration measurements, Glisson's capsule characterization, and the corresponding data analysis procedures.[1] The procedure for intra-operative measurements on humans must be non-traumatic, operate under sterile conditions and comply with the time- and space-limitations in the operating room, while at the same time allowing to maintain control over the mechanical boundary conditions and the protocol applied in the test.

26.2.1 Aspiration Device

The working principle of the aspiration device is illustrated in Fig. 26.1. The procedure is based upon the so called 'pipette aspiration' technique. The instrument consists of a tube closed on one extremity by a disk containing the circular opening (diameter: 10 mm) for tissue aspiration. The internal pressure in the tube can

[1]The work described here constitutes the main contribution of the PhD Thesis of the first author, see Hollenstein (2011). For this reason, text passages, figures, and tables from Hollenstein (2011) are used in this article.

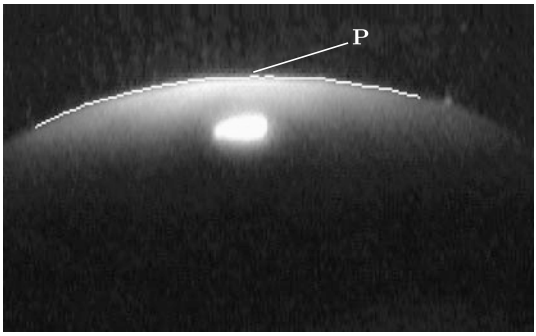

Fig. 26.2 Side view of a human liver as captured by the CCD-camera of the aspiration probe; the extracted contour is indicated as white line with the apex defined as point with the maximum deflection along the contour, denoted '*P*' on the picture

be controlled according to a prescribed time history. The experiment is performed by establishing thorough contact between the probe head and the tissue, and creating a time-variable vacuum in the aspiration tube such that the tissue is sucked in through the aspiration hole. A sufficiently smooth surface region of the organ of about 30 mm diameter is required to enable proper contact. During a typical experiment on human liver, a maximum suction pressure of 200 mbar is applied such that the displacement of the tissue apex is in the order of 3 mm (point P, Figs. 26.2 and 26.3). Nominal strains up to 30 % are induced into the involved tissue portion. Tissue from the surface down to about 10–15 mm is considered to contribute to the observed response, i.e. represents the characterized tissue volume. A monochrome CCD-camera at the top of the body captures the full side view profile of the deforming tissue mirrored in a prism installed in the probe head. A cold light source is used to illuminate the tissue surface by dint of an optical fiber. A pressure sensor is installed in the handle of the device. The silicone pressure conduit, the optical fibers and electronic cables for the pressure sensor are maintained and sealed in a standard medical cable tube suitable for sterilization. Pressure data and images are recorded at 25 Hz. The assembled probe weighs approximately 0.5 kg. The probe is designed such that it can be completely disassembled for cleaning and ethylene oxide (EO) gas sterilization. The pneumatic system is composed of a diaphragm pump, an air reservoir, two pressure sensors, and two three-way isolation valves. The pressure sensors, the valves, the pump, and the CCD-camera are linked to a computer for controlling and data acquisition by means of a custom-written LabView program. The pictures are processed off-line with Matlab to extract the contour of the side view of the aspirated tissue. Time histories of measured pressure and deformation profiles are the input data for further analysis. Further technical details and descriptions of all components are reported in Hollenstein (2011).

26.2.1.1 Inverse Analysis

The time histories of applied negative pressure and resulting tissue deformation profiles are used to determine parameters describing the mechanical behavior of the tissue. One possible evaluation method is based on the iterative comparison between predicted and measured tissue response, i.e. on the solution of the so called

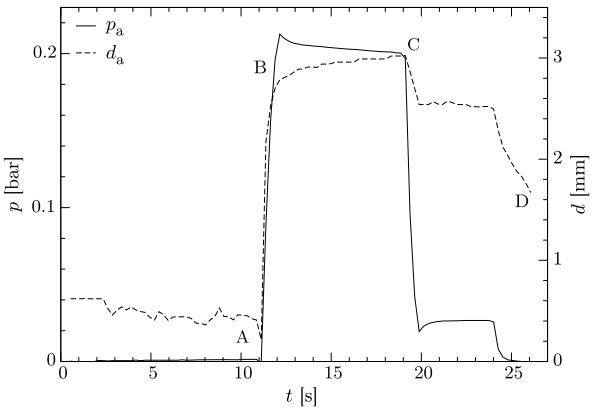

Fig. 26.3 Typical pressure profile applied on human liver and corresponding tissue response as the displacement history of the apex point 'P', see Fig. 26.2

'inverse problem'. This approach uses the finite element method to simulate the experimental procedure and aims at determining constitutive model parameters of the soft tissues involved. The commercial FE-software Abaqus was applied here. An axisymmetric model incorporating parenchyma and capsule as separate tissues is used. Both tissues are assumed to be isotropic, homogeneous, incompressible, and initially unstressed. Previous studies (Nava, 2007; Mazza et al., 2008; Hollenstein et al., 2009), identified the influence of probe geometry, contact conditions and friction, size of the modeled tissue portion, applied boundary conditions, and preload in terms of the initial contact force applied prior to test onset; the latter leads to probe indentation. A Matlab script was written to generate structured meshes with a high refinement level in the contact region and near the aspirated surface. Several transition regions were included to coarsen the mesh towards the bottom and lateral boundary. The capsule was represented with linear membrane elements (MAX1) with their nodes (slave) tied and prescribed to follow the nodes of the underlying quadrilateral elements (master). The aspiration probe was modeled as analytic rigid surface fully clamped at the reference point. The contact between aspirator and tissue was left frictionless, which is not only consistent with previous findings (Nava, 2007; Hollenstein et al., 2009), but is as well physically plausible as the capsule during the intraoperative measurements was moisturized with saline and thus was wet and slippery. The reduced polynomial strain energy potential form and quasi-linear viscoelasticity were used to describe the parenchyma. The capsule was represented hyperelastic using the Rubin-Bodner strain energy potential (Rubin and Bodner, 2002), with parameters determined, as described in Sect. 26.2.2. This model formulation was shown to suitably represent tissue response in equibiaxial stress state.

26.2.1.2 Scalar Parameters

An alternative approach providing an immediate evaluation of the measured response is based on scalar parameters extracted directly from the pressure and apex

point (P, Fig. 26.2) displacement histories. The course of the apex displacement exhibits characteristic points, A–D, see Fig. 26.3. The displacement history can thus be characterized by relative displacement measures, such as $d_0 := d_B - d_A$, $d_1 := d_C - d_A$, $d_2 := d_C - d_B$, $d_3 := d_D - d_A$. The ratio between the maximum aspiration pressure P_{max} and the induced apex-displacement defines a measure for the instantaneous stiffness. The ratio between d_2 and d_0 might be used to quantify the degree of 'creep' in the tissue. A few scalar parameters related to the time and history dependent mechanical behavior of soft biological tissue were analyzed in previous studies, see, e.g., Bauer et al. (2009). The parameter $\eta = P_{max}/d_0$ will be reported for the intraoperative liver measurements in this paper.

26.2.1.3 Patient Election and Ethical Aspects

Intraoperative aspiration measurements on human livers were conducted under given approval of the Swiss ethics commission and informed consent by the patient (SPUK Chirg/Anäst/Patho USZ, Stv-Nr.: 007-2004). Elective were patients of 18 years or older planned for routine hepatectomy with primary or secondary liver tumors, and benign tumors.

26.2.2 Characterization of Glisson's Capsule

Characterization of the liver capsule aimed mainly at quantifying its influence on the analysis of the aspiration experiment. In fact, the aspiration measurement does not provide sufficient information for characterizing both, capsule and parenchyma. An average capsule model based on uniaxial and biaxial experiments on liver capsule was implemented in the inverse finite element model described in Sect. 26.2.1.1. The present section briefly introduces the methods applied for experimental characterization of Glisson's capsule. The long-term response of 69 bovine and 8 human liver capsule samples has been recorded in uniaxial tension, and of 18 bovine samples in biaxial inflation experiments. One healthy human liver could be obtained postmortem from an 80-year-old subject for mechanical tests from the Institute of Surgical Pathology, University Hospital Zurich. The decedent gave informed consent for the autopsy. Mechanical tests were complemented with a morphological and biochemical characterization (Hollenstein, 2011). The human and the bovine liver capsule turned out to scale with a factor of about 3 in terms of membrane stiffness, thickness, collagen content, and the diameter of the collagen fibers, whereas their general microstructure was found very similar. The bovine equibiaxial stress characteristic, as obtained from the inflation test, were thus used to estimate the homeostatic point, to calibrate the Rubin-Bodner model (Rubin and Bodner, 2002), and to scale the corresponding parameters for inclusion in the finite element analysis of the aspiration experiment on the human liver.

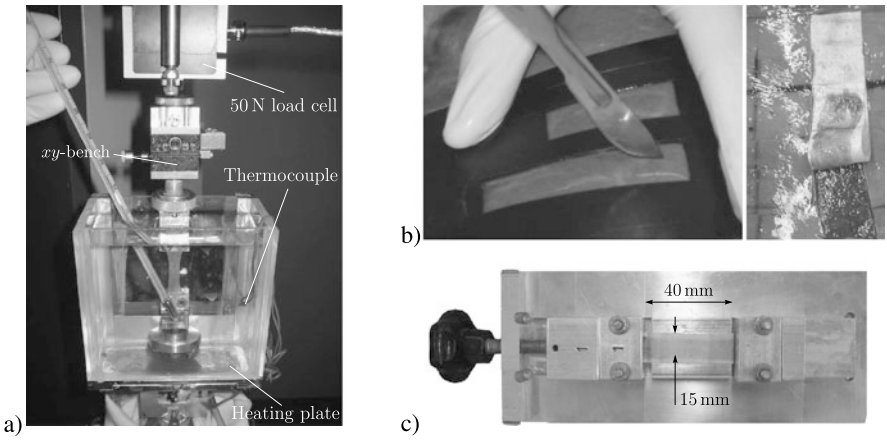

Fig. 26.4 Experimental setup and sample preparation for uniaxial tensile testing. (**a**) Situation on the uniaxial testing machine: the installed sample inside the bio-chamber, the clamping interfaces, the xy-positioning stage, and the load cell are visible. (**b**) Excision of the capsule samples from the parenchyma using a scalpel and a plastic template. On the *right*, a sample with paper backing is shown on the site of extraction. The underlying parenchyma is visible. (**c**) The custom-made assembling jig for precise and gentle alignment and mounting of the samples on the clamps

26.2.2.1 Uniaxial Tests

The liver capsule samples were tested in a Zwick 1456 universal materials testing machine. The axial force was measured with a 50 N load cell. A custom-made biochamber was used to simulate physiological conditions. During testing, the samples remained entirely immersed in the saline with its temperature controlled to 37.0 °C. A two-axis linear positioning stage was installed on the load cell to precisely align the sample with the tensile axis of the machine in order to prevent shearing. The test setup is shown in Fig. 26.4. Samples were delicately excised using a surgical scalpel and a thin plastic sheet template. The samples were approximately 15 mm in width and 60 mm in length. The sample thickness was assumed equal within the same sample and was assessed by averaging three measurements taken at random locations using a micrometer caliper. The time between sample preparation and mechanical test never exceeded 1 h.

A preload of 0.065 N was applied at the beginning of the tests; note that the choice of the preload has significant influence on the definition of the reference configuration and thus on the strain calculation. Tests were carried out under displacement-controlled conditions with an elongation rate of 0.5 %/s nominal strain. In order to obtain a preconditioned state of the tissue samples, the samples underwent 10 cycles of loading and unloading between 0 and 15 % nominal strain prior to ultimate loading until tissue rupture. Given the sample width of $w = 15$ mm, the displacement of the cross bar, the free gauge length at preload, and the exerted tensile force, the nominal strain and the nominal membrane tension in uniaxial tension were computed.

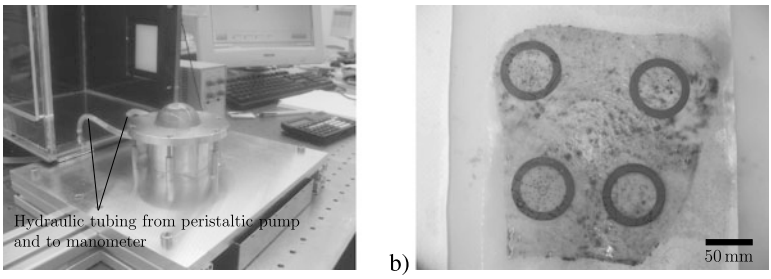

Fig. 26.5 (**a**) Inflation cylinder with cover ring bolted down with 6 screws. An inflated soft polymer is visible. (**b**) Part of a liberated bovine liver capsule with the sandpaper rings attached

26.2.2.2 Inflation Tests

Inflation experiments allow to easily investigate the response of membranous tissue to a biaxial loading. The circular sample is placed over a hollow cylinder filled with saline solution and clamped using a rigid ring. Increased liquid pressure leads to membrane inflation and the side view profile of the deforming sample is measured with a video extensometer. The theoretical framework for data analysis is more involved than that for the classic material tests such as uniaxial or in-plane biaxial tests. In fact, the induced state of stress and strain is inhomogeneous, with equibiaxial stress state at the center of the testpiece and a configuration of pure shear at the clamping interface. For isotropic material behavior, the problem becomes truly axisymmetric. The effective strain and stress fields must be computed using FE-simulations postulating a particular constitutive behavior, or they must be estimated from analytic approximations (Hollenstein, 2011).

The setup is depicted in Fig. 26.5. It consists of the inflation-cylinder, which is connected by sidewise bores to an external pressure sensor and a peristaltic pump, a mounting rail for the extensometer CCD-camera, an LCD-backlight to enhance the image contrast, a control box that contained the peristaltic pump and all the electronic measuring equipment, and a control-PC. The inflation-cylinder was made of aluminum with an inner diameter of 50 mm, an outer diameter of 60 mm. A cover ring of 1 mm thickness with an inner diameter of 50 mm and an outer diameter of 60 mm, and with a chamfer radius at its inner perimeter of 0.5 mm was used to clamp the samples to the cylinder by dint of 6 screws. Physiological saline solution was used to inflate the liver capsule samples to rupture at room temperature without preconditioning. For the tests on the liver capsule, the final experimental data included the pressure course inside the inflation cylinder and the displacement history of the apex of the inflated specimen, i.e. the maximal vertical displacement progression of the specimen. More details about the setup can be found in Egger (2008) and Hollenstein (2011). Sandpaper rings were used to improve the effectiveness of the clamping. They were prepared with inner and outer diameters of 50 mm and 70 mm, respectively. A commercial cyanoacrylate based glue was applied on the outer margin of the smooth surface of these precut sandpaper rings. The sandpaper rings with the glue were then gently applied onto capsule regions devoid of any

visible defects. In this way, the underside of the capsule was prepared according to the desired number of samples (Fig. 26.5b). Subsequently, the capsule was turned to its other side and sandpaper rings were glued onto the upside opposing the rings on the underside. This procedure resulted in capsule samples sandwiched between two sandpaper rings with their rough side facing away from the capsule. Finally, the sandwiched samples were cut out with surgical scissors along the outer margin of the sandpaper rings.

26.3 Results

A representative constitutive model for Glisson's capsule is required in order to analyze the aspiration experiments on human liver. Correspondingly, the mechanical characterization of liver capsule is presented first, Sect. 26.3.1. The capsule model is then used in the analysis of the sensitivity of the aspiration experiment described in Sect. 26.3.2. Next we present results from more than 200 measurements during open surgery.

26.3.1 Mechanical Behavior of Glisson's Capsule

Uniaxial test results provided qualitatively similar results for human and bovine samples. The characteristics of all stress-strain curves are consistent with the typical J-shaped behavior of soft tissues. They exhibit large scatter in the initial stiffness and in the toe- and heel-part of the curves. This scatter can be considerably reduced by increasing the reference preload. In contrast, the stiffness in the part of the curves at larger strains is fairly consistent. The high-strain tangent stiffness in uniaxial stress was evaluated with reference to the free gauge length at 0.2 N preload, see Fig. 26.6. The uniaxial mechanical data indicate that human capsule is about a factor of 3 more compliant as compared to bovine tissue. Corresponding microstructural analysis (Hollenstein, 2011) yield a similar factor for the thickness of these membranes, as well as for the collagen content, or the diameter of collagen fibers bundles. The human tissue available was not sufficient in quantity for performing corresponding inflation experiments. The observations from inflation tests on bovine tissue were used as a basis for determination of a human capsule model, scaled with the factor of 3.

A typical uniaxial and a typical equibiaxial tension-strain characteristic, as derived from the uniaxial tension and the inflation test, are compared in Fig. 26.7. To this end, the equibiaxial characteristic was adjusted for the preload of the inflation test to be consistent with the uniaxial tensile test in terms of pretension. The respective high strain slopes show that liver capsule is 2–3 times stiffer in an equibiaxial than in an uniaxial state of stress; note that the uniaxial characteristic, in contrast to the equibiaxial characteristic, is based on a preconditioned sample. Analytical

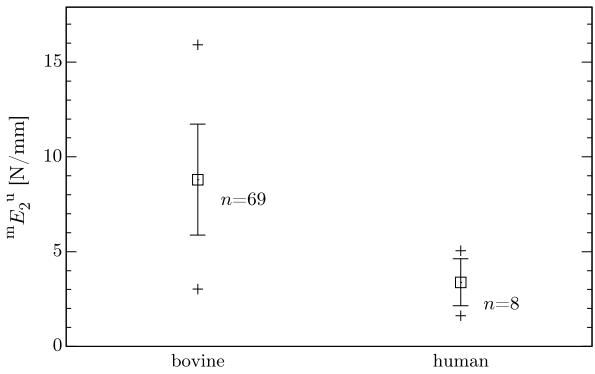

Fig. 26.6 Uniaxial high strain membrane tangent modulus $^{m}E_2^{u}$ for bovine and human samples

and FE based analysis of the inflation data enabled determining constitutive model equations for the long term response of liver capsule. As shown in Fig. 26.7, both types of loading, uniaxial and equibiaxial stress, can only be reproduced simultaneously by a 2nd order polynomial form of the strain energy potential in the strain invariant I_2.

Based on average biaxial data, a calibrated and physiologically representative constitutive model was determined in order to include the capsule as an individual structure in computer simulations, Sect. 26.2.1.1. To this end, the elastic and isotropic part of Rubin-Bodner model (Rubin and Bodner, 2002) was considered for describing the equibiaxial characteristic of bovine liver capsule. The reference configuration in the inflation experiment however is different from the *in vivo* reference state, i.e. before performing the aspiration experiment. In fact, the capsule is subjected to internal pressure. The intra-hepatic blood pressure averages up to about 50–60 mmHg, i.e. 6.7–8.0 kPa. Assuming that the parenchyma is non-load-bearing and the liver has a characteristic diameter of 17.5 cm, a guess for the physiological true tension in the liver capsule at equilibrium yields 0.64 N/mm. The associated biaxial strain is about 7 %. By means of the multiplicative nature of the stretch, the 'typical' equibiaxial tension-strain characteristic was shifted to this point and the Rubin-Bodner model calibrated with respect to this new reference curve. To adjust the model for the human capsule, the finding that the human capsule is about three times thinner and softer than the bovine capsule was implied, i.e. they 'scale' with a factor of 3, and thus the Rubin-Bodner parameter μ_0 was corrected accordingly, see Table 26.1.

26.3.2 Finite Element Analysis of the Aspiration Experiment

The FE-model introduced in Sect. 26.2.1.1 was used to analyze the determination of constitutive model parameters of liver capsule and parenchyma from the inverse analysis of aspiration measurements. The Rubin-Bodner formulation was

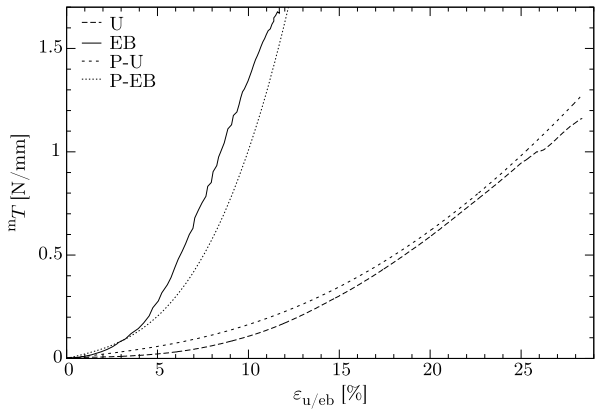

Fig. 26.7 Comparison of the uniaxial and the equibiaxial membrane tension response of bovine liver capsule based on typical nominal tension-strain characteristics; the equibiaxial characteristic is based on the analytic solution of the inflation test. Indicated by *dashed lines* is the combined fit of the 2nd order polynomial strain energy form with C_{10}, C_{20}, C_{11} set to zero, and $C_{01} = 0.320$ N/mm and $C_{02} = 2.964$ N/mm. *U*: uniaxial stress, *EB*: equibiaxial stress, *P-U*: response in uniaxial stress of the 2nd order polynomial form, *P-EB*: response in equibiaxial stress of the 2nd order polynomial form

used for liver capsule and a quasi-linear viscoelastic model for the parenchyma, see Table 26.1. The parameter values are consistent with typical observations from aspiration experiments on healthy human liver tissue. The capsule was shown to be about 3-times more significant for the local response of the organ to aspiration as compared to parenchyma. Furthermore, when investigating the impact of the capsule properties on the apex-displacement by varying the initial shear moduli of capsule by ± 25 %, changes of ± 10 % of the reference apex-displacement were observed. For corresponding changes in the parenchyma properties variations were in the range of less than 1 %. Note however that all constitutive parameters are well-determined for the chosen low-order constitutive models.

The effects of a tumor or diffuse cirrhosis were estimated by assigning considerably stiffer constitutive behavior to particular subregions of the FE-model. Tumoral tissue was assumed as very stiff nodules and modeled three-orders of magnitude stiffer than the peripheral parenchymal tissue. In contrast, diffuse fibrosis was included 10-times stiffer as the peripheral tissue, in accordance with the findings in Sandrin et al. (2003). Tumors were modeled as cylindrical disks of 15 mm radius and 5 mm height just underneath the aspirator embedded at different depths. Similarly, diffuse cirrhosis was assigned to subregions of 15 mm radius and spread between varying depths. This analysis showed that aspiration measurements are only marginally affected in case of lesions starting at a depth of more than 5 mm from the surface.

Table 26.1 Condensation for the parameter setup of constitutive models for parenchyma and capsule as used for the FE-analysis of the aspiration test. The tissues were modeled fully incompressible. RP: reduced polynomial, QLV: quasi-linear viscoelasticity in terms of Prony-series, RB: Rubin-Bodner. Note that the capsule model is expressed in terms of membrane properties

	RP		QLV				RB	
	C_{10}^{∞} (kPa)	C_{20}^{∞} (kPa)	g_1 (–)	τ_1 (s)	g_2 (–)	τ_2 (s)	${}^{m}\mu_0$ (N/mm)	q (–)
Parenchyma	0.7	4.5	0.49	1.9	0.19	6.5		
Capsule							4.81	0.052

26.3.3 Open Surgery Measurements

Aspiration measurements were performed on the fully perfused organ after opening of the abdomen and mobilization of the liver for resection. Typically the whole measurement procedure did not exceed 5 min. The measuring sites were defined on the part of the organ to be resected, which then was available for biopsy acquisition. First, the aspiration measurement was realized 3-times on normal tissue for reference. Subsequently, the measurement was repeated 3-times on the lesion. The tissue was not preconditioned. The aspiration cycle was set for a step decrease to a target suction pressure of 200 mbar with a hold time of 9 s. One measuring cycle took about 30 s. The measurement procedure was established based on initial trials, as follows: the probe head is kept perpendicular and just in contact with the organ surface, keeping the downforce as small as possible, while the surgeon visually tracks the motion of the organ due to the artificial respiration of the patient; once a stable situation has been accomplished, the operator initiates the measurement; the surgeon tracks the motion of the liver keeping the probe in a constant relative position to avoid changes in the contact conditions and dependence of the measurement on the far-field boundary conditions; at the end of each measuring cycle, the surgeon carefully retracts the probe and visually checks the measurement site.

The repeatability of the measurements was assessed based on the stiffness parameter (Sect. 26.2.1.2). The coefficient of variation was calculated as the standard deviation of normalized with respect to the measuring site mean value. The coefficient of variation for the present data resulted in 3.9 % for the reference sites, 4.8 % for the lesion sites, and 4.2 % overall. Considering previous data (Mazza et al., 2007; Nava et al., 2008), with typical values of the coefficient of variation in the range of 20 %, a fivefold increase in repeatability was achieved. Most probably these improvements are due to the minimization and better control of the contact force, and are due to the fact that always the same surgeon performed the measurements.

Figure 26.8(a) reports all measured stiffness values for normal tissue and lesion with the corresponding connective tissue content as measured by histo-pathological analysis (Hollenstein, 2011). Although a weak separation between lesion (higher values) and normal tissue can be observed, no significant correlation could be found between stiffness value and connective tissue content. More interesting findings can be worked out when considering the relative difference between the ‘reference’ site

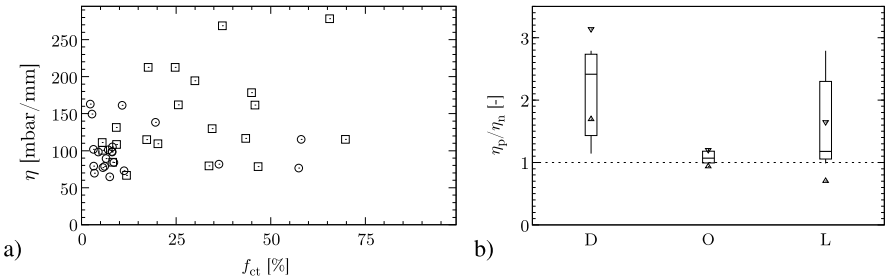

Fig. 26.8 (**a**) Stiffness η vs connective tissue content f_{ct} *circles* and *squares* indicate the reference and the target measuring sites, respectively. (**b**) Box plots of the relative differences in the stiffness parameter η_p/η_n divided into the categories 'desmoplasia' ('D'), 'other' ('O'), and 'lesion' ('L'); 'n' stands for the reference measuring site and 'p' for the target measuring site. The relative increase in the stiffness parameter is significant and 100 % sensitive for the category 'desmoplasia'

and the 'target' site. Figure 26.8(b) shows the box plots for the relative increase in η with separated evaluation of lesion type 'desmoplasia', 'other', and all 'lesion'. On the current database, it was possible to reach 100 % sensitivity with η for detection of 'desmoplasia'; the confidence interval is large, but it is still highly significant, the median indicating at 2.4-fold increase in the stiffness parameter. For the selected threshold value the corresponding specificity is 63 %.

The acquired aspiration data enabled the calibration of constitutive models, based on the FE-model and the inverse analysis procedure. The results obtained for average observations from measurements on normal tissue were reported in Sect. 26.3.2, assuming a given model for liver capsule.

26.4 Discussion

26.4.1 Protocol for Open Surgery Measurements

A significant improvement was achieved in the repeatability of intraoperative aspiration experiments in the present study. In all previous applications the aspiration test was performed as combination of indentation and aspiration without measurement of the contact force, where the former led to unknown contact and far-field boundary conditions. This is considered as the main reason for the pronounced scatter in the measuring data of previous studies (Nava, 2007). The new measuring protocol minimizes the contact force between probe head and organ, with the surgeon following as much as possible the motion of the liver during the measurement. This provided better-defined and hence more repeatable kinetic and kinematic initial and boundary conditions. It was possible to reduce the systematic error by a factor of 5 to a coefficient of variation of about 5 %. One other reason for better reproducibility was the fact that always the same surgeon trained to operate the aspiration device performed the measurements. This is good accuracy for intraoperative measurements,

which drastically improved the data quality and makes possible to repeat an identical experiment between different measuring sites and subjects. Actually, the possibility to conduct locally-confined measurements independent of the far-field is a key strength of the aspiration test. Unknown initial and boundary conditions is one of the major issues with other invasive measurement techniques: for the analysis of large indentation, for example, knowledge not only of the contact condition and the indentation-depth (near-field) are required, but similarly the organ geometry and its embedding in the abdomen (far-field) are relevant, but these latter are typically not available. For comparison, the coefficients of variation of data reported in the literature for the liver are as follows: for indentation Zheng et al. (2000), Tay et al. (2006) and Samur et al. (2007) show data with coefficients of variation of 15 %, 20 %, and 29 %, while as to dynamic elastography Sandrin et al. (2003), Huwart et al. (2006), and Rouvière et al. (2006) have coefficients of variation of 3.2 % (intra-operator cv), 10.3 %, and 5.6 % (on a tissue phantom), respectively.

26.4.2 Mechanical Behavior of Glisson's Capsule

Conventional uniaxial tensile tests with simple inflation experiments were combined to provide information on the multiaxial mechanical behavior of liver capsule. The inflation test complements well the uniaxial tension test in that, for a homogeneous and isotropic membrane, it subjects the membrane to different modes of distortion from 'uniaxial strain' at the clamping interface to 'equibiaxial strain' at the sample apex over a large strain range; these modes are all of high stress-biaxiality and typical for physiologically relevant deformations of biological membranes. Thus uniaxial tension and inflation test together characterize tissues response over a wide region of the strain space.

Besides the physiologically relevant loading, advantages of the inflation test are the easy sample preparation and test realization, and the well-defined boundary and initial conditions. However, the test is restricted in the control of the test kinematics and kinetics, the applicable nominal strain rate does usually not exceed 10 %/s, the tension and strain values are typically derived from less-precise video extensometer data and the total measurement of the distension pressure. Furthermore, sample inhomogeneities, irregular deformations, and surface imperfections influence the interpretation of the test.

Uniaxial and biaxial data were analyzed in order to determine corresponding constitutive model equations able to describe both experiments. Good predictions are obtained when the model formulation is based on the second invariant I_2 of the right Cauchy-Green tensor. As illustrated in Fig. 26.9, the invariant I_1 can be interpreted as the average (squared) stretch of the sides of an infinitesimal volume element. For an incompressible material I_2 is proportional to the average area stretch of the faces of an infinitesimal volume element. It is thus interesting to note that Glisson's capsule behaves as a I_2 material. This might be associated with a network arrangement of collagen fibers in the capsule, leading to a response closer to the one

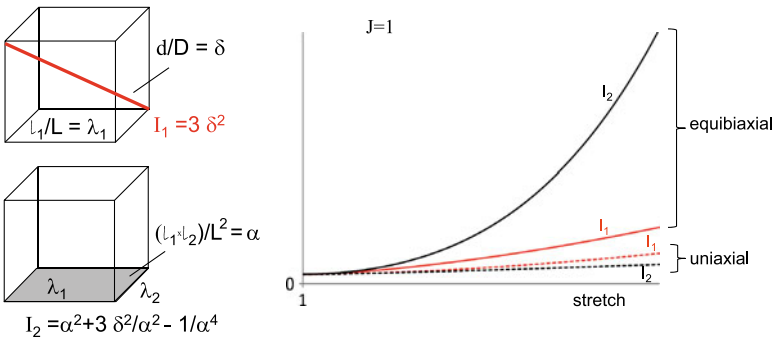

Fig. 26.9 Illustration of the interpretation of the invariants I_1 and I_2 of the *right* (*left*) Cauchy-Green tensor as related to change in length or surface area of an infinitesimal volume element

of a textile with much higher resistance to area stretch in the plane of the membrane than to elongations in uniaxial stress state. Similar observations were reported from the multiaxial characterization of fetal membranes (Bürzle et al., 2012), indicating that this behavior might be common to several biological membranes.

Attention was given to the definition of the reference configuration in both, the mechanical test set-up and the *in vivo* physiological reference state. The influence of setting a threshold membrane tension value for the analysis of uniaxial and biaxial data was demonstrated. Liver capsule, as many other biological membranes, is subjected to a preload due to the homeostatic pressure at their reference physiological state. Thus, a mechanical model describing the response of the capsule in the vicinity of that reference state might be defined with respect to a preloaded configuration, i.e. the state corresponding to the *in vivo* membrane tension. This approach was adopted here for determining a constitutive model of Glisson's capsule. It is interesting to note that the scatter of the experimental results is drastically reduced in case the physiological membrane tension is taken as threshold force value.

26.4.3 Diagnostic Relevance of Aspiration Measurements

As demonstrated with corresponding finite element investigations, the aspiration technique cannot detect moderate changes in consistency of parenchyma, mainly due to the shielding effect of the capsule. However at least for dense lesions with a high connective tissue content, which are larger than the aspiration hole and not located deeper than 15 mm, a trend to a stiffer response was observed. The reduced sensitivity of the technique motivated the analysis in terms of relative stiffness, i.e. to assess the base properties of normal parenchyma, such as a stiffness-level, and then to assess the suspected lesion site relative to its peripheral parenchyma characterized from the reference measurement. This strategy leads to a real significant result: lesions with a high connective tissue content, a larger diameter than the aspiration hole, and not located deeper than 15 mm beneath the capsule lead to a detectable

increase in the stiffness parameter relative to the peripheral parenchyma. For the current database, the median increase is 2.4-fold, where the lower significance bound is located at 1.7.

The absolute values of the aspiration parameters and corresponding elastic moduli derived from the aspiration data, 'normal', 'desmoplasia', and 'connective tissue', are in good agreement with literature data and agree with the finding from elastography (Sandrin et al., 2003). It is interesting to note that the diagnostic performance of tissue aspiration and digital palpation were similar (Hollenstein, 2011). Both reached 100 % empirical sensitivity for desmoplastic lesions at specificities of 63 % and 85 %, respectively. Other cases are not likely to be detected with both techniques. Observe that aspiration is probably more limited to superficial lesions, where palpation might as well detect deeper lesions. Also it should be noted that digital palpation was non-blinded and always conducted by the same surgeon, which might have biased the outcome.

26.4.4 Mechanical Behavior of Human Livers

The solution of the inverse problem enabled determining model parameters for capsule and parenchyma which are considered as representative of the behavior observed in aspiration experiments on normal liver tissue. From the FE-analysis of the aspiration experiment and despite the shielding-effect of the capsule, it was surprising to learn that for the proposed macrostructural two-layer model of the liver, the constitutive parameters for both, the capsule and the parenchyma, are well-determined for the implied Rubin-Bodner and 2nd order reduced polynomial form, respectively. This was quantitatively evaluated in Hollenstein (2011). The degree of determination will rapidly decrease for higher-order models, especially regarding the parenchyma. The inverse FE-analysis based solely on the apex-displacement in the objective function cannot possess a unique solution: for instance, the optimization kernel could drive the elasticity of the parenchyma down to zero and adjust the capsule properties to capture the measured course of the apex-displacement by itself. Thus it takes a good initial guess for the parameters in order to find a meaningful local solution to the optimization problem.

26.5 Conclusions

The present study improved with respect to existing models of liver tissue in that (i) parenchyma and capsule were separately modeled, (ii) a wide range mechanical characterization of liver capsule was provided, (iii) data were used from intra-operative *in vivo* mechanical measurements.

The aspiration technique was applied in an extensive clinical study with over 200 measurements during open abdominal surgery. All procedures related to this experiment were optimized leading to an excellent repeatability of the intra-operative measurements.

Inverse analysis of the aspiration measurements enabled defining a representative liver model including Glisson's capsule and parenchyma. The results of this work can also be used as a relevant benchmark for simulation of the mechanical behavior of human liver.

The cases in which aspiration data can provide diagnostic information were identified. The aspiration technique was shown to yield to a sensitivity similar to the one of (un-blinded) digital palpation by an experienced surgeon.

As a note, by now the aspiration technique has been further developed for application during laparoscopy. Technical details for this novel setup and first results from corresponding *in vivo* measurements are found in Hollenstein et al. (2011).

Acknowledgements We thank Dr. S. Breitenstein, University Hospital Zurich, for performing the intraoperative measurements with the aspiration device. This work was partly supported by the CO-ME/NCCR research network of the Swiss National Science Foundation.

References

Bauer M, Mazza E, Jabareen M, Sultan L, Bajka M, Lang U, Zimmermann R, Holzapfel GA (2009) Assessment of the in vivo biomechanical properties of the human uterine cervix in pregnancy using the aspiration test: a feasibility study. Eur J Obstet Gynecol Reprod Biol 144:S77–S81

Brown JD, Rosen J, Kim YS, Chang L, Sinananand M, Hannaford B (2003) In-vivo and in-situ compressive properties of porcine abdominal soft tissues. In: Westwood JD, Hoffman HM, Mogel GT, Phillips R, Robb RA, Stredney D (eds) Medicine meets virtual reality 11. Studies in health technology and informatics, vol 94. IOS Press, Amsterdam, pp 26–32

Bürzle W, Haller C, Ehrbar M, Mazza E (2012) Experimental investigations of fetal membrane mechanics. In: Holzapfel GA (ed) CD-ROM proceedings of the European solid mechanics conference 2012, Graz, Austria

Carter FJ, Frank TG, Davies PJ, McLean D, Cuschieri A (2001) Measurement and modelling of the compliance of human and porcine organs. Med Image Anal 5:231–236

Chui C, Kobayashi E, Chen X, Hisada T, Sakuma I (2007) Transversely isotropic properties of porcine liver tissue: experiments and constitutive modelling. Med Biol Eng Comput 45:99–106

Egger J (2008) An inflation device for testing human fetal membranes. Master's Thesis, ETH, Zurich

Gao Z, Lister K, Desai JP (2010) Constitutive modeling of liver tissue: experiment and theory. Ann Biomed Eng 38:505–516

Hollenstein M (2011) PhD Thesis, No. 19587, ETH, Zurich

Hollenstein M, Jabareen M, Breitenstein S, Riener M-O, Clavien P-A, Bajka M, Mazza E (2009) Intraoperative mechanical characterization of human liver. Proc Appl Math Mech 9:83–86

Hollenstein M, Bugnard G, Joos R, Kropf S, Villiger P, Mazza E (2011) Towards laparoscopic tissue aspiration. Med Image Anal (submitted)

Huwart L, Peeters F, Sinkus R, Annet L, Salameh N, ter Beek LC, Horsmans Y, Van Beers BE (2006) Liver fibrosis: non-invasive assessment with MR elastography. NMR Biomed 19:173–179

Kerdok A, Ottensmeyer M, Howe R (2006) Effects of perfusion on the viscoelastic characteristics of liver. J Biomech 39:2221–2231

Mazza E, Nava A, Hahnloser D, Jochum W, Bajka M (2007) The mechanical response of human liver and its relation to histology: an in vivo study. Med Image Anal 11:663–672

Mazza E, Grau P, Hollenstein M, Bajka M (2008) Constitutive modeling of human liver based on in vivo measurements. Med Image Comput Comput Assist Interv 11:726–733

Nava A (2007) In vivo characterization of the mechanical response of soft human tissue. ETH Zurich Diss., 17060

Nava A, Mazza E, Furrer M, Villiger P, Reinhart WH (2008) In vivo mechanical characterization of human liver. Med Image Anal 12:203–216

Ottensmeyer MP (2002) TeMPeST I-D: an instrument for measuring solid organ soft tissue properties. Exp Tech 26:48–50

Rouvière O, Yin M, Dresner MA, Rossman PJ, Burgart LJ, Fidler JL, Ehman RL (2006) MR elastography of the liver: preliminary results. Radiology 240:440–448

Rubin MB, Bodner SR (2002) A three-dimensional nonlinear model for dissipative response of soft tissue. Int J Solids Struct 39:5081–5099

Samur E, Sedef M, Basdogan C, Avtan L, Duzgun O (2007) A robotic indenter for minimally invasive measurement and characterization of soft tissue response. Med Image Anal 11:361–373

Sandrin L, Fourquet B, Hasquenoph J, Yon S, Fournier C, Mal F, Christidis C, Ziol M, Poulet B, Kazemi F, Beaugrand M, Palau R (2003) Transient elastography: a new noninvasive method for assessment of hepatic fibrosis. Ultrasound Med Biol 29:1705–1713

Schwartz J, Denninger M, Rancourt D, Moisan C, Laurendeau D (2005) Modelling liver tissue using a visco-elastic model for surgery simulation. Med Image Anal 9:103–112

Tay BK, Kim J, Srinivasan MA (2006) In vivo mechanical behavior of intra-abdominal organs. IEEE Trans Biomed Eng 53:2129–2138

von Siebenthal M, Székely G, Lomax AJ, Cattin PC (2007) Systematic errors in respiratory gating due to intrafraction deformations of the liver. Med Phys 34:3620–3629

Zheng YP, Leung SF, Mak AFT (2000) Assessment of neck tissue fibrosis using an ultrasound palpation system: a feasibility study. Med Biol Eng Comput 38:497–502

Chapter 27
In Vivo Validation of Predictive Models for Bone Remodeling and Mechanobiology

Alina Levchuk and Ralph Müller

Abstract *In silico* modeling is a powerful tool for the prediction of bone remodeling and mechanobiology. As the method is gaining popularity a standardized measure for the *in vivo* validation of the quality of the produced simulations is required. In this review, we discuss current validity assessment approaches, as well as the validation 'gold standard', in which the experimental and computational parts are carried out concomitantly, and by the same research team. A novel validation framework for the tissue level model, based on the true geometry is introduced.

27.1 Introduction

Our understanding of bone remodeling and its governing mechanisms has come a long way since the first attempts to explain these complex processes (Roux, 1881; Wolff, 1892). In fact, it is now often left to the biologists to characterize the elaborate signaling processes in bone, while a new branch of computational biomechanics has emerged, with the focus on creating realistic models of these biological events. *In silico* modeling, supported by experimental investigations, is a powerful tool that allows translation of biological phenomena into mathematical laws, thus facilitating detailed analyses of distinct biological processes. The true value of *in silico* modeling is, however, in its predictive power, which, if close enough to the *in vivo* events can not only save large efforts in the experimental domain both resource and time wise, but also introduce treatment prediction options in clinics, thus improving therapeutic outcomes.

The transition from theoretical modeling to *in silico* simulations required a major improvement in the available computational capabilities. The advent of the finite element (FE) analysis in the second part of the 20th century has become such a breakthrough for the field of biomechanics. The first published investigation, which

A. Levchuk · R. Müller (✉)
ETH Zurich, Zurich, Switzerland
e-mail: ram@ethz.ch

A. Levchuk
e-mail: alevchuk@ethz.ch

G.A. Holzapfel, E. Kuhl (eds.), *Computer Models in Biomechanics*,
DOI 10.1007/978-94-007-5464-5_27,

incorporated the technique, was performed by Brekelmans et al. (1972). The popularity of the application grew exponentially ever since, many of the prominent publications of the first decade of its existence being reviewed in Huiskes and Chao (1983).

Micro-computed tomography (micro-CT), introduced several years later (Feldkamp et al., 1989), allowed not only three-dimensional (3D) visualization of bone architecture, but also a more reliable image-based validation method for the computational models. However, the first validation of an *in silico* model against the corresponding biological data was reported only in 1997, in a study that compared FE models of trabecular bone with contact radiographs both quantitatively and qualitatively (Silva and Gibson, 1997).

In the meantime, both computational and visualization advances have provided a framework for accurate simulations of bone remodeling and mechanobiology throughout the hierarchical levels of its complexity, while algorithm validation with experimental data collected within the same study was deemed 'gold standard' for model confirmation (Anderson et al., 2007). This review focuses on different approaches of *in vivo* validation across multiscale modeling of bone remodeling and mechanobiology from cell to tissue and on to the organ level.

27.2 Cell Level

Bone is a tissue subject to frequent remodeling due to various mechanically triggered remodeling processes as well as micro- and macro-fractures. The study of bone mechanobiology, thus, remains relevant throughout the lifetime of the organism. However, understanding and prediction of the cell mechanics is particularly significant for the multiscale applications, such as implant selection and fixation, and fracture healing (Van der Meulen and Huiskes, 2002). Nevertheless, even with the focus of research narrowed down to the single cell level, *in silico* studies range from the simulations of cellular interactions, to signaling pathway modeling, and all the way to the intracellular predictions of cytoskeletal reorganization.

The first validated model in mechanobiology described osteocyte excitation by mechanical stresses in mathematical terms (Weinbaum et al., 1994). The model was based on the experimental observations, and attempted to quantify mechanical stimuli sensed by osteocytes within the bone tissue. For validation purposes, the calculations were compared to experimentally measured results, reported by a collaborating group (Fritton et al., 2000).

Incorporation of the FE analysis into the mechanobiological models was initially an attempt to provide analytical perspectives on observed *in vivo* events; this trend later developed quantification and even prediction of the mechanical changes on the local level. Nevertheless, comparison with literature remained a preferred method of validation in the field (Carter et al., 1998; Knothe Tate and Niederer, 1998; Bonivtch et al., 2007).

In an effort to create more realistic and sophisticated *in silico* models researchers started incorporating true geometries obtained by various imaging methods (McGarry et al., 2005; Anderson and Knothe Tate, 2008). The study by Anderson and collaborators, for example, was based on high-resolution transmitted electron micrographs to analyze stresses imposed on osteocytes by fluid drag, while McGarry and colleagues incorporated previously reported images of cell spreading (Frisch and Thoumine, 2002) to assess the effect of fluid shear stress and strain on the mechanical response of bone cells using FE analysis. Nevertheless, while computational and experimental components of the investigations are rarely carried out within a single integrative study addressing the same research question using both *in silico* and *in vivo* modalities concomitantly, the possibility of direct validation remains slim.

A computational model for signaling pathways and interactions between osteoblast and osteoclasts has attempted to predict the effects of catabolic treatment with parathyroid hormone (PTH), as well as to simulate the interaction between receptor activator of nuclear factor-$\kappa\beta$, its ligand, and osteoprotegerin (RANK-RANKL-OPG pathway), which is essential for osteoclast formation (Lemaire et al., 2004). This complex *in silico* framework has reportedly been able to correctly predict cellular interaction, and the effects of the common metabolic diseases, such as estrogen deficiency, calcitriol deficiency, senescence and glucocorticoid excess. The results of the simulation find convincing evidence in the extensive comparison with literature; however no other direct validation has been undertaken. Other theoretical models with the focus on the prediction of molecular signaling pathways and mechanobiology have also been presented (Potter et al., 2005; Pivonka et al., 2008; Lio et al., 2011); unfortunately, despite the fact that all of them strive to predict bone adaptation on the micro scale, none of them have been verified against corresponding *in vivo* data, and thus are lacking confirmation of the level of fidelity.

The need for validation has also been emphasized for *in silico* models of cellular chemotaxis and cytoskeletal reorganization (Loosli et al., 2010; Landsberg et al., 2011). Both investigations compare results of the computational simulations with the *in vitro* experiments. In both reports sample geometries and boundary conditions for the models were derived directly from the experimental data. For example, the study by Landsberg and colleagues used a tetrahedral mesh for micro-CT reconstruction, as a starting point for the chemotaxis simulation, while Loosli and colleagues reconstructed the shapes of the adhesive islands from the *in vitro* study to computationally predict the adhesion sites of the cells (Fig. 27.1). Such complementary experimental and *in silico* studies tend to enable better understanding of the model limitations. For example, Landsberg and colleagues refer to a similar ongoing experimental study, utilizing signaling molecules, for further model validation. Loosli and colleagues, on the other hand, mention the algorithm's failure to predict adhesion formation at curved geometries, due to a missing model parameter, as one of the limitations, requiring further improvements.

The overall lack of adequate validation for the predictive value of microscale models in bone mechanobiology has also been noted by other authors (Jacobs and Kelly, 2011; Webster and Müller, 2011; Isaksson, 2012). A particular concern of validating models with *in vivo* data provided by collaborating investigators is that

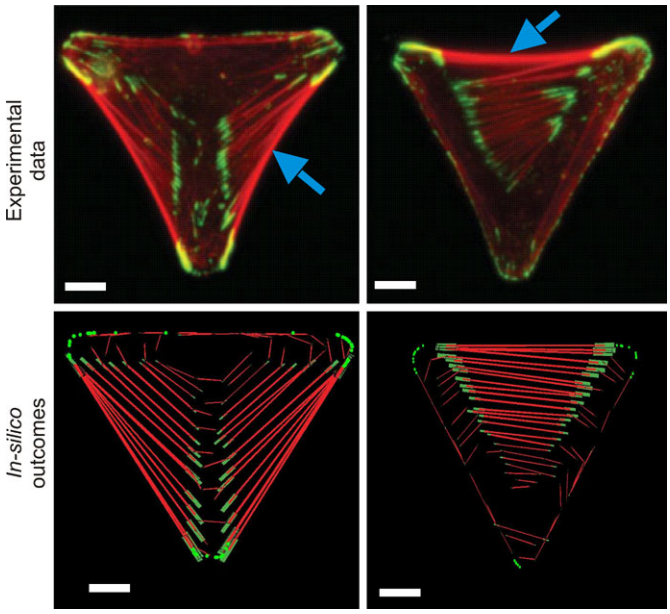

Fig. 27.1 Experimental (*top row*) and *in silico* (*bottom row*) results of controlled spreading on T- and V-shaped adhesive islands. Adapted with permission from Loosli et al. (2010)

important details of experimental setup, and measurements relevant for the confirmation of the computational results, might be omitted. This is often the case for boundary conditions and mechanical properties of the material, which generally hold true only for the exact conditions of the testing setup. Consequently, while numerous experimental reports can be found in literature, extrapolations or estimations of such data for validation purposes could be misleading and erroneous.

27.3 Tissue Level

It has long been shown that trabecular bone is more susceptible to the effects of osteoporosis than cortical bone (Leichter et al., 1987). Non-surprisingly, most predictive models for bone adaptation on the tissue level focus on this particular component of bone. While a large number of existing models have already been extensively reviewed (Gerhard et al., 2009; Webster and Müller, 2011), validation of those studies has never been comprehensively discussed. This section covers bone remodeling algorithms which have been validated in one way or another. Additionally, a new *in vivo* validation technique for a recently developed model of mechanically triggered trabecular remodeling is discussed.

The first algorithm based on true bone geometry comprised a phenomenological model for bone resorption and was performed on the high resolution quantitative

computed tomography (QCT) images (Müller and Rüegsegger, 1996). In the study, 3D FE models were paired with controlled Gaussian filtration to derive two models of moderate and pronounced bone atrophy. While the resulting apparent Young's moduli were the only mode of validation for this early attempt of *in silico* simulation of bone adaptation, the reported methods became the foundation for subsequent models. Thus, a follow-up study introduced further improvement to the application by using 3D micro CT scans as the input for the algorithm (Müller and Hayes, 1997). The isotropic resolution of the input images increased from 170 to 14 μm. In addition, the original simulated bone atrophy (SIBA) model was expanded to follow the mechanostat hypothesis (Frost, 1964), allowing controlled formation and resorption. This, in turn, facilitated simulation of various stages of bone loss, as well as a more realistic 'age-match'. For validation the results were compared to the experimental measurement of the post-menopausal group both qualitatively and quantitatively, and proved to be in good agreement. Finally, the model was applied to the 3D micro CT scans of human iliac crest and lumbar spine biopsies selected from the pre- and post-menopausal groups, in an attempt to simulate pre-, peri-, and post-menopausal bone states (Müller, 2005). In this study strong emphasis was placed on the validation of the results against biological data. Thus, visual comparison after the simulation of 43 years confirmed that the model produced realistic trabecular architecture when compared to the *in vivo* group, while quantitative bone morphometry, carried out for both groups produced a 100 % match for the bone volume density (BV/TV) parameter, and excellent agreement for the other parameters.

Another *in silico* simulation, based on true bone geometry and verified against *in vivo* biological data, employed a voxel-based surface adaptation under uniaxial compression (Adachi et al., 2001). In this algorithm, micro-CT measurements of canine cancellous bone were obtained from the previously published investigation (Goldstein et al., 1991), and the results of the simulation were compared to the corresponding animals at the end of the *in vivo* study (Guldberg et al., 1997). The validation was performed based on a comparison of the calculated morphometric indices for the *in silico* and *in vivo* experiments respectively. The results from the two approaches were in good agreement with values for bone volume fraction (BV/TV) being 0.230 and 0.222 for the experimental and simulated samples, respectively.

Several other notable studies, presenting elaborate models with realistic results, should be mentioned. For example, long-term investigation performed on the 3D micro-CT scans of human vertebra modeled the period of 50 years (Van der Linden et al., 2001). Morphometric indices, calculated for the resulting structures, correlated closely with the values reported in literature. Unfortunately, no validation against experimental data has been performed for this study. Another remarkable algorithm has been presented by Ruimerman et al. (2005a). The simulation was carried out on computer generated cubes of trabecular bone, and investigated the ability of bone to adapt in response to elevated strains. In addition to implementing the theory for metabolic expression under load (Huiskes et al., 2000), an extensive examination of osteocytic stimuli, such as maximal principal strain, volumetric strain, and strain energy density (SED) have been carried out as part of the study (Ruimerman et al., 2005b). While the model parameters themselves are largely based on the

values found in literature, the results of the simulations have not received any validity confirmation past the 'circumstantial evidence' validation, a term the authors used to summarize the similarity of the assumption-based prediction and biological reality.

A different algorithm for stochastic simulation of bone adaptation via the exchange of discrete bone packets and an accompanying novel approach for validation has recently been introduced (Hartmann et al., 2011). The study was subdivided into the investigation of the most effective signal integration for this *in silico* model, as well as validation of the results with quantitative backscattered electron imaging (qBEI) data. The model assumed that resorption takes place randomly on the bone surface, while deposition is mechanically controlled. The investigation of collective (summed), individual (maximal) and total (the sum of the previous two) signaling modalities indicated that using collective signal from the osteocyte network will introduce effective surface tension, which the authors argue plays a key role in bone morphogenesis and cell sorting. Validation of the simulation results against experimental qBEI data centered on correlating the values of quantified material heterogeneity. For this purpose, the age of bone packets (voxels) has been converted to represent corresponding mineral content (Ruffoni et al., 2007). When comparing simulated structures to the experimental images, bone mineralization density distribution (BMDD) exhibited similar trends, where older bone was enclosed under layers of younger bone. Notably, this validation method helped identify one of the limitations of the algorithm, as it did not comply with the proposed theory that older bone is more likely to be remodeled than younger bone (Taylor et al., 2007), and was capable of remodeling only bone surface voxels.

More recently, Schulte et al. (2011) introduced an algorithm to simulate bone thickening in response to cyclic mechanical loading using an open control loop. This *in silico* model is based on the assumption that a single remodeling signal submitted as an input for the simulation is sufficient to predict the long-term outcome of the remodeling process. Micro-CT scans of whole murine caudal vertebrae measured at the beginning of the *in vivo* study were used as the input for the simulation and the results computed from the time-lapsed *in vivo* images were compared to the simulated time points. This approach allowed not only comparison of the morphometric indexes and relative geometries *in vivo* and *in silico*, but also quantification and spatial distribution of the errors produced by the algorithm for each individual animal. The authors report a maximum error of 2.4 % for bone volume fraction and 5.4 % for other morphometric parameters. In addition, similarly to the previous study, the appropriate validation method helped detect one of the less obvious model limitations, namely that in the simulation remodeling occurred rather homogeneously in the surface layers, while a similar assessment of the *in vivo* data revealed localized areas of stronger deposition.

Finally, a similar approach has been extended for the validation of a newly developed algorithm for bone remodeling employing Frost's mechanostat theory and using SED values calculated after each remodeling iteration, in a closed feedback loop (Schulte, 2011). The growth velocity was calculated with a set of iteratively solved non-linear equations, and the mechanical thresholds for resorption, formation or homeostasis were selected interactively. The algorithm was applied for a

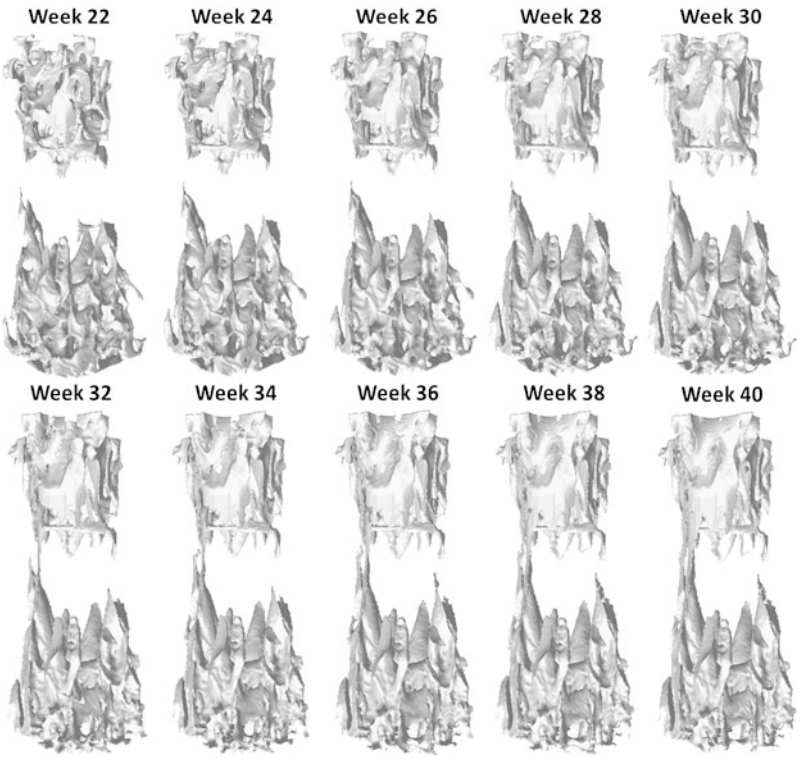

Fig. 27.2 Long-term simulation of the catabolic effect of PTH treatment combined with cyclic mechanical loading in a murine caudal vertebra

short-term prediction of the effects of hormone depletion due to ovariectomy, cyclic loading, and pharmaceutical treatments with anabolic (parathyroid hormone (PTH)), and anti-resorptive (bisphosphonate (BIS)) agents, as well as for the control studies for all groups. The model is also capable of long-term prediction (Fig. 27.2). The input micro-CT images of the murine caudal vertebra were obtained from a concomitant *in vivo* study. The results of both *in silico* and *in vivo* study have been assessed qualitatively as described elsewhere (Schulte, 2011). For the quantitative evaluation, both static and dynamic morphometric parameters were calculated, and comparative physiome maps were constructed for each parameter showing again strong agreement between experiment and simulation.

27.4 Organ Level

Due to their place in the hierarchy of bone modeling, organ-level simulations often treat bone as a continuum, disregarding local architecture, and biological events. Instead, such models focus on global stresses and strains, as well as on the interaction

of bone tissue with other materials. Thus, computational models on the organ level can be an invaluable tool for the pre-clinical studies of orthopedic implant performance and whole bone fracture healing. Since such investigations have the potential to go to clinics, thorough and well planned validation is mandatory in order to assess practicality and applicability of such *in silico* efforts.

The questions of importance of validation and its existing modalities have been comprehensively discussed by Huiskes (1997). In the same study, the author presented a three-tier approach to validation of the augmented femur model. According to the model, periprosthetic remodeling runs under the effects of stress shielding, and can be estimated according to the adaptive bone-remodeling theory. The levels in the proposed validation included quantitative validity of the results at large, the validity of the outcome in a specific population, which was verified again with results from a canine study (Sumner et al., 1992), and the validity of the prediction relative to a single specimen in the population, assessed with the human post-mortem retrieval study (Engh et al., 1992). Remarkably, the suggested model performed well on all levels, and was deemed clinically relevant. Another two studies that attempted to predict pre-operative implant fit and fill (Testi et al., 2004), as well as to analyze different mechanical signals (Schmitz et al., 2004) for the total hip arthroplasty application have been validated with a similar approach. The presented algorithms were first validated against the *in vitro* CT data for the surface assessment and distance map accuracy in the first study, and performance of the FE code in the second study. Following this validation step, both algorithms were tested *in vivo* on patient specific clinical data. Eventually, both models were declared clinically applicable, with only the cortical penetration parameter performing slightly lower than expected in the sensitivity test of the first investigation. The second study also demonstrated that SED and deviatoric strains were the best candidates for the *in silico* mechanical signal used in the remodeling algorithm.

In addition, as both the need for computational modeling, and validation of such models is getting increasing recognition among researchers, several groups have focused on generating and collecting potential validation data (Lengsfeld et al. 2002, 2005; Sangiorgio et al., 2011), where micro CT imaging was performed either pre-operatively, and/or in the follow up studies, with the hope of making this data useful for future *in silico* studies, needing validation.

Another common validation method for the organ level computer models is comparison with the *in vivo* performed dual-energy X-ray absorptiometry (DXA). Several studies reported successful use of bone mineral density (BMD) measurements obtained from the 2D DXA images to validate and improve their algorithms (Kerner et al., 1999; Coelho et al., 2009; Santos et al., 2010). Thus, Kerner and colleagues were able to demonstrate that the results of both *in silico* patient specific model and clinical results agree in that bone loss corresponds to the inverse of the pre-operative bone mineral content (BMC). This result suggests that the model can be used to improve current implant design, by taking into account predicted bone loss. An investigation by Coelho et al. (2009) proposes a hierarchical model on the organ and tissue levels, where each scale of complexity was represented by density based variables. The model correlated apparent density distribution with that measured

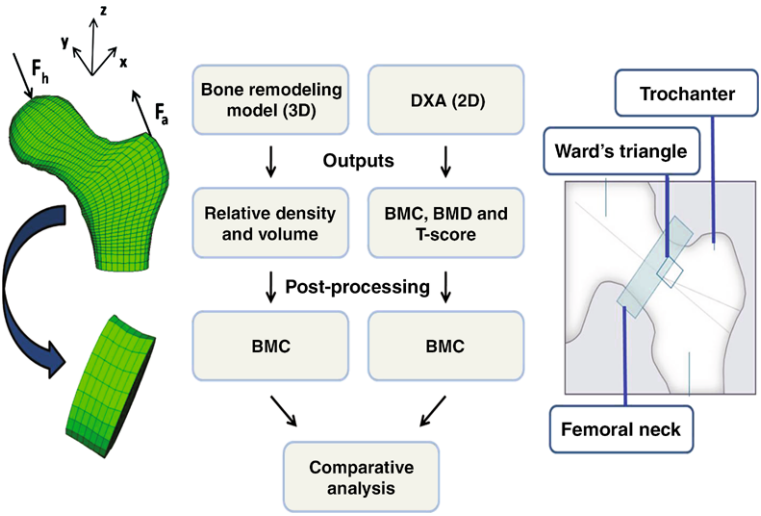

Fig. 27.3 Methodology framework for comparative analysis of the *in silico* and *in vivo* studies on the organ level. Reprinted with permission from Santos et al. (2010)

with clinical DXA, and found good agreements in both quantitative and qualitative results. The latest of the validated studies (Santos et al., 2010) was based on the patient-specific model for the prediction of BMD (Fig. 27.3). When quantitatively compared to the DXA derived results for the normal, osteopenic, and osteoporotic bone, the maximum discrepancy between the *in silico* and *in vivo* measurements was only 3.92 %. In addition, the authors report, that comparison with the clinical data has helped them improve the model by selecting the parameters that lead to the biologically relevant results.

Fracture healing is another area of interest that borders on the cellular and organ levels, in that it focuses on an event associated with the cellular level, such as sheer forces or angiogenic processes, but the algorithm is still based on a continuum assumption. One of the first computational models attempting to simulate tissue differentiation during fracture healing was based on the biphasic poroelastic FE algorithm that started at granulation and traced the process all the way to bone resorption (Lacroix and Prendergast, 2002). The model was validated against histomorphometric data from literature, with different fracture gap sizes. The validation confirmed that the proposed mechanobiological model produced realistic results for different gap sizes and loading magnitudes on the rate of reduction in interfragmentary strains. Isaksson and colleagues have performed a comparative review of the existing approaches, and determined that deviatoric strain is the most significant parameter for the modeling of tissue differentiation (Isaksson et al., 2006). Unfortunately, since fracture healing is an inflammatory time-dependent process that is difficult to monitor, this investigation relied only on previous reports for validation.

27.5 Conclusions

While *in silico* simulations are gaining popularity, and have even been referred to as the 'third method of science', following logic and experiment (Kelly, 1998), adequate validation is the only way to ascertain the level of fidelity, and thus, the advantage of such studies. It is generally accepted that the 'gold standard' method of validation is a complementary *in vivo* investigation, ideally carried out within the same research group. Both *in silico* and *in vivo* approaches should focus on the same research questions, and match boundary conditions, time scales, and other relevant parameters on the sample basis. Additionally, current imaging capabilities allow the use of the experiment data as direct input for the computational models, an improvement that should be taken advantage of for all suitable studies. Finally, it is important that both qualitative and quantitative modules of validation are comprehensively evaluated for the convincing evidence of the algorithm's capability to produce realistic results.

Acknowledgements The authors gratefully acknowledge funding from the European Union for the Osteoporotic Virtual Physiological Human project (VPHOP FP7-ICT2008-223865) and computational time from the Swiss National Supercomputing Center (CSCS, Manno, Switzerland).

References

Adachi T, Tsubota K, Tomita Y, Hollister SJ (2001) Trabecular surface remodeling simulation for cancellous bone using microstructural voxel finite element models. J Biomech Eng 123:403–409

Anderson AE, Ellis BJ, Weiss JA (2007) Verification, validation and sensitivity studies in computational biomechanics. Comput Methods Biomech Biomed Eng 10:171–184

Anderson EJ, Knothe Tate ML (2008) Idealization of pericellular fluid space geometry and dimension results in a profound underprediction of nano-microscale stresses imparted by fluid drag on osteocytes. J Biomech 41:1736–1746

Bonivtch AR, Bonewald LF, Nicolella DP (2007) Tissue strain amplification at the osteocyte lacuna: a microstructural finite element analysis. J Biomech 40:2199–2206

Brekelmans W, Slooff T, Poort H (1972) New method to analyze mechanical behavior of skeletal parts. Acta Orthop Scand 43:301–317

Carter DR, Beaupré GS, Giori NJ, Helms JA (1998) Mechanobiology of skeletal regeneration. Clin Orthop Relat Res S355:S41–S55

Coelho PG, Fernandes PR, Rodrigues HC, Cardoso JB, Guedes JM (2009) Numerical modeling of bone tissue adaptation—a hierarchical approach for bone apparent density and trabecular structure. J Biomech 42:830–837

Engh CA, Mcgovern TF, Bobyn JD, Harris WH (1992) A quantitative-evaluation of periprosthetic bone-remodeling after cementless total hip-arthroplasty. J Bone Jt Surg, Am Vol 74:1009–1020

Feldkamp LA, Goldstein SA, Parfitt AM, Jesion G, Kleerekoper M (1989) The direct examination of three-dimensional bone architecture *in vitro* by computed tomography. J Bone Miner Res 4:3–11

Frisch T, Thoumine O (2002) Predicting the kinetics of cell spreading. J Biomech 35:1137–1141

Fritton SP, McLeod KJ, Rubin CT (2000) Quantifying the strain history of bone: spatial uniformity and self-similarity of low-magnitude strains. J Biomech 33:317–325

Frost HM (1964) The laws of bone structure. Thomas, Springfield
Gerhard FA, Webster DJ, van Lenthe GH, Müller R (2009) The relative significance of trabecular and cortical bone-density as a diagnostic index for osteoporosis. Philos Trans R Soc A 367:2011–2030
Goldstein SA, Matthews LS, Kuhn JL, Hollister SJ (1991) Trabecular bone remodeling—an experimental model. J Biomech 24:135–150
Guldberg RE, Richards M, Caldwell NJ, Kuelske CL, Goldstein SA (1997) Trabecular bone adaptation to variations in porous-coated implant topology. J Biomech 30:147–153
Hartmann MA, Dunlop JW, Brechet YJ, Fratzl P, Weinkamer R (2011) Trabecular bone remodelling simulated by a stochastic exchange of discrete bone packets from the surface. J Mech Beh Biomed Mat 4:879–887
Huiskes R (1997) Validation of adaptive bone-remodeling simulation models. Stud Health Technol Inform 40:33–48
Huiskes R, Chao EYS (1983) A survey of finite element analysis in orthopedic biomechanics: the first decade. J Biomech 16:385–409
Huiskes R, Ruimerman R, van Lenthe GH, Janssen JD, (2000) Effects of mechanical forces on maintenance and adaptation of form in trabecular bone. Nature 405:704–706
Isaksson H (2012) Recent advances in mechanobiological modeling of bone regeneration. Mech Res Commun 42:22–31
Isaksson H, Wilson W, van Donkelaar CC, Huiskes R, Ito K (2006) Comparison of biophysical stimuli for mechano-regulation of tissue differentiation during fracture healing. J Biomech 39:1507–1516
Jacobs CR, Kelly DJ (2011) Cell mechanics: the role of simulation. In: Fernandes PR, Bártolo PJ (eds) Advances on modeling in tissue engineering. Computational methods in applied sciences, vol. 20, pp 1–14
Kelly K (1998) The third culture. Science 279:992–993
Kerner J, Huiskes R, van Lenthe GH, Weinans H, van Rietbergen B, Engh CA, Amis AA (1999) Correlation between pre-operative periprosthetic bone density and post-operative bone loss in THA can be explained by strain-adaptive remodelling. J Biomech 32:695–703
Knothe Tate ML, Niederer P (1998) A theoretical FE-based model developed to predict the relative contribution of convective and diffusive transport mechanisms for the maintenance of local equilibria within cortical bone. In: Clegg S (ed) Advances in heat and mass transfer in biotechnology. The American Society of Mechanical Engineers, New York, pp 133–142
Lacroix D, Prendergast PJ (2002) A mechano-regulation model for tissue differentiation during fracture healing: analysis of gap size and loading. J Biomech 35:1163–1171
Landsberg C, Stenger F, Deutsch A, Gelinsky M, Rosen-Wolff A, Voigt A (2011) Chemotaxis of mesenchymal stem cells within 3D biomimetic scaffolds—a modeling approach. J Biomech 44:359–364
Leichter I, Bivas A, Giveon A, Margulies JY, Weinreb A (1987) The relative significance of trabecular and cortical bone-density as a diagnostic index for osteoporosis. Phys Med Biol 32:1167–1174
Lemaire V, Tobin FL, Greller LD, Cho CR, Suva LJ (2004) Modeling the interactions between osteoblast and osteoclast activities in bone remodeling. J Theor Biol 229:293–309
Lengsfeld M, Gunther D, Pressel T, Leppek R, Schmitt J, Griss P (2002) Validation data for periprosthetic bone remodelling theories. J Biomech 35:1553–1564
Lengsfeld M, Burchard R, Gunther D, Pressel T, Schmitt J, Leppek R, Griss P (2005) Femoral strain changes after total hip arthroplasty–patient-specific finite element analyses 12 years after operation. Med Eng Phys 27:649–654
Lio P, Merelli E, Paoletti N, Viceconti M (2011) A combined process algebraic and stochastic approach to bone remodeling. Electron Notes Theor Comput Sci 277:41–52
Loosli Y, Luginbuehl R, Snedeker JG (2010) Cytoskeleton reorganization of spreading cells on micro-patterned islands: a functional model. Philos Trans R Soc, Math Phys Eng Sci 368:2629–2652

McGarry JG, Klein-Nulend J, Mullender MG, Prendergast PJ (2005) A comparison of strain and fluid shear stress in stimulating bone cell responses—a computational and experimental study. FASEB J 19:482–484

Müller R (2005) Long-term prediction of three-dimensional bone architecture in simulations of pre-, peri- and post-menopausal microstructural bone remodeling. Osteoporos Int 16:S25–S35

Müller R, Hayes WC (1997) Biomechanical competence of microstructural bone in the progress of adaptive bone remodeling. Proc SPIE 3149:69–81

Müller R, Rüegsegger P (1996) Analysis of mechanical properties of cancellous bone under conditions of simulated bone atrophy. J Biomech 29:1053–1060

Pivonka P, Zimak J, Smith DW, Gardiner BS, Dunstan CR, Sims NA, Martin TJ, Mundy GR (2008) Model structure and control of bone remodeling: a theoretical study. Bone 43:249–263

Potter LK, Greller LD, Cho CR, Nuttall ME, Stroup GB, Suva LJ, Tobin FL (2005) Response to continuous and pulsatile PTH dosing: a mathematical model for parathyroid hormone receptor kinetics. Bone 37:159–169

Roux W (1881) Der Kampf der Theile im Organismus. Ein Beitrag zur Vervollständigung der mechanischen Zweckmässigkeitslehre. Leipzig

Ruffoni D, Fratzl P, Roschger P, Klaushofer K, Weinkamer R (2007) The bone mineralization density distribution as a fingerprint of the mineralization process. Bone 40:1308–1319

Ruimerman R, Hilbers P, van Rietbergen B, Huiskes R (2005a). A theoretical framework for strain-related trabecular bone maintenance and adaptation. J Biomech 38:931–941

Ruimerman R, van Rietbergen B, Hilbers P, Huiskes R (2005b). The effects of trabecular-bone loading variables on the surface signaling potential for bone remodeling and adaptation. Ann Biomed Eng 33:71–78

Sangiorgio SN, Longjohn DB, Dorr LD, Ebramzadeh E (2011) Challenges in relating experimental hip implant fixation predictions to clinical observations. J Biomech 44:235–243

Santos L, Romeu JC, Canhao H, Fonseca JE, Fernandes PR (2010) A quantitative comparison of a bone remodeling model with dual-energy X-ray absorptiometry and analysis of the inter-individual biological variability of femoral neck T-score. J Biomech 43:3150–3155

Schmitz MJ, Clift SE, Taylor WR, Hertig D, Warner MD, Ploeg HL, Bereiter H (2004) Investigating the effect of remodelling signal type on the finite element based predictions of bone remodelling around the thrust plate prosthesis: a patient-specific comparison. Proc Inst Mech Eng, H J Eng Med 218, pp 417–424

Schulte FA (2011) *In silico* bone biology in a murine model of bone adaptation. Diss. ETH No. 19679, Zurich

Schulte FA, Lambers FM, Webster DJ, Kuhn G, Müller R (2011) *In vivo* validation of a computational bone adaptation model using open-loop control and time-lapsed micro-computed tomography. Bone 49:1166–1172

Silva MJ, Gibson LJ (1997) Modeling the mechanical behavior of vertebral trabecular bone: effects of age-related changes in microstructure. Bone 21:191–199

Sumner DR, Turner TM, Urban RM, Galante JO (1992) Remodeling and ingrowth of bone at two years in a canine cementless total hip-arthroplasty model. J Bone Jt Surg, Am Vol 74:239–250

Taylor D, Hazenberg JG, Lee TC (2007) Living with cracks: damage and repair in human bone. Nat Mater 6:263–268

Testi D, Cappello A, Sgallari F, Rumpf M, Viceconti M (2004) A new software for prediction of femoral neck fractures. Comput Methods Programs Biomed 75:141–145

Van der Linden JC, Verhaar JAN, Weinans H (2001) A three-dimensional simulation of age-related remodeling in trabecular bone. J Bone Miner Res 16:688–696

Van der Meulen MCH, Huiskes R (2002) Why mechanobiology? A survey article. J Biomech 35:401–414

Webster D, Müller R (2011) *In silico* models of bone remodeling from macro to nano-from organ to cell. Wires Syst Biol Med 3:241–251

Weinbaum S, Cowin SC, Zeng Y (1994) A model for the excitation of ostecytes by mechanical loading-induced bone fluid shear stresses. J Biomech 27:339–360

Wolff J (1892) Das Gesetz der Transformation der Knochen. Hirschwald, Berlin

Chapter 28
Bridging Scales in Respiratory Mechanics

Lena Yoshihara, Mahmoud Ismail, and Wolfgang A. Wall

Abstract In this paper, we review different types of overall lung models developed recently in our group. The first approach is based on three-dimensional (3D) continuum models of both the airways and the tissue. As only parts of the lung can be resolved in detail in the model, advanced multi-scale techniques are utilized to adequately consider the unresolved parts. Alternatively, we have proposed a comprehensive reduced-dimensional lung model allowing to effectively study pressure and flow characteristics in the entire conducting region of the lung, albeit at the cost of detailed information on local tissue stresses and strains. To combine the advantages of detailed and simplified lung models, we have developed a novel approach for the coupling of 3D and 0D airway models.

28.1 Introduction

Compared to other areas in biomechanics like the circulatory or the musculoskeletal system, surprisingly many open questions related to structural-functional correlations in the lung remain. Much of the uncertainty stems from the difficulties in documenting lung mechanics on the 'micro-level', given the small size of corresponding interior structures and the large movement of the lung during breathing. Therefore, a sound standing 'virtual lung model' can be a valuable tool for various applications ranging from the better understanding of lung diseases to progress on individual therapeutic approaches.

Our current main motivation for modeling the respiratory system is related to the treatment of patients suffering from the Acute Respiratory Distress Syndrome (ARDS). This severe diffuse lung disease is characterized by a number of symptoms such as reduced overall lung compliance, edema, severe hypoxemia, and general inflammation of the lung tissue. Although many therapeutic approaches have been developed, the mortality associated with ARDS remains relatively high (Tsushima

L. Yoshihara · M. Ismail · W.A. Wall (✉)
Institute for Computational Mechanics, Technische Universität München, Boltzmannstr. 15, 85747 Garching, Germany
e-mail: wall@lnm.mw.tum.de

G.A. Holzapfel, E. Kuhl (eds.), *Computer Models in Biomechanics*,
DOI 10.1007/978-94-007-5464-5_28,

et al., 2009). An indispensable tool in the treatment for ARDS is mechanical ventilation. However, heterogeneity of the ARDS lung predisposes patients towards a number of complications which are collectively termed ventilator associated lung injuries (VALI) and deemed one of the most important factors in the pathogenesis of ARDS (Ranieri et al., 1999). VALI mainly occurs in the walls of the small lung compartments constituting the blood-gas barrier. In these so-called alveoli, both primary mechanical and secondary inflammatory injuries occur (DiRocco et al., 2005). Primary injuries are consequences of alveolar overexpansion or frequent recruitment and derecruitment inducing high shear stresses. Since mechanical stimulation of cells can result in the release of proinflammatory mediators—a phenomenon commonly called mechanotransduction—secondary inflammatory injuries often directly follow, possibly starting a cascade of events leading to sepsis and multi-organ failure. Understanding the reason why the lungs still become damaged despite recent developments towards more 'protective' ventilation protocols (Amato et al., 1998) is a key question sought by the medical community.

Computational models of the respiratory system can provide essential insights into involved phenomena and open up new vistas towards improved patient-specific ventilation protocols. In particular, computational models offer the possibility to predict data that cannot be measured in vivo such as local alveolar strains and stresses which are relevant for the development and progress of VALI. However, establishing reasonable models is difficult since the lung comprises more than 20 generations of bifurcating airways ending in approximately 500 million alveoli. This complexity inhibits a direct numerical simulation resolving all levels of the respiratory system from the onset. Therefore, we currently pursue two distinct modeling strategies, which will be reviewed in the following. The first approach is based on three-dimensional (3D) continuum models of both the airways and the tissue. As only parts of the lung can be resolved in detail in the model, advanced multi-scale techniques are utilized to adequately consider the unresolved parts. After having discussed the 3D approach in Sect. 28.2, an alternative reduced-dimensional (0D) lung model will be presented in Sect. 28.3. This approach allows to effectively study pressure and flow characteristics in the entire conducting region of the lung, albeit at the cost of detailed information on local alveolar stresses and strains. In Sect. 28.4, the presented models will be briefly summarized and an outlook to future work will be provided.

28.2 3D Lung Model

To enable the quantification of local stresses and strains during ventilation, we have established a comprehensive 3D continuum model of the respiratory system. In the following, the basic building blocks and their combination to one overall lung model will be surveyed.

28.2.1 3D Model of Individual Alveoli

Since alveoli are the main site of VALI, a detailed knowledge of all involved phenomena on this 'micro-level' is crucial. Therefore, as a first step, we have developed a comprehensive computational model of individual alveoli. Alveolar tissue can be characterized as an irregular open foam consisting of mainly polyhedral structures with average dimensions ranging around 200 μm. Our computational model is based on both artificial (Wiechert et al., 2008) and imaging-based geometries (Rausch et al., 2011a).

For modeling of alveolar tissue behavior, a hyperelastic constitutive law introduced originally by Holzapfel et al. (2000) for arterial tissue has been adapted (Wiechert et al., 2009). The chosen isotropic strain-energy density function is composed of two main parts related to the major stress-bearing elements, i.e. the matrix material including elastin fibers and the collagen fiber network. To satisfy the quasi-incompressibility constraint typical of all soft biological tissues, the penalty function proposed by Balzani et al. (2006) has been implemented. Due to the lack of experimental data for individual alveolar walls, the material model has been fitted to available stress-strain curves of lung tissue sheets (Al Jamal et al., 2001).

Since alveolar walls are covered with a thin fluid film, the interaction of tissue and liquid lining mechanics has also been included in the computational model. However, instead of explicitly discretizing the fluid film, we have proposed a novel approach based on integrating the interfacial energy in the alveolar wall model (Wiechert et al., 2009). To model the complex behavior of the surface active agents in the liquid lining, the constitutive law of Otis et al. (1994) relating the local concentration of these substances to the surface stresses has been employed.

The simulation of small alveolar ensembles already becomes computationally very expensive. Hence, modeling all 500 million alveoli in the human lung is obviously not feasible. To overcome this problem, we have established an advanced multi-scale model of lung tissue which will be discussed in the following section.

28.2.2 3D Multi-scale Model of Lung Tissue

Although neighboring lung regions influence each other strongly—a phenomenon known as interdependence (Mead et al., 1970)—this effect has been completely neglected in previous alveolar models (Kowe et al., 1986; Gefen et al., 2001; Denny and Schroter, 2006). Due to the lack of physiologically reasonable boundary conditions for alveolar models, clinically relevant predictions of local stresses and strains during mechanical ventilation were not feasible up to now. Therefore, instead of restricting analyses to isolated alveolar domains, it seems reasonable to model lung parenchyma—i.e., lung tissue at a global scale—as a whole. In this case, suitable boundary conditions can be easily derived, e.g., from 4D CT imaging. Since the alveolar micro-structure cannot be resolved everywhere, we have proposed to employ two complementary approaches. The bulk of lung parenchyma is

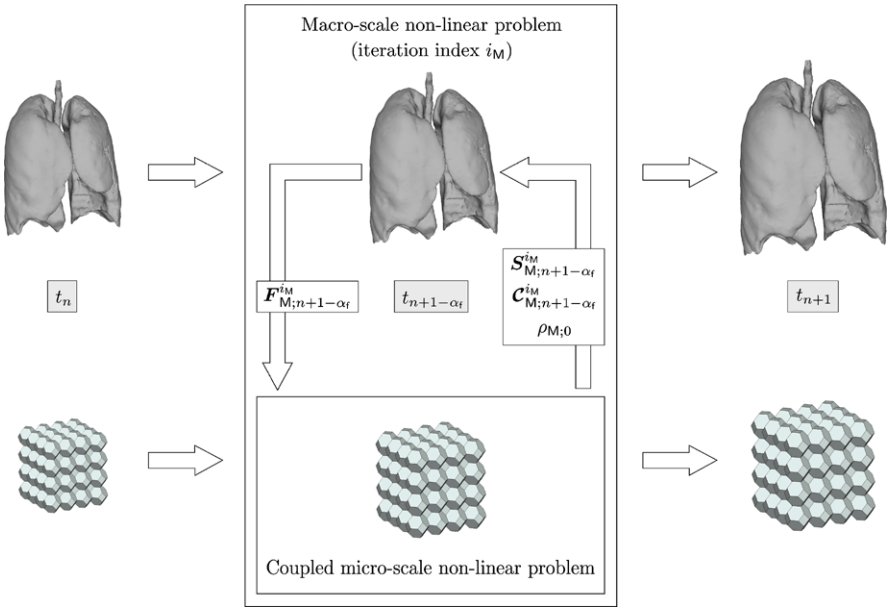

Fig. 28.1 Schematic overview on nested dynamic multi-scale method for a given time step. The deformation of the RVE boundary is prescribed according to the macroscopic deformation gradient. After having solved the RVE problem, the macroscopic density, stress, and constitutive tensor are determined by volume averaging. Nonlinearities on both scales are taken into account. For time discretization of the dynamic macro-scale problem, the generalized alpha scheme is utilized

modeled using a homogenized, phenomenological constitutive law fitted to experiments (Rausch et al., 2011b). At certain hotspots in our model, however, we want to zoom in on the alveolar micro-structure in order to quantify local stresses and strains relevant for VALI. To bridge the gap between the global parenchyma and the local alveolar level, we have developed a novel computational multi-scale approach based on the nested solution of the boundary value problems on both levels. The benefit of this so-called FE^2 strategy is twofold; firstly, improved global properties are derived due to the detailed modeling of the underlying complex micro-structure. Secondly, the global parenchyma model serves as an 'embedding' of the locally resolved micro-structure, thereby providing physiologically reasonable boundary conditions for alveolar simulations.

Our approach extends existing methods (Feyel and Chaboche, 2000; Kouznetsova et al., 2001; Miehe, 2003; Geers et al., 2010; Peric et al., 2010) to coupled and dynamic scenarios inherent to (mechanical) ventilation. To account for the transient effects, we have proposed to couple a dynamic simulation on the global level with a quasi-static simulation of the discretized alveolar level (Wiechert and Wall, 2010). This procedure enables us to investigate the time-dependent behavior of lung parenchyma as a whole and local alveolar ensembles simultaneously without necessitating to resolve the alveolar micro-structure completely. Instead, representative volume elements (RVEs) of the underlying alveolar microstructure including inter-

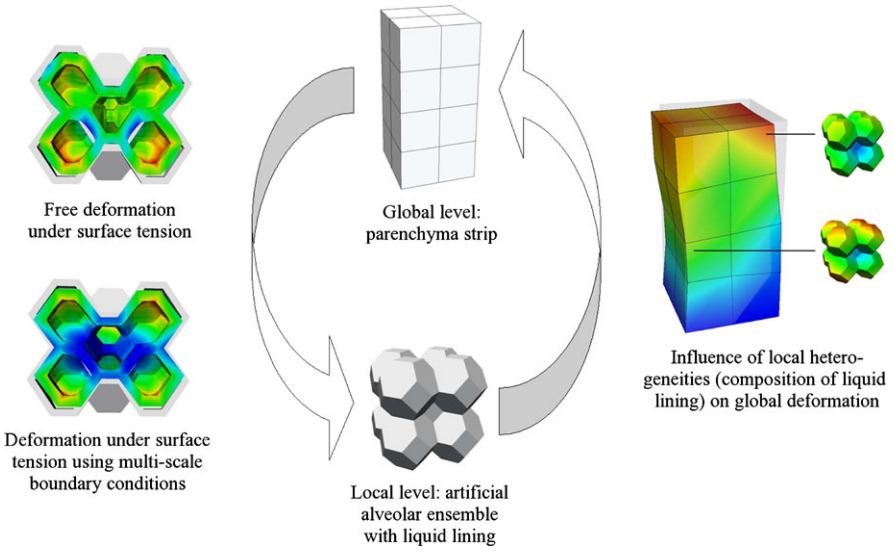

Fig. 28.2 Simple numerical example illustrating the mutual coupling of parenchyma and alveolar levels in the multi-scale model. *Right*: heterogeneous deformation of simplified lung parenchyma strip due to locally different alveolar liquid lining compositions. *Left*: deformation states for alveolar assemblages under surface tension load using traction-free (*top*) and multi-scale boundary conditions (*bottom*)

facial effects are defined and associated with selected macro-scale Gauss integration points. For the macro-micro scale transition, currently displacement boundary conditions are utilized. Since the boundary deformation of each RVE is prescribed according to the associated macro-scale deformation state, RVEs of neighboring Gauss points influence each other indirectly via the macro-level. Hence, the important interdependence effect is inherently considered in our model. After solution of the local, constrained micro-problem, computational homogenization procedures are employed to determine volume-averaged densities, stresses, and constitutive tensors for the macroscopic simulation. A schematic representation of the dynamic multi-scale method is shown in Fig. 28.1.

Since global parenchyma and local alveolar models are simulated simultaneously, a mutual information transfer is enabled. The right hand side of Fig. 28.2 shows exemplarily the overall heterogeneous deformation of an idealized lung parenchyma strip due to locally different compositions of the alveolar liquid lining. A diseased state was modeled by assuming a deficiency of surface active agents, i.e. a purely aqueous liquid lining, in some of the associated alveolar micro-structures. This phenomenon is known to occur in case of lung failure. On the left hand side of Fig. 28.2, the effect of the multi-scale boundary conditions on local alveolar deformations is illustrated. For comparison, the behavior of an alveolar ensemble with traction-free boundary conditions was simulated. This type of boundary condition has been standardly employed in alveolar simulations so far. For a given surface tension load on the interior surfaces, considerable differences in the resulting defor-

mation states can be observed. Although imposed multi-scale boundary conditions are still very simple, alveolar deformation can be simulated more realistically than in the comparative simulation neglecting the influence of the surrounding tissue completely.

28.2.3 Coupling of 3D Parenchyma and Airway Models

Although VALI is known to occur primarily in the alveolar region, the conducting part of the lung also has to be included in the model. After all, local parenchyma deformations are determined by the distribution of airflow into the peripheral domains. Hence, we have been recently focusing on completing our 'bridging of scales' by combining our multi-scale parenchyma model with 3D airway models (cf., e.g., Wall and Rabczuk, 2008; Comerford et al., 2010). Again, due to limited computational resources and the insufficient resolution of CT imaging techniques (minimum voxel size of $0.5 \times 0.5 \times 0.5$ mm), a detailed modeling of all relevant airway structures from the trachea—where the endotracheal tube is situated during mechanical ventilation—down to the alveoli is not possible. Therefore, airway models are usually restricted to the first generations of the tracheo-bronchial tree.

To compensate for the gap between resolvable airways and the alveolar region, we have proposed a general concept for the homogenization of unresolvable structures (Yoshihara and Wall, 2012). Briefly, our approach considers two different types of interactions of airway and tissue models. Firstly, lung parenchyma surrounds the main part of the airway tree, thereby affecting airflow and inducing an interdependence of neighboring airways not present in the isolated airway tree. This effect can be considered by means of fluid-structure interaction (FSI) procedures (see, e.g., Gee et al., 2010; Küttler et al., 2010). Secondly, the parenchyma is inflated by the air transported in the conducting part. To consider this coupling, we divide the parenchyma model into subdomains associated with the outlets of the resolved three-dimensional airway tree. Each subdomain can be thought of as a homogenized continuum consisting of smaller airways and alveoli that is provided with air by the associated 3D airway. Hence, the volume of air passing through each outlet has to equal the change in volume of the corresponding tissue subdomain. To enforce this constraint within the framework of FSI problems, we utilize a Lagrange multiplier technique. For the parallel and iterative solution of the resulting linear systems, a specific preconditioning algorithm has been introduced.

The simple numerical example shown in Fig. 28.3 illustrates the novel volume-coupled FSI approach. A cuboidal parenchyma model is split into two parts consistent with the two outlets of the embedded deformable cylindrical airways. If both parenchyma blocks exhibit the same material properties, a perfectly symmetric distribution of parenchyma deformations and airflow develops for a prescribed inflow. However, if the Young's modulus of the left block is doubled, most of the inflowing air is transported into the softer right parenchyma block resulting in a heterogeneous deformation state. In combination with the multi-scale approach of lung

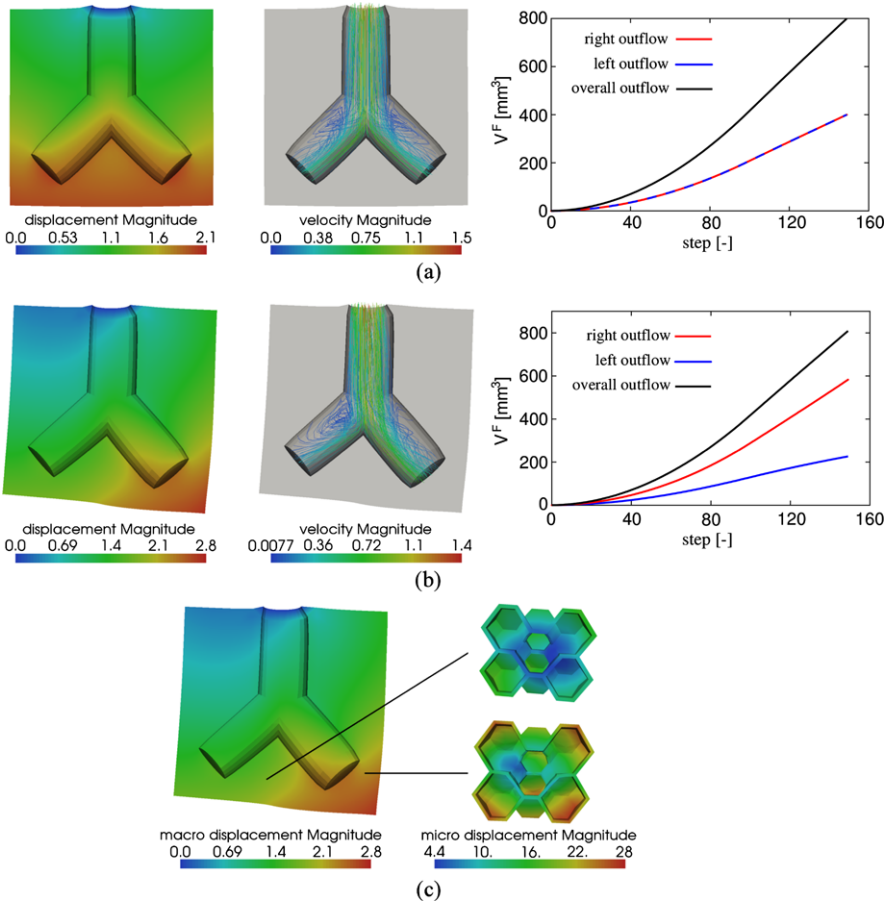

Fig. 28.3 Deformation of parenchyma model and distribution of airflow velocities for a given prescribed inflow. Diagrams on the *right* visualize how air volumes split between the two outlets. (**a**) Tissue parameters are homogeneous throughout the parenchyma model. (**b**) Young's modulus of the *left half* of the parenchyma model is twice as large as the one of the *right half*. (**c**) Combination of volume-coupling and multi-scale approach enabling the determination of local alveolar stresses and strains depending on the airflow in the associated airways

parenchyma, the developed models allow to simulate airflow in the airways and coupled local alveolar deformation realistically for the first time.

Currently, we are working on simulating coupled airflow and parenchyma deformation using CT-based instead of simplified geometries. In this case, however, the number of subdivisions of the parenchyma model is limited since only few airway generations can be resolved. To overcome this problem and enable more realistic predictions of the distribution of gases and local deformations, we have recently proposed an efficient reduced-dimensional model of the conducting region which will be reviewed in the following section.

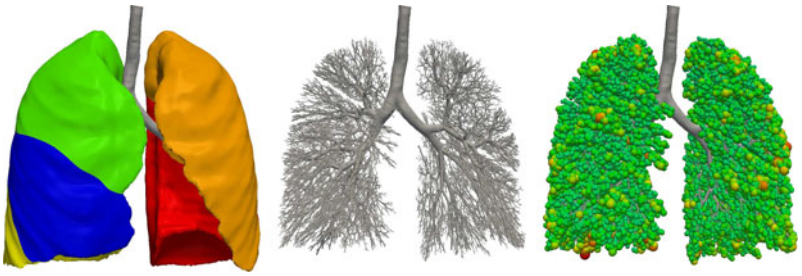

Fig. 28.4 Generation of 0D lung models. (**a**) Lobes segmented from CT images. (**b**) Space-filling airway tree generated within the lobes. (**c**) Acini generated within the lobes

28.3 Reduced-Dimensional Lung Model

An effective alternative to 3D lung models are reduced-dimensional models such as 1D, 0D, and impedance models. Corresponding approaches are generally based on electrical analogies, where flow resistance, fluid inertia, and tissue compliance are represented by resistors, inductors, and capacitors, respectively. Reduced-dimensional models were shown to well capture the averaged physiological and physical behavior of lung mechanics (Pedley et al., 1970; Horsfield et al., 1971; Lambert et al., 1982; Bates, 2009; Comerford et al., 2010; Ismail et al., 2012a). To enable the spatial representation of flow in the lung, our reduced-dimensional model is based on patient-specific CT images and morphological information for the unresolvable generations (cf. Fig. 28.4). We utilize a methodology similar to the one presented by Tawhai et al. (2000) to generate a space-filling tree of 0D airways. With each terminal airway, the volume of a so-called acinus representing a cluster of alveolar ducts is associated. In the following, the building blocks of our reduced-dimensional lung model will be briefly reviewed.

28.3.1 Tree of 0D Airways

Following Pedley et al. (1970) and van Ertbruggen et al. (2005), we model the airway tree as a combination of pipes with nonlinear resistances. Pre-integration in radial as well as longitudinal direction leads to a 0D model of the individual segments which are then combined to an overall model. To validate our approach, we compared the results obtained in fully 0D and coupled 3D–0D simulations (Ismail et al., 2012a). To create the 3D–0D model, we coupled a 3D airway model segmented from CT scans with a space-filling tree of 0D airways for the lower generations (cf. also Sect. 28.3.3). The results shown in Fig. 28.5 demonstrate that the 0D model can indeed mimic the space-averaged 3D results.

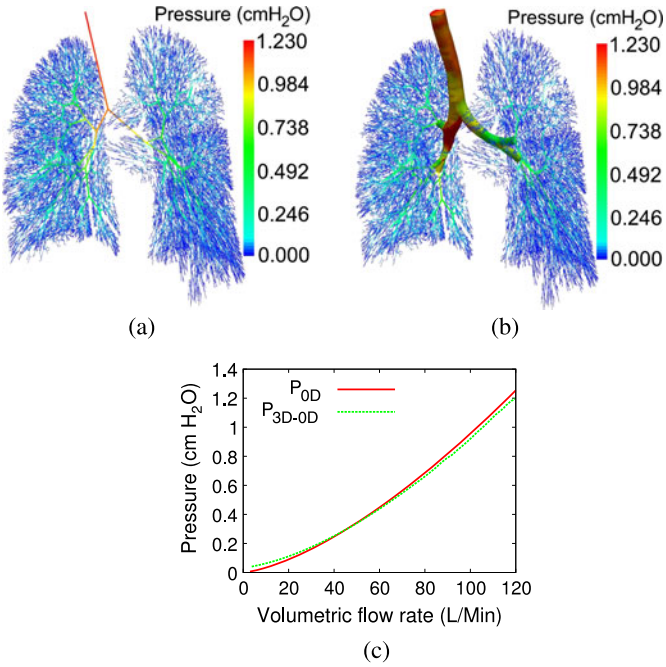

Fig. 28.5 Pressure distribution obtained in (**a**) a fully 0D simulation and (**b**) a coupled 3D–0D simulation. In both cases, the trachea flowrate was 120 l/min. The pressure at the terminal airways was taken to be zero. (**c**) Total bronchial pressure drop of models (**a**) and (**b**) at different inlet flowrates

28.3.2 0D Model of Acini

To account for the influence of alveolar dynamics, we have proposed to introduce simplified acinar models at all ends of the airway tree (Ismail et al., 2012a). Each acinus is constructed from a tree of several alveolar ducts which are approximated by Maxwell models (see Fig. 28.6). Corresponding parameters have been determined by calibrating the Maxwell model with 3D simulation results from the literature.

28.3.3 3D–0D Coupling

If detailed flow patterns in the larger airways are of interest, it seems reasonable to utilize a combination of 3D and 0D airway models. Recently, we have developed a novel coupling algorithm of 3D and reduced-dimensional models (Ismail et al., 2012b) based on the Neumann inflow boundary condition presented by Gravemeier et al. (2012). This approach was shown to reproduce correct pressure levels and resolve potential instabilities on inflow boundaries. Briefly, we first evaluate the pressure on the 0D boundary using the flowrate of the 3D boundary. Subsequently,

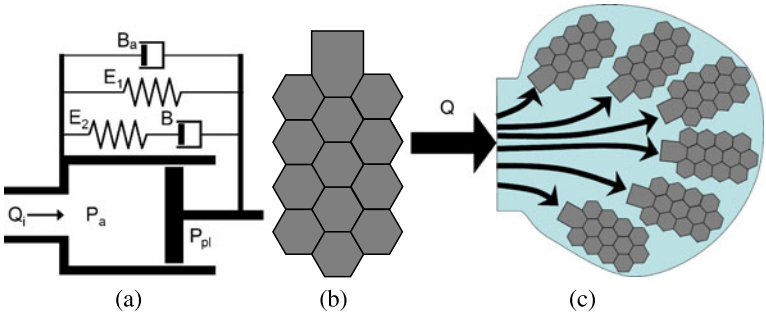

Fig. 28.6 (**a**) Maxwell model for a single alveolar duct. (**b**) 3D alveolar duct model of Denny and Schroter (2000) utilized to calibrate the 0D model. (**c**) Construction of an acinus from a tree of alveolar ducts

both 0D pressure and 3D flowrate are utilized to evaluate the total traction, which is then applied as a Neumann boundary condition to the 3D boundary. In Fig. 28.7, selected simulation results are provided for an overall lung model containing nine 3D airways, 55,000 0D airways, and 28,000 0D acini. The validity of our coupling approach is illustrated by the perfect matching of pressure curves at associated 3D and 0D boundaries. The simulated tracheal flowrate is in excellent agreement with reported physiological flowrates.

28.4 Conclusion and Outlook

In this paper, we have reviewed different types of overall lung models developed recently in our group. If detailed information about local flow patterns or tissue stresses and strains are of interest, utilization of 3D models is indispensable. As a first step, we have established a comprehensive 3D model of individual alveoli considering not only tissue behavior but also the influence of the covering surfactant film. Since it is impossible to resolve all 500 million alveoli in the human lung, we have proposed an advanced multi-scale methodology enabling the simulation of tissue dynamics at a global level while still resolving alveolar scales locally. To complete the 'bridging of scales', a novel approach for the coupling of 3D parenchyma and airway models into one overall lung model has been developed. The number of resolvable 3D airways is, however, limited.

Therefore, we have proposed an alternative reduced-dimensional lung model allowing to effectively study pressure and flow characteristics in the entire conducting region of the lung. For this purpose, a space-filling artificial airway tree with attached acini is generated using patient-specific morphological information. Each airway is modeled as a pipe with nonlinear resistance. The 0D acinus model is based on a combination of Maxwell models fitted to 3D simulation results from the literature. The resulting reduced-dimensional lung model was shown to reproduce global physiological data in a very efficient manner.

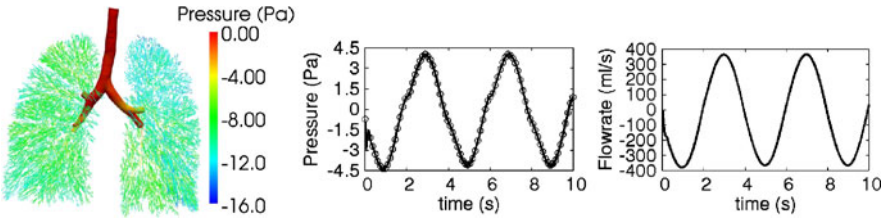

(a) (b) (c)

Fig. 28.7 3D–0D simulation results for spontaneous breathing. (**a**) Bronchial pressure distribution at maximum inspiration. (**b**) Pressure curve at the 3D boundary (*line*) and at the 0D boundary (*circles*) in the right bottom lobe. (**c**) Simulated flowrate at the inlet of the trachea

Recently, we have also developed a novel approach for the coupling of 3D and 0D airway models. Hence, we can resolve in detail local flow patterns in larger airways, whereas a reduced-dimensional model is utilized to approximate the distribution of pressure and flow in the peripheral region.

To determine tissue stresses and strains relevant to VALI, though, a 3D model of the alveolar region is essential. Therefore, future work will be concerned with a novel 3D–0D–3D coupling based on a modification of our volume coupling approach. This way, we can combine the advantages of 3D and 0D airways and enable a reasonable investigation of alveolar mechanics during (mechanical) ventilation for the first time. In order to validate our computational models, we plan to correlate simulation results with medical data obtained from, e.g., positron emission tomography (PET) or electrical impedance tomography (EIT). Although developed against the background of VALI, our approaches are by no means restricted to this particular application. Hence, we believe that our models can promote further understanding of the lung under healthy and diseased conditions. Thus, they will be valuable for answering a number of questions brought up by the medical and biological community.

Acknowledgements Support by the German Science Foundation/Deutsche Forschungsgemeinschaft (DFG) through projects WA1521/6-2, WA1521/9-2, and WA1521/9-2 within the priority program 'Protective Artificial Respiration' (PAR) is gratefully acknowledged.

References

Al Jamal R, Roughley PJ, Ludwig MS (2001) Effect of glycosaminoglycan degradation on lung tissue viscoelasticity. Am J Physiol, Lung Cell Mol Physiol 280:L306–L315

Amato MBP, Barbas CSV, Medeiros DM, Magaldi RB, Schettino GPP, Lorenzi-Filho G, Kairalla RA, Deheinzelin D, Munoz C, Oliveira R, Takagaki TY, Carvalho CRR (1998) Effect of a protective-ventilation strategy on mortality in the acute respiratory distress syndrome. N Engl J Med 338:347–354

Balzani D, Neff P, Schröder J, Holzapfel GA (2006) A polyconvex framework for soft biological tissues. Adjustment to experimental data. Int J Solids Struct 43:6052–6070

Bates J (2009) Lung mechanics: an inverse modeling approach. Cambridge University Press, Cambridge

Comerford A, Förster C, Wall WA (2010) Structured tree impedance outflow boundary conditions for 3D lung simulations. J Biomech Eng 132:081002

Denny E, Schroter RC (2000) Viscoelastic behavior of a lung alveolar duct model. J Biomech Eng 112:143–151

Denny E, Schroter RC (2006) A model of non-uniform lung parenchyma distortion. J Biomech 39:652–663

DiRocco JD, Carney DE, Nieman GF (2005) The mechanism of ventilator-induced lung injury: role of dynamic alveolar mechanics. In: Yearbook of intensive care and emergency medicine 2005, vol 2005, pp 80–92, Part 2

Feyel F, Chaboche J-L (2000) FE^2 multiscale approach for modelling the elastoviscoplastic behaviour of long fibre SiC/Ti composite materials. Comput Methods Appl Mech Eng 183:309–330

Gee MW, Küttler U, Wall WA (2010) Truly monolithic algebraic multigrid for fluid-structure interaction. Int J Numer Methods Eng 85:987–1016

Geers MGD, Kouznetsova V, Brekelmans WAM (2010) Multi-scale computational homogenization: trends & challenges. J Comput Appl Math 234:2175–2182

Gefen A, Halpern P, Shiner RJ, Schroter RC, Elad D (2001) Analysis of mechanical stresses within the alveolar septa leading to pulmonary edema. Technol Health Care 9:257–267

Gravemeier V, Yoshihara L, Comerford A, Ismail M, Wall WA (2012) Neumann inflow boundary conditions in biomechanics. Int J Numer Methods Biomed Eng 28:560–573

Holzapfel GA, Gasser TC, Ogden RW (2000) A new constitutive framework for arterial wall mechanics and a comparative study of material models. J Elast 61:1–48

Horsfield K, Dart G, Olson D, Filley G, Cumming G (1971) Models of the human bronchial tree. J Appl Physiol 31:207–217

Ismail M, Comerford A, Wall W (2012a) Coupled and reduced dimensional modeling of respiratory mechanics during spontaneous breathing. Int J Numer Methods Biomed Eng (submitted)

Ismail M, Gravemeier V, Comerford A, Wall W (2012b) A computational approach for simulating coupled 3D–0D biofluid networks using Neumann inflow boundary conditions (in preparation)

Kouznetsova V, Brekelmans WAM, Baaijens FPT (2001) An approach to micro-macro modeling of heterogeneous materials. Comput Mech 27:37–48

Kowe R, Schroter RC, Matthews FL, Hitchings D (1986) Analysis of elastic and surface tension effects in the lung alveolus using finite element methods. J Biomech 19:541–549

Küttler U, Gee MW, Förster C, Comerford A, Wall WA (2010) Coupling strategies for biomedical fluid-structure interaction problems. Int J Numer Methods Biomed Eng 26:305–321

Lambert RK, Wilson TA, Hyatt RE, Rodarte JR (1982) A computational model for expiratory flow. Respir Physiol 52:44–56

Mead J, Takishima T, Leith D (1970) Stress distribution in lungs: a model of pulmonary elasticity. J Appl Physiol 28:596–608

Miehe C (2003) Computational micro-to-macro transitions for discretized microstructures of heterogeneous materials at finite strains based on the minimization of averaged incremental energy. Comput Methods Appl Mech Eng 192:559–591

Otis DR, Ingenito EP, Kamm RD, Johnson M (1994) Dynamic surface tension of surfactant TA: experiments and theory. J Appl Physiol 77:2681–2688

Pedley TJ, Schroter RC, Sudlow MF (1970) The prediction of pressure drop and variation of resistance within the human bronchial airways. Respir Physiol 9:387–405

Peric D, de Souza Neto EA, Feijoo RA, Partovi M, Molina AJC (2010) On micro-to-macro transitions for multi-scale analysis of non-linear heterogeneous materials: unified variational basis and finite element implementation. Int J Numer Methods Eng 87:149–170

Ranieri VM, Suter PM, Tortorella C, De Tullio R, Dayer JM, Brienza A, Bruno F, Slutsky AS (1999) Effect of mechanical ventilation on inflammatory mediators in patients with acute respiratory distress syndrome: a randomized controlled trial. J Am Med Assoc 282:54–61

Rausch S, Haberthuer D, Stampanoni M, Schittny JC, Wall WA (2011a) Local strain distribution in real three-dimensional alveolar geometries. Ann Biomed Eng 39:2835–2843

Rausch S, Martin C, Bornemann PB, Uhlig S, Wall WA (2011b) Material model of lung parenchyma based on living precision-cut lung slice testing. J Mech Beh Biomed Mat 4:583–592

Tawhai MH, Pullan AH, Hunter PJ (2000) Generation of an anatomically based three-dimensional model of the conducting airways. Ann Biomed Eng 28:793–802

Tsushima K, King LS, Aggarwal NR, De Gorordo A, D'Alessio FR, Kubo K (2009) Acute lung injury review. Int Med 48:621–630

van Ertbruggen C, Hirsch C, Paiva M (2005) Anatomically based three-dimensional model of airways to simulate flow and particle transport using computational fluid dynamics. J Appl Physiol 98:970–980

Wall WA, Rabczuk T (2008) Fluid-structure interaction in lower airways of CT-based lung geometries. Int J Numer Methods Fluids 57:653–675

Wiechert L, Wall WA (2010) A nested dynamic multi-scale approach for 3D problems accounting for micro-scale multi-physics. Comput Methods Appl Mech Eng 199:1342–1351

Wiechert L, Rabczuk T, Comerford A, Metzke R, Wall WA (2008) Towards stresses and strains in the respiratory system. ESAIM Proc 23:98–113

Wiechert L, Metzke R, Wall WA (2009) Modeling the mechanical behavior of lung tissue at the microlevel. J Eng Mech 135:434–438

Yoshihara L, Wall WA (2012) Fluid-structure interaction including volume coupling of homogenized subdomains for treating artificial boundaries (in preparation)

Index

G.A. Holzapfel, E. Kuhl (eds.), *Computer Models in Biomechanics*,
DOI 10.1007/978-94-007-5464-5,